NASA Conference Publication 3300

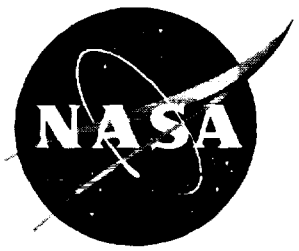

ICASE/LaRC Workshop on Benchmark Problems in Computational Aeroacoustics (CAA)

Edited by
J. C. Hardin
Langley Research Center • Hampton, Virginia

J. R. Ristorcelli
Institute for Computer Applications in Science and Engineering • Hampton, Virginia

C. K. W. Tam
Florida State University • Tallahassee, Florida

Proceedings of a workshop sponsored by the National Aeronautics and Space Administration, Washington, D.C., and the Institute for Computer Applications in Science and Engineering (ICASE), Hampton, Virginia and held in Hampton, Virginia October 24–26, 1994

National Aeronautics and Space Administration
Langley Research Center • Hampton, Virginia 23681-0001

May 1995

Cover Photo:

Contours of acoustic pressure from the numerical simulation of a flat plate in a Mach 0.5 gust (figure 1 from "Aeroacoustic Computation of a Gust-Plate Interaction via MacCormack Schemes," by James E. Martin).

This publication is available from the following sources:

NASA Center for AeroSpace Information
800 Elkridge Landing Road
Linthicum Heights, MD 21090-2934
(301) 621-0390

National Technical Information Service (NTIS)
5285 Port Royal Road
Springfield, VA 22161-2171
(703) 487-4650

PREFACE

This volume contains the proceedings of the ICASE/LaRC Workshop on Benchmark Problems in Computational Aeroacoustics (CAA). CAA is a relatively new area of research addressing issues relevant to the acoustic propagation of sound generated by fluid flow. Advances in computer technology make addressing these issues in a more detailed manner a possibility. Such advances allow the treatment of the fully nonlinear propagation problem as well as the direct computation of the acoustic sources, the sound generation problem. These possibilities are expected to benefit both the validation of models that have been developed as well as help develop better models for more complex flows. In situations where calculations are not prohibitively expensive a direct computation of the acoustic and source fields becomes possible.

When research in this area was first considered several technical challenges were apparent. The intention of these proceedings is to more fully investigate a subset of these numerical issues and make some progress in their resolution. These issues include:

1. The small magnitude of the acoustical quantities of interest and the need to distinguish and extract them from the larger background fields.

2. The sensitive dependence of the acoustical field on phase, dissipation and dispersion when propagated over large spatial distances.

3. The potentially higher frequencies of the quantities of interest in comparison to those of interest in the problems more typically addressed in unsteady aerodynamics or structural vibrations.

4. For the computation of acoustical spectra long time solutions are necessary for computing averages; numerical codes are required to be stable and accurate for long time integrations.

5. Many codes are designed for stationary problems in which the path of approach to the asymptotic solution is not important (except from the viewpoint of cost). These schemes are potentially inadequate for aeroacoustical problems in which time accurate computations are required. The dissipation, dispersion, and anisotropic biases in these schemes are now very relevant to the aeroacoustical problems of interest.

6. Time dependent boundary conditions are also required which will not reflect acoustic waves from imposed computational boundaries yet reflect acoustic waves properly from real physical boundaries.

7. As many flows of interest occur at high Mach number nonlinear effects on the sound propagation problem are to be anticipated. This is in addition to the nonlinear effects of the sound generation problem and its additional complexity in higher Mach number situations.

8. The wide range of spatial and temporal scales that require resolution when both the sound generation and propagation problem are simultaneously considered.

The benchmark problems addressed in this Workshop were chosen with some of these issues in mind. The primary focus has been on numerical accuracy - dissipation, dispersion - and on boundary condition issues. There are, in addition, problems on the nonlinear propagation and on the sound propagation in a non-uniform prescribed mean flow. While no problems addressing the sound generation problem are posed, there is a sample problem in which the acoustical field, due to a prescribed fluctuating velocity field, is required. In general, the problems chosen are simple requiring little computational effort; it is for that reason computational effort has not been used as a criteria in assessing the different schemes.

Jay C. Hardin, NASA Langley Research Center
J. Ray Ristorcelli, ICASE, NASA Langley Research Center
Christopher K.W. Tam, Florida State University

ORGANIZING COMMITTEE

This workshop was organized by a Scientific Committee which consisted of:

Ramesh K. Agarwal	McDonnell Douglas Aerospace
Sanford Davis	NASA Ames Research Center
Phillip R. Gliebe	General Electric Company
Jay C. Hardin	NASA Langley Research Center
M. Yousuff Hussaini	ICASE
Wen-Huei Jou	Boeing Commercial Airplane Group
J. R. Ristorcelli	ICASE
Lakshmi Sankar	Georgia Institute of Technology
Christopher K.W. Tam	Florida State University
Jay Webb	ICASE

CONTENTS

Preface iii

Benchmark Problems and Solutions 1
Christopher K.W. Tam

Application of Essentially Nonoscillatory Methods to Aeroacoustic Flow Problems 15
Harold L. Atkins

Computational Aeroacoustics Using Hyperbolic Wave Primitives 27
Sanford S. Davis

Comparative Study of Numerical Schemes of TVD3, UNO3-ACM and Optimized Compact Scheme 47
Duck-Joo Lee, Chang-Jeon Hwang, Duck-Kon Ko, and Jae-Wook Kim

A Compact Solution to Computational Acoustics 59
K.-Y. Fung, Raymond S. O. Man, and Sanford Davis

Application of Low Dissipation and Dispersion Runge-Kutta Schemes to Benchmark Problems in Computational Aeroacoustics 73
F. Q. Hu, M. Y. Hussaini, and J. Manthey

Results of Two New Methods for Aeroacoustics Benchmark Problems 99
H. T. Huynh

Solution of Acoustic Workshop Problems by a Spectral Multidomain Method 117
David A. Kopriva and John H. Kolias

Computation of Wave Propagation in a Complex Flow 125
Philippe Lafon

Second-Order Numerical Solution of Time-Dependent, First-Order Hyperbolic Equations 133
Patricia L. Shah and Jay Hardin

Lattice Gas Methods for Computational Aeroacoustics 143
Victor W. Sparrow

Solutions of the Benchmark Problems by the Dispersion-Relation-Preserving Scheme 149
C.K.W. Tam, H. Shen, K. A. Kurbatskii, L. Auriault, Z. Dong, and J. C. Webb

The Construction of High-Accuracy Schemes for Acoustic Equations 173
Lei Tang and James D. Baeder

A Comparative Study of Upwind and MacCormack Schemes for CAA Benchmark Problems 185
K. Viswanathan and L. N. Sankar

Application of Traditional CFD Methods to Nonlinear Computational Aeroacoustics Problems 197
Thomas S. Chyczewski and Lyle N. Long

Evaluation of High Order Schemes for Nonlinear Wave Computations 203
M. Ehtesham Hayder

Time Accurate Application of the MacCormack 2-4 Scheme on Massively Parallel Computers 209
Dale A. Hudson and Lyle N. Long

Nonlinear Wave Propagation using Three Different Finite Difference Schemes 217
D. Stuart Pope and J. C. Hardin

Wave Propagation and Scattering in Computational Aeroacoustics 225
Cathy Chung and Philip J. Morris

The Use of Staggered Schemes and an Absorbing Buffer Zone for Computational Aeroacoustics 233
Douglas M. Nark

A Numerical Solution Method for Acoustic Radiation from Axisymmetric Bodies 245
John E. Caruthers and G. K. Raviprakash

Application of a New Finite Difference Algorithm for Computational Aeroacoustics 255
John W. Goodrich

Computational Aeroacoustics on Massively Parallel Computers 261
Yusuf Özyörük and Lyle N. Long

Category 5 Problem Solution using an Unstructured Finite Volume Algorithm 267
Trong T. Bui and Reda R. Mankbadi

Comparison of Spatial Numerical Operators for Duct-Nozzle Acoustics 273
A. B. Cain and W. W. Bower

High-Order Essentially Non-Oscillatory Methods for Computational Aeroacoustics 279
Jay Casper

Numerical Simulations of Small Amplitude Acoustic Wave Propagation in a Converging-Diverging Nozzle 285
Thomas Z. Dong and Reda R. Mankbadi

The Pressure Field of a Gust Interacting with a Flat Plate 291
Hafiz M. Atassi and Sheryl M. Patrick

Aeroacoustic Computation of a Gust-Plate Interaction via MacCormack Schemes 297
James E. Martin

Evaluation of Numerical Schemes for the Analysis of Sound Generation by Blade-Gust Interaction 303
J. N. Scott, S. I. Hariharan and R. Mankbadi

Overview of Computed Results 313
Christopher K.W. Tam

Industry Panel Presentations and Discussions 377
N. N. Reddy

Participants 389

N95-30134

BENCHMARK PROBLEMS AND SOLUTIONS

Christopher K.W. Tam

The Scientific Committee, after careful consideration, adopted six categories of benchmark problems for the workshop. These problems do not cover all the important computational issues relevant to Computational Aeroacoustics (CAA). The deciding factor to limit the number of categories to six was the amount of effort needed to solve these problems. For reference purpose, the benchmark problems are provided below. They are followed by the exact or approximate analytical solutions. At present, an exact solution for the Category 6 problem is not available.

BENCHMARK PROBLEMS

Category 1

Problems to test the numerical dispersion and dissipation properties of a computation scheme (linear waves).

Use nondimensional variables with the following scales

$$\Delta x = \Delta r = \text{ length scale}$$

$$a_\infty \text{ (ambient sound speed)} = \text{ velocity scale}$$

$$\frac{\Delta x}{a_\infty} = \text{ time scale}$$

$$\rho_\infty = \text{ density scale}$$

$$\rho_\infty a_\infty^2 = \text{ pressure scale}$$

1. Solve the initial value problem

$$\frac{\partial u}{\partial t} + \frac{\partial u}{\partial x} = 0$$

$$t = 0 \quad u = 0.5 \exp\left[-(\ln 2)\left(\frac{x}{3}\right)^2\right]$$

Give numerical solution at $t = 100$, 200, 300 and 400 over $-20 \leq x \leq 450$. State the size of Δt used.

2. Solve the spherical wave problem

$$\frac{\partial u}{\partial t} + \frac{u}{r} + \frac{\partial u}{\partial r} = 0$$

over the domain $5 \leq r \leq 450$, with initial condition $t = 0$, $u = 0$. The boundary condition at $r = 5$ is:

$$r = 5, \qquad u = \sin \omega t$$

(a) $\omega = \dfrac{\pi}{4}$

(b) $\omega = \dfrac{\pi}{3}$

Give the numerical solution at $t = 100$, 200, 300 and 400 for each case. (Do not recast the equation in a plane wave form.) State the size of Δt used.

Category 2

Problems to test the nonlinear wave propagation properties of a computational scheme.

Use dimensionless variables with the following scales

$$\Delta x = \text{ length scale}$$

$$a_\infty \text{ (ambient sound speed)} = \text{ velocity scale}$$

$$\frac{\Delta x}{a_\infty} = \text{ time scale}$$

$$\rho_\infty = \text{ density scale}$$

$$\rho_\infty a_\infty^2 = \text{ pressure scale}$$

In both problems, the one-dimensional Euler equations are to be solved.

$$\frac{\partial \rho}{\partial t} + \frac{\partial \rho u}{\partial x} = 0$$

$$\rho \left(\frac{\partial u}{\partial t} + u \frac{\partial u}{\partial x} \right) = -\frac{\partial p}{\partial x}$$

$$\frac{\partial p}{\partial t} + u \frac{\partial p}{\partial x} + \gamma p \frac{\partial u}{\partial x} = 0$$

(You may use an equivalent form of the Euler equations.)

1. Solve the initial value problem

$$t = 0 \qquad u = 0.5 \exp \left[-(\ln 2) \left(\frac{x}{5} \right)^2 \right]$$

$$p = \frac{1}{\gamma}\left(1 + \frac{\gamma - 1}{2}u\right)^{\frac{2\gamma}{\gamma-1}}$$

$$\rho = \left(1 + \frac{\gamma - 1}{2}u\right)^{\frac{2}{\gamma-1}}; \quad \gamma = 1.4$$

Use a computational domain $-50 \leq x \leq 350$. Give the spatial distribution of u, ρ, and p at $t = 10$, 20, 30, 40, 50, 100, 150, 200 and 300.

2. Solve the one-dimensional shock tube problem using the following initial conditions

$$t = 0 \qquad u = 0$$

$$p = \begin{cases} 4.4, & x < -2 \\ 2.7 + 1.7\cos\left[\frac{(x+2)\pi}{4}\right], & -2 \leq x \leq 2 \\ 1, & x > 2 \end{cases}$$

$$\rho = (\gamma p)^{\frac{1}{\gamma}}, \qquad \gamma = 1.4$$

Use a computational domain $-100 \leq x \leq 100$. Give the spatial distribution of p, ρ and u at $t = 40$, 50, 60 and 70.

Category 3

Problems to test the effectiveness of radiation boundary conditions, inflow and outflow boundary conditions and the isotropy property of the computation algorithm.

Use dimensionless variables with the following scales

$$\Delta x = \text{ length scale}$$

$$a_\infty \text{ (ambient sound speed)} = \text{ velocity scale}$$

$$\frac{\Delta x}{a_\infty} = \text{ time scale}$$

$$\rho_\infty = \text{ density scale}$$

$$\rho_\infty a_\infty^2 = \text{ pressure scale}$$

In both problems, the linearized two-dimensional Euler equations on a uniform mean flow are to be solved.

$$\frac{\partial \mathbf{U}}{\partial t} + \frac{\partial \mathbf{E}}{\partial x} + \frac{\partial \mathbf{F}}{\partial y} = 0$$

where

$$\mathbf{U} = \begin{bmatrix} \rho \\ u \\ v \\ p \end{bmatrix}, \quad \mathbf{E} = \begin{bmatrix} M_x\rho + u \\ M_x u + p \\ M_x v \\ M_x p + u \end{bmatrix} \mathbf{F} = \begin{bmatrix} M_y\rho + v \\ M_y u \\ M_y v + p \\ M_y p + v \end{bmatrix}$$

M_x and M_y are constant mean flow Mach number in the x and y direction, respectively. (You may use an equivalent form of the above equations.)

Use a computational domain $-100 \leq x \leq 100$, $-100 \leq y \leq 100$ embedded in free space.

1. Let $M_x = 0.5$, $M_y = 0$. Solve the initial value problem, $t = 0$.

$$p = \exp\left[-(\ln 2)\left(\frac{x^2+y^2}{9}\right)\right]$$

$$\rho = \exp\left[-(\ln 2)\left(\frac{x^2+y^2}{9}\right)\right] + 0.1\exp\left[-(\ln 2)\frac{(x-67)^2+y^2}{25}\right]$$

$$u = 0.04y\exp\left[-(\ln 2)\frac{(x-67)^2+y^2}{25}\right]$$

$$v = -0.04(x-67)\exp\left[-(\ln 2)\frac{(x-67)^2+y^2}{25}\right]$$

Give the distributions of p, ρ, u and v at $t = 30$, 40, 50, 60, 70, 80, 100, 200 and 600.

2. Let $M_x = M_y = 0.5\cos(\frac{\pi}{4})$. Solve the initial value problem, $t = 0$.

$$p = \exp\left[-(\ln 2)\left(\frac{x^2+y^2}{9}\right)\right]$$

$$\rho = \exp\left[-(\ln 2)\left(\frac{x^2+y^2}{9}\right)\right] + 0.1\exp\left[-(\ln 2)\frac{(x-67)^2+(y-67)^2}{25}\right]$$

$$u = 0.04(y-67)\exp\left[-(\ln 2)\frac{(x-67)^2+(y-67)^2}{25}\right]$$

$$v = -0.04(x-67)\exp\left[-(\ln 2)\frac{(x-67)^2+(y-67)^2}{25}\right]$$

Note: The mean flow is in the direction of the diagonal of the computational domain.

Give the distributions of p, ρ, u and v at $t = 60$, 70, 80, 90, 100, 200, 600 and 1000.

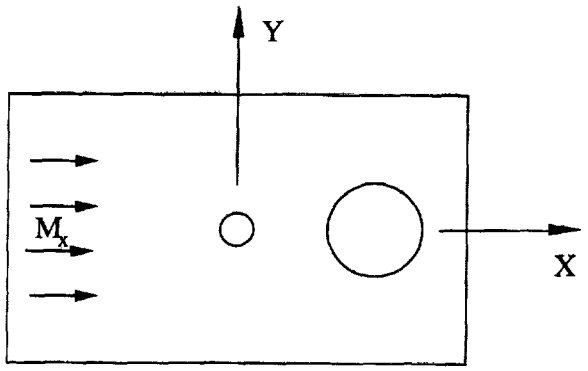

Figure for Problem 1, Category 3

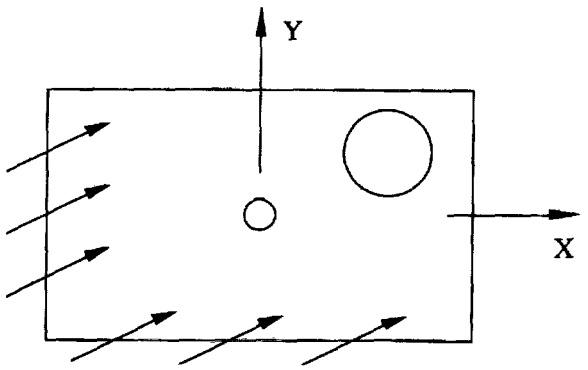

Figure for Problem 2, Category 3

Category 4

Problems to test the effectiveness of wall boundary conditions.

Use dimensionless variables with the following scales

$$\Delta x = \Delta r = \text{ length scale}$$
$$a_\infty \text{ (ambient sound speed) } = \text{ velocity scale}$$
$$\frac{\Delta x}{a_\infty} = \text{ time scale}$$
$$\rho_\infty = \text{ density scale}$$
$$\rho_\infty a_\infty^2 = \text{ pressure scale}$$

1. Reflection of an acoustic pulse off a wall in the presence of a uniform flow in semi-infinite space.

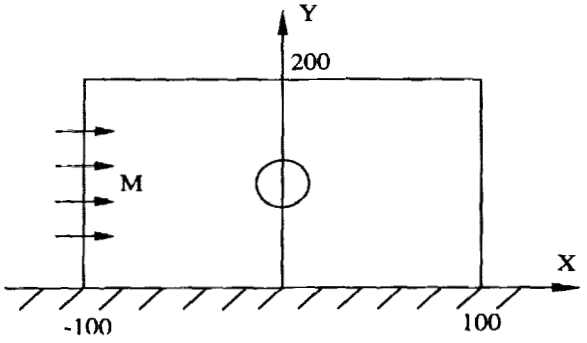

Figure for Problem 1, Category 4

Use a computational domain $-100 \leq x \leq 100, 0 \leq y \leq 200$. The wall is at $y = 0$. The linearized Euler equation in two dimensions are

$$\frac{\partial}{\partial t}\begin{bmatrix}\rho\\ u\\ v\\ p\end{bmatrix} + \frac{\partial}{\partial x}\begin{bmatrix}M\rho + u\\ Mu + p\\ Mv\\ Mp + u\end{bmatrix} + \frac{\partial}{\partial y}\begin{bmatrix}v\\ 0\\ p\\ v\end{bmatrix} = 0$$

where $M = 0.5$. The initial condition is

$$t = 0, \qquad u = v = 0$$

$$p = \rho = \exp\left\{-(\ln 2)\left[\frac{x^2 + (y-25)^2}{25}\right]\right\}$$

Give the pressure field at $t = 15$, 30, 45, 60, 75, 100 and 150.

2. Acoustic radiation from an oscillating circular piston in a wall

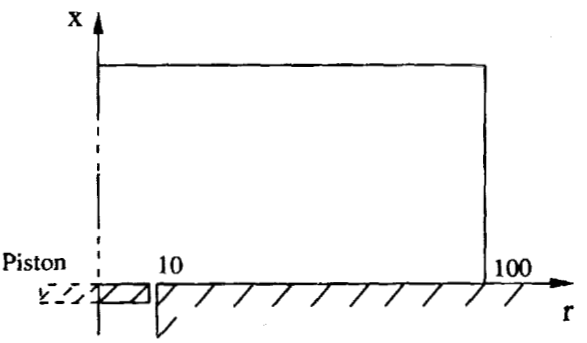

Figure for Problem 2, Category 4

Radius of piston = 10. Velocity of piston $u = 10^{-4}\sin(\frac{\pi t}{5})$. Use a computational domain $0 \leq x \leq 100, 0 \leq r \leq 100$. The wall and the piston are at $x = 0$. The cylindrical coordinate system is centered at the center of the piston. With axisymmetry, the linearized Euler

equations are

$$\frac{\partial}{\partial t}\begin{bmatrix}\rho\\ u\\ v\\ p\end{bmatrix}+\frac{\partial}{\partial r}\begin{bmatrix}v\\ 0\\ p\\ v\end{bmatrix}+\begin{bmatrix}\frac{v}{r}\\ 0\\ 0\\ \frac{v}{r}\end{bmatrix}+\frac{\partial}{\partial x}\begin{bmatrix}u\\ p\\ 0\\ u\end{bmatrix}=0$$

The initial conditions are:

$$t=0 \qquad \rho=u=v=p=0$$

Give the time harmonic pressure distribution at the beginning, $\frac{1}{4}$, $\frac{1}{2}$ and $\frac{3}{4}$ of a period of piston oscillation.

Category 5

Problem to test the suitability of a numerical scheme for direct numerical simulation of very small amplitude acoustic waves superimposed on a non-uniform mean flows in a semi-infinite duct.

Use nondimensional variables with the following scales

$$\Delta x = \text{ length scale}$$

$$a_\infty \text{ (sound speed far upstream) } = \text{ velocity scale}$$

$$\frac{\Delta x}{a_\infty} = \text{ time scale}$$

$$\rho_\infty \text{ (density of gas upstream) } = \text{ density scale}$$

$$\rho_\infty a_\infty^2 = \text{ pressure scale}$$

A small amplitude sound wave is incident on a convergent-divergent nozzle as shown

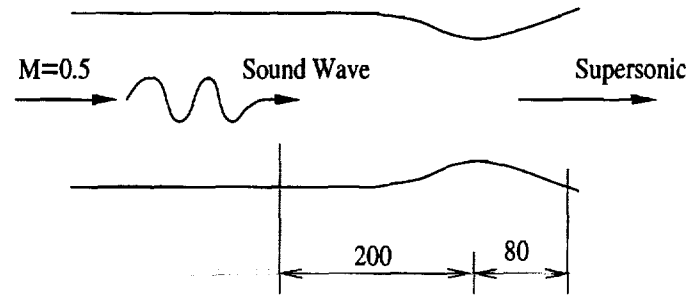

Figure for Category 5 Problem

Use a computational domain $-200 \le x \le 80$. The area of the nozzle is given by

$$A(x) = \begin{cases} 134 & x \le -100 \\ 117 - 17\cos\left(\frac{\pi x}{100}\right) & -100 \le x \le 19 \\ 97.2 + 0.3x & 19 \le x \le 80 \end{cases}$$

The quasi-one-dimensional unsteady flow equations are

$$\frac{\partial \rho A}{\partial t} + \frac{\partial \rho u A}{\partial x} = 0$$
$$\rho\left(\frac{\partial u}{\partial t} + u\frac{\partial u}{\partial x}\right) + \frac{\partial p}{\partial x} = 0$$
$$\frac{\partial pA}{\partial t} + \frac{\partial puA}{\partial x} + (\gamma - 1)p\frac{\partial uA}{\partial x} = 0$$

Far upstream $x \le -200$, there is an incoming acoustic wave. Together with the steady inflow, the velocity, pressure and density are given by

$$\begin{bmatrix} u \\ p \\ \rho \end{bmatrix} = \begin{bmatrix} M \\ \frac{1}{\gamma} \\ 1 \end{bmatrix} + \begin{bmatrix} 1 \\ 1 \\ 1 \end{bmatrix} \varepsilon \sin\left[\omega\left(\frac{x}{1+M} - t\right)\right]$$

Take $\gamma = 1.4$, $M = 0.5$, $\varepsilon = 10^{-6}$, $\omega = 0.1\pi$, calculate the transmitted sound wave at the nozzle exit. Give $p(t) - \overline{p}$ over a time period; $\overline{p}$ is the time averaged pressure.

Category 6

Problems to test the ability of a numerical scheme to calculate aeroacoustic source.

Use dimensionless variables with the following scales

$$\Delta x = \text{ length scale}$$
$$a_\infty \text{ (ambient sound speed)} = \text{ velocity scale}$$
$$\frac{\Delta x}{a_\infty} = \text{ time scale}$$
$$\rho_\infty = \text{ density scale}$$
$$\rho_\infty a_\infty^2 = \text{ pressure scale}$$

1. Sound generation by gust-blade interaction (two-dimensional)

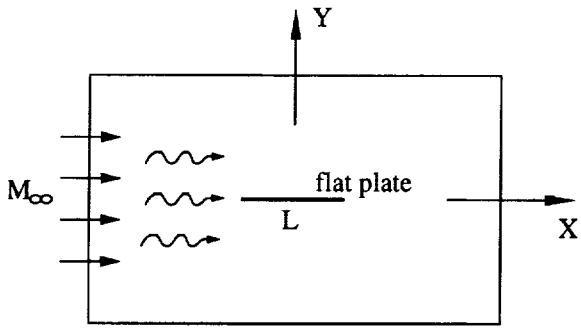

Figure for Category 6 Problem

Use a computational domain $-100 \leq x \leq 100$, $-100 \leq y \leq 100$. The blade is a flat plate of length L ($L = 30$) lying along the x-axis centered at the origin. There is a Mach 0.5 uniform mean flow in the x-direction. The mean flow carries a gust with velocity component in the y-direction given by

$$v = 0.1 \sin\left[\frac{\pi}{8}\left(\frac{x}{M_\infty} - t\right)\right], \quad M_\infty = 0.5$$

The linearized Euler equations are

$$\frac{\partial}{\partial t}\begin{bmatrix}\rho\\ u\\ v\\ p\end{bmatrix} + \frac{\partial}{\partial x}\begin{bmatrix}M_\infty\rho + u\\ M_\infty u + p\\ M_\infty v\\ M_\infty p + u\end{bmatrix} + \frac{\partial}{\partial y}\begin{bmatrix}v\\ 0\\ p\\ v\end{bmatrix} = 0$$

Determine the intensity of radiated sound, $\overline{p}^2$, along the coordinate lines $x = \pm 95$ and $y = \pm 95$.

SOLUTIONS

Category 1

Problem 1. The solution is

$$u(x,t) = 0.5 \exp\left[-(\ell n\, 2)\left(\frac{x-t}{3}\right)^2\right]$$

Problem 2. The solution is

$$u(r,t) = \begin{cases} 0, & r > t+5 \\ \frac{5}{r}[\sin\omega(t-r+5)], & r \leq t+5. \end{cases}$$

Category 2

Problem 1. An approximate solution can be found by using the simple wave assumptions (Chapter 6, G.B. Whitham, "Linear and nonlinear waves"). These assumptions are

1. The flow is isentropic
2. The Riemann invariant $\frac{2a}{\gamma-1} - u = \frac{2}{\gamma-1}$, which starts from the uniform region ahead of the pulse, is valid everywhere.

With these assumptions, the Euler equations reduces to the nonlinear simple wave equation

$$\frac{\partial u}{\partial t} + \left(1 + \frac{\gamma+1}{2}u\right)\frac{\partial u}{\partial x} = 0$$

This quasi-linear first-order equation can be solved by the method of characteristics. For the given initial conditions, a shock will form at the front of the pulse as the disturbance propagates to the right. The location of the shock may be found approximately by the use of Whitham's equal area rule.

Problem 2. The standard shock tube solution is a good approximate solution. The standard solution is available in most books on gas dynamics.

Category 3

Problem 1. Let $\alpha_1 = \frac{(\ell n 2)}{9}$, $\alpha_2 = \frac{(\ell n 2)}{25}$, $M = 0.5$, $\eta = [(x - Mt)^2 + y^2]^{\frac{1}{2}}$.

The solution is

$$u = \frac{(x - Mt)}{2\alpha_1 \eta} \int_0^\infty e^{\frac{-\xi^2}{4\alpha_1}} \sin(\xi t) J_1(\xi\eta)\xi \, d\xi + 0.04ye^{-\alpha_2[(x-67-Mt)^2+y^2]}$$

$$v = \frac{y}{2\alpha_1 \eta} \int_0^\infty e^{\frac{-\xi^2}{4\alpha_1}} \sin(\xi t) J_1(\xi\eta)\xi \, d\xi - 0.04(x - 67 - Mt)e^{-\alpha_2[(x-67-Mt)^2+y^2]}$$

$$p = \frac{1}{2\alpha_1} \int_0^\infty e^{\frac{-\xi^2}{4\alpha_1}} \cos(\xi t) J_0(\xi\eta)\xi \, d\xi$$

$$\rho = p + 0.1e^{-\alpha_2[(x-67-Mt)^2+y^2]}$$

where $J_0(\ \ )$ and $J_1(\ \ )$ are Bessel functions of order 0 and 1.

(Reference: C.K.W. Tam and J.C. Webb, "Dispersion-Relation-Preserving finite difference schemes for computational acoustics," J. Computational Phys., Vol. 107, pp. 262–281, 1993.)

Problem 2. The solution can be obtained from that of problem 1 by a coordinate transformation.

Category 4

Problem 1. Let $\alpha = \frac{(\ell n 2)}{25}$, $\eta = [(x-Mt)^2 + (y-25)^2]^{\frac{1}{2}}$, $\zeta = [(x-Mt)^2 + (y+25)^2]^{\frac{1}{2}}$.
The solution is

$$u = \frac{(x-Mt)}{2\alpha\eta}\int_0^\infty e^{-\frac{\xi^2}{4\alpha}}\sin(\xi t)J_1(\xi\eta)\xi\,d\xi + \frac{(x-Mt)}{2\alpha\zeta}\int_0^\infty e^{-\frac{\xi^2}{4\alpha}}\sin(\xi t)J_1(\xi\zeta)\xi\,d\xi$$

$$y = \frac{(y-25)}{2\alpha\eta}\int_0^\infty e^{-\frac{\xi^2}{4\alpha}}\sin(\xi t)J_1(\xi\eta)\xi\,d\xi + \frac{(y-25)}{2\alpha\zeta}\int_0^\infty e^{-\frac{\xi^2}{4\alpha}}\sin(\xi t)J_1(\xi\zeta)\xi\,d\xi$$

$$p = \rho = \frac{1}{2\alpha}\int_0^\infty e^{-\frac{\xi^2}{4\alpha}}\cos(\xi t)[J_0(\xi\eta) + J_0(\xi\zeta)]\xi\,d\xi$$

Problem 2. Let $\varepsilon = 10^{-4}$, $R = 10$, $\omega = \frac{\pi}{5}$.
The solution is

$$p = \rho = \mathrm{Re}\left[\varepsilon R\omega\int_0^\infty \frac{J_1(\xi R)}{(\xi^2-\omega^2)^{\frac{1}{2}}}J_0(\xi r)e^{-(\xi^2-\omega^2)^{\frac{1}{2}}x - i\omega t}d\xi\right]$$

$$u = \mathrm{Im}\left[-\varepsilon R\int_0^\infty J_1(\xi R)J_0(\xi r)e^{-(\xi^2-\omega^2)^{\frac{1}{2}}x - i\omega t}d\xi\right]$$

$$v = \mathrm{Im}\left[-\varepsilon R\int_0^\infty \frac{J_1(\xi R)}{(\xi^2-\omega^2)^{\frac{1}{2}}}\xi J_1(\xi r)e^{-(\xi^2-\omega^2)^{\frac{1}{2}}x - i\omega t}d\xi\right]$$

where Re[ ] = the real part of and Im[ ] = the imaginary part of.

Note: $(\xi^2-\omega^2)^{\frac{1}{2}} = -i|\xi^2-\omega^2|^{\frac{1}{2}}$ for $\xi < \omega$.

A fairly accurate solution of this problem can be found by first determining the governing equations for the amplitude functions of the time-periodic disturbances inside the nozzle. These equations are ordinary differential equations but with variable coefficients. They can be integrated numerically.

Let the solution be separated into a mean and a time-periodic part in the form

$$\begin{bmatrix} \rho \\ u \\ p \end{bmatrix} = \begin{bmatrix} \overline{\rho} \\ \overline{u} \\ \overline{p} \end{bmatrix} + \mathrm{Re}\left\{ \begin{bmatrix} \widehat{\rho}(x) \\ \widehat{u}(x) \\ \widehat{p}(x) \end{bmatrix} e^{-i\omega t} \right\}$$

The physical quantities of the mean flow at the nozzle throat will be denoted by a subscript $*$. With the area ratio A_*/A_1 known, where A_1 is the area of the uniform duct, ρ_* is first found by solving the equation

$$\rho_*^{\gamma+1}\left(\frac{A_*}{A_1}\right)^2 + \frac{2}{\gamma-1} = \frac{\gamma+1}{\gamma-1}\rho_*^{\gamma-1}$$

The other variables at the nozzle throat are given by

$$p_* = \frac{1}{\gamma}\rho_*^{\gamma}, \qquad u_* = \rho_*^{\frac{\gamma-1}{2}}$$

The mean flow solution is

$$\overline{\rho}\,\overline{u}\,A = \rho_* u_* A_*$$

$$\frac{\overline{p}}{p_*} = \left(\frac{\overline{\rho}}{\rho_*}\right)^{\gamma}$$

$$\frac{\overline{u}^2}{2} + \frac{\gamma}{\gamma-1}\frac{p_*}{\rho_*^{\gamma}}\overline{\rho}^{\gamma-1} = \frac{u_*^2}{2} + \frac{\gamma}{\gamma-1}\frac{p_*}{\rho_*}$$

The linearized governing equations for the amplitude functions $\widehat{\rho}$, $\widehat{u}$ and $\widehat{p}$ are

$$\begin{aligned}
\frac{d\widehat{u}}{dx} &= \frac{1}{(\overline{\rho}\,\overline{u}^2 - \gamma\overline{p})}\left[-\overline{u}^2\frac{d\overline{u}}{dx}\widehat{\rho} + \left(i\omega\overline{\rho}\,\overline{u} - \overline{\rho}\,\overline{u}\frac{d\overline{u}}{dx} + \frac{d\overline{p}}{dx} - \frac{\gamma\overline{p}}{A}\frac{dA}{dx}\right)\widehat{u} - \left(i\omega - \frac{\gamma}{A}\frac{d(\overline{u}\,\overline{A})}{dx}\right)\widehat{p}\right] \\
\frac{d\widehat{p}}{dx} &= \frac{1}{(\overline{\rho}\,\overline{u}^2 - \gamma\overline{p})}\left[\gamma\overline{p}\,\overline{u}\frac{d\overline{u}}{dx}\widehat{\rho} + \left(-i\omega\gamma\overline{p}\,\overline{\rho} + \gamma\overline{p}\,\overline{\rho}\frac{d\overline{u}}{dx} - \overline{\rho}\,\overline{u}\frac{d\overline{p}}{dx} - \frac{\gamma\overline{p}\,\overline{\rho}\,\overline{u}}{A}\frac{dA}{dx}\right)\widehat{u}\right. \\
&\qquad \left. + \left(i\omega\overline{\rho}\,\overline{u} - \frac{\gamma\overline{\rho}\,\overline{u}}{A}\frac{d(\overline{u}\,A)}{dx}\right)\widehat{p}\right] \qquad (1) \\
\frac{d\widehat{\rho}}{dx} &= -\frac{\overline{\rho}}{\overline{u}}\frac{d\widehat{u}}{dx} + \left(i\omega A - \frac{d(\overline{u}\,A)}{dx}\right)\frac{1}{\overline{u}\,A}\widehat{\rho} - \frac{1}{\overline{u}\,A}\frac{d(\overline{\rho}\,A)}{dx}\widehat{u}
\end{aligned}$$

In the uniform region of the duct, the solution of (1) that matches the incoming acoustic wave is

$$\begin{bmatrix} \widehat{\rho} \\ \widehat{u} \\ \widehat{p} \end{bmatrix} = -i\varepsilon \begin{bmatrix} 1 \\ 1 \\ 1 \end{bmatrix} e^{\frac{i\omega x}{1+M}} + c \begin{bmatrix} 1 \\ -1 \\ 1 \end{bmatrix} e^{\frac{i\omega x}{1-M}} \tag{2}$$

In (2), the second term represents the reflected acoustic wave. The unknown amplitude c is to be determined later.

Equations (1) have a regular singular point at the nozzle throat ($x = 0$). Near the throat, there are two non-singular series solutions. The first two terms of these solutions are

$$\begin{aligned} \widehat{\rho} &= \left\{ \frac{i\omega\rho_*}{u_*^2[\frac{1}{(\gamma+1)A_*}(\frac{d^2A}{dx^2})_*]^{\frac{1}{2}}} - \frac{2\rho_*}{u_*} \right\} u_0 + \left\{ \frac{-i\omega}{u_*^3[\frac{1}{(\gamma+1)A_*}(\frac{d^2A}{dx^2})_*]^{\frac{1}{2}}} + \frac{\gamma}{u_*^2} \right\} p_0 + \rho_1 x + \dots \\ \widehat{u} &= u_0 + u_1 x + \dots \\ \widehat{p} &= p_0 + p_1 x + \dots \end{aligned} \tag{3}$$

where u_0 and p_0 are arbitrary constants. ρ_1, u_1 and p_1 are functions of u_0 and p_0.

A numerical solution of (1) can be constructed by starting the solution slightly upstream of the nozzle throat at $x = -\delta$ ($\delta << 1$) using (3) as the starting solution. (For small δ, the terms of the series involving δ and powers of δ may be neglected.) The numerical integration proceeds upstream until the uniform duct region is reached. At this point, the numerical solution must match solution (2). This provides three algebraic equations for the three unknowns p_0, u_0 and c. Once these constants are found, the solution upstream of the nozzle throat is known.

For the solution downstream of the nozzle throat one can start integrating (1) numerically at a point just downstream, say at $x = \delta$. Again (3) is used as the starting solution. The numerical integration proceeds downstream until the nozzle exit is reached. With p_0, u_0 already found, the amplitude functions are now completely determined along the entire length of the nozzle.

Christopher K.W. Tam
Department of Mathematics
Florida State University
Tallahassee, FL 32306-3027

Application of Essentially Nonoscillatory Methods to Aeroacoustic Flow Problems

Harold L. Atkins
NASA Langley Research Center
Hampton, VA

SUMMARY

A finite-difference essentially nonoscillatory (ENO) method has been applied to several of the problems prescribed for the workshop sponsored jointly by the Institute for Computer Applications in Science and Engineering and by NASA Langley Research Center entitled "Benchmark Problems in Computational Aeroacoustics." The workshop focused on computational challenges specific to aeroacoustics. Among these are long-distance propagation of a short-wavelength disturbance, propagation of small-amplitude disturbances, and nonreflective boundary conditions. The shock capturing-capability inherent to the ENO method effectively eliminates oscillations near shock waves without the need to add and tune dissipation or filter terms. The method-of-lines approach allows the temporal and spatial operators to be chosen separately in accordance with the demands of a particular problem. The ENO method was robust and accurate for all problems in which the propagating wave was resolved with 8 or more points per wavelength. The finite-wave-model boundary condition, a local nonlinear acoustic boundary condition, performed well for the one-dimensional problems. The buffer-domain approach performed well for the two-dimensional test problem. The amplitude of nonphysical reflections were less than 1 percent of the exiting wave's amplitude.

INTRODUCTION

Essentially nonoscillatory (ENO) methods have been under development at NASA Langley Research Center (LaRC) since 1988. The algorithms are intended for flow simulations that require a high degree of accuracy but that also contain shock waves or other fluid discontinuities. One early use of the method was in the simulation of supersonic shear-layer instabilities (ref. 1) in which small "eddy shocklets" appear. Both control-volume (ref. 2) and finite-difference (ref. 1) approaches have been implemented and applied to a variety of validation cases (ref. 3) to compare their strengths and weaknesses. Recent recognition that the methodology is an appropriate tool for the study of high-speed jet noise has prompted some ground-laying work in the area of aeroacoustics. Work in this area includes the development of nonreflective boundary conditions (ref. 4), and improved spatial operators based on bandwidth resolution rather than strict order properties (ref. 5). Applications of ENO methods have included studies of shock-wave interaction with various other waves (ref. 6) and the combination of ENO methods with

Kirchhoff's method for far-field noise prediction (ref. 7).

The works cited above demonstrate that although the ENO approach is intended for problems that contain discontinuities the method also performs well for smooth problems. The problems prescribed for this workshop focus on several difficulties specific to aeroacoustics. Among these are long-distance propagation of a short-wavelength disturbance, propagation of small-amplitude disturbances, and nonreflective boundary conditions. This work describes the performance of the finite-difference ENO method for several of these problems. The first section gives a brief description of the method; a more detailed description can be found in ref. 1. The following section describes the results of applying the method to the workshop problems in categories 1, 2, 3, and 5.

METHODOLOGY

The program used for the benchmark problems implements the finite-difference form of ENO for the Euler or Navier-Stokes equations in a full three-dimensional curvilinear form. The program runs efficiently in one- or two-dimensional modes and has quasi-one-dimension and axisymmetric capability. The program is third order in time and up to fifth order in space (user selected). The program was modified for the category 3 problem, which prescribes the linear form of the Euler equations; however no attempt was made to optimize the implementation to take advantage of the linearity. The category 1 problem, which involved scalar advection, was solved by using a linear algorithm with operators similar to the "preferred" operator of the Euler/Navier-Stokes program. The meaning of "preferred" will be addressed later in this work. The basic method is described here for a one-dimensional conservation law:

$$\frac{\partial U}{\partial t} + \frac{\partial F}{\partial x} = 0$$

The finite-difference form of ENO was proposed by Shu and Osher (ref. 8) as an efficient means of implementing the ENO strategy in multiple dimensions. The approach is well suited to a method-of-lines approach, and one-dimensional forms are easily extended to two or three dimensions. The time integration is performed with the following three-stage third-order Runge-Kutta method due to Shu (ref. 9):

$$\begin{aligned} V^0 &= U(t^n) \\ V^k &= \alpha_k V^0 + (1-\alpha_k)\left(V^{k-1} - \Delta t\, S^{k-1}\right) \qquad k = 1,2,3 \\ U(t^{n+1}) &= V^3 \end{aligned}$$

where $\alpha_1 = 1$, $\alpha_2 = 3/4$, $\alpha_3 = 1/3$, and S denotes the spatial operator. This form of Runge-Kutta is total-variation diminishing (TVD), which is important to the overall stability of the ENO approach. High-order forms have been developed; however, the third-order form was chosen as a trade-off between storage and accuracy.

The spatial operator is evaluated with a conservative flux-splitting approach. A split numerical flux $\hat{F}^{\pm}$ is defined as an expansion of the split physical flux that achieves an approximation of the spatial

derivative to the desired order of accuracy.

$$S \equiv \frac{\delta\left(\widehat{F}^{+} + \widehat{F}^{-}\right)}{\Delta x} = \frac{\partial F}{\partial x} + O\left[(\Delta x)^{N}\right]$$

$$\widehat{F}^{\pm} \equiv \sum_{n=0}^{N} a_n \Delta x^n \frac{\partial^n F^{\pm}}{\partial x^n}$$

$$F^{\pm} = F \pm \widetilde{\lambda} U$$

$$a_0 = 1, \quad a_2 = \frac{-1}{24}, \quad a_4 = \frac{7}{5670}, \quad \cdots, \quad a_{10} = \frac{-73}{3,503,554,560}$$

$$a_3 = a_5 = a_7 = \cdots = 0$$

In this splitting, $\widetilde{\lambda}$ is a smooth function that is larger than the absolute value of the largest eigenvalue of the Jacobian of F. The split numerical flux is evaluated by fitting a polynomial through the split physical flux and differentiating as needed. Polynomials with different stencils may be used for each element of each flux; however, they must be chosen such that they are upwind in some sense.

The polynomial stencil is chosen by a solution adaptive procedure that results in the essentially-nonoscillatory property. Because the spatial operator depends on the solution, the algorithm is inherently nonlinear even if the problem to be solved is linear. The original adaptation procedure of Harten et al. (ref. 10) makes use of the divided-difference table of the solution to construct a polynomial whose stencil covers the smoothest segment of the solution that contains a specified starting point. Hence, the stencils for F^{+} and F^{-} can be biased upwind by choosing a starting point that is upwind. Although this adaptation procedure ensures the desired ENO property, it has convergence problems that affect long-time calculations (refs. 11and 12). The adaptation procedure used here avoids these problems by making the stencil choice a continuous and smooth function of the solution. With this procedure, for a smooth solution the stencil choice approaches a predetermined preferred stencil as the mesh is refined. The preferred stencils for F^{+} and F^{-} are one-half-cell upwind and result in a linearly stable scheme. To increase the computational efficiency, all elements of a given flux use the same stencil, which is chosen by examining a single test function (e.g., the density).

RESULTS OF BENCHMARK CASES

The finite-difference ENO method has been applied to the problems in categories 1, 2, 3, and 5. Results for categories 2 and 5 are presented first because these problems required little or no changes to the program and the algorithm described above. A discussion of the results for categories 1 and 3 follows. Unless otherwise noted, all results are third order in time and fifth order in space, with 64-bit precision and a Courant-Friedrichs-Lewy (CFL) number of 0.5. Also, all problems prescribed a uniform grid with unit spacing; hence, the size of the domain also indicates the number of grid point used.

Category 2 prescribed two problems that were designed to test nonlinear wave propagation. Both involve the one-dimensional Euler equations, but they have different initial conditions. Problem 1 starts

with a Gaussian pressure distribution and velocity and density distributions that are appropriate for a right-traveling acoustic wave. The wave quickly steepens into a shock wave that propagates to the right and weakens. The initial Gaussian distribution is resolved with 10 points across its half-width. Figure 1 shows the pressure and density for t = 0, 50, 100, and 300. The inset in the pressure plot reveals no oscillations in the neighborhood of the shock at $t = 100$. The dip in density near $x = 50$ is due to entropy produced by the shock formation.

The initial conditions for problem 2 of this category consist of two piecewise-constant pressure regions connected by a cosine function over a four-point region. The initial velocity is zero and the density is given by the isentropic relation. This initial distribution quickly evolves into a left-traveling acoustic wave, a convecting entropy wave, and a right-traveling shock wave. Figure 2 shows the pressure and density distributions for t = 0, 30, 50, and 70. The inset shows the density in the neighborhood of the entropy wave for $t = 50$. As before, no discernible oscillations exist near the shock. For both problems 1 and 2, the shock wave has exited the domain by the final time. The finite-wave model (ref. 4) used for the boundary condition allows the shock to exit the domain without any visible reflection. For comparison, an additional simulation was performed in which the domain was extended by 10 points so that the shock did not leave the domain. The results of this case overlay the results of the workshop test case.

The purpose of the category 5 problem is to assess the ability of the method to resolve a low-amplitude disturbance in a nonuniform flow. The test case consists of a shock-free quasi-one-dimensional flow in which a periodic disturbance with an amplitude of $p/p_\infty = 1.4 \times 10^{-6}$ is added at the inflow boundary. The mean flow is accelerated from a Mach number of 0.5 to supersonic conditions through a converging-diverging nozzle. The area distribution is defined by three regions that have second-derivative discontinuities at their interfaces. These discontinuities in the geometry were expected to produce some error (ref. 3); however, the effect was less than anticipated.

The problem has been solved in two ways. The first approach is to obtain a discrete steady-state solution simply by a long time-accurate simulation. The residual is reduced to machine zero to ensure that the small disturbance to be added is well resolved. The simulation is restarted from the discrete steady state solution and is continued for 21 periods, during which the disturbance is imposed at the inflow boundary. The requested measurements of $[p(t) - \overline{p}]/(\rho a_\infty^2)$ are taken during the 21st period. An alternative approach is to force the exact quasi-one-dimensional solution to satisfy the discrete spatial operator by adding a forcing function. The forcing function that achieves this is simply the usual spatial operator evaluated for the exact quasi-one-dimensional solution. The procedure is easily implemented by computing and storing the residual for the initial solution and then subtracting that residual from the instantaneous residual during the time integration procedure. The results of the two methods are identified by the terms "direct approach" for the first method and "residual subtraction" for the second method.

Figure 3 illustrates the convergence history and the mean-flow solution of the direct approach. The dashed line in fig. 3(b) indicates the difference between the discrete mean-flow solution and the exact quasi-one-dimensional solution. As expected, jumps in the error occur at the point where the area definition has discontinuous second derivatives. Figure 4 shows the perturbation pressure $(p - \overline{p})/p_\infty$

for times of 2, 4, and 8 periods obtained with both the direct and residual subtraction methods. Both methods give the same prediction for the perturbation in spite of the error in the mean-flow solution for the direct approach.

The problems in category 1 are intended to test the dispersion and dissipation properties of the method for a linear advection problem. Because the Euler/Navier-Stokes code could not be easily or efficiently modified to solve a scalar equation, a linear algorithm that uses the same preferred spatial operator and time integration was written for this case. However, the use of a linear algorithm may actually be more appropriate than the application of the nonlinear ENO algorithm. As in the category 5 problem, an acoustic disturbance will most likely be small in amplitude; thus, assuming the mean flow is smooth, the ENO adaptation process will essentially return the preferred stencil. Because the category 1 problems prescribe waves with amplitudes on the order of one, the adaptation procedure would respond to the wave itself.

Category 1 consists of two problems that are similar to those of category 2 and 5; however, these problems have more demanding resolution requirements. The initial condition for the first problem is a Gaussian distribution similar to that of problem 1 from category 2; however, the Gaussian half-width is resolved with only 6 points instead of the 10 points used in the earlier problem. The second problem in category 1 has two cases, both of which are similar to the category 5 problem in that a periodic wave is specified at the inflow boundary. The major difference is that the wavelengths prescribed for the category 1 problems are much shorter, with only 6 or 8 points per wavelength instead of the 30 points per wavelength specified for the category 5 problem. An important consequence is that the waves of the category 1 problems are examined for propagation distances as large as 75 wavelengths, whereas in the category 5 problem the wave propagated less than 10 wavelengths to reach the exit.

Figure 5(a) shows the solution at t = 100, 200, 300, and 400 for the first problem of category 1. Results are shown for both fifth-order (solid line) and fourth-order (dashed line) spatial operators. Only the fourth-order operator was presented at the workshop. Figures 5(b) and 5(c) show an enlarged view of a portion of the solution at t = 400; the solutions are similar, and the error of the fifth-order case is approximately 10 percent.

Problem 2 of this category is governed by a nonhomogeneous equation that produces a decaying solution, as illustrated in figs. 6 and 7. The solid line indicates the amplitude envelope of the exact solution; the numerical solution is shown as a dashed line. At t = 300 (figs. 6(a) and 6(b)), the wave front for the case with 8 points per wavelength has propagated 37.5 wavelengths. At this time, both the fourth-order and fifth-order methods show the effects of dissipation; however, the fifth-order method is noticeably improved. At the same time, the solution that is resolved with 6 points per wavelength (figs. 7(a) and 7(b)) is completely damped for the fourth-order method and nearly so for fifth-order method. This result was expected based on earlier work (ref. 5) in which a set of optimized operators were developed. The large transient at the front of the wave is a result of the abrupt start-up of the simulation. If the amplitude of the wave imposed at the boundary is smoothly increased from zero, the transient is eliminated; however, this procedure has little effect on the solution behind the front.

The category 3 problem employes the linear Euler equations in two dimensions to test nonreflective

boundary conditions and scheme isotropy. The category defines two problems, only the first of which is solved here. This problem consists of a rectangular domain with initial conditions that prescribe a circular convective wave and a circular acoustic wave, as shown in fig. 8. The origin of the waves are such that both waves reach the right boundary at the same time.

Due to its modular nature, the Euler/Navier-Stokes program was modified to solve the linear Euler equations with relative ease. All boundary conditions, including the inflow, are implemented by a buffer domain approach. This method involves adding a region of points around the physical domain (also shown in fig. 8), in which the governing equations are modified such that all eigenvalues at the outer boundary of the buffer domain are indicative of outbound waves. For the linear Euler equations, this modification is easily accomplished by defining the linear Mach parameter as follows:

$$\widehat{M}_x \equiv M_x + (\pm 1.3 - M_x)\left[\frac{(i - i_b)}{(i_e - i_b)}\right]^{\kappa}$$

$$\widehat{M}_y \equiv M_y + (\pm 1.3 - M_y)\left[\frac{(j - j_b)}{(j_e - j_b)}\right]^{\kappa}$$

where M_x and M_y are the interior values and $\widehat{M}_x$ and $\widehat{M}_y$ are the values in the buffer domain. Subscripts b and e denote the boundary between the physical domain and the buffer domain and the outer edge of the buffer domain. The $\pm$ sign switches between $+$ on the right and top boundaries and $-$ on the left and bottom boundaries. The parameter κ allows some control over the smoothness of $\widehat{M}$ at the interface of the physical and buffer regions. In addition to modifying the equations, the grid in the buffer region was stretched slightly so that the maximum CFL number did not occur in the buffer region.

Figure 9 shows the density obtained with $\kappa = 2$ and with 20 points in the buffer domain at t = 100, 200, and 250. The dark band indicates the boundary between the physical domain and the buffer domain. The waves remain cylindrical, and reflections are small. The minimum contour level is ± 0.0025. Figure 10 shows the pressure on the horizontal (y = 0) and vertical (x = 0) centerlines of the domain. The scale has been reduced for the plots in which the prescribed wave has left the domain, so that the nonphysical reflection can be seen. On both axes, the reflected wave is less than 1 percent of the wave that exited the domain.

CONCLUSIONS

The finite-difference essentially nonoscillatory (ENO) method performed well for all problems solved with adequate resolution. The fifth-order spatial operator gave accurate results for waves resolved with 8 or more points per wavelength, although the dissipation was noticeable in cases with long propagation distances; 6 points per wavelength was not adequate. Shock waves were captured without large oscillations and without additional dissipation. The finite-wave-model boundary condition was accurate and robust (shocks were able to exit without reflection) for the one-dimensional cases in which it was applied. The buffer-domain approach was easy to implement and worked surprisingly well,

even at inflow boundaries. The method-of-lines approach offered flexibility, and allowed temporal and spatial operators to be optimized as needed.

ACKNOWLEDGMENTS

The author is grateful for the assistance of Dr. Freda Porter Locklear of Pembroke University for her assistance in setting up the program for several of the benchmark cases.

REFERENCES

1 Atkins, H. L.: High-Order ENO Methods for the Unsteady Compressible Navier-Stokes Equations. AIAA–90–1557, July 1990.

2 Casper, J.; and Atkins, H. L.: A Finite-Volume High-Order ENO Scheme for Two-Dimensional Hyperbolic Systems. *Journal of Computational Physics*, vol. 106, no. 1, 1993, pp. 62–76.

3 Casper, J.; Shu, C.-W.; and Atkins, H.: Comparison of Two Formulations for High-Order Essentially Nonoscillatory Schemes. *AIAA Journal*, vol. 32, no. 10, 1994, pp. 1970–1977.

4 Atkins, H.; and Casper, J.: Nonreflective Boundary Conditions for High-Order Methods. *AIAA Journal*, vol. 32, no. 3, 1994, pp. 512–518.

5 Lockard, D. P.; Brentner, K. S.; and Atkins, H. L.: High-Accuracy Algorithms for Computational Aeroacoustics. AIAA–94–0460, Jan. 1994.

6 Meadows, K. R.; Caughy, D. A.; and Casper, J.: Computing Unsteady Shock Waves for Aeroacoustic Applications. AIAA–93–4329, Oct. 1993.

7 Meadows, K. R.; and Atkins, H. L.: An Evaluation of a Hybrid Kirchhoff–CFD Approach for Computational Aeroacoustics. *Proceedings of the Imacs 14th World Congress*, vol. 2, July 1994, pp. 824–827.

8 Shu, C.-W.; and Osher, S.: Efficient Implementations of Essentially Non-oscillatory Shock-Capturing Schemes. *Journal of Computational Physics*, vol. 83, no. 1, 1989, pp. 32–78.

9 Shu, C.-W.: Total-Variation-Diminishing Time Discretizations. *SIAM J. Sci. Stat. Comput.*, vol. 9, no. 6, 1988, pp. 1073–1084.

10 Harten, A.; Engquist, B.; Osher, S.; and Chakravarthy, S. R.: Uniformly High Order Accurate Essentially Non-oscillatory Schemes III. *Journal of Computational Physics*, vol. 71, no. 2, 1987, pp. 231–323.

11 Rogerson, A. M.; and Meiburg, E.: A Numerical Study of the Convergence Properties of ENO Schemes. *Journal of Scientific Computing*, vol. 5, no. 2, 1990, pp. 151–167.

12 Shu, C.-W.: Numerical Experiments on the Accuracy of ENO and Modified ENO Schemes. *Journal of Scientific Computing*, vol. 5, no. 2, 1990, pp. 127–150.

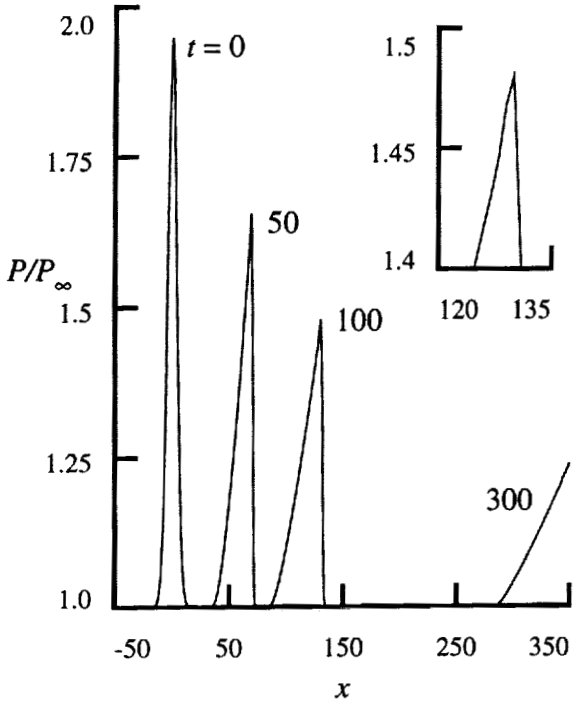

a) Pressure Distribution.

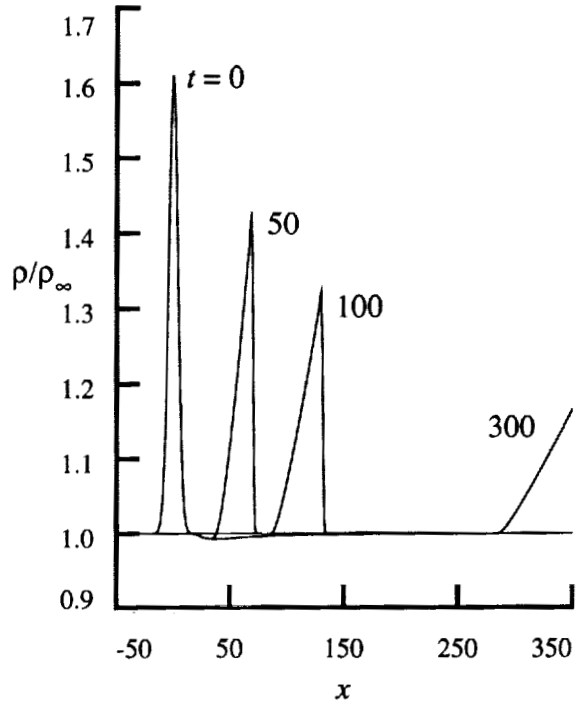

b) Density Distribution.

Figure 1. Solutions for problem 1 of category 2 at t = 0, 50, 100, and 300. Insert shows pressure near the shock at t = 100.

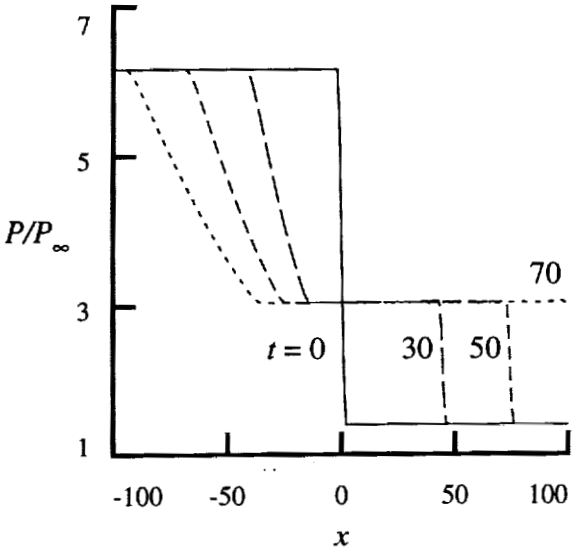

a) Pressure distribution.

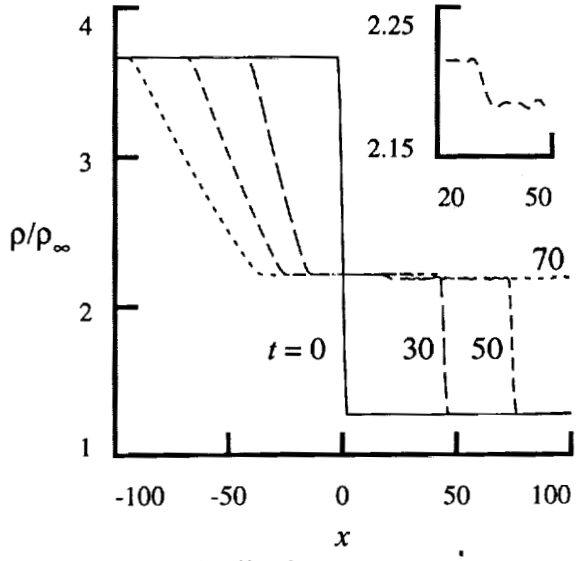

b) Density distribution.

Figure 2. Solutions for problem 2 of category 2 at t = 0, 30, 50, and 70. Insert shows density near entropy wave at t = 50.

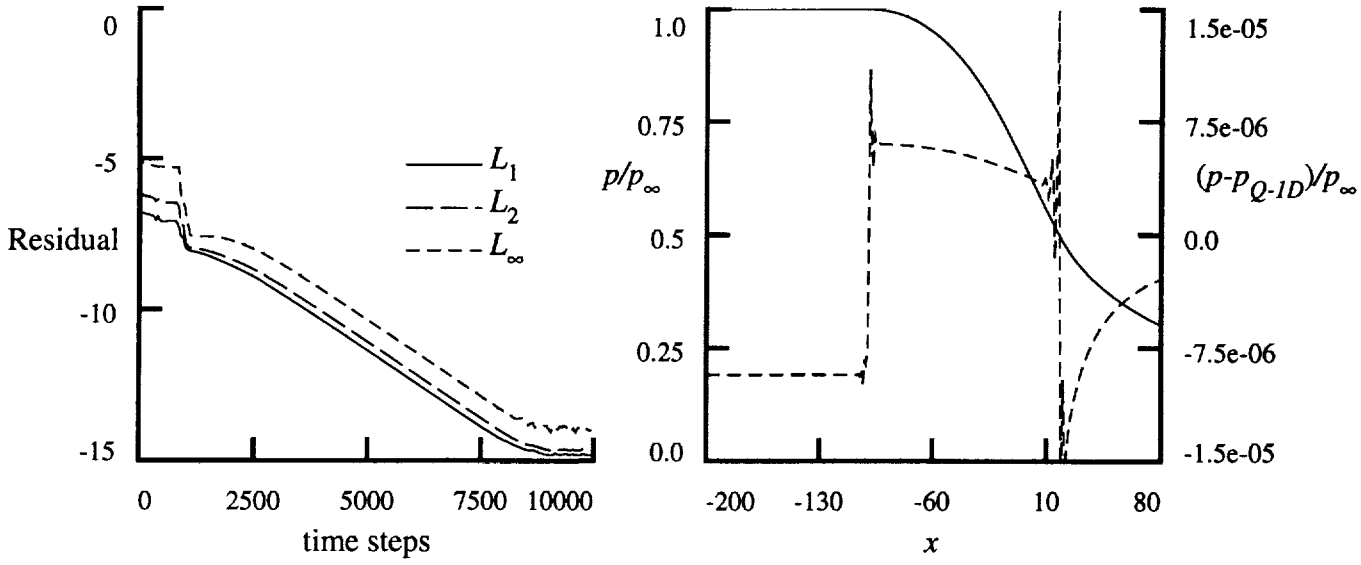

a) Convergence history.

b) Mean-flow pressure (—) and $(p-p_{Q\text{-}1D})/p_\infty$ (- -).

Figure 3. Mean-flow solution for the category 5 problem.

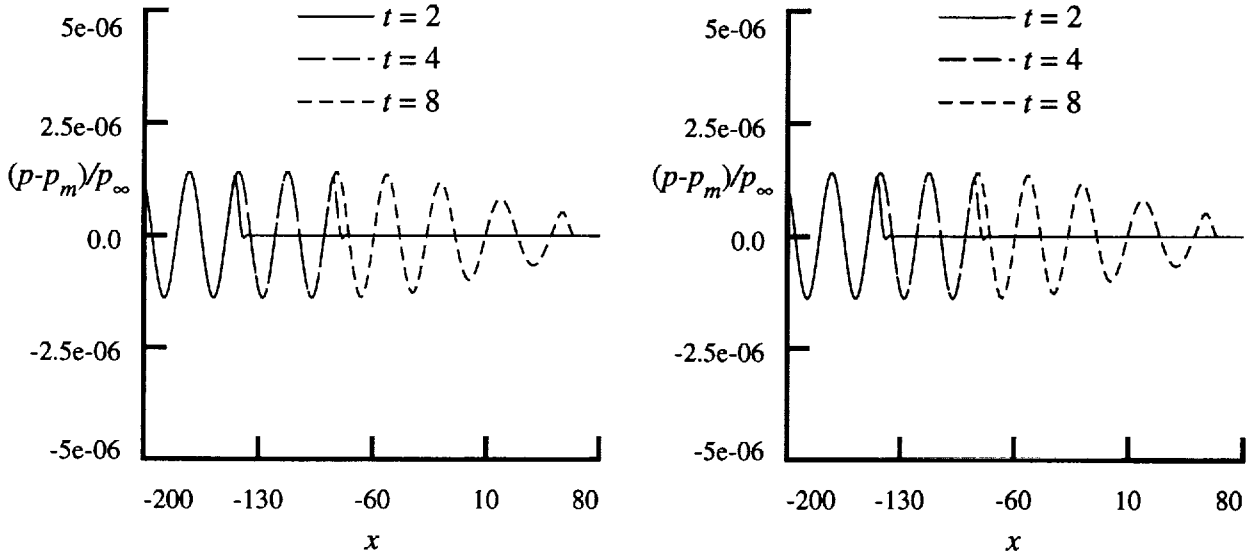

a) Direct method.

b) Residual subtraction method.

Figure 4. Perturbation pressures for the category 5 problem at various t.

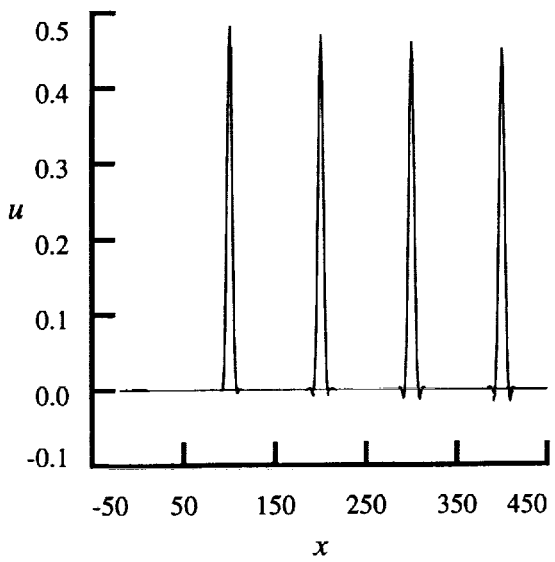

a) Solutions at t = 100, 200, 300 and 400.

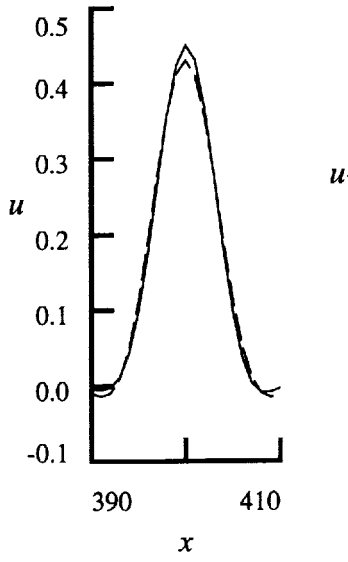

b) Solutions at t = 400.

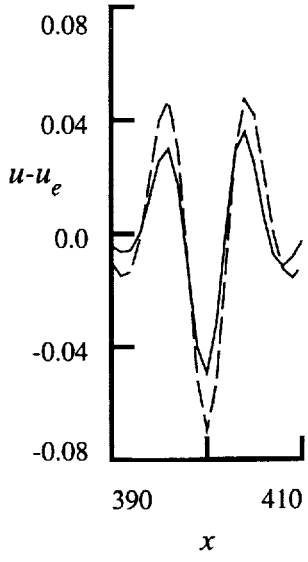

c) Error at t = 400.

Figure 5. Solutions for problem 1 of category 1 with fourth-order (dashed) and fifth-order (solid) methods.

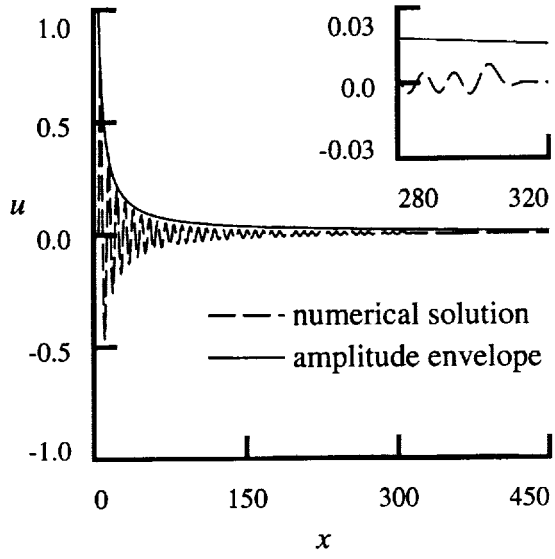

a) Fourth-order method.

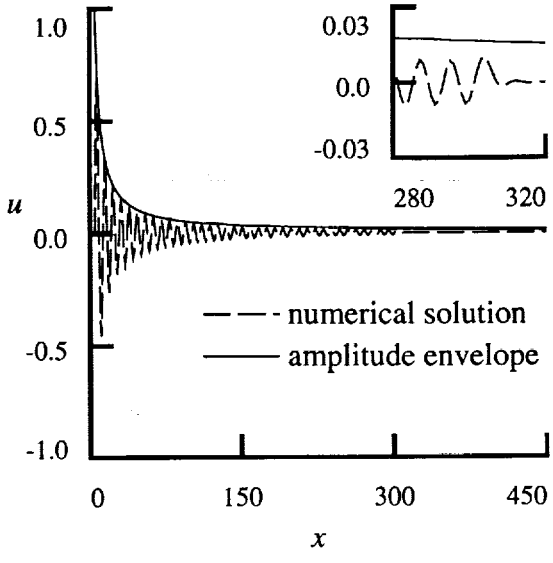

b) Fifth-order method.

Figure 6. Solution for problem 2 of category 1 with 8 points per wavelength at t = 300.

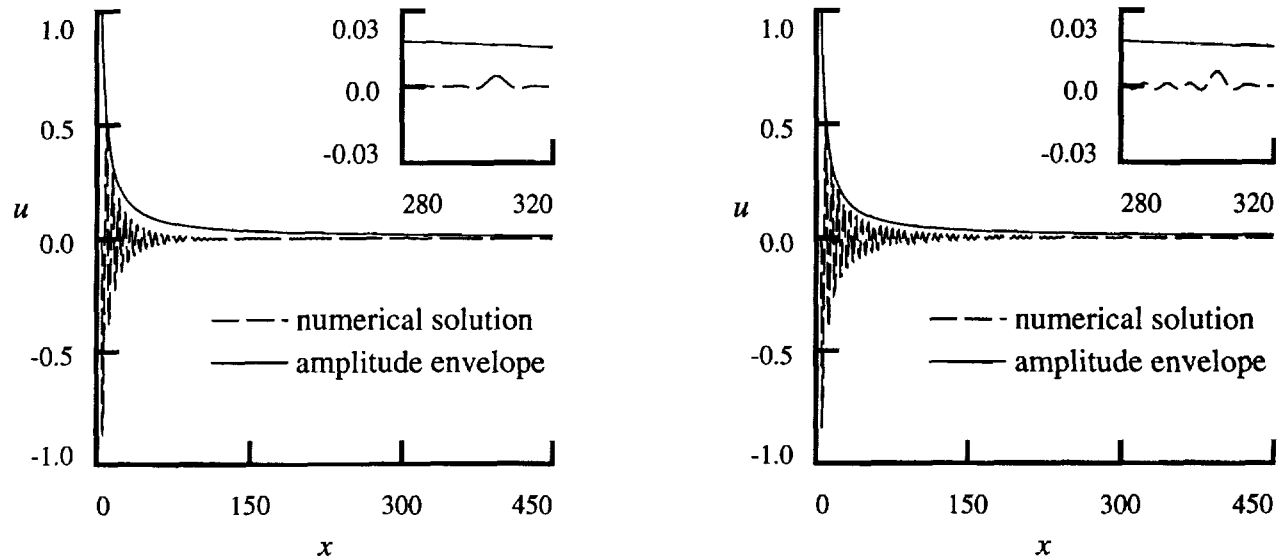

a) Fourth-order method.

b) Fifth-order method.

Figure 7. Solution for problem 2 of category 1 with 6 points per wavelength at t = 300.

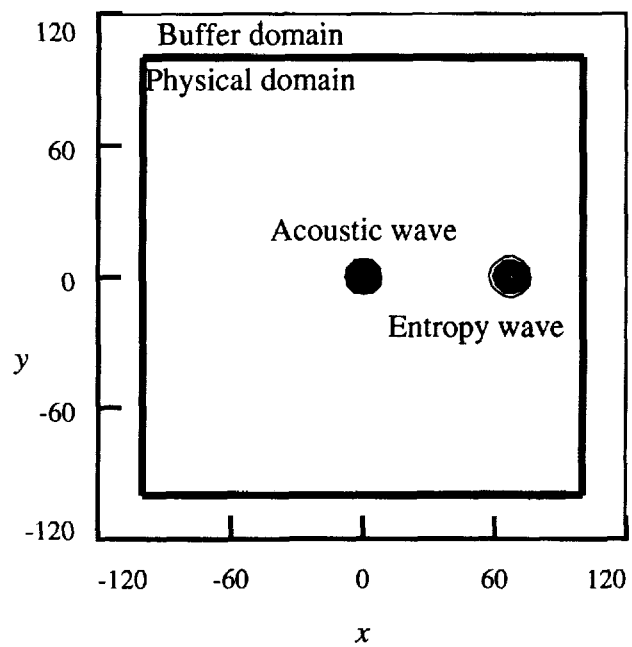

Figure 8. Initial density for problem 1 of category 3 with buffer domain around physical domain.

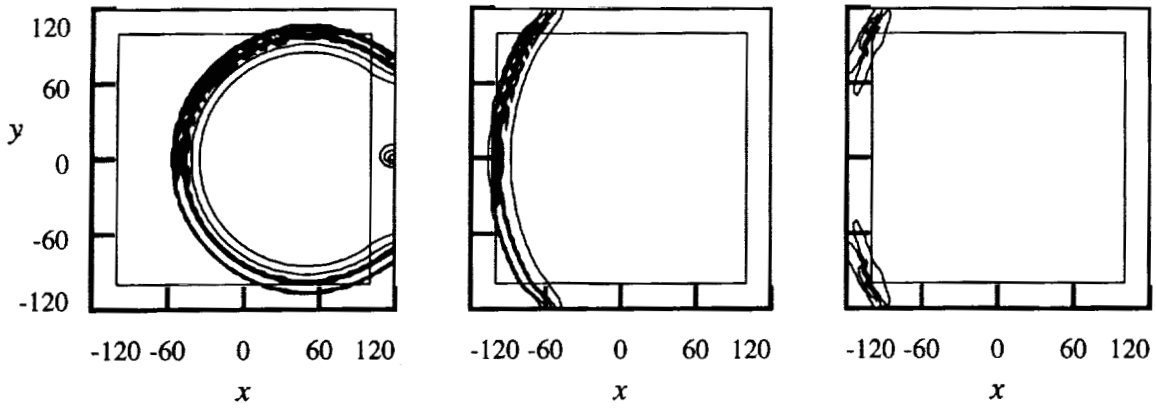

a) $t = 100$. b) $t = 200$. c) $t = 300$.

Figure 9. Density contours for problem 1 of category 3: contour increment = 0.005.

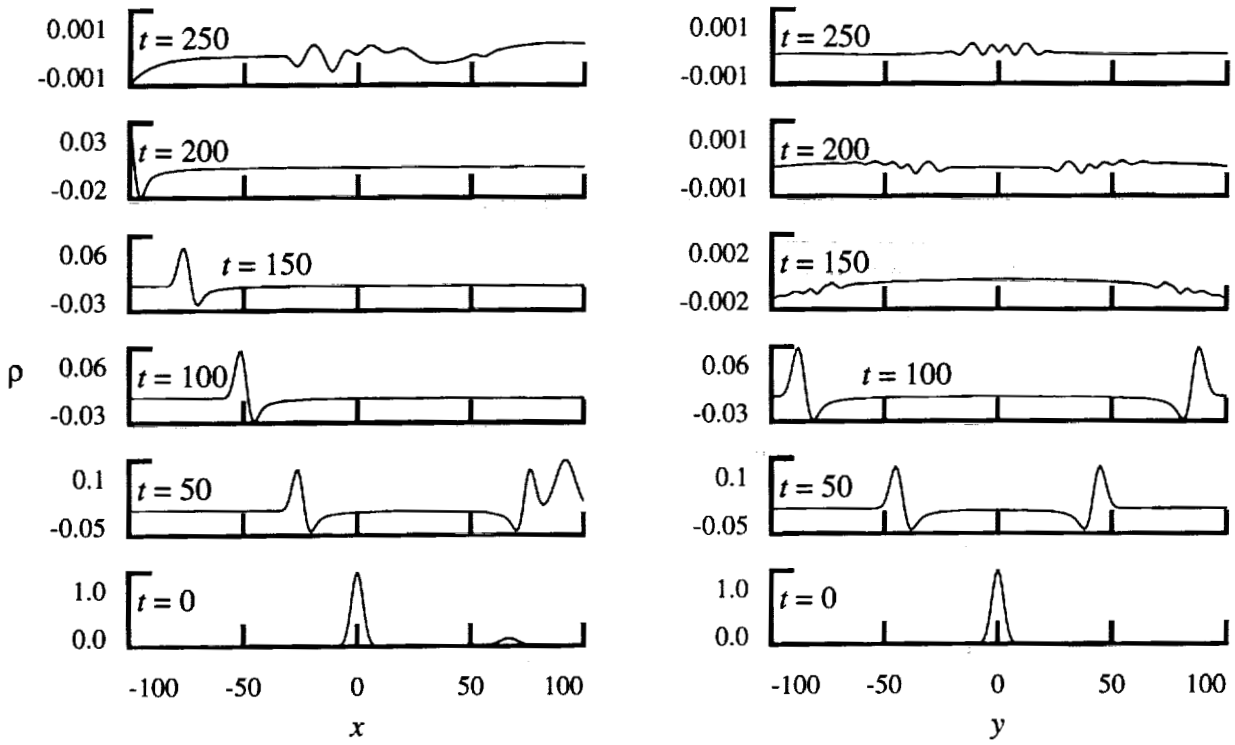

a) Solution on $y = 0$ b) Solution on $x = 0$.

Figure 10. Density for problem 1 of category 3 at t = 0, 50, 100, 150, 200, and 250.

COMPUTATIONAL AEROACOUSTICS USING HYPERBOLIC WAVE PRIMITIVES

Sanford S Davis
Fluid Mechanics Laboratory
NASA Ames Research Center
Moffett Field CA 94035

SUMMARY

A compact high order three-spatial point, two-time level dissipationless scheme is derived by matching amplification factors from differential and difference forms hyperbolic systems of partial differential equations. This approach has the advantage of allowing large time steps (Courant numbers of one) and imposing boundary conditions that are globally compatible with the wave operators. Solutions are presented for planar and spherical one dimensional acoustic waves and more complex wave patterns in two dimensions.

INTRODUCTION

Computation of steady-state solutions to fluid flow problems are now well established. In some cases the same algorithms are used for unsteady flow, but results to date are mixed. A problem with these CFD-type algorithms is dispersive error that distort propagating waves. Dispersion is caused by numerical artifacts that selectively alter phase shifts among the component wavelengths at each time step. In complex problems, it is not possible to separate algorithmic dispersion from true physical dispersion. These effects are more subtle than amplitude related artifacts (dissipation) that cause either catastrophic failure or excessive smoothing.

A new approach to dissipationless finite difference schemes was reported in Ref. 1 where dispersion errors are analyzed and compared with other published schemes. In Ref. 2 the algorithm was used to compute simple acoustic waves. In this paper, the algorithm will be rederived for a system of first order hyperbolic partial differential equations in two space dimensions. A process of operator splitting and diagonalization into primitive scalar wave equations is used to simplify the multidimensional problem. Once split into its simplest components, a basic fourth order implicit algorithm is used to advance each primitive. Solutions are presented for Category One and Category Three benchmark problems.

FINITE DIFFERENCE FORMULATION

Consider a one dimensional first order hyperbolic system $\frac{\partial \overline{U}}{\partial t} + A\frac{\partial \overline{U}}{\partial x} = 0$. If A is a constant matrix with real eigenvalues, it can be diagonalized into $P^{-1}\Lambda P$ and the system reduced to the uncoupled normal form $\frac{\partial \overline{Z}}{\partial t} + \Lambda\frac{\partial \overline{Z}}{\partial x} = 0$. The physical solution to the matrix system is simply $\overline{U} = P^{-1}\overline{Z}$ at each time step. It is sufficient to examine only the simple scalar wave equation $\frac{\partial u}{\partial t} + a\frac{\partial u}{\partial x} = 0$ to solve the one dimensional system. The dispersion relation associated with the simple wave operator is $i\omega + ika = 0$ where ω is the radian frequency and k a spatial wavenumber. The dispersion relation connects space

and time scales in a simple manner. If τ is a discrete time increment, the ratio of harmonic solutions at two subsequent times at the same spatial location x is: $\frac{u(t+\tau)}{u(t)} = \frac{e^{i(\omega(n+1)\tau+kx)}}{e^{i(\omega(n)\tau+kx)}} = e^{i\omega\tau}$. Introducing the dispersion relation to eliminate the radian frequency, the amplification factor involves two important parameters: the Courant number Cn = aτ/h and the nondimensional wavenumber kh = 2πh/λ.

$$u^{n+1} = u^n e^{-iCn\,kh} \tag{1}$$

The amplification factor has magnitude unity and its phase is directly proportional to both Cn and kh.

Next consider a plane wave defined on a uniform grid (x,t) = (jh,nτ) such that $u_j^n = e^{-i(\omega n\tau + kjh)}$. This generic plane wave is used as an intermediary to find the best *local* approximation on a two time-level, three-spatial point stencil. The molecule is:

$$a_0 u_j^{n+1} + a_1 u_{j-1}^{n+1} + a_2 u_{j+1}^{n+1} = b_0 u_j^n + b_1 u_{j-1}^n + b_2 u_{j+1}^n \tag{2}$$

Substitute the discrete plane wave into Eq. (2) and use Eq. (1) to obtain the formula:

$$\frac{u^{n+1}}{u^n} = \frac{b_0 + b_1 e^{-ikh} + b_2 e^{ikh}}{a_0 + a_1 e^{-ikh} + a_2 e^{ikh}} = e^{-iCn\,kh} \tag{3}$$

If the constants are real, and if $b_1 = a_2$, $b_0 = a_0$, and $b_2 = a_1$, the ratios are complex conjugates and Eq. (2) is dissipation free. The two remaining constants are computed by matching the first and third terms in Taylor series expansions about kh = 0. The constants depend only on the Courant number and the final fourth order algorithm is:

$$\begin{aligned}(Cn-1)(Cn-2)u_{j-1}^{n+1} - 2(Cn-2)(Cn+2)u_j^{n+1} + (Cn+1)(Cn+2)u_{j+1}^{n+1} = \\ (Cn+1)(Cn+2)u_{j-1}^n - 2(Cn-2)(Cn+2)u_j^n + (Cn-1)(Cn-2)u_{j+1}^n\end{aligned} \tag{4}$$

This algorithm has been derived previously by others using conventional finite difference approaches. It can be considered "compact" since fourth order is achieved not with five spatial grid points at each time level, but by using the space-time connection afforded by the dispersion relation to maximize accuracy. If five points at each time level are allowed, an eighth order algorithm may be derived (Ref. 1).

Some features of this derivation are: (1) It does not rely on separate finite difference approximations in space and time; (2) It yields maximum accuracy for a given mesh stencil; (3) The procedure can be extended to systems with non constant coefficients (which can arise from linear but variable coefficient problems, non linear effects, stretched meshes, or combinations thereof); and (4) Explicit recognition of the wavenumber kh=2πh /λ as a fundamental parameter in the analysis.

The two dimensional first order system $\frac{\partial \overline{U}}{\partial t} + A\frac{\partial \overline{U}}{\partial x} + B\frac{\partial \overline{U}}{\partial y} = 0$ is analyzed in a similar manner but with a significant difference: As above, a local harmonic solution of the form $e^{ikx+ily+i\omega t}$ is inserted into the equation to define the matrix dispersion relation $i\omega I + ikA + ilB = 0$. Following the same sequence as above, solutions at subsequent time

steps are related by $U(t+\tau) = e^{il\omega\tau}U(t)$ or, in terms of the spatial scales $U(t+\tau) = e^{-iApkh\,-iBplh}U(t)$. In this formula, p is the ratio τ/h, kh is 2πh/λ in the x direction and lh is 2πh/λ in the y direction. The basic formula now involves matrix exponentials. Next consider a plane wave defined on a discrete grid (x,y,t) = (jh,mh,nτ) such that $u^n_{j,m} = e^{-i(\omega\, n\tau + k\, jh + l\, mh)}$. The discrete form of the incremental solution is now $U^{n+1}_{j,m} = e^{-iApkh\,-iBplh}U^{\,n}_{j,m}$. One could attempt to split the operator in an obvious manner, but this would not be appropriate since matrix exponential do not commute; e.g. $e^{A+B} \neq e^Ae^B \neq e^Be^A$.

Instead, a process attributed to G. Strang in Ref. 3 is used that is formally correct to second order in the matrix exponentials:

$$U^{n+1}_{j,m} = \frac{1}{2}(e^{-iApkh}e^{-iBplh} + e^{-iBplh}e^{-iApkh})\; U^n_{j,m} \qquad (5)$$

This alternating splitting was found to be very accurate; the order of computed solutions seem to be closer to fourth than second order. Each stage in the splitting is equivalent to a one dimensional matrix equation in the indicated coordinate direction; that is the formula $U^* = e^{-iApkh}\; U^n$ implies that U* is the solution of $\frac{\partial \overline{U}}{\partial t} + A\frac{\partial \overline{U}}{\partial x} = 0$. These one dimensional matrix equations can be solved using the eigenfunction procedure outlined at the beginning of this section.

BOUNDARY CONDITIONS FOR ONE DIMENSIONAL INITIAL-BOUNDARY-VALUE PROBLEMS

Classical explicit methods such as Lax-Wendroff and its variants are suitable tools for the numerical integration of initial-value hyperbolic systems. Difficulties arise when boundary conditions are imposed. This point is discussed in Refs. 4 and 5. There are three cases to be considered depending on the eigenvalue spectrum of A. If A is positive definite and initial values are given on the half line t=0, x>0, boundary values along the line x=0, then the problem is well posed in the first quadrant. If A is negative definite and initial values are given on the half line t=0, x<0, boundary values along the line x=0, then the problem is well posed in the second quadrant. If a two-point boundary value problem is given, and A possesses both positive and negative eigenvalues, forward and backward waves are generated. The problem is now well posed if components of $\overline{U}$ on each boundary match the number of positive and negative eigenvalues. This is rarely true in practical problems.

The new method used here for radiation boundary conditions is to impose boundary conditions on the left for normal solutions with positive eigenvalues and boundary conditions on the right for those with negative eigenvalues. In practice, these imposed boundary conditions are not given explicitly, but must be deduced from the solution at the previous time step. Each one dimensional matrix equation is solved as described and then reassembled as outlined in the previous section.

CATEGORY ONE, PROBLEM ONE

The initial pulse is given as $u(x) = .5e^{(-x/3)^2 \ln 2}$ and the exact solution of $\frac{\partial u}{\partial t} + \frac{\partial u}{\partial x} = 0$ is u(x,t) = u(x-t). A numerical solution is required on the domain -20(1)450. This simple problem can be analyzed precisely from an analysis of dispersion errors. The dispersion plot for two Courant numbers are shown in Fig. 1. Over the allowable range of wavenumbers from 0 to π the exact slope is -Cn from Eq. (1) and is depicted by the straight lines. The discrete part of Eq. (3) is shown as a solid line and a second order form of Eq. (2) -- a standard Crank-Nicolson scheme centered at the half-time step -- is shown dashed. The dispersion plot shows that if Cn=1 the algorithm is an exact solution while at Cn=.5 only wave numbers to about 1.3 are correctly resolved. The initial pulse has significant energy content to about kh=1.8 from the chosen mesh. Predicted pulses at t=100,200,300, and 400 are shown in Fig. 2 for Cn=.5. The incorrect phase resolution of short waves in the range kh=1.3-1.8 leaves a small but growing "tail." Note that the amplitude of the signal is reduced due to redistribution of wave energy into the tail as this algorithm has no dissipation. Figure 3 presents the same information but at Cn=1. The wave is predicted exactly and will remain exact for all times. This behavior could have been predicted from Fig. 1 alone.

CATEGORY ONE, PROBLEM TWO

The simple spherical wave $\frac{\partial u}{\partial t} + \frac{u}{r} + \frac{\partial u}{\partial r} = 0$ is to be solved on the domain 5(1)450. The exact solution is $u(r,t) = 5\sin(\omega t - \omega r + 5\omega)/r$. The presence of the term not involving first derivatives in the equation requires some analysis. Consider a plane wave solution $e^{i(\omega t + kx)}$ from which follows the dispersion relation $i\omega + ik + 1/r = 0$. Using this relation to eliminate the radian frequency from the amplification factor, the analog to Eq. (1) is:

$$u^{n+1} = u^n e^{-iCn\,kh - \tau/r} = u^n e^{-iCn\,kh} e^{-\tau/r} \qquad (6)$$

This splitting property of the scalar exponential suggests a two step approach. (1) The formula $u^* = u^n e^{-\tau/r}$ implies that u* is the solution of the ordinary time-domain differential equation $\frac{\partial u}{\partial t} + \frac{u}{r} = 0$. This equation can be solved at any r using standard methods. (2) The formula $u^{n+1} = u^* e^{-iCn\,kh}$ is simply a representation of the scalar wave equation. The outcome after two steps (which commute with one another from properties of the exponential) is the updated solution. Note that the first step does not involve the wavenumber k since no spatial derivatives are involved.

Solutions are required for the two radian frequencies $\omega=\pi/3$ and $\omega=\pi/4$ corresponding to 6 and 8 points per wavelength respectively. Only the more severe test case $\omega=\pi/4$ will be presented here. Computations for Cn (equivalent to time step τ) of 0.125 and 1.0 will be shown. Figure 4 presents the general character of the solution. The value of Cn is 0.125 and the time is 400. The wave envelope decays at 1/r and the wave front, although decayed, has progressed to r=405. The problem for Cn=1 looks similar at this scale. A microscopic view near the wave front for these two Courant numbers is shown in Figs. 5 and 6. Thirty two hundred time steps were required for the wave to reach x=405 at Cn=.125 as depicted in Fig. 5. Dispersion errors have severely compromised the wave front. Figure 6 indicates the case where Cn was increased to the "perfect resolution" value of 1.0. The wave is predicted exactly. Even though a microscopic analysis of the simulation shows significant differences, the global patterns as exemplified by Fig. 4 for

Cn=.125 may be adequate for certain applications. At any rate, it is always desirable to use the largest time step possible.

CATEGORY THREE, PROBLEM ONE

The problem to be solved is

$$\frac{\partial}{\partial t}\begin{bmatrix}\rho\\u\\v\\p\end{bmatrix}+\begin{bmatrix}U & a & 0 & 0\\0 & U & 0 & a\\0 & 0 & U & 0\\0 & a & 0 & U\end{bmatrix}\frac{\partial}{\partial x}\begin{bmatrix}\rho\\u\\v\\p\end{bmatrix}+\begin{bmatrix}0 & 0 & a & 0\\0 & 0 & 0 & 0\\0 & 0 & 0 & a\\0 & 0 & a & 0\end{bmatrix}\frac{\partial}{\partial y}\begin{bmatrix}\rho\\u\\v\\p\end{bmatrix}=0 \qquad (7)$$

where x, y, and t are physical quantities and the Mach number M = U/a = 0.5. The perturbation density, velocities, and pressure are normalized by ρ_∞, a, and $\rho_\infty a^2$ respectively. Initial conditions are given as a combination of an acoustic pulse at the origin and a combined entropy/vortex centered at (x,y)=(67,0). Numerical solutions are required on a 201 x 201 mesh centered at the origin with step size one. Initial conditions were chosen so that the acoustic and entropy/vortex wave fronts first meet at the outflow boundary x = 100. This problem was designed to test the propagation algorithm and imposition of radiation boundary conditions.

The solution process follows the following steps: (1) Reduce the equation to component one dimensional matrix equations as described above. The matrices A and B have eigenvalues [U+a,U-a,U,U] and [a,-a,0,0] respectively. An eigenvector decomposition reduces each direction to four individual scalar wave equations with wave speeds indicated by the eigenvalues. (2) Solve each of the primitive scalar wave equations using the fourth order algorithm given in Eq. (4). Choose the time step so that the Courant number based on the step size and sound speed is unity. This will give exact simulation for the component acoustic sweeps. There is a second Courant number based on the convection speed and it is 0.5. (3) Boundary conditions are applied to scalar waves that exit the computational domain using a four point two time-level implicit scheme at and just inside the boundary. (4) Boundary conditions for waves that enter the computational domain must be imposed. They are extrapolated from known solutions at the previous time level one grid point beyond the boundary. (5) Reassemble the physical components at each time step. In summary, four one-dimensional vector PDEs are solved at each time step. Each matrix problem, in turn, reduces to four primitive scalar problems. A total of sixteen elementary primitives of the form $\frac{\partial u}{\partial t}+\lambda\frac{\partial u}{\partial x}=0$ are solved at each time step. Much of this work is mutually independent and may be natural for parallel processing applications.

Initial computations are presented to show the effect of not commuting matrix operations as in Eq. (5). Figures 7 and 8 show contour plots of density from numerical solutions of Eq. (7) at time t=30. Figure 7 compares density contours at t=30 with initial condition shown dotted. The acoustic waves are the larger circles that convect in the x direction and propagate with the speed of sound in all directions. The wave behaves as a ripple with a long tail (not shown here) that is similar to throwing a pebble in a moving stream. The entropy wave is physically translated 15 steps to the right based on its speed M = 0.5. Figure 8 shows the same information except that an x sweep is followed by a y sweep, e.g. only half the algorithm in Eq. (5). The acoustic waves seem to be unaffected, but the entropy wave is no longer isotropic. Numerical experiments show that a computation

with the sweeps reversed would reverse the sense of the distorted entropy wave. Alternating directions at each time step is also a viable strategy. These simulations were compared with other strictly second order methods. The second order method left an oscillatory trail that is a severely limiting numerical artifact.

Figures 9 and 10 present line graphs of the solution vector at time 60. Figure 9 shows the waves on the axis of symmetry, y=0. The backward acoustic wave is characterized by $\rho = p = -u$. The forward wave is interfering with the entropy/vortex and results in the complex pattern near the right outflow boundary. The tail of the clockwise vortex is visible in the v profile and is almost halfway out of the computational domain. The pressure is unaffected by the entropy/vortex wave and only the acoustic portion of the pressure is evident near the boundary. Constructive interference of the density is apparent near the right boundary.

Figure 10 shows the solution vector along the vertical outflow boundary x=100. The density field should be exactly symmetric about the horizontal centerline y=0. The fact that there is some asymmetry indicates that the boundary conditions are not exactly correct. However, this misalignment does not seem to have a long range effect as shown in Fig. 11 where the acoustic wave (all that remains) is shown on the vertical boundary at time 100.

CONCLUSIONS

A class of dissipationless algorithms were used to compute one and two dimensional wave problems with high fidelity. Simple one dimensional waves were examined and distortion traced to phase error artifacts of the finite difference scheme. Spherical wave were found to be well predicted using a simple splitting scheme. Finally, relatively complex two dimensional acoustic/propagation problems were found to be well suited to a splitting scheme using a sequence of elementary one dimensional wave solutions.

The decomposition into wave primitives has the following advantages: (1) it allows large time steps corresponding to Courant numbers of about one, and (2) it allows the imposition of natural boundary conditions without any *a priori* assumptions regarding solution behavior.

The class of linear systems of hyperbolic equations in two independent variables with constant coefficients can be analyzed completely. These equations always admit exponential solutions that can be Fourier analyzed and discretized as shown here. Other problems using equation sets with non-constant coefficients (or variable meshes) and nonlinear problems are under study.

REFERENCES

1. Davis, S. S.: A Space-Time Discretization Procedure for Wave Propagation Problems. NASA TM-102215, November 1989.

2. Davis, S. S: Low Dispersion Finite Difference Methods for Acoustic Waves in a Pipe. *J. Acoust. Soc. Amer.*, vol. 90, no. 5, November 1991, pp. 2775-2781.

3. Burstein, S. Z,: Numerical Methods in Multidimensional Shock Flow. *AIAA J.*, vol. 12, no. 12, December 1964, pp. 2111-2117.

4. Strikwerda, John C.: *Finite Difference Schemes and Partial Differential Equations.* Wadsworth & Brook/Cole, 1989, pp. 9-11.

5. Mitchell, A. R.: *Computational Methods in Partial Differential Equations,* John Wiley & Sons, 1969, pp.168-170.

FIGURE CAPTIONS

Figure 1. Dispersion plot for second and fourth order dissipationless finite difference schemes. The curves for exact resolution are straight lines with slope -Cn. Curves for Cn of 0.5 and 1.0 are shown. Solid: Fourth order algorithm, Dash: Second order algorithm.

Figure 2. Pulse profiles at time 100, 200, 300, and 400. Step size (Courant number) = .5.

Figure 3. Pulse profiles at time 100, 200, 300, and 400. Step size (Courant number) = 1.0.

Figure 4. Spherical wave spatial pattern at time 400. The Courant number is 0.125.

Figure 5. Spherical wave spatial pattern at time 400 near the leading edge. The Courant number is 1.0. Symbols: Computed solutions at discrete mesh points. Dash: Exact solution.

Figure 6. Spherical wave spatial pattern at time 400 near the leading edge. The Courant number is 0.125. Symbols: Computed solutions at discrete mesh points. Dash: Exact solution.

Figure 7. Density contours at initial instant and at time 30. Contours of density 0.01, 0.02, and 0.03 shown.

Figure 8. Density contours at time 30. Same as figure 7 except on x-sweep followed by y-sweep with no contributions from communed operator.

Figure 9. Solution vector along the horizontal axis of symmetry Y=0 at time 60.

Figure 10. Solution vector along the outflow boundary at X=100 at time 60.

Figure 11. Acoustic wave along the outflow boundary at X=100 at time 100.

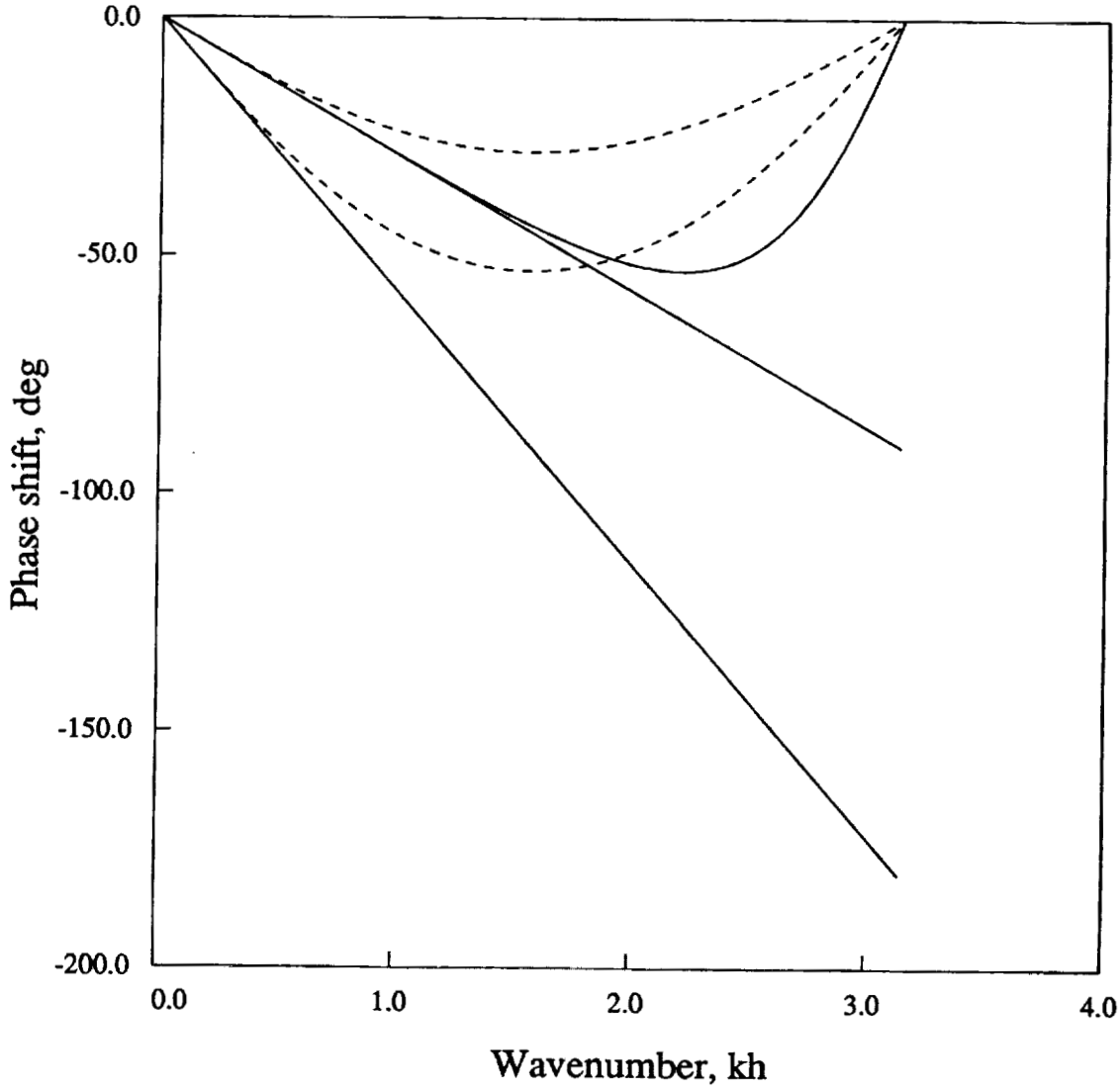
0.0
-50.0
-100.0
-150.0
-200.0
Phase shift, deg
0.0
1.0
2.0
3.0
4.0
Wavenumber, kh

Figure 1

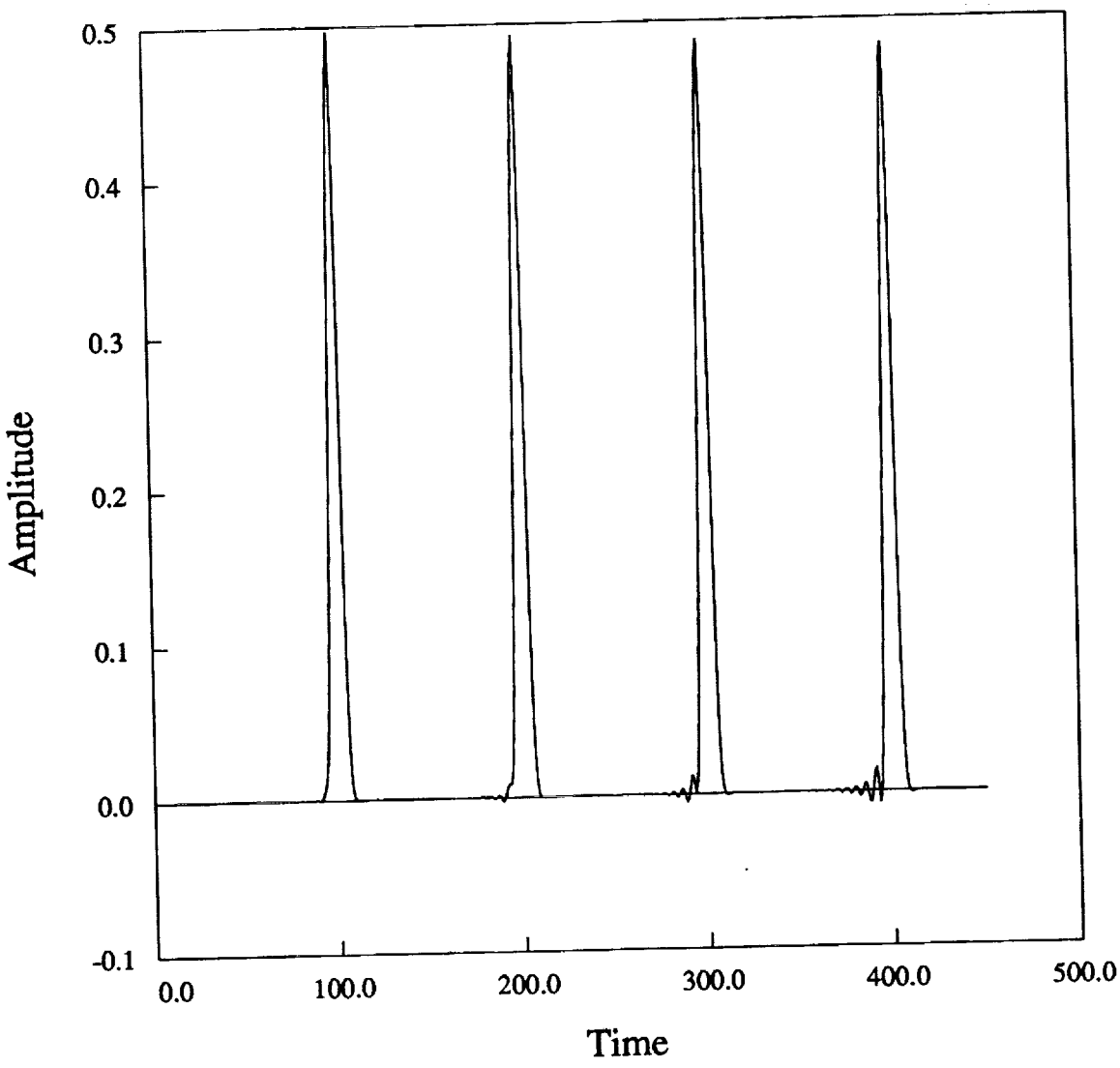

Figure 2

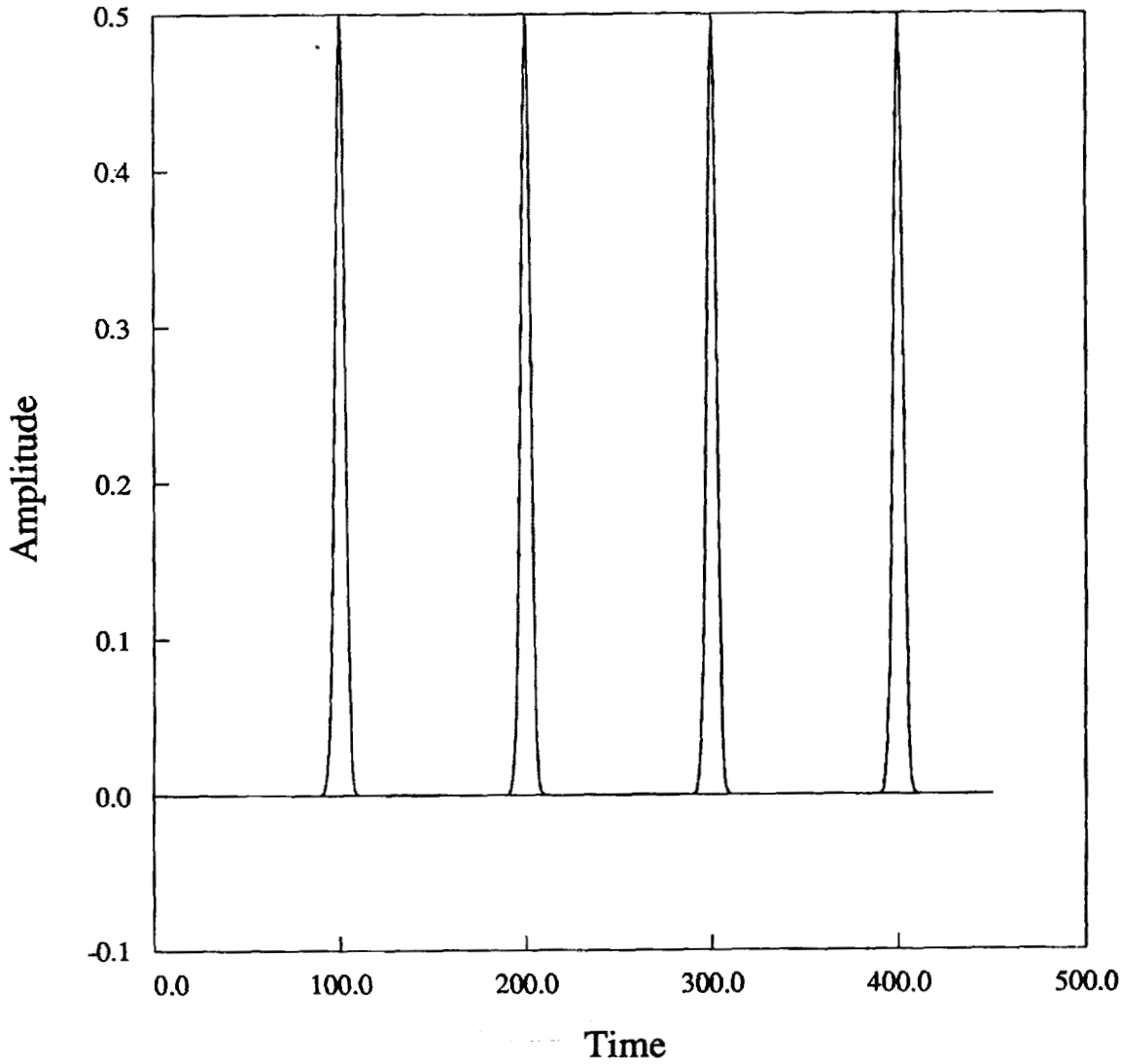

Figure 3

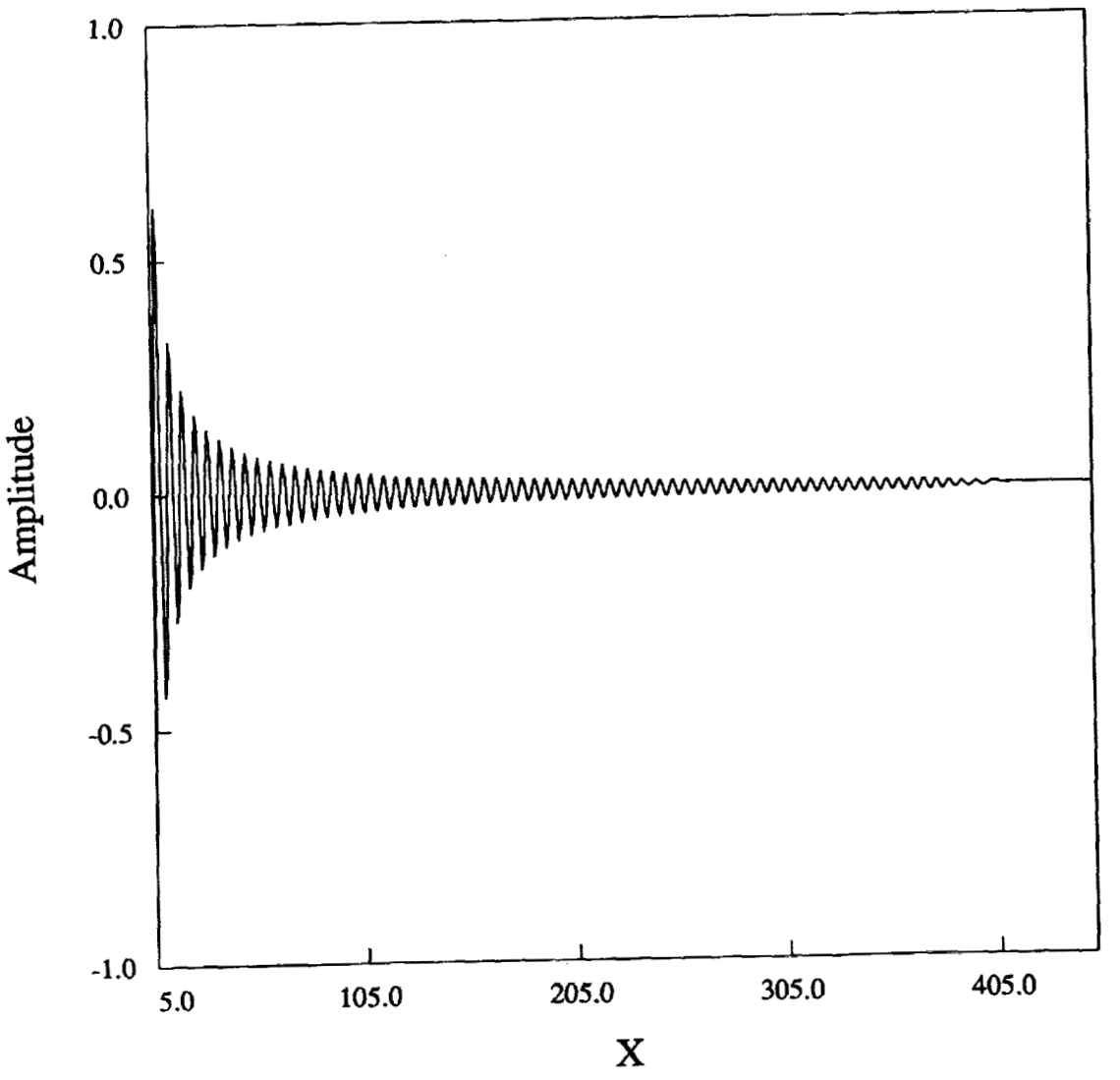

Figure 4

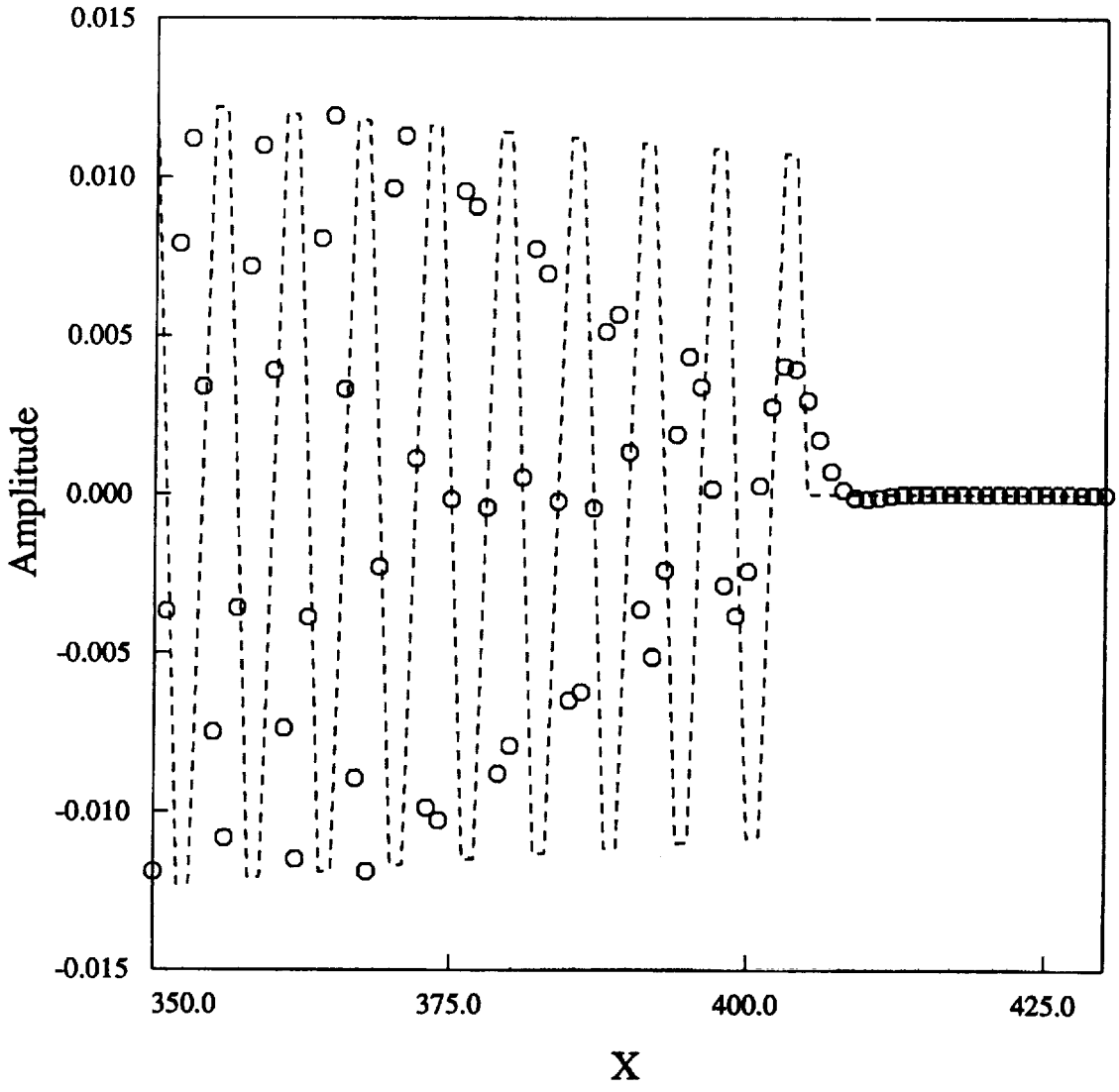
0.015
0.010
0.005
0.000
-0.005
-0.010
-0.015
Amplitude
350.0
375.0
400.0
425.0
X

Figure 5

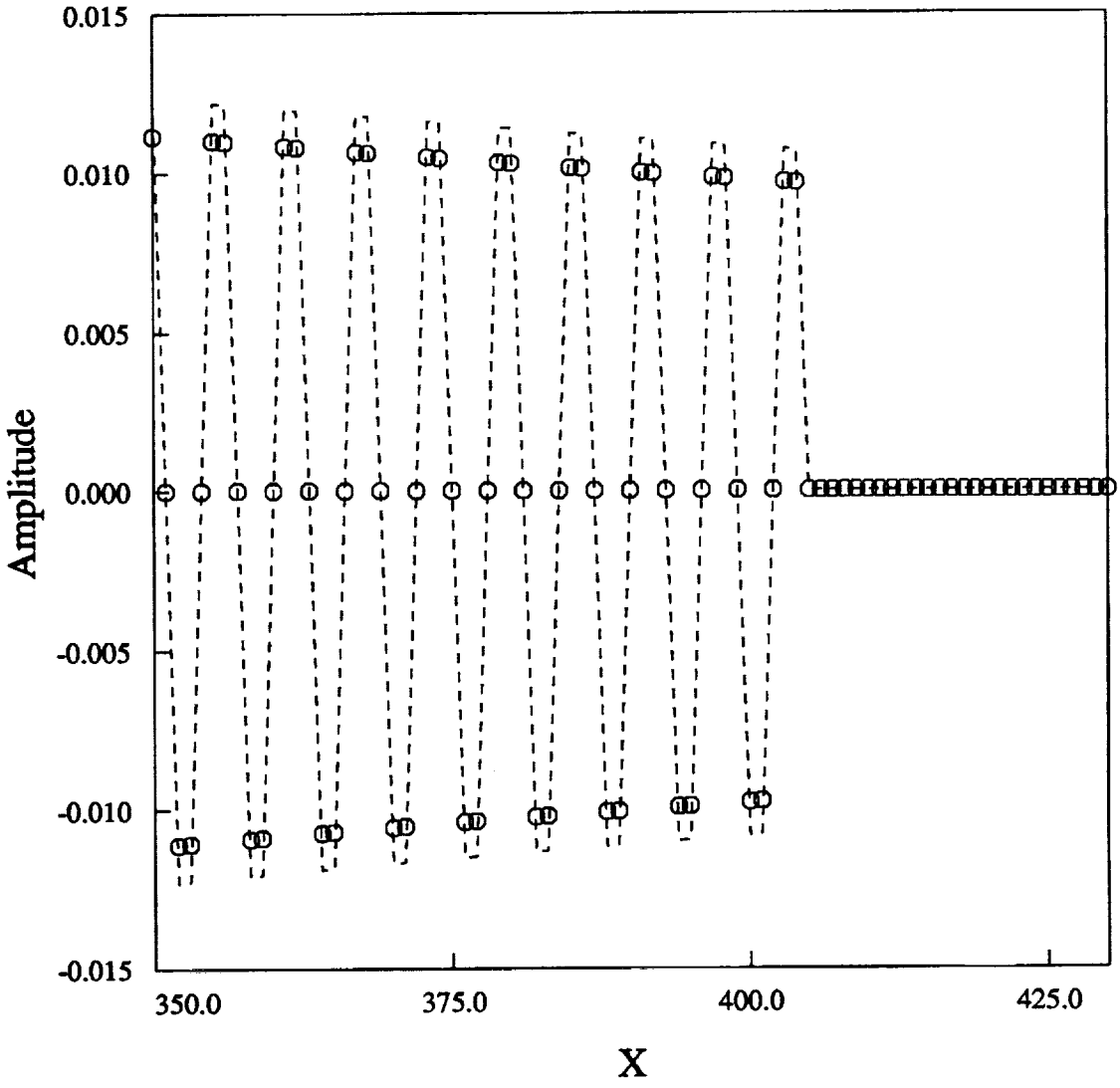
0.015
0.010
0.005
0.000
-0.005
-0.010
-0.015
Amplitude
350.0
375.0
400.0
425.0
X

Figure 6

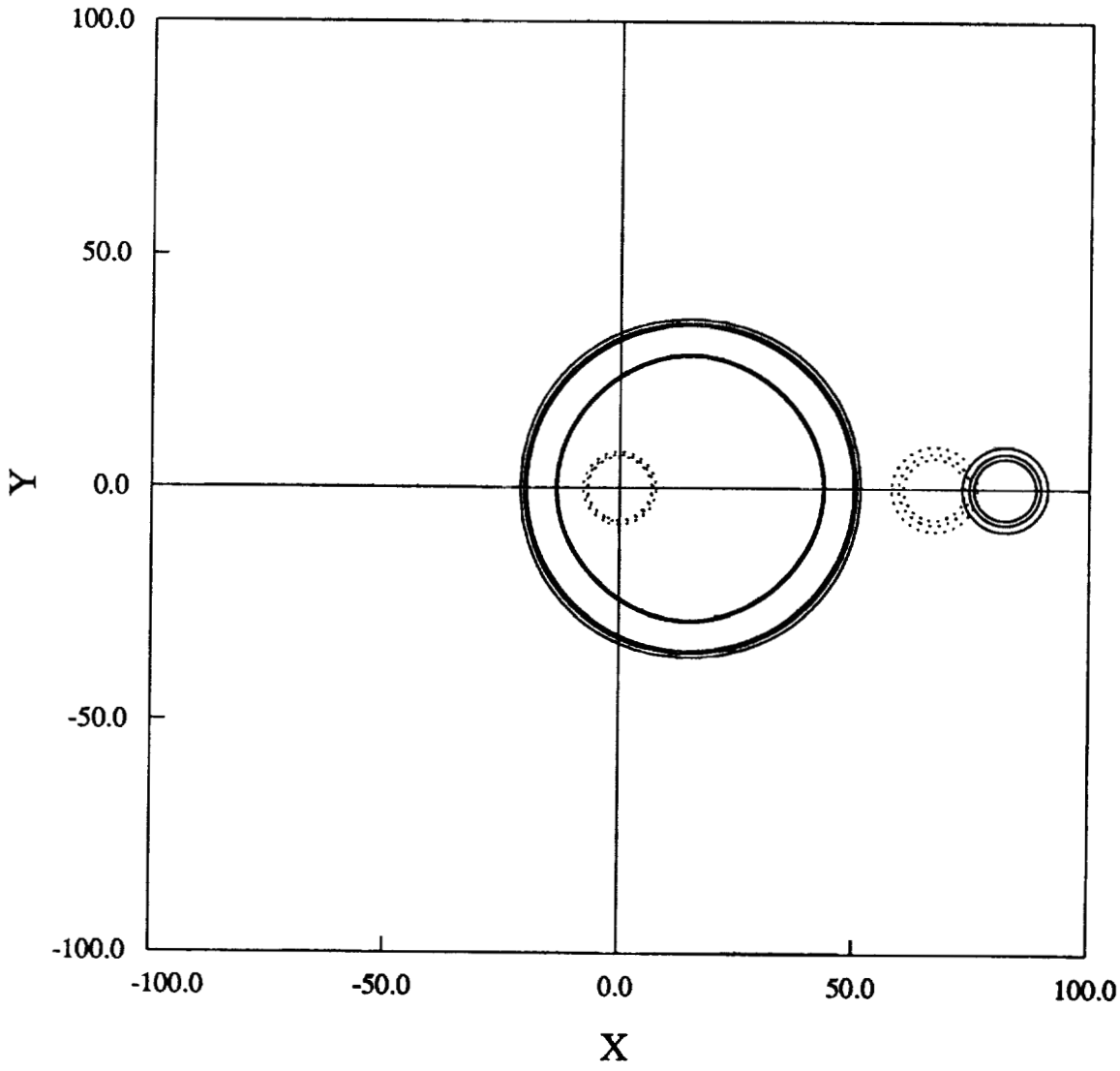

Figure 7

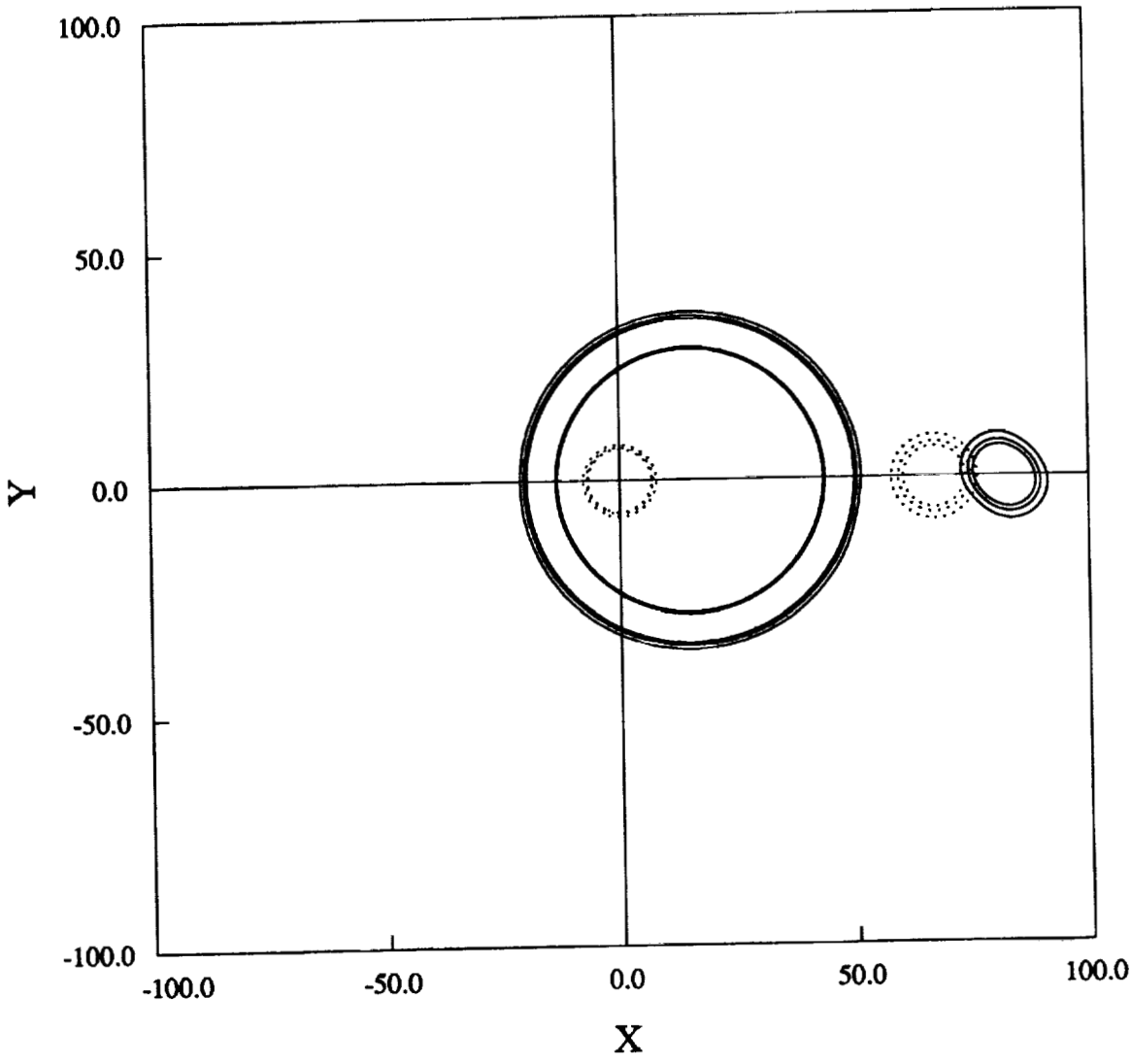

Figure 8

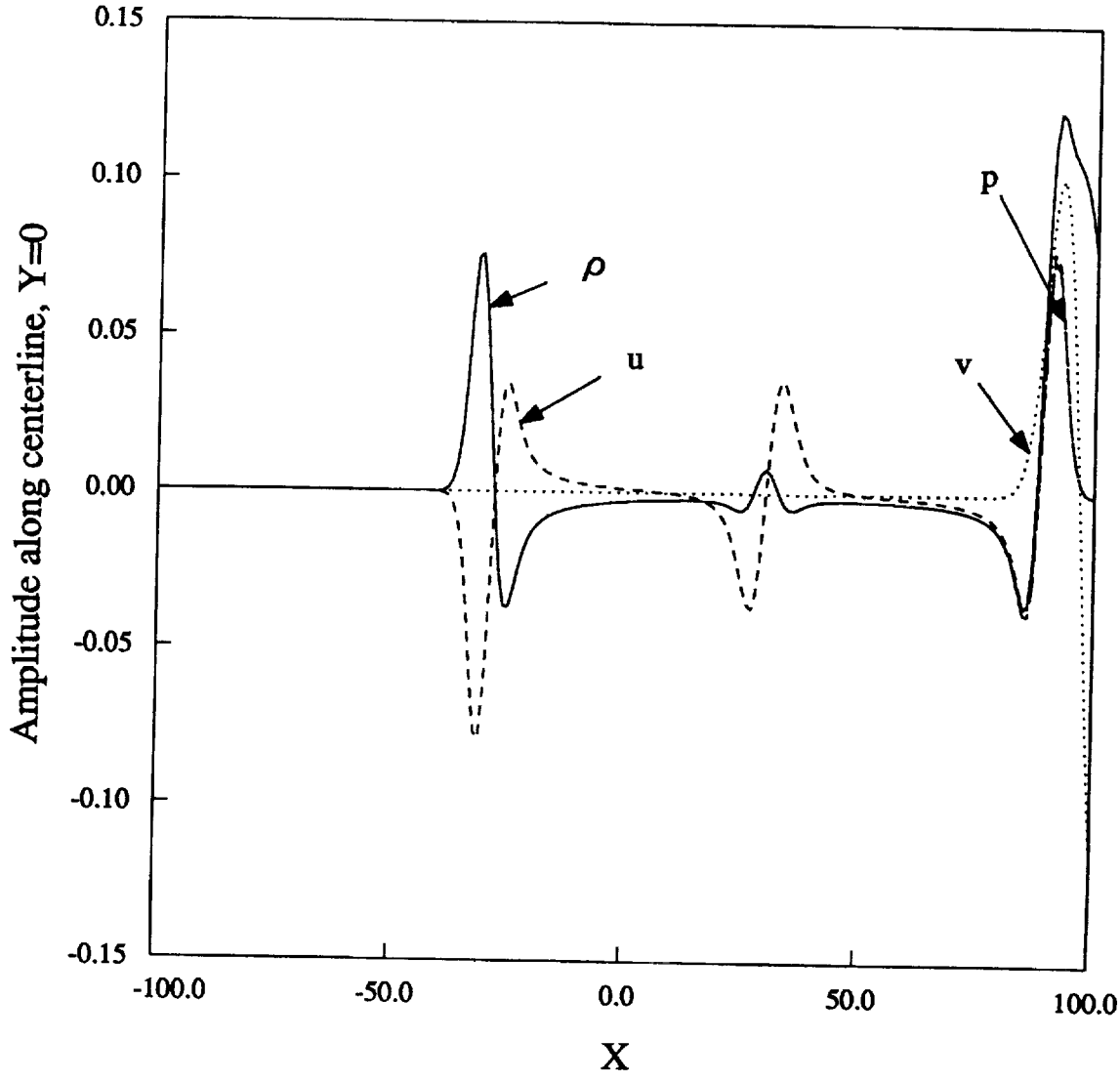
0.15
0.10
0.05
0.00
-0.05
-0.10
-0.15
Amplitude along centerline, Y=0
-100.0
-50.0
0.0
50.0
100.0
X
ρ
u
v
p

Figure 9

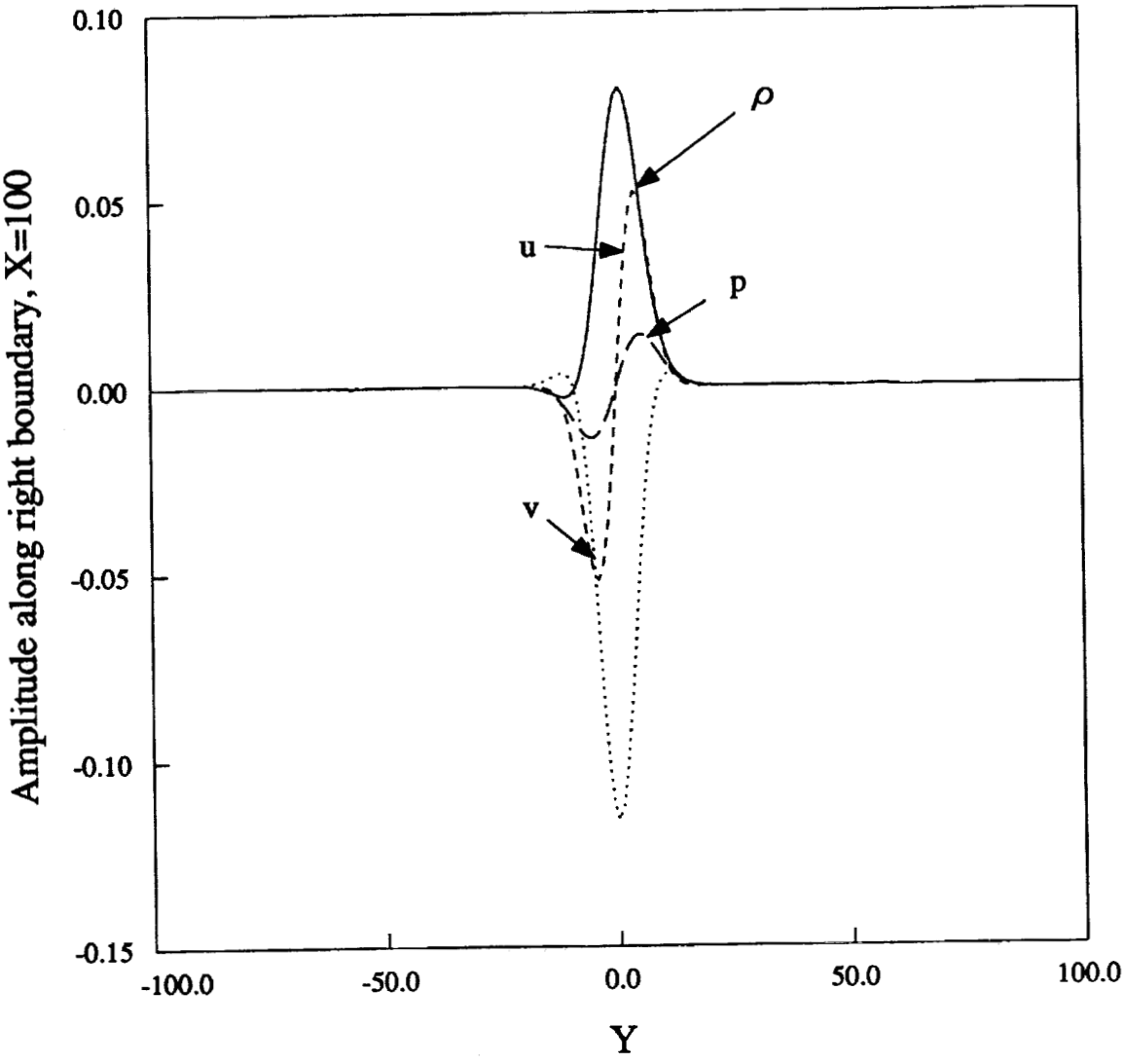
0.10
0.05
0.00
-0.05
-0.10
-0.15
-100.0
-50.0
0.0
50.0
100.0
Y
Amplitude along right boundary, X=100
ρ
u
p
v

Figure 10

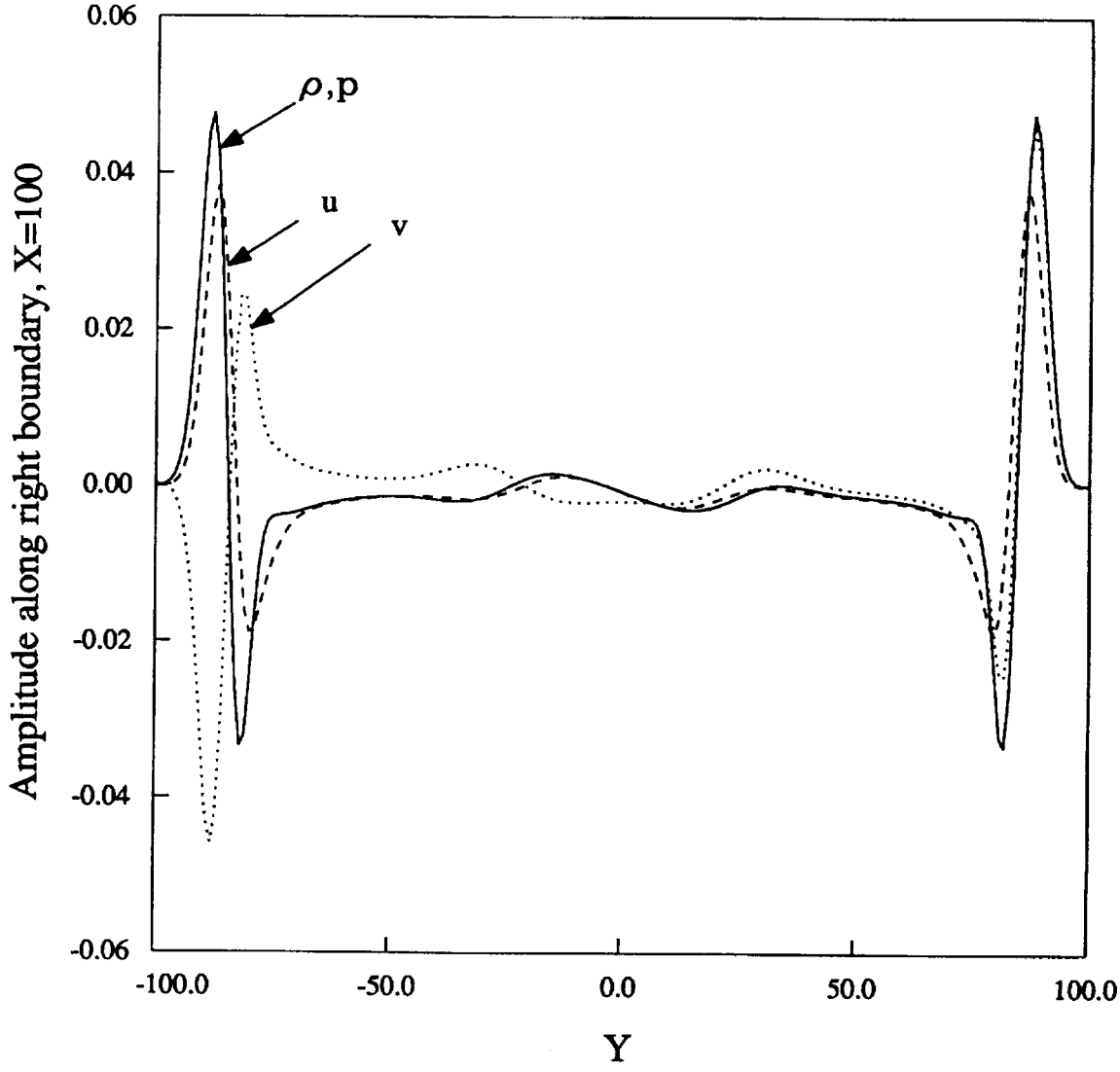
0.06
0.04
0.02
0.00
-0.02
-0.04
-0.06
Amplitude along right boundary, X=100
ρ,p
u
v
-100.0
-50.0
0.0
50.0
100.0
Y

Figure 11

COMPARATIVE STUDY OF NUMERICAL SCHEMES OF TVD3, UNO3-ACM AND OPTIMIZED COMPACT SCHEME

Duck-Joo, Lee*, Chang-Jeon, Hwang**, Duck-Kon, Ko** and Jae-Wook, Kim**
Department of Aerospace Engineering
Korea Advanced Institute of Science and Technology
Taejon, Korea

SUMMARY

Three different schemes are employed to solve the benchmark problem. The first one is a conventional TVD-MUSCL(Monotone Upwind Schemes for Conservation Laws) sheme. The second scheme is a UNO3-ACM(Uniformly Non-Oscillatory-Artifitial Compression Method) scheme. The third scheme is an optimized compact finite difference scheme modified by us: the 4th order Runge Kutta time stepping, the 4th order pentadiagonal compact spatial discretization with the maximum resolution characteristics. The problems of category 1 are solved by using the second(UNO3-ACM) and third(Optimized Compact) schemes. The problems of category 2 are solved by using the first(TVD3) and second(UNO3-ACM) schemes. The problem of category 5 is solved by using the first(TVD3) scheme. It can be concluded from the present calculations that the Optimized Compact scheme and the UNO3-ACM show good resolutions for category 1 and category 2 respectively.

INTRODUCTION

Schemes of high accuracy and resolution have been developed with two different viewpoints. One is to have high resolutions of discontinuities such as shock and contact discontinuity. The other is to have a overall high resolution with spectral accuracy. The former has been concerned by aerodynamists, on the otherhand, the latter has been developed by turbulence researchers using DNS(Direct Numerical Simulation). In the meantime, reseachers of CAA(Computational AeroAcoustics) have been devised the better scheme which have minimal dissipation and dispersion errors in order to simulate not only acoustic propagation but also source generations in aeroacoustic field.

Three different schemes are employed here. The first one is the conventional Roe-MUSCL-TVD3 scheme, which is widely used in the CFD field. The second scheme is a UNO3-ACM scheme. The resolution of UNO3 scheme is enhanced by ACM at contact discontinuity. The last one is an Optimized Compact scheme modified by us for maximum resolution characteristics and minimum dispersion errors. The problems of category 1 are solved by using the second(UNO3-ACM) and third(Optimized Compact) schemes. The problems of category 2 are solved by using the first(TVD3) and second(UNO3-ACM) schemes. The problem of category 5 is solved by using the first(TVD3) scheme.

---

* **Associate Professor**
** **Graduate Student**

NUMERICAL ALGORITHM

TVD3-MUSCL

In order to know the performance of the convetional TVD scheme for CFD, we employ the 3rd order TVD-MUSCL-Roe scheme. Detailed descriptions are as follows(ref.1):

Governing Equations

$$\frac{\partial \mathbf{U}}{\partial t} + \frac{\partial \mathbf{F}}{\partial x} = \alpha \frac{dA}{Adx}\mathbf{Q} \tag{1}$$

where

$$\mathbf{U} = (\rho,\ \rho u,\ e)^T$$
$$\mathbf{F} = (\rho u,\ \rho u^2 + p,\ (e+p)u)^T$$
$$\mathbf{Q} = -(\rho u,\ \rho u^2,\ (e+p)u)^T$$

Here, α is set to 0 for the category 2 problem and 1 for the category 5 problem.

We employ the 2nd order Runge-Kutta method for time stepping as below(ref.1):

1st step

$$\mathbf{U}_j^* = \mathbf{U}_j^n - (\Delta t/2)[\ (\tilde{\mathbf{F}}_{j+1/2}^n - \tilde{\mathbf{F}}_{j-1/2}^n)/\Delta x + \alpha(dA/Adx)\mathbf{Q}^n\ ] \tag{2}$$

2nd step

$$\mathbf{U}_j^{n+1} = \mathbf{U}_j^n - \Delta t[\ (\tilde{\mathbf{F}}_{j+1/2}^* - \tilde{\mathbf{F}}_{j-1/2}^*)/\Delta x + \alpha(dA/Adx)\mathbf{Q}^*\ ] \tag{3}$$

The numerical flux, $\tilde{F}$ based on Roe's approximate Riemann solver with entropy fix is employed(ref.2).

$$\tilde{\mathbf{F}}_{j+1/2} = (1/2)(\mathbf{U}_{j+1/2}^R + \mathbf{U}_{j+1/2}^L + \mathbf{R}_{j+1/2}\,\Phi_{j+1/2}) \tag{4}$$

where the lth element $\phi_{j+1/2}^l$ of $\Phi_{j+1/2}$ are written as:

$$\phi_{j+1/2}^l = -\psi(a_{j+1/2}^l)\alpha_{j+1/2}^l \tag{5}$$

where

$$\alpha_{j+1/2} = \mathbf{R}_{j+1/2}^{-1}(\mathbf{U}^R - \mathbf{U}^L)_{j+1/2}$$

and

$$\psi(z) = \begin{cases} |z| & \text{if } |z| \geq \delta_1 \\ (z^2 + \delta_1^2)/2\delta_1 & \text{if } |z| < \delta_1 \end{cases} \tag{6}$$

where δ_1 is some small number, and Ψ is the so-called entropy fix function. The right eigen matrix, $\mathbf{R}_{j+1/2}$ and eigen values, $a_{j+1/2}^l$, are evaluated using Roe's average,

$$a_{j+1/2}^l = a^l(\mathbf{U}^R, \mathbf{U}^L)_{j+1/2} \tag{7}$$

$$\mathbf{R}_{j+1/2} = \mathbf{R}(\mathbf{U}^R, \mathbf{U}^L)_{j+1/2} \tag{8}$$

Higher order schemes can be constructed from MUSCL as follows(ref.2):

$$\mathbf{U}_{j+1/2}^L = \{\ 1 + [\ (1-\kappa)\Delta\bar{\mathbf{U}}_{j+1/2} + (1+\kappa)\Delta\tilde{\mathbf{U}}_{j+1/2}\ ]/4\ \} \tag{9}$$

$$\mathbf{U}_{j+1/2}^R = \{\ 1 - [\ (1-\kappa)\Delta\tilde{\mathbf{U}}_{j+1/2} + (1+\kappa)\Delta\bar{\mathbf{U}}_{j+1/2}\ ]/4\ \} \tag{10}$$

where

$$\Delta\bar{\mathbf{U}}_{j+1/2} = minmod[\Delta\mathbf{U}_{j+1/2}, b\Delta\mathbf{U}_{j+1/2}],\quad \Delta\tilde{\mathbf{U}}_{j+1/2} = minmod[\Delta\mathbf{U}_{j+1/2}, b\Delta\mathbf{U}_{j+1/2}],\quad \Delta\mathbf{U}_{j+1/2} = \mathbf{U}_{j+1} - \mathbf{U}_j \tag{11}$$

Here, κ is 1/3 to obtain the 3rd order spatial accuracy and b is 2. The minmod slope limiter function is used to prevent the numerical solution from oscillations as below(ref.2):

$$\mathbf{minmod}(x,y) = \mathbf{sgn}(x)\,\mathbf{max}[0, \mathbf{min}(|x|, y\ \mathbf{sgn}(x))]$$

$$\overline{m}(x,y)=[x \ \ when\ |x|\le|y|,\ \ otherwise \ \ y] \tag{12}$$

So, the resulting scheme has the 2nd order temporal accuracy and the 3rd order spatial accuracy.

UNO3-ACM

The UNO3-ACM scheme uses 1 step time integration. Its formulation is as below (ref.6). In Eq.(4), the term Φ controls the upwind properties(ref.2).

$$\Phi_{j+1/2}=\left[\phi^1_{j+1/2} \quad \phi^2_{j+1/2} \quad \phi^3_{j+1/2} \quad \phi^4_{j+1/2}\right]^T \tag{13}$$

where

$$\phi^l_{j+1/2}=g^l_j+g^l_{j+1}-\psi(a^l_{j+1/2}+\gamma^l_{j+1/2}) \tag{14}$$

$$\gamma^l_{j+1/2}=\frac{g^l_{j+1}-g^l_j}{\alpha^l_{j+1/2}} \quad if\ \alpha^l_{j+1/2}\neq 0$$
$$\gamma^l_{j+1/2}=0 \quad elseif\ \alpha^l_{j+1/2}=0 \tag{15}$$

The term $\gamma^l_{j+1/2}$ compliments the characteristic speed, $a^l_{j+1/2}$, to be the proper accuracy.

The expression of the term g^l_j, which makes the scheme to the 3rd order accuracy, is described in a new compact form in this paper as below

$$g^l_j=\bar{a}^l_j\beta^l_j+\begin{Bmatrix}\bar{a}^l_j\tilde{\beta}_j & |\alpha^l_{j-1/2}|\le|\alpha^l_{j+1/2}| \\ \hat{a}^l_j\hat{\beta}_j & otherwise\end{Bmatrix} \tag{16}$$

and the characteristic speed is expressed in a new compact form as below

$$\bar{a}^l_j=\left|a^l_{j+1/2}\right|\left(\frac{1-|\sigma|}{2}\right)_j \tag{17}$$

$$\tilde{a}^l_j=a^{l+}_{j+1/2}\left(\frac{2-3|\sigma|+\sigma^2}{6}\right)_j+a^{l-}_{j+1/2}\left(\frac{\sigma^2-1}{6}\right)_j \tag{18}$$

$$\hat{a}^l_j=a^{l+}_{j+1/2}\left(\frac{\sigma^2-1}{6}\right)_j+a^{l-}_{j+1/2}\left(\frac{2-3|\sigma|+\sigma^2}{6}\right)_j \tag{19}$$

where

$$\sigma=a^l_{j+1/2}\frac{\Delta t}{\Delta x}, \qquad a^{l\pm}_{j+1/2}=\frac{a^l_{j+1/2}\pm\left|a^l_{j+1/2}\right|}{2}$$

The derivatives β^l_j, $\tilde{\beta}^l_j$ and $\hat{\beta}^l_j$ in the equation (16) is obtained by using the function (12) respectively(ref.4, ref.5).

$$\beta^l_j=m(\alpha^l_{j-1/2},\alpha^l_{j+1/2}) \qquad \tilde{\beta}^l_j=\overline{m}(\Delta_-\alpha^l_{j-1/2},\Delta_+\alpha^l_{j-1/2}) \qquad \hat{\beta}^l_j=\overline{m}(\Delta_-\alpha^l_{j+1/2},\Delta_+\alpha^l_{j+1/2}) \tag{20}$$

The above new expressions (13)-(20) correctly describe symmetric behaviors for the left and right going waves.

ACM(Artificial Compression Method)

Most interpolation functions including the ENO interpolation have smooth properties in computation domain. Therefore, those interpolation functions have limitations in capturing the physical discontinuities such as contact surfaces and shocks. Even though a shock has the tendency to sustain the steep solution of itself, a contact surface cannot keep its discontinuities to be much smeared. Therefore, a special technique is required to resolve the discontinuities. To increase the resolutions of the scheme, we adopted a ACM(Artificial Compression Method) technique.

$$\text{if } l \neq 1 \quad \frac{d^l}{d^l}(\hat{\mathbf{R}}(x,v)) = \frac{d^l}{d^l}(\mathbf{R}(x,v))$$

$$\text{else } l = 1 \quad \frac{d}{d}(\hat{\mathbf{R}}(x,v)) = \frac{d}{d}(\mathbf{R}(x,v)) + \frac{ds_j}{dx} \tag{26}$$

where l : Order of the derivatives
x : Arbitrary position in cell
v : A variable

Here, $\mathbf{R}(x,v)$ and $\hat{\mathbf{R}}(x,v)$ are reconstruction functions.

The function modifying the slope, ds_j^l, is as below

$$ds_j^l = 2 \cdot \mathbf{m}(\alpha_j^c \cdot \mathbf{m}(\delta_{j+1/2}, \delta_{j-1/2}), \mathbf{m}(\tilde{\Delta}_{j+1/2}, \hat{\Delta}_{j-1/2})) \tag{27}$$

where $\delta_{j+1/2} = v_{j+1/2}^{N+}(\sigma=0) - v_{j-1/2}^{N-}(\sigma=0)$ $\tilde{\Delta}_{j+1/2} = v_{j+1} - v_{j+1/2}^{N+}(\sigma=0)$ $\hat{\Delta}_{j+1/2} = v_{j-1/2}^{N-}(\sigma=0) - v_{j-1}$

The minmod function ,$\mathbf{m}(x,y)$, was expressed as equation (12). The coefficient α_j^c controls the quality of the solution. We adopted $\alpha_j^c = 1.5$.

Optimized Compact Finite Difference Scheme

For the purpose of obtaining high order accuracy and high resolution characteristics, we use the compact finite discretization as follow(ref.7):

$$\beta f'_{i-2} + \alpha f'_{i-1} + f'_i + \alpha f'_{i+1} + \beta f'_{i+2} = c\frac{f_{i+3} - f_{i-3}}{6h} + b\frac{f_{i+2} - f_{i-2}}{4h} + a\frac{f_{i+1} - f_{i-1}}{2h} \tag{28}$$

The Fourier Transform of the left and right side of Eq.(28) is as follow(ref.7):

$$i\omega(\beta e^{-2i\omega\Delta x} + \alpha e^{-i\omega\Delta x} + 1 + \alpha e^{i\omega\Delta x} + \beta e^{2i\omega\Delta x})\tilde{f} = \left[\frac{c}{6\Delta x}(e^{3i\omega\Delta x} - e^{-3i\omega\Delta x}) + \frac{b}{4\Delta x}(e^{2i\omega\Delta x} - e^{-2i\omega\Delta x}) + \frac{a}{2\Delta x}(e^{i\omega\Delta x} - e^{-i\omega\Delta x})\right] \tag{29}$$

The Fourier analysis provides an effective way to quantify the resolution characteristics of Eq.(28). From the equation(29), modified-wavenumber is derived as :

$$\overline{\omega}\Delta x \equiv \frac{a\sin(\omega\Delta x) + \frac{b}{2}\sin(2\omega\Delta x) + \frac{c}{3}\sin(3\omega\Delta x)}{1 + 2\alpha\cos(\omega\Delta x) + 2\beta\cos(2\omega\Delta x)} \tag{30}$$

where $\overline{\omega}\Delta x$ is a defined modified-wavenumber. To assure that the Fourier transform of Eq.(28) is a good approximation of that of the partial derivative, the modified-wavenumber should coincide with the true-wavenumber(=$\omega\Delta x$) in wide range(i.e. $0 \le \omega\Delta x \le \pi$).

Let's define the weighted deviation(integrated error) as(ref.8):

$$E \equiv \int_0^{r\pi} (\omega\Delta x - \overline{\omega}\Delta x)^2 W(\omega\Delta x)\, d(\omega\Delta x) \tag{31}$$

where W($\omega\Delta x$) is a weighting function and 'r' is a factor to determine the optimizing range($0 < r \le 1$). The weighting function and the range factor give important effects to the optimization of Eq.(28).

The integrated error defined in Eq.(31) is a function of each coefficients a,b,c,α and β. It is necessary to find the optimal values of the coefficients that would minimize the integrated error. The conditions that E is a minimum are :

$$\frac{\partial E}{\partial \beta} = 0 \quad (32) \quad , \quad \frac{\partial E}{\partial \alpha} = 0 \quad (33) \quad , \quad \frac{\partial E}{\partial c} = 0 \quad (34) \quad , \quad \frac{\partial E}{\partial b} = 0 \quad (35) \quad , \quad \frac{\partial E}{\partial a} = 0 \quad (36)$$

These equations(32)-(36) and the constraints to match the Taylor series coefficients of various orders provide a system of linear algebraic equations by which the coefficients can be determined.

The weighting function and the optimizing range factors for each scheme are as follows :

$$W(\kappa) = \left[(1+2\alpha\cos(\kappa)+2\beta\cos(2\kappa))\, e^{\kappa}\right]^2 \tag{37}$$

(where $\kappa = \omega\Delta x$)

1. Tridiagonal
   - 2nd order : r = 0.820 4th order : r = 0.790
   - 6th order : r = 0.715
2. Pentadiagonal
   - 2nd order : r = 0.90 4th order : r = 0.890
   - 6th order : r = 0.865 8th order : r = 0.815

The coefficients a,b,c,α and β are finally determined with the above constraints, i.e. they are optimized to obtain the maximum resolution characteristics for each scheme and given truncation order of accuracy. The optimized coefficients are presented in Table1 and Table2 for the tridiagonal and the pentadiagonal schemes, respectively.

Table 1. Optimized Coefficients for the Maximum Resolution : Tridiagonal Schemes

Tridiagonal	a	b	c	α	β
2nd order	1.545790417	0.434249728	-0.078236437	0.450901855	0
4th order	1.551941906	0.361328195	-0.042907397	0.435181352	0
6th order	1.568098212	0.271657107	-0.022576781	0.408589269	0

Table 2. Optimized Coefficients for the Maximum Resolution : Pentadiagonal Schemes

Pentadiagonal	a	b	c	α	β
2nd order	1.265667929	1.079904285	0.053798648	0.596631925	0.103053504
4th order	1.280440844	1.049309076	0.044465832	0.589595521	0.097512355
6th order	1.323482375	0.944394243	0.027596356	0.566458285	0.081278202
8th order	1.373189728	0.814447053	0.016707870	0.537265947	0.064906379

RESULTS AND DISCUSSION

Category 1

In Fig.1(a)-(d), we present the solved results of the problems in Catagory1 and compare the numerical dispersion and dissipation properties of three numerical schemes(Optimized Compact, UNO3 with and without ACM). Time step, $\Delta\tau$ is 0.5 and Δx is 1. It is shown that the UNO3-ACM can obtain solutions that have less dispersive and dissipative errors than UNO3, i.e. the ACM contributes to the resolution characteristics of UNO3. Thus the ACM is combined with the UNO3 successfully. The Optimized

Compact scheme shows the best solutions that have little dispersive and dissipative errors, thus retains the amplitudes and geometric symmetries of the waves for a long time. It was so optimized to achieve the maximum resolution characteristics for a given truncation order that it can resolve the waves very accurately. It has the central difference form in space and there are no dissipative errors resulted from the spatial discretization, so it shows very small dissipative errors as well as small dispersive errors.

Category 2

Three different scheme of TVD3 and UNO3 without and with ACM are employed to solve the category 2. Time step, $\Delta\tau$ is 0.2 and Δx is 1. In Fig.2(a), it is shown that the same accuracy in most regions is obtained except the maxima region of the shock at $t=200$. It is because the UNO3 and UNO3-ACM have the uniformly third order accuracy in every region while the accuracy of TVD3 come down to 1st order at the maxima or minima point (ref.2). We used the ACM only to isentropic characteristics value. Therefore, there is no differece in figures of the shock between UNO3 and UNO3-ACM. In Fig.2(b), the differences near the contact discontinuity are shown. In the box of Fig.2(b), we can tell the obvious differeces among the three methods. The UNO3-ACM method gives better results than the others. The results of UNO3 are slightly better than those of TVD3 because of the uniformly third order accuracy.

Category 5

The results of category 5 solved by the TVD3 are shown in Fig.3(a)-(c). Figure 3(a) shows the convegence history to obtain the steady solution for a initial condition. We obtain the machine accuracy of double precision i.e. 10^{-16} after 15,000 iterations. The converged steady state solutions are shown in Fig.3(c) The numerical solutions are described well the sonic behaviors at the throat. Figure 3(b) is shown the periodic solution due to the inlet excitation with 10^{-6} amplitude. For this problem, time step, $\Delta\tau$ is 0.05 and Δx is 1. The amplitude of the outlet trasmitted signal decrease due to the reflection of the incident wave at the throat. The conventional TVD scheme for the CFD field is useful for simple problems of CAA field with a appropriate grid points(PPW-points per wavelength).

CONCLUSION

It can be concluded that the optimized compact scheme shows good resolutions for the category 1 problems and the UNO3-ACM for the category 2 problems. However, the UNO3-ACM may have the best results among the three schemes if the mixed problems of category 1 and category 2 are concerned. But in these calculation, we employed the ACM to isentropic characterics only. The ACM can be applied to all caracteristics, it enhances the resolutions in one dimensional calculation. But multi-dimensional problems makes some oscillations. So we typically use the ACM on the isentropic characteristic only.

REFERENCES

1. Hirsch, C., *Numerical Computation of Internal and External Flows*, 1st ed., Vol. 2, John Wiley & Sons, New York, 1990, pp. 408-594
2. Yee, H. C., " A Class of High-Resolution Explicit and Implicit Shock-Capturing Methods," *NASA TM* 101088, Feb. 1989
3. Harten, A. and Osher, S., "Uniformly High-Order Accurate Non-oscillatory schemes I", *SIAM Journal,* Vol. 24, No. 2, 1987
4. Hsu, C.A. and Yang, J.Y., "High-Resolution Non-oscillatory schemes for Unsteady Compressible Flows", *AIAA Jounal,* Vol. 30, No. 6, 1992
5. Yang, H., "An Artificial Compression Method for ENO Schemes", *Journal of Computational Physics*, 1990, pp. 89
6. Ko, D.K. and Lee, D.J., "Third Order Uniformly Nonoscillatory Scheme with Artificial Compression Technique for Unsteady Compression Flows", *proceedings of the 5th international symposium on computational fluid dynamics*, Volume II, pp.59
7. Lele, S. K. , "Compact Finite Difference Schemes with Spectral-like Resolution," *Journal of Computational Physics*, Vol. 103, 1992, pp. 16-42.
8. Tam, C. K. W. and Webb, J. C. , "Dispersion-Relation-Preserving Schemes for Computational Aeroacoustics," *Proceedings of the DGLR/AIAA 14th Aeroacoustics Conference*, Vol. 1, DGLR, Eurogress Center Aachen, 1992, pp. 214-222 (DGLR/AIAA Paper 92-02-033).

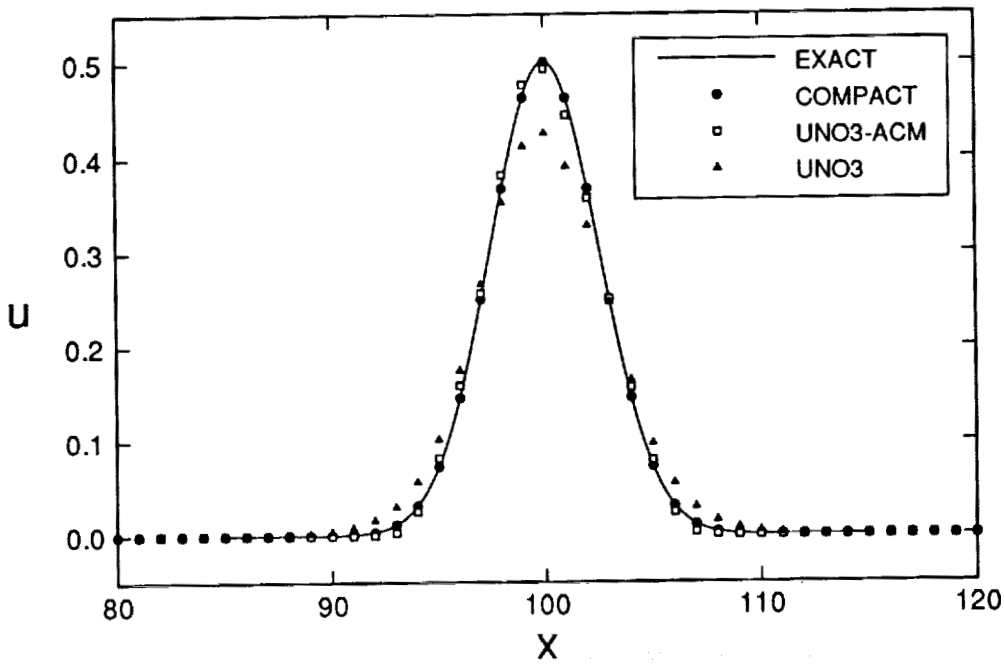

(a) Problem 1 (Time = 100).

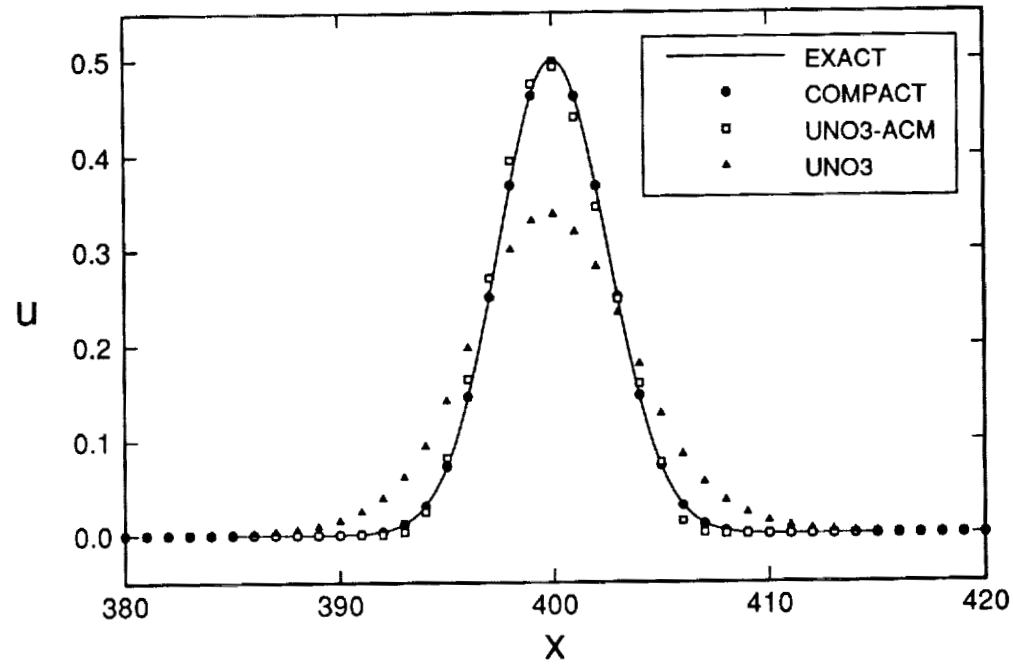

(b) Problem 1 (Time = 400).

Figure 1. Catagory 1

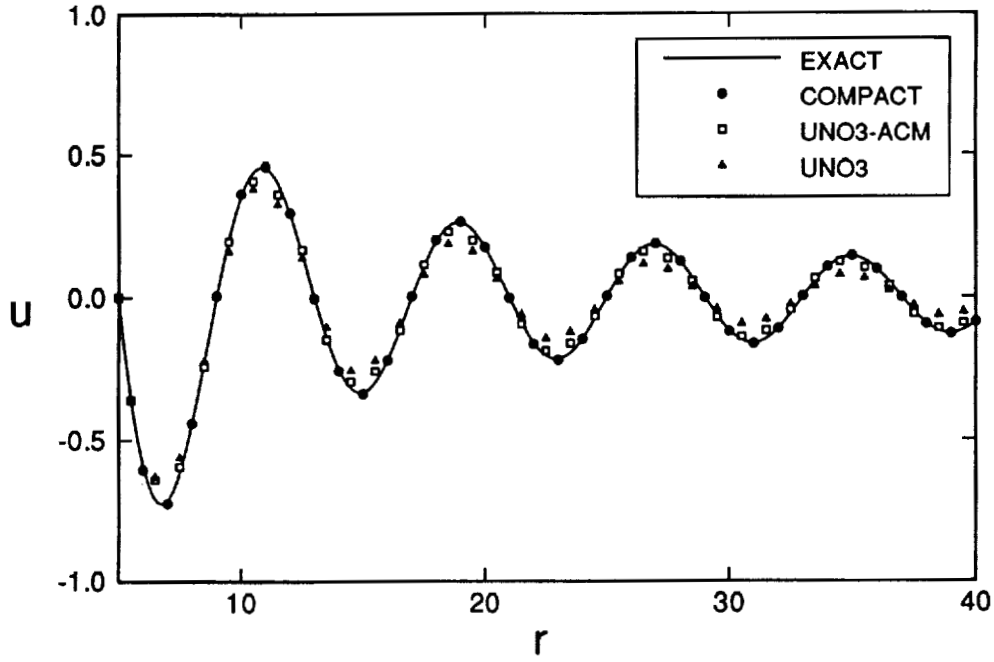

(c) Problem 2(a) (Time = 400).

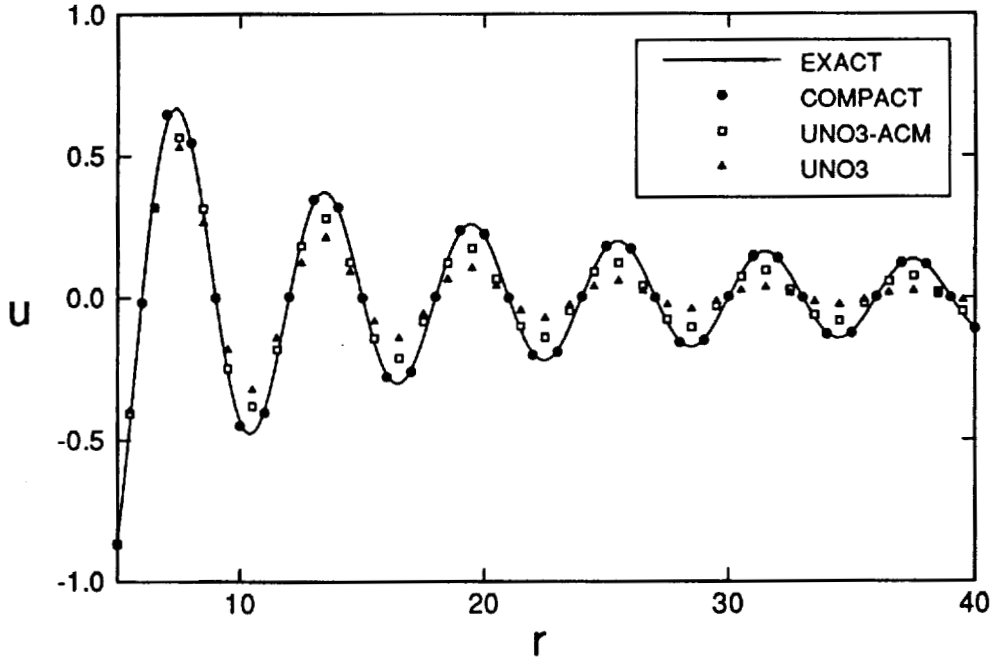

(d) Problem 2(b) (Time = 400).

Figure 1. Catagory 1

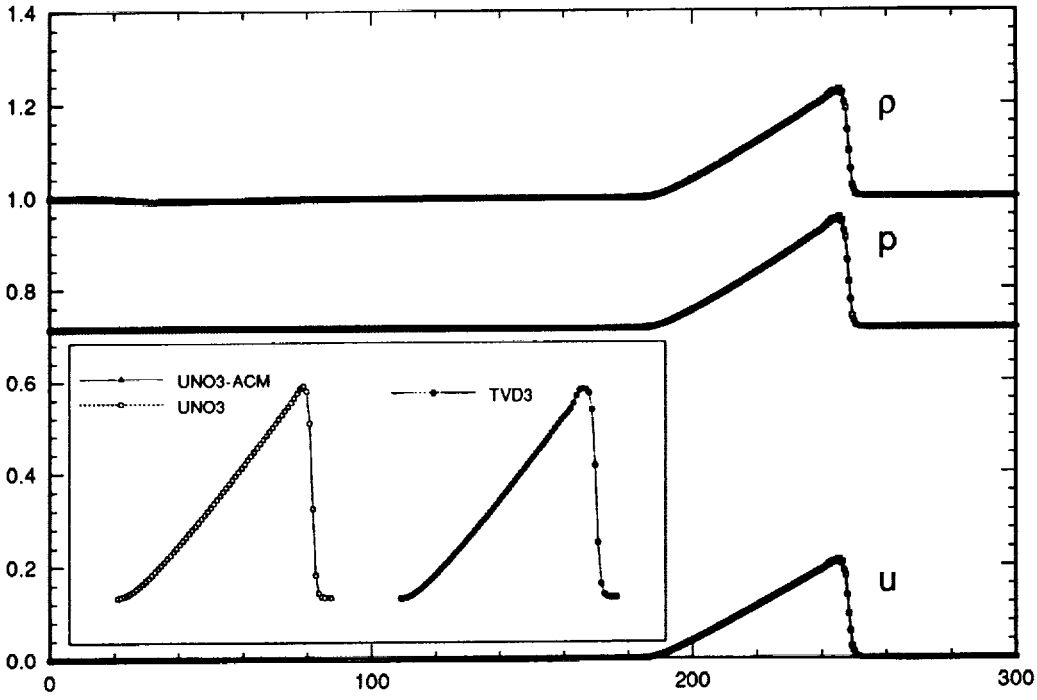

(a) Problem 1 (Time=200).

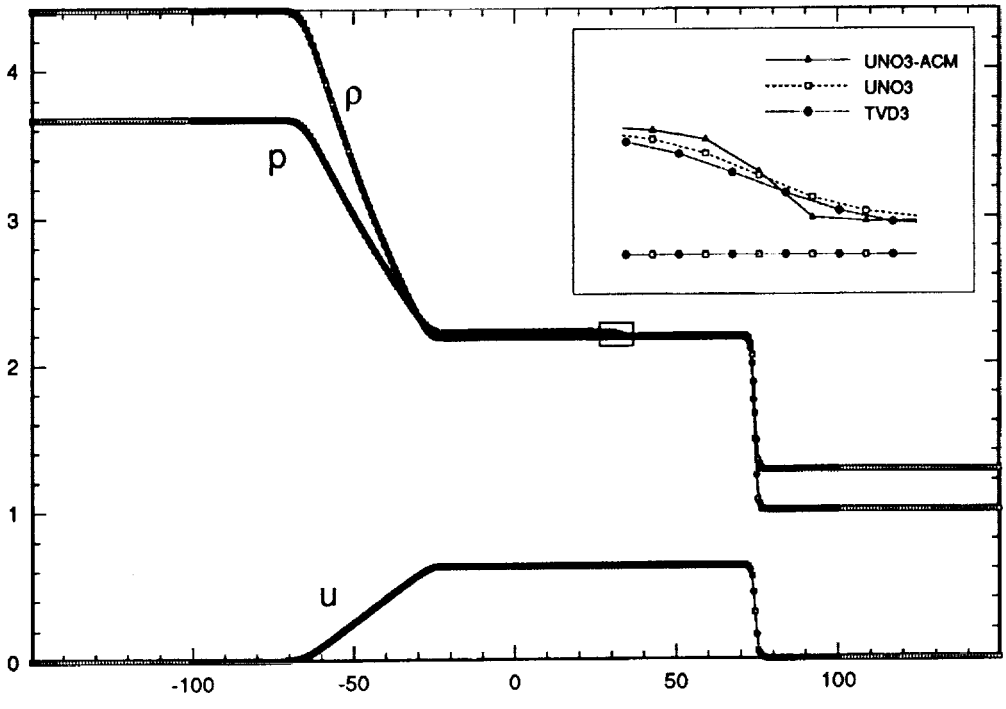

(b) Problem 2 (Time=50).

Figure 2. Category 2

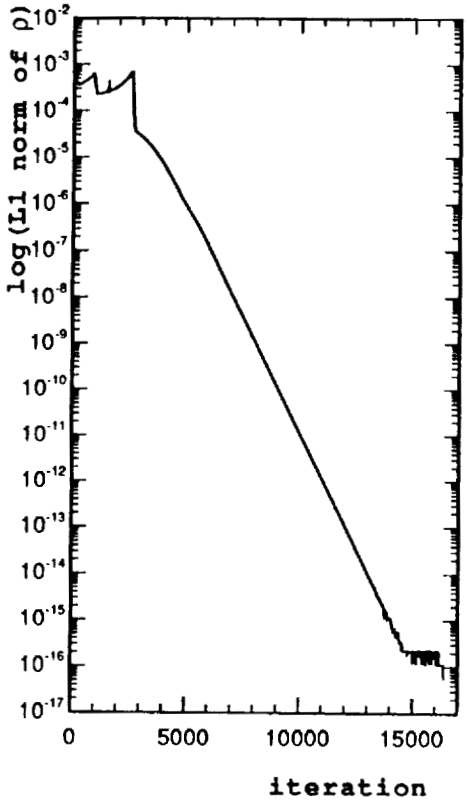

(a) Convergence history.

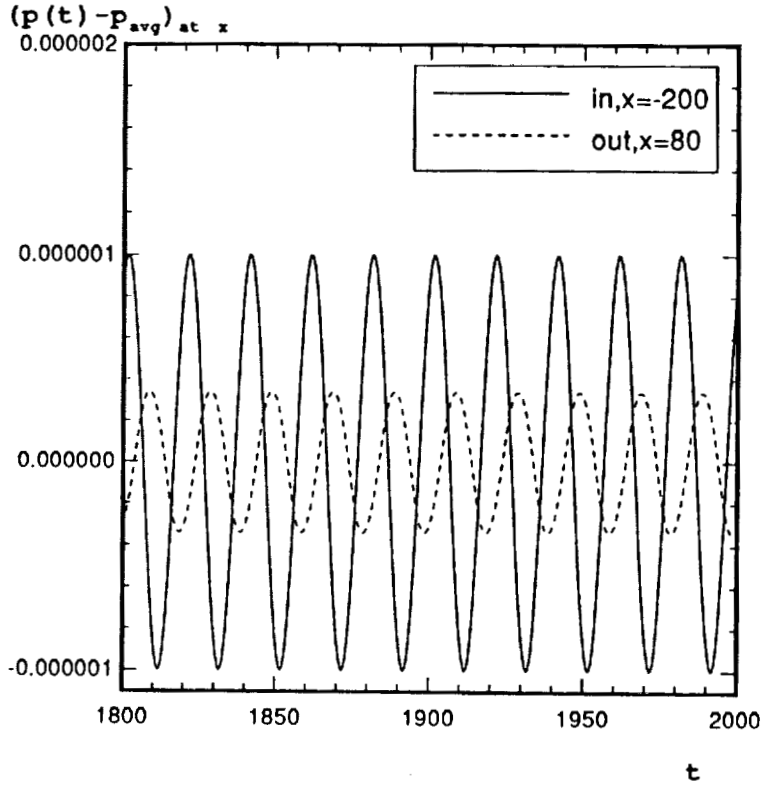

(b) Time histories of pressure.

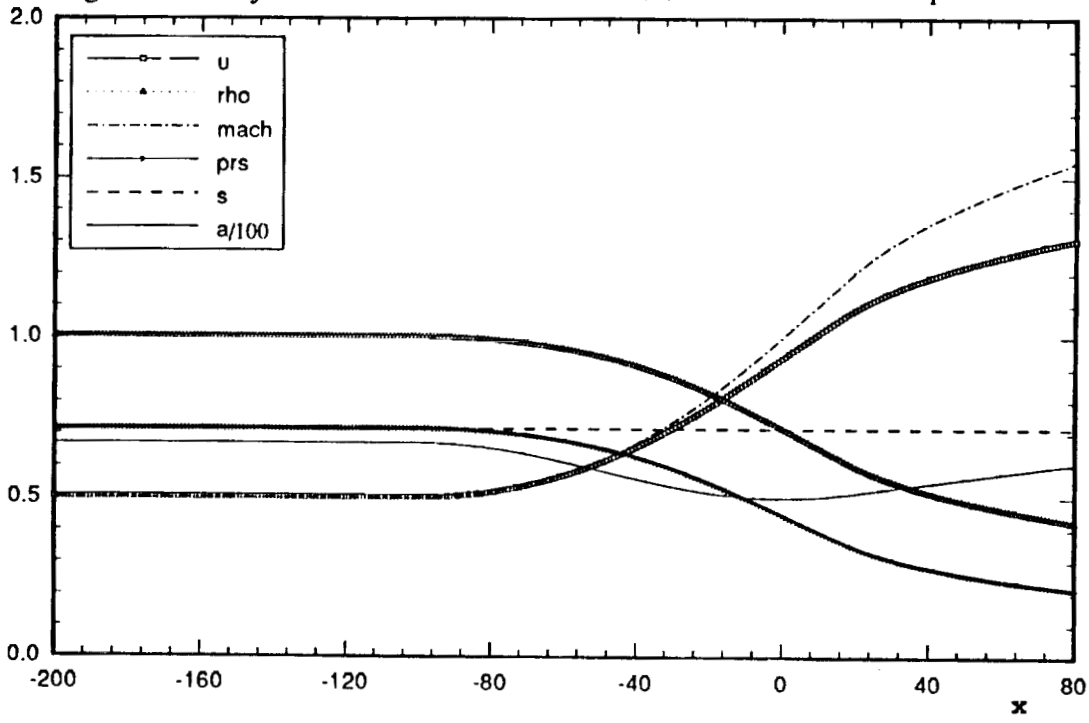

(c) Steady state solution.

Figure 3. Category 5

A COMPACT SOLUTION TO COMPUTATIONAL ACOUSTICS

K.-Y. Fung
University of Miami
Coral Gables, FL

Raymond S. O. Man*
University of Arizona
Tucson, AZ

Sanford Davis
NASA-Ames Research center
Moffett Field, CA

SUMMARY

This paper demonstrates that the linearized, dimensional Euler equations for acoustic computation can be accurately solved as a set of decoupled first-order wave equations, and that if ordered properly, this system of simple waves has unambiguous, easily implemented boundary conditions, allowing waves of same group speeds to pass through numerical boundaries or comply with wall conditions. Thus, the task of designing a complex multi-dimensional scheme with approximate far-field boundary conditions reduces to the design of higher order schemes for the one-dimensional simple wave equation.

A compact finite-difference scheme and a characteristically exact but numerically n^{th} order accurate boundary condition are introduced for solving the first order wave equation. Spanning a three-point two-level stencil, this low-dispersion implicit scheme has a third order spatial accuracy when used on nonuniform meshes, fourth order accurate on uniform meshes, and a temporal accuracy of second order due to the choice of trapezoidal integration for algorithmic simplicity. The robustness and accuracy of the scheme are demonstrated through a series of numerical experiments and comparisons with published results. When tested on the one-dimensional wave equation on a uniform grid, this scheme allows a Gaussian wave packet to pass through any finite domain with low numerical dispersion characteristic of a spatially fourth-order scheme and reflections at numerical boundaries maintained below truncation error. On highly stretched and irregular grids, only mild dispersions are found in the solution while solutions by other methods fail or were severely distorted. Yet, this scheme is no more sophisticated to solve or implement than the Crank-Nicolson scheme.

This scheme has been tested on four categories of the ICASE/LaRC benchmark problems, which include propagation of acoustic and convective waves in Cartesian and cylindrical domains, reflection of acoustic wave at stationary/moving boundaries, and sound generation by gust-blade interaction.

INTRODUCTION

For various reasons, direct time-domain solution by finite difference methods, especially of the implicit type, has not been a widely accepted numerical approach to wave propagation problems[1]. Chief among the reasons cited for its unpopularity is the inability of a majority of popular, robust, and successful numerical schemes to track waves with low dispersion and dissipation for large distances[2]. Successful, popular approaches to wave propagation problems, e.g. underwater acoustics, by finite differences do

* partial support for this author under NASA Grant NCA2-707 is gratefully acknowledged.

exist, but are predominantly indirect, spatial approximations of the so-called parabolic wave equation[3] (Helmholtz) in the frequency domain. Many space-time higher order explicit schemes have been proposed, e.g., Tam and Webb[4]. Being explicit and higher order these schemes inevitably involve multi-level, broad band data structure and algorithmic non-uniformity at domain boundaries. Higher order schemes with simple data structure, two time levels and tridiagonal matrices, are possible, e.g., Refs. 5 & 6, but it is not clear how these schemes can be implemented for solution of practical problems involving more than one spatial dimension without compromising solution accuracy.

Here, a class of high order schemes for solving the convection (simple wave) equation on nonuniform meshes is derived. A commonality of these schemes is the absence of purely spatial truncation error terms lower than second order. Due to the absence of a truncation error term proportional to the third spatial derivative of the dependent variable, this class of schemes has low dispersion comparable to the most accurate scheme possible for a three-point two-level stencil on uniform mesh. Among the schemes derived here, the most accurate scheme has fourth order temporal-spatial accuracy but is not suitable for systematically stretched grid or extension to systems of conservation laws. A compact spatial fourth order scheme is possible, but may not be in conservation law form unless the grid is stretched appropriately and may allow the growth of high wave number components on grids with large stretching ratio. Lastly, a compact, spatial third order, low-dispersion scheme with damping for all high wave number components and in conservation form, regardless of the stretching ratio, is introduced. The robustness of these schemes is tested and compared on grids with stretching ranges from random to systematic.

These schemes, like all other schemes for simple wave propagation that involve a centered stencil, by themselves without an alternate scheme for the end points are incomplete and insufficient to ensure accuracy. Here, a class of higher order one-sided schemes based on the method of characteristic is derived for the end point where waves are propagating out, and shown to be progressively more effective in minimizing reflections due to the artificial boundary regardless of its location, or the size of the domain.

The third order compact scheme together with an n-th order interpolated end value based on the method of characteristics constitute the building block for construction of solution of wave propagation here.

For problems of more than one spatial dimensions, the key issue is whether they can be converted into a system of simple waves for each of which the direction of propagation is known a priori and the corresponding boundary condition is known or enforceable. It will be shown through the benchmarking cases indeed the propagation of aeroacoustic waves, consisting of a combination of acoustic, entropy and vorticity waves, is reduceable to a system of simple waves. This equivalence implies that algorithms developed for one spatial dimension is immediately applicable for multi-dimensions, that the computation for each simple wave can be advanced in parallel with that of the others, and that the size of the computational domain can be as small as the region of interest.

LOW DISPERSION COMPACT SCHEMES

In his 1986 review paper[1], Candel remarked that implicit finite difference schemes had not been reported in acoustic wave applications, and illustrated the potential savings due to their unconditional stability over the CFL-restricted explicit schemes by an application of the Crank-Nickolson scheme to the propagation of acoustic wavelets in a close-end duct. However, it is arguable, e.g. Ref. 2, that since the time step restriction for solution accuracy is comparable to that for algorithmic stability, the advantage of implicit methods is seen only when the spatial resolution of the spectral contents of the solution is amply sufficient. Clearly, the choice can not be made on the basis of stability or accuracy alone. Algorithmic simplicity, including implementation of boundary conditions, especially in multi-dimensional applications is equally, if not more, important. A prime reason for using explicit methods, despite their inefficiency which nowadays can be compensated by massively parallel computer architecture, is the simplicity in the data structure, if only all boundary conditions are also explicit. Unfortunately, this is not the case in

unsteady problems. Pressure, being of prime interest in most cases, is not known a priori and can not simply be given at the boundary as a function of time. However, aside from having to cope with the difficulty of implementing certain types of boundary condition, implicit methods, as illustrated by Davis[6] using his optimum space-time fourth-order difference scheme, can afford a data structure as simple as three-point two-level and a savings of as much as 60% fewer mesh points per wave length per dimension than a three-point explicit method. Whereas a comparable explicit method, the DPR scheme of Tam and Webb[4] for instance, involves a five-point four-level data structure and seven-point one-sided schemes for boundary points. If the ultimate application of these schemes involves other distinct flow features and/or complex boundaries that necessitate the used of nonuniform grids, accuracy, algorithm robustness, data structure simplicity, and solution efficiency must all be considered together for a fair assessment of their effectiveness.

For uniform mesh, weighted differencing has been used on a three-point two-level computational molecule to produce all known finite difference methods[5], including a temporal second order spatial fourth order accurate compact scheme and the temporal and spatial fourth order scheme derived and proposed separately by Davis[6]. Here, similar techniques are used to derive schemes suitable for propagation of phase-sensitive waves over nonuniform meshes.

The most general stencil for the convection equation

$$\frac{\partial u}{\partial t} + c\frac{\partial u}{\partial x} = 0 \tag{1}$$

is

$$a_0 u_j^{n+1} + a_1 u_{j-1}^{n+1} + a_2 u_{j+1}^{n+1} = b_0 u_j^n + b_1 u_{j-1}^n + b_2 u_{j+1}^n \tag{2}$$

Here, u_j^n denotes the solution u(x,t) at the spatial node x_j and n-times the temporal advancement Δt. The coefficients, a_j and b_j chosen by design, characterize the accuracy, stability and usefulness of a scheme.

Let a locally plane wave of the form $e^{i\omega t + ikx}$ propagate through the nonuniform mesh. The amplitudes at the two time levels are related by Eq. (2):

$$e^{i\omega(n+1)\Delta t} e^{-ikx}(a_0 + a_1 e^{-ik\Delta x} + a_2 e^{ikr\Delta x}) = e^{i\omega n\Delta t} e^{-ikx}(b_0 + b_1 e^{-ik\Delta x} + b_2 e^{ikr\Delta x}) \tag{3}$$

where $t = n\Delta t$, $\Delta x = x_j - x_{j-1}$, and the grid stretching ratio $r = \dfrac{(x_{j+1} - x_j)}{(x_j - x_{j-1})} = \dfrac{(x_{j+1} - x_j)}{\Delta x}$.

Whence the amplification factor is obtained:

$$e^{i\omega\Delta t} = \frac{b_0 + b_1 e^{-ik\Delta x} + b_2 e^{ikr\Delta x}}{a_0 + a_1 e^{-ik\Delta x} + a_2 e^{ikr\Delta x}} \tag{4}$$

If, instead, in Eq. (2) Taylor-series expansion is used to express the values at different points of the stencil, the truncation error can be obtained. For example, the Crank-Nicolson type (CNT) scheme with

centered differencing for the spatial derivative, $\frac{\partial u}{\partial x} = \frac{u_{j+1} - u_{j-1}}{x_{j+1} - x_{j-1}}$, has the truncation error:

T.E. $= -\frac{c\,(r-1)\,\Delta x}{2} u_{xx} - \frac{c^3 \Delta t^2}{12} u_{xxx} - \frac{c\,(r^2 - r + 1)\,\Delta x^2}{6} u_{xxx} + O\left((\Delta x, \Delta t)^3\right)$, which is formally only first order accurate when used on a nonuniform grid, i.e. $r \neq 1$. In that case, the scheme has coefficients:

$$a_0 = 1 \ , \ a_1 = -\frac{\nu}{2\,(r+1)} \ , \ a_2 = \frac{\nu}{2\,(r+1)} \ , \ b_0 = 1 \ , \ b_1 = \frac{\nu}{2\,(r+1)} \ , \ b_2 = -\frac{\nu}{2\,(r+1)}$$

where the Courant number $\nu = \frac{c\,\Delta t}{\Delta x}$.

The compact difference approximant for spatial derivative, $\delta_x u_j$, can be written as:

$$\left(a_m E^{-1} + a + a_p E\right)\delta_x u_j = \frac{\left(b_m E^{-1} + b + b_p E\right)u_j}{\Delta x} \tag{5}$$

where the shift operators are so defined: $E\,u_j = u_{j+1}$, $E^{-1}\,u_j = u_{j-1}$, and the coefficients to be determined are: a_m, a, a_p, b_m, b, b_p. For simplicity, these coefficients are chosen to be functions of the grid stretching ratio r only. Since five of the above coefficients are independent, the spatial gradient can at best be approximated to fourth order accuracy. With trapezoidal integration, the finite difference equivalent of Eq. (1), $\Delta t\,\delta_t u + \Delta x\,\nu\,\delta_x u = 0$, when put into the form of Eq. (2), will have the coefficients,

$$a_0 = 1 + \frac{\nu\, b}{2} \ , \ a_1 = a_m + \frac{\nu\, b_m}{2}, \ a_2 = a_p + \frac{\nu\, b_p}{2}$$

$$b_0 = 1 - \frac{\nu\, b}{2} \ , \ b_1 = a_m - \frac{\nu\, b_m}{2}, \ b_2 = a_p - \frac{\nu\, b_p}{2}$$

where a=1 is set for convenience. The maximum spatial accuracy of fourth order is obtained when the coefficients are:

$$a_m = \frac{r^2}{(r+1)^2} \ , \qquad a = 1 \ , \qquad a_p = \frac{1}{(r+1)^2} \ ,$$

$$b_m = -\frac{2r^2\,(r+2)}{(r+1)^3} \ , \ b = \frac{2(r-1)}{r} \ , \ b_p = \frac{2(2r+1)}{r(r+1)^3}$$

This Compact Fourth order scheme for Nonuniform mesh (C4N), as it will be referred here, has truncation error, T.E. $= -\frac{c^3\,\Delta t^2}{12} u_{xxx} + \frac{c^3\, r\,(r-1)\Delta x \Delta t^2}{24(r^2 + r + 1)} u_{xxxx} + O\left((\Delta x,\, \Delta t)^4\right)$. This scheme reduces to Noye's fourth order linear finite element scheme (LFE)[5] on a uniform mesh and maintains its accuracy on a nonuniform grid as well. This is because the spatial approximant reduces back to the (2,2) Padé Approximant for three-point two-level differencing for uniform mesh (r=1), with amplification and phase error identical to what has been shown by Beam and Warming[7] for the fourth order version of their scheme when used with trapezoidal time integration.

As mentioned, C4N has only a second order temporal accuracy but there is no pure spatial error term lower than fourth order. However, the second term on the right hand side above is a third order cross term involving both Δx and Δt. It can be seen by a comparison of the complex amplification factors that due to the absence of spatial second order truncation error term that is proportional to the third derivative of u the improvement in phase over CNT is comparable to that of LFE, whereas the absence of the third order pure spatial error term (r=1) only brings a very slight reduction of the error in the amplification magnitude. As the switch to compact differencing introduces two more coefficients, five instead of the original three, and only one is needed to eliminate that second order term, a free coefficient can be used for the design of a scheme with some other desirable characteristic instead of the marginal improvement of the amplification magnitude. This defines a family of schemes which will be spatially third order accurate in general.

For instance, by stipulating $b = 0$, the resulting approximant has coefficients,

$$a_m = -\frac{r(r-2)}{(r+1)^2} \quad , \quad a = 1 \quad , \quad a_p = \frac{2r-1}{(r+1)^2} \quad ,$$

$$b_m = -\frac{6r}{(r+1)^3} \quad , \quad b = 0 \quad , \quad b_p = \frac{6r}{(r+1)^3}$$

A rather simple result which will again reduce back to the Padé Approximant for uniform mesh. The scheme, which is called the compact third order scheme for nonuniform mesh (C3N) here, has truncation error: $\text{T.E.} = -\frac{c^3 \Delta t^2}{12} u_{xxx} - \frac{c^3 (r-1) \Delta x \Delta t^2}{24} u_{xxxx} + \frac{c (r-1)(r+1)^2 \Delta x^3}{72} u_{xxxx} + O\left((\Delta x, \Delta t)^4\right)$. The amplification factor for the C3N scheme differs from that of the C4N scheme mainly by a spatial third order damping term proportional to the fourth derivative of u. This desirable feature especially for damping high frequency waves on an expanding grid ($r > 1$) in the direction of propagation is in fact a result of setting b=0. For r close to unity, both Compact schemes have phase accuracy essentially that of the LFE scheme because the spatially related third order truncation error terms all have a factor of (r - 1).

First, the schemes are tested on a domain with periodic boundary condition to avoid having to address effects of alternate schemes for end points and boundary conditions. Following Noye[5], a Gaussian pulse, i.e. $u(x,0)=e^{-100(x-0.5)^2}$, is placed in the domain, $0 \le x \le 1$, as initial condition. The domain is discretized into 50 points, a slightly higher resolution, and a smaller time step of 0.008 is used to give the same Courant number of 0.4 as in the above reference. Four different grids are used. Grid A is a simple uniform grid. The others are nonuniform. Two of them represent the extremes in systematic variation and the last one is completely lacking in order except the inherent periodicity. Grid B is called a sawtooth grid where the spacing between grid points alternates between wide and narrow, with about 1.1 as r, the ratio of wide to narrow spacing. Grid C is called a compressed-expanded grid because points are clustered near the periodic ends and dispersed in the middle. The stretching ratio r varies smoothly from around 1.3 in the expanding region to the reciprocal value of about 0.87 in the compressing region. Gird D is a grid obtained by displacing each grid point of the uniform grid by a random amount less than a quarter of the nominal spacing. Therefore, the absolute minimum spacing possible will be half while maximum twice. The probability of any amount of displacement is intended to be equal. The solutions after 4 periods, or 500 time steps, are plotted.

Figure 1a almost reproduces a similar figure in Ref. 5, showing that the Crank-Nicolson type (CNT) scheme is highly dispersive and incapable of resolving the Gaussian pulse on the uniform grid. Figure 1b shows that, on the sawtooth grid, with cancellation of alternating errors due to the sawtooth nonuniformity, the CNT scheme behaves as on a uniform grid. Figure 1c shows that, on the compressed-expanded grid, the CNT scheme behaves much worse, loosing completely any phase coordination, while Figure 1d shows that, on the random grid, same phase coordination as on the uniform grid but with embedded wiggles due to the randomness.

Figure 1a, CNT Scehme on Uniform Grid

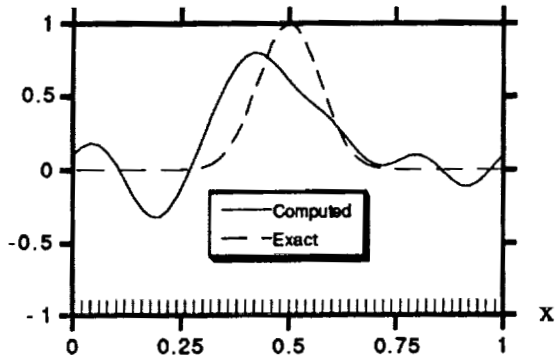

Figure 1b, CNT Scheme on Sawtooth Grid

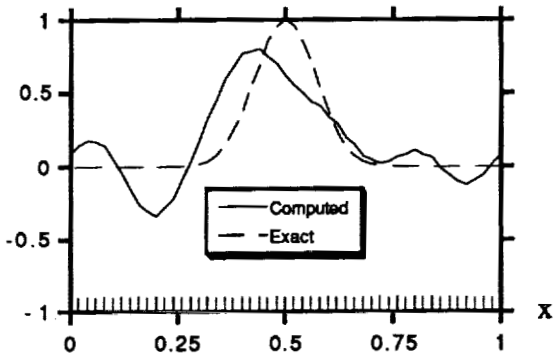

Figure 1c, CNT on Compressed-Expanded Grid

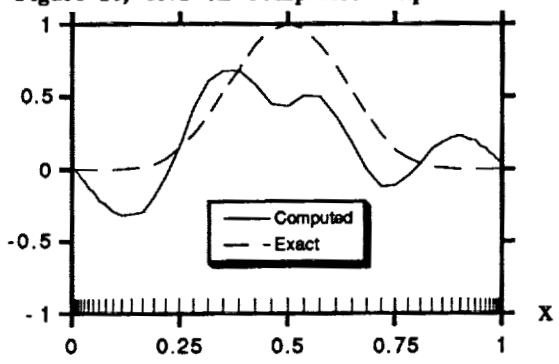

Figure 1d, CNT Scheme on Random Grid

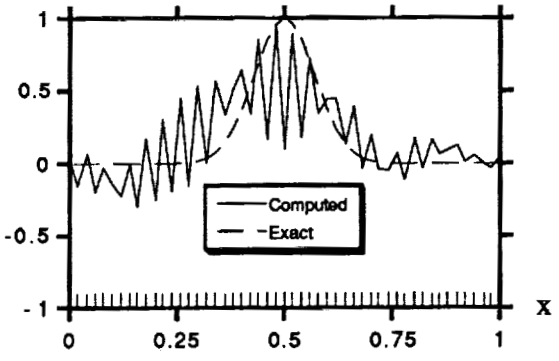

Figure 2a, C4N/C3N on Uniform Grid

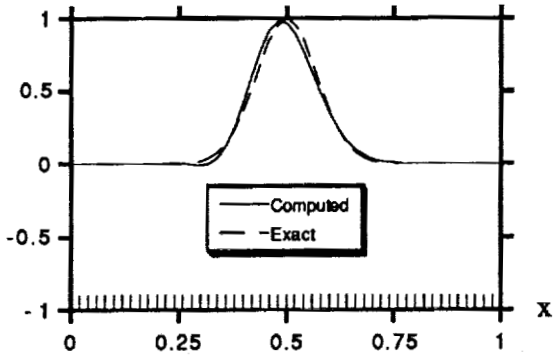

Figure 2b, C3N on Sawtooth Grid

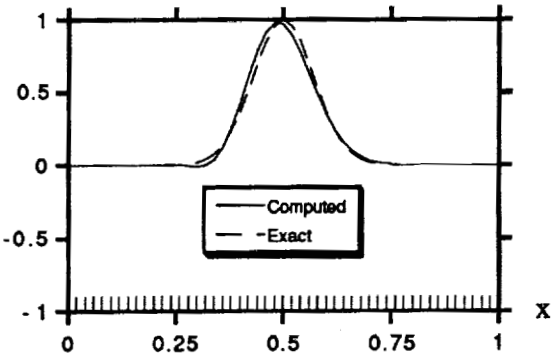

Figure 2c, C3N on Compressed-Expanded Grid

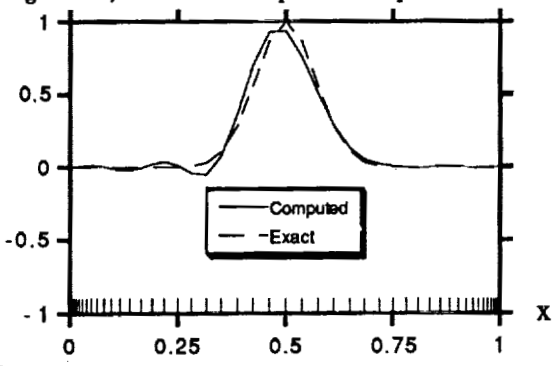

Figure 2d, C3N on Random Grid

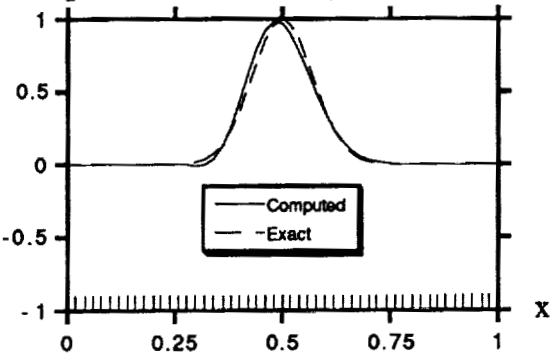

Of all three-point two-level schemes of Eq. (2) the temporal-spatial fourth order scheme TS4 proposed by Noye[5] and independently by Davis[6] gives the optimum and close to exact solution on the uniform mesh for which it was derived and almost as good on the other types except that on the compressed-expanded grid the solution becomes unstable and fails after fives time steps. Being identical to each other and equivalent to the LFE scheme[5] on the uniform grid, the compact schemes, C4N and C3N, give solutions far better than those of CNT, Figures 2a-d, nearly as good as TS4 on the other grids except for some slight dispersion of high frequency most noticeably on the compressed-expanded grid which has lower resolution in the expanding region.

Schemes for End Points

By itself, Equation (2) is incomplete for a solution of Eq. (1), which describes the propagation of a wave from point a to point b, left to right assuming c>0. At the end opposite to the direction of propagation u(a,t) must be specified, while at the other end u(b,t) should obey the same equation in theory but in practice can not follow Eq. (2) as an interior point. A common remedy is to approximate the spatial derivative using one-sided difference formulae, which pose no difficulty of implementation for explicit schemes. For implicit schemes, one-sided formulae for the spatial and temporal derivatives inevitably either complicate the data structure or degrade the scheme to a lower order. Since the schemes considered here are of higher order, to preserve the tridiagonal structure the following scheme is proposed,

$$u_{Ni}^{n+1} = u_c = \begin{cases} \sum_{k=0,K} L_k(x_c) u_{Ni-k}^{n} & ; \nu \le 1 \\ \sum_{k=0,1} L_k(t_c) u_{Ni-1}^{n+1-k} & ; \nu > 1 \end{cases} \qquad (6)$$

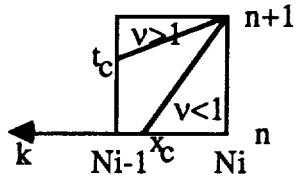

Here, for the end point Ni the value u_{Ni}^{n+1} is updated according to the method of characteristics as the value at x_c, depicted in the sketch between points Ni and Ni-1 when $\nu \le 1$, interpolated from K interior values u_{Ni-k}^{n} using a Kth order interpolant L_k, or at t_c interpolated implicitly from u_{Ni-1}^{n} and u_{Ni-1}^{n+1} using a linear interpolant when $\nu > 1$— for it is only necessary that the temporal accuracy of Eq. (6) be comparable to that of the compact schemes which by choice is only second order. Equation (6) maintains the implicitness and simplicity of a tridiagonal data structure while allowing choices of spatial accuracy.

Category I Problems

For the nondimensional time t<400 based on grid points travelled, the Gaussian pulse, initially $u(x,0) = 0.5\exp\left[-\ln 2(\frac{x}{3})^2\right]$, remains within the domain -20≤x≤450 and should be insensitive to boundary conditions. Figure 3 shows the computed pulses at t=100,200,300,400 using the numerically optimum time step of Δt=0.125, for further reduction of which led to no significant improvement. The fourth order accuracy and the small but increasing trailing dispersion of high frequency are clear from a comparison with the exact solution and other known higher order schemes. The effort to solve Eq. (2) is the same as that for CNT, one inversion of a tridiagonal matrix for each time step, but a comparable solution using CNT requires a grid roughly eight time finer, or the savings of using compact differencing is eight times fewer storage and correspondingly eight times faster. It is of interest to know for comparisons with other schemes that no discernible dispersion was found if a grid spacing of Δx=0.5 instead of 1.0 was used.

To test the effectiveness of Eq. (6), the same pulse is computed as it is exiting the reduced domain $20 \geq x \geq -20$ at the right boundary where a fourth order Lagrange interpolant is used. Figure 4a shows at t=27 trailing packets of spurious fluctuations of magnitude 5×10^{-4} propagating in the opposite direction as the pulse is moving within a few grid points out of the domain. After the pulse completely left the domain at t=40, Fig. 4b, the fluctuations congregate at the left boundary where no wave is allowed to escape and rebound towards the right boundary where some reflection is bound to occur for Eq. (6), being one-sided, has different dispersion characteristics than a centered scheme. The spurious fluctuations linger on with a slowly reducing magnitude even after long times, Fig. 4c. However, the use of an eighth order interpolant instead of same fourth order as the compact schemes reduces the magnitude of the spurious reflection by a factor of 20 for four additional additions and multiplications which amounts to the work of adding one grid point.

Figure 3, Application of C3N to Prob. 1 of Cat. I

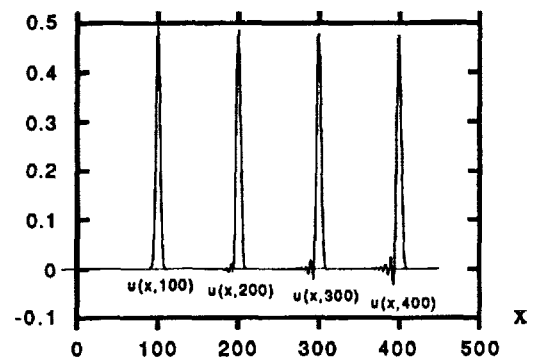

Figure 4a, Spurious Fluctuations due to 4th order B.C.

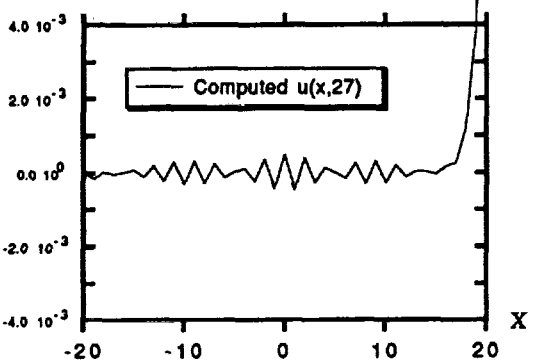

Figure 4b, Congregation of Dispersed Reflections.

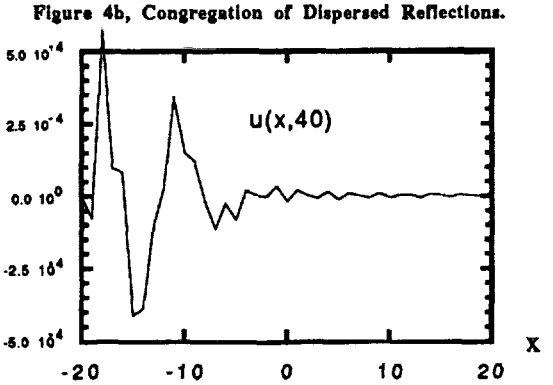

Figure 4c, Trapped Dispersion Residues

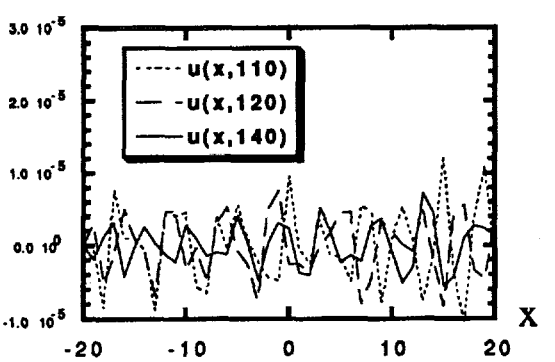

Figure 5a, Application of C3N to Spherical Wave
u(5,t)=sinωt, (ω=π/4, Δt=0.125)

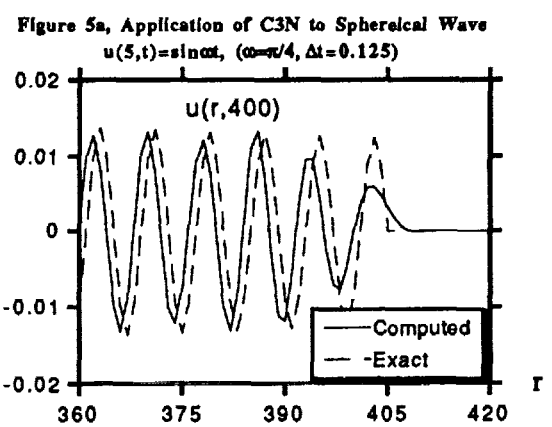

Figure 5b, Application of C3N to Spherical Wave
u(5,t)=sinωt, (ω=π/3, Δt=0.125)

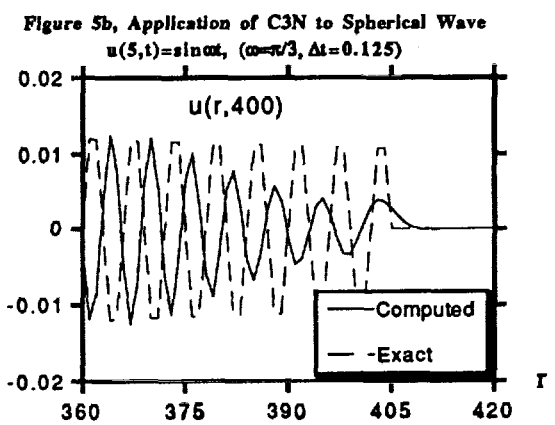

Application of C3N to the spherical wave equation is achieved by modifying the coefficients of Eq. (2) according to the difference equation: $\left(a_m E^{-1} + a + a_p E\right)\left(\delta_t u + \frac{u}{r}\right) + v\left(b_m E^{-1} + b + b_p E\right)u = 0$. Figure 5a shows the computed wave as the front reaches r=400. The r^{-1} decay is well captured up to the second peak with a small phase shift, but at the higher frequency, Fig. 5b, the first five peaks are significantly damped with a phase shift of π, which can be easily improved by slightly increasing the spatial resolution.

MULTI-DIMENSIONAL EXTENSIONS

One drawback in the application of implicit schemes to multi-dimensional problems is the drastic increase in system bandwidth for each additional dimension unless operator splitting or approximate factorization is used. However, a factorized or split scheme often involves intermediate variables that have no clear connection to the physical variables on which certain constraints are to be satisfied. Hence, the success of an implicit scheme for multidimensional problems hinges on whether the dependent variable in each factorized or split step can be consistently related to the physical constraints at boundary. This seems to be the case for aeroacoustic problems governed by the linearized Euler equations in Cartesian coordinates:

$$\frac{\partial U}{\partial t} + \frac{\partial AU}{\partial x} + \frac{\partial BU}{\partial y} = 0; \text{ where } U = \begin{bmatrix} \rho \\ u \\ v \\ p \end{bmatrix}, A = \begin{bmatrix} M_x,1,0,0 \\ 0,M_x,0,1 \\ 0,0,M_x,0 \\ 0,1,0,M_x \end{bmatrix} \text{ and } B = \begin{bmatrix} M_y,0,1,0 \\ 0,M_y,0,0 \\ 0,0,M_y,1 \\ 0,0,1,M_y \end{bmatrix} \tag{7}$$

Equation (7) can be split into two sets of equations $\begin{cases} \delta_t U + \delta_x AU = 0 \\ \delta_t U + \delta_y BU = 0 \end{cases}$, which can then be transformed into two sets of first order decoupled equations $\begin{cases} \delta_t \overline{U}_A + \delta_x \Lambda_A \overline{U}_A = 0 \\ \delta_t \overline{U}_B + \delta_y \Lambda_B \overline{U}_B = 0 \end{cases}$ corresponding to the characteristic variables $\overline{U}_A = \begin{bmatrix} \rho - p \\ v \\ u - p \\ u + p \end{bmatrix}$, $\overline{U}_B = \begin{bmatrix} \rho - p \\ v - p \\ u \\ v + p \end{bmatrix}$ and eigenvalues $\Lambda_A = \begin{bmatrix} M_x\ ,\ 0,0,0 \\ 0,M_x\ ,\ 0,0 \\ 0,0,M_x - 1,0 \\ 0,0,0,M_x + 1 \end{bmatrix}$, $\Lambda_B = \begin{bmatrix} M_y,\ 0,0,0 \\ 0,M_y - 1,0,0 \\ 0,0,M_y,\ 0 \\ 0,0,0,M_y + 1 \end{bmatrix}$.

Interestingly, subscripts A and B correspond to the coefficient Matrices A and B, which define the transformation from the physical variables to the characteristic variables, or the corresponding processes of wave propagation for each spatial dimension. It is clear that the last three equations in both transformed sets can be solved independently of the first, that only p affects ρ, and thus the first equation is needed only to find ρ after knowing p. The first equations in transformed sets A and B describe the convection of entropy ρ-p in two distinct directions at corresponding speeds M_X, M_Y. Being linear and independent, these equations, or processes, can be advanced in any order. The second equation in set A describes the convection of a vortical disturbance v at the speed M_X, while the third and fourth equations describe the propagation of acoustic disturbances at the receding speed M_X-1 and advancing speed M_X+1. The advancements of v and u in set A follow two distinct processes, hence are independent, whereas the roles of u and v exactly reverse in set B. Thus the linearized Euler equations, Eq. (7), which describe the convection of entropy and vorticity and the propagation of acoustic pulses, can be seen as eight one-dimensional modes of wave propagation at speeds corresponding to their eigenvalues. Unlike

factorization, which approximates the governing equation for easier inversions, splitting simply acknowledges the decomposition of vectors and the possibility of advancing their components in separate fashions. The two sets are indeed coupled through the common scalar variable p, which adjusts to the vortical and acoustical disturbances from all directions, and through which mass conservation is assured. The extension of Eq. (7) to three spatial dimensions is straight forward since all the preceding arguments for splitting remain valid.

Once split, the system becomes a set of one-dimensional wave equations, which can be solved using the compact schemes, or any appropriate schemes. A problem is set by specifying a value for each wave mode at the incoming end. Take for example the set A variables

$$\overline{U}_A = \begin{bmatrix} \rho_a - p_a \\ v_a \\ u_b - p_b \\ u_a + p_a \end{bmatrix}, \text{ which correspond to the eigenvalue matrix } \Lambda_A = \begin{bmatrix} M_x, & 0,0,0 \\ 0, M_x, & 0,0 \\ 0,0, M_x - 1, 0 \\ 0,0,0, M_x + 1 \end{bmatrix}, \text{ and assume that}$$

$0<M_x<1$. All variables corresponding to right running characteristics must be specified at the left boundary x=a except the third specified at the right x=b. For an undisturbed upstream or downstream, these values are unambiguously given. However, as disturbances propagate outward beyond b, the information for the third variable which should come from the value at a location beyond b is lost. Depending on the type of disturbance and approximation used, different degrees of reflection are found in the solutions as they are presented and discussed later.

Category III Test Problems

Figure 6a shows the density contours of a vortical pulse and an expanding acoustic pulse after being convected horizontally 15 grid points downstream from their initial positions. Perfect numerical symmetry is found in both pulses before their fronts hit the sides, confirming the one-dimensional nature of linear wave propagation. As the wave front of the acoustic pulse catches up with the vortical pulse at the downstream boundary, a slight asymmetry is observed in the density contours around the exiting vortex due to the boundary condition, Fig. 6b.

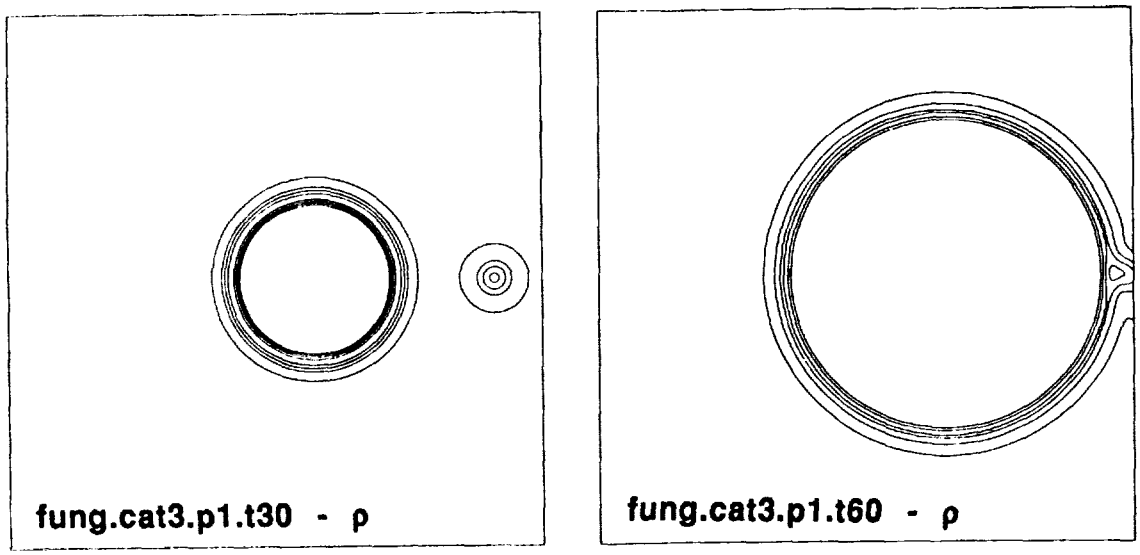

Figure 6a, Convected Acoustic and Vortical Pulses at t=30, and Figure 6b, t=60

A similar plot of pulses convected diagonally is shown in Fig. 7a, where the vortical pulse is not visible in pressure contours, but appears in density contours in Fig. 7b as it exits the domain at the upper right corner. Again slight contour distortion can be detected due to the boundary condition as the wave exits the domain.

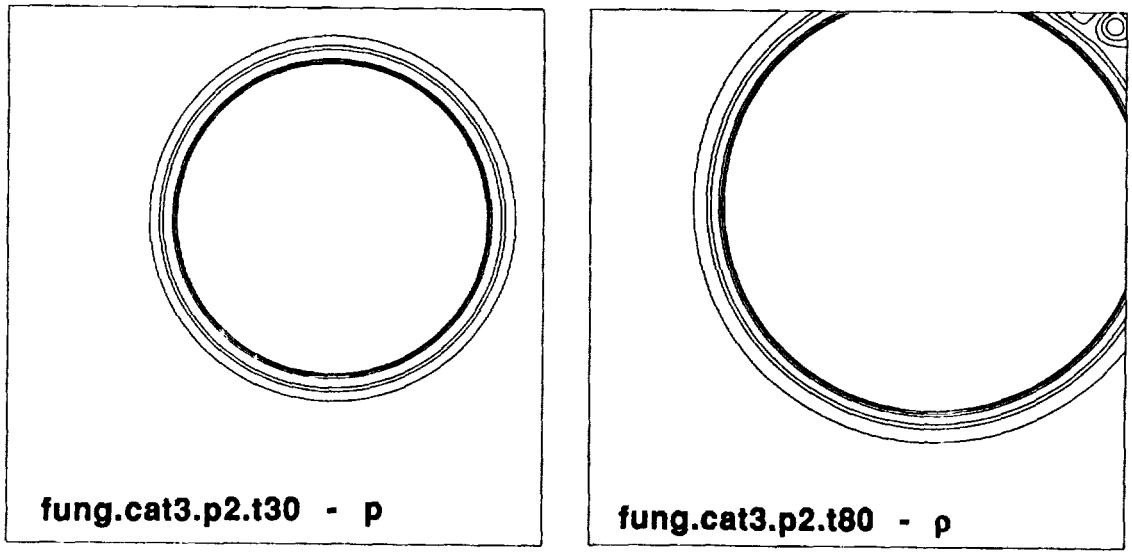

Figure 7a, Convected Acoustic and Vortical Pulses at t=30, and Figure 7b, t=80

The flow at any location is undisturbed until the arrival of a wave. At an exit plane, the incoming characteristic variable, e.g. u-p, for an undisturbed flow is zero, corresponding to u equals p. However, u and p are not always equal for a wave. A specification of $u-p|_b=0$, referred to as BC0 here on, could cause a phase shift and correspondingly a reflection to enter the domain along the incoming characteristics. Much weaker reflections are found when u-p is kept at the updated value from the sweep in the alternate direction, referred here on as BC1, or even weaker ones when it is corrected by a fraction α of its change from the previous value, $u-p=u-p+\alpha\Delta(u-p)$, referred as BC2.

The authors have not investigated the use of asymptotic expressions for the far field, since they are domain and problem dependent.

Category IV and VI Problems

The reflection of an acoustic pulse from wall or the satisfaction of a wall condition when the velocity component normal to the wall is constrained is achieved by ordering the characteristic variables and solving the one approaching the wall first, e.g. v-p, and setting v+p to comply with any condition on v, such as v+p=-(v-p) to enforce v=0. This ordering establishes a causality relation between the acoustic components, which should be solved one after the other as two arrays or merged into a large array with the first element of the second connected to the last element of the first to satisfy the wall constraint. If wall constraints are to be imposed on both ends, the joint array has cyclic boundary condition which can be solved using standard cyclic tridiagonal solvers.

Figure 8a shows the reflection of an acoustic pulse from wall, at y=0 v=0, and Fig. 8b shows the exit of the wave fronts from the right boundary at a later time (t=60) and a spike of reflection due to applying BC0. A much weaker reflection, less than 10% of the frontal magnitude, is found when BC1 is used, Fig. 8c, and practically no reflection, less than 5%, when BC2 and α=0.15 are used instead.

Figure 8a, Pressure Contours of a Reflected Acoustic Pulse at t=20

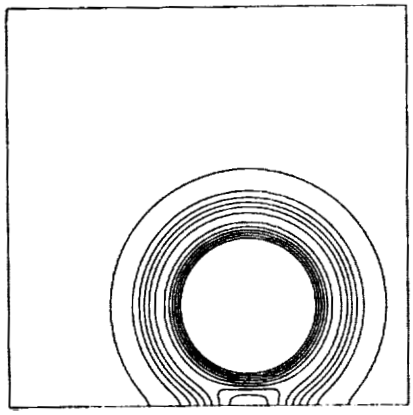

Figure 8b, Pressure Contour of Fronts Exiting Numerical Boundary at x=50 Using BC0

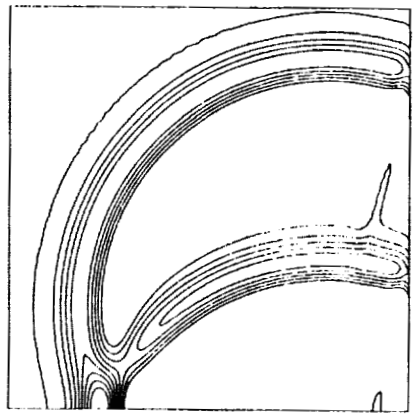

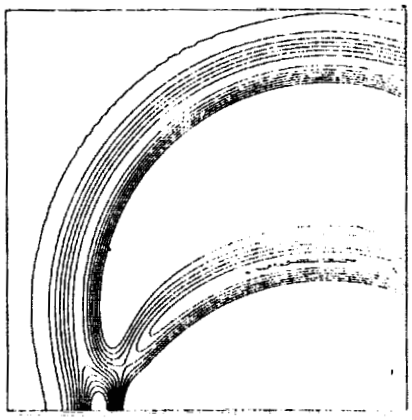

Figure 8c, Pressure Contour of Fronts Exiting Numerical Boundary at x=50 Using BC1

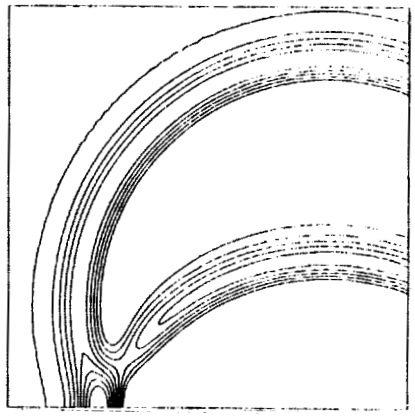

Figure 8d, Pressure Contour of Fronts Exiting Numerical Boundary at x=50 Using BC2

The extension to problems in cylindrical coordinates is nontrivial in that unlike in Cartesian coordinates the acoustic part of the split equations in the radial direction can not be transformed into uncoupled characteristic components due to the source-like term v/r, viz.,

$$\delta_t \begin{bmatrix} u_1 \\ u_2 \\ u_3 \\ u_4 \end{bmatrix} + \delta_r \begin{bmatrix} 0,0, & 0,0 \\ 0,0, & 0,0 \\ 0,0, & -1,0 \\ 0,0, & 0,1 \end{bmatrix} \begin{bmatrix} u_1 \\ u_2 \\ u_3 \\ u_4 \end{bmatrix} + \begin{bmatrix} 0 \\ 0 \\ -(u_3+u_4)/2r \\ (u_3+u_4)/2r \end{bmatrix} = 0.$$

However, it is found that the coupling between the acoustic components is only a weak one, and the source-like term can be treated explicitly to a second order in time to maintain the same simplicity in data structure as in Cartesian coordinates, e.g., $u_3^{n+1} = u_3^n + \frac{\Delta t}{2}\delta_r(u_3^{n+1} + u_3^n) + \frac{\Delta t}{2r}\left(u_4^n + u_3^n + \frac{\Delta t}{2}\delta_r(u_4^n - u_3^n)\right)$.

Another complication arises due to the transformation singularity at the radial symmetry point r=0. Numerically this is just a boundary point where the incoming characteristic variable v-p turns into the outgoing variable v+p to satisfy the condition at r=0, where v also vanishes, but not necessarily v/r. Fortunately, the assumption that v/r is regular and hence, approaches the adjacent value at r=Δr proved

adequate for the application of the acoustic field of a harmonically moving piston. Figure 9a shows a plot of pressure contours at t=160, and Fig. 9b gives the pressure variations at two instances ($\pi/4$ & 2π) along and normal to the piston axis.

Figure 9a, Acoustic Field of a Piston

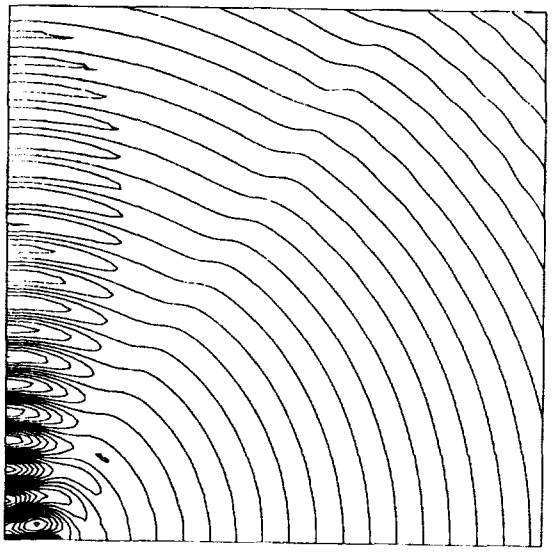

Figure 9b, Axial and Radial Pressure Variations

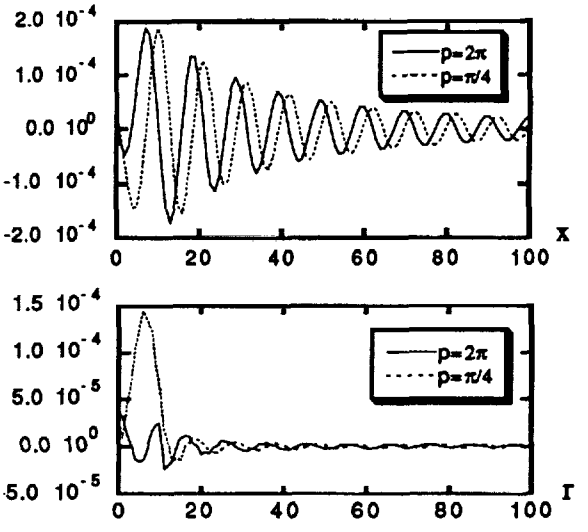

The compact schemes presented here are nondissipative but dispersive for short waves whose presence is unavoidable whenever a discontinuity is involved in the boundary condition. In the case of a piston, for example, the edge of a piston at r=R is a source of discontinuity where the axial velocity changes abruptly from the piston velocity to zero wall velocity. Spurious waves immediately disperse unless they are either filtered or damped. Here, a damping, ε=0.01, consistent with a three-point scheme and proportional to the second derivative, $\varepsilon\frac{\Delta t}{\Delta x^2}\delta_x^2\frac{u^{n+1}+u^n}{2}$, is found adequate for the present applications.

The last application here is to compute the acoustic field of an airfoil encountering a sinusoidal gust, or a sinusoidally deforming airfoil in a subsonic stream. An extra array is needed to represent the jumps in pressure and correspondingly in tangential velocity component across the airfoil slit at y=0 and $|x|\le c/2$. The acoustic components are ordered differently for the upper and lower half planes such that the one towards the airfoil is solved before the other. For points other than the airfoil slit on y=0, pressure assumes the average value while jumps in tangential velocity are allowed. Figure 10a shows the acoustic field, and Figure 10b&c shows the powers p^2 radiated at x,y=±95 respectively.

Figure 10a, Acoustic Field of an Airfoil in a Gust

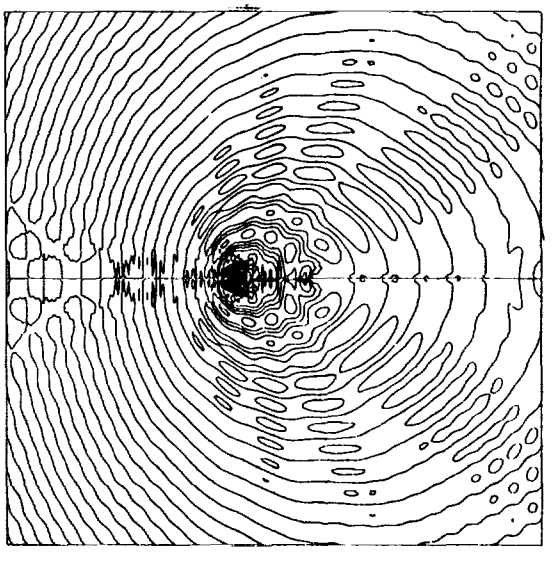

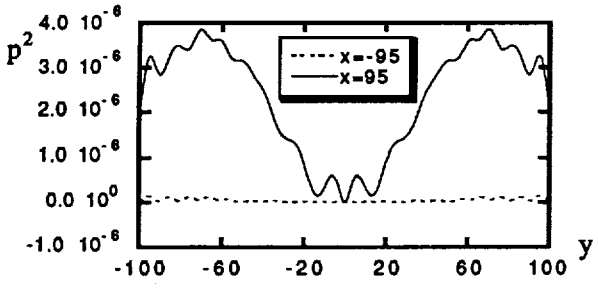

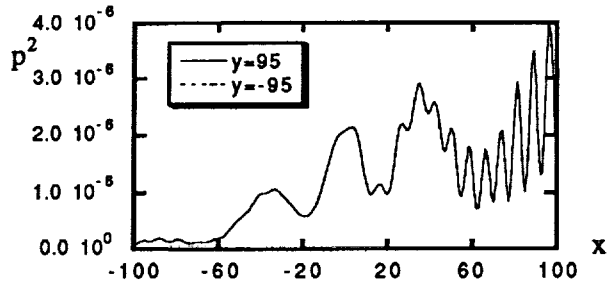

CONCLUDING REMARKS

The effectiveness of C3N and a class of outgoing boundary conditions has been established on various wave propagation problems and nonuniform grids. This compact scheme, though not the most accurate one on a uniform grid, is simple to implement, robust under all conditions tested, and requires standard tridiagonal solvers to invert and negligible overhead storage.

The equivalence between the propagation of acoustic waves in two spatial dimensions and that of a system of one-dimensional simple waves is shown, and conversion to characteristic variables allows decoupling and ordering of the wave components. All solutions presented, regardless of the number of spatial dimensions, are obtained by passing segments of self-contained, one-dimensional arrays through the same solver, which can occupy concurrently a massive array of computers for rapid data processing.

Contrary to others, the present approach requires specification of the incoming components into the far field boundaries. This component must be compatible with the outgoing ones to ensure no spurious reflection. It is shown here how the spurious reflections are reduced but not completely eliminated, for which further research is warranted.

REFERENCES

1. Candel S., "A review of Numerical Methods in Acoustic Wave Propagation," in Recent Advances in Aeroacoustics, edited by Krothapalli and Smith, Springer-Verlag, 1986, pp. 339-410.

2. Roe, P., "Technical Prospects for Computational Aeroacoustics," DGLR/AIAA paper 92-02-032

3. Lee, D., Botseas, G., and Papadakis, J. S. " Finite Difference Solutions to the Parabolic Wave Equation," J. Acoust. Soc. Am., 70 (1981), 795-800.

4. Tam, C. K. W. and Webb J. C., "Dispersion-Relation-Preserving Difference Schemes," for Computational Acoustics," J. Comp. Phys. 107, 262-281, 9993.

5. Noye, J., "Three-point, Two-level Finite Difference Methods for the One-dimensional Advection Equation," in Computational Techniques and Applications, CTAC-85, edited by Noye and R. May (North-Holland, Amsterdam, 1986), pp. 159-192.

6. Davis, S., "Low-Dispersion Finite Difference Methods for Acoustic Waves in a Pipe," J. Acoust. Soc. Am. 90 (5), Nov. 1991.

7. Beam, R. M. and Warming, R. F., "An Implicit Finite-Difference Algorithm for Hyperbolic Systems in Conservation-Law Form", J. Comp. Phys., 22, pp 87-110, 1976.

APPLICATION OF LOW DISSIPATION AND DISPERSION RUNGE-KUTTA SCHEMES TO BENCHMARK PROBLEMS IN COMPUTATIONAL AEROACOUSTICS

F. Q. Hu[†], M. Y. Hussaini[‡] and J. Manthey[†]
[†]Department of Mathematics and Statistics, Old Dominion University
Norfolk, VA 23529

[‡]Institute for Computer Applications in Science and Engineering
NASA Langley Research Center, Hampton, VA 23681

ABSTRACT

We investigate accurate and efficient time advancing methods for computational aeroacoustics, where non-dissipative and non-dispersive properties are of critical importance. Our analysis pertains to the application of Runge-Kutta methods to high-order finite difference discretization. In many CFD applications, multi-stage Runge-Kutta schemes have often been favored for their low storage requirements and relatively large stability limits. For computing acoustic waves, however, the stability consideration alone is not sufficient, since the Runge-Kutta schemes entail both dissipation and dispersion errors. The time step is now limited by the tolerable dissipation and dispersion errors in the computation. In the present paper, it is shown that if the traditional Runge-Kutta schemes are used for time advancing in acoustic problems, time steps greatly smaller than that allowed by the stability limit are necessary. Low Dissipation and Dispersion Runge-Kutta (LDDRK) schemes are proposed, based on an optimization that minimizes the dissipation and dispersion errors for wave propagation. Optimizations of both single-step and two-step alternating schemes are considered. The proposed LDDRK schemes are remarkably more efficient than the classical Runge-Kutta schemes for acoustic computations. Numerical results of each Category of the Benchmark Problems are presented. Moreover, low storage implementations of the optimized schemes are discussed. Special issues of implementing numerical boundary conditions in the LDDRK schemes are also addressed.

1. INTRODUCTION

Computational acoustics is a recently emerging tool for acoustic problems. In this approach, the acoustic waves are computed directly from the governing equations of the compressible flows, namely, the Euler equations or the Navier-Stokes equations. Special needs of numerical schemes for computational acoustics have been indicated in recent works (eg. [9], [12]). It has been recognized that numerical schemes that have minimal dispersion and dissipation errors are desired, since the acoustic waves are non-dispersive and non-dissipative in their propagations. In this regard, it has appeared that high-order schemes would be more suitable for computational acoustics than the lower-order schemes since the former are usually less dispersive and less dissipative. Recently, high-order spatial discretization schemes have gained considerable interests in computational acoustics, among them the explicit DRP [12], implicit (or compact) [8,11] and ENO schemes[6]. In this paper, we

This work was supported by the National Aeronautics and Space Administration under NASA Contract NAS1-19480 while the authors were in residence at the Institute for Computer Applications in Science and Engineering, NASA Langley Research Center, Hampton, VA 23665, USA.

investigate accurate and efficient time advancing schemes for computational acoustics. In particular, the family of Runge-Kutta methods is considered. The present analysis pertains to the application of Runge-Kutta methods to high-order finite difference schemes.

In many CFD applications, popular time advancing schemes are the classical 3rd- and 4th-order Runge-Kutta schemes because they provide relatively large stability limits [10]. For acoustic calculations, however, the stability consideration alone is not sufficient, since the Runge-Kutta schemes retail both dissipation and dispersion errors. The numerical solutions need to be *time accurate* to resolve the wave propagations. In Category 1 problems, we show that when the classical Runge-Kutta schemes are used in wave propagation problems using high-order spatial finite difference, time steps much smaller than that allowed by the stability limit are necessary in the long-time integrations. This certainly undermines the efficiency of the classical Runge-Kutta schemes.

Runge-Kutta schemes are multi-stage methods. Traditionally, the coefficients of the Runge-Kutta schemes are chosen such that the maximum possible order of accuracy is obtained for a given number of stages. However, it will be shown that it is possible to choose the coefficients of the Runge-Kutta schemes so as to minimize the dissipation and dispersion errors for the propagating waves, rather than to obtain the maximum possible formal order of accuracy. The optimization also does not compromise the stability considerations. The optimized schemes will be refereed to as Low Dissipation and Dispersion Runge-Kutta (LDDRK) schemes. Consequently, remarkably larger time steps can be used in the LDDRK schemes, which increases the efficiency of the computation. The optimized 4-, 5-, and 6-stage schemes are proposed. In addition, optimized two-step schemes are also given in which different coefficients are used in the alternating steps. It is found that when two steps are coupled for optimization, the dispersion and dissipation errors can be further reduced and higher formal order of accuracy be retained.

Optimization of numerical schemes for wave propagation problems has been conducted in several recent studies (e.g., [8], [12], [16]). In [12], a Adam-Bashforth type multi-step time integration scheme was optimized for acoustic calculations. In that work, the optimization was carried out to preserve the numerical frequency in the development of Dispersion-Relation-Preserving finite difference schemes. In [16], a 6-stage Runge-Kutta scheme was optimized for the linear wave propagations. Most recently, optimization of 5-stage Runge-Kutta schemes was considered in [8] for long-time integration, in which optimized coefficients were given depending on the spectrum of initial condition. There are, however, differences between the present and previous works in several aspects. First, the optimization of time advancing is separate from the spatial discretization schemes. The optimization is done once and for all. The proposed LDDRK schemes are applicable to different spatial discretization methods. Second, the optimization is carried out only for the resolved frequencies/wavenumber in the spatial discretization. It will be shown that LDDRK schemes preserves the frequency in the time integration and thus is Dispersion-Relation-Preserving in the sense of [12]. Third, optimizations of two coupled Runge-Kutta steps are considered for the first time. Our results indicate that the two-step schemes offer better properties and are more efficient than the optimized single-step schemes.

The advantages of Runge-Kutta methods also include low storage requirements in their implementations, as compared to Adam-Bashforth type multi-step methods. The low storage requirement is important for computational aeroacoustics applications where large memory use is expected. In the past, it has been shown that the 3-stage 3rd-order scheme can be implemented with only two levels of storages. Recently, the 4th-order scheme has been put into a two-level format using 5 stages in [4]. We point out that, in light of recent studies, most of the LDDRK schemes proposed here can be

implemented with two levels of storages, since the number of stages are larger than the formal order of accuracy retained in all schemes except one.

In section 2, results of Fourier analysis of high-order finite difference schemes are reviewed briefly. Time advancing with Runge-Kutta methods is described in section 3, Optimization process and LDDRK schemes are given in section 4 and low storage implementations are discussed in section 5. Special issues of implementing boundary conditions are discussed in section 6. Numerical results are discussed in section 7. Concluding remarks are given in section 8.

2. FOURIER ANALYSIS OF HIGH-ORDER SPATIAL DISCRETIZATION

In this section, results of Fourier analysis of high-order finite difference schemes are reviewed briefly [14]. For simplicity of discussions, we consider the convective wave equation

$$\frac{\partial u}{\partial t} + c\frac{\partial u}{\partial x} = 0 \tag{2.1}$$

Let the spatial derivative be approximated by a central difference scheme with an uniform mesh of spacing Δx as

$$\left(\frac{\partial u}{\partial x}\right)_j = \frac{1}{\Delta x}\sum_{\ell=-N}^{N} a_\ell u_{j+\ell} \tag{2.2}$$

in which a central difference stencil has been used. In (2.2) u_j represents the value of u at $x = x_j$ and a_ℓ's are the coefficients of the difference scheme. Applying the spatial discretization (2.2) to (2.1), a semi-discrete equation is obtained as

$$\frac{\partial u_j}{\partial t} + \frac{c}{\Delta x}\sum_{\ell=-N}^{N} a_\ell u_{j+\ell} = 0$$

at interior points. Using Fourier analysis, it is easy to show that the semi-discrete equation yields

$$\frac{\partial \tilde{u}}{\partial t} + \mathrm{i}ck^*\tilde{u} = 0 \tag{2.3}$$

where $\tilde{u}$ is the spatial Fourier transform of u and k^* is effective wavenumber :

$$k^* = \frac{-\mathrm{i}}{\Delta x}\sum_{\ell=-N}^{N} a_\ell e^{\mathrm{i}\ell k\Delta x} \tag{2.4}$$

and k is the actual wavenumber. $\mathrm{i} = \sqrt{-1}$.

Thus k^* of (2,4) is seen as an approximation to the actual wavenumber k. Moreover, we note that the non-dimensionalized effective wavenumber $k^*\Delta x$ as a function of $k\Delta x$ is a property of the finite difference scheme, depending only on the coefficients of the scheme, a_ℓ. (Similar analysis can also be performed for implicit finite difference schemes, such as the compact schemes [8, 11]). In Figure 1, $k^*\Delta x$ as a function of $k\Delta x$ is plotted for several high-order spatial discretization schemes.

It is observed that $k^*\Delta x$ approximates $k\Delta x$ adequately for only a limited range of the long waves. For convenience, the maximum resolvable wavenumber will be denoted by k_c^*. Using a criterion of $|k^*\Delta x - k\Delta x| < 0.005$, a list of $k_c^*\Delta x$ values for high-order central difference schemes is given in Table I. Often the "resolution" of spatial discretization is represented by the minimum points-per-wavelength needed to reasonably resolve the wave. Here the points-per-wavelength value will be computed as $2\pi/k_c^*\Delta x$.

TABLE I

Values of $k_c^*\Delta x$ and $k_{max}^*\Delta x$ for several high-order central difference schemes of the spatial derivative. † indicates that the scheme has been optimized to have maximum $k_c^*\Delta x$.

Spatial Discretization	$k_c^*\Delta x$	Resolution (Point-Per-Wavelength)	$k_{max}^*\Delta x$
5-point 4th-order [7]	0.7	9.0	1.4
7-point 4th-order† [13]	1.16	5.4	1.65
9-point 6th-order†	1.31	4.8	1.77
11-point 6th-order†	1.48	4.2	1.9
5-point compact [11]	1.36	4.6	2.0

Also listed in Table I are the values of maximum effective wavenumber $k_{max}^*\Delta x$. Clearly, when finite difference schemes are used for the spatial discretization, only the long waves (i.e. for $k \leq k_c^*$) are resolved within a given accuracy.

3. TIME ADVANCING WITH RUNGE-KUTTA SCHEMES

We now consider the time advancing schemes. In particular, the Runge-Kutta methods will be considered. For convenience of discussions, a general explicit Runge-Kutta scheme is described below. Let the time evolution equation be written as

$$\frac{\partial \mathbf{U}}{\partial t} = F(\mathbf{U}) \tag{3.1}$$

An explicit, p-stage Runge-Kutta scheme advances the solution from time level $t = t_n$ to $t_n + \Delta t$ as follows :

$$\mathbf{U}^{n+1} = \mathbf{U}^n + \sum_{i=1}^{p} w_i \mathbf{K}_i \tag{3.2}$$

where

$$\mathbf{K}_i = \Delta t F(\mathbf{U}^n + \sum_{j=1}^{i-1} \beta_{ij} \mathbf{K}_j), \qquad i = 1, 2, ..., p \tag{3.3}$$

In the above, w_i and β_{ij} are the constant coefficients of the particular scheme.

The choice of the time step Δt is an important issue in the Runge-Kutta schemes. One criterion for the time step is that the time integration be stable. The time integration would be considered as stable if the step size is limited by the stability boundary, usually from the "foot print" of the particular Runge-Kutta scheme. For references, the stability "foot prints" of the classical 3rd- and 4th-order Runge-Kutta schemes are shown in Figure 2 in the complex $\lambda\Delta t$ plane, where λ is the eigenvalue of the linearized operator of $F(\mathbf{U})$ in (3.1).

To get time accurate solutions, however, the time step size Δt is now limited by the tolerable dissipation and dispersion errors, in addition to the stability considerations. Consider, for example, the semi-discrete equation (2.3) of the convective wave equation (2.1) and suppose that the classical 4th-order Runge-Kutta schemes is used. Here, the eigenvalue is $-\mathbf{i}\,c\,k^*$ and k^* is real for central difference schemes. Thus, from Figure 2, the 4th-order Runge-Kutta scheme should be stable if Δt is chosen such that

$$c\,k^*_{max}\,\Delta t \leq 2.83$$

in which k^*_{max} is the maximum effective wavenumber of the spatial difference scheme. Figure 3 shows the computational results of Category 1 problem 1 where several different values of Δt have been used, i.e. $c\,k^*_{max}\,\Delta t = 2.83,\ 2.0,\ 1.0$. Numerical results at $t = 400$ are shown. Since our purpose is to demonstrate the time integration schemes, a 9-point central difference scheme has been used in the spatial discretization for the calculations presented. The numerical solutions exhibit serious dissipation and dispersion errors for the first two cases. This example shows that, to get time accurate solutions, time steps much smaller than that allowed by the stability limit is necessary when the classical Runge-Kutta schemes are used.

To analyze the numerical errors in the Runge-Kutta schemes, we consider the amplification factor of the schemes, i.e. the ratio of the numerical solution at time levels $n+1$ and n in the wave number domain. From the semi-discrete equation (2.3), it is easy to find that the Runge-Kutta scheme leads a numerical amplification factor,

$$r = \frac{\tilde{\mathbf{U}}^{n+1}_k}{\tilde{\mathbf{U}}^{n}_k} = 1 + \sum_{j=1}^{p} c_j(-\mathbf{i}\sigma)^j \tag{3.4}$$

where $\sigma = c\,k^*\,\Delta t$. $\tilde{\mathbf{U}}^n_k$ is the spatial Fourier transform of $\mathbf{U}^n$. The *exact* amplification factor, on the other hand, is found to be

$$r_e = e^{-\mathbf{i}\,c\,k^*\,\Delta t} = e^{-\mathbf{i}\sigma} \tag{3.5}$$

The numerical amplification factor r in (3.4) is seen as a polynomial approximation to the exact factor $e^{-\mathbf{i}\sigma}$. In fact, the order of a Runge-Kutta scheme is indicated by the number of leading coefficients in (3.4) that match the Taylor series expansion of $e^{-\mathbf{i}\sigma}$. To compare the numerical and exact amplification factors, we express the ratio r/r_e as

$$\frac{r}{r_e} = |r|e^{-\mathbf{i}\delta} \tag{3.6}$$

In this expression, $|r|$ represents the dissipation rate (or the dissipation error) where the exact value should be 1, and δ represents the phase error (or the dispersion error) where the exact value should be 0. It is easily seen from (3.4) that $|r|$ and δ are functions of $ck^*\Delta t$. The dissipation rate $|r|$ and the dispersion error δ of the classical 3rd- and 4th-order Runge-Kutta scheme are plotted in Figure 4. Only the values for positive $ck^*\Delta t$ are shown, since $|r|$ and δ are even and odd functions, respectively.

Using the criteria, say, that $\left||r|-1\right| \leq 0.001$ and $|\delta| \leq 0.001$, it is found that the numerical solution would be *time accurate* for $c\,k^*\,\Delta t \leq 0.5$ and $c\,k^*\,\Delta t \leq 0.67$ in the 3rd- and 4th-order Runge-Kutta schemes, respectively.

Following above analysis, we let R denote the *stability limit* of $c\,k^*\,\Delta t$, i.e. the scheme is stable for $c\,k^*\,\Delta t \leq R$, and L denote the *accuracy limit*, i.e. the solution is time accurate for $c\,k^*\,\Delta t \leq L$. Then, it is necessary for the time advancing scheme to be both stable for *all* wavenumbers and accurate for *resolved* wavenumbers. These considerations lead to the following conditions of determining Δt for the convective wave equation :

$$c\,k_c^*\,\Delta t \leq L \tag{3.7a}$$

$$c\,k_{max}^*\,\Delta t \leq R \tag{3.7b}$$

That is, in non-dimensional terms,

$$c\,\frac{\Delta t}{\Delta x} = min\left(\frac{L}{k_c^*\,\Delta x},\ \frac{R}{k_{max}^*\,\Delta x}\right) \tag{3.8}$$

Thus, the accuracy limit would give a smaller time step whenever $\frac{L}{R} < \frac{k_c^*}{k_{max}^*}$. .

4. LOW DISSIPATION AND DISPERSION RUNGE-KUTTA SCHEMES

4.1 Minimizing the dissipation and dispersion errors

To optimize the Runge-Kutta schemes, we modify the coefficients c_j in the amplification factor (3.4) such that the dissipation and the dispersion errors are minimized and the accuracy limit L is extended as much as possible. This is in contrast to the traditional choice of c_j that maximizes the possible order of accuracy. The optimized schemes will be to as Low Dissipation and Dispersion Runge-Kutta (LDDRK) schemes. The optimization is carried out by minimizing $|r-r_e|^2$ as a function of $ck^*\Delta t$. It can be shown that this minimizes the total of the dissipation and dispersion errors. Certain formal order of accuracy has been retained in the optimization processes. In other words, the coefficients c_j will be determined such that the following integral is a minimum :

$$\int_0^\Gamma \left| 1 + \sum_{j=1}^{p} c_j(-\mathrm{i}\sigma)^j - e^{-\mathrm{i}\sigma} \right|^2 d\sigma = MIN \tag{4.1}$$

where Γ specifies the range of $c\,k^*\,\Delta t$ in the optimization. This leads to a simple constrained minimum problem which yields a linear system for c_j. Once the values of c_j have been determined, the actual coefficients of the Runge-Kutta schemes, i.e. w_i and β_{ij}, can be found accordingly. This optimization process can also be viewed as preserving the frequency (Appendix A) and thus is Dispersion-Relation-Preserving in the sense of [12].

Optimizations of 4-, 5-, and 6-stage schemes have been carried out. At least a 2nd order accuracy has been maintained, i.e., $c_1 = 1$ and $c_2 = 1/2$ for all the schemes and 4th-order accuracy has been retained in the optimized 6-stage schemes. The optimized coefficients are given in Table II. Also listed are the respective accuracy and stability limits of the optimized schemes. The accuracy limits

L are determined using the criteria $\left||r|-1\right| \leq 0.001$ and $|\delta| \leq 0.001$. The value of Γ used in (4.1) has been varied such that the accuracy limit L is as large as possible. The dissipation and dispersion errors of the optimized schemes are plotted in Figure 5. Plotted in dotted lines are the errors of un-optimized scheme in which the coefficients c_j equal to the that of the Taylor expansion of $e^{-i\sigma}$.

Table II shows that the optimized 5-stage scheme can be more efficient than the 4-stage scheme, as the increase in the accuracy limit out-weights the cost of the additional stage incurred. On the other hand, the optimized 6-stage scheme has a smaller stability limit than the 5-stage scheme, although the accuracy limit is larger. This scheme, perhaps, is more useful for spectral methods than finite difference methods [3].

TABLE II

Optimized coefficients for the amplification factor (3.4). L and R are the accuracy and stability limits, respectively. All the schemes have at least second-order formal accuracy , i.e. $c_1 = 1$, $c_2 = 1/2$.

Stages	c_3	c_4	c_5	c_6	L	R
4	0.162570	0.0409464	—	—	0.86	2.85
5	0.166344	0.0395041	0.00781071	—	1.36	3.54
6	1/3!	1/4!	0.00781005	0.00132141	1.75	1.75

4.2 Optimized two-step alternating schemes

In two-step alternating schemes, we consider schemes in which different coefficients are employed in the alternating steps. The advantages of the alternating schemes are that, when two steps are combined in the optimization, the dispersion and dispersion errors can be further reduced and higher order of accuracy can be maintained.

Let the amplification factors of the first and the second step be

$$r_1 = 1 + \sum_{j=1}^{p_1} a_j(-i\sigma)^j \tag{4.2a}$$

$$r_2 = 1 + \sum_{j=1}^{p_2} b_j(-i\sigma)^j \tag{4.2b}$$

where p_1 and p_2 are the number of stages of the two steps, respectively. Accordingly, the scheme will be denoted as p_1-p_2 scheme below. It is easy to see that the amplification factor for these two steps combined equals to $r_1 r_2$. The exact amplification factor, on the other hand, is r_e^2. Again, we now choose the coefficients a_j and b_j such that $|r_1 r_2 - r_e^2|$ is minimized. That is, the coefficients in the alternating steps will be determined such that the following integral is minimum

$$\int_0^{\Gamma} \left| \left(1 + \sum_{j=1}^{p1} a_j(-\mathbf{i}\sigma)^j \right) \left(1 + \sum_{j=1}^{p2} b_j(-\mathbf{i}\sigma)^j \right) - e^{-2\mathbf{i}\sigma} \right|^2 d\sigma = MIN \tag{4.3}$$

Optimized coefficients for 4-6 and 5-6 schemes are given in Table III. In both schemes, a 4th-order accuracy has been maintained for each step. Thus, the first step in 4-6 scheme is actually the same as the traditional 4-stage 4th-order Runge-Kutta scheme. The dissipation and dispersion errors are shown in Figure 6 and the stability foot prints are given in Figure 7. For efficiency, we note that the computational cost of the 4-6 alternating scheme is comparable to that of 5-stage schemes while the 5-6 scheme is slightly higher. However, the 4-6 and 5-6 schemes are 4th-order accurate whereas the optimized single-step 5-stage scheme is 2nd order.

TABLE III

Optimized coefficients for the 4-6 and 5-6 schemes of (4.2). 4th-order accuracy has been retained in each step, i.e. $a_1 = b_1 = 1$, $a_2 = b_2 = 1/2$, $a_3 = b_3 = 1/6$, $a_4 = b_4 = 1/24$. L and R are the accuracy and stability limits of each step, respectively.

Scheme	Step	Stages	a_5/b_5	a_6/b_6	L	R
4-6	1	4	—	—	1.65	2.52
	2	6	0.0162571	0.00286365		
5-6	1	5	0.00366849	—	2.05	2.85
	2	6	0.0121101	0.00285919		

Numerical results of Category 1 are shown in Figure 7. By and large, it has been observed that the optimized two-step alternating schemes appear to be more efficient than the single-step optimized schemes.

Finally, we point out that, unlike [8], the condition $|r| \leq 1$ has not been forced explicitly in the optimization processes. Although this gives a simpler optimization problem, the optimized schemes are, consequently, very slightly unstable for some narrow region of the wavenumber within the given stability limits R. However, $|r| < 1.001$ in all cases. Such weak instability is not expected to cause numerical problem and can be overcome in practical computations, for instance by artificial damping or viscous effects.

5. LOW STORAGE IMPLEMENTATION OF LDDRK SCHEMES

In this section, we study the implementation of the LDDRK schemes. Particularly, we will be interested in the implementations that require low memory storages. For linear problems, the following implementation is convenient for a p-stage scheme. Let the time evolution equation be given as (3.1). Then,

1. For $i = 1 \ldots p$, compute (with $\bar{\beta}_1 = 0$)

$$\mathbf{K}_i = \Delta t\, F(\mathbf{U}^n + \bar{\beta}_i \mathbf{K}_{i-1}) \tag{5.1b}$$

2. Then,

$$\mathbf{U}^{n+1} = \mathbf{U}^n + \mathbf{K}_p \tag{5.1c}$$

The coefficients $\bar{\beta}_i$ in (5.1) are related to the coefficients c_j of the amplification factor of LDDRK schemes as follows :

$$\begin{aligned} c_2 &= \bar{\beta}_p \\ c_3 &= \bar{\beta}_p\, \bar{\beta}_{p-1} \\ &\cdots\cdots \\ c_p &= \bar{\beta}_p\, \bar{\beta}_{p-1} \ldots \bar{\beta}_2 \end{aligned} \tag{5.2}$$

The above scheme can also be applied to non-linear problems, but it will be formally second-order in general [3,10]. This implementation requires at most three levels of storage.

6. IMPLEMENTATION OF BOUNDARY CONDITIONS

Numerical boundary condition is another important issue in computational aeroacoustics. Often the physical boundary conditions are given in the form of differential equations, such as the characteristics-based boundary conditions or the boundary conditions based on the asymptotic forms of the far field solutions [1, 12]. When boundary conditions are coupled with governing equations of the interior grids, it is not immediately clear as to how the $\mathbf{K}_i$'s in the Runge-Kutta time integration process should be computed at the boundaries.

For simplicity, we assume that the problem is linear or can be linearized at the boundaries. To examine the situation around the boundary grid points, we note that $\mathbf{K}_i$ is related to the time derivatives of the solution $\mathbf{U}$, rather than being some "intermediate" value of the solution [5]. Specifically, for the iterations of (5.1) for linear problems, we have

$$\begin{aligned}
\mathbf{K}_1 &= \Delta t \frac{\partial \mathbf{U}}{\partial t} \\
\mathbf{K}_2 &= \Delta t \frac{\partial \mathbf{U}}{\partial t} + \bar{\beta}_2 \Delta t^2 \frac{\partial^2 \mathbf{U}}{\partial t^2} \\
\mathbf{K}_3 &= \Delta t \frac{\partial \mathbf{U}}{\partial t} + \bar{\beta}_3 \Delta t^2 \frac{\partial^2 \mathbf{U}}{\partial t^2} + \bar{\beta}_3 \bar{\beta}_2 \Delta t^3 \frac{\partial^3 \mathbf{U}}{\partial t^3} \\
\mathbf{K}_4 &= \Delta t \frac{\partial \mathbf{U}}{\partial t} + \bar{\beta}_4 \Delta t^2 \frac{\partial^2 \mathbf{U}}{\partial t^2} + \bar{\beta}_4 \bar{\beta}_3 \Delta t^3 \frac{\partial^3 \mathbf{U}}{\partial t^3} + \bar{\beta}_4 \bar{\beta}_3 \bar{\beta}_2 \Delta t^4 \frac{\partial^4 \mathbf{U}}{\partial t^4} \\
\mathbf{K}_5 &= \Delta t \frac{\partial \mathbf{U}}{\partial t} + \bar{\beta}_5 \Delta t^2 \frac{\partial^2 \mathbf{U}}{\partial t^2} + \bar{\beta}_5 \bar{\beta}_4 \Delta t^3 \frac{\partial^3 \mathbf{U}}{\partial t^3} + \bar{\beta}_5 \bar{\beta}_4 \bar{\beta}_3 \Delta t^4 \frac{\partial^4 \mathbf{U}}{\partial t^4} + \bar{\beta}_5 \bar{\beta}_4 \bar{\beta}_3 \bar{\beta}_2 \Delta t^5 \frac{\partial^5 \mathbf{U}}{\partial t^5} \\
\mathbf{K}_6 &= \Delta t \frac{\partial \mathbf{U}}{\partial t} + \bar{\beta}_6 \Delta t^2 \frac{\partial^2 \mathbf{U}}{\partial t^2} + \bar{\beta}_6 \bar{\beta}_5 \Delta t^3 \frac{\partial^3 \mathbf{U}}{\partial t^3} + \bar{\beta}_6 \bar{\beta}_5 \bar{\beta}_4 \Delta t^4 \frac{\partial^4 \mathbf{U}}{\partial t^4} + \bar{\beta}_6 \bar{\beta}_5 \bar{\beta}_4 \bar{\beta}_3 \Delta t^5 \frac{\partial^5 \mathbf{U}}{\partial t^5} + \bar{\beta}_6 \bar{\beta}_5 \bar{\beta}_4 \bar{\beta}_3 \bar{\beta}_2 \Delta t^6 \frac{\partial^6 \mathbf{U}}{\partial t^6}
\end{aligned} \tag{6.1}$$

The above relations are exact. Thus, it becomes clear that, if $\mathbf{U}$ is known at the boundary, $\mathbf{K}_i$ at the boundary points should be computed according to (6.1). On the other hand, when the boundary condition is given in the form of differential equations, $\mathbf{K}_i$ at the boundary points should be computed from the boundary equations using the *same* Runge-Kutta scheme as at the interior points.

7. RESULTS OF BENCHMARK PROBLEMS

The proposed LDDRK schemes have been applied to each category of the workshop benchmark problems. Very favorable agreements between the numerical results and known analytic solutions were found. The results of Category 1 have been shown in sections 2-5. In this section, brief discussions of numerical solutions of Category 2-6 are given.

7.1 Category 2

We solve one-dimensional non-linear equations. Spatial derivatives are discretized by a 7-point central difference scheme [13] and the time integration is done by the optimized LDDRK scheme. At boundary points (3 points inward), backward differences are used [7]. Moreover, at left boundary, $x = -50, -49, -48$, the following linearized equations, supporting only left-going waves, are used :

$$\frac{\partial \rho}{\partial t} - \frac{\partial \rho}{\partial x} = 0$$

$$\frac{\partial u}{\partial t} - \frac{\partial u}{\partial x} = 0$$

$$\frac{\partial p}{\partial t} - \frac{\partial p}{\partial x} = 0$$

The boundary equations are integrated using the same Runge-Kutta scheme as the interior equations.

Artificial damping has been used in the shock region. In particular, the semi-discrete temporal equation (3.1) is modified to be

$$\frac{\partial u_j}{\partial t} + L(U) = \epsilon \sum_{\ell=-N}^{N} d_\ell u_{j+\ell}$$

where ϵ if proportional the variation of u_j. The coefficients d_ℓ were chosen such that only the unresolved short waves are damped [13].

Another artificial damping method, filtering, has also been experimented. In this case, the temporal equation becomes

$$\frac{\partial \mathbf{U}}{\partial t} + L(\mathbf{U}) = 0$$

$$\frac{\partial u_j}{\partial t} = \epsilon \sum_{\ell=-N}^{N} d_\ell u_{j+\ell}$$

Similar numerical results are observed in the two methods of damping. The computational solutions are shown in Figure 8.

7.2 Category 3

Linearized Euler equation is solved. Schematic of the computational grid is shown in Figure 9. Radiation and out-flow conditions of [12] are used for boundary grid (3 points inward). These boundary equations are based on the asymptotic form of the far field solution. They are integrated using the same Runge-Kutta scheme as the interior Euler equation. It has been experimented in which the boundary equations were applied on grids 3, 5 and 10 points inward from the numerical boundary. No significant differences were found. Backward differences are used where central difference can not be applied. Specifically, 5-point 4th-order closure scheme of [7] gives

$$f_1' = -\frac{25}{12}f_1 + \frac{48}{12}f_2 - \frac{36}{12}f_3 + \frac{16}{12}f_4 - \frac{3}{12}f_5$$
$$f_2' = -\frac{3}{12}f_1 - \frac{10}{12}f_2 + \frac{18}{12}f_3 - \frac{6}{12}f_4 + \frac{1}{12}f_5$$
$$f_3' = \frac{1}{12}f_1 - \frac{8}{12}f_2 + \frac{8}{12}f_4 - \frac{1}{12}f_5$$

Density contours of Problem 2 are shown in Figure 9 for $t = 50, 70, 90$. For the calculation presented, 5-6 LDDRK scheme have been used with $\Delta t = 0.84$.

7.3 Category 4

In Problem 1, solid wall boundary condition is applied at $y = 0$. Physically, the boundary condition at solid wall is that the normal velocity equals to zero for inviscid flows. That is, $v = 0$ at $y = 0$. Then, from (6.1), since all the time derivatives of v are also zero, the numerical implementation in the Runge-Kutta schemes is

$$\mathbf{K}_i = 0 \quad \textit{for the normal velocity components} \tag{6.3}$$

No additional condition is applied on the wall. The schematic of the computational grid is shown in Figure 10. The explicit 5-point boundary closure scheme of [7] is applied for backward differences. The radiation and out-flow boundary conditions of [12] are applied at upper, left and right boundary, respectively. Pressure contours are shown in Figure 10.

In Problem 2, we solve

$$\frac{\partial}{\partial t}\begin{pmatrix}\rho\\ u\\ v\\ p\end{pmatrix} + \frac{\partial}{\partial r}\begin{pmatrix}v\\ 0\\ p\\ v\end{pmatrix} + \begin{pmatrix}v/r\\ 0\\ 0\\ v/r\end{pmatrix} + \frac{\partial}{\partial x}\begin{pmatrix}u\\ p\\ 0\\ u\end{pmatrix} = 0$$

The above equation becomes undefined at $r = 0$. However, at $r = 0$, $v = 0$. By L'Hospital's rule, $\frac{v}{r} \to \frac{\partial v}{\partial r}$. The equations at $r = 0$ becomes

$$\frac{\partial \rho}{\partial t} + 2\frac{\partial v}{\partial r} + \frac{\partial u}{\partial x} = 0$$

$$\frac{\partial u}{\partial t} + \frac{\partial p}{\partial x} = 0$$

$$\frac{\partial p}{\partial t} + 2\frac{\partial v}{\partial r} + \frac{\partial u}{\partial x} = 0$$

No additional conditions are specified along the symmetry line $r = 0$. Along the boundary $x = 0$, following condition for u is applied :

$x = 0,\ r \leq 9,\ u = 10^{-4}\sin(\pi t/5)$
$x = 0,\ r = 10,\ u = 0.5 \times 10^{-4}\sin(\pi t/5)$
$x = 0,\ r \geq 11,\ u = 0$

Computational grid and numerical results are shown in Figure 11.

7.4 Category 5

The given equations are integrated directly with the boundary condition at $x = -200$:

$$\begin{pmatrix} \rho \\ u \\ p \end{pmatrix} = \begin{pmatrix} 1 \\ M \\ 1/\gamma \end{pmatrix} + 10^{-6} \begin{pmatrix} 1 \\ 1 \\ 1 \end{pmatrix} \sin\Big(\omega\left(x/(1+M) - t\right)\Big)$$

The initial state at $t = 0$ for ρ, u and p is the linear profile shown in Figure 12. The spatial discretization is the 7-point central difference and the time integration is the 5-6 LDDRK scheme. The $\mathbf{K}_i$ at left boundary $x = -200$ in the RK scheme is calculated according to (6.1), since here the boundary conditions as functions of t are know.

The time history of pressure at exit $x = 80$ is shown in Figure 13. After time greater than around 2500, the solution appears to reach a periodic stead state, as shown in the very fine scale. The variation of $p - p_{mean}$ is also shown for time between 3900 and 4000, demonstrating a well defined periodic oscillation of amplitude 0.36×10^{-6}. The state of ρ, u and p at $t = 4000$ is plotted in Figure 12.

7.5 Category 6

In this problem, acoustic waves are generated as the gust passes the flat plate. Since the gust satisfies the convective linearized Euler equation, it is convenient computationally to separate the gust and the secondary flow generated by the plate. This leads to the following boundary condition on the plate for scattered field : at $y = \pm 0$ and $-15 \leq x \leq 15$, $v = 0.1\sin\left(\frac{\pi}{8}(x/M - t)\right)$

Two calculations with different computational domains were carried out. The first is the full domain of $[-100, 100] \times [-100, 100]$ and the second is a half domain of $[-100, 100] \times [0, 100]$. Physically, with a mean flow M_∞, a wake is formed after the trailing edge. Consequently, the velocity is discontinuous across the wake. It is convenient to use the half domain to allow the discontinuity of velocity. In this case, an anti-symmetry condition for p, i.e. $p = 0$, is imposed at $y = 0$. However, numerical results of the two calculations do not show significant differences in the radiated sound field, although the velocity in the wake region are different.

Since the flow field has discontinuities around the leading and trailing edges of the plate, artificial damping is applied on the grids around the edges. Since the damping scheme is designed to damp the unresolved high frequency wave only, the radiated acoustics wave, which has a wavelength of resolved waves, is not expected to be affected by the damping. However, no quantitative study has been conducted.

Figure 14 shows the instantaneous pressure p and velocity u contours. A well defined vorticity wave is convected downstream in the wake region. The directivity pattern of rp^2 is given in Figure 15.

8. CONCLUDING REMARKS

An analysis of dissipation and dispersion properties of Runge-Kutta time integration methods has been given for high-order finite difference discretization. Low Dissipation and Dispersion Runge-Kutta (LDDRK) schemes are proposed, based on an optimization that minimizes the dissipation and dispersion errors for wave propagations.

The importance of dispersion relations of the finite difference schemes have been emphasized in recent works of computational aeroacoustics. The proposed condition of determining the time step, (3.8), is based on the wave propagation properties of the the finite difference schemes. It takes account of both the spatial and temporal discretizatons. This ensures the correct wave propagation of resolved waves and, thus, improves the robustness of the computation.

APPENDIX A: OPTIMIZATION VIEWED AS PRESERVING THE FREQUENCY

In section 4, the optimization is carried out by minimizing the difference of the numerical and the exact amplification factors. This actually minimizes the total of dissipation and dispersion errors. In this appendix, we show that minimizing integral (4.1) also preserves the frequency in the time integration. As such the LDDRK scheme is dispersion relation preserving in the sense of [12]. By (6.1) for linearized problems, it is easy to show that the Runge-Kutta scheme leads to

$$\mathbf{U}(t_n+\Delta t) \approx \mathbf{U}(t_n) + c_1\Delta t\frac{\partial \mathbf{U}}{\partial t}(t_n) + c_2\Delta t^2\frac{\partial^2 \mathbf{U}}{\partial t^2}(t_n) + \cdots\cdots + c_p\Delta t^p\frac{\partial^p \mathbf{U}}{\partial t^p}(t_n) \qquad (A1)$$

where c_i are identical to the coefficients of the amplification factor (3.4). This will be true regardless of the particular form of partial differential equations concerned. The above relation only involves the time derivatives of the solution. Upon replacing t_n by t and applying Laplace transforms on both sides of (A1), it is found that

L.H.S.

$$\frac{1}{2\pi}\int_0^\infty \mathbf{U}(t+\Delta t)e^{i\omega t}dt = e^{-i\omega\Delta t}\tilde{\mathbf{U}} \qquad (A2)$$

R.H.S.

$$\frac{1}{2\pi}\int_0^\infty [\mathbf{U}(t) + c_1\Delta t\frac{\partial \mathbf{U}}{\partial t}(t) + c_2\Delta t^2\frac{\partial^2 \mathbf{U}}{\partial t^2}(t) + \cdots\cdots + c_p\Delta t^p\frac{\partial^p \mathbf{U}}{\partial t^p}(t)]e^{i\omega t}dt$$

$$= [1 + c_1(-i\omega\Delta t) + c_2(-i\omega\Delta t)^2 + \cdots\cdots + c_p(-i\omega\Delta t)^p]\tilde{\mathbf{U}} \qquad (A3)$$

where $\tilde{\mathbf{U}}$ is the Laplace transform of $\mathbf{U}$ (For simplicity, we assume that $\mathbf{U} = 0$ for $t \le \Delta t$). Next we express

$$1 + c_1(-i\omega\Delta t) + c_2(-i\omega\Delta t)^2 + \cdots\cdots + c_p(-i\omega\Delta t)^p \equiv e^{-i\omega^*\Delta t} \qquad (A4)$$

C-2

(A4) equals to the amplification factor r in (3.4) when ω is replaced by ck^*. By comparing (A4) and (A2), it is seen that ω^* represents the numerical frequency in the Runge-Kutta time integration scheme. By replacing ck^* with ω, we have

$$|r - r_e|^2 = \left|e^{-i\omega^*\Delta t} - e^{-i\omega\Delta t}\right|^2 = \left|e^{-i(\omega^*\Delta t - \omega\Delta t)} - 1\right|^2 \approx \left|\omega^*\Delta t - \omega\Delta t\right|^2 \qquad (A5)$$

for $\left|\omega^*\Delta t - \omega\Delta t\right|$ small. From above, it is easy to see that the optimization integral (4.1) results in the preservation of the frequency.

REFERENCES

[1] A. Bayliss and Eli Turkel, "Radiation boundary conditions for wave-like equations", *Communications on Pure and Applied Mathematics*, **33**, 708-725, 1980.

[2] J. C. Butcher, *The numerical analysis of ordinary differential equations, Runge-Kutta and general linear methods*, 1987, Wiley.

[3] C. Canuto, M. Y. Hussaini, A. Quarteroni and T. A. Zang, *Spectral Methods in Fluid Dynamics*, Springer-Verlag, 1988.

[4] M. H. Carpenter and C. A. Kennedy, "Fourth-order 2N-Storage Runge-Kutta schemes", NASA Technical Memorandum 109112, 1994.

[5] M. H. Carpenter, D. Gottlieb, S Abarbanel and W.-S. Don, "The theoretical accuracy of Runge-Kutta time discretizations for the initial boundary value problem: a careful study of the boundary error", ICASE Report 93-83, 1993.

[6] J. Casper, C.-W. Shu and H. Atkins, "Comparison of two formulations for high-order accurate essentially non-oscillatory schemes", *AIAA J.*, **32** (10), 1994.

[7] J. Gary, "On boundary conditions for hyperbolic difference schemes", *Journal of Computational Physics*, **26**, 339-351, 1978.

[8] Z. Haras and S. Ta'asan, "Finite difference schemes for long-time integration", *Journal of Computational Physics*, **114**, 265-279, 1994.

[9] J. Hardin, M. Y. Hussaini, *Computational Aeroacoustics*, Springer-Verlag, 1992.

[10] A. Jameson, W. Schmidt and E. Turkel, "Numerical solutions of the Euler equations by finite volume methods using Runge-Kutta time-stepping schemes", AIAA paper 81-1259, 1981.

[11] S. K. Lele, "Compact finite difference schemes with spectral-like resolution", *Journal of Computational Physics*, **103**, 16, 1992.

[12] C. K. W. Tam and J. C. Webb, "Dispersion-Relation-Preserving schemes for computational acoustics", *Journal of Computational Physics*, **107**, 262-281, 1993.

[13] C. K. W. Tam and H. Shen, "Direct computation of nonlinear acoustic pulses using high order finite difference schemes", AIAA paper 93-4325, 1993.

[14] R. Vichnevetsky and J. B. Bowles, *Fourier analysis of numerical approximations of hyperbolic equations*, SIAM, 1982.

[15] J. H. Williamson, "Low-storage Runge-Kutta schemes", *Journal of Computational Physics*, **35**, 48-56, 1980.

[16] D. W. Zingg, H. Lomax and H. Jurgens, "An optimized finite-difference scheme for wave propagation problems", AIAA paper 93-0459, 1993.

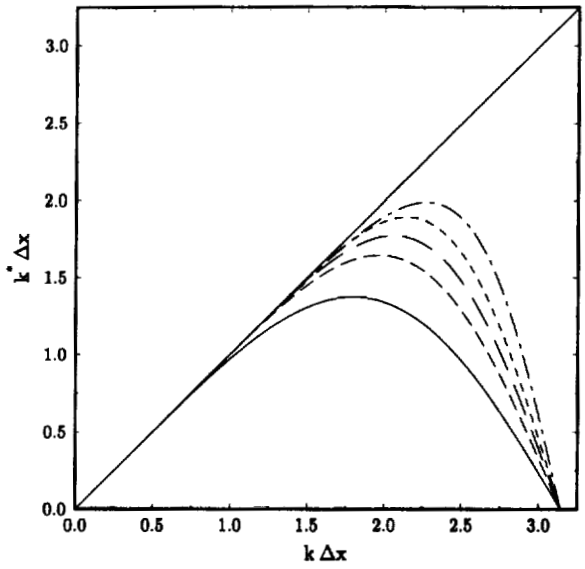

Figure 1. Numerical wave number $k^*\Delta x$ v.s. the actual wave number $k\Delta x$ for several high-order finite difference schemes. ——— 5-point 4th-order [7], — — — 7-point 4th-order [13], —— —— —— 9-point 6th-order, - - - - - - 11-point 6th-order, — - — - — 5-point compact [11].

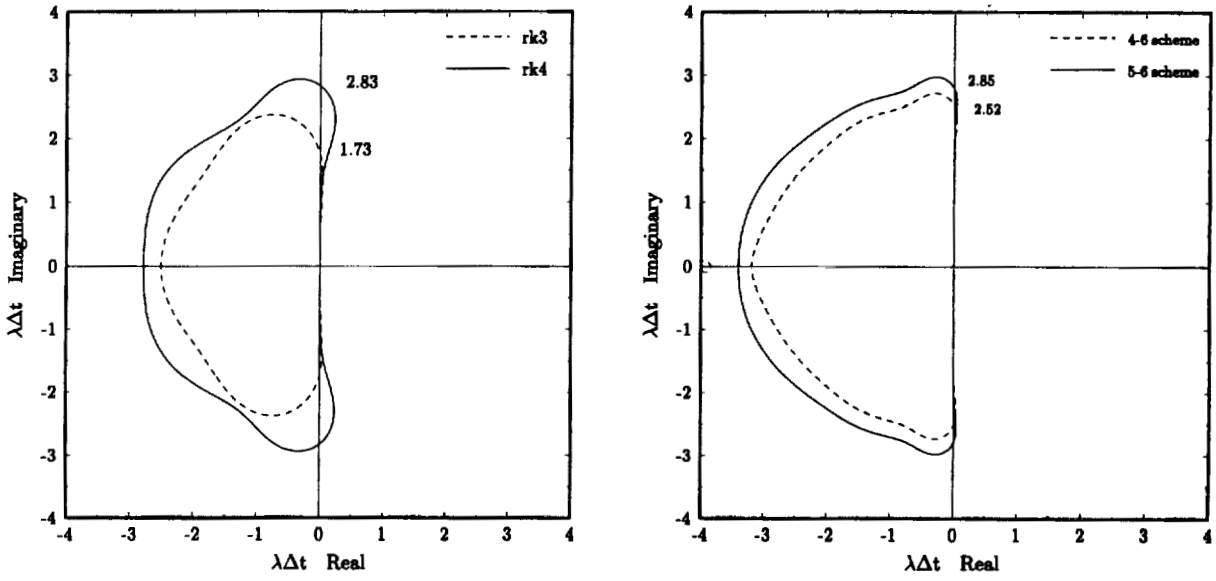

Figure 2. Stability foot prints of the 3rd-order (rk3) and 4th-order (rk4) schemes (left). λ is the eigenvalue of the linearized operator F in (3.1). Indicated are the stability limits on the imaginary axis. Also shown are the stability limits of optimized 4th-order LDDRK schemes (right).

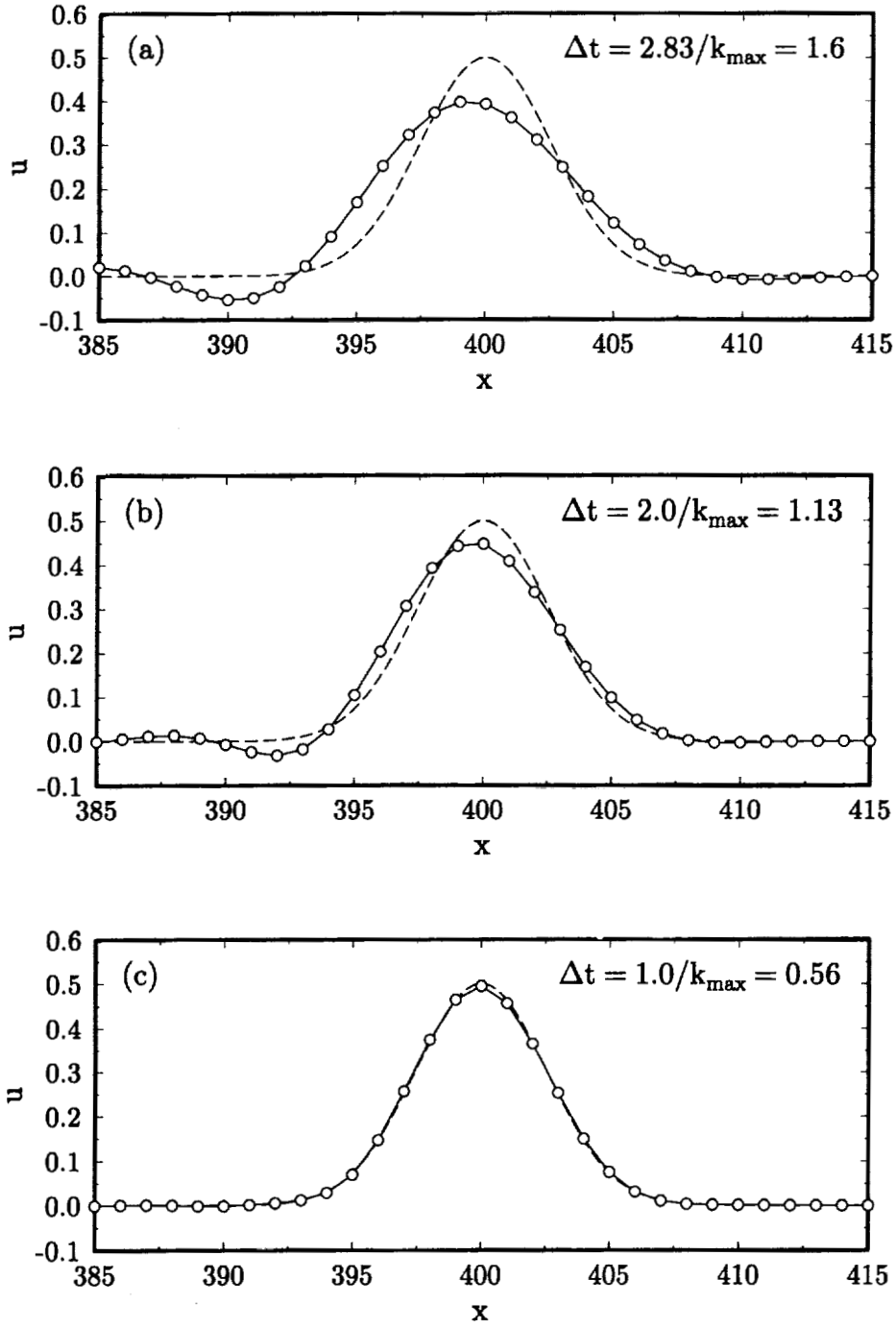

Figure 3. Numerical results of Category 1 Problem 1. The classical 4-stage 4th-order Runge-Kutta scheme is used. A 9-point central difference scheme has been used for the spatial discretization. - - - - - - exact, —o— numerical. t=400.

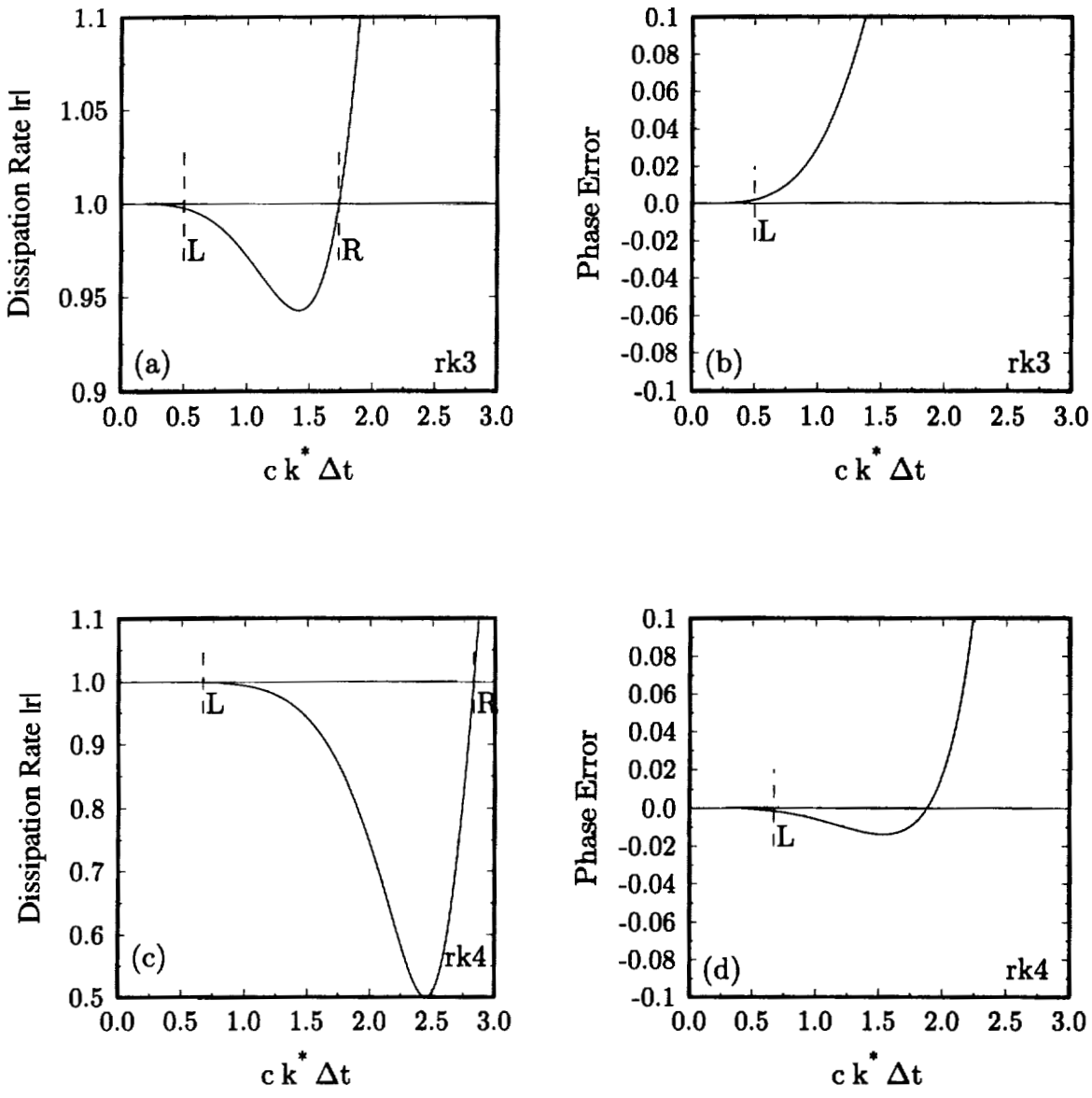

Figure 4. Dissipation and phase errors of the classical 3-stage 3rd-order (rk3) and 4-stage 4th-order (rk4) Runge-Kutta schemes. L and R are the accuracy and stability limits, respectively.

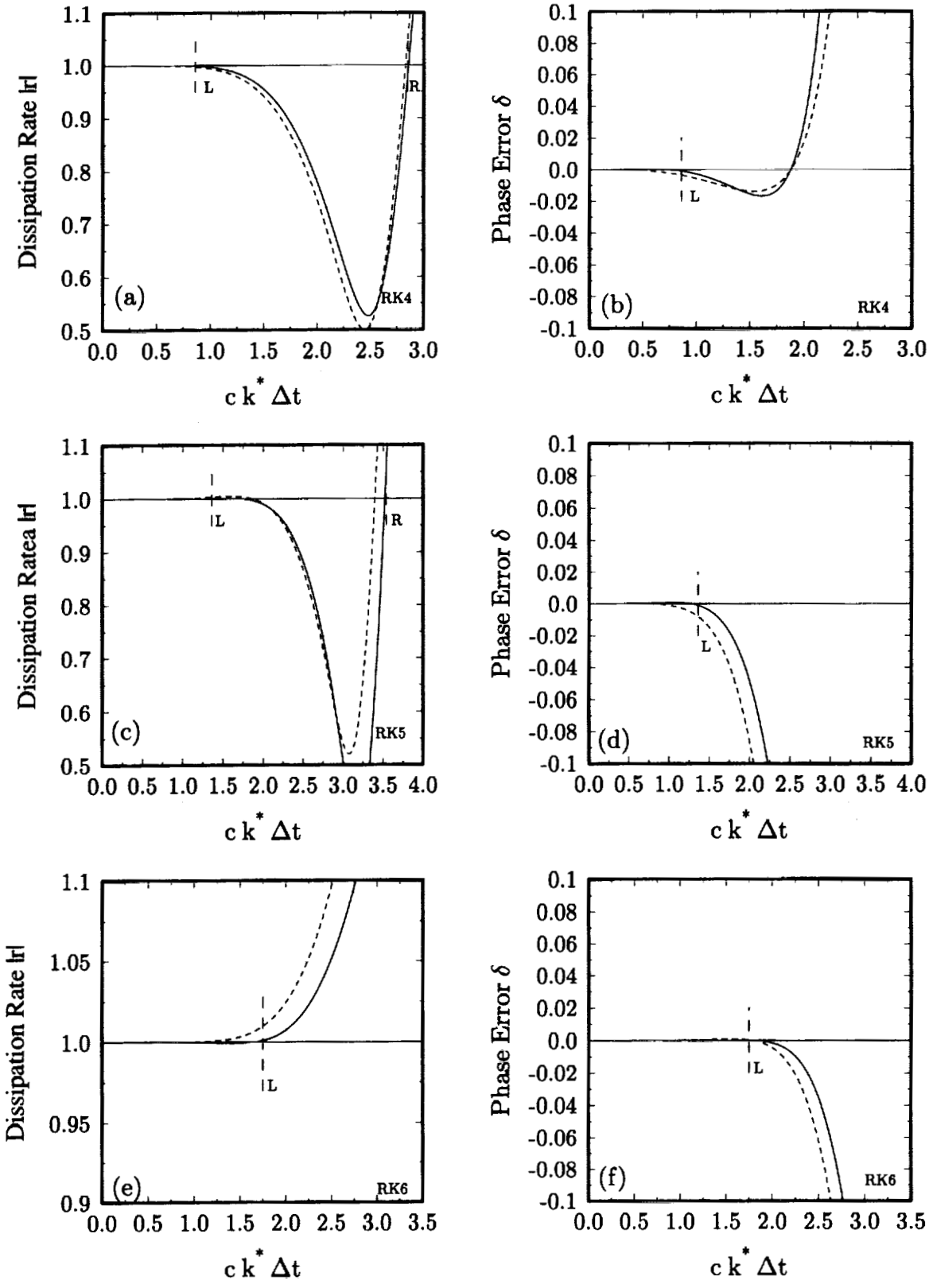

Figure 5. Dissipation and phase errors of the optimized schemes. Dotted line is the un-optimized scheme. (a) and (b) : 4-stage; (c) and (d) : 5-stage; (e) and (f) : 6-stage.

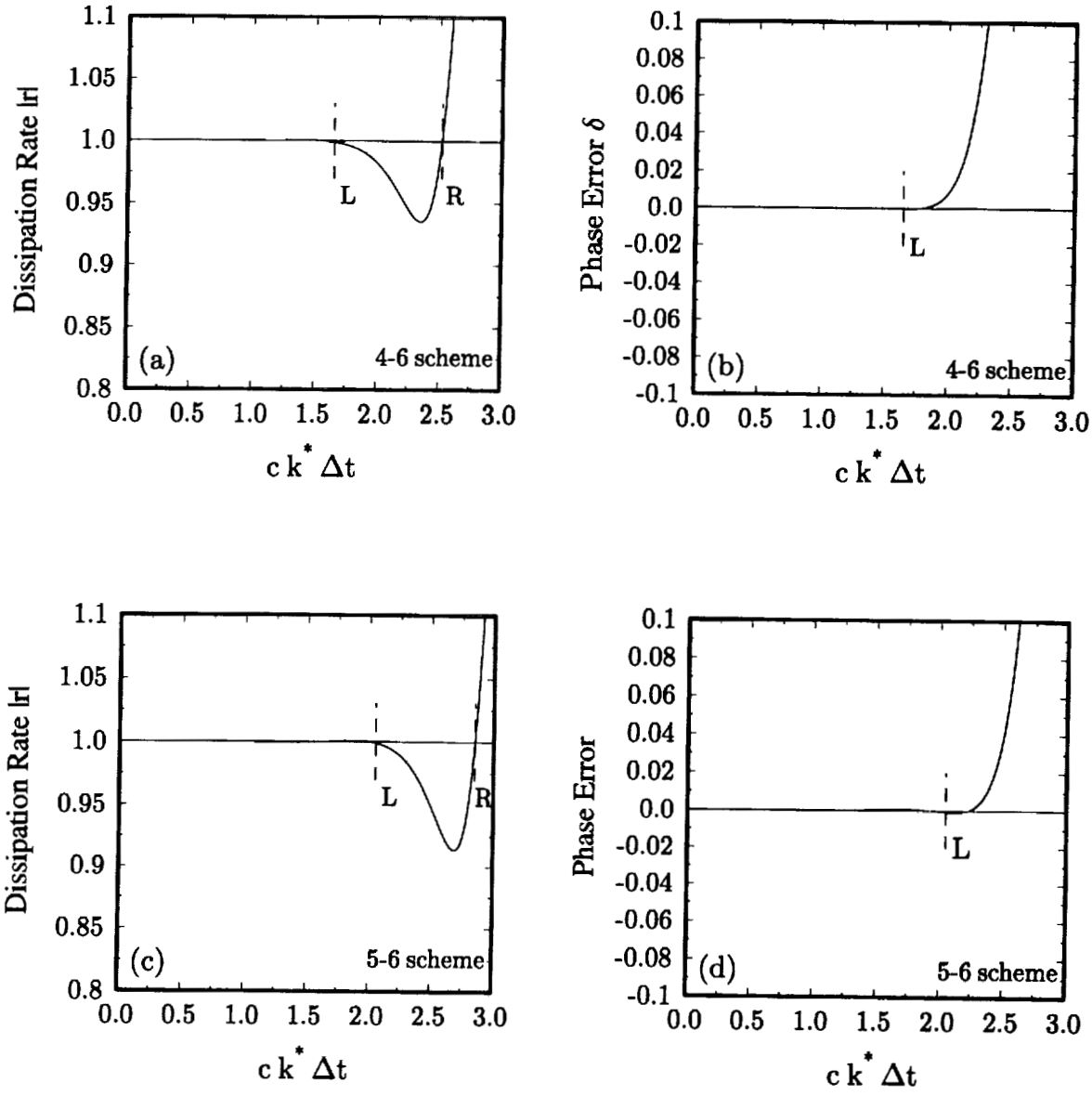

Figure 6. Dissipation and phase errors of the optimized 4th-order two step alternating schemes. (a) and (b) : 4-6 scheme; (c) and (d) : 5-6 scheme.

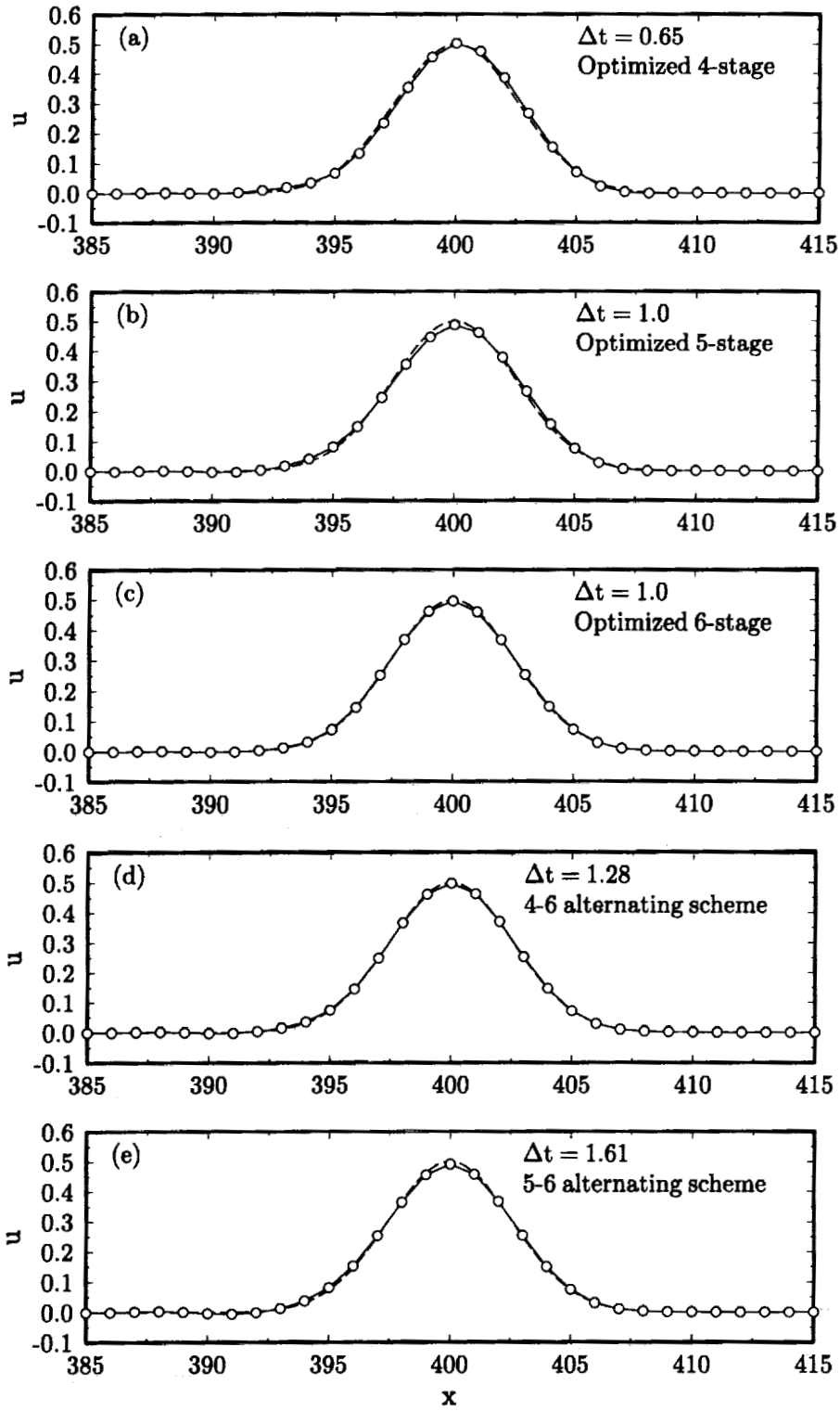

Figure 7. Numerical results of Category 1 Problem 1. using optimized schemes. - - - - - - exact, —o— numerical. t=400.

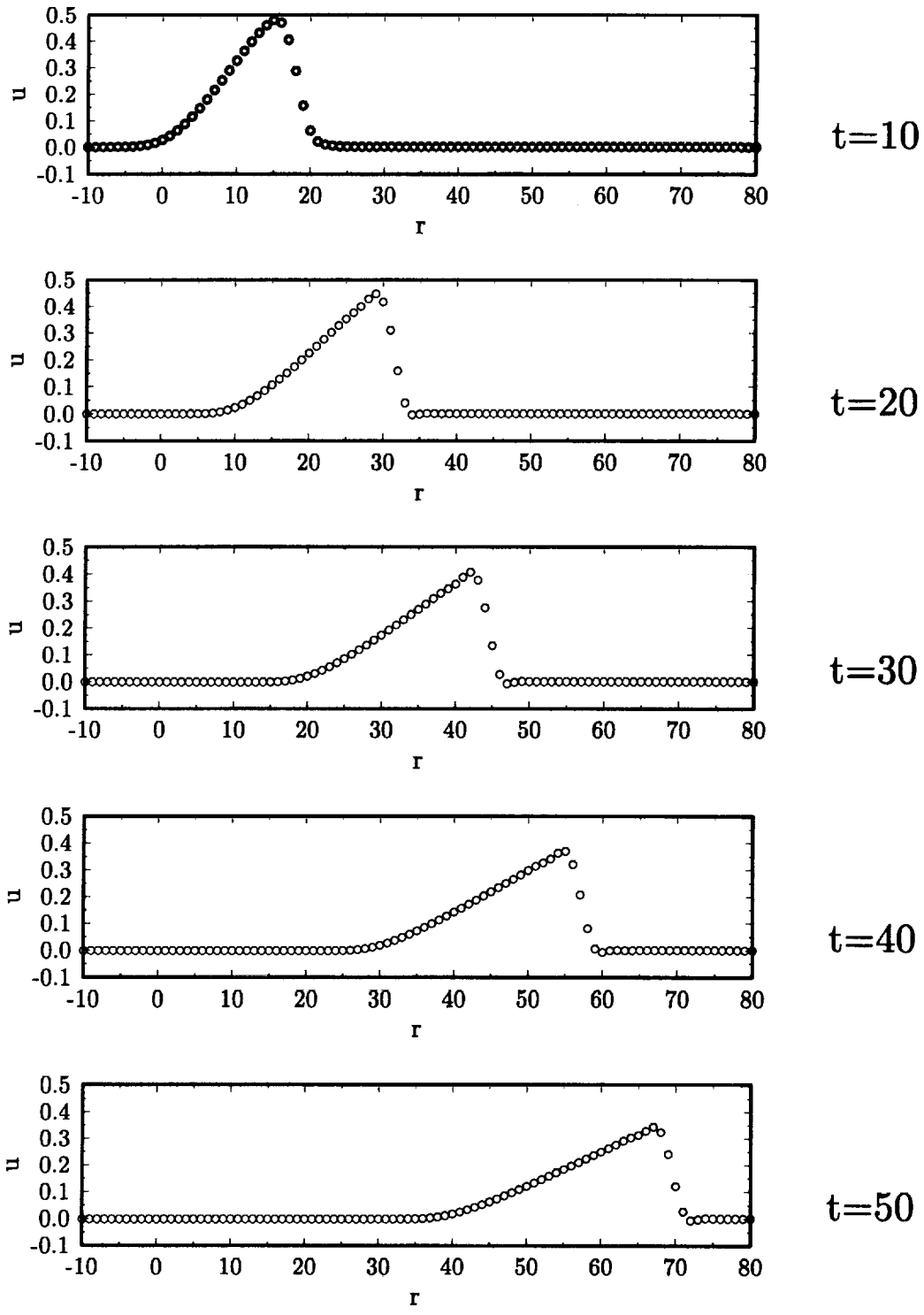

Figure 8. Numerical solutions of Category 2 problem 1. Shown are the values of u at t = 10, 20, 30, 40, 50.

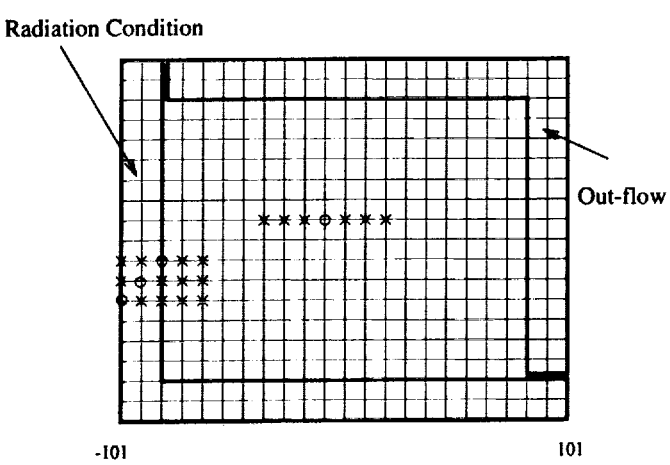

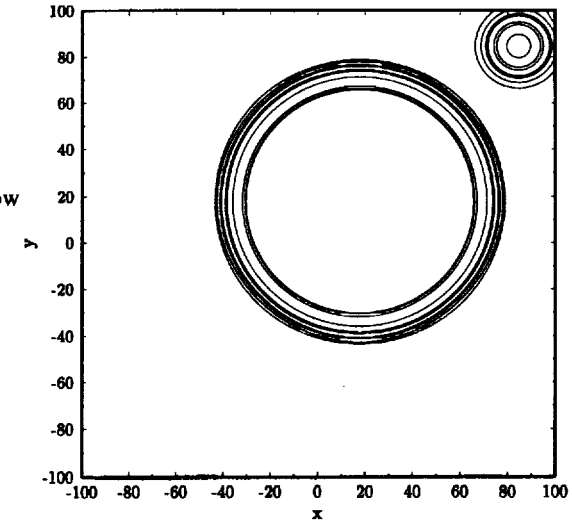

Density Contours 0.00001 to 0.1
t=50

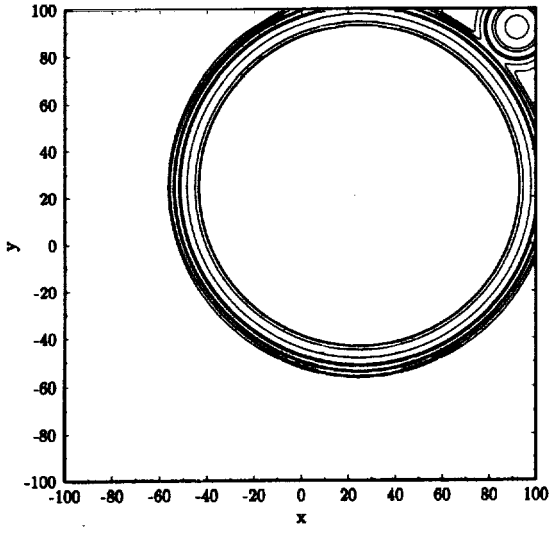

Density Contours 0.00001 to 0.1
t=70

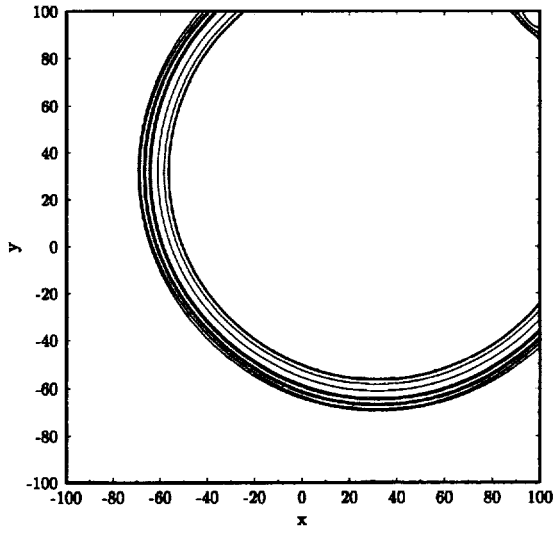

Density Contours 0.00001 to 0.1
t=90

Figure 9. Grids and density contours of Category 3 Problem 2.

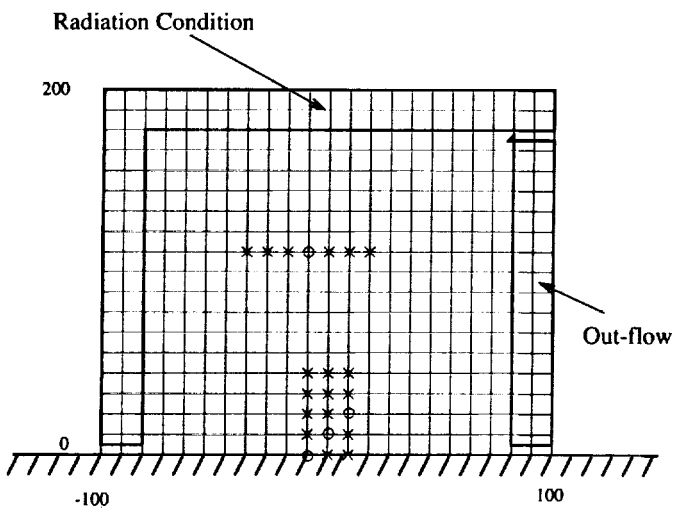

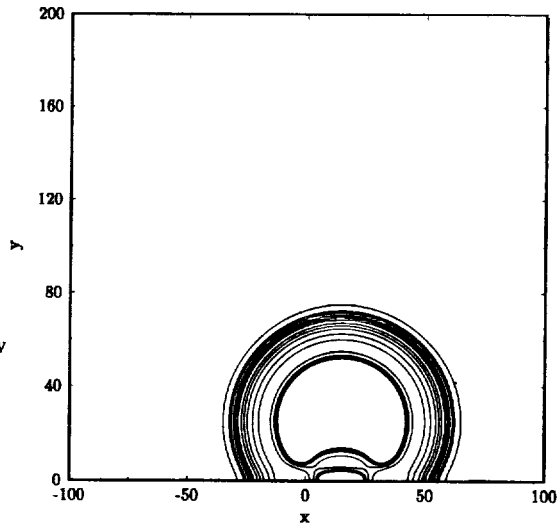

Pressure Contours 0.000001 to 0.1

t=30

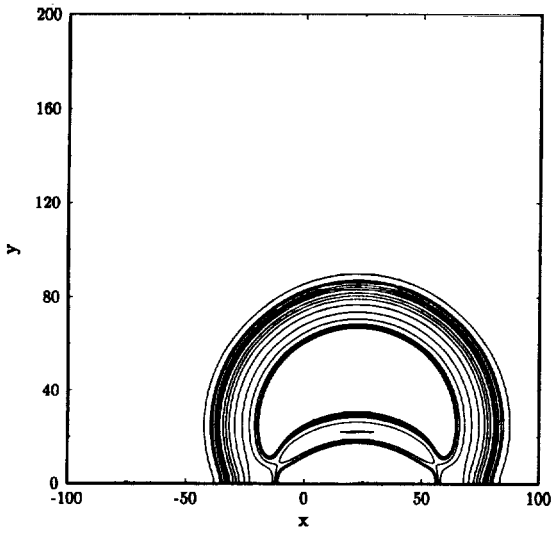

Pressure Contours 0.000001 to 0.1

t=45

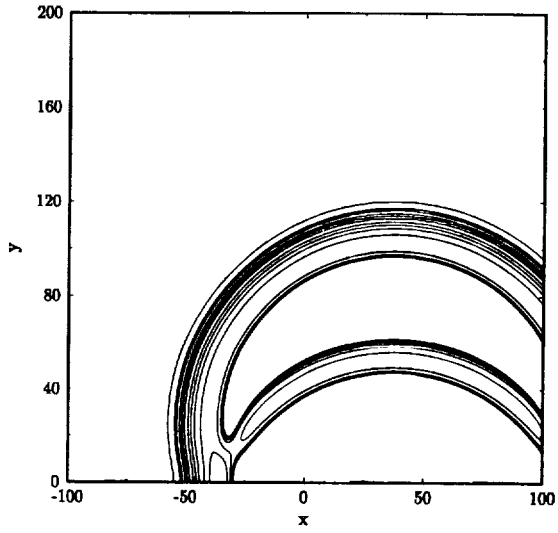

Pressure Contours 0.000001 to 0.1

t=75

Figure 10. Grids and density contours of Category 4 Problem 1.

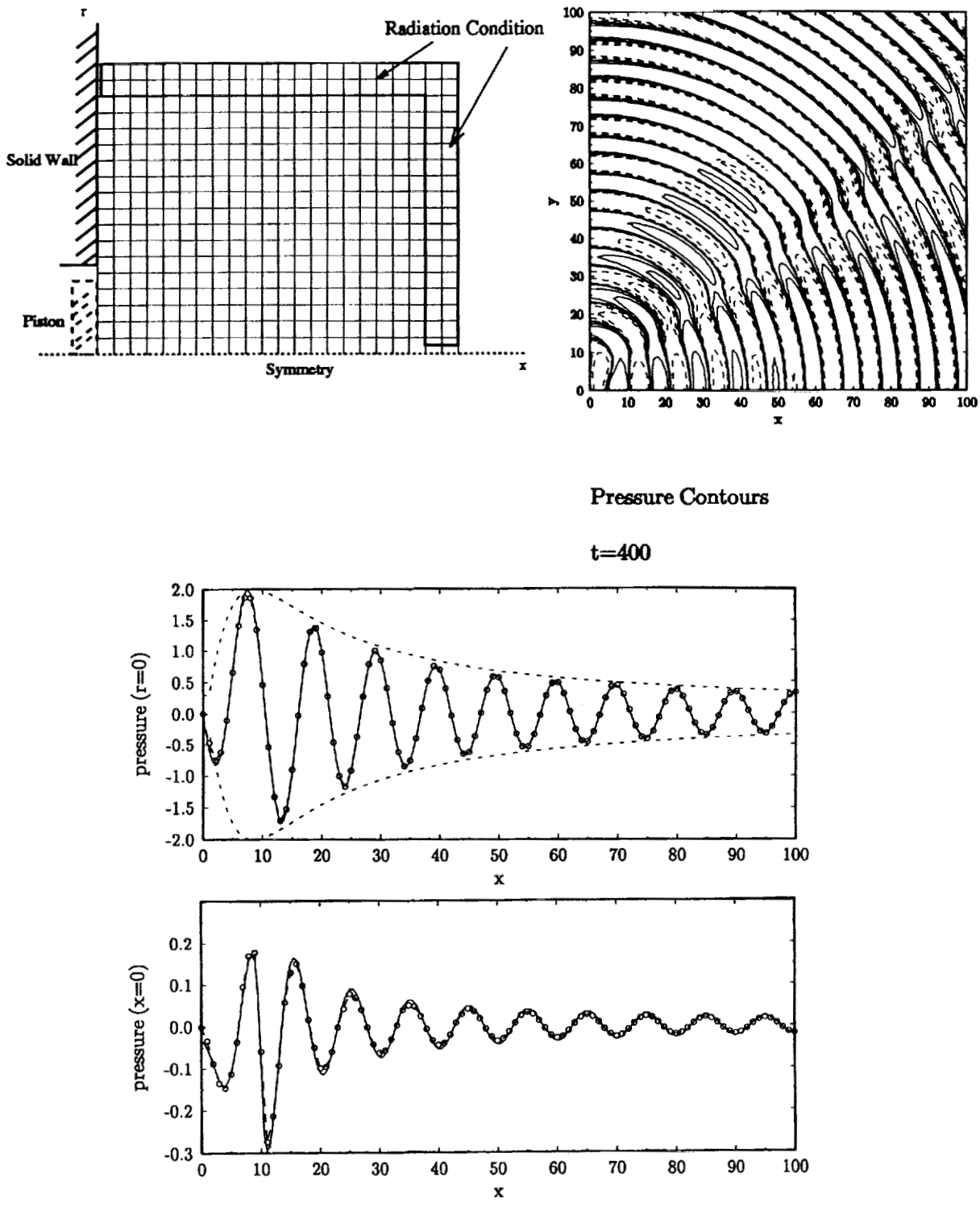

Figure 11. Pressure contours of Category 4 Problem 2 (above) and profiles along $x = 0$ and $r = 0$ (below). Cirles are the computed results and the solid lines are the analytic solution (courtesy of D. Nark, NASA Langley).

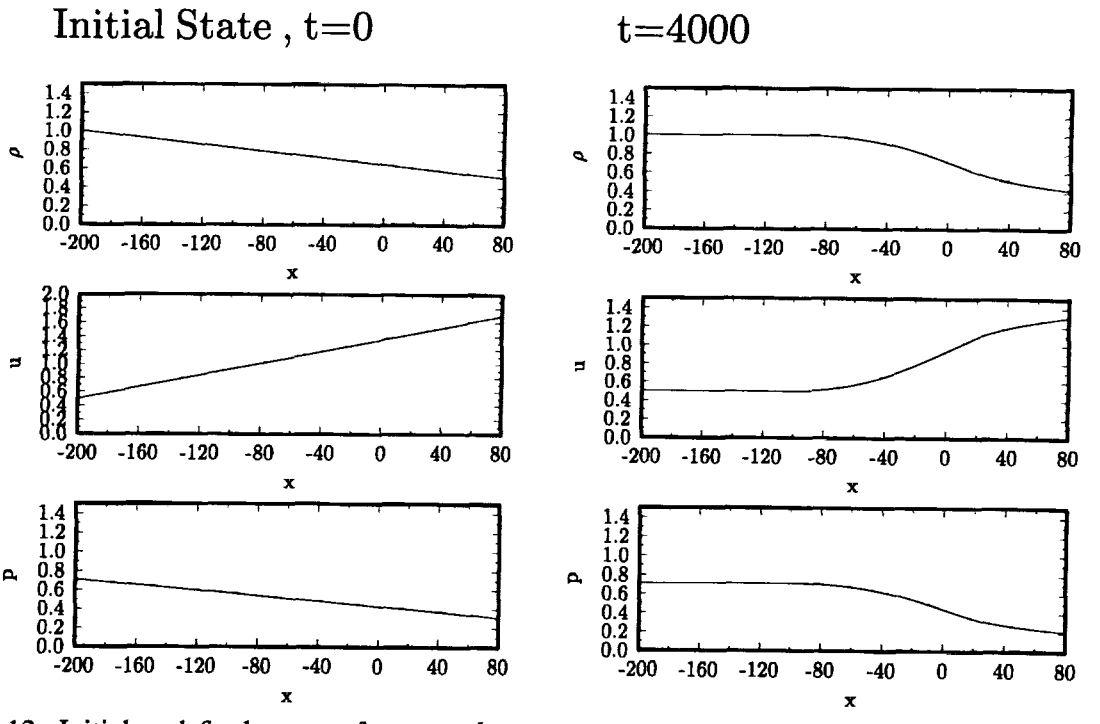

Figure 12. Initial and final states of ρ, u and p.

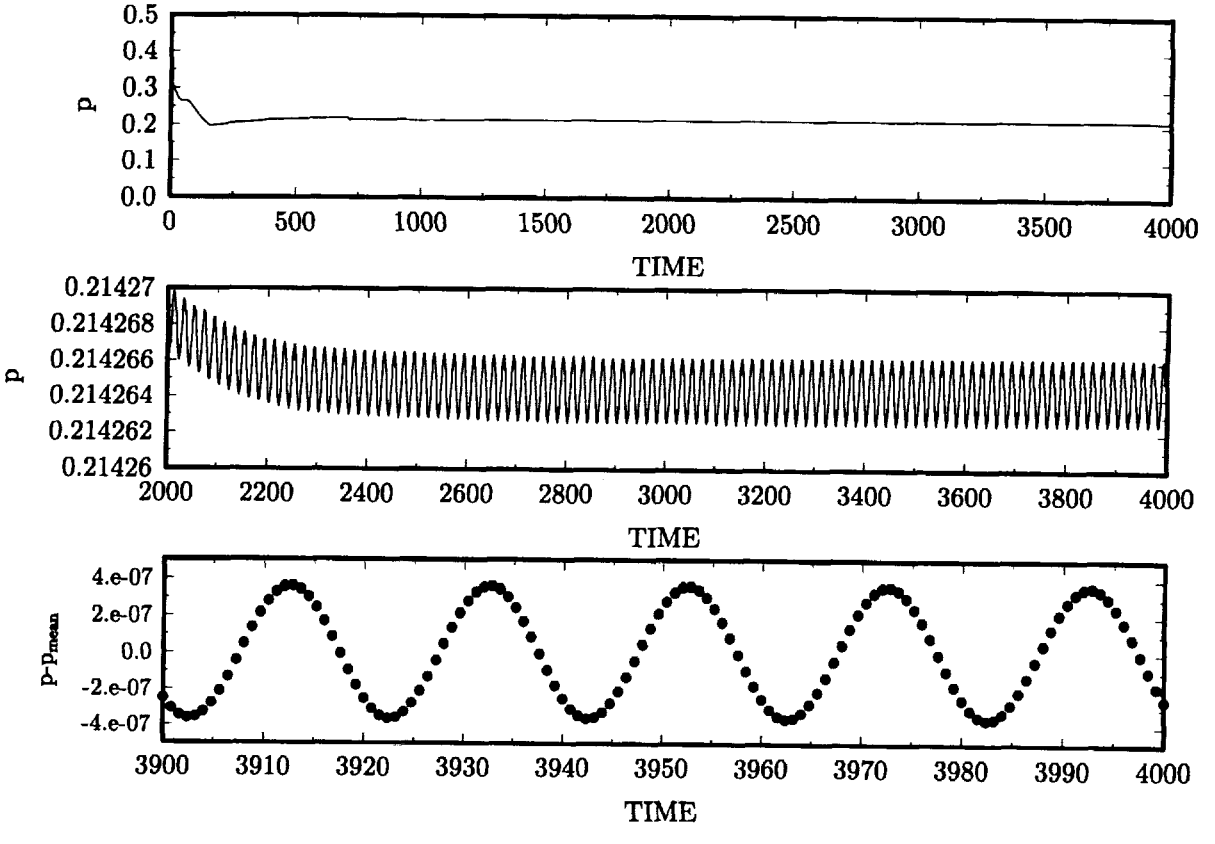

Figure 13. Time history of p at exit $x = 80$.

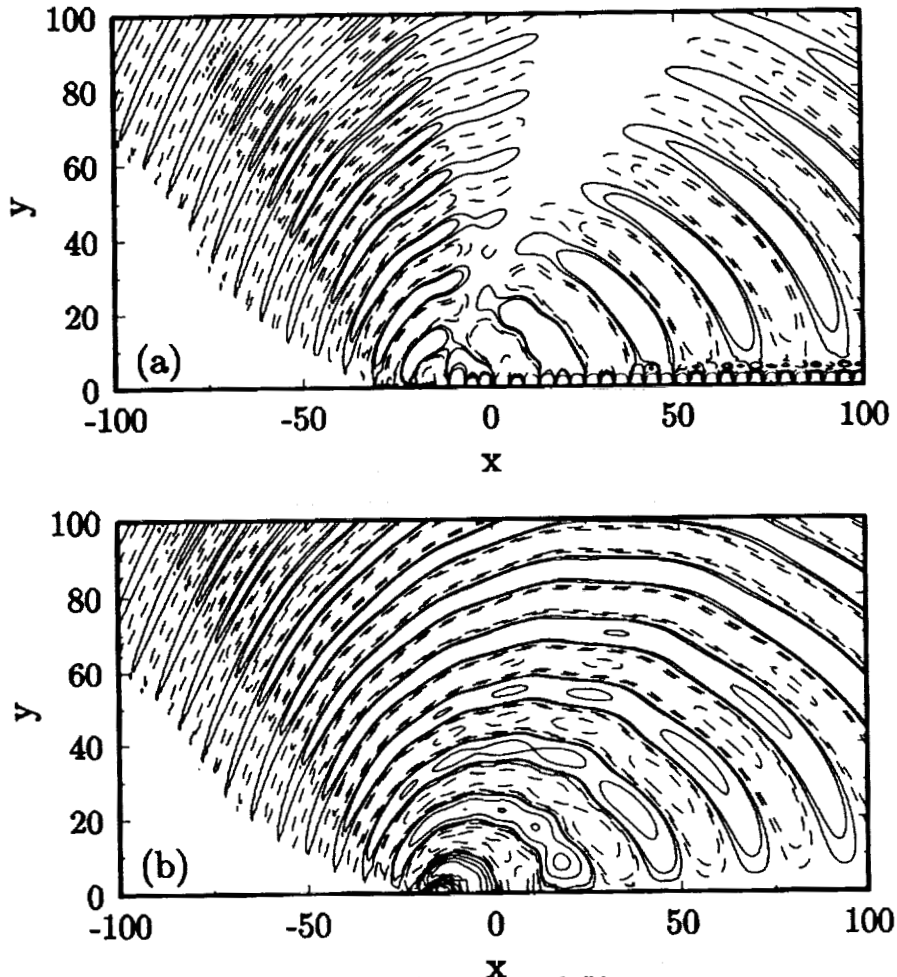

Figure 14. Instantaneous contours of (a) velocity u and (b) pressure p.

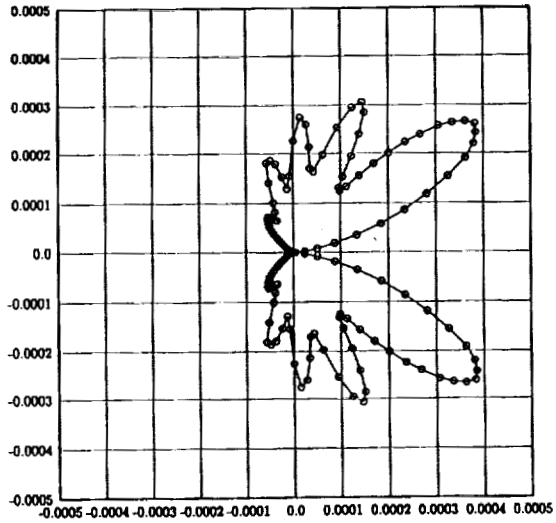

Figure 15. Directivity of $\overline{rp^2}$. Lower-half obtained by symmetry.

RESULTS OF TWO NEW METHODS FOR AEROACOUSTICS BENCHMARK PROBLEMS

H. T. Huynh
NASA Lewis Research Center, MS 5-11
Cleveland, Ohio 44135

Phone: (216) 433-5852; Fax: (216) 433-5802
E-mail: tohung@freya.lerc.nasa.gov

Summary. Two new methods for the numerical solution of conservation laws (the Euler equations in particular) are presented: a uniformly second-order accurate upwind scheme and a third-order accurate centered scheme. Results of these schemes are shown for problems in categories 1, 2, and 5.

1. Introduction. Problems in aeroacoustics generally require fourth- or higher-order accurate schemes. In this article, we present two lower-order schemes that are considerably more accurate than standard low order methods. These two schemes are designed to resolve discontinuities without oscillations. They perform well for a wide class of problems in fluid dynamics, and they can capture shocks with high resolution. The question is how well can these schemes resolve acoustic waves? In addition, can the concepts and techniques employed to derive these methods be applied to high-order schemes in acoustics?

The first method is a second-order accurate upwind scheme. It consists of two key steps (of MUSCL type): a reconstruction step which estimates the slopes in each cell (piecewise linear), followed by an upwind step which obtains the fluxes at each interface. For the upwind step, Roe's flux-difference splitting (1981) is employed. We present here a simple explanation of this splitting: it is identical to a flux-vector splitting via linearization and diagonalization. The reconstruction step, however, is different from those in the literature. We start with the slope of the quartic through five points. To avoid oscillations near a discontinuity, we introduce a monotonicity constraint that preserves uniform second-order accuracy. The constraint consists of two bounds (limits). The lower bound, which preserves accuracy, is defined by a slope 'closest' to zero among all second-order accurate slopes. This bound can also be defined by the UNO slope of Harten and Osher (1987). The upper bound, which prevents the slope from becoming too steep, is derived by making use of the upper limit of Van Leer's MUSCL scheme. The constraint requires the final slope to lie between these two limits. This requirement is conveniently enforced by using the median function: the final slope is the median of the quartic slope and the above two limits. To save computing time, we present a simple criterion that detects the smooth part of the data: if a cell is in the smooth region, then the monotonicity constraint has no effect, and the slope reduces to the quartic formula.

The second method is a third-order accurate centered scheme. It carries not only the average of the conserved variables in each cell but also the interface values of these variables. For this reason, the dispersion error is small even for the highest frequency waves (Van Leer 1977). Similar to upwind schemes, this method employs a reconstruction step which, for third-order accuracy,

is piecewise quadratic. Oscillations in the solutions are avoided by limiting the interface values. Here, as in the linear reconstruction case, we introduce a simple monotonicity constraint that does not cause a loss of accuracy near extrema. What is different from an upwind scheme, however, is that instead of an upwind step, a dual-mesh (staggered) system is employed (Sanders and Weiser 1989, 1992, and Nessyahu and Tadmor 1990). This mesh system facilitates the updating of both variables (averages and point values) and yields a centered scheme.

We present these schemes first for the advection equation and then for the Euler equations.

2. Second-order upwind scheme for advection equation. Consider the advection equation with constant speed a,

$$\frac{\partial u}{\partial t} + a\frac{\partial u}{\partial x} = 0, \tag{2.1a}$$

$$u(x,0) = u_0(x), \tag{2.1b}$$

where the initial condition $u_0(x)$ is assumed to be of compact support or periodic. As a result, boundary conditions are straightforward. Other boundary conditions will be addressed as needed. The derivation below facilitates the extensions to systems of equations.

Let x_j be the cell center, $x_{j+1/2}$ the interface between the j-th and $j+1$-th cells, and h the cell width; the mesh is uniform. At time $t^n = n\tau$ where τ is the time step, assume that we know u_j^n which approximates the solution u at x_j for all j. We wish to calculate u_j^{n+1}. Here, the time step τ is assumed to satisfy the CFL condition

$$|a|(\tau/h) \le 1. \tag{2.2}$$

By applying the midpoint rule, we obtain a second-order accurate scheme:

$$u_j^{n+1} = u_j^n + (\tau/h)(au_{j-1/2}^{n+1/2} - au_{j+1/2}^{n+1/2}). \tag{2.3}$$

The flux $f_{j+1/2}^{n+1/2} = au_{j+1/2}^{n+1/2}$ is obtained in two steps.

The first step is called the reconstruction step: in each jth cell and for $t^n \le t \le t^{n+1}$, we approximate $u(x,t)$ by a linear function $r_j(x,t)$. Suppose, for the moment, $(u_x)_j$ is known. We can calculate $(u_t)_j$ via (2.1a):

$$(u_t)_j = -a(u_x)_j. \tag{2.4}$$

Thus, r_j is known:

$$r_j(x,t) = u_j + (x - x_j)(u_x)_j + (t - t^n)(u_t)_j. \tag{2.5}$$

At time $t^{n+1/2}$ and at the two interfaces of the jth cell, Taylor series expansions yield

$$r_j(x_{j-1/2}, t^{n+1/2}) = u_j - \tfrac{1}{2}h(u_x)_j + \tfrac{1}{2}\tau(u_t)_j; \qquad r_j(x_{j+1/2}, t^{n+1/2}) = u_j + \tfrac{1}{2}h(u_x)_j + \tfrac{1}{2}\tau(u_t)_j. \tag{2.6}$$

The second step is the upwind step. At each interface $j+1/2$, we now have two values for u: one from the Taylor series expansion in the jth cell, namely, $r_j(x_{j+1/2}, t^{n+1/2})$; and one from that in the $j+1$ cell, $r_{j+1}(x_{j+1/2}, t^{n+1/2})$. Denote these two values respectively by u_L and u_R. The flux is obtained simply by upwinding:

$$f_{j+1/2}^{n+1/2} = \begin{cases} au_L & \text{if } a \ge 0, \\ au_R & \text{otherwise.} \end{cases} \tag{2.7}$$

Equivalently,

$$f_{j+1/2}^{n+1/2} = \tfrac{1}{2}(au_L + au_R) - \tfrac{1}{2}|a|(u_R - u_L). \tag{2.8}$$

The problem therefore reduces to defining $(u_x)_j$.

In the rest of this section, time is frozen at level n. For simplicity of notation, we omit the superscript n and, when it does not cause confusion, the subscript j is set equal to 0. One of the simplest formulas for $(u_x)_0$ which does not cause oscillations near a discontinuity is a weighted average employed by Van Albada, Van Leer, and Roberts (1982): with

$$s_- = (u_0 - u_{-1})/h \qquad \text{and} \qquad s_+ = (u_1 - u_0)/h, \tag{2.9}$$

$$(u_x)_0 = (s_-^2 s_+ + s_+^2 s_-)/(s_-^2 + s_+^2 + 10^{-20}). \tag{2.10}$$

The above slope works well for a wide class of problems, but it is quite diffusive and is only first-order accurate near an extremum. We present below a uniformly second-order accurate slope which has a much smaller diffusion error.

The key idea is to preserve monotonicity of the data by a constraint that does not cause a loss of accuracy. To be precise, we need a few definitions. Let the median of three numbers be the one that lies between the other two. With real numbers x and y, denote by $I[x,y]$ the closed interval whose two end points are x and y. In addition, let $\text{minmod}(x,y)$ be defined as the median of x, y, and 0. Then for the purpose of coding,

$$\text{minmod}(x,y) = \tfrac{1}{2}[\text{sgn}(x) + \text{sgn}(y)]\ \min(|x|,|y|), \tag{2.11}$$

where $\text{sgn}(x) = 1$ if x is positive; $\text{sgn}(x) = -1$ if x is negative. Note that if $x = 0$, the above minmod function returns 0, and it does not matter whether $\text{sgn}(x)$ is defined as 1 or -1. Conversely, the median function can be expressed in terms of minmod:

$$\begin{aligned} \text{median}(x,y,z) &= x + \text{minmod}(y-x, z-x) = y + \text{minmod}(x-y, z-y) \\ &= x + \tfrac{1}{2}[\text{sgn}(y-x) + \text{sgn}(z-x)]\ \min(|y-x|, |z-x|). \end{aligned} \tag{2.12}$$

The minmod function of three arguments will also be used: with $\alpha = \min(z_1,z_2,z_3)$ and $\beta = \max(z_1,z_2,z_3)$, define $\text{minmod}(z_1,z_2,z_3) = \text{median}(0,\alpha,\beta)$. Equivalently,

$$\text{minmod}(z_1,z_2,z_3) = \tfrac{1}{4}\{\text{sgn}(z_1) + \text{sgn}(z_2)\}\ |\text{sgn}(z_1) + \text{sgn}(z_3)|\ \min(|z_1|,|z_2|,|z_3|). \tag{2.13}$$

We are now ready for the constraint. It requires the final slope to lie in a certain interval. Between the two ends of this interval, the one closer to 0 is called the lower bound; the other, the upper bound. Let p_-, p_0, and p_+ be the slopes at $j = 0$ of the three quadratics defined respectively by $\{u_{-2}, u_{-1}, u_0\}$, $\{u_{-1}, u_0, u_1\}$, and $\{u_0, u_1, u_2\}$:

$$p_- = (u_{-2} - 4u_{-1} + 3u_0)/(2h), \quad p_0 = (u_1 - u_{-1})/(2h), \quad p_+ = (-u_2 + 4u_1 - 3u_0)/(2h). \tag{2.14}$$

The lower bound, denoted by q_*, is given by (see Fig. 2.1)

$$q_* = \text{minmod}(p_-, p_0, p_+). \tag{2.15}$$

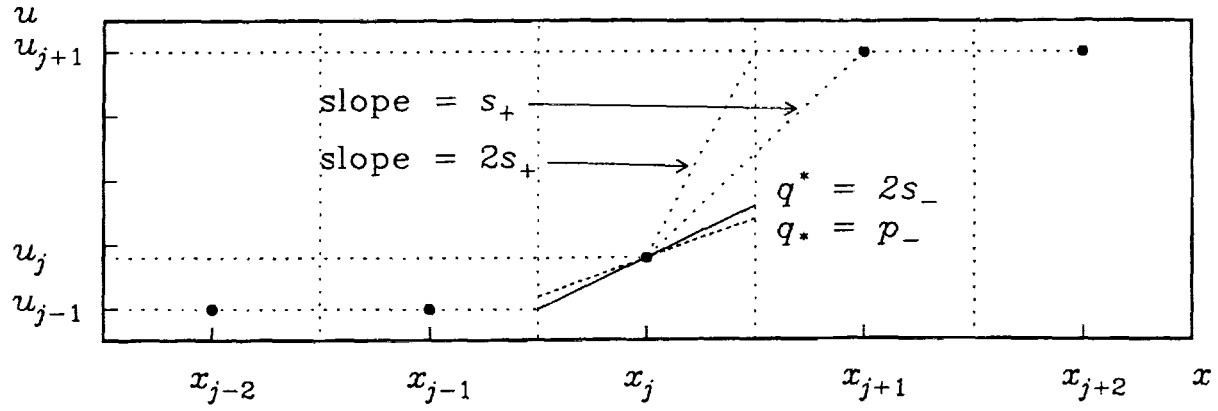

Figure 2.1. *The constraints.*

Clearly, the three slopes (2.14) are accurate to $O(h^2)$; as a result, q_* is accurate to the same order. Loosely put, q_* is the slope closest to 0 among the (three) second-order accurate slopes.

For the upper bound, the argument to the right of $j = 0$ is carried out first. In our context, Van Leer's constraint requires that for $x_0 \le x \le x_{1/2}$, the reconstruction $r_j(x, t^n)$ takes values in $I[u_0, u_1]$; that is, the final slope $(u_x)_0$ lies between 0 and $2s_+$ (Fig. 2.1). It is the limit 0 that causes accuracy to degenerate near extrema. To obtain uniform second-order accuracy, we require the final slope to lie between q_* and $2s_+$. The requirement to the left of $j = 0$ is for $(u_x)_0$ to lie between q_* and $2s_-$. The two requirements together result in the following constraint: the final slope lies in the intersection of the two intervals $I[q_*, 2s_-]$ and $I[q_*, 2s_+]$. Clearly, one end of this intersection interval is q_*; the other is

$$q^* = \text{median}\,(q_*, 2s_-, 2s_+). \tag{2.16}$$

And the constraint requires the slope $(u_x)_0$ to lie in $I[q_*, q^*]$.

Our next task is to define an accurate slope. Using the quartic (five-point) formula, set

$$q_5 = (u_{-2} - 8u_{-1} + 8u_1 - u_2)/(12h). \tag{2.17}$$

The above slope is highly accurate; however, near a discontinuity, it may have the wrong sign (see Fig. 2.2(a)). We avoid this problem by requiring q_5 to lie between p_0 and p_m where

$$p_m = \text{median}\,(p_-, p_+, p_0). \tag{2.18}$$

To bring q_5 into the interval $I[p_0, p_m]$, we once again use the median function:

$$q_6 = \text{median}\,(q_5, p_m, p_0). \tag{2.19}$$

Note that at the smooth part of the data, one can show via a Taylor series argument that q_6 is generally identical to q_5; that is, p_m and p_0 provide plenty of room for an accurate slope.

Finally, using the median function, we limit q_6,

$$(u_x)_0 = \text{median}\,(q_6, q_*, q^*). \tag{2.20}$$

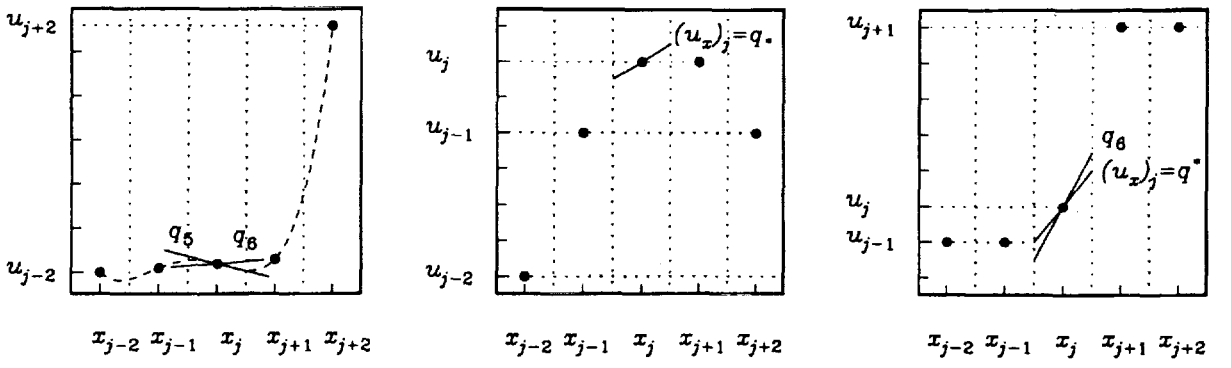

(a) q_5 *has a wrong sign* (b) $(u_x)_j$ *near an extremum* (c) $(u_x)_j$ *near a discontinuity*

Figure 2.2. *Effects of the constraints.*

Since q_* and q_6 are accurate to $O(h^2)$, the above $(u_x)_0$ is also accurate to the same order.

The following remark shows the effect of the above constraint. At the smooth part of the data where the slope is nonzero, expression (2.20) yields $(u_x)_0 = q_6$ because q_* is closer to 0 than q_6, and q^* is further from 0. Near an extremum, the interval $I[q_*, q^*]$ may reduce to the point $\{q_*\}$ and, in this case, $(u_x)_0 = q_*$ (see Fig. 2.2(b)). It is here that our monotonicity constraint preserves second-order accuracy while Van Leer's may not. Near a discontinuity, or where the data change rapidly, the slope q_6 is generally steeper than q^*, and the final slope is identical to q^*, which is either $2s_+$ or $2s_-$ (see Fig. 2.2(c)).

An alterative definition for q_* is the UNO slope:

$$q_- = \text{median}\,(s_-, p_-, p_0), \qquad q_+ = \text{median}\,(s_+, p_+, p_0), \qquad q_* = \text{minmod}\,(q_+, q_-). \quad (2.21a,b,c)$$

We can also steepen the slope near a discontinuity: after (2.19) and before (2.20), we reset q_6,

$$q_6 \leftarrow \text{sgn}\,(q_6)\max(5|q_+ - q_-|, |q_6|). \tag{2.22}$$

Here, the factor 5 is found by numerical experiments. At smooth regions, $|q_+ - q_-|$ is a small number of order $O(h^2)$, and the above modification does not alter q_6. Near a discontinuity, on the other hand, q_- and q_+ are far apart, and (2.22) steepens q_6 considerably.

Next, we present a simple criterion which detects the smooth regions where the constraint has no effect. Let $\Delta_j^2 u$ be the second difference of u:

$$\Delta_j^2 u = u_{j-1} - 2u_j + u_{j+1}. \tag{2.23}$$

For each index j, if

$$\tfrac{2}{3} \le \Delta_{j-1}^2 u / \Delta_j^2 u \le \tfrac{3}{2}, \quad \text{and} \quad \tfrac{2}{3} \le \Delta_{j+1}^2 u / \Delta_j^2 u \le \tfrac{3}{2}, \tag{2.24a,b}$$

then the solution is considered to be 'smooth' in the jth cell, and it can be shown that a constraint slightly more general than the above has no effect on the quartic slope. In this case, there is no need to carry out the constraint, and the final slope is given by the quartic formula (2.17). (See

also Huynh 1993a, 1993b.) For the Euler equations, this test is generally performed only on the density field.

3. Second-order upwind scheme for the Euler equations. The one-dimensional flow of an inviscid and compressible gas obeys the conservation laws for mass, momentum, and energy:

$$\frac{\partial \mathbf{U}}{\partial t} + \frac{\partial \mathbf{F}(\mathbf{U})}{\partial x} = 0, \tag{3.1}$$

$$\mathbf{U} = \begin{pmatrix} \rho \\ m \\ e \end{pmatrix}, \qquad \mathbf{F} = \begin{pmatrix} m \\ (m^2/\rho) + p \\ (e+p)m/\rho \end{pmatrix} = \begin{pmatrix} \rho u \\ \rho u^2 + p \\ (e+p)u \end{pmatrix} \tag{3.2, 3}$$

where t is time, x distance, ρ density, m momentum, e total energy per unit volume, u velocity, and p pressure. Let γ be the ratio of specific heats, then for a perfect gas,

$$p = (\gamma - 1)(e - \tfrac{1}{2}\rho u^2). \tag{3.4}$$

At smooth regions of $\mathbf{U}$, (3.1) is equivalent to the non-conservation form

$$\frac{\partial \mathbf{U}}{\partial t} + \mathbf{A}_c \frac{\partial \mathbf{U}}{\partial x} = 0, \qquad \text{where} \qquad \mathbf{A}_c = \frac{\partial \mathbf{F}}{\partial \mathbf{U}} = \left(\frac{\partial \mathbf{F}}{\partial \rho}, \frac{\partial \mathbf{F}}{\partial m}, \frac{\partial \mathbf{F}}{\partial e}\right). \tag{3.5, 6}$$

And after some algebra,

$$\mathbf{A}_c = \begin{pmatrix} 0 & 1 & 0 \\ (\gamma-3)u^2/2 & (3-\gamma)u & \gamma - 1 \\ (\gamma-1)u^3 - \gamma u e/\rho & -3(\gamma-1)u^2/2 + \gamma e/\rho & \gamma u \end{pmatrix}. \tag{3.7}$$

For the primitive variable $\mathbf{V}$ (more precisely, the vector of primitive variables),

$$\mathbf{V} = \begin{pmatrix} \rho \\ u \\ p \end{pmatrix}, \qquad \frac{\partial \mathbf{V}}{\partial t} + \mathbf{A}_p \frac{\partial \mathbf{V}}{\partial x} = 0, \qquad \text{where} \qquad \mathbf{A}_p = \begin{pmatrix} u & \rho & 0 \\ 0 & u & 1/\rho \\ 0 & \gamma p & u \end{pmatrix}. \tag{3.8, 9, 10}$$

Denote the Jacobian matrix of the transformation between the primitive and conservative variables by $\mathbf{M}$ (Warming, Beam, and Hyett 1975):

$$\mathbf{M} = \frac{\partial \mathbf{U}}{\partial \mathbf{V}} = \left(\frac{\partial \mathbf{U}}{\partial \rho}, \frac{\partial \mathbf{U}}{\partial u}, \frac{\partial \mathbf{U}}{\partial p}\right). \tag{3.11}$$

Then

$$\mathbf{M} = \begin{pmatrix} 1 & 0 & 0 \\ u & \rho & 0 \\ u^2/2 & \rho u & 1/(\gamma-1) \end{pmatrix}, \qquad \mathbf{M}^{-1} = \begin{pmatrix} 1 & 0 & 0 \\ -u/\rho & 1/\rho & 0 \\ (\gamma-1)u^2/2 & -(\gamma-1)u & \gamma - 1 \end{pmatrix}. \tag{3.12a, b}$$

Using the chain rule, (3.5, 9, 11) imply

$$\mathbf{A}_p = \mathbf{M}^{-1} \mathbf{A}_c \mathbf{M}. \tag{3.13}$$

Next, we diagonalize $\mathbf{A}_p$ and then $\mathbf{A}_c$. Let c be the speed of sound, $c = (\gamma p/\rho)^{1/2}$. Equation (3.13) implies $\mathbf{A}_p$ and $\mathbf{A}_c$ have the same eigenvalues. They are

$$\lambda^{(1)} = u - c, \qquad \lambda^{(2)} = u, \qquad \lambda^{(3)} = u + c. \tag{3.14}$$

Let $\mathbf{L}_p$ be the matrix of the left eigenvectors of $\mathbf{A}_p$; $\mathbf{R}_p$, that of the right. Let Λ be the diagonal matrix whose diagonal entries are $\lambda^{(1)}$, $\lambda^{(2)}$, and $\lambda^{(3)}$. Then

$$\mathbf{L}_p = \begin{pmatrix} 0 & -\rho/(2c) & 1/(2c^2) \\ 1 & 0 & -1/c^2 \\ 0 & \rho/(2c) & 1/(2c^2) \end{pmatrix}, \qquad \mathbf{R}_p = \begin{pmatrix} 1 & 1 & 1 \\ -c/\rho & 0 & c/\rho \\ c^2 & 0 & c^2 \end{pmatrix}, \tag{3.15a, b}$$

and

$$\mathbf{L}_p = \mathbf{R}_p^{-1}, \qquad \mathbf{L}_p \mathbf{A}_p \mathbf{R}_p = \Lambda, \qquad \mathbf{A}_p = \mathbf{R}_p \Lambda \mathbf{L}_p. \tag{3.16, 17a, b}$$

The diagonalization of $\mathbf{A}_c$ follows from (3.13):

$$\mathbf{L}_c \mathbf{A}_c \mathbf{R}_c = \Lambda, \qquad \text{where} \qquad \mathbf{L}_c = \mathbf{L}_p \mathbf{M}^{-1}, \qquad \mathbf{R}_c = \mathbf{M} \mathbf{R}_p. \tag{3.18, 19, 20}$$

Let H be the total enthalpy, $H = (e + p)/\rho$. Expressions (3.20, 12a, 15b) lead to

$$\mathbf{R}_c = \begin{pmatrix} 1 & 1 & 1 \\ u - c & u & u + c \\ H - uc & u^2/2 & H + uc \end{pmatrix}. \tag{3.21}$$

To define the characteristic variables, let $\hat{\mathbf{U}}$ be a fixed state, and let $\mathbf{U}$ vary. Equation (3.5) can be linearized around $\hat{\mathbf{U}}$:

$$\frac{\partial \mathbf{U}}{\partial t} + \hat{\mathbf{A}}_c \frac{\partial \mathbf{U}}{\partial x} = 0. \tag{3.22}$$

The characteristic variable $\mathbf{W}_c$ and the corresponding characteristic equation are

$$\mathbf{W}_c = \hat{\mathbf{L}}_c \mathbf{U}, \qquad \frac{\partial \mathbf{W}_c}{\partial t} + \hat{\Lambda} \frac{\partial \mathbf{W}_c}{\partial x} = 0. \tag{3.23, 24}$$

Similarly, for the primitive variable $\mathbf{V}$, with a fixed state $\hat{\mathbf{V}}$,

$$\frac{\partial \mathbf{V}}{\partial t} + \hat{\mathbf{A}}_p \frac{\partial \mathbf{V}}{\partial x} = 0, \qquad \mathbf{W}_p = \hat{\mathbf{L}}_p \mathbf{V}, \qquad \frac{\partial \mathbf{W}_p}{\partial t} + \hat{\Lambda} \frac{\partial \mathbf{W}_p}{\partial x} = 0. \tag{3.25, 26, 27}$$

3.1. Reconstruction step. For the Euler equations, given $\{\mathbf{U}_j\}$, we first calculate $\{\mathbf{V}_j\}$. If the weighted average (2.10) is employed, we can simply apply it on $\mathbf{V}_j$ to obtain $(\mathbf{V}_x)_j$. Since (2.10) is quite diffusive, it damps out oscillations (if any) quickly. We can also apply (2.10) on $\mathbf{U}_j$; because $\mathbf{A}_c$ is more complex than $\mathbf{A}_p$, the algorithm is slightly costlier.

As shown by (3.24, 27), however, the quantities being advected are the characteristic variables. With a more accurate reconstruction step such as (2.14-20), we need to employ $\mathbf{W}_p$ as follows. For each index j, if conditions (2.24) are satisfied for the density field, the slopes $(\mathbf{V}_x)_j$ are given by (2.17). Otherwise, for $-2 \le l \le 2$ (five-point stencil), employing (3.26) with $\hat{\mathbf{V}} = \mathbf{V}_j$, set

$(\mathbf{W}_p)_l = \hat{\mathbf{L}}_p \mathbf{V}_{j+l}$. Algorithm (2.14–20) is carried out for each component of $(\mathbf{W}_p)_l$, and the result is denoted by $\mathbf{W}_x$. Finally, $(\mathbf{V}_x)_j = \hat{\mathbf{R}}_p \mathbf{W}_x$.

Note that when the constraints have no effect, because $\hat{\mathbf{L}}_p$ and $\hat{\mathbf{R}}_p$ are the inverse of each other, the above interpolation of $(\mathbf{W}_p)_l$ yields a $(\mathbf{V}_x)_j$ identical to the interpolation of $\mathbf{V}_j$.

Knowing $(\mathbf{V}_x)_j$, one can calculate $(\mathbf{V}_t)_j$ via (3.9). For each interface $j + 1/2$, Taylor series expansions from the two adjacent cells j and $j + 1$ yield $\mathbf{V}_L$ and $\mathbf{V}_R$ at time $t^{n+1/2}$.

3.2. Upwind step. Given $\mathbf{V}_L$ and $\mathbf{V}_R$, we next define the upwind flux. For linear advection, the speed is known; here, to obtain the characteristic speeds, which depend on $\mathbf{V}_L$ and $\mathbf{V}_R$, we need to linearize. The simplest and most obvious state for linearization is $\hat{\mathbf{V}} = \frac{1}{2}(\mathbf{V}_L + \mathbf{V}_R)$. As shown by (3.24, 27), the Euler equations can then be approximated by three advection equations. The speeds of advection are $\hat{\lambda}^{(i)}$ given in (3.14). Denote $\mathbf{F}_L = \mathbf{F}(\mathbf{V}_L)$. The characteristic flux and characteristic variables are

$$\mathbf{G}_L = \hat{\mathbf{L}}_c \mathbf{F}_L, \qquad (\mathbf{W}_c)_L = \hat{\mathbf{L}}_c \mathbf{U}_L, \qquad (\mathbf{W}_p)_L = \hat{\mathbf{L}}_p \mathbf{V}_L.$$

Similar expressions hold with subscript L replaced by R. The upwind characteristic flux, denoted $\mathbf{G}_U$, is given by the sign of $\hat{\lambda}^{(i)}$, $1 \le i \le 3$. Omitting the superscript (i), each component of $\mathbf{G}_U$ is given by:

$$g_U = \tfrac{1}{2}(g_L + g_R) - \tfrac{1}{2}\,\mathrm{sgn}\,(\hat{\lambda})(g_R - g_L). \tag{3.28}$$

Here there is a problem. When $\hat{\lambda} = 0$, should we select g_L or g_R as the upwind flux? This problem no longer exists, however, if the state of linearization $\hat{\mathbf{V}}$ has the property that

$$\text{if} \qquad \hat{\lambda} = 0, \qquad \text{then} \qquad g_L = g_R. \tag{3.29}$$

For convenience, let Δ be the difference operator R minus L, e.g., $\Delta\mathbf{F} = \mathbf{F}_R - \mathbf{F}_L$. From (3.6), $\partial\mathbf{F} = \mathbf{A}_c \partial\mathbf{U}$. Suppose $\tilde{\mathbf{V}}$ (to be determined) is a fixed state that satisfies

$$\Delta\mathbf{F} = \tilde{\mathbf{A}}_c \Delta\mathbf{U}. \qquad \text{Then,} \qquad \Delta\mathbf{G} = \tilde{\mathbf{\Lambda}} \Delta\mathbf{W}_c, \tag{3.30, 3.31}$$

where $\Delta\mathbf{W}_c = \tilde{\mathbf{L}}_c \Delta\mathbf{U}$. Expression (3.31) implies that property (3.29) holds with $\hat{\mathbf{V}}$ replaced by $\tilde{\mathbf{V}}$. Rewriting (3.28) in vector form and employing (3.31),

$$\mathbf{G}_U = \tfrac{1}{2}(\mathbf{G}_L + \mathbf{G}_R) - \tfrac{1}{2}\,|\tilde{\mathbf{\Lambda}}| \tilde{\mathbf{L}}_c \Delta\mathbf{U}. \tag{3.32}$$

Multiplying the above on the left by $\tilde{\mathbf{R}}_c$, we obtain the upwind flux:

$$\mathbf{F}_U = \tfrac{1}{2}(\mathbf{F}_L + \mathbf{F}_R) - \tfrac{1}{2}\,\tilde{\mathbf{R}}_c |\tilde{\mathbf{\Lambda}}| \tilde{\mathbf{L}}_c \Delta\mathbf{U}. \tag{3.33}$$

Further simplification can be made by requiring—and the motivation is (3.11)—that $\tilde{\mathbf{V}}$ satisfies

$$\Delta\mathbf{U} = \tilde{\mathbf{M}} \Delta\mathbf{V}. \tag{3.34}$$

Multiplying the above on the left by $\tilde{\mathbf{L}}_c$, we obtain, by (3.19), $\Delta\mathbf{W}_c = \tilde{\mathbf{L}}_c \tilde{\mathbf{M}} \Delta\mathbf{V} = \tilde{\mathbf{L}}_p \Delta\mathbf{V} = \Delta\mathbf{W}_p$. Thus,

$$\mathbf{F}_U = \tfrac{1}{2}(\mathbf{F}_L + \mathbf{F}_R) - \tfrac{1}{2}\,\tilde{\mathbf{R}}_c |\tilde{\mathbf{\Lambda}}| \tilde{\mathbf{L}}_p \Delta\mathbf{V}. \tag{3.35}$$

Since $\tilde{\mathbf{L}}_p$ is simpler than $\tilde{\mathbf{L}}_c$, (3.35) is more economical than (3.33).

Finally, to determine $\tilde{\mathbf{V}}$, the first component of (3.30) turns out to be useless (redundant). The second yields a quadratic in $\tilde{u}$; among the two solutions of this quadratic, only one always makes sense and yields $\tilde{u}$. The third component gives $\tilde{H}$. Similarly, the last two components of (3.34) lead to $\tilde{\rho}$ and $\tilde{u}$. Expressions (3.30) and (3.34) together define $\tilde{\mathbf{V}}$ uniquely:

$$\tilde{\rho} = \sqrt{\rho_L \rho_R}; \qquad \beta_L = \rho_L/(\rho_L + \tilde{\rho}), \qquad \beta_R = 1 - \beta_L = \rho_R/(\rho_R + \tilde{\rho}); \qquad (3.36, 37a, b)$$

$$\tilde{u} = \beta_L u_L + \beta_R u_R; \qquad \tilde{H} = \beta_L H_L + \beta_R H_R. \qquad (3.38, 39)$$

For more details as well as a simple entropy fix, see (Huynh 1993b).

Expression (3.35) is very simple, but it involves all three components (waves). Employing a conditional statement, (3.35) can be coded economically by stepping across only one wave as follows. Let $\tilde{\mathbf{V}}$ be given by (3.36–39), and $\tilde{c}$, the corresponding speed of sound.

If $\tilde{u} - \tilde{c} \geq 0$, then $\mathbf{F}_U = \mathbf{F}_L$;
else if $\tilde{u} \geq 0$, then with $\Delta w_p^{(1)}$ the first component of $\tilde{\mathbf{L}}_p \Delta \mathbf{V}$, $\mathbf{F}_U = \mathbf{F}_L + (\tilde{u} - \tilde{c}) \Delta w^{(1)} \tilde{\mathbf{R}}_c^1$;
else if $\tilde{u} + \tilde{c} \geq 0$, then $\mathbf{F}_U = \mathbf{F}_R - (\tilde{u} + \tilde{c}) \Delta w^{(3)} \tilde{\mathbf{R}}_c^3$;
else, $\mathbf{F}_U = \mathbf{F}_R$.

Note that for the tilde state, (3.28), (3.33), and (3.35) yield identical upwind fluxes. With a different state of linearization, e.g., $\hat{\mathbf{V}}$, they yield different fluxes; for (3.33) and (3.35) the results still depend continuously on the data; for (3.28), however, the result no longer depend continuously. In fact, with $\hat{\mathbf{V}}$ in place of $\tilde{\mathbf{V}}$, (3.33) and (3.35) work well for most problems, but (3.28) does not.

4. Third-order centered scheme for advectionequation. At time t^n, as in §2, let x_j be the cell center and $x_{j+1/2}$ the cell interface. Assume that we know $\bar{u}_j$ and $u_{j+1/2}$ which respectively approximate the average value in the j-th cell and the interface point value at $x_{j+1/2}$ of the solution u, for all j. (For a parabolic reconstruction, as shown by (4.2c) below, the cell average $\bar{u}_j$ is generally different from the point value u_j. Again the superscript n is understood.) We wish to calculate, and note the changes in the subscripts, $\bar{u}_{j+1/2}^{n+1/2}$ and $u_j^{n+1/2}$, which respectively approximate the cell average and the interface point value of the solution at time $t^{n+1/2} = t^n + \tau/2$. Here, τ is assumed to satisfy the CFL condition (2.2). Notice that we take only half of a regular time step and, at time $t^{n+1/2}$, the mesh is staggered. See Fig. 4.1.

The algorithm proceeds as follows. Set

$$u_{L,j} = u_{j-1/2}, \qquad u_{R,j} = u_{j+1/2}. \qquad (4.1)$$

(When monotonicity constraints are introduced, $u_{L,j}$ and $u_{R,j}$ will be defined differently.) At time level n and in each cell j, we reconstruct the solution by a parabola denoted by $P_j(x)$ using the three pieces of information: the cell average $\bar{u}_j$ and the two point values $u_{L,j}$ and $u_{R,j}$. The second and first derivatives and the point value at x_j of the parabola P_j are, respectively,

$$D_x^2 u_j = 6(u_{L,j} + u_{R,j} - 2\bar{u}_j)/h^2, \quad D_x u_j = (u_{R,j} - u_{L,j})/h, \quad u_j = \bar{u}_j - (D_x^2 u_j)h^2/24. \quad (4.2a, b, c)$$

The time partial derivatives can be evaluated by differentiating the advection equation (1.1a):

$$D_t u_j = -a(D_x u_j), \qquad D_t^2 u_j = a^2(D_x^2 u_j). \tag{4.3a,b}$$

We can now update the point value $u_j^{n+1/2}$ via a Taylor series expansion:

$$u_j^{n+1/2} = u_j + (D_t u_j)(\tau/2) + (1/2)(D_t^2 u_j)(\tau/2)^2. \tag{4.4}$$

Observe that since the half time step corresponds to a CFL number less than 1/2, the discontinuity in slope at $(x_{j+1/2}, t^n)$ has not arrived at x_j or x_{j+1} when $t = t^{n+1/2}$. For this reason, the dual-mesh formulation does not need an upwind step; nevertheless, upwinding takes effect when we employ the differential equations to calculate the time derivatives from the spatial ones.

The values $u_j^{n+1/4}$, $u_{j+1/4}$, and $u_{j-1/4}$ can be obtained by expressions similar to (4.4). Define the average flux $\tilde{f}_j$ (in time) by

$$\tilde{f}_j = a(u_j + 4u_j^{n+1/4} + u_j^{n+1/2})/6. \tag{4.5}$$

The same calculations as in (4.2–5) are then carried out for the cell $j+1$. The cell average $\bar{u}_{j+1/2}^{n+1/2}$ is updated by balancing the fluxes for the control volume whose four corners are (x_j, t^n), (x_{j+1}, t^n), $(x_j, t^{n+1/2})$, and $(x_{j+1}, t^{n+1/2})$ (shown in Fig. 4.1),

$$\bar{u}_{j+1/2}^{n+1/2} = (u_j + 4u_{j+1/4} + u_{R,j})/12 + (u_{j+1} + 4u_{j+1-1/4} + u_{L,j+1})/12 - (1/2)(\tau/h)(\tilde{f}_{j+1} - \tilde{f}_j). \tag{4.6}$$

The next half time step is identical to the above except for obvious changes in indices due to the staggering of the mesh system. We then obtain $\{\bar{u}_j^{n+1}\}$ and $\{u_{j+1/2}^{n+1}\}$, and this completes the basic algorithm.

Note that the single-mesh version of the above scheme was presented by Van Leer (1977). For a single-mesh system, the scheme must be formulated as an upwind scheme. This formulation makes extensions to systems of equations very difficult since it is not clear how to update the interface values. The above dual-mesh piecewise-parabolic formulation is due to Sanders (1988), except for the following key difference. Instead of evolving in time via the partial differential equations and a Taylor series expansion as in (4.3–4), he employed characteristic tracing. This characteristic tracing makes preserving third-order accuracy a nontrivial task. Our monotonicity constraint below is also considerably simpler than Sanders'. If we discard the interface values and reconstruct the function in each cell by interpolating the cell average quantities via a limiter such as (2.10), we obtain the staggered-mesh scheme of Nessyahu and Tadmor (1990). They also employed the time evolution (4.3a) above. Due to the linear reconstruction, their algorithm is simple. It takes very little work, however, to carry the point values, and as shown by the analysis in (Van Leer 1977, scheme 1 and 2), the resulting scheme (Chang and To 1992) is more accurate. Finally, these dual-mesh methods can be considered as higher-order extensions of the Lax-Friedrichs scheme.

Next, we move to the subject of preventing oscillations. Colella and Woodward (1984) presented a constraint which assures that the reconstruction parabolas are always monotone. This constraint, however, causes accuracy to degenerate to first-order near extrema. Sanders (1988)

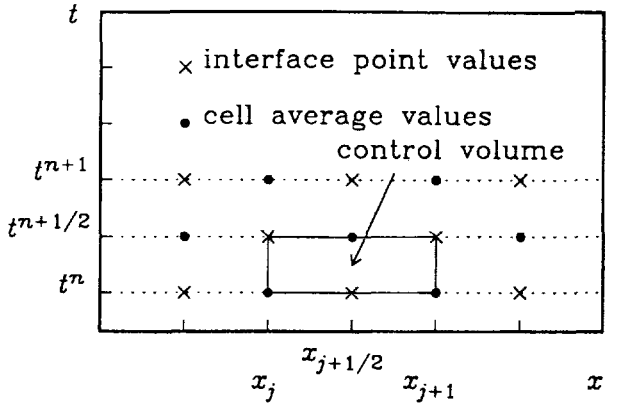

Fig. 4.1. *Dual-mesh system.*

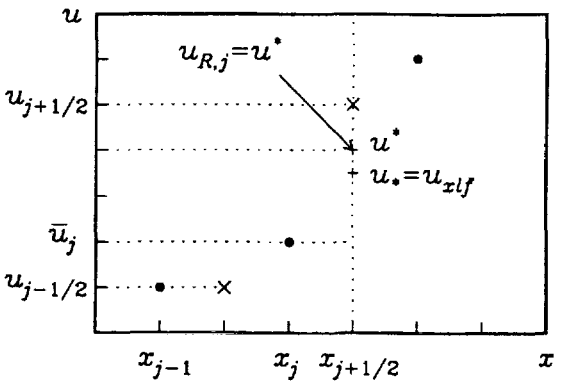

Fig. 4.2. *Monotonicity constraint.*

derived a constraint that preserves at least second-order accuracy near extrema, but it is complex and costly. We introduce below a simple constraint that preserves accuracy.

Due to symmetry (reflection), we carry out the constraint only for $u_{R,j}$. This constraint has two bounds: a lower bound u_* and an upper bound u^*, and $u_{R,j}$ is required to lie between these two bounds. To obtain the lower bound, consider the parabola defined by the three quantities $\bar{u}_j$, $u_{j-1/2}$, and $\bar{u}_{j-1}$. The value of this parabola at $x_{j+1/2}$ is

$$u_{xfl} = \tfrac{5}{2}\,\bar{u}_j - 2u_{j-1/2} + \tfrac{1}{2}\,\bar{u}_{j-1}; \tag{4.7}$$

here, the subscript xfl stands for 'extrapolating from left'. And,

$$u_* = \text{median}(\bar{u}_j, u_{j+1/2}, u_{xfl}), \qquad u^* = \bar{u}_j + 2(\bar{u}_j - u_{j-1/2}). \tag{4.8a,b}$$

See Fig. 4.2. Note since $u_{j+1/2}$ and u_{xfl} are accurate to $O(h^3)$, so is the lower bound u_*. This is why accuracy is preserved. Finally,

$$u_{R,j} = \text{median}(u_{j+1/2}, u_*, u^*). \tag{4.9}$$

Loosely put, u_* is generally too close to $\bar{u}_j$, and u^* too far from $\bar{u}_j$; as a result, at most smooth regions, $u_{R,j}$ is identical to $u_{j+1/2}$, i.e., the constraint that $u_{R,j}$ lies between u_* and u^* has no effect on $u_{j+1/2}$. Near a discontinuity, however, $u_{j+1/2}$ often lies outside the interval formed by u_* and u^*, and expression (4.9) yields u^* as shown in Fig. 4.2.

Although the constraint (4.7–9) is very simple, for the Euler equations we apply it to the characteristic variables, which are somewhat expensive to calculate. Since the constraint has no effect at most smooth regions, it would save considerable computing time if we can derive simple criteria to detect when it has no effect, and in that case, $u_{L,j}$ and $u_{R,j}$ are respectively identical to $u_{j-1/2}$ and $u_{j+1/2}$ as in (4.1). Such a criterion is presented below.

Again, for the j-th cell, let D_L^2 be the second derivative of the parabola defined by $\bar{u}_j$, $u_{j-1/2}$, and $\bar{u}_{j-1}$; D_R^2, that of the parabola defined by $\bar{u}_j$, $u_{j+1/2}$, and $\bar{u}_{j+1}$. Then if

$$\tfrac{2}{3} \le D_L^2/D_x^2 u_j \le \tfrac{3}{2} \qquad \text{and} \qquad \tfrac{2}{3} \le D_R^2/D_x^2 u_j \le \tfrac{3}{2}, \tag{4.10}$$

the data are considered to be 'smooth' in the j-th cell, and the interface values are left unchanged. For the Euler equations, this test is performed only on the density field. Therefore, the resulting scheme is economical.

5. Third-order centered scheme for the Euler equations. The above formulation facilitates the extensions to systems of equations. For the Euler equations, if condition (4.10) is satisfied for density, the interface values $\mathbf{U}_{L,j}$ and $\mathbf{U}_{R,j}$ are given respectively by $\mathbf{U}_{j-1/2}$ and $\mathbf{U}_{j+1/2}$. Otherwise, the monotonicity constraints (4.7–9) are carried out for the characteristic variables $\mathbf{W}_c$, and then these characteristic interface values are transferred back to the conservative quantities. Note that the characteristic variables and the constraints are generally needed at only a few cells near a discontinuity. Next, the x-derivatives of the conserved variables are given by (4.2). The t-derivatives are calculated by differentiating (3.5). The updating of the conserved variables are then straightforward: the point values via (4.4) and the nonconservation form; the averages, via (4.5–6) and the conservation form.

6. Numerical results. In the following numerical examples, unless otherwise stated, the CFL number is 0.8; thus, for the dual-mesh scheme, each half time step corresponds to a CFL number of 0.4. The continuous lines (curves) represent the exact solutions, and the circles the numerical ones.

The first problem of category 1 is the advection equation (1.1a) with a gaussian initial condition. Here, to see how the schemes advect discontinuities, in addition to the gaussian, we also have a square, a triangle, and a semi-ellipse wave. The results after propagating a distance of 200 cells ($t = 200$) are shown in Fig. 6.1. We also present the results of a steepening technique for the third-order method (due to space limitation, the details of this technique were omitted).

The second problem of category 1 is a spherical wave problem. The results for the second-order scheme are shown in Fig. 6.2, and the third-order in Fig. 6.3. For $\omega = \pi/3$, the waves are damped out by the second-order scheme very quickly (the plot is omitted).

For problems in categories 2 and 5, the two schemes yield essentially identical results. Therefore, we present only the results of the second-order upwind scheme. For category 2, the solutions of the first problem at $t = 200$ and the second problem at $t = 60$ are shown in Fig. 6.4. Note that for shocktube problems, the first few time steps corresponding to a fixed CFL number are generally too big because the flow has not developed. These big time steps may cause oscillations. To avoid this problem, the first 4 time steps τ_k $(k = 1, \ldots, 4)$ are replaced by $(k/5)\tau_k$.

The results by the second-order upwind scheme for category 5 are presented in Fig. 6.5(a). Here, several snapshots of the spatial distribution of the pressure disturbances are plotted by a continuous curve. A similar result with a shock in the steady state solution is shown in Fig. 6.5(b). The steady state solution with shock is shown in Fig. 6.5(c). Note that for this problem, we employ the standard characteristic boundary conditions.

7. Conclusion and discussion. A second-order accurate upwind scheme and a third-order dual-mesh centered scheme are presented. These schemes are simple, and they can capture discontinuities well. For nonlinear acoustic problems, the results are highly accurate if waves are represented by 15 or more mesh points. Waves with too few mesh points are damped out.

To resolve waves with only 6 to 8 mesh points per period, higher-order schemes are preferred. Conceptually, the techniques presented here can be applied to several of these high-order schemes. Indeed, high-order schemes often can be formulated in conservation form; more specifically, the interpolation yields the interface values for the conserved variables rather than the slopes at a cell center. The constraint or limiting technique can then be applied to these interface values. At smooth regions, the constraint has no effect. Near a discontinuity, however, the constraints for the two sides of each interface yield two different values. We can then employ a flux splitting to define an upwind flux. Such a scheme employed with, e.g., a Runge-Kutta time stepping, reduces to a centered scheme at smooth regions, and turns into an upwind scheme only when the constraint takes effect, i.e., near discontinuities. Whether such schemes are capable of accurately resolving shocks and acoustic waves remains to be shown.

References.

S.-C. Chang and W.-M. To, *A brief description of a new numerical framework for solving conservation laws–the method of space-time conservation element and solution element*, 13th International Conference on Numerical Methods in Fluid Dynamics, Rome, Italy, July 6–10, 1992.

P. Colella and P. Woodward, *The piecewise parabolic method (PPM) for gas-dynamical simulations*, J. Comp. Phys., 54 (1984), pp. 174–201.

A. Harten and S. Osher, *Uniformly high-order accurate nonoscillatory schemes.* I, SIAM J. Numer. Anal., 24 (1987), pp. 279–309.

H. T. Huynh, *Accurate monotone cubic interpolation*, SIAM J. Numer. Anal., 30 (1993a), pp. 57–100.

H. T. Huynh, *Accurate upwind methods for the Euler equations*, SIAM J. Numer. Anal., to appear; also NASA TM 106388 (1993b).

H. Nessyahu and E. Tadmor, *Non-oscillatory central differencing for hyperbolic conservation laws*, J. Comp. Phys., 87 (1990), pp. 408–463.

P. L. Roe, *Approximate Riemann solvers, parameter vectors, and difference schemes*, J. Comp. Phys., 43 (1981), pp. 357–372.

P. L. Roe, *Characteristic-based schemes for the Euler equations*, Ann. Rev. Fluid Mech., 18 (1986), pp. 337–365.

R. Sanders, *A third-order accurate variation nonexpansive difference scheme for single nonlinear conservation laws*, Math. Comp. 51 (1988), pp. 535–558.

R. Sanders and A. Weiser, *A high order staggered grid method for hyperbolic systems of conservation laws in one space dimension*, Computer Methods in Applied Mechanics and Engineering, 75 (1989), pp. 91–107.

R. Sanders and A. Weiser, *A high resolution staggered mesh approach for nonlinear hyperbolic systems of conservation laws*, J. Comp. Phys., 101 (1992), pp. 314–329.

G. D. van Albada, B. van Leer, and W. W. Roberts, Jr., *A comparative study of computational methods in cosmic gas dynamics*, Astronom. and Astrophys., 108 (1982), pp. 76–84.

B. van Leer, *Towards the ultimate conservative difference scheme.* IV. *A new approach to numerical convection*, J. Comp. Phys., 23 (1977), pp. 276–298.

B. van Leer, *Towards the ultimate conservative difference scheme.* V. *A second-order sequel to Godunov's method*, J. Comp. Phys., 32 (1979), pp. 101–136.

R. F. Warming, R. M. Beam, and B.J. Hyett, *Diagonalization and simultaneous symmetrization of the gas-dynamic matrices*, Math. Comput., 29 (1975) pp. 1037–1045.

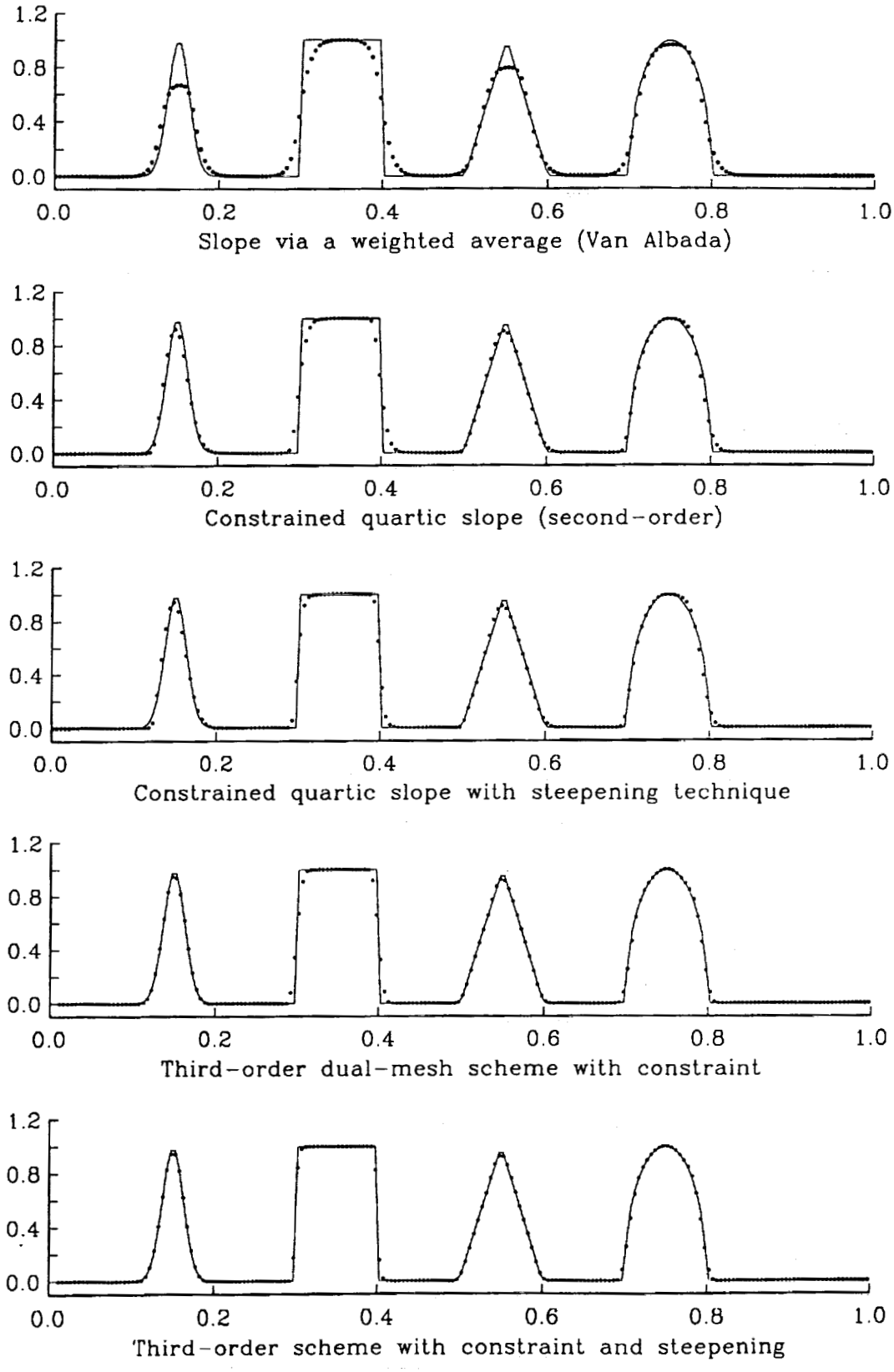

Fig. 6.1. *Linear advection; CFL=0.8; the waves have advected 200 cells.*

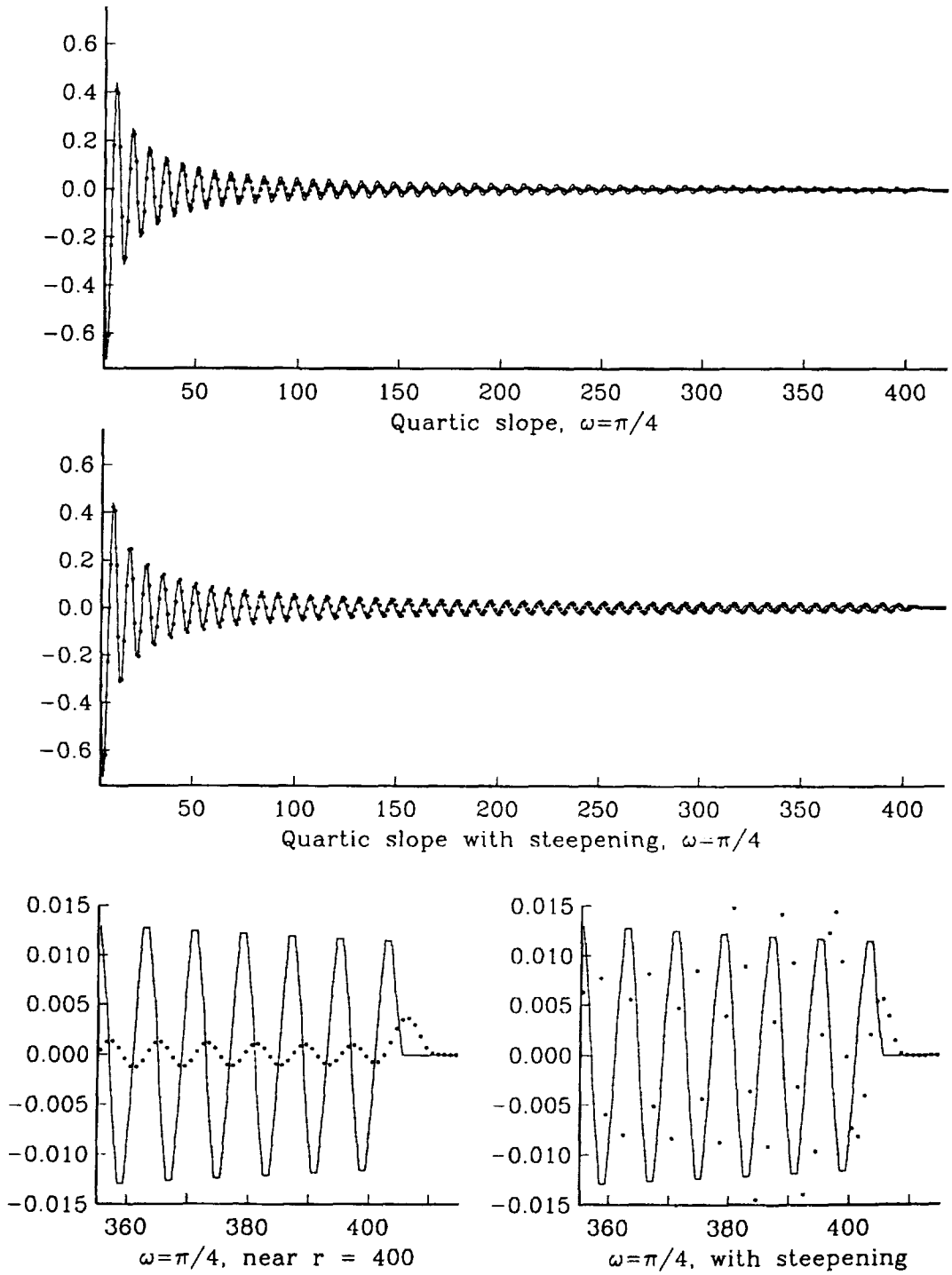

Fig. 6.2. *Second-order scheme for problem 2 of category 1; CFL=0.4.*

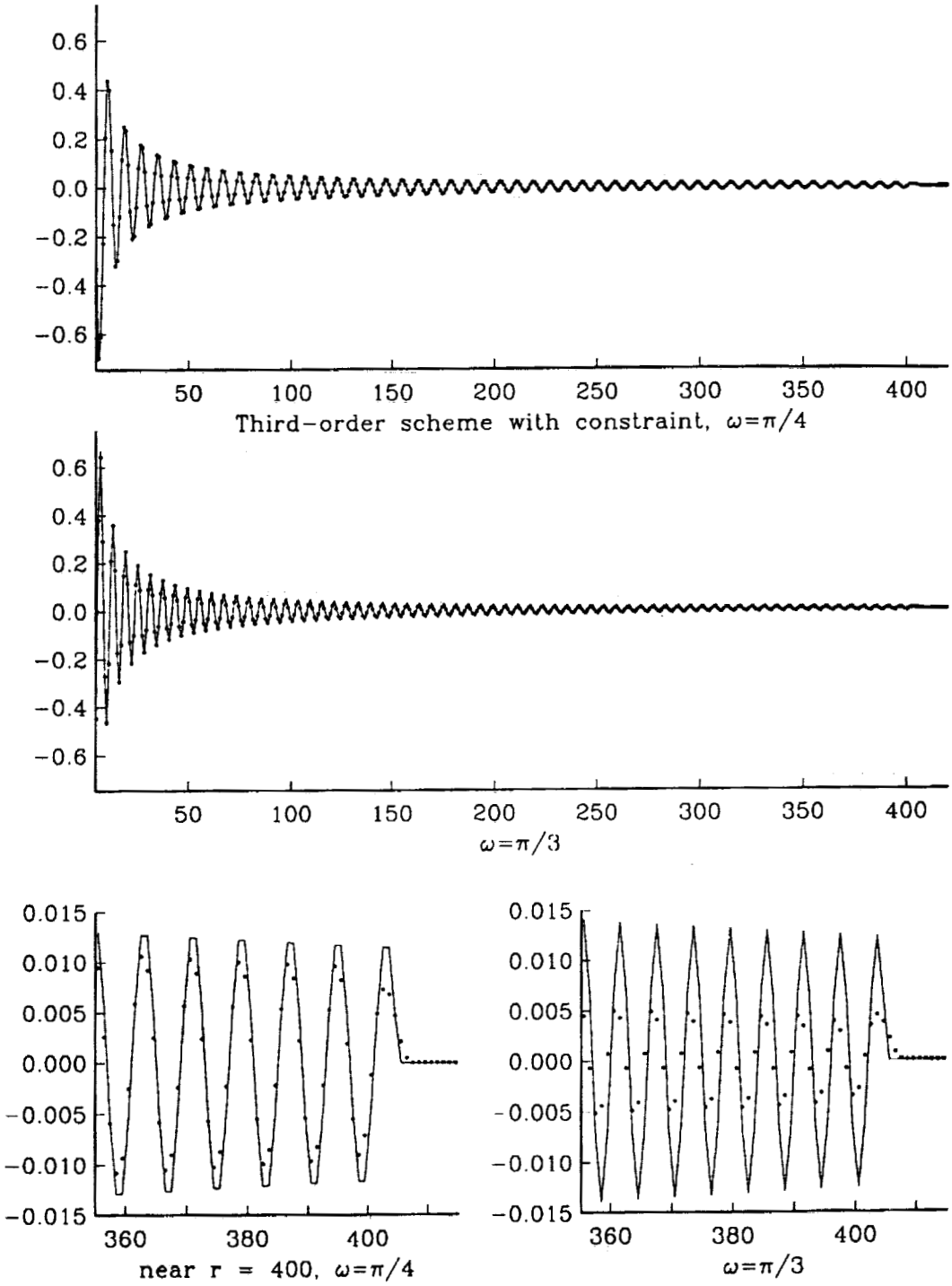

Fig. 6.3. *Third-order scheme for problem 2 of category 1; CFL=0.8.*

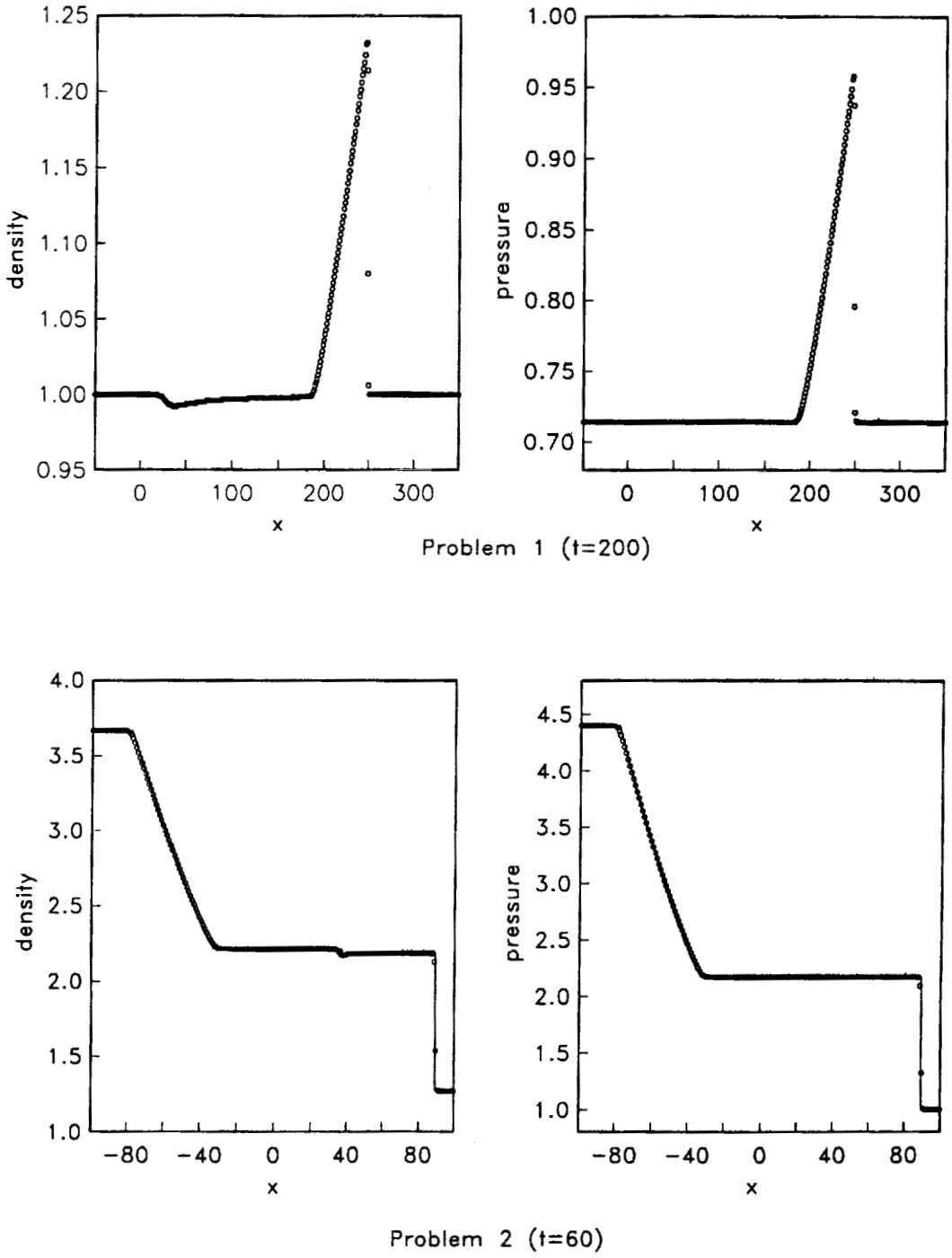

Fig. 6.4. *Second-order scheme (quartic slope with constraint) for problems of category 2.*

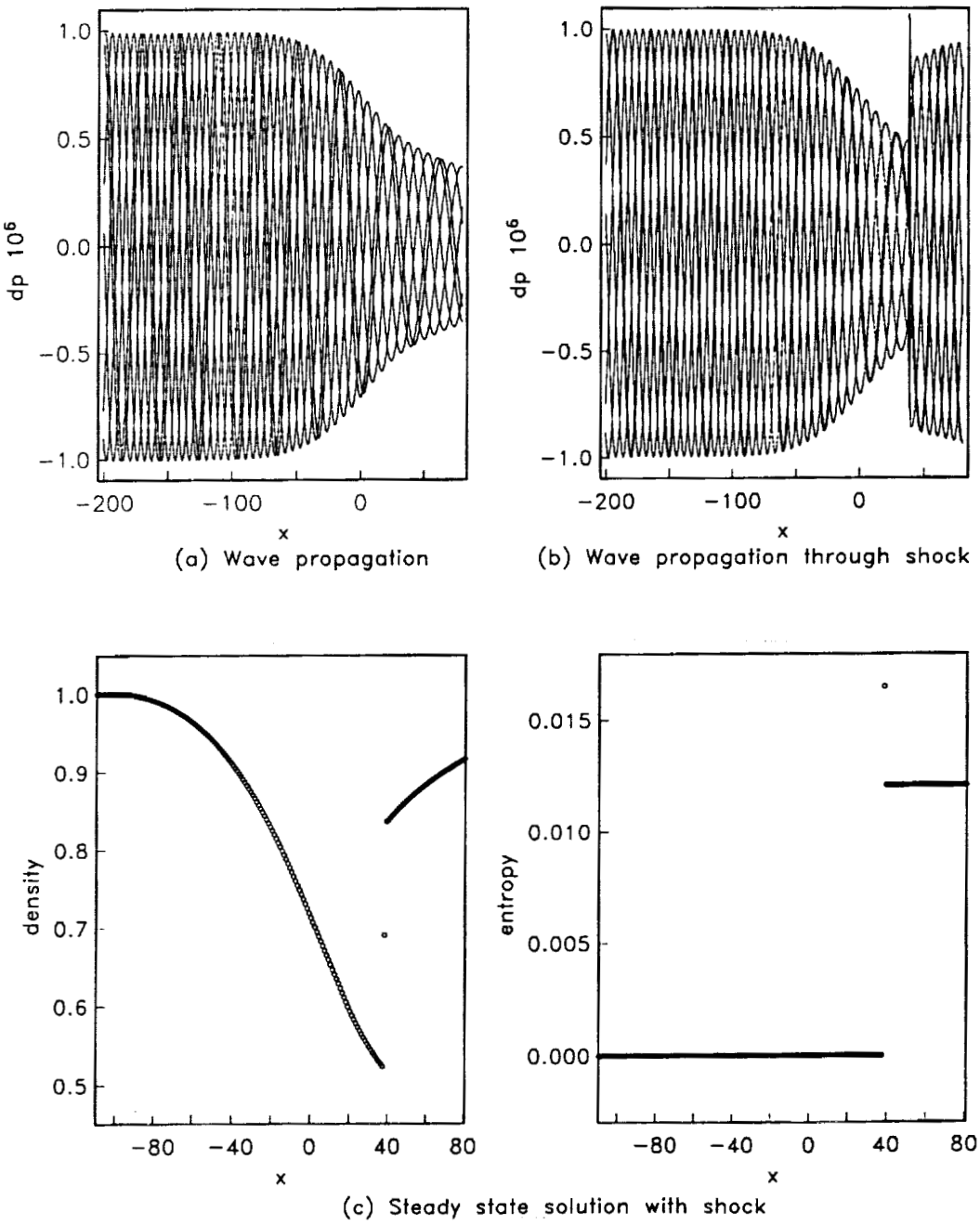

Fig. 6.5. *Second-order scheme (quartic slope with constraint) for category 5.*

SOLUTION OF ACOUSTIC WORKSHOP PROBLEMS BY A SPECTRAL MULTIDOMAIN METHOD*

David A. Kopriva
Supercomputer Computations Research Institute
and
Department of Mathematics
The Florida State University
Tallahassee, FL 32306

John H. Kolias
Department of Mechanical Engineering
The Florida State University
Tallahassee, FL 32306

SUMMARY

We use a new staggered grid Chebyshev spectral multidomain method to solve three of the Workshop benchmark problems. The method defines solution unknowns at the nodes of the Chebyshev Gauss quadrature, and the fluxes at the nodes of the Chebyshev Gauss-Lobatto quadrature. The Chebyshev spectral method gives exponentially convergent phase and dissipation errors. The multidomain approximation gives the method flexibility. Using the method, we solve problems in Categories 1 and 5.

INTRODUCTION

In this paper we demonstrate the use of a new staggered grid spectral multidomain method on the Category 1 and Category 5 Workshop problems. The desirable features of spectral methods regarding the solution of wave-propagation problems are their excellent phase and dissipation properties, and the fact that special boundary approximations are not needed to avoid overhang of the computational stencil. It has long been known that Chebyshev spectral methods require a minimum of π modes per wavelength to resolve a sine wave (Ref. 1). Exponential convergence of the phase and dissipation errors for Chebyshev spectral methods was demonstrated in Ref. 2. For large computational domains, however, large numbers of points are required even if only π points per wavelength are required to resolve a propagating wave. To reduce the inflexibility associated with a single global approximating polynomial through all those points, multidomain spectral methods were introduced. See Ref. 3, Chapter 13 for a review of early work.

* This research was supported in part by the U.S. Department of Energy through Contract # DE-FC05-85ER250000 and by the National Science Foundation through Grant DMS-9404322.

The multidomain methods that have been used in the past defined all solution values at the Gauss-Lobatto quadrature points. Characteristic upwinding at subdomain interfaces was imposed by using upwind values of the derivatives (Ref. 4) or by correcting the solution values obtained by integrating the equations directly on either side of the interface (Ref. 5). The advantage of the former is that the high order temporal accuracy required for wave-propagation problems can be obtained, at the expense of flexibility in two space dimensions. The latter approach is more geometrically flexible, but is limited in temporal accuracy.

The new multidomain method uses a staggered grid and does not have the same limitations of the single grid methods. Solution unknowns are defined on a grid defined by the Gauss quadrature points. This grid interlaces the Gauss-Lobatto grid on which the fluxes are evaluated. Interface conditions require only flux continuity and can be evaluated to any temporal order of accuracy. The increased flexibility is balanced by the extra cost of a spectral interpolation from the Gauss to Gauss-Lobatto grids.

THE STAGGERED GRID APPROXIMATION

The staggered grid approximation computes the solution values and the advective fluxes on two different grids. Unlike the common approximation (Ref. 3), which uses only the nodes of the Chebyshev Gauss-Lobatto quadrature as collocation points, the new method uses both the Gauss and the Gauss-Lobatto points. We denote the Lobatto points by X_j and the Gauss points by $\overline{X}_{j+1/2}$, defined by

$$\begin{aligned} X_j &= \frac{1}{2}\left(1-\cos\left(\frac{j\pi}{N}\right)\right) \quad j=0,1,\ldots,N \\ \overline{X}_{j+1/2} &= \frac{1}{2}\left(1-\cos\left(\frac{2j+1}{2N+2}\pi\right)\right) \quad j=0,1,\ldots,N-1 \end{aligned} \tag{1}$$

In (1), we have mapped the usual collocation points defined on [-1,1] to the more convenient unit interval. The use of the overbar and half point notation for the Gauss points is used only for its value as an analogy to staggered grid finite difference methods. It must be understood that the Gauss points do not lie halfway between the Lobatto points (Ref. 3).

Two polynomial approximations are defined, one for each grid. Let the space of polynomials of degree less than or equal to N to be denoted $\mathsf{P}_N = \{\text{Polynomials of Degree } \le N\}$. Let $\ell_j(\xi) \in \mathsf{P}_N$ be the Lagrange interpolating polynomial

$$\ell_j(\xi) = \prod_{\substack{i=0 \\ i\neq j}}^{N}\left(\frac{\xi - X_j}{X_i - X_j}\right) \tag{2a}$$

defined on the Lobatto grid. On the Gauss grid, we define $h_{j+1/2} \in \mathsf{P}_{N-1}$ to be the polynomial

$$h_{j+1/2}(\xi) = \prod_{\substack{i=0 \\ i\neq j}}^{N-1}\left(\frac{\xi - \overline{X}_{i+1/2}}{\overline{X}_{j+1/2} - \overline{X}_{i+1/2}}\right) \tag{2b}$$

Finally, let Q_j be a grid point value on the Lobatto grid and $\overline{Q}_{j+1/2}$ be a value defined on the Gauss grid. Then we write the polynomials that interpolate these values as

$$Q(X) = \sum_{j=0}^{N} Q_j \ell_j(X) \tag{3a}$$

$$\overline{Q}(X) = \sum_{j=0}^{N-1} \overline{Q}_{j+1/2} h_{j+1/2}(X). \tag{3b}$$

The workshop problems called for uniform unit grid spacing. The spectral approximation, however, uses the non-uniform spacing defined by (1). To be consistent, the calculations were performed so that the *average* grid spacing was unitary. In this paper, all results are reported on the non-uniform grid. However, the spectral results reported in the overview by Tam in this volume are interpolated to a uniform grid using the representations (3).

We first consider the approximation of scalar problems of the form

$$\begin{cases} u_t + f_x(u) = 0 \quad \partial f / \partial u > 0, x \in [a,b], t > 0 \\ u(x,0) = u_0(x) \\ u(a,t) = g(t) \end{cases} \tag{4}$$

The interval [a,b] is subdivided into multiple, non-overlapping subdomains, $\Omega^k = [a_k, b_k]$, $k = 1,2,\ldots,K$, which are ordered left to right, as shown in Fig. 1. A simple linear transformation can be made to the unit interval, so that on each subdomain we solve the problem

$$u_t + \frac{1}{x_X} f_X(u) = 0 \quad X \in [0,1], t > 0 \tag{5}$$

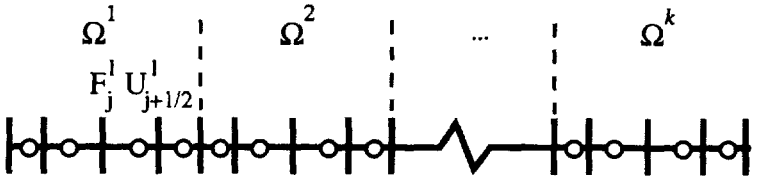

Figure. 1 Diagram of the domain decomposition in one space dimension.

On each subdomain is placed the staggered grid defined by (1). For convenience, we will assume that the same number of points is used in each subdomain, but this is not required by the method. We then let $\overline{U}^k(X) \in \mathsf{P}_{N-1}$, defined by (3a), approximate the exact solution, u on Ω^k. Similarly, the flux is approximated by the polynomial $F^k(X) \in \mathsf{P}_N$, defined by (3b). Substitution of these approximations into (5) gives

$$\overline{U}_t^k + \frac{1}{x_X}\frac{\partial F^k(X)}{\partial X} = R^k(X) \quad k = 1,2,\ldots,K \tag{6}$$

To obtain the equations that define the solution unknowns at the Gauss points, we require that the residual, R, be zero at the Gauss points of the subdomain. This leads to the collocation approximation

$$\frac{d\overline{U}_{j+1/2}^k}{dt} + \frac{1}{x_X}\frac{\partial F^k(\overline{X}_{j+1/2})}{\partial X} = 0 \quad j = 0,1,\ldots,N-1 \tag{7}$$

Eq. (7) can be used to update the grid point values of the approximate solution, $\overline{U}_{j+1/2}^k$, from which the interpolant $\overline{U}^k(X)$ is computed.

The spatial derivative operation in (7) can be evaluated as the multiplication of the vector of flux values that are defined at the Lobatto points, by a derivative matrix, **D**. From (3a), we see that

$$\frac{\partial F^k(\overline{X}_{j+1/2})}{\partial X} = \sum_{n=0}^{N} \ell_n'\left(\overline{X}_{j+1/2}\right)F_n = \sum_{n=0}^{N} d_{jn}F_n \tag{8}$$

Thus, we write

$$\left.\frac{\partial F^k}{\partial X}\right|_{j+1/2} = (\mathbf{DF})_{j+1/2} = \sum_{n=0}^{N} d_{jn}F_n^k \tag{9}$$

and the collocation approximation can be written in vector form as

$$\frac{d\overline{\mathbf{U}}^k}{dt} + \mathbf{DF}^k = 0 \quad k = 1,2,\ldots,N \tag{10}$$

where $\overline{\mathbf{U}}^k = \left[U_{1/2}^k\ U_{3/2}^k \ldots U_{N-1/2}^k\right]^T, \mathbf{F}^k = \left[F_0^k\ F_1^k \ldots F_N^k\right]^T$.

To compute the flux values, we first evaluate the interpolant $\overline{U}^k(X) \in \mathsf{P}_{N-1}$ at the Lobatto points. This can be computed by the multiplication of the vector of solution values in the Gauss grid times an interpolation matrix, **I**, i.e.,

$$\overline{U}(X_j) = \sum_{n=0}^{N-1} \overline{U}_{n+1/2}h_{n+1/2}(X_j) = \sum_{n=0}^{N-1} I_{j,n+1/2}\overline{U}_{n+1/2} \tag{11}$$

Since the characteristics of (4) run left to right, we expect that extrapolation to the left to be an unstable procedure. Instead, we use the boundary condition to define the $j = 0$ value on the furthest left subdomain. At subdomain interfaces, where two values $\overline{U}^{k-1}(1), \overline{U}^k(0)$ are available, we choose the value computed from the upwind, i.e., left, side of the interface. The result is an upwind evaluated approximation at both the left boundary and at the interfaces. The fluxes F_j, are then computed from these solution values.

Equation (10) is a system of ordinary differential equations that must be integrated in time to get the approximate solution values at the Gauss points. In principle, any common integration procedure can be used. We have chosen to use low storage Runge-Kutta methods that require only 2-N storage locations per subdomain. In particular, the third order 2-N storage method of Ref. 6 and a new fourth order method by Carpenter and Kennedy (private communication).

The method can be easily extended to systems of hyperbolic equations of the form

$$\begin{cases} \mathbf{Q}_t + \mathbf{F}_x(\mathbf{Q}) = 0 \quad x \in [a,b], t > 0 \\ \mathbf{Q}(x,0) = \mathbf{Q}_0(x) \end{cases} \tag{12}$$

where $\mathbf{Q}$ and $\mathbf{F}$ are m-vectors. The approximation of the system follows that of the scalar equation, except for the treatment of boundary and interface conditions.

At a subdomain interface between two subdomains k-1 and k, there are two values of the interpolated solution available, $\mathbf{Q}_N^{k-1}$ and $\mathbf{Q}_0^k$. The flux computed at the interface must use these two values in such a way that waves are allowed to propagate freely through the interfaces. For constant coefficient linear problems, we can write

$$\mathbf{F} = \mathbf{A}\mathbf{Q} = \mathbf{Z}\Lambda\mathbf{Z}^{-1}\mathbf{Q} = \mathbf{Z}\Lambda^{+}\mathbf{Z}^{-1}\mathbf{Q} + \mathbf{Z}\Lambda^{-}\mathbf{Z}^{-1}\mathbf{Q} \tag{13}$$

where $\Lambda^{\pm} = \Lambda \pm |\Lambda|$. The first term represents waves moving left to right, and the second waves moving right to left. To define an upwind approximation we choose $\mathbf{Q}_N^{k-1}$ for the right going components, and $\mathbf{Q}_0^k$ for the left going components. Thus, at each interface, we compute the flux

$$F_N^{k-1} = F_0^k = \mathcal{F}\left(\mathbf{Q}_N^{k-1}, \mathbf{Q}_0^k\right) \equiv \mathbf{Z}\Lambda^{+}\mathbf{Z}^{-1}\mathbf{Q}_N^{k-1} + \mathbf{Z}\Lambda^{-}\mathbf{Z}^{-1}\mathbf{Q}_0^k \tag{14}$$

Characteristic decompositions for the nonlinear case have been addressed extensively in the finite difference community (e.g. Ref. 7)

Boundaries can be considered to be interfaces between the computed solution and the solution assumed to exist outside the computational region. Thus, at boundary points, we can compute the flux by

$$F_0^1 = \mathcal{F}\left(\mathbf{Q}(a,t), \mathbf{Q}_0^1\right) \text{ and } F_N^K = \mathcal{F}\left(\mathbf{Q}_N^K, \mathbf{Q}(b,t)\right) \tag{15}$$

where $\mathbf{Q}$ represents the exterior solution at the boundary.

A solution of the Category 1a problem using the method described above is shown in Fig. 2. The calculation shown here was performed on the interval [-20,420]. That interval was subdivided into 22 subdomains of equal length on which 20 Lobatto points were used. The fourth order low storage Runge-Kutta method was used for the time integration. The match between the exact and computed solutions are evidence of the excellent phase and dissipation properties of the method for smooth solutions. In fact, the resolution required by the problem specification is greater than that required to get an acceptable answer. Fig. 3 shows a plot of the maximum error as a function of the number of points per subdomain. As expected, the error decays exponentially fast. The box marks the error of 10^{-4} obtained for the resolution requested in the problem.

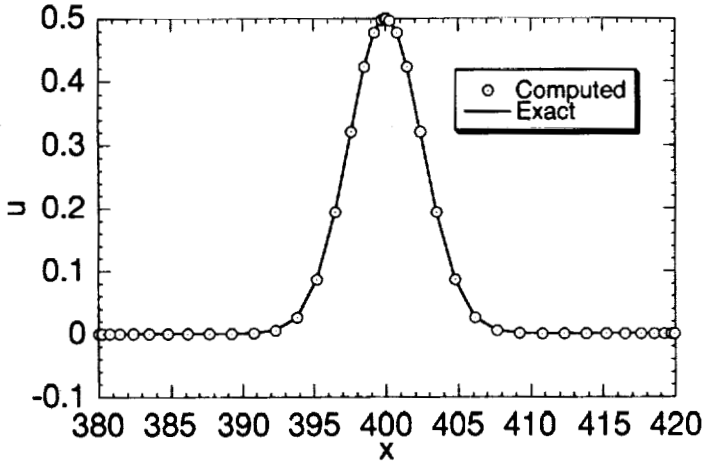

Fig. 2. Solution of Gaussian pulse at time t = 400.

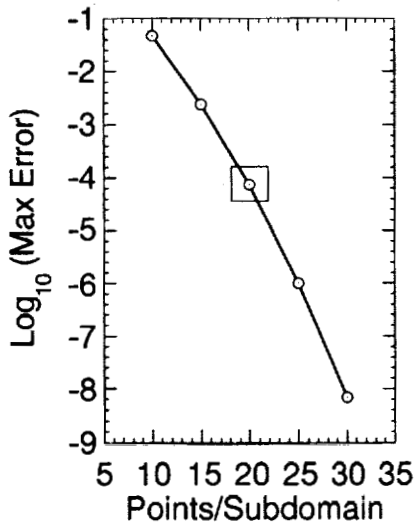

Fig. 3 Error as a function of resolution for the Gaussian pulse of Fig. 2.

The second problem of Category 1 computed a long sinusoidal wavetrain. Results for time t=300 at the requested resolution are shown in Figures 4 and 5. These calculations used Again, we see excellent agreement between the exact and computed solutions for both wave numbers, with no evidence to graphical precision of phase and dissipation errors. The errors we do see, however, are from the Gibbs' phenomenon that results from the discontinuity in the first derivative at the front of the wave. It is possible to filter the oscillations at the front, but we have not done it here.

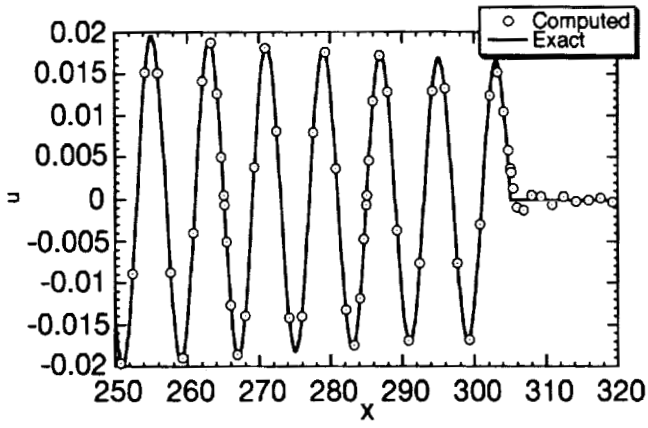

Figure 5. Solution of the spherical wave problem, $\omega = \pi/4$, t = 300.

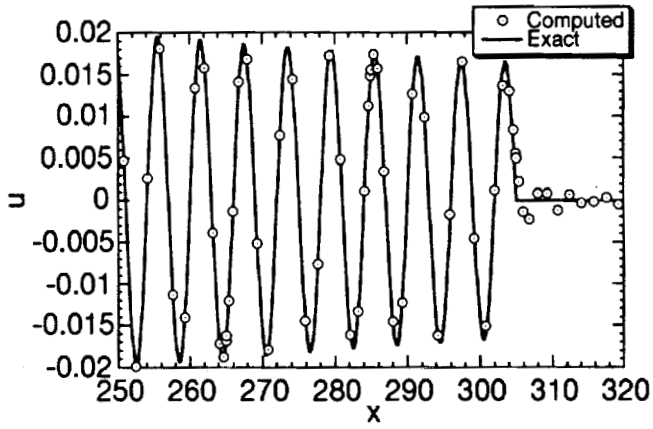

Figure 6. Solution of the spherical wave problem, $\omega = \pi/3$, t = 300.

SOLUTION OF THE CATEGORY 5 PROBLEM

The Category 5 problem is flow in a quasi-one-dimensional nozzle. We solved the equations in the standard conservation form, using the density, momentum and energy equations (Ref. 7). The calculation presented here was performed with 19 subdomains of equal size and 16 Lobatto points per subdomain, which is at lower resolution than that required by the problem. At the interfaces, Van Leer's (Ref. 8) flux vector splitting was used to upwind the approximation. The inflow boundary condition was specified by computing the incoming Riemann invariant from the boundary values, and computing the outgoing Riemann invariant from the interpolation of the solution. Those Riemann invariants, plus the entropy give enough equations to determine the flux at the boundary. The time integration was done by the third order Runge-Kutta.

Both steady and unsteady solutions were computed, and the difference between the two is shown in Fig. 6. Also plotted on Fig. 6 is the exact solution for the envelope of the acoustic wave. A comparison of the exit pressure and the exact linear wave solution is included in the overview by Tam.

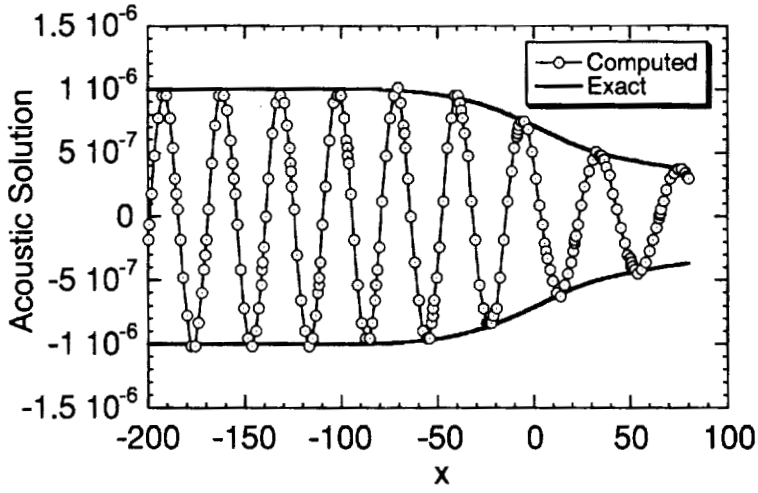

Figure 7. Acoustic wave pattern for the Cat. 5 problem with the envelope of the exact solution.

ACKNOWLEDGMENTS

The authors would like to thank Mr. Laurent Auriault for his computation of the envelope of the acoustic wave for the Category 5 problem.

REFERENCES

1. Gottlieb, D; and Orszag, S.A.: Numerical analysis of Spectral Methods: Theory and Applications. SIAM, 1977.

2. Kopriva, D.A.: Spectral Solution of Acoustic Wave-Propagation Problems. AIAA-90-3916, Oct. 1990.

3. Canuto, C.; Hussaini, M.Y.; Quarteroni A.; and Zang,T.A.: Spectral Methods in Fluid Mechanics, Springer-Verlag, 1987.

4. Kopriva, D. A.; and Hussaini, M.Y. : Multidomain Spectral Solution of Shock-Turbulence Interactions. In Domain Decomposition Methods (T.F. Chan, R. Glowinski, J. Periaux and O. B. Widlund, eds.) SIAM, 1989, pp. 340 - 350.

5. Kopriva, D.A. : Multidomain Spectral Solution of the Euler Gas-Dynamics Equations. *J. Comp. Phys.* vol. 96, no. 2., 1991, pp 428-450.

6. Williamson, J.H. : Low Storage Runge-Kutta Schemes . *J. Comp. Phys.* vol. 35, 1980, pp. 48-56.

7. Hirsch, C. : Numerical Computation of Internal and External Flows Vol II. John Wiley and Sons, 1990.

8. Van Leer, B. : Flux vector splitting for the Euler equations. ,In. Proc. 8th International Conference on Numerical Methods in Fluid Dynamics, Springer Verlag, 1982).

COMPUTATION OF WAVE PROPAGATION IN A COMPLEX FLOW

Philippe Lafon
Electricité de France - Direction des Etudes et Recherches
Département Acoustique et Mécanique Vibratoire
1, avenue du Général de Gaulle
92141 Clamart - France

SUMMARY

A numerical method has been developed in order to address aeroacoustic problems modeled by the linearized Euler equations. A weak formulation of the equations leads to a time-dependent equation for the test functions. The basic solver being one dimensional, two dimensional problems are handled by directional splitting. This method shows low dissipation and dispersion errors.

INTRODUCTION

Since 1952, Aeroacoustics has been dominated by Lighthill's Acoustic Analogy (ref. 1, 2). In this formulation, an inhomogeneous wave equation is derived from the exact equations of fluid motion. The wave operator accounts for the propagation of acoustic fluctuations in an external medium at rest. The flow effects are taken into account in the source term. The source term cannot be calculated without some assumptions and simplifications. If one choose a statistical approach, it is possible to model the sources of Lighthill's analogy from the knowledge of mean quantities given by codes using statistical models for Navier-Stokes equations (ref. 3, 4). If one wants to solve directly the Lighthill equation, instantaneous solutions of the Navier-Stokes equations are needed (ref. 5). These two approaches can be applied to turbulent jet noise. The problem is more complicated for confined flows. In this case, the flow might be complex, and the best way for tackling the problem of sound generation and propagation is to solve the Euler linearized equations (ref. 6). It is known that accurate algorithms are needed in order to minimize dissipation and dispersion errors.

We shall present in the next section the numerical method used. Results obtained for the proposed problems of category 1 and 4 are presented and discussed.

THE NUMERICAL PROCEDURE

Equations

The flow is assumed to be isentropic. A propagation operator for the acoustic waves can be derived from the linearization of Euler's equations about a mean steady flow:

$$\frac{\partial p}{\partial t} + \overline{U}_j \frac{\partial p}{\partial y_j} + \gamma \overline{P} \frac{\partial u_j}{\partial y_j} + \gamma p \frac{\partial \overline{U}_j}{\partial y_j} + u_j \frac{\partial \overline{P}}{\partial y_j} = 0$$

$$\frac{\partial u_i}{\partial t} + \overline{U}_j \frac{\partial u_i}{\partial y_j} + \frac{1}{\overline{\rho}} \frac{\partial p}{\partial y_i} + u_j \frac{\partial \overline{U}_i}{\partial y_j} - \frac{p}{\overline{\rho}^2 \overline{c}^2} \frac{\partial \overline{P}}{\partial y_i} = 0 \qquad (1)$$

Overbared quantities denote steady flow parameters. Two dimensional problems are handled by directional splitting.The set of equations (1) leads to the following one dimensional matrix equation:

$$\frac{\partial \vec{W}}{\partial t} + \vec{\vec{A}} \frac{\partial \vec{W}}{\partial x} + \vec{\vec{B}}\, \vec{W} + \vec{C} = 0 \quad \text{where} \quad \vec{W} = \begin{pmatrix} p \\ u \end{pmatrix} \tag{2}$$

The equations (1), (2) are hyperbolic and have to be solved on a segment [a,b] between the time steps t^n and t^{n+1}. Characteristics method is combined with a weak formulation of the equations (ref. 7). An adjoint problem, where the unknowns are the test functions, is obtained . The weak formulation reads:

$$\left\langle \frac{\partial \vec{W}}{\partial t} + \vec{\vec{A}} \frac{\partial \vec{W}}{\partial x} + \vec{\vec{B}}\, \vec{W} + \vec{C}\ ,\ \vec{\psi} \right\rangle = 0 \quad \text{where } \vec{\psi} \text{ is the test function and } \langle \vec{f}, \vec{g} \rangle = \int_a^b \int_{t^n}^{t^{n+1}} \vec{f}.\vec{g}\, dx\, dt \tag{3}$$

Discretization

The discretization of a scalar function is performed using linear finite elements and basic function $g_i(x)$:

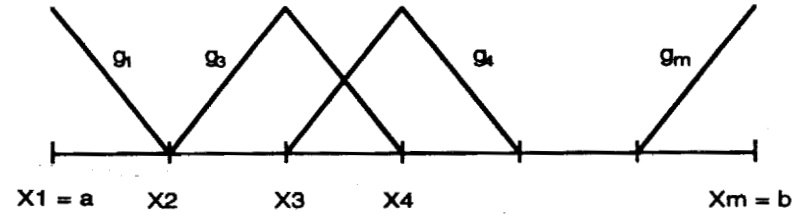

Discretized scalar and vector fields read:

$$p(x,t) = \sum_{i=1}^{m} p_i(t)\, g_i(x) \quad \text{and} \quad \vec{W}(x,t) = \sum_{i=1}^{2m} W_i(t)\, \vec{\varphi}_i(x) \quad \text{where} \begin{cases} \varphi_i = \begin{bmatrix} g_i \\ 0 \end{bmatrix} & \text{if } i \in [1,m] \\ \varphi_i = \begin{bmatrix} 0 \\ g_{i-m} \end{bmatrix} & \text{if } i \in [m+1,2m] \end{cases} \tag{4}$$

Application of the weak formulation

The weak formulation (3) applied to the discretized field gives:

$$\forall\, k \in [1,2m] \quad \int_a^b \int_{t^n}^{t^{n+1}} \left(\frac{\partial \vec{W}}{\partial t}\, \vec{\psi_k} + \vec{\vec{A}} \frac{\partial \vec{W}}{\partial x}\, \vec{\psi_k} + \vec{\vec{B}}\, \vec{W}\, \vec{\psi_k} + \vec{C}\, \vec{\psi_k} \right) dx\, dt = 0 \tag{6}$$

Neglecting boundary and source terms, an integration by parts with respect to time and space yields:

$$\forall\, k \in [1,2m] \quad \left| \int_a^b \vec{W}\, \vec{\Psi}_k\, dx \right|_{t^n}^{t^{n+1}} - \int_a^b \int_{t^n}^{t^{n+1}} \vec{W} \left[\frac{\partial \vec{\Psi}_k}{\partial t} + \frac{\partial \left[\vec{\vec{A}}^T \vec{\Psi}_k \right]}{\partial x} - \vec{\vec{B}}^T \vec{\Psi}_k \right] dx\, dt = 0 \tag{7}$$

The second term can be set to zero with an appropriate choice of the test functions.

Determination of test functions

It is assumed that test and basic functions coincide at time t^{n+1}. In order to determine the test functions at time t^n, the following problem has to be solved:

$$\frac{\partial \vec{\Psi}_k}{\partial t} + \frac{\partial \left[\overrightarrow{\overrightarrow{A^T}} \vec{\Psi}_k \right]}{\partial x} - \overrightarrow{\overrightarrow{B^T}} \vec{\Psi}_k = 0 \quad \text{for } t^n \le t \le t^{n+1} \text{ with } \vec{\Psi}_k^{n+1} = \vec{\varphi}_k \tag{8}$$

The resolution is performed using a lagrangian transport of the test functions along the characteristics curves. Finally, (7) gives:

$$\forall\, k \in [1,2m] \quad \sum_{i=1}^{2m} W_i(t^{n+1}) \int_a^b \varphi_i \varphi_k dx = \sum_{i=1}^{2m} W_i(t^n) \int_a^b \varphi_i \psi_k^n dx \tag{9}$$

The left hand side of (9) consists of a three diagonal linear system and the right hand side is known.

PROBLEMS OF CATEGORY 1

The aim of this category of problems is to test the dispersion and dissipation properties of a computation scheme.

Problem 1

The problem 1 consists in solving the following initial value problem:

$\frac{\partial u}{\partial t} + \frac{\partial u}{\partial x} = 0$ over the domain $-20 \le x \le 450$ with initial condition $t = 0$, $u = 0.5\, exp\left[- ln\, 2 \left(\frac{x}{3}\right)^2 \right]$

Figure 1 displays the time evolution of the gaussian pulse at t = 100, 200, 300, 400. The mesh size is 1 and the time step is 1. For this problem, the computation gives the exact solution.

Problem 2

The problem 2 consists in solving the spherical wave problem:

$\frac{\partial u}{\partial t} + \frac{u}{r} + \frac{\partial u}{\partial r} = 0$ over the domain $5 \le r \le 450$ with initial condition $t = 0$, $u = 0$.

The boundary condition at $r = 5$ is:

$$u = sin \omega t \quad \text{with } (a)\ \omega = \frac{\pi}{4},\ (b)\ \omega = \frac{\pi}{3}$$

Figures 2 and 3 show the theoritical (solid line) and the numerical (dashed line) solutions at $t = 200$ over the domain $100 \le r \le 150$ for the two frequency values. The mesh size is 1 and the time step is 1. No dispersion appears in the solutions. Some dissipation affects the solutions but it has a limited influence.

PROBLEMS OF CATEGORY 4

The aim of this category of problems is to test the effectiveness of wall boundary conditions.

Problem 1

The problem 1 deals with the reflection of an acoustic pulse off a wall in the presence of a uniform flow in semi-infinite space. One uses a computational domain $-100 \le x \le 100$, $0 \le y \le 200$ and the wall is at $y = 0$. The flow Mach number M_x is 0.5. The initial condition is:

$$t = 0, \quad u = v = 0 \quad p = \rho = exp\left\{-ln\,2\left[\frac{x^2 + (y - 25)^2}{25}\right]\right\}$$

Figures 4 and 5 display the pressure isolines at $t = 45$ and $t = 100$. The mesh size is 1 and the time step is 0.5. It appears that the numerical treatment of the wall boundary condition does not introduce any disturbances in the propagation process.

Problem 2

The problem 2 deals with the axisymmetric radiation of an oscillating circular piston in a wall. The wall and the piston are at $x=0$ and one uses a domain $0 \le x \le 100$, $0 \le r \le 100$. The radius of the piston is 10 and its velocity u is $10^{-4} sin\left(\frac{\pi t}{5}\right)$. The initial conditions are: $t=0$, $\rho = u = v = p = 0$.

Figure 6 shows the pressure isolines at half a period. The mesh size is 1 and the time step is 1. An axisymmetric boundary condition is applied on the axis $r = 0$. No oscillations are produced at the edge of the piston.

CONCLUSION

In this paper, an original computational method for the resolution of the linearized Euler equations is described. The applications carried out on the proposed problems show low dispersion and dissipation errors.

The aim of developing such numerical methods is to build computational codes in order to deal with the noise generation and propagation in complex flows. Additional work is necessary to obtain accurate time dependent informations about the turbulent sources.

REFERENCES

1. Lighthill, M. J.: On Sound Generated Aerodynamically: I. General Theory. *Proc. Roy. Soc. (A)* 211, pp. 564-587

2. Lighthill, M. J.: On Sound Generated Aerodynamically: I. Turbulence as a source of sound. *Proc. Roy. Soc. (A)* 222, pp. 1-32

3. Bailly, C.; Lafon, P.; Candel, S.: Computation of Subsonic and Supersonic Jet Mixing Noise Using a Modified k-ε Model for Compressible Free Shear Flows. *Acta Acustica*, vol. 2, no. 2, April 1994, pp. 101-112

4. Bailly, C.; Béchara, W. ; Lafon, P.; Candel, S.: Jet noise predictions using a k-ε turbulence model. *15th Aeroacoustics Conference*, AIAA-93-4412, Long Beach, 1993

5. Bastin, F.; Lafon, P.; Candel, S.: Analysis in (k,ω) space of plane jet noise computations. *Flow acoustics: a new technology audit*, Ecole Centrale de Lyon, July 1994

6. Béchara, W.; Bailly, C.; Lafon, P.; Candel, S.: Stochastic Approach to Noise Modelling for Free Turbulent Flows. *AIAA Journal*, vol. 32, no. 3, March 1994, pp. 455-463.

7. Esposito, P.: A New Numerical Method for Wave Propagation in a Complex Mean Flow. *5th International Conference on Numerical Methods in Laminar and Turbulent Flow*, Montréal, 1987

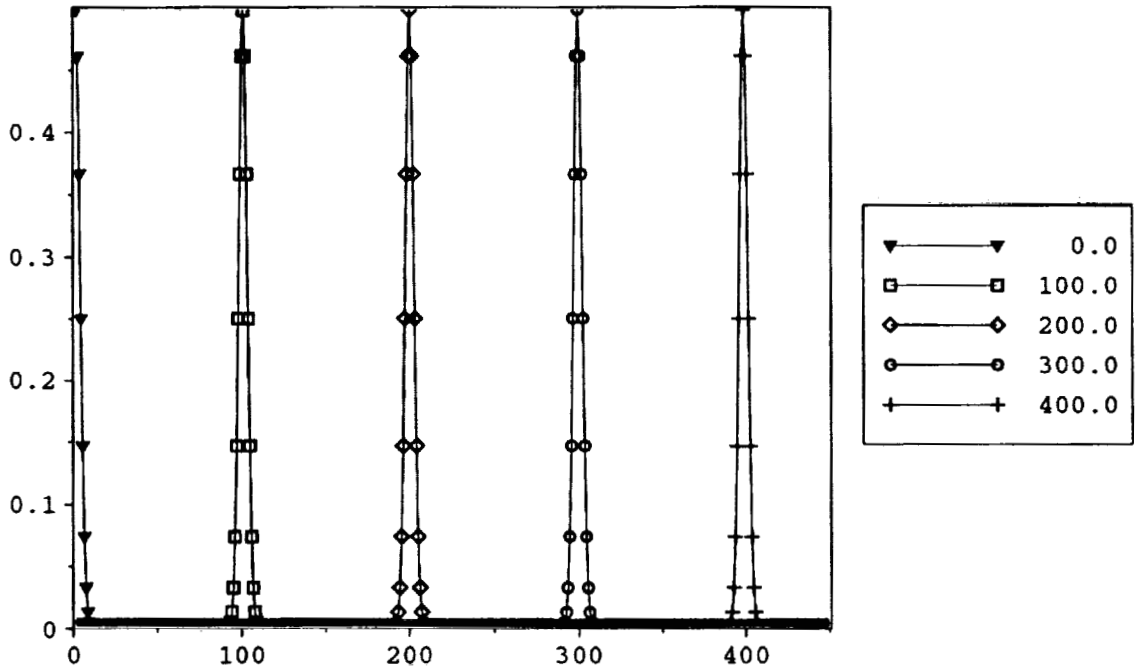

Figure 1. Problem 1 of category 1: time history of the convection of a gaussian pulse.

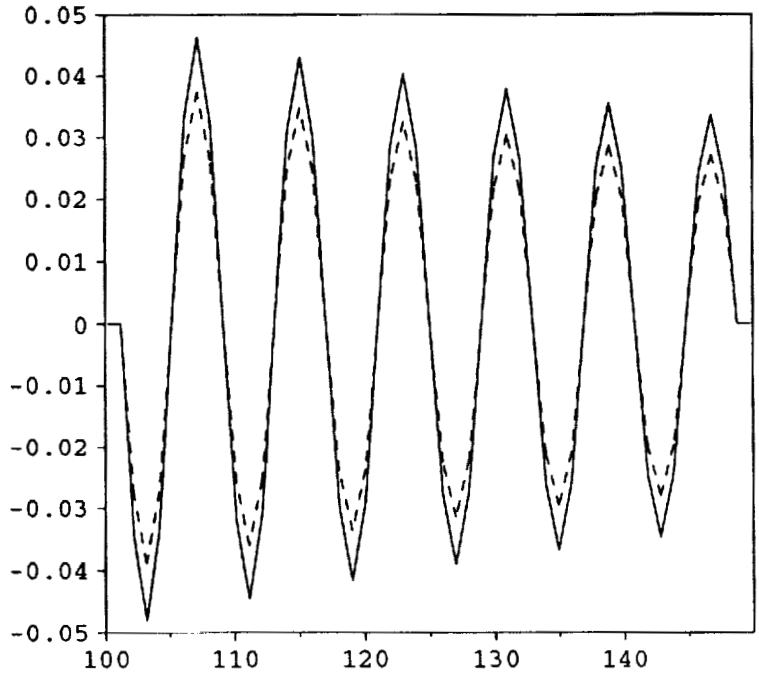

Figure 2. Problem 2 of category 1: solution at $t = 200$ for $\omega = \frac{\pi}{4}$.

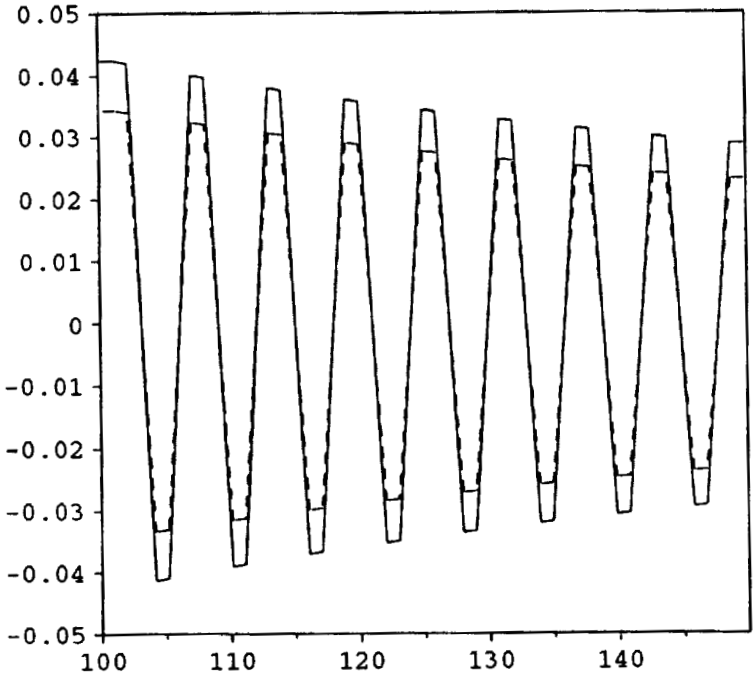

Figure 3. Problem 2 of category 1: solution at $t = 200$ for $\omega = \frac{\pi}{3}$.

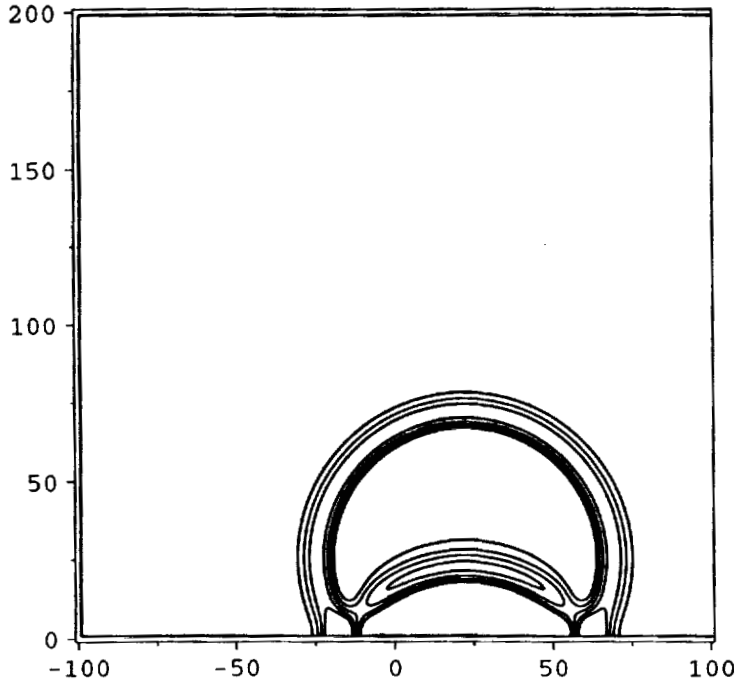

Figure 4. Problem 1 of category 4: pressure isolines at t = 45 .

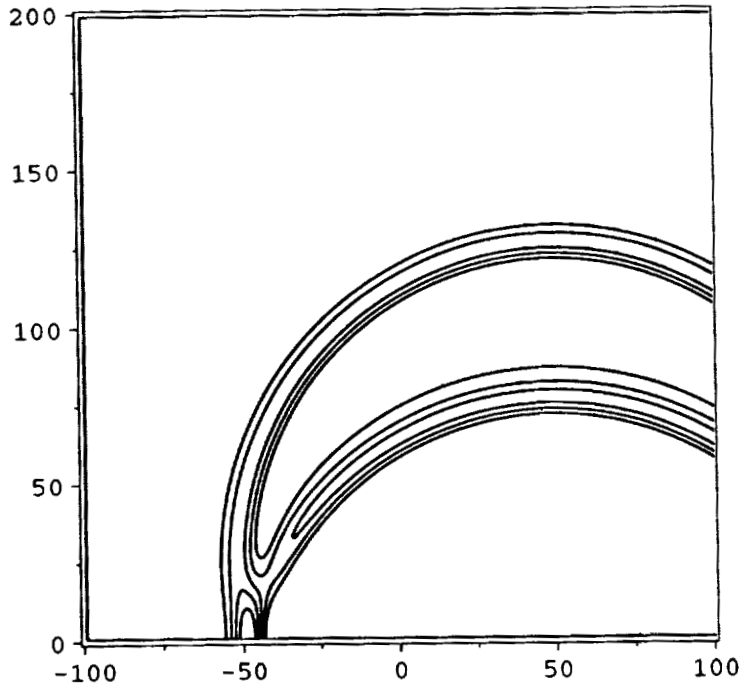

Figure 5. Problem 1 of category 4: pressure isolines at t = 100 .

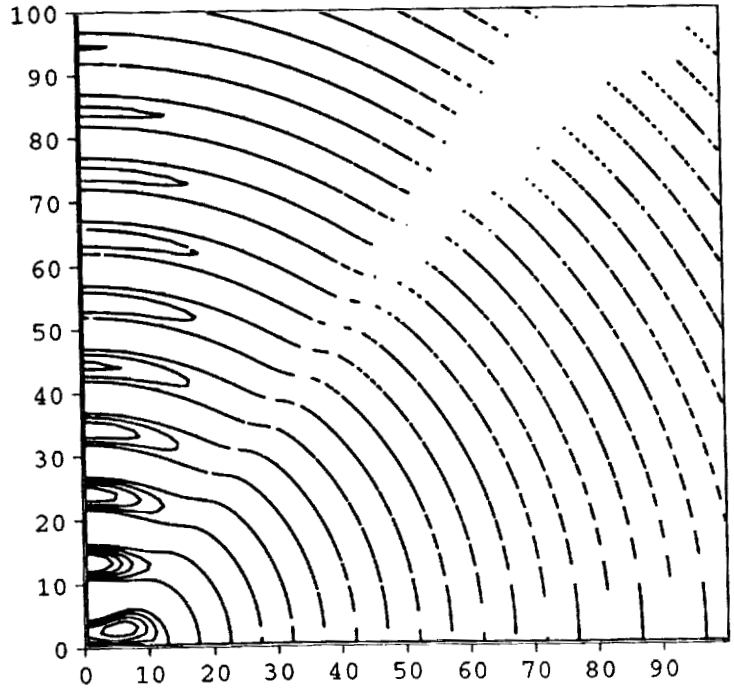

Figure 6. Problem 2 of category 4: pressure isolines at half a period .

SECOND-ORDER NUMERICAL SOLUTION OF TIME-DEPENDENT, FIRST-ORDER HYPERBOLIC EQUATIONS

Patricia L. Shah*
Boston University
Boston, MA

Jay Hardin
NASA Langley Research Center
Hampton, VA

SUMMARY

A finite difference scheme is developed to find an approximate solution of two similar hyperbolic equations, namely a first-order plane wave and spherical wave problem. Finite difference approximations are made for both the space and time derivatives. The result is a conditionally stable equation yielding an exact solution when the Courant number is set to one.

INTRODUCTION

Many different numerical schemes have been developed to solve problems such as those under consideration in this paper. These include the MacCormack finite difference scheme (the two-two scheme) which is second-order accurate in time and space, or the fourth-order extension of the MacCormick scheme by Gottlib and Turkel[1]. Other approaches are the Dispersion- Relation- Preserving (DRP) schemes of Tam[2] and Essentially Non- Oscillatory (ENO) schemes proposed by Shu and Osher[3]. All of these schemes have certain characteristics associated with them which influence the solutions. The characteristics of particular interest in this paper are dissipation and dispersion from the discretization process. Rather than test an existing scheme, such as the ones mentioned above, which have been developed for fluid problems, we have used the basic principles of finite differences to discretize the wave problems under consideration. The schemes developed here are interesting because although the time and space discretizations both exhibit dissipation and dispersion, when they are coupled by the partial differential equation, they yield an exact result. The reason for this is that the discretized equation has the same solution as the continuous equation if the Courant number is properly chosen. The existence of such schemes for simple wave equations suggests that it may be possible to develop similar schemes for more difficult equations.

*Work performed while residing at ICASE under NASA contract number NAS1-19480.

Plane Wave

We consider first an initial value problem for the equation

$$u_t + u_x = 0 \tag{1}$$

solved to the initial conditions

$$u(x,0) = f(x) = 0.5e^{\left[-ln2\left(\frac{x}{3}\right)^2\right]}. \tag{2}$$

The computational range in space is $-20 \leq x \leq 450$. The exact solution to this initial value problem is

$$u(x,t) = f(x-t) = 0.5e^{\left[-ln2\left(\frac{x-t}{3}\right)^2\right]}. \tag{3}$$

Numerical Algorithm

Finite differences were used to discretize the space and time derivatives in equation (1). Since $u(x,t)$ is a function of both x and t, the mesh size for each variable will have to be specified. A second-order time derivative is approximated by a Taylor expansion of u_i^{n+1} and u_i^{n-1}, where $u(i\Delta x, n\Delta t) \sim u_i^n$. Therefore,

$$u_t = \frac{u_i^{n+1} - u_i^{n-1}}{2\Delta t} + O(\Delta t^2). \tag{4}$$

A similar Taylor expansion for the spatial derivative allows equation (1) to be discretized and solved for u_i^{n+1}, namely;

$$u_i^{n+1} = u_i^{n-1} - \sigma[u_{i+1}^n - u_{i-1}^n]. \tag{5}$$

Since $u(x,t)$ is a function of both x and t, the mesh size for each variable will have to be specified. This is accomplished by the Courant number, σ, which is a ratio of the mesh sizes. For this problem,

$$\sigma = \frac{\Delta t}{\Delta x}. \tag{6}$$

Initial Conditions

Inspection of equation (5) suggests that it is second-order in time differences and therefore requires two initial conditions. The second initial condition is found by using equation (1),

$$u_t(x,0) = -u_x(x,0) = -f'(x). \tag{7}$$

Moreover,

$$u_{tt}(x,0) = -u_{xt}(x,0) = u_{xx}(x,0) = f''(x). \tag{8}$$

Therefore a Taylor expansion of $u_i^{\Delta t}$ using the above expressions yields the second condition,

$$u_i^{\Delta t} = f(x - \Delta t). \tag{9}$$

Boundary Conditions

Recall the grid spans $-20 \leq x \leq 450$. To implement the algorithm, the solution at $x = -21$ and $x = 451$ is required. The downstream boundary condition (the boundary at the right edge of the spacial domain) is determined by substituting into equation (1) a time derivative approximated by a Taylor expansion backward in time and a spacial derivative expanded forward in space. This yields the boundary condition

$$u^n_{450} = u^{n-1}_{449}. \tag{10}$$

However at the upstream boundary, the solution must be specified as it enters the domain. By the initial condition of the problem, there is a wave entering our domain at the left boundary, given by

$$u^n_{-20} = f(-20 - n). \tag{11}$$

Stability

The Courant number, σ, plays a crucial role in the stability of any algorithm developed; it is important to know what are the admissible values of σ for which the solution is stable. This was accomplished by separating the time from the spacial components in equation (5), following the method described by Strauss[4]. The result is that although the scheme is stable for $\sigma \leq 1$, for an exact result the time mesh grid needs to lie on the characteristics, which in this problem, are along $x = t$. Therefore, $\Delta x = \Delta t$, and $\sigma = 1$. Since we were told in the problem statement that $\Delta x = 1$, we must take $\Delta t = 1$. Note that this condition holds true for the spherical wave problem as well.

Results and Discussion

The numerical results from the plane wave problem are compared with the exact solution in Figure 1 for $\sigma = 1$. The results show that an exact solution was obtained using this algorithm. Moreover, an approximation for this problem was also obtained for $\sigma = 0.5$. Figure 2 shows the solution at a $t = 100$, which clearly shows deviations from the exact solution, which is a Gaussian pulse passing through the computational domain with time. This result illustrates the fact that, although such algorithms are exact when the proper Courant number is utilized, they rapidly deteriorate for other values of the Courant number.

Spherical Wave

The second problem concerns the spherical wave equation

$$u_t + \left(\frac{u}{r}\right) + u_r = 0 \tag{12}$$

solved to the conditions

$$u(r, 0) = 0 \tag{13}$$

and

$$u(5, t) = sin\omega t \tag{14}$$

over the range $5 \leq x \leq 450$, and for $\omega = \frac{\pi}{4}$ and $\omega = \frac{\pi}{3}$. It is easy to prove that the exact solution to this problem is

$$u(r, t) = \frac{5}{r} sin[\omega(t - (r - 5))]U[t - (r - 5)] \tag{15}$$

where U is the Heaviside Function.

Numerical Algorithm

The space and time derivatives are approximated by second-order finite differences, as in the one-dimensional problem. The term $\frac{u}{r}$ is approximated by the radial average of $u(r,t)$, namely

$$\frac{u_i^n}{r} = \frac{u_{i+1}^n + u_{i-1}^n}{2r}. \tag{16}$$

The discretized formula is therefore

$$u_i^{n+1} = u_i^{n-1} - \sigma\left[\frac{(i+1)u_{i+1}^n}{i}\right] + \sigma\left[\frac{(i-1)u_{i-1}^n}{i}\right] \tag{17}$$

where the Courant number, σ, is again defined to be

$$\sigma = \frac{\Delta t}{\Delta r}. \tag{18}$$

Initial Conditions

The initial condition given in equation (13) gives rise to the other required initial condition for implementation of the algorithm. By means of the procedure used in the plane wave problem, it can be shown that

$$u_i^{\Delta t} = 0. \tag{19}$$

Boundary Conditions

The numerical algorithm of equation (17) requires that the entrance and exit conditions on the spacial grid be defined. While one boundary condition $u(5,t)$ is specified, an exit condition is also required. Following the procedure used in the plane wave problem, it can be shown that

$$u_{450}^{n+1} = u_{449}^n. \tag{20}$$

Results and Discussion

The numerical results for $\omega = \frac{\pi}{4}$ are plotted next to the exact solution in Figure 3 for the spherical wave problem. A comparison of the data shows that an exact solution was obtained for $\sigma = 1$. Figure 4 shows the numerical and exact results for $\omega = \frac{\pi}{5}$ for $\sigma = 1$; again, exact results are obtained.

Conclusions

Numerical solutions that are formally exact have been obtained for two first-order hyperbolic problems. The finite difference discretization of both time and space provides a simple means of obtaining the solutions; the only

requirement is the specification of the solution as it enters and exits the domain. The algorithms are exact for a Courant number of 1, but deteriorate for the Courant number less than one.

Appendix

1. Tam, C.K.W.; and Webb, J.C.: Dispersion- Relation- Preserving Finite Difference Schemes for Computational Acoustics. *Journal of Computational Physics*, vol. 107, 1993, pp. 262-281.

2. Gottlieb, D.; and Turkel, E.: Dissipative Two-Four Methods for Time Dependent Problems. *Math. Comp.*, vol. 30, 1976, pp. 703-723.

3. Shu, C.; and Osher, S.: Efficient Implementation of Essentially Non- Oscillatory Shock Capturing Schemes. *Journal of Computational Physics.*, vol. 77, 1988, pp. 439-471.

4. Strauss, W.A.; *Partial Differential Equations.* John Wiley Sons, Inc., 1992.

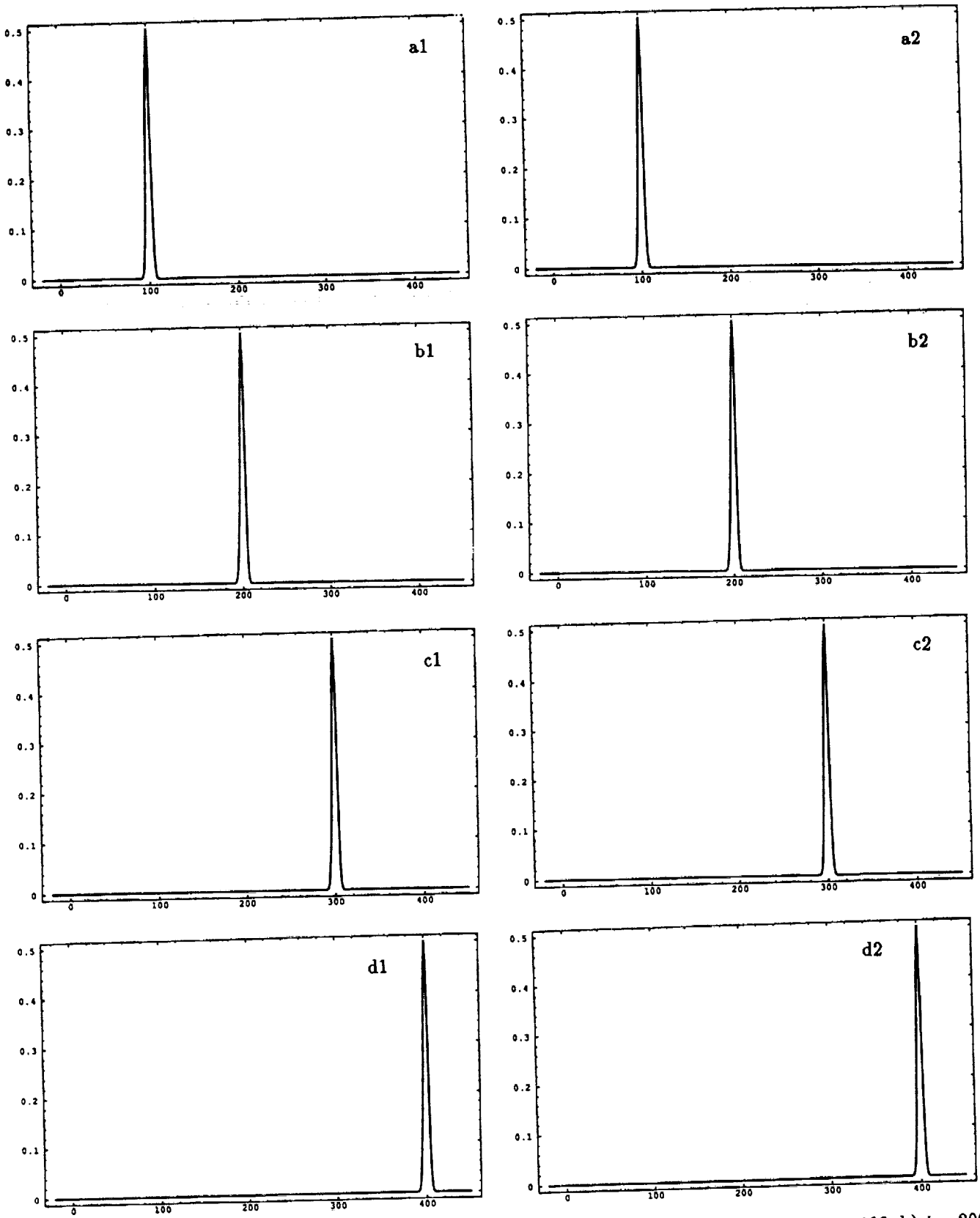

Figure 1. Comparison of numerical solution (1) and exact solution (2) of $u(x,t)$ verses x at a) $t = 100$, b) $t = 200$, c) $t = 300$, d) $t = 400$.

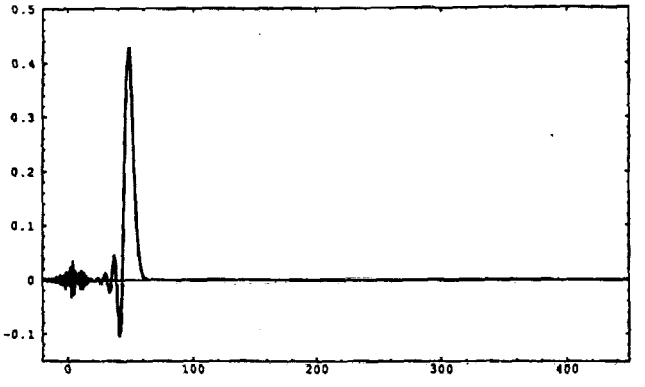

Figure 2. Numerical solution of $u(x, 100)$ verses x.

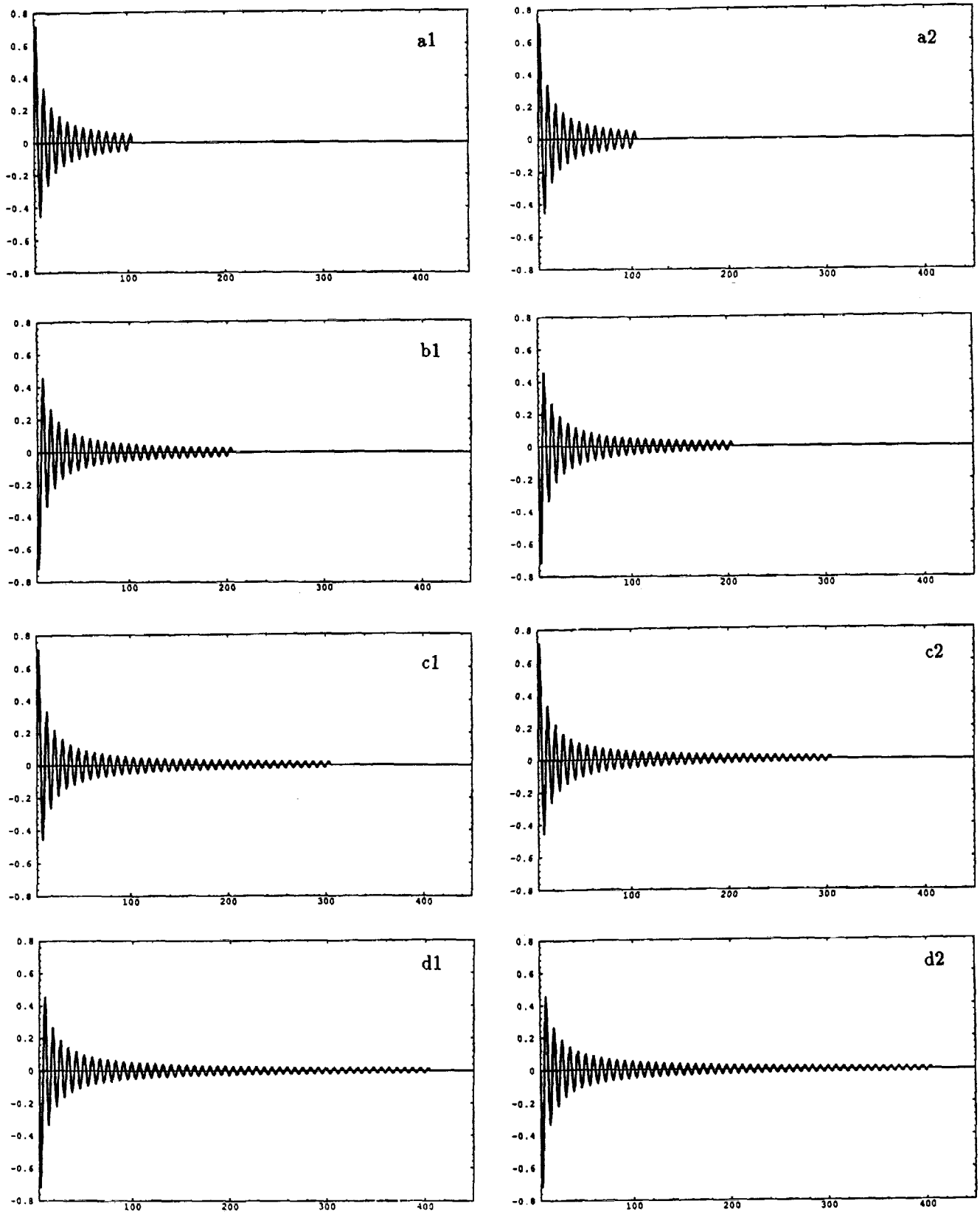

Figure 3. Comparison of numerical solution (1) and exact solution (2) of $u(r,t)$ verses r for $\omega = \frac{\pi}{4}$ at a) $t = 100$, b) $t = 200$, c) $t = 300$, d) $t = 400$.

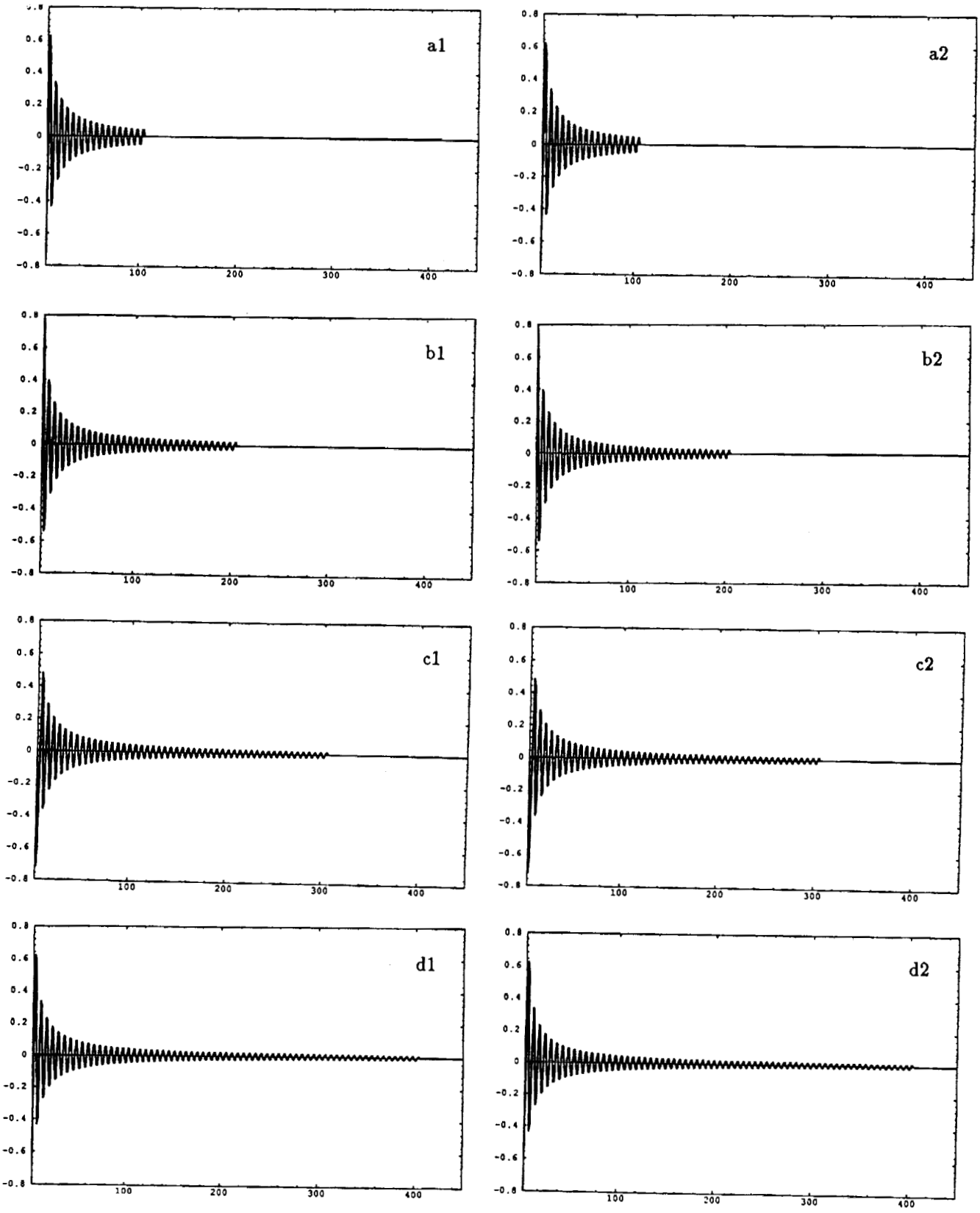

Figure 4. Comparison of numerical solution (1) and exact solution (2) of $u(r, r)$ verses r for $\omega = \frac{\pi}{3}$ at a) $t = 100$, b) $t = 200$, c) $t = 300$, d) $t = 400$.

LATTICE GAS METHODS FOR COMPUTATIONAL AEROACOUSTICS

Victor W. Sparrow
Graduate Program in Acoustics
The Pennsylvania State University, University Park, PA 16802

SUMMARY

This paper presents the lattice gas solution to the category 1 problems of the ICASE/LaRC Workshop on Benchmark Problems in Computational Aeroacoustics, held 24–26 October 1994. The first and second problems were solved for $\Delta t = \Delta x = 1$, and additionally the second problem was solved for $\Delta t = 1/4$ and $\Delta x = 1/2$. The results are striking: even for these large time and space grids **the lattice gas numerical solutions are almost indistinguishable from the analytical solutions.** A simple bug in the *Mathematica* code was found in the solutions submitted for comparison, and the comparison plots shown at the end of this volume show the bug. An Appendix to the present paper shows an example lattice gas solution with and without the bug.

INTRODUCTION

Lattice gas methods are new simulation methods which have great potential in computational aeroacoustics, CAA. Lattice gas methods are tailor-made for massively parallel processing computers since only nearest neighbor communication is needed between grid points. This is in contrast to high order finite difference schemes whose stencils require communication between grid points separated by several spatial steps.

Unlike finite difference methods, lattice gas methods exhibit zero anomalous dispersion and dissipation both for one-dimensional problems [1] and along all coordinate axes for multidimensional problems [2]. It is well known that one can attain such excellent agreement for the plane wave propagation problem (problem 1 of category 1) by using certain finite difference methods with $\Delta t = \Delta x = 1$. The lattice gas solutions generated for this Workshop, however, also show excellent agreement with the analytical solutions for the spherical wave problem for all source frequencies (problem 2 of category 1).

This paper will first give a nutshell explanation of the underlying principles behind the lattice gas method, and then it will demonstrate the excellent results. All of the work was done using the symbolic manipulation program *Mathematica* [3]. A small bug was found in the results submitted for comparison for this Workshop. This bug is pointed out in an Appendix. Although beyond the scope of this paper, it is worth mentioning that the lattice gas method already has been extended, separately, to problems with dissipation, nonlinearity, and mean flow [4].

METHOD

Overview

The lattice gas method is fundamentally different from finite differences in that a cellular

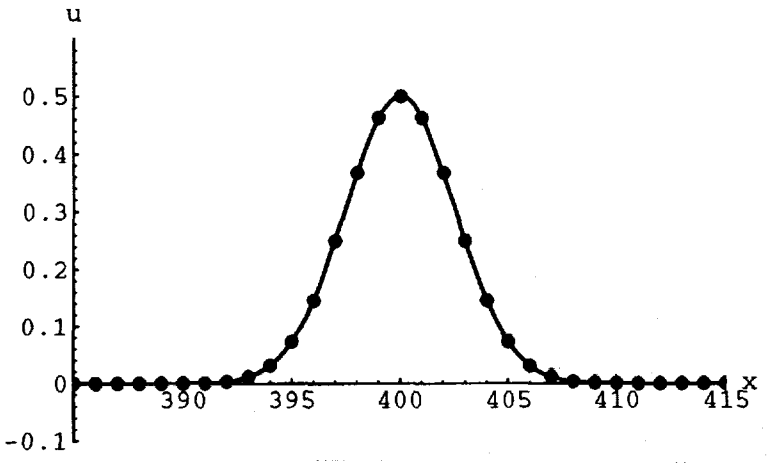

Figure 1. Comparison between lattice gas simulation and analytical result for problem 1 at $t = 400$.

automaton approach is taken. To represent acoustic waves, one uses finite amounts (or numbers) of particles moving under specific rules in a discrete spatial lattice.

As is described elsewhere [1], the most important *caveat* in the lattice gas method for CAA is that the CFL number, $c\,\Delta t/\Delta x$, must be a ratio of integers. Throughout this paper the speed of sound c will equal unity. Then the CFL number for a simulation with $\Delta t = 1/4$ and $\Delta x = 1/2$ will be taken as the ratio of integers

$$\frac{\Delta t = 1/4}{\Delta x = 1/2} = \frac{1}{2} \quad . \tag{1}$$

Here the denominator, equal to 2 in this example, gives the number of temporary values, called *states*, needed at every spatial position in the spatial lattice. The numerator, equal to 1, gives the number of states which are associated with propagation. The remaining states are associated with resting. Carefully defining which states propagate or rest ensures that information always is accounted for, and no data falls "in between" nodal positions.

Algorithms for the Benchmark Problems

For problem one of category one, solving the the plane wave advection equation, $\partial u/\partial t + \partial u/\partial x = 0$, the following lattice gas algorithm was used:

$$u_j(x, t+1) = \delta_{\nu_{j\ominus 1},1}\, u_{j\ominus 1}(x-1, t) + \delta_{\nu_{j\ominus 1},0}\, u_{j\ominus 1}(x, t) \tag{2}$$

where δ is the Kronecker delta, $\nu_j = 1$ if a state is a propagation state, 0 otherwise, and where $\ominus$ is a circular shift operator. One finds the total field at each spatial position by summing over the states:

$$u(x, t) = \sum_j u_j(x, t) \quad . \tag{3}$$

For problem 2 the spherical advection equation, $\partial u/\partial t + u/r + \partial u/\partial r = 0$, is solved using the lattice gas algorithm

$$u_j(r, t+1) = \delta_{\nu_{j\ominus 1},1}\, u_{j\ominus 1}(r-1, t) \left(\frac{(r-1)}{r}\right) + \delta_{\nu_{j\ominus 1},0}\, u_{j\ominus 1}(r, t) \quad . \tag{4}$$

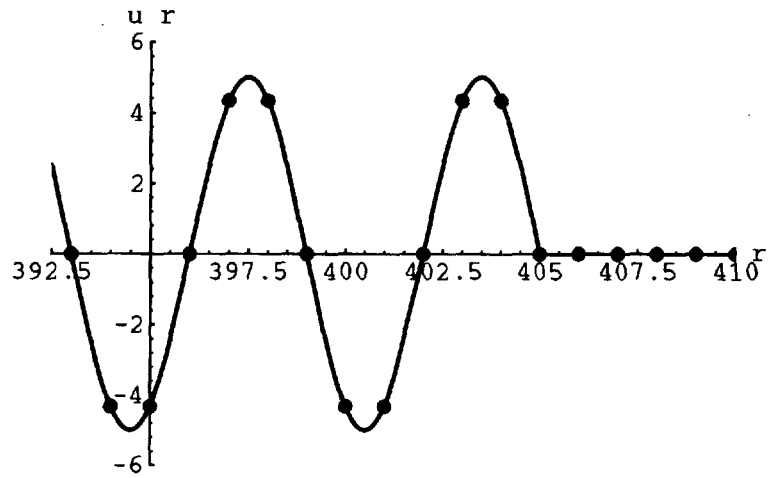

Figure 2. Comparison between lattice gas and analytical for problem 2, 6 points/λ, at $t = 400$.

The only change from Eq. (2) is the factor of $(r-1)/r$ that represents the decrease in the amplitude of u over a single spatial step.

CATEGORY ONE RESULTS

Problem One

For brevity, only selected results for each simulation run will be shown. Using a CFL $= 1.0$, $\Delta t = 1.0$, and $\Delta x = 1.0$, a blow up of the interesting part of the field at the final time of $t = 400$ is shown in Fig. 1. Here $\{\nu_j\} = \{1\}$ was used. The lattice gas result, given by the round dots, is indistinguishable from the analytical result, given as a continuous line. Other CFL give similarly spectacular results.

Problem Two

Here only the 6 point/λ results will be shown, as the 8 point/λ results were all similar. For the 6 point/λ cases, excellent results were obtained for any CFL being the ratio of integers. Figure 2 shows a result for CFL $= 1.0$ with $\Delta t = 1.0$ and $\Delta x = 1.0$ at the final time of $t = 400$. Again $\{\nu_j\} = \{1\}$ was employed. The plot is scaled by multiplying the data by r. This blow up of the leading portion of the spherical wavefront shows that the "kink" is propagated with zero dispersion. Figure 3 further shows a 12 point/λ case at the midpoint of the run, $t = 200$, for a CFL $= 0.5$ using $\Delta t = 0.25$ and $\Delta x = 0.5$. Here $\{\nu_j\} = \{1, 0\}$ was used.

CONCLUSIONS

The lattice gas simulation results in this paper show that zero anomalous dispersion and dissipation can be achieved for any CFL that is the ratio of integers. Certainly the lattice gas method should be explored further for direct application to CAA.

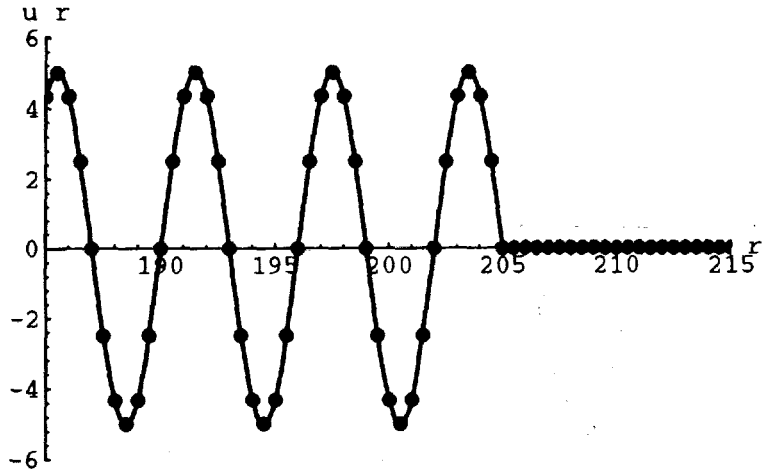

Figure 3. Comparison between lattice gas and analytical for a 12 point/λ case at $t = 200$.

ACKNOWLEDGMENTS

The author would like to thank Y. Sudo for many conversations related to this work, as well as Drs. J. Hardin and K. Brentner of NASA Langley Research Center.

REFERENCES

[1] Sudo, Y. and Sparrow, V.: A new lattice gas model for 1-D sound propagation. *J. Comp. Acoust.* vol. 1, no. 4, December 1993, pp. 423-454.

[2] Sudo, Y. and Sparrow, V.: Sound propagation simulations using lattice gas methods. AIAA-93-4404, Oct. 1993.

[3] Wolfram Research, Inc.: Mathematica, version 2.1. Wolfram Research, Champaign, IL, 1994.

[4] Sudo, Y.: Lattice gas models for sound propagation simulation. Ph.D. thesis. The Pennsylvania State University, May 1994.

APPENDIX

The lattice gas solutions submitted for this Workshop were produced with a *Mathematica* program which contained a simple bug. This bug is reflected in the plots shown at the end of this volume. The Workshop problem 2 solutions were to be printed at times $t = 0$, 100, 200, 300, and 400. The bug caused the wave source to reset to time $t = 0$ at each time the solution was printed. Figure 4 shows the results of the 8 point/λ run at the final time of $t = 400$, with the bug included. Figure 5 shows the result with the bug removed. It is interesting to note that the "kinks" created by the bug in Figure 4 are propagated with no dissipation or dispersion.

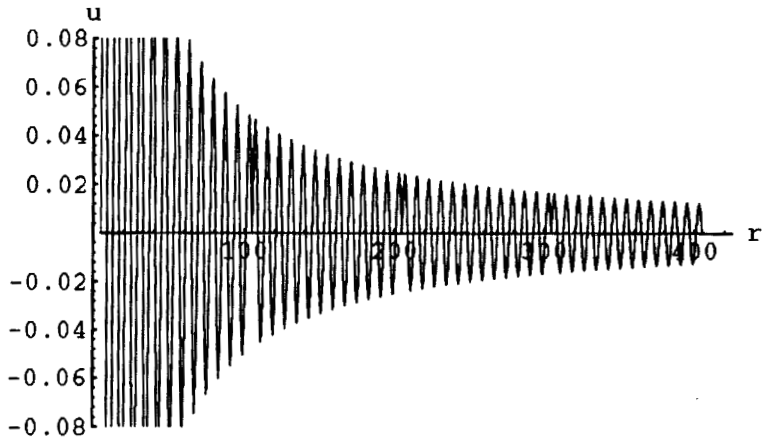

Figure 4. Lattice gas solution (WITH BUG) for problem 2, 8 points/λ, at $t = 400$.

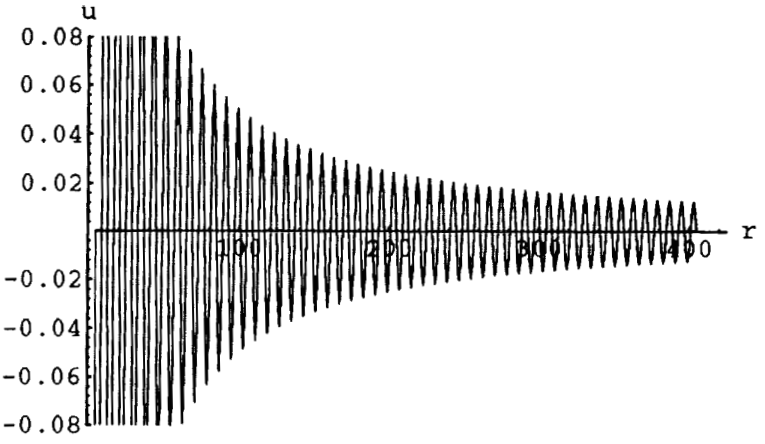

Figure 5. Lattice gas solution (WITHOUT BUG) for problem 2, 8 points/λ, at $t = 400$.

SOLUTIONS OF THE BENCHMARK PROBLEMS BY THE DISPERSION-RELATION-PRESERVING SCHEME

C.K.W. Tam, H. Shen, K.A. Kurbatskii,
L. Auriault, Z. Dong, and J.C. Webb
Department of Mathematics
Florida State University
Tallahassee, FL 32306-3027

SUMMARY

The 7-point stencil Dispersion-Relation-Preserving scheme of Tam and Webb is used to solve all the six categories of the CAA benchmark problems. The purpose is to show that the scheme is capable of solving linear, as well as nonlinear aeroacoustics problems accurately. Nonlinearities, inevitably, lead to the generation of spurious short wave length numerical waves. Often, these spurious waves would overwhelm the entire numerical solution. In this work, the spurious waves are removed by the addition of artificial selective damping terms to the discretized equations. Category 3 problems are for testing radiation and outflow boundary conditions. In solving these problems, the radiation and outflow boundary conditions of Tam and Webb are used. These conditions are derived from the asymptotic solutions of the linearized Euler equations. Category 4 problems involved solid walls. Here, the wall boundary conditions for high-order schemes of Tam and Dong are employed. These conditions require the use of one ghost value per boundary point per physical boundary condition. In the second problem of this category, the governing equations, when written in cylindrical coordinates, are singular along the axis of the radial coordinate. The proper boundary conditions at the axis are derived by applying the limiting process of $r \to 0$ to the governing equations. The Category 5 problem deals with the numerical noise issue. In the present approach, the time-independent mean flow solution is computed first. Once the residual drops to the machine noise level, the incident sound wave is turned on gradually. The solution is marched in time until a time-periodic state is reached. No exact solution is known for the Category 6 problem. Because of this, the problem is formulated in two totally different ways, first as a scattering problem then as a direct simulation problem. There is good agreement between the two numerical solutions. This offers confidence in the computed results. Both formulations are solved as initial value problems. As such, no Kutta condition is required at the trailing edge of the airfoil.

1. INTRODUCTION

All the six categories of benchmark problems are solved by using the 7-point stencil

Dispersion-Relation-Preserving (DRP) scheme (ref. 1).

In wave propagation theory, it is known that the propagation characteristics of the waves, governed by a linear system of partial differential equations, are completely determined by the dispersion relations. Thus, to ensure that the characteristics of the waves of a system of finite difference equations are (nearly) identical to those of the partial differential equations, it is sufficient that both systems have (nearly) identical dispersion relations. The first step in constructing such dispersion-relation-preserving finite difference algorithms is to determine what is the wave number and angular frequency of a finite difference scheme. In ref. 1, Tam and Webb demonstrated how this can be done using Fourier-Laplace transforms.

1.1. Wave Number of a Finite Difference Scheme

Suppose a 7-point central difference is used to approximate the first derivative $\frac{\partial f}{\partial x}$ at the ℓ^{th} node of a grid with spacing Δx; i.e.

$$\left(\frac{\partial f}{\partial x}\right)_\ell \simeq \frac{1}{\Delta x}\sum_{j=-3}^{3} a_j f_{\ell+j}. \tag{1}$$

Equation (1) is a special case of the following finite difference equation with x as a continuous variable,

$$\frac{\partial f}{\partial x}(x) \simeq \frac{1}{\Delta x}\sum_{j=-3}^{3} a_j f(x+j\Delta x). \tag{2}$$

The Fourier transform of (2) is,

$$i\alpha\,\tilde{f} \simeq \left(\frac{1}{\Delta x}\sum_{j=-3}^{3} a_j e^{ij\alpha\Delta x}\right)\tilde{f} \tag{3}$$

where $\tilde{}$ denotes the Fourier transform and α is the Fourier wave number. By comparing the two sides of (3), it is evident that the quantity,

$$\overline{\alpha} = \frac{-i}{\Delta x}\sum_{j=-3}^{3} a_j e^{ij\alpha\Delta x} \tag{4}$$

is effectively the wave number of the finite difference scheme (2) or (1). Tam and Webb (ref. 1) suggested to choose coefficients a_j so that (1) is accurate to order $(\Delta x)^4$ when expanded in Taylor series. The remaining unknown coefficient is chosen so that $\overline{\alpha}$ is a close approximation of α over a wide band of wave numbers. This can be done by minimizing the integrated error

$$E = \int_{-\eta}^{\eta} |\overline{\alpha}\Delta x - \alpha\Delta x|^2 d(\alpha\Delta x). \tag{5}$$

Tam and Shen (ref. 2) recommended to set $\eta = 1.1$. The numerical values of a_j determined this way are (see also ref. 3)

$$a_0 = 0 \quad a_1 = -a_{-1} = 0.770882380518$$
$$a_2 = -a_{-2} = -0.166705904415$$
$$a_3 = -a_{-3} = 0.208431427703$$

Figure 1 shows the relation $\overline{\alpha}\,\Delta x$ versus $\alpha\Delta x$. Over the range of $\alpha\Delta x$ up to 1.0 the curve is nearly the same as the straight line $\overline{\alpha} = \alpha$. This is the range of wave number in which the finite difference scheme will behave almost identically to the original partial differential equation.

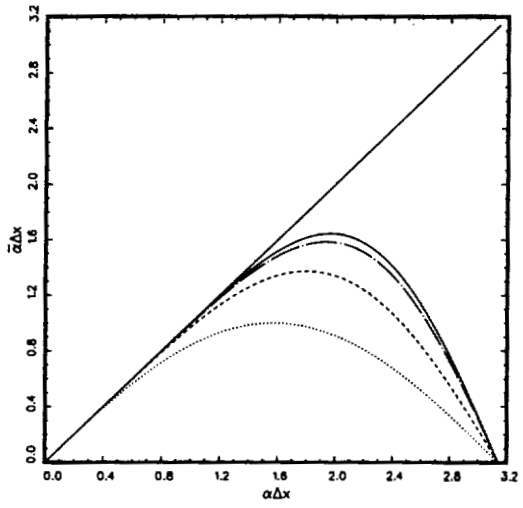

Figure 1. $\overline{\alpha}\Delta x$ versus $\alpha\Delta x$ relation for the standard central difference second order, ·····; fourth order, - - - -; sixth order, —·—; and the DRP scheme, ——.

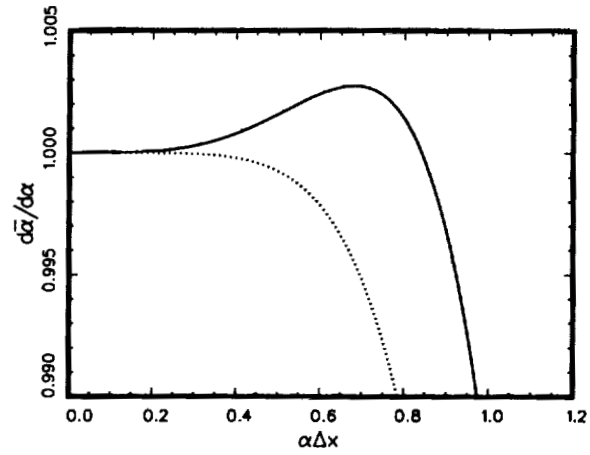

Figure 2. $d\overline{\alpha}/d\alpha$ versus $\alpha\Delta x$ for the DRP scheme, ——; and the sixth order standard central difference scheme, ·····.

1.2. Angular Frequency of a Finite Difference Scheme

For time discretization, ref. 1 proposed to use the following four levels marching scheme,

$$f^{(n+1)} - f^{(n)} = \Delta t \sum_{j=0}^{3} b_j \left(\frac{df}{dt}\right)^{(n-j)} \tag{6}$$

where the superscript indicates the time level. The Laplace transform of (6) with zero initial condition (for nonzero initial condition, see ref. 1) yields

$$-i\frac{i(e^{-i\omega\Delta t} - 1)}{\Delta t \sum_{j=0}^{3} b_j e^{ij\omega\Delta t}}\,\widetilde{f} = \frac{\widetilde{df}}{dt} \tag{7}$$

where $\widetilde{\ }$ represents Laplace transform and ω is the angular frequency (transform variable). The Laplace transform of the time derivative, i.e., the right side of (7), is equal to $-i\omega\,\widetilde{f}$. On compar-

ing the two sides of (7), the quantity

$$\overline{\omega} = \frac{i(e^{-i\omega\Delta t} - 1)}{\Delta t \sum_{j=0}^{3} b_j e^{ij\omega\Delta t}} \tag{8}$$

is identified as the effective angular frequency of the time marching scheme (6). The coefficients b_j are determined by requiring (6) to be second order accurate. Tam and Webb found the remaining coefficient by minimizing a weighted integral error which forces $\overline{\omega}$ to be a good approximation of ω. The numerical values of b_j are

$$\begin{aligned} b_0 &= 2.302558088838 \\ b_1 &= -2.491007599848 \\ b_2 &= 1.574340933182 \\ b_3 &= -0.385891422172. \end{aligned}$$

For a given value of $\overline{\omega}\,\Delta t$, (8) yields four roots of $\omega\Delta t$. In order that the scheme is numerically stable, all the roots must have a negative imaginary part. Numerical investigations reveal that this is true as long as $\overline{\omega}\,\Delta t$ is less than 0.4. Hence by choosing a sufficiently small Δt, the scheme is stable. A detailed discussion of the numerical stability of the DRP scheme is provided in ref. 1.

1.3. Group Velocity and Numerical Dispersion

Numerical dispersion is caused by the variation of the group velocity of the wave components of different wave numbers. For example, consider Category 1, Problem 1. The governing equation and the finite difference equations of the DRP scheme are

$$\frac{\partial u}{\partial t} + \frac{\partial u}{\partial x} = 0 \tag{9}$$

$$u_\ell^{(n+1)} = u_\ell^{(n)} - \Delta t \sum_{j=0}^{3} b_j K_\ell^{(n-j)} \tag{10}$$

$$K_\ell^{(n)} = \sum_{j=-3}^{3} a_j u_{\ell+j}^{(n)}. \tag{11}$$

It is easy to find, by using Fourier-Laplace transforms, that the dispersion relation of (9) and finite difference equations (10) and (11) are

$$\omega = \alpha, \qquad \overline{\omega}(\omega) = \overline{\alpha}(\alpha).$$

Formally, therefore, the dispersion relations of the two systems are the same.

The speed of propagation of a wave component of a particular wave number is given by the group velocity $\frac{d\omega}{d\alpha}$. For the DRP scheme, we have $\frac{d\omega}{d\alpha} = \frac{d\overline{\alpha}}{d\alpha} / \frac{d\overline{\omega}}{d\omega}$. For small Δt, $\frac{d\overline{\omega}}{d\omega} \simeq 1.0$ so that the group velocity is directly related to the slope of the $\overline{\alpha}(\alpha)$ curve (figure 2). Over the wave number range of $\alpha\Delta x \leq 0.9$, $\frac{d\overline{\alpha}}{d\alpha}$ differs from unity by no more than 0.3%. With a group velocity deviation of 0.3%, the wave component will be misplaced by 1.2 mesh spacings after propagating a distance of 400 mesh spacings. This is not excessive numerical dispersion. With this dispersion error regarded as acceptable, the 7-point DRP scheme may be considered as adequate for wave propagation computation for waves with wavelengths longer than 7 mesh spacings ($\alpha\Delta x \leq 0.9$).

1.4. Numerical Dissipation

Numerical dissipation can arise from spatial discretization or temporal discretization or both. The 7-point DRP scheme is a central difference scheme so that $\overline{\alpha}(\alpha)$ is real for real α. In this case, there is no numerical dissipation due to spatial discretization. On the other hand, for upwind scheme $\overline{\alpha}$ is complex for real α. Now for a given set of governing equations, the angular frequency $\overline{\omega}(\omega)$ is related to $\overline{\alpha}$ through the dispersion relation. Thus, if $\overline{\alpha}$ is complex, $\overline{\omega}$ and hence ω is complex as well. The numerical damping rate is given by $\mathrm{Im}(\omega)$ for the particular wave number.

For a marching scheme such as (6), ω is complex although α, $\overline{\alpha}$ and $\overline{\omega}$ are all real. The damping rate is again given by $\mathrm{Im}(\omega)$. This time, the origin of damping is temporal discretization. In general, by using a small Δt, $\mathrm{Im}(\omega)$ is reduced over the range of resolved frequencies. This is an effective way to reduce numerical damping. For the DRP scheme, a way to determine the size of the time step Δt for a prescribed amount of dissipation is discussed in ref. 1.

1.5. The Order versus the Dispersion Relation of a Finite Difference Scheme

In computational fluid dynamics, the order of a finite difference scheme is used as a yardstick to measure the anticipated quality of the computed results. For instance, a fourth-order scheme is expected to provide more accurate results than a second-order scheme. For computational aeroacoustics problems in which numerical dispersion, numerical dissipation errors and the accurate reproduction of the wave speeds are important, the order of a scheme is less relevant. The formal order of a scheme sheds no light on the accuracy of the wave speeds, anisotropy and other wave propagation characteristics. But these characteristics are contained in the dispersion relations of the scheme. Thus, it would be more beneficial to judge a numerical scheme through how good its dispersion relations approximate those of the original partial differential equations than to rely on the traditional formal order criterion.

2. CATEGORY 1 PROBLEMS

2.1. Problem 1

The initial value problem is solved by the 7-point stencil DRP scheme; equations (9) and (10). The calculated waveform and the exact solution at $t = 400$ are shown in figure 3. Shown in this figure also are the numerical solutions using the standard fourth-order and sixth-order central difference schemes. The results of the standard schemes reveal appreciable numerical dispersion. There is much smaller dispersion error in the computed result of the DRP scheme even though the stencil size is the same as the sixth-order scheme. For the given initial condition Fourier transform analysis indicates that a 9-point stencil DRP scheme is needed to reduce the effect of dispersion to a not-easily-observable level at $t = 400$.

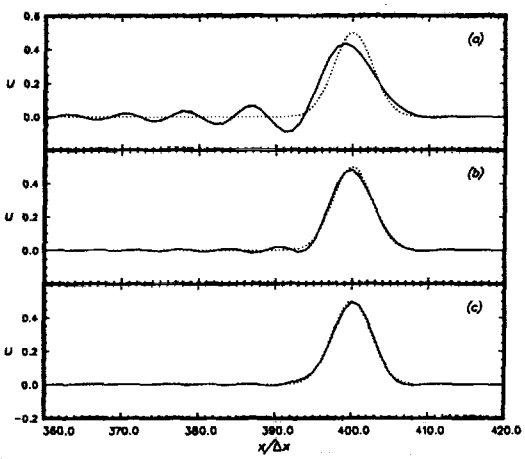

Figure 3. Comparison between computed and exact solutions of the simple one dimensional wave equation. —— numerical solution; ····· exact solution. (a) Fourth order central difference scheme. (b) Sixth order central difference scheme. (c) DRP scheme (7-point stencil).

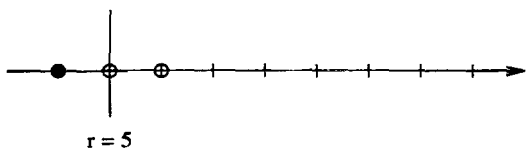

Figure 4. Ghost point and boundary points at r=5

2.2. Problem 2

This initial boundary value problem is again solved by the 7-point stencil DRP scheme. There is a nonhomogeneous boundary condition at $r = 5$. To ensure that the discretized governing equation, as well as the boundary conditions, are satisfied at $r = 5$, the method of ghost point (ref. 4) is employed. Figure 4 shows the configuration of the ghost point and the two boundary points where backward difference stencils (see ref. 3) are used to approximate the spatial derivative.

The computed results for case (a) with $\omega = \frac{\pi}{4}$ at $t = 400$ are shown in figure 5 and 6. Shown in dotted lines are the exact solution. Overall, there is good agreement between the numerical and the exact solution as can be seen in figure 5. Near the wavefront in figure 6, the agreement

is not as good due to dispersion effect. The computed results for case (b) with $\omega = \frac{\pi}{3}$ at $t = 400$ are shown in figures 7 and 8. The spatial resolution as prescribed by the benchmark problem is 6 mesh points per wavelength. This is near the resolution limit (with acceptable dispersion error) of the 7-point stencil DRP scheme. The agreement between the numerical and the exact solution is comparable to that of case (a).

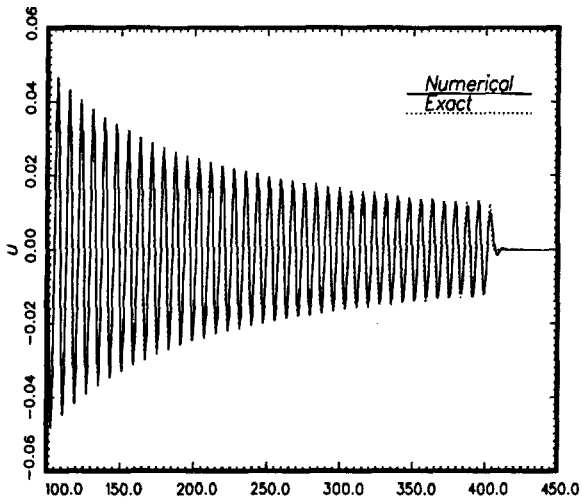

Figure 5. Spatial distribution of waves at $t = 400$, $\omega = \pi/4$.

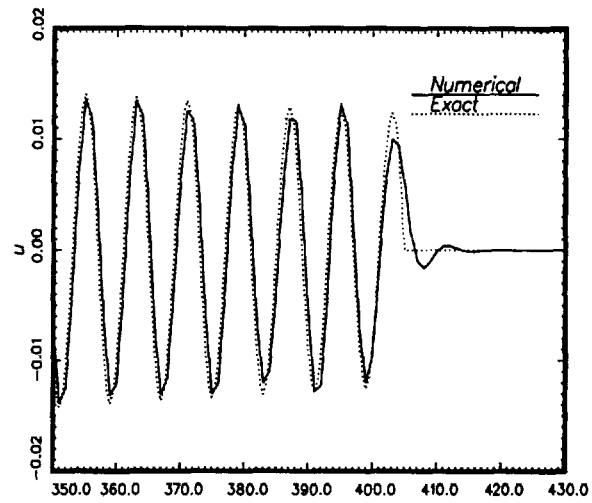

Figure 6. Spatial distribution of waves at $t = 400$, $\omega = \pi/4$.

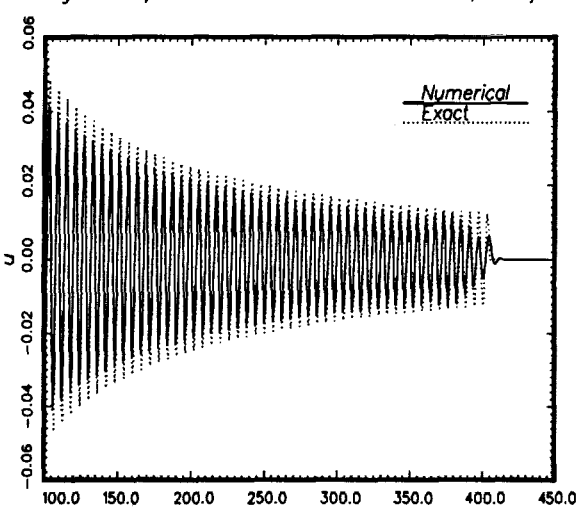

Figure 7. Spatial distribution of waves at $t = 400$, $\omega = \pi/3$.

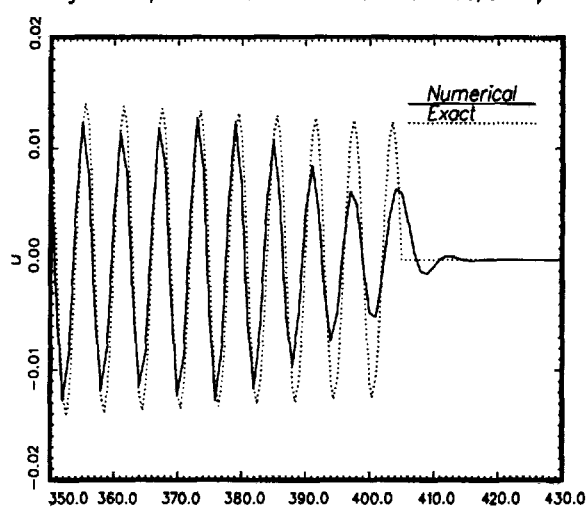

Figure 8. Spatial distribution of waves at $t = 400$, $\omega = \pi/3$.

3. CATEGORY 2 PROBLEMS

3.1. Artificial Selective Damping

We use the 7-point stencil DRP scheme to solve both problems of this category. It is known that during the propagation of a strong acoustic pulse the nonlinear steepening process causes

high-order finite difference scheme to generate spurious spatial oscillations. When unchecked, these spurious oscillations would overwhelm the entire numerical solution. The origin of these spurious spatial oscillations has recently been studied by Tam and Shen (ref. 2). They suggest to eliminate these oscillations by the addition of artificial selective damping terms (see ref. 5). Here our computation follows essentially the method of ref. 2.

The discretized one-dimensional Euler equations written in conservation form according to the DRP scheme are

$$\mathbf{Q}_\ell^{(n)} = \begin{bmatrix} \rho \\ \rho u \\ \rho e \end{bmatrix}_\ell^{(n)}, \qquad \mathbf{E}_\ell^{(n)} = \begin{bmatrix} \rho u \\ \rho u^2 + p \\ (\rho e + p)u \end{bmatrix}_\ell^{(n)} \tag{12}$$

$$\mathbf{Q}_\ell^{(n+1)} = \mathbf{Q}_\ell^{(n)} + \Delta t \sum_{j=0}^{3} b_j \mathbf{K}_\ell^{(n-j)} \tag{13}$$

$$\mathbf{K}_\ell^{(n)} = -\sum_{j=-3}^{3} a_j \mathbf{E}_{\ell+j}^{(n)} - \frac{u_{\text{stencil}}}{R_a} \sum_{j=-3}^{3} d_j \mathbf{Q}_{\ell+j}^{(n)}. \tag{14}$$

The last term on the right side of (14) represents the variable artificial damping. The coefficients d_j are given in ref. 2 and 3. $u_{\text{stencil}} = |u_{\max} - u_{\min}|$ is the difference between the maximum and the minimum velocity in the 7-point stencil. R_a is the artificial Reynolds number. We use $R_a = 0.05$ as suggested by numerical experiments.

3.2. Problem 1, Nonlinear Acoustic Pulse

The initial value problem was solved using the DRP algorithm (13) and (14). Figures 9 and 10 show the acoustic pulse density and velocity waveforms at time $t = 200$. At this time a shock has been formed at the front of the pulse. Also showing in these figures (in dotted line) are the approximate analytical solution using the nonlinear simple wave equation. The location of the shock is determined by the equal area rule of Whitham (ref. 6). According to the approximate analytical solution, at $t = 200$, the pulse has already become triangular in shape. This solution matches well with the numerical result. The equal area rule gives a slower shock. The shock in the numerical solution is smeared out to about 5 mesh spacings. If a sharper shock is desired, a scheme specifically designed for shock capturing should be used. Such a scheme may reduce the shock thickness to 3 mesh spacings but at substantial additional computation costs.

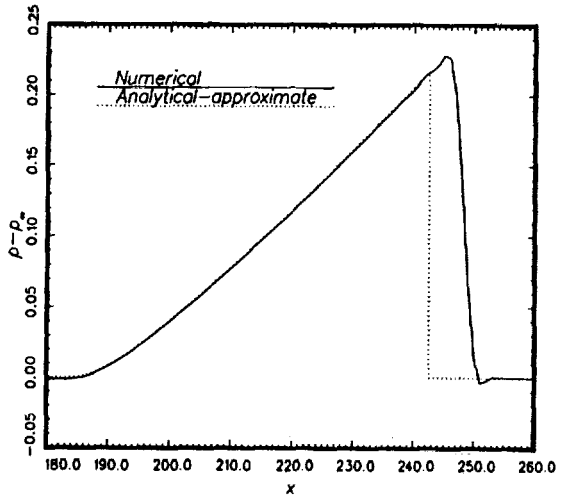

Figure 9. Density distribution at $t = 200$.

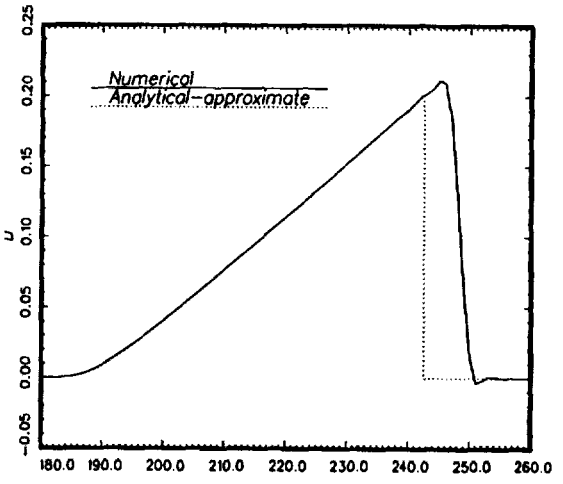

Figure 10. Velocity distribution at $t = 200$.

3.3. Problem 2, The Shock Tube Problem

Finite difference equations (13) and (14) of the DRP scheme are used to generate a shock tube solution numerically using the given initial conditions. Computationally, there is no difference between the nonlinear acoustic pulse problem above and the present shock tube problem. Only the initial conditions are different.

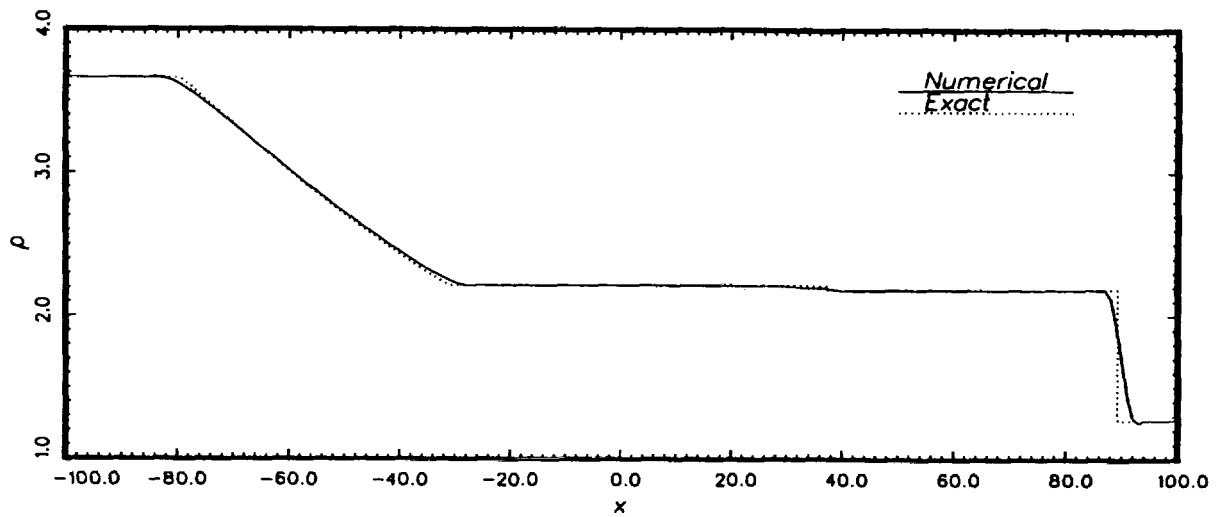

Figure 11. Density distribution at $t = 60$.

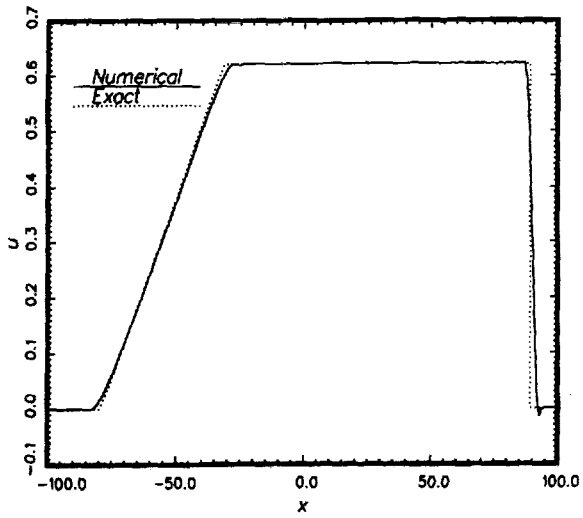

Figure 12. Velocity distribution at $t = 60$.

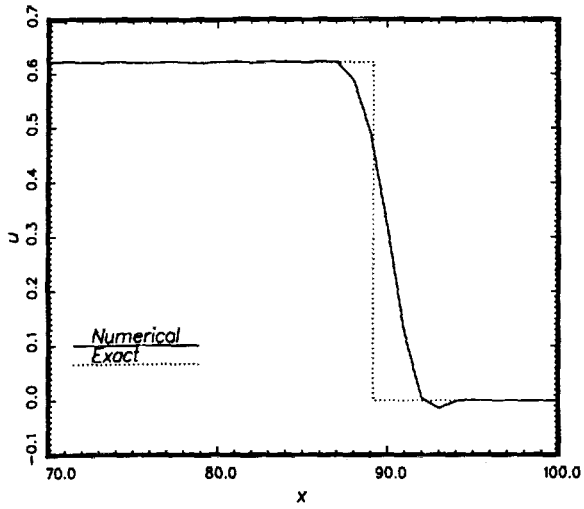

Figure 13. Velocity distribution near the propagating shock at $t = 60$.

Figure 11 shows a comparison between the computed density profile and the standard shock tube solution at $t = 60$. Overall, there is good agreement. The contact discontinuity of the numerical solution is, however, not very sharp. It spreads over a considerable distance. Figure 12 shows the corresponding computed velocity profile. There is, again, good overall agreement. The DRP scheme is a high-order finite difference algorithm. It cannot faithfully reproduce the discontinuities in the computed variable, such as shocks and contact discontinuities. In addition, it cannot faithfully reproduce discontinuities of the first derivatives of the solution variables, such as the first derivative discontinuities that occur at the beginning and the end of the expansion fan. Figure 13 is an enlarged profile of the shock front. The shock is smeared out over 5 mesh spacings as in Problem 1 above.

4. CATEGORY 3 PROBLEMS

4.1. Formulation of Radiation and Outflow Boundary Conditions

Broadly speaking, there are three general ways of formulating radiation and outflow boundary conditions. They are,

1. By the use of characteristics,
2. By the use of asymptotic solutions,
3. By the addition of an absorbing layer outside the computation domain.

In one-dimensional problems, the solution of the Euler equations can be constructed by means of the three sets of characteristics of the equations. The information concerning the solution are transmitted in space and time by these characteristics. Thus, at the boundary of the computation domain the characteristics provide a natural way to formulate the radiation and outflow boundary conditions. Radiation and outflow boundary conditions developed this way

have the advantage that they are valid even for nonlinear waves. One important drawback for characteristics based radiation and outflow boundary conditions is that there are no true characteristics in two- or three-dimensional problems. As an approximation, some investigators ignore the multi-dimensionality of the problem near the boundary of the computation domain. They treat the problem as if it is one-dimensional with the distance normal to the boundary as the only coordinate variable. This approximation has been found to lead to significant reflections when the wave incident angle is oblique to the boundary and also when there is a strong mean flow tangential to the boundary.

Absorbing layers are, by and large, empirical in nature. In general, it is difficult, if not impossible, to assess the error and reflection characteristics of such layers.

In this paper, we use the radiation and outflow boundary conditions derived from the asymptotic solutions of the linearized Euler equations (ref. 1). Here the asymptotic solutions form the extension of the numerical solution; all the way to the far-field outside the computation domain. With respect to a polar coordinate system (2-dimensional problems) with coordinates (r, θ) centered at the center of the computation domain, the radiation boundary conditions given in ref. 1 may be written in the form

$$\left(\frac{1}{V(\theta)}\frac{\partial}{\partial t}+\frac{\partial}{\partial r}+\frac{1}{2r}\right)\begin{bmatrix}\rho\\ u\\ v\\ p\end{bmatrix}=0 \tag{15}$$

where $V(\theta) = [M\cos\theta + (1 - M^2\sin^2\theta)^{\frac{1}{2}}]$. M is the mean flow Mach number and θ is measured from the direction of the mean flow. (15) is applied to boundary regions without an outflow where the outgoing disturbances are acoustic waves only.

In regions with outflow, the outgoing disturbances consist of a combination of acoustic, entropy and vorticity waves. The latter two types of waves are convected out by the mean flow. Tam and Webb (ref. 1) derived the following outflow boundary conditions that are used in the present computation.

$$\begin{aligned}
&\frac{\partial\rho}{\partial t}+M\frac{\partial\rho}{\partial x}=\frac{\partial p}{\partial t}+M\frac{\partial p}{\partial x}\\
&\frac{\partial u}{\partial t}+M\frac{\partial u}{\partial x}=-\frac{\partial p}{\partial x}\\
&\frac{\partial v}{\partial t}+M\frac{\partial v}{\partial x}=-\frac{\partial p}{\partial y}\\
&\frac{1}{V(\theta)}\frac{\partial p}{\partial t}+\frac{\partial p}{\partial r}+\frac{p}{2r}=0
\end{aligned} \tag{16}$$

4.2. Problem 1

The 7-point stencil DRP scheme is used to obtain the solution of the initial value problem.

The discretized linearized Euler equations and radiation and outflow boundary conditions are given in ref. 1. In this problem, the mean flow is parallel to the x-direction. As a result, radiation boundary conditions are imposed on the left, top and bottom boundaries of the computation domain. At the right boundary, there is outflow. Here, outflow boundary condition (16) is used.

Figure 14 shows the computed density contours at $t = 30$. The exact solution is shown in dotted lines. But the dotted lines cannot be seen because the difference between the numerical and the exact solution is less than the thickness of the lines. Figure 15 gives the computed density waveform and the exact solution at $t = 30$ along the line $y = 0$. At this time, the acoustic pulse and the entropy pulse are separated from each other. Figures 16 and 17 show the computed density contours and waveform along $y = 0$ at $t = 60$. At this time, the acoustic pulse catches up and merges with the entropy pulse. The merged pulse leaves the right boundary of the computation domain as a single entity. By examining the numerical solution at later times, we find no significant reflections off the boundaries of the computation domain.

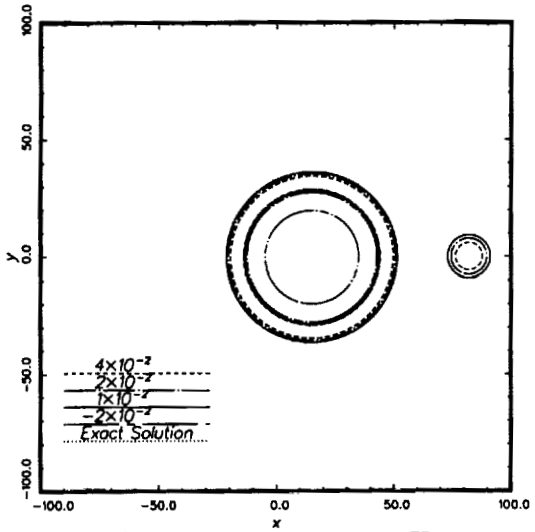

Figure 14. Density contours at $t = 30$.

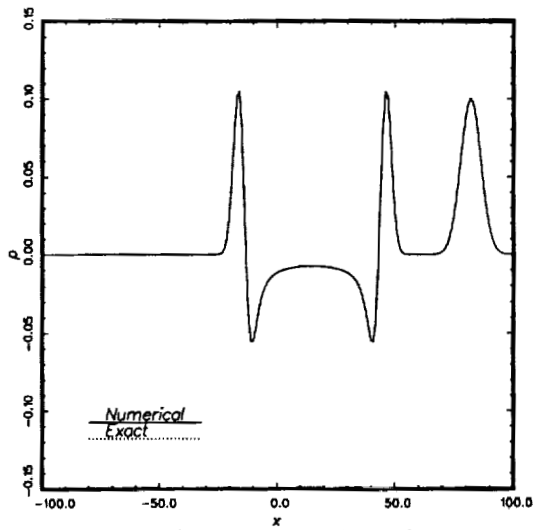

Figure 15. Density waveform along the x−axis at $t = 30$.

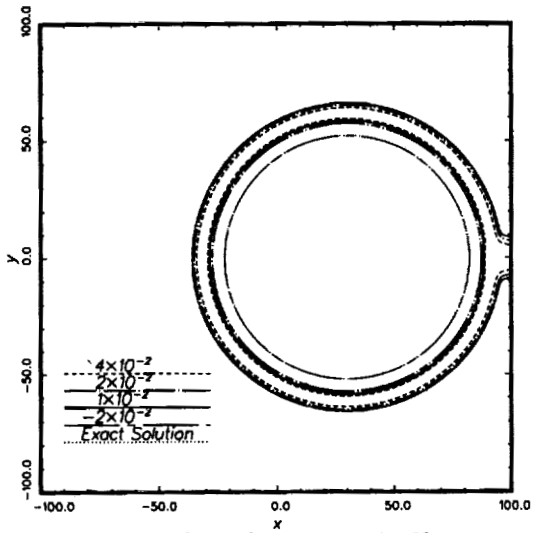

Figure 16. Density contours at $t = 60$.

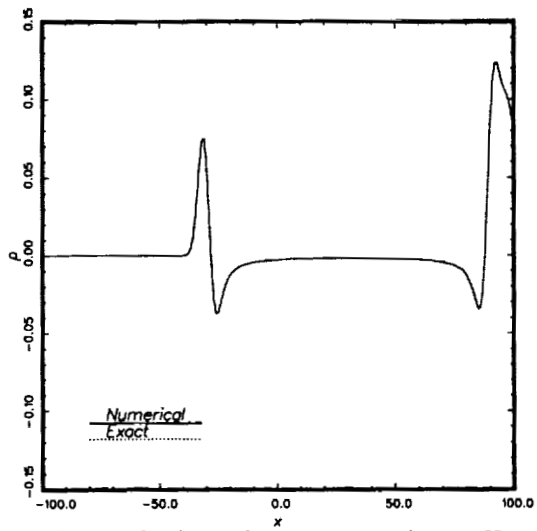

Figure 17. Density waveform along the x−axis at $t = 60$.

4.3. Problem 2

This problem can be made identical to Problem 1 by applying a coordinate rotation of 45 degrees. In this case, radiation boundary conditions are imposed at the bottom and left boundaries of the computation domain where there is an inflow. Outflow boundary conditions are imposed on the top and right side of the computation domain.

Figures 18 and 19 show the computed density contours and the waveform along the line $x = y$ together with the exact solution at $t = 80$. Again, the difference between the computed and the exact contours are too small to be noticed. At $t = 80$, the entropy pulse and the acoustic wave pulse are about to merge and then exit through the upper right-hand corner of the computation domain. A careful examination of the computed results at different time levels reveals that no significant reflection of waves occurs at the boundaries. Based on the above and other examples, we believe that radiation boundary condition (15) and outflow boundary condition (16) are almost transparent to outgoing disturbances provided they are in the resolved wave number range.

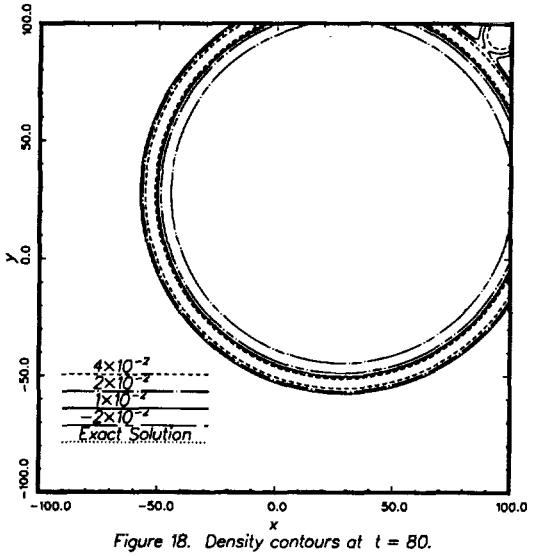

Figure 18. Density contours at $t = 80$.

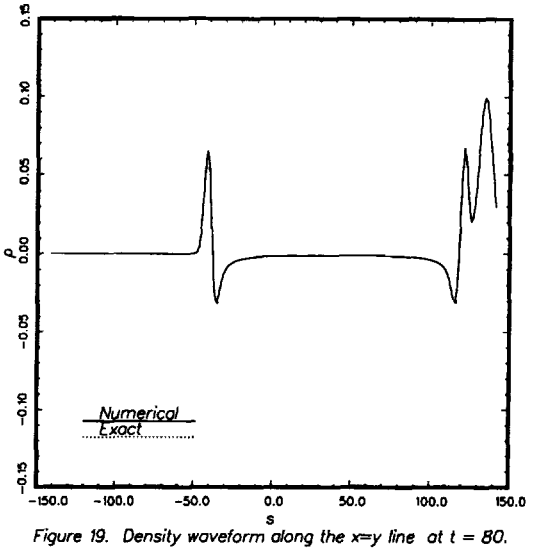

Figure 19. Density waveform along the x=y line at $t = 80$.

5. CATEGORY 4 PROBLEMS

5.1. Wall Boundary Conditions for High-Order Schemes

Unless all the first-order derivatives of the Euler equations are approximated by first-order finite difference, the order of the resulting finite difference equations is higher than that of the original partial differential equations. When this is the case, the finite difference equations will support solutions that have no counterpart in the original partial differential equations. Those

are spurious solutions. They can be excited by initial conditions or generated at the surface of discontinuity such as at a wall. Also, with higher-order governing equations, the number of boundary conditions required for a unique solution is larger. The set of wall boundary conditions, appropriate for the Euler equations, is no longer sufficient. For high-order schemes, we, therefore, need a new set of wall boundary conditions that would provide a unique solution without producing spurious waves. Here the wall boundary conditions of ref. 4, developed with the above reasonings in mind, are used.

5.2. Problem 1, Reflection by a Flat Plate

This problem was considered in ref. 4. To ensure that the solution of the finite difference scheme satisfied the governing equations as well as the boundary condition at the boundary points on the surface of the plate, a set of wall boundary conditions based on the use of ghost values was developed in ref. 4. In this reference, the qualities of these wall boundary conditions were examined quantitatively through an analysis of the problem of a plane acoustic wave train incident on a plane wall. The results indicated that only an insignificant amount of spurious numerical waves was generated. Further, the numerical boundary layer adjacent to the wall, formed by the spatially damped spurious numerical waves of the computation scheme, was no more than two mesh points thick. This strongly suggested that the proposed wall boundary conditions could yield high-quality numerical solution. In this work, the wall boundary treatment of ref. 4 is used. Figures 20 and 21 show the computed pressure contours at $t = 30$ and 60. By comparing the contour patterns of the two figures, the mean flow convection effect becomes evident. To an accuracy corresponding to the thickness of the contour lines shown, the computed results are identical to the exact solution.

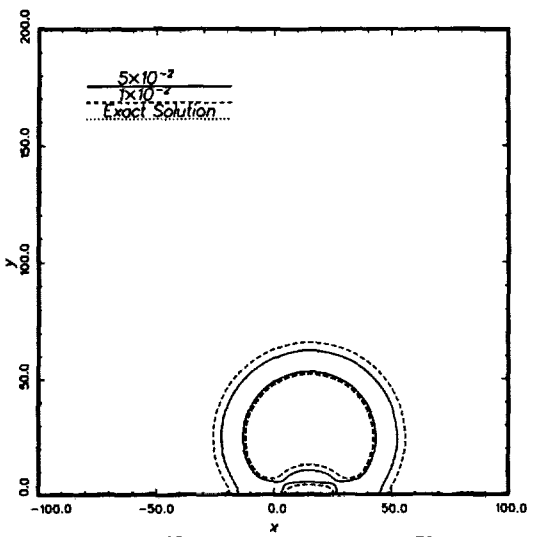

Figure 20. Pressure contours at $t = 30$.

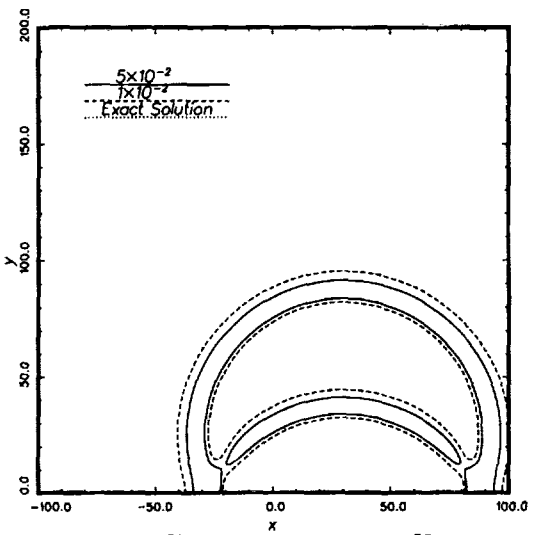

Figure 21. Pressure contours at $t = 60$.

5.3. Problem 2, Oscillating Piston in a Wall

The problem is axisymmetric. Here it is solved as a two-dimensional problem in the r-x-plane where (r, x, θ) are the cylindrical coordinates with origin centered at the center of the piston. The governing equations are

$$\frac{\partial u}{\partial t} + \frac{\partial p}{\partial x} = 0 \tag{17}$$

$$\frac{\partial v}{\partial t} + \frac{\partial p}{\partial r} = 0 \tag{18}$$

$$\frac{\partial p}{\partial t} + \frac{\partial v}{\partial r} + \frac{v}{r} + \frac{\partial u}{\partial x} = 0. \tag{19}$$

The boundary condition on the wall surface, $x = 0$, is

$$u = \begin{cases} 0, & x > R \\ \varepsilon \sin \omega t, & x < R \end{cases}$$

where R is the radius of the piston.

At the axis of symmetry, $r = 0$, equation (19) is singular and should not be used. We note that as $r \to 0$, $v \to 0$ so that $\frac{v}{r} \to \frac{\partial v}{\partial r}$. Thus, for the mesh points lying on the axis of symmetry, the following equation is used in lieu of (19).

$$r = 0, \qquad \frac{\partial p}{\partial t} + 2\frac{\partial v}{\partial r} + \frac{\partial u}{\partial x} = 0. \tag{20}$$

The present problem is three-dimensional. Radiation boundary condition (15) is not appropriate. The three-dimensional version of (15) applicable to this problem is

$$\left(\frac{\partial}{\partial t} + \frac{\partial}{\partial R} + \frac{1}{R}\right) \begin{bmatrix} u \\ v \\ p \end{bmatrix} = 0 \tag{21}$$

where $R = (x^2 + r^2)^{\frac{1}{2}}$.

We solve equations (17), (18) and (19) by the 7-point stencil DRP scheme. Figure 22 shows the computation domain. Along the axis of symmetry (17), (18) and (20) are used. On the top and right boundary regions radiation boundary condition (21) is used. Below the wall and piston surface, a row of ghost points, each with a single ghost value $p_{\ell,-1}$ ($\ell = 0, 1, \ldots, 100$), are included in the computation. The ghost values are chosen so that the wall and piston surface boundary conditions are satisfied as in Category 1, Problem 2 and Category 4, Problem 1. The mesh point at $\ell = 10$, $m = 0$ (ℓ, m are the indices in the r- and x-directions) corresponds to the edge of the piston. Here, the boundary condition is discontinuous. In the computation, we choose to set u to be equal to the mean value at this location.

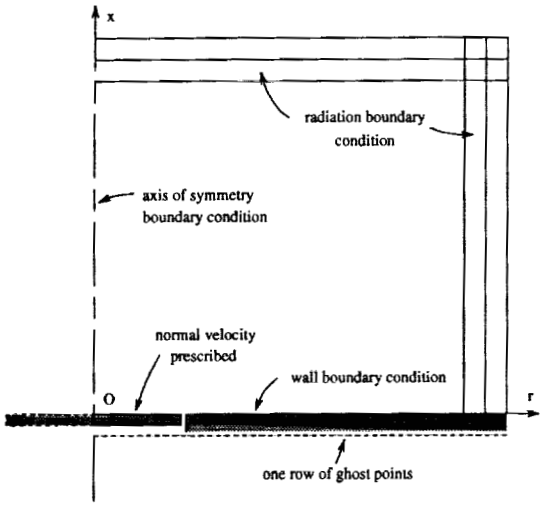

Figure 22. The computation domain and boundary conditions.

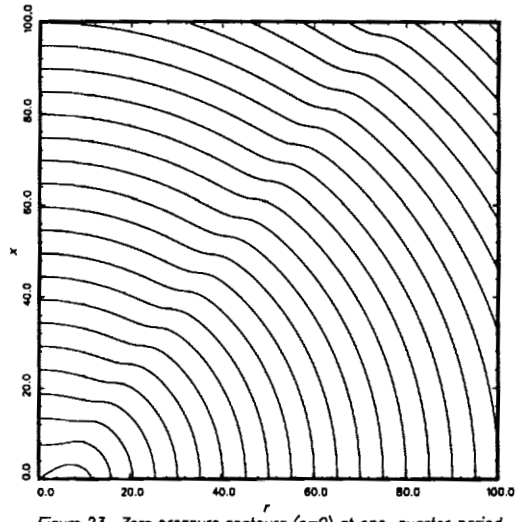

Figure 23. Zero pressure contours (p=0) at one-quarter period of a cycle. —— numerical solution, ····· exact solution.

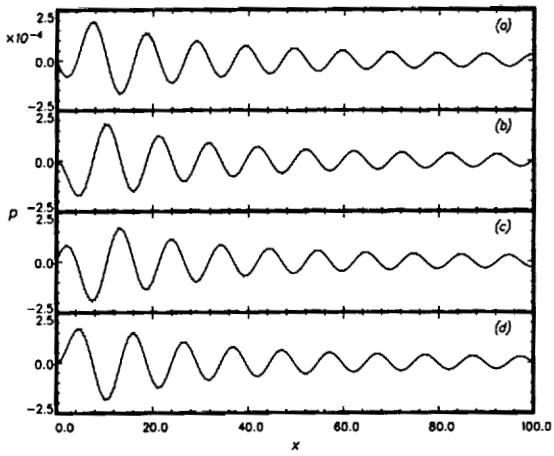

Figure 24. Pressure distribution along the axis of the piston (r=0) at (a) the beginning of a circle, (b) one quarter of a cycle, (c) half cycle, (d) three quarters of a cycle, —— numerical solution, ····· exact solution.

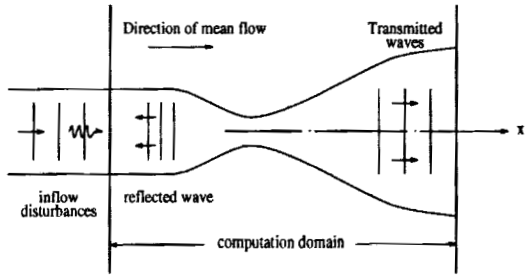

Figure 25. Schemetic diagram of the computation domain for a one dimensional flow in a variable area duct with constant area termination. Inflow disturbances at the left boundary may consist of sound and entropy waves.

In this problem, because of the use of equation (20) instead of (19) at $r = 0$, there is an abrupt change in the governing finite difference equations between the first two columns of mesh points on the left side of the computation domain. In addition, there is a rapid change in the boundary condition at the edge of the piston. Short wave length spurious numerical waves are often generated in these regions of rapid changes. This was noticed immediately in our trial runs. To eliminate these waves, artificial damping terms are added to the DRP scheme as discussed in section 3. An artificial mesh Reynolds number, $R = (\Delta x)\frac{a_0}{\nu_0}$, of 5 is used in the numerical computation. With the inclusion of the artificial selective damping terms, spurious waves are effectively eliminated in the numerical solution.

Figure 23 shows the computed zero-pressure contours ($p = 0$) at one-quarter period of a cycle. There is excellent agreement with the exact solution. Figure 24 shows the computed pressure waveform along the axis of the piston at each quarter cycle. As can be seen, the agreement with the exact solution is very good. It is believed that for problems of this kind, the DRP scheme,

together with the wall boundary condition of ref. 4, can provide very accurate time-domain solutions.

6. CATEGORY 5, THE NOZZLE PROBLEM

6.1. Formulation

The one-dimensional nozzle flow equations are solved by the 7-point stencil DRP scheme. At the left boundary of the computation domain, see figure 25, radiation boundary conditions, which allow the incoming sound wave to propagate into the computation domain and at the same time permit the reflected waves to leave the computation domain, are to be imposed. Here, these radiation boundary conditions are developed from the asymptotic solutions of the governing equations.

To the left of the computation domain, the duct has a constant area. In this region, the governing equations for small amplitude disturbances are

$$\frac{\partial}{\partial t}\begin{bmatrix}\rho\\ u\\ p\end{bmatrix}+\frac{\partial}{\partial x}\begin{bmatrix}M\rho+u\\ Mu+p\\ Mp+u\end{bmatrix}=0 \tag{22}$$

where M is the mean flow Mach number. The general solution of (22), which is valid outside the computation domain all the way to $x\rightarrow-\infty$, consists of three arbitrary functions, F, G and H. It may be written in the form,

$$\begin{bmatrix}\rho\\ u\\ p\end{bmatrix}=\begin{bmatrix}1\\ 1\\ 1\end{bmatrix}F\left(\frac{x}{1+M}-t\right)+\begin{bmatrix}1\\ 0\\ 0\end{bmatrix}G\left(\frac{x}{M}-t\right)+\begin{bmatrix}1\\ -1\\ 1\end{bmatrix}H\left(\frac{x}{1-M}+t\right). \tag{23}$$

In (13), F represents the incoming acoustic wave. To match the given incoming wave, we let

$$F=\varepsilon\sin\left[\omega\left(\frac{x}{1+M}-t\right)\right].$$

G represents an incoming entropy wave that is zero for the present problem. H represents the reflected acoustic waves that is unknown until after the problem is solved. By eliminating H through differentiation, we derive the following nonhomogeneous radiation boundary condition

$$\left(\frac{1}{1-M}\frac{\partial}{\partial t}-\frac{\partial}{\partial x}\right)\begin{bmatrix}\rho\\ u\\ p\end{bmatrix}=-\begin{bmatrix}1\\ 1\\ 1\end{bmatrix}\frac{2\omega\varepsilon}{1-M^2}\cos\left[\omega\left(\frac{x}{1+M}-t\right)\right]. \tag{24}$$

This equation is used to update the solution at the left boundary points of the computation domain.

The outflow at the right boundary is supersonic. All the disturbances will be convected out of the computation domain automatically. No special outflow boundary condition is needed. The spatial derivatives of the governing equations are discretized using backward difference stencils at the right boundary points.

6.2. Steady State Solution

A two-step procedure is used to compute the transmitted sound waves. The first step involves the computation of the mean flow. For this purpose, the right side of (24) is set equal to zero. To speed up the computation, the exact analytical solution is used as the initial condition. But this is not the solution of the finite difference equations of the DRP scheme. The difference between the exact and the numerical solution contributes to the initial residuals. The initial residual (based on infinite norm) is of the order of 10^{-3}. This is shown in figure 26. As the computation proceeds in time the residual decreases gradually. But the rate of decrease is very slow. Figure 26 shows the time history of the convergence of the numerical solution to the steady state.

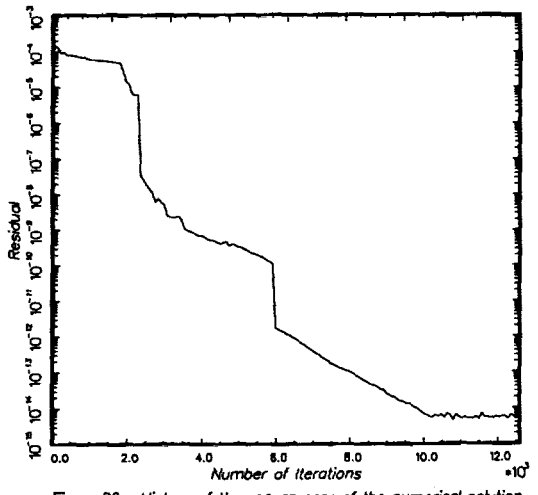

Figure 26. History of the convergence of the numerical solution to steady state. (Residual according to infinite norm)

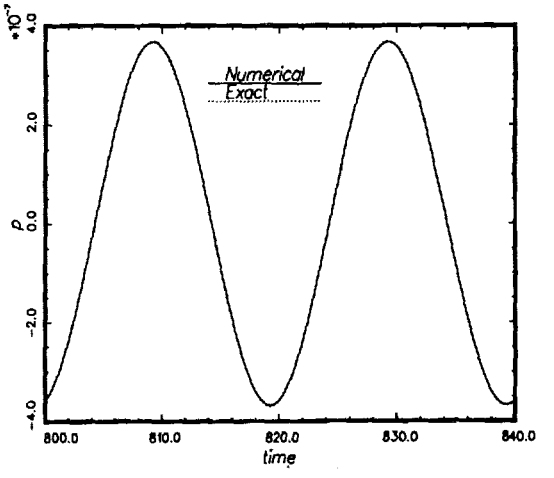

Figure 27. Time variation of the pressure field of the transmitted acoustic wave at the nozzle exit.

To accelerate the rate of convergence, we use the technique of "canceling-the-residual" discussed in ref. 7. In this method, small source terms are added to the right side of the governing equations to momentarily reduce the residual to zero. But when the computation resumes, the residual in the next time step is not completely zero. However, because of the added source terms, it is usually several orders of magnitude smaller than before. In figure 26, the two abrupt decreases in the residual is due to the application of this accelerated convergence technique. Of course, when small source terms are added to the finite difference equations, the steady state solution is slightly changed. But the exact numerical solution differs from the exact analytical so-

lution generally by the order of 10^{-3}. Thus, as long as the added source terms are of the order 10^{-5} or smaller, the change in the numerical steady state solution is of no consequence to the overall accuracy of the result. In the present computation, the steady state solution has a numerical noise level limited only by the machine truncation error as shown in figure 26.

6.3. Numerical Solution

After the numerical solution settles down to a steady state condition (with low numerical noise level), the right-hand side of equation 24 is turned on slowly at the boundary points on the left. This allows the incoming acoustic waves to enter the computation domain. The numerical computation continues until a time-periodic state is attained. The time variation of the computed pressure field of the transmitted acoustic waves at the nozzle exit is shown in figure 27. Plotted in this figure also is the exact solution. There appears to be very little difference between the numerical and the exact solution. This good agreement indicates that although the sound wave is many orders of magnitude smaller than the mean flow, it can be directly computed with high accuracy by the DRP scheme.

7. CATEGORY 6, GUST-BLADE INTERACTION PROBLEM

We formulate the mathematical problem in two entirely different ways. Both problems are solved by the 7-point stencil DRP scheme. The good agreement between the two solutions assures that the numerical solution is correct.

7.1. Gust-Blade Problem as a Scattering Problem

We will regard the gust as the incident disturbance. When impinging on the flat plate, a scattered field of acoustic and vorticity waves is generated. The total disturbance field near the plate is the sum of the incident disturbance and the scattered pressure and velocity fluctuations. Let the scattered field be denoted by a prime then

$$\begin{bmatrix} u \\ v \\ p \end{bmatrix} = 0.1 \sin\left[\frac{\pi}{8}\left(\frac{x}{M} - t\right)\right] \begin{bmatrix} 0 \\ 1 \\ 0 \end{bmatrix} + \begin{bmatrix} u' \\ v' \\ p' \end{bmatrix}. \tag{25}$$

On substituting (25) into the linearized momentum and energy equations, the governing equations for the scattered field are found that may be written as

$$\frac{\partial}{\partial t}\begin{bmatrix} u \\ v' \\ p \end{bmatrix} + \frac{\partial}{\partial x}\begin{bmatrix} Mu + p \\ Mv' \\ Mp + u \end{bmatrix} + \frac{\partial}{\partial y}\begin{bmatrix} 0 \\ p \\ v' \end{bmatrix} = 0 \tag{26}$$

The wall boundary condition on the plate becomes

$$v' = -0.1 \sin\left[\frac{\pi}{8}\left(\frac{x}{M} - t\right)\right](1 - e^{-\frac{t}{\tau}}). \tag{27}$$

To allow the scattered field to be turned on gradually, we have added the last factor to the right side of (27). This factor becomes unity when t is much larger than τ.

The problem is antisymmetric with respect to the plate so that we may use a reduced computation domain as shown in figure 28. On the left and top boundaries, the radiation boundary condition (15) is imposed. On the right boundary, the outflow boundary condition (16) is imposed. On the bottom boundary, (27) is to be satisfied over the region of the flat plate. This is enforced by adding a row of ghost points below the plate. For the rest of the boundary, the antisymmetric conditions

$$\begin{aligned} p(x, -y, t) &= -p(x, y, t) \\ u(x, -y, t) &= -u(x, y, t) \\ v'(x, -y, t) &= v'(x, y, t) \end{aligned} \tag{28}$$

are used. The present problem is solved as an initial value problem (zero initial disturbances) so that no Kutta condition is required.

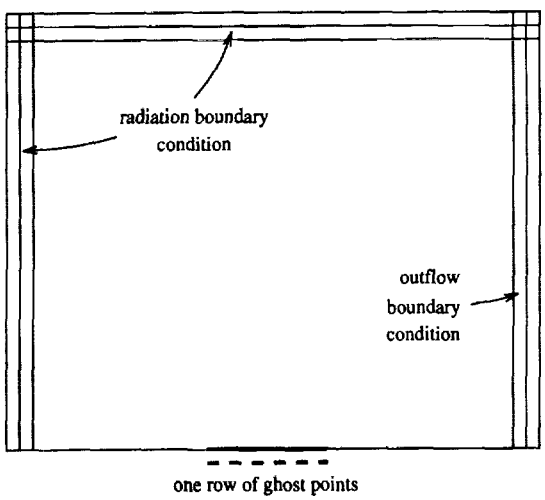

Figure 28. Computation domain for the scattered field.

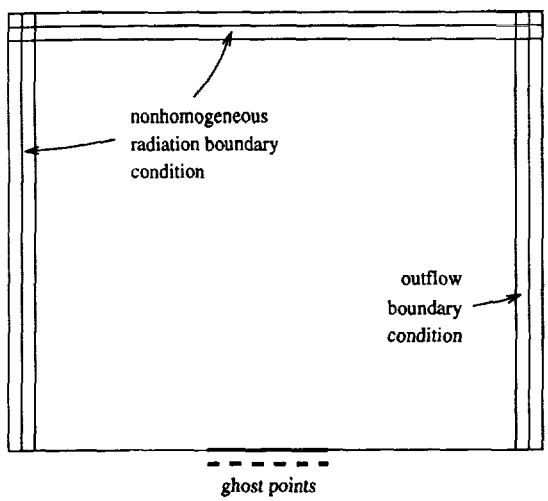

Figure 29. Computation domain for direct simulation.

At the leading and trailing edge of the plate there is an abrupt change in the boundary condition. This inevitably results in the generation of spurious numerical waves. To eliminate these waves, artificial selective damping terms are added to the DRP scheme. Since artificial damping is needed primarily around the plate, the mesh Reynolds number is taken to be $\frac{1}{1.5}$ for all mesh points lying in the rectangular region within 3 mesh points from the plate. Far away from the plate, a mesh Reynolds number of 10 is found to be adequate. A Gaussian distribution with a half-width of 3 mesh points is used for transition from the former value of mesh Reynolds number to the latter.

Instead of solving for the scattered field, one can compute the total field directly. The governing equations are the linearized momentum and energy equations that are the same as (26) except that v' is to be replaced by v. For the total field, the boundary conditions are

$$v = 0.1 \sin\left[\frac{\pi}{8}\left(\frac{x}{M} - t\right)\right] \tag{29}$$

at the boundaries of the computation domain away from the plate and

$$v = 0 \tag{30}$$

at the wall.

Now at the left and top boundaries of the computation domain, we have a combination of the inflow gust disturbance given by (29) and the radiated sound field. On using the asymptotic solution of ref. 1 to represent the outgoing acoustic field, the velocity and pressure field in the boundary region may be written in the form

$$\begin{bmatrix} u \\ v \\ p \end{bmatrix} = \frac{F(\frac{r}{V(\theta)-t,\theta})}{r^{\frac{1}{2}}} \begin{bmatrix} \hat{u}(\theta) \\ \hat{v}(\theta) \\ 1 \end{bmatrix} + 0.1 \sin\left[\frac{\pi}{8}\left(\frac{x}{M} - t\right)\right] \begin{bmatrix} 0 \\ 1 \\ 0 \end{bmatrix} \tag{31}$$

where $V(\theta) = [M\cos\theta + (1 - M^2\sin^2\theta)^{\frac{1}{2}}]$. (r, θ) are the polar coordinates with origin at the center of the plate. The unknown function F of the outgoing acoustic waves may be eliminated by differentiation. This gives the nonhomogeneous radiation boundary condition

$$\left(\frac{1}{V(\theta)}\frac{\partial}{\partial t} + \frac{\partial}{\partial r} + \frac{1}{2r}\right)\begin{bmatrix} u \\ v \\ p \end{bmatrix} = \left\{0.1\frac{\pi}{8}\left(\frac{\cos\theta}{M} - \frac{1}{V(\theta)}\right)\cos\left[\frac{\pi}{8}\left(\frac{x}{M} - t\right)\right] + \frac{0.1}{2r}\sin\left[\frac{\pi}{8}\left(\frac{x}{M} - t\right)\right]\right\}\begin{bmatrix} 0 \\ 1 \\ 0 \end{bmatrix}. \tag{32}$$

Figure 29 shows the computation domain and the various boundary conditions. Nonhomogeneous radiation boundary condition (32) is to be satisfied at the left and upper boundary of the computation domain. The nonhomogeneous terms are turned on slowly by multiplying them with the factor $(1 - e^{-\frac{t}{\tau}})$. On the outflow region, the gust solution satisfies the outflow boundary condition identically. Thus, the same homogeneous outflow boundary conditions as before are applied to the right boundary region of the computation domain. Antisymmetry condition (28) is, again, used at the bottom boundary outside the flat plate. Artificial selective damping is also required around the flat plate. The same mesh Reynolds number distribution as discussed above is used.

In implementing the second formulation, it was found, because of the use of backward difference stencil in the boundary region, low intensity acoustic waves were radiated out from the upper left corner of the computation domain. This spurious source of noise caused a slight contamination of the numerical results. The first formulation was implemented by Z. Dong. In this case, the nonhomogeneities were on the plate boundary condition. No spurious source of noise was created.

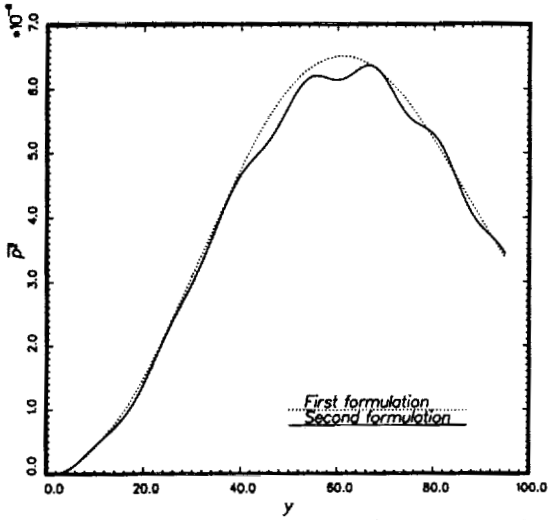

Figure 30. Distribution of radiated sound intensity along x=95

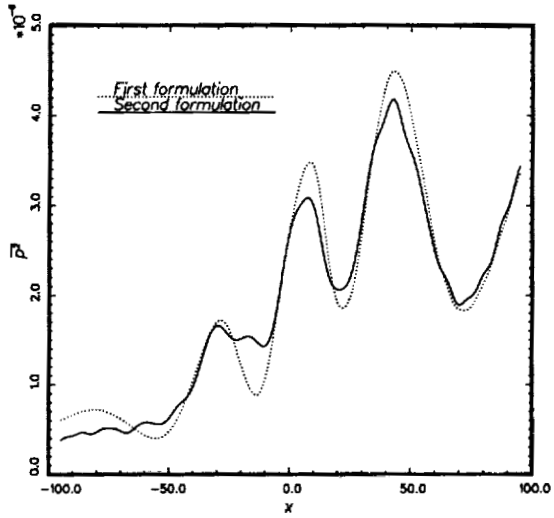

Figure 31. Distribution of radiated sound intensity along y=95

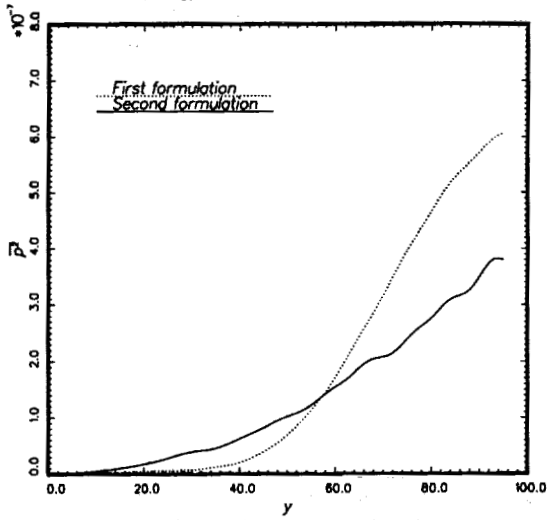

Figure 32. Distribution of radiated sound intensity along x=−95

Figure 30 shows the calculated distribution of radiated sound intensity along the line $x = 95$. Figure 31 and 32 show the corresponding distribution along the lines $y = 95$ and $x = -95$, respectively. In spite of the fact that the computed results of the second formulation are slightly contaminated by spurious numerical noise, there is good agreement between the two sets of results. All the local directions of peak noise radiation are in agreement with each other. Time

constraint has prevented us from developing a counter-measure to eliminate the numerical noise. We believe that had we been able to suppress the spurious noise source at the upper left corner, the two formulations would give identical results indicating strongly that the computed results are correct.

ACKNOWLEDGMENT

This work was supported by the NASA Lewis Research Center Grant NAG 3-1267.

REFERENCES

1. Tam, C.K.W.; and Webb, J.C.: Dispersion-Relation-Preserving Finite Difference Schemes for Computational Acoustics. *J. Computational Phys.*, vol. 107, Aug. 1993, pp. 262–281.
2. Tam, C.K.W.; and Shen, H.: Direct Computation of Nonlinear Acoustic Pulses Using High-Order Finite Difference Schemes. AIAA–93–4325, Oct. 1993.
3. Tam, C.K.W.: Computation Aeroacoustics: Issues and Methods. AIAA–95–0677, Jan. 1995.
4. Tam, C.K.W.; and Dong, Z.: Wall Boundary Conditions for High-Order Finite-Difference Schemes in Computational Aeroacoustics. *Theoret. Comput. Fluid Dynamics*, vol. 6, Oct. 1994, pp. 303–322..
5. Tam, C.K.W.; Webb, J.C.; and Dong, Z.: A Study of the Short Wave Components in Computational Acoustics. *J. Computational Acoustics*, vol. 1, Mar. 1993, pp. 1–30.
6. Whitham, G.B.: *Linear and Nonlinear Waves.* Wiley-Interscience, New York, 1974.
7. Tam, C.K.W.; and Dong, Z.: Radiation and Outflow Boundary Conditions for Direct Computation of Acoustic and Flow Disturbances in a Nonuniform Mean Flow. Proceeding of the First Joint CEAS/AIAA Aeroacoustics Conference (16^{th} AIAA Aeroacoustics Conference), 12–15 June 1995, Munich, Germany.

THE CONSTRUCTION OF HIGH-ACCURACY SCHEMES FOR ACOUSTIC EQUATIONS

Lei Tang and James D. Baeder
University of Maryland
College Park, MD

SUMMARY

An accuracy analysis of various high order schemes is performed from an interpolation point of view. The analysis indicates that classical high order finite difference schemes, which use polynomial interpolation, hold high accuracy only at nodes and are therefore not suitable for time-dependent problems. Thus, some schemes improve their numerical accuracy within grid cells by the near-minimax approximation method, but their practical significance is degraded by maintaining the same stencil as classical schemes. One-step methods in space discretization, which use piecewise polynomial interpolation and involve data at only two points, can generate a uniform accuracy over the whole grid cell and avoid spurious roots. As a result, they are more accurate and efficient than multistep methods. In particular, the Cubic-Interpolated Psuedo-particle (CIP) scheme is recommended for computational acoustics.

INTRODUCTION

The emergence of computational acoustics as a discipline has focused more attention on the numerical accuracy requirements for time-dependent problems, which classical finite difference schemes seem to satisfy poorly. Thus, several improved schemes have been proposed. Two typical examples of them are: the Dispersion-Relation Preserving (DRP) finite difference schemes[1], and the compact finite difference schemes with spectral-like resolution[2], which indeed generate a higher accuracy within grid cells. Unfortunately, they have the same computational costs as classical high order schemes. Since the ultimate goal of applying a high accuracy scheme is to reduce the necessary number of grid points, and therefore improve numerical efficiency, these improved schemes are not much better than classical schemes in practice.

This paper analyzes various high order schemes from an interpolation point of view in order to determine their suitability for time-dependent problems. The analysis shows that the accuracy deficiency of classical high order schemes results from the application of polynomial interpolation. If one applies one-step methods in space discretization, which use piecewise polynomial interpolation, then high computational cost can be avoided. Numerical results indicate that third order one-step schemes can satisfy the accuracy requirements of computational acoustics. In particular, the Cubic-Interpolated Psuedo-particle (CIP) scheme[3] is recommended for computational acoustics, which is the most efficient third-order accuracy scheme.

At last, note that in order to clearly indicate the role of interpolation in the numerical solution of differential equations, only the linear convection equation

$$\frac{\partial u}{\partial t}+a\frac{\partial u}{\partial x}=0 \qquad (a>0) \tag{1.1}$$

is discussed in this paper.

THE ANALYSIS OF CLASSICAL HIGH ORDER SCHEMES

Standard textbooks (e.g. ref. [4]) indicate two approaches to construct high order finite difference schemes in space: explicit and implicit formulas. If one considers the approximation of the first order derivative $\partial u/\partial x$ at the ith node of a uniform grid of spacing Δx, and use the nodal values of u and $\partial u/\partial x$ at the M nodes to the right and N nodes to the left of the point i, then the corresponding finite difference scheme is

$$\sum_{j=-N}^{M}\alpha_j u_{i+j}=\Delta x\cdot\sum_{j=-N}^{M}\beta_j(u_x)_{i+j} \tag{2.1}$$

where α_j and β_j are constants, and not all α_j are zero, and $\beta_0\neq 0$. The scheme (2.1) is explicit if $\beta_j=0$, and implicit (or compact) if $\beta_j\neq 0$ when $j\neq 0$.

Expanding both sides of (2.1) in Taylor series of Δx, e.g.

$$u_{i+1}=u_i+(u_x)_i\Delta x+\frac{1}{2!}(u_{xx})_i\Delta x^2+\frac{1}{3!}(u_{xxx})_i\Delta x^3+\ldots+\frac{1}{n!}(u_{nx})_i\Delta x^n+\ldots$$

$$u_{i-1}=u_i-(u_x)_i\Delta x+\frac{1}{2!}(u_{xx})_i\Delta x^2-\frac{1}{3!}(u_{xxx})_i\Delta x^3+\ldots+\frac{(-1)^n}{n!}(u_{nx})_i\Delta x^n+\ldots$$

the second order central scheme for $(u_x)_i$ is

$$(u_x)_i=\frac{u_{i+1}-u_{i-1}}{2\Delta x}-\frac{1}{6}(u_{xxx})_i\Delta x^2+\ldots \tag{2.2}$$

Notice that the second order of such a scheme does not come from accurately evaluating the second order derivative term in the Taylor series expansions of the solution, but from balancing the contribution of second order derivative terms from different points $i-1$ and $i+1$ at a certain grid point i. Obviously, such balances occur only at nodes. Thus, the second order accuracy of such a scheme only holds at nodes, not within the grid cells. Furthermore, if we classify our solutions into two categories: low curvature components (e.g. sin(x/10)), and high curvature components (e.g. sin(10x)), then such balances would have a significant influence on the numerical accuracy within grid cells only for high curvature components.

For time independent problems, the accuracy deficiency of such a scheme does not appear explicitly because the nodal values of the solution are fixed. One is only interested in the nodal values of the solution. So "the quality of CFD schemes is generally ranked by the order of (Taylor series) truncation"[1]. However, for time dependent problems, this criterion is not sufficient. For example, the exact solution of the linear convection equation (1.1) is $U(x-at)$, and if $U_i^n(x)$ represents the solution function over the grid cell $[x_{i-1},x_i]$ at n time step, the nodal value of solution at the ith node and n+1 time step would be

$$u_i^{n+1} = U_i^n(x_i - a\Delta t) \tag{2.3}$$

So, if local CFL number $\mu = a\Delta t/\Delta x$ is less than one, u_i^{n+1} would be equal to the solution value at a certain interior point within the grid cell $[x_{i-1}, x_i]$ at n time step, i.e. $U_i^n(\xi)$, where

$$x_{i-1} < \xi = x_i - \mu\Delta x < x_i$$

Therefore, different from time independent problems, one is now interested in the accuracy of a numerical scheme over the whole grid cell, not only at nodes. This motivates further examining finite difference schemes from an interpolation point of view.

A classical finite difference scheme is equivalent to locally representing the solution by a Taylor polynomial. The truncation error of a nth order Taylor polynomial $p_n(x)$ is

$$e_n(x) = u(x) - p_n(x) = \frac{(x-x_1)(x-x_2)...(x-x_n)}{n!}(u_{nx})_{x=\xi}$$

$$x_1 < x_2 < ... < x_n \tag{2.4}$$

where $x_1 < \xi < x_n$. For low curvature components, the truncation error is very small because of $(u_{nx})_{x=\xi} << 1$. Also the behavior of the polynomial

$$\phi_n(x) = (x-x_1)(x-x_2)...(x-x_n) \tag{2.5}$$

is not important. Thus, classical high order schemes are still suitable for time-dependent low-curvature solutions.

However, for high curvature components, the behavior of the polynomial $\phi_n(x)$ significantly influences the truncation error $e_n(x)$ because of a large $(u_{nx})_{x=\xi}$. Consider the standard sixth order central scheme for $(u_x)_i$:

$$(u_x)_i = \frac{1}{60\Delta x}(-u_{i-3} + 9u_{i-2} - 45u_{i-1} + 45u_{i+1} - 9u_{i+2} + u_{i+3}) \tag{2.6}$$

The solution is approximated locally in the range $x_{i-3} \le x \le x_{i+3}$ by a polynomial $p_6(x)$:

$$p_6(x) = ax^6 + bx^5 + cx^4 + dx^3 + ex^2 + fx + g$$

with $p_6(x_{i+j}) = u_{i+j}$, j=-3, -2, -1, 0, 1, 2, 3. The truncation error of this approximation is

$$e_6(x) = u(x) - p_6(x) = \frac{(x-x_{i-3})...(x-x_{i+3})}{7!}(u_{7x})_{x=\xi} \tag{2.7}$$

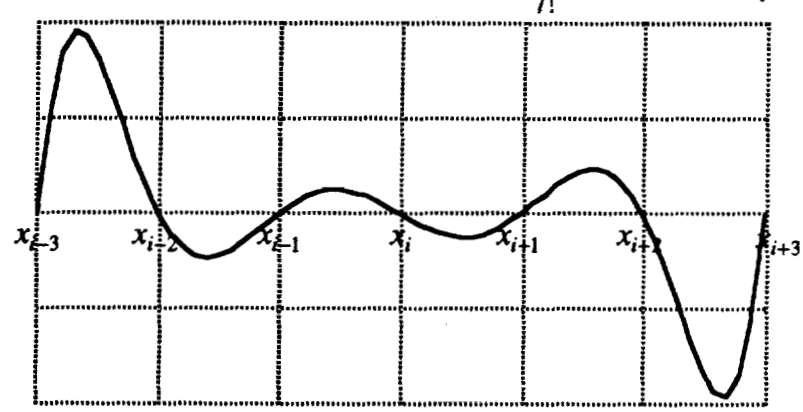

Fig.1 The distribution of $\phi_7(x)$

where $x_{i-3} \le \xi \le x_{i+3}$. Fig.1 is a plot of $\phi_7(x)$:

$$\phi_7(x) = (x - x_{i-3})...(x - x_{i+3}) \tag{2.8}$$

which shows that for large values of n, say, n≥7, the values of $\phi_n(x)$ vary greatly throughout the interval $x_{i-3} \le x \le x_{i+3}$. The values in $[x_{i-3}, x_{i-2}]$ and $[x_{i+2}, x_{i+3}]$ become much larger than the values in the middle of $[x_{i-1}, x_{i+1}]$. As n increases, this disparity also increases[5].

Theorem 2.1 For each n, let $p_n(x)$ be the polynomial interpolant to $f(x) = e^{i\alpha x}$, $\alpha \in \Re$, in the points 0, 1, ..., n. Then

$$\|f - p_n\|_{[0,n]} \to 0 \quad \text{as} \quad n \to \infty$$

if and only if $|\alpha| \le \pi/3$.[6]

This means that increasing the order of a Taylor polynomial interpolant does not necessarily increase the interpolation accuracy, and at least six points per wavelength are required for a good interpolation of solution. Further, repeatedly applying the standard sixth order central scheme (2.6) on the intervals $[x_0, x_6], [x_1, x_7], ..., [x_{N-6}, x_N]$, there are six eigenmodes within each cell[7]. The large truncation errors in $[x_{i-3}, x_{i-2}]$ and $[x_{i+2}, x_{i+3}]$ will appear as spurious roots.

So, for time-dependent high-curvature components which are typical for computational acoustics, if one reduces the number of grid points to make less points than this critical value per wavelength for classical finite difference method, then "a consistent, stable, and convergent high order scheme does not guarantee a good quality numerical wave solution"[1].

THE NEAR-MINIMAX APPROXIMATION METHODS

The last section demonstrates that for time-dependent high-curvature solutions, it is necessary to reduce $\phi_n(x)$ within grid cells. Naturally, the first approach considered is the near-minimax approximation methods, i.e. applying a polynomial interpolant at the Chebyshev points.

Consider once more the sixth order central scheme (2.6). Equivalent to (2.8),

$$\phi_7(x) = (x + 3\Delta x)(x + 2\Delta x)...(x - 3\Delta x) \qquad (-3\Delta x \le x \le 3\Delta x)$$

If we set $\Delta x = 1/3$, then the interpolation points are:

$$0, \ \pm 1/3, \ \pm 2/3, \ \pm 1 \tag{3.1}$$

Theorem 3.1 Let n≥1 be an integer, and consider all possible monic polynomials of degree n. Then the degree n monic polynomial with the smallest maximum on [−1,1] is the modified Chebyshev polynomial $\tilde{T}_n(x)$, and its maximum value on [−1,1] is $1/2^{n-1}$.[5]

So, the smallest possible value of $\max_{x_{i-3} \le x \le x_{i+3}} |\phi_7(x)|$ can be attained with a polynomial

$$\phi_7(x) = \frac{T_7(x)}{2^6} = x^7 - \frac{7}{4}x^5 + \frac{7}{8}x^3 - \frac{7}{64}x \qquad (-1 \le x \le 1)$$

Then one obtains the Chebyshev points:

$$0,\ \pm 0.4338837388,\ \pm 0.7818314826,\ \pm 0.9749279125 \tag{3.2}$$

Consider the construction of the sixth order central scheme on a more general grid:

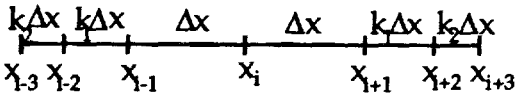

It can be shown, after some algebraic operations, that

$$(\frac{\partial u}{\partial x})_i = \sum_{j=1}^{3} a_j (u_{i+j} - u_{i-j}) \tag{3.3}$$

where $a_1 = 1/e_1 f$, $a_2 = -(1/e_1 + 1/e_2)/d_1^3 f$, $a_3 = 1/d_2^3 e_2 f$, and $d_1 = 1 + k_1$, $d_2 = 1 + k_1 + k_2$, $e_1 = k_1(2 + k_1)$, $e_2 = k_2(2 + 2k_1 + k_2)$, $f = 2\Delta x[1/e_1 - (1/e_1 + 1/e_2)/d_1^2 + 1/d_2^2 e_2]$. Thus for the equally spaced interpolation points of (3.1),

$$a_1 = 2.25,\ a_2 = -0.45,\ a_3 = 0.5 \tag{3.4}$$

and for the Chebyshev points of (3.2), $k_1 = 0.801937737$, $k_2 = 0.445041868$, $\Delta x = 0.4338837388$ and then

$$a_1 = 2.076521402,\ a_2 = -0.797473384,\ a_3 = 0.228243471 \tag{3.5}$$

Fig.2 is a plot of modified wavenumber $\bar{k}$ vs wavenumber k for (3.4) and (3.5), which indicates that a polynomial interpolant at the Chebyshev points can significantly enlarge the resolution range of a numerical scheme. However, the resulting oscillatory behavior of a minimax method is not desired. Therefore, the DRP schemes directly apply the dispersion relation to modify classical high order explicit formulas [1] (the same idea is used on the implicit formulas by the compact finite difference methods with spectral-like resolution [2]).

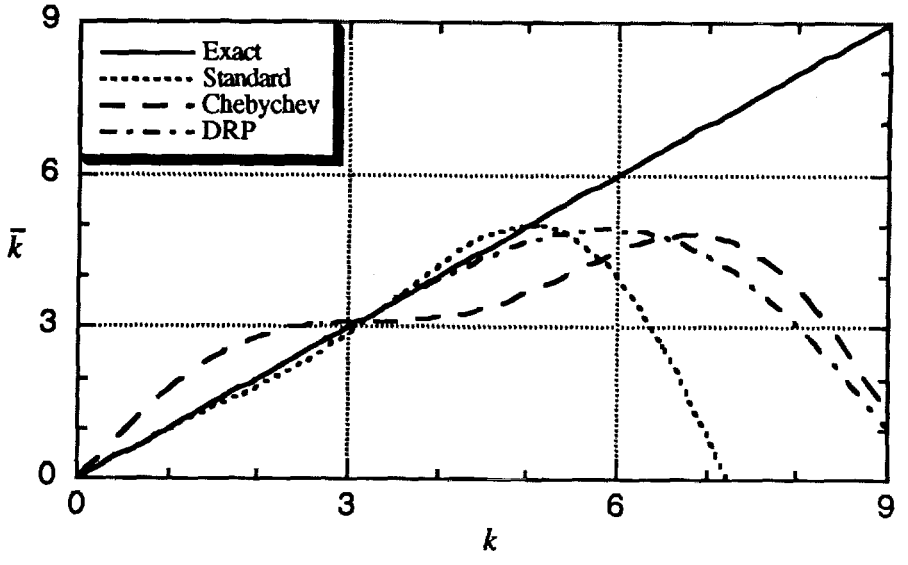

Fig.2 The curve of $\bar{k}$ vs k

More general than (2.1),

$$u_x(x) = \frac{1}{\Delta x}\sum_{j=-N}^{M}\alpha_j u(x+j\Delta x) \tag{3.6}$$

The DRP schemes apply a Fourier transformation to (3.6), then

$$ik\tilde{u}(k) = (\frac{1}{\Delta x}\sum_{j=-N}^{M}\alpha_j e^{ijk\Delta x})\tilde{u}(k)$$

where $\tilde{u}(k) = \frac{1}{2\pi}\int_{-\infty}^{\infty} u(x)e^{-ikx}dx$, and k is the wave number. Define the discrete representation of the exact wave number as

$$\bar{k} = -\frac{i}{\Delta x}\sum_{j=-N}^{M}\alpha_j e^{ijk\Delta x} \tag{3.7}$$

The phase error can be expressed as

$$E = \int_{-\eta}^{\eta}\left|k\Delta x - \bar{k}\Delta x\right|^2 d(k\Delta x) = \int_{-\eta}^{\eta}\left|iK - \sum_{j=-N}^{M}\alpha_j e^{ijK}\right|^2 dK \tag{3.8}$$

Then, for the sixth order central scheme (3.3), the DRP schemes choose α_2 and α_3 to attain fourth order, and determine α_1 to minimize the phase error of (3.8). The data of Tam and Webb are [1]:

$$a_1 = 2.39779929,\ a_2 = -0.56823942,\ a_3 = 0.07955985 \tag{3.9}$$

And Tam and Shen improve them further to[8]:

$$a_1 = 2.31264714,\ a_2 = -0.5001177,\ a_3 = 0.06252942 \tag{3.10}$$

which are closer to the standard values of (3.4).

From Fig.2, it is observed that the result for the DRP scheme (3.10) agrees very well with the dispersion relation to the extent that it is very close to the result for (3.5). It indicates that high order schemes are not necessarily equivalent to high accuracy schemes. If a Taylor polynomial of some degree is being used, then there exists another polynomial of much lower degree that will be of equal accuracy. More importantly, different from classical schemes, increasing the order of the DRP schemes necessarily improves their numerical accuracy within grid cells. Unfortunately, on the other hand, the DRP scheme (3.10) still use the same stencil as the sixth order central scheme (2.6), so the numerical efficiency is not improved. This is because they keep the polynomial interpolation, which is very sensitive to the choice of interpolation points. Then some parameters are needed to attain a certain order, and some to satisfy the dispersion relation. If the accuracy of approximating $U_i^n(x)$ can be automatically improved by increasing the order of an interpolant, then the necessary number of free parameters would be reduced. Actually, such an approach exists, i.e. one-step methods in space discretization, which use piecewise polynomial interpolation.

THE CONSTRUCTION OF HIGH ACCURACY SCHEMES

Numerical solution of differential equations involves two steps: 1) discretize the differential equations; 2) solve the resulting algebraic equations. The numerical stability and accuracy are related to the first step. Indeed, as we discussed above, the discretization step

C-3

includes an interpolation or approximation of solution. Each discretization scheme is equivalent to a certain interpolant. Then a good interpolant would lead to a more accurate and also more stable numerical scheme. Now let us see how to interpolate the solutions of differential equations accurately.

Consider the linear convection equation (1.1):

$$\frac{\partial u}{\partial t} + a\frac{\partial u}{\partial x} = 0 \qquad (a > 0) \tag{1.1}$$

If we approximate the time derivative u_t alone, and leave the space derivative u_x analytic, then (1.1) can be converted into a set of O.D.E.:

$$a\frac{d\vec{u}}{dx} = [A]\vec{u} - \vec{f}(x) \tag{4.1}$$

Define the left- and right-hand eigenvector matrices to be $[X]^{-1}$ and $[X]$ respectively, and $[\Lambda]$ as the diagonal matrix with the eigenvalues λ_i of $[A]$ along the diagonal, then the solutions of (4.1) are

$$\vec{u}(x) = \sum_{i=1}^{IMAX} C_i e^{\lambda_i x/a}\vec{t}_i + [X][\Lambda]^{-1}[X]^{-1}\vec{f} \tag{4.2}$$

where $\vec{t}_i$ are the eigenvectors.

Further, from the so-called $\sigma \sim \lambda$ relation, one finds that indeed, the finite difference methods use the Taylor polynomial to approximate the exponential functions $e^{\lambda_i x/a}$. Therefore, the first order approximation of solution is the piecewise linear interpolation:

$$U_i^n(x) = u_i^n + (u_x)_i^n \cdot (x - x_i) \tag{4.3}$$

and within $[x_{i-1}, x_i]$,

$$(u_x)_i^n = \frac{u_i^n - u_{i-1}^n}{\Delta x} \tag{4.4}$$

which is the first order backward scheme, and within $[x_i, x_{i+1}]$,

$$(u_x)_i^n = \frac{u_{i+1}^n - u_i^n}{\Delta x} \tag{4.5}$$

which is the first order forward scheme. From the exact solution $u(x-at)$, it is natural to introduce the " upwind " concept which is very important to numerical stability:

$$u_i^{n+1} = u_i^n + \frac{u_i^n - u_{i-1}^n}{\Delta x}(-a\Delta t) \tag{4.6}$$

Actually, (4.6) is the first order form of the CIP scheme.

In this level, almost all numerical methods give the same result, and also the same accuracy, i.e. first order. However, from constructing second order schemes, the difference between each method will appear, and lead to the different accuracy within grid cells.

Define a second order approximation as

$$U_i^n(x) = u_i^n + (u_x)_i^n(x - x_i) + \frac{1}{2!}(u_{xx})_i^n(x - x_i)^2 \tag{4.7}$$

The CIP scheme sets $(u_x)_i^n$ as a free parameter to evaluate $(u_{xx})_i^n$:

$$(u_{xx})_i^n = \frac{2}{\Delta x}(u_x)_i^n - \frac{2}{\Delta x^2}(u_i^n - u_{i-1}^n) \tag{4.8}$$

then

$$\begin{cases} u_i^{n+1} = u_i^n + (u_x)_i^n(-a\Delta t) + [\frac{1}{\Delta x}(u_x)_i^n - \frac{1}{\Delta x^2}(u_i^n - u_{i-1}^n)](-a\Delta t)^2 \\ (u_x)_i^{n+1} = (u_x)_i^n + 2[\frac{1}{\Delta x}(u_x)_i^n - \frac{1}{\Delta x^2}(u_i^n - u_{i-1}^n)](-a\Delta t) \end{cases} \tag{4.9}$$

which is second order accurate in both time and space.

A more general way is to evaluate $(u_x)_i$ explicitly by u_i, u_{i-1}, and $(u_x)_{i-1}$:

$$u_{i-1} = u_i - (u_x)_i\Delta x + \frac{1}{2}(u_{xx})_i\Delta x^2 \tag{4.10}$$

$$(u_x)_{i-1} = (u_x)_i - (u_{xx})_i\Delta x \tag{4.11}$$

then

$$(u_x)_i = \frac{2}{\Delta x}(u_i - u_{i-1}) - (u_x)_{i-1} \tag{4.12}$$

$$(u_{xx})_i = \frac{2}{\Delta x^2}(u_i - u_{i-1}) - \frac{2}{\Delta x}(u_x)_{i-1} \tag{4.13}$$

where (4.12) is the second order implicit formula. Obviously, it is also second order accurate, because the second order of this scheme comes from accurately evaluating the second order derivative term. If one uses $(u_x)_i$ instead of $(u_x)_{i-1}$ in (4.13) by (4.12), one would get (4.8) again.

Moreover, there are three second order explicit formulas. As mentioned above, these schemes are equivalent to locally representing the solution in the range $[x_{i-2}, x_i]$, or $[x_{i-1}, x_{i+1}]$, or $[x_i, x_{i+2}]$ by a quadratic polynomial. Apparently, compared with the above two second order accuracy schemes, the "effective stepsize" of these explicit formulas doubles, and therefore in order to keep the same accuracy as one-step methods, it is necessary to reduce the stepsize. More importantly, these explicit formulas generate spurious roots which degrade their numerical accuracy within grid cells. So, increasing the order of a numerical scheme by a larger stencil is not a good idea.

A numerical example illustrates this fact. Consider the linear convection equation (1.1) with $a = 1$, and initial condition

$$u(x,0) = 0.5exp[-ln2(\frac{x}{3})^2] \qquad (-20 \le x \le 450) \tag{4.14}$$

Apply the Trapezoidal scheme in time discretization:

$$u^{n+1} = u^n + \frac{\Delta t}{2}[(u_t)^{n+1} + (u_t)^n] \tag{4.15}$$

which is second order accurate in time and unconditionally stable. In space discretization, the second order implicit formula (4.12), and two different second order explicit formulas are considered: one is the second order central scheme given by (2.2), and the other is second order upwind scheme:

$$(u_x)_i = \frac{1}{\Delta x}\cdot(\frac{3}{2}u_i - 2u_{i-1} + \frac{1}{2}u_{i-2}) \tag{4.16}$$

Also considered is the second order form of the CIP scheme (4.9).

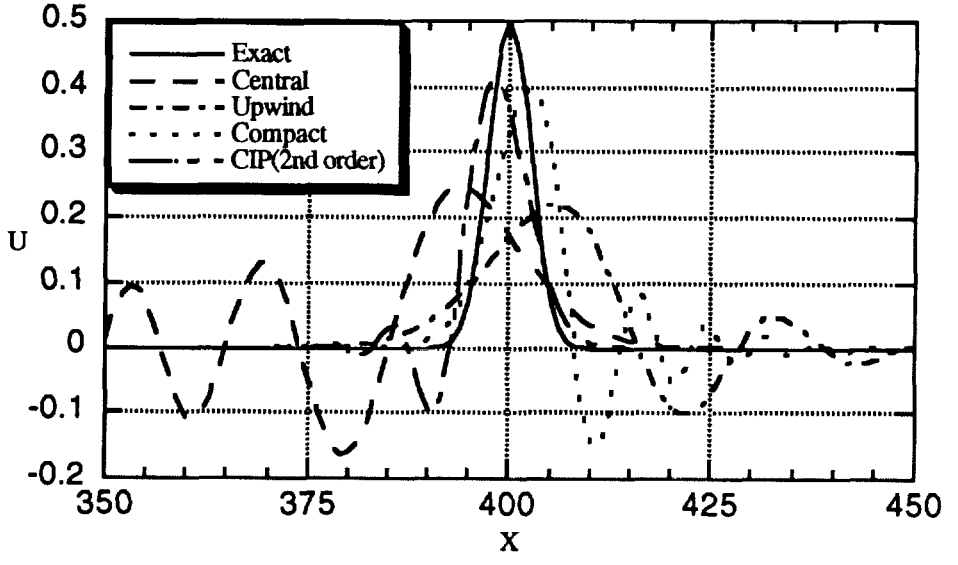

Fig.3 The comparison of various 2nd order schemes $(\Delta x = 1, \mu = 0.8, t = 400)$

Fig.3 shows that although the structures of truncation errors are different for two explicit formulas, and they generate different oscillation positions, the difference between their accuracy is small. Also it is true for the accuracy difference between the second order implicit formula and the second order form of the CIP scheme. However, as expected, there is a large accuracy difference between the second order explicit formulas and the second order accuracy schemes (4.9) and (4.12).

It is also noteworthy that even for continuous solutions, similar to 2nd order central scheme, the 2nd order upwind scheme produces numerical oscillations. So, numerical oscillation is not related to "the apparent contradiction between the physical one-way propagation of waves and the symmetrical central differenced schemes which are direction independent"[9] which is only important to numerical stability. The numerical oscillation results from the accuracy deficiency of the numerical scheme. It will be shown later that with accuracy improvement, the numerical oscillation will disappear.

Continue to think about a third order accuracy scheme:

$$U_i^n(x) = u_i^n + (u_x)_i^n (x - x_i) + \frac{1}{2!}(u_{xx})_i^n (x - x_i)^2 + \frac{1}{3!}(u_{xxx})_i^n (x - x_i)^3 \qquad (4.17)$$

The CIP scheme introduces an additional parameter $(u_x)_{i-1}^n$ combined with the previous nodal condition u_{i-1}^n:

$$\begin{cases} u_{i-1}^n = u_i^n - (u_x)_i^n \Delta x + (u_{xx})_i^n \Delta x^2/2 - (u_{xxx})_i^n \Delta x^3/6 \\ (u_x)_{i-1}^n = (u_x)_i^n - (u_{xx})_i^n \Delta x + (u_{xxx})_i^n \Delta x^2/2 \end{cases}$$

to evaluate $(u_{xx})_i^n$ and $(u_{xxx})_i^n$:

$$\begin{cases}(u_{xx})_i^n = -6(u_i^n - u_{i-1}^n)/\Delta x^2 + [4(u_x)_i^n + 2(u_x)_{i-1}^n]/\Delta x \\ (u_{xxx})_i^n = 6[(u_x)_i^n + (u_x)_{i-1}^n]/\Delta x^2 - 12(u_i^n - u_{i-1}^n)/\Delta x^3\end{cases}$$

Finally one gets

$$\begin{cases}u_i^{n+1} = u_i^n + (u_x)_i^n(-a\Delta t) + [-3(u_i^n - u_{i-1}^n)/\Delta x^2 + (2(u_x)_i^n + (u_x)_{i-1}^n)/\Delta x](-a\Delta t)^2 \\ +\{[(u_x)_i^n + (u_x)_{i-1}^n]/\Delta x^2 - 2(u_i^n - u_{i-1}^n)/\Delta x^3\}(-a\Delta t)^3 \\ (u_x)_i^{n+1} = (u_x)_i^n + 2[-3(u_i^n - u_{i-1}^n)/\Delta x^2 + (2(u_x)_i^n + (u_x)_{i-1}^n)/\Delta x](-a\Delta t) \\ +3\{[(u_x)_i^n + (u_x)_{i-1}^n]/\Delta x^2 - 2(u_i^n - u_{i-1}^n)/\Delta x^3\}(-a\Delta t)^2\end{cases} \tag{4.18}$$

which is third order accurate in both time and space.

However, similar to the difficulty which the explicit formulas meet for constructing a second order accuracy scheme, there is no additional nodal conditions for the implicit formulas to construct a third order accuracy scheme without balances. If the solution within the grid cell $[x_{i-1}, x_i]$ is approximated by $D^4u = 0$, we find that the CIP scheme makes full use of the nodal conditions: u_i, u_{i-1}, $(u_x)_i$, $(u_x)_{i-1}$. So, we would like to say that the CIP scheme is the most efficient third order accuracy scheme.

If one wishes to extend the CIP scheme approach to construct a fourth order accuracy scheme, one must introduce an extra condition besides those four nodal conditions. One could introduce a higher order derivative, or an additional evaluation, or an extra interior point within the grid cell $[x_{i-1}, x_i]$. However, then the numerical efficiency will degrade. Recall that the ultimate goal of using high order schemes is to reduce the number of grid points necessary for a certain accuracy requirement, and thus to enhance the numerical efficiency. So, if the numerical efficiency of a higher order scheme degrades, we would rather choose a lower order scheme with a finer grid, especially an adaptive grid.

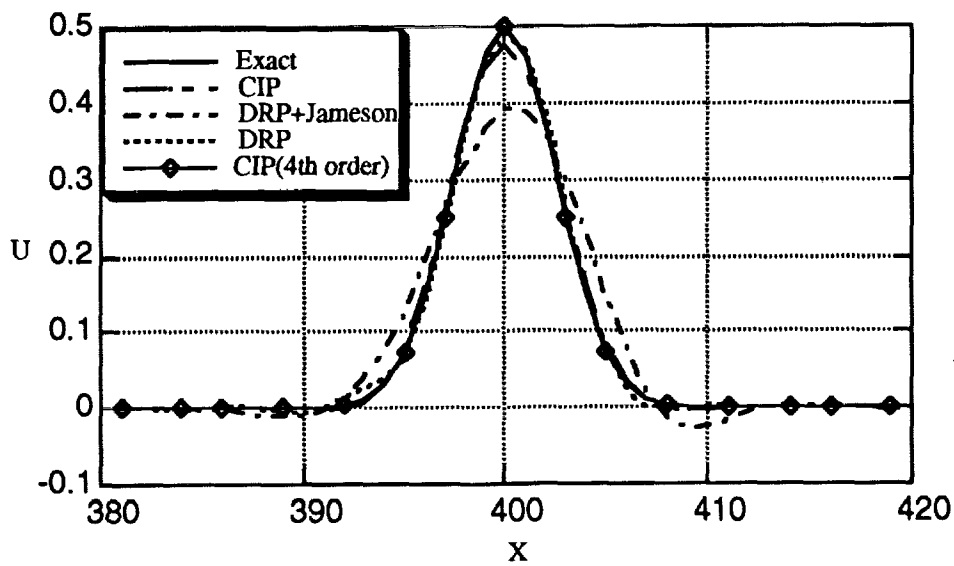

Fig.4 The comparison of DRP schemes and CIP schemes $(\Delta x = 1, t = 400)$

Fortunately, the CIP scheme satisfies the general accuracy requirements well. In Fig.4, the results of the CIP scheme are compared with that of the DRP scheme in space[8] and the third order Jameson scheme in time for the problem (4.14). Both the dissipation and dispersion errors of the CIP scheme are smaller. Further, consider the DRP scheme in both time and space[8], which is a fourth order scheme in space and an optimized four-level scheme in time. Fig.4 shows that the dispersion error of the CIP scheme is still smaller, and the DRP scheme reduces the dissipation error only a little. Moreover, the stability limit of the DRP scheme is: $\mu \leq 0.22857$, and 2000 iterations with $\mu = 0.2$ are used to obtain this result at t=400. On the other hand, a similar result is obtained by the CIP scheme after only 500 iterations with $\mu = 0.8$. In Fig.4, the result of a fourth order form of the CIP scheme which includes the information from second order derivative term is also shown. It is seen that the amplitude is further improved such that the result is indistinguishable from the exact solution.

CONCLUSION

The definition of numerical accuracy according to the order of (Taylor series) truncation is not sufficient for time-dependent problems, especially for computational acoustics. A uniform accuracy over the whole grid cell is required, which is represented by the order of the corresponding piecewise polynomial interpolant. In general, a third-order one-step scheme can satisfy the accuracy requirement. We recommend the CIP scheme for computational acoustics. Further work should be concentrated on the treatment of discontinuity.[10]

REFERENCES

1. C.K.W. Tam and J.C. Webb, J. Comput. Phys. 107, 262 (1993).
2. S.K. Lele, J. Comput. Phys. 103, 16 (1992).
3. T. Yabe and T. Aoki, Comput. Phys. Commun. 66, 219 (1991).
4. C. Hirsch, Numerical Computation of Internal and External Flows Vol.1, 1992.
5. K. Atkinson, Elementary Numerical Analysis (2nd edition), 1993.
6. L.N. Trefethen and J.A.C. Weideman, J. Approx. Theory 65, 247 (1991).
7. J.D. Lambert, Computational Methods in Ordinary Differential Equations, 1973.
8. C.K.W. Tam and H. Shen, AIAA paper 93-4325, 1993.
9. C. Hirsch, Numerical Computation of Internal and External Flows Vol.2, p.408, 1992.
10. L. Tang and J.D. Baeder: The construction of high-order Godunov-type schemes for acoustic equations. (in preparation).

A COMPARATIVE STUDY OF UPWIND AND MACCORMACK SCHEMES* FOR CAA BENCHMARK PROBLEMS

K. Viswanathan
Lockheed Aeronautical Systems Company
Marietta, GA

L. N. Sankar
Georgia Institute of Technology
Atlanta, GA

SUMMARY

In this study, upwind schemes and MacCormack schemes are evaluated as to their suitability for aeroacoustic applications. The governing equations are cast in a curvilinear coordinate system and discretized using finite volume concepts. A flux splitting procedure is used for the upwind schemes, where the signals crossing the cell faces are grouped into two categories: signals that bring information from outside into the cell, and signals that leave the cell. These signals may be computed in several ways, with the desired spatial and temporal accuracy achieved by choosing appropriate interpolating polynomials. The classical MacCormack schemes employed here are fourth order accurate in time and space. Results for category 1, 4, and 6 are presented. Comparisons are also made with the exact solutions, where available. The main conclusions of this study are finally presented.

INTRODUCTION

Application of numerical techniques for the evaluation of acoustic wave propagation has been the subject of recent research, with the current emphasis on reducing community noise and developing quieter aircraft. Higher order schemes are necessary for the evaluation of wave propagation. In this paper, the resolution properties of upwind and MacCormack schemes are evaluated. Both second and fourth order accurate time discretizations have been employed. The upwind schemes discussed in this work have the following advantages. They have built-in dissipation and do not require an explicitly-

* Work done under contract NAS1-20102.

added numerical viscosity. At the far field boundaries, the signals entering the computational domain may be turned off, eliminating reflection of all normal waves. A spatially third-order accurate version of the present class of upwind scheme has been applied to a number of classical aeroacoustics problems. For comparisons, Gottlieb and Turkel's [1] extension of the MacCormack scheme, the 2-4 scheme, and a fourth order accurate temporal discretization of the MacCormack scheme, the 4-4 scheme, have also been used for the solution of the benchmark problems.

NUMERICAL SCHEMES AND SOLUTION PROCEDURE

Category 1 problems test the dissipation and dispersion properties of computational schemes for one dimensional wave propagation. The discretizations used in the upwind and MacCormack schemes are first given. The two stage time integration is illustrated for the upwind scheme and the four stage time integration for the MacCormack scheme. Consider the model problem,

$$\frac{\partial U}{\partial t}+\frac{\partial U}{\partial x}=0 \tag{1}$$

The 2-3 upwind scheme may be written,

$$U_i^{(p)}=U_i^{(n)}-\frac{\Delta t}{\Delta x}\left[U_i^R-U_i^L\right]^{(n)} \tag{2a}$$

$$U_i^{(n+1)}=\frac{1}{2}\left[U_i^{(n)}+U_i^{(p)}-\frac{\Delta t}{\Delta x}\left\{U_i^R-U_i^L\right\}^{(p)}\right] \tag{2b}$$

where superscript (p) denotes the predictor stage. The quantities U_i^R and U_i^L are defined as,

$$U_i^R=U_i+\frac{1}{3}\left[U_{i+1}-U_i\right]+\frac{1}{6}\left[U_i-U_{i-1}\right] \tag{3a}$$

$$U_i^L=U_{i-1}+\frac{1}{3}\left[U_i-U_{i-1}\right]+\frac{1}{6}\left[U_{i-1}-U_{i-2}\right] \tag{3b}$$

The 4-4 MacCormack scheme may be written,

$$U_i^{(1)}=U_i^{(n)}-\frac{\Delta t}{2\Delta x}\left[\Delta Q_1\right] \tag{4a}$$

$$U_i^{(2)}=U_i^{(n)}+\frac{\Delta t}{2\Delta x}\left[\Delta Q_2\right] \tag{4b}$$

$$U_i^{(3)} = U_i^{(n)} - \frac{\Delta t}{\Delta x}[\Delta Q_3] \tag{4c}$$

$$U_i^{(n+1)} = U_i^{(n)} + \frac{\Delta t}{6\Delta x}[\Delta Q_1 + 2\Delta Q_2 + 2\Delta Q_3 + \Delta Q_4] \tag{4d}$$

where the superscripts (1), (2), and (3) denote the intermediate stages. The difference operators ΔQ's are given by

$$\Delta Q_1 = \frac{1}{6}[7U_i - 8U_{i-1} + U_{i-2}]^{(n)} \tag{5a}$$

$$\Delta Q_2 = \frac{1}{6}[7U_i - 8U_{i+1} + U_{i+2}]^{(1)} \tag{5b}$$

$$\Delta Q_3 = \frac{1}{6}[7U_i - 8U_{i-1} + U_{i-2}]^{(2)} \tag{5c}$$

$$\Delta Q_4 = \frac{1}{6}[7U_i - 8U_{i+1} + U_{i+2}]^{(3)} \tag{5d}$$

Problems in categories 4 and 6 involve the solution of the linearized 2-D Euler equations. The effectiveness of wall boundary conditions are tested in category 4. The noise radiated by a flat plate subjected to a gust is computed in category 6. The numerical methodology, using explicit time integration for the solution of the governing Euler equations, was developed by Sankar and is reported in Sankar et al [2]. A brief description is provided here. The computational formulation starts with the 3-D compressible Euler equations in a Cartesian coordinate system:

$$q_t + E_x + F_y + G_z = 0 \tag{6}$$

Here q is the flow properties vector,

$$q = [\rho, \rho u, \rho v, \rho w, e]^T \tag{7}$$

E, F, and G are the inviscid fluxes. The flow field q is decomposed into a mean flow component and a perturbation component,

$$q = \overline{q} + q' \tag{8}$$

The magnitude of the perturbations are usually much smaller than the mean flow. Therefore, the instantaneous fluxes may be expressed as perturbations about the mean flow fluxes. A linearization about the mean quantities permits the evaluation of the flow fluxes from the mean quantities,

$$A = \partial E / \partial q; B = \partial F / \partial q; C = \partial G / \partial q \tag{9}$$

The matrices A, B, and C are the Jacobians of the fluxes E, F, and G, respectively. When the above decompositions are substituted into equation (6), and the unsteady Euler equations for the mean flow are subtracted, a system of equations for the perturbation results,

$$(q')_t + (Aq')_x + (Bq')_y + (Cq')_z = 0 \tag{10}$$

Equation (10) is discretized using standard finite volume schemes as follows. Consider a control volume surrounding node (i,j,k). The governing equation may be cast in an integral form on such a control volume. The divergence theorem is invoked to convert the volume integral to surface integrals, to yield

$$\int_V \frac{\partial q'}{\partial t} dV + \oiint_S [Aq'\hat{i} + Bq'\hat{j} + Cq'\hat{k}].\hat{n} dS = 0 \tag{11}$$

If the coefficient matrices A, B, and C could be computed at the centers of the cell faces in some fashion, the above equation may be written

$$Vol_{i,j,k}\left[\frac{dq'}{dt}\right]_{i,j,k} + \Sigma\left\{\left[A\hat{i} + b\hat{j} + C\hat{k}\right].n\Delta S\right\}q' = 0 \tag{12}$$

where $Vol_{i,j,k}$ is the volume (3-D) or area (2-D) of the control volume.

A number of schemes may be devised for the solution of equation (12), which may be written in a form suitable for time integration as,

$$\frac{dq'}{dt} = -\frac{1}{V}\Sigma Hq' \tag{13}$$

Both two and four stage Runge-Kutta time integrations have been implemented in the code. For the upwind scheme, the matrix H may be split and grouped into two matrices which have only positive or negative eigenvalues, using a similarity transformation. These matrices are computed at the cell faces (i+1/2,j), (i-1/2,j), etc. using Roe averages of the mean flow. The positive eigenvalues correspond to the waves traveling downstream and the negative values to the upstream propagating waves. The flux Hq' is finally computed as

$$Hq' = H^+ q'_L + H^- q'_R \tag{14}$$

The term $H^+ q'_L$, which represents the flux associated with waves traveling from left to right, is computed using the q' values that are weighted towards the nodes upstream or left of the (i+1/2) plane.

Similarly, the term $H^{-}q'_R$, which represents the flux associated with waves traveling from right to left, is computed using an interpolation that is weighted towards the nodes that are to the right of the face (i+1/2). With a sufficiently high order of upwind-weighted interpolation, high formal accuracy may be achieved. In the current calculations, though, a third order upwind-biased interpolation has been used. The difference operators for the x direction are given by

$$q'_L = q'_{i,j} + \frac{1}{3}\left(q'_{i+1,j} - q'_{i,j}\right) + \frac{1}{6}\left(q'_{i,j} - q'_{i-1,j}\right) \tag{15a}$$

$$q'_R = q'_{i+1,j} + \frac{1}{3}\left(q'_{i} - q'_{i+1,j}\right) + \frac{1}{6}\left(q'_{i+1,j} - q'_{i+2,j}\right) \tag{15b}$$

The MacCormack scheme adopts a procedure similar to the one used for the 1-D problem. The fluxes are evaluated using the node points to the left/bottom of the cell face or those on the right/top during alternate sweeps.

RESULTS AND DISCUSSION

Results for categories 1, 4, and 6 are now presented. Figures 1a, 1b, and 1c show the computed and exact solutions for the Gaussian pulse propagation problem at time t=100, 200, 300, and 400. The CFL number for all the calculations is 0.2. In figure 1a, the 2-4 MacCormack scheme with Δx=1.0 and Δt=0.2 is seen to produce oscillations and has a large dissipation. In figure 1b, the 2-3 upwind scheme has a much larger dissipation. There was only a marginal improvement when the CFL number was reduced. Use of a four stage time integration also did not improve the solution when the value of Δx was fixed at 1.0. But there is a dramatic improvement when the spatial resolution is increased. The results from the 2-4 MacCormack scheme with Δx=0.25 is compared with the exact solution in figure 1c. There is a small amount of dissipation but there is very little difference even at t=400. This clearly shows that spatial resolution is a critical factor in wave propagation studies.

Figures 2a, 2b, and 2c show the computed and exact solutions for the spherical wave propagation problem at time t=400. Figure 2a depicts the results from the 4-4 MacCormack and the 4-3 upwind schemes. Here, the frequency $\omega=\pi/8$, Δx=1.0 and Δt=0.01. There are 16 points per wavelength and the MacCormack scheme resolves the wave accurately. The upwind scheme exhibits some dissipation and furthermore, propagates the wave not at the correct speed at large distances from the source. In figure 2b the frequency $\omega=\pi/4$, with the same Δx and Δt. Now there are only 8 points per wavelength and the computed solutions are not good. The upwind scheme has substantial dissipation and damps out the

wave beyond x=100. To further illustrate the importance of spatial resolution, the same case was run with a step size Δx=0.5. In addition, the two stage time integration was used and the CFL number was purposely increased to be 20 times the value used in figure 2b. The comparison, though not very good, is still much better in figure 2c.

For the category 4 problem, the following wall boundary conditions were specified:

$$\frac{\partial p'}{\partial n} = 0 \qquad \frac{\partial \rho'}{\partial n} = 0 \qquad \frac{\partial u'}{\partial n} = 0 \qquad v' = 0 \tag{16}$$

At the other three boundaries, boundary conditions were specified as follows. For the MacCormack schemes, all the flow variables were set to zero. Radiation conditions were not enforced and this is expected to produce some reflections. For the flux splitting scheme, there is an easy way of ensuring that no external waves enter the computational domain. This is achieved by setting the incoming wave (either H^+q_L' or H^-q_R') to zero, as shown in the diagram. At the top boundary $B^-q_R' = 0$.

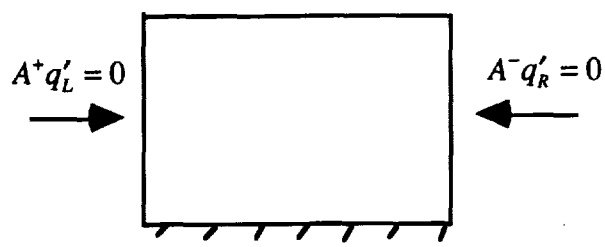

The pressure distributions for problem 1 in category 4, shown in figures 3a and 3b at t=45 and t=100, respectively, have been obtained using the 4-4 MacCormack scheme with Δx=1.0 and Δt=0.25. In figure 3a the pressure distribution is seen to be symmetric. At the later time, there are some oscillations in the solution close to the outflow boundary due to reflection. These oscillations were seen to be less pronounced when the flux splitting scheme was implemented. Figures 4a, 4b, 4c and 4d show comparisons of the wall pressure at different time levels from the two schemes. The pressure distributions at earlier time levels of t=30, 45, and 60, before the pulse reaches the downstream boundary, are compared with the exact solutions in figures 4a and 4b. As can be seen in 4a, the 4-4 MacCormack scheme provides excellent agreement, except for some dissipation at the peaks. The 4-3 upwind scheme has a larger dissipation and the peaks are under-predicted in 4b.

The pressure distributions at time levels t=75, 100, and 150 are shown in figures 4c and 4d. Again, the 4-4 MacCormack scheme produces excellent results away from the outflow boundary. Due to the implementation of simple outflow conditions, reflections from the boundary are seen to produce oscillations which propagate farther into the computational domain with time. In figure 4d, the 4-3

upwind scheme exhibits more dissipation, but the reflections are not quite as severe as for the MacCormack scheme.

Results for the noise radiated by a flat plate in a gust are now presented. The root mean squared pressure is required at a distance of x=±95 and y=±95. For this problem, the MacCormack scheme was chosen because of the large dissipation in the upwind scheme. At the four boundaries, the fluxes were computed using the appropriate conditions for the outgoing waves. Thus, the incoming waves represented by the terms A^+ and B^+ at the left and bottom boundaries, and A^- and B^- at the right and top boundaries, respectively, were set equal to zero. Figure 5a shows the rms pressure contours. Five dominant lobes on the top and bottom may be identified. Also, the solution is seen to be symmetric above and below the plate. The pressure distributions at x=±95 for the top half plane ($0 \le y \le 100$) are shown in figure 5b. As expected, the values at the upstream plane are very low. But in the downstream direction there is a single well-defined peak, the location of which is in good agreement with the solutions presented by Atassi and Tam et al in this workshop. For the pressure distributions at y=±95 (not shown here), the rear lobes are well predicted. But the signal drops off in the forward direction due to dissipation, even with the MacCormack scheme.

CONCLUDING REMARKS

A spatially fourth order accurate MacCormack scheme and a third order upwind scheme have been applied for the solution of the benchmark problems. Both two and four stage Runge-Kutta time integrations have been implemented. The MacCormack scheme provides very good solutions, while the upwind scheme exhibits significant dissipation. The importance of adequate spatial resolution has been emphasized. The use of appropriate one-sided fluxes at the boundaries allows one to turn off non-physical incoming waves. Radiation boundary conditions are necessary to prevent reflected waves from contaminating the solution in the computational domain.

REFERENCES

1. Gottlieb, D.; and Turkel, E.: Dissipative Two-Four Methods for Time Dependent Problems. *Math. Comp.*, vol. 30, 1976, pp. 703-723.

2. Sankar, L. N.; Reddy, N. N.; and Hariharan, N.: A Third Order Upwind Scheme for Aeroacoustic Applications. AIAA-93-0149, January, 1993.

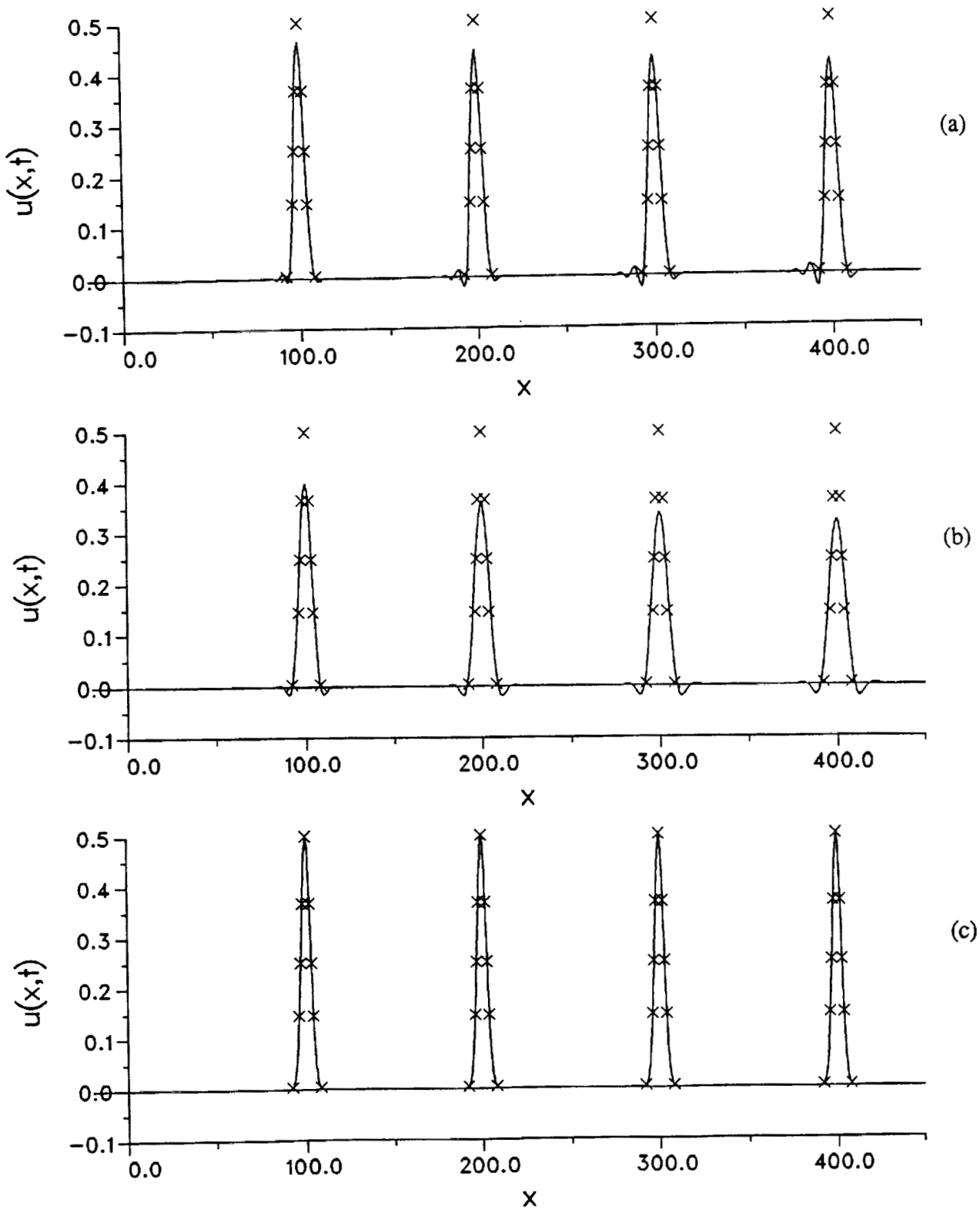

Figure 1. Comparison of exact and computed solutions of Gaussian pulse propagation. Symbols: exact solution, lines: computed solution. (a) 2-4 MacCormack scheme, $\Delta x=1$, CFL=0.2 (b) 2-3 upwind scheme, $\Delta x=1$, CFL=0.2 (c) 2-4 MacCormack scheme, $\Delta x=0.25$, CFL=0.2.

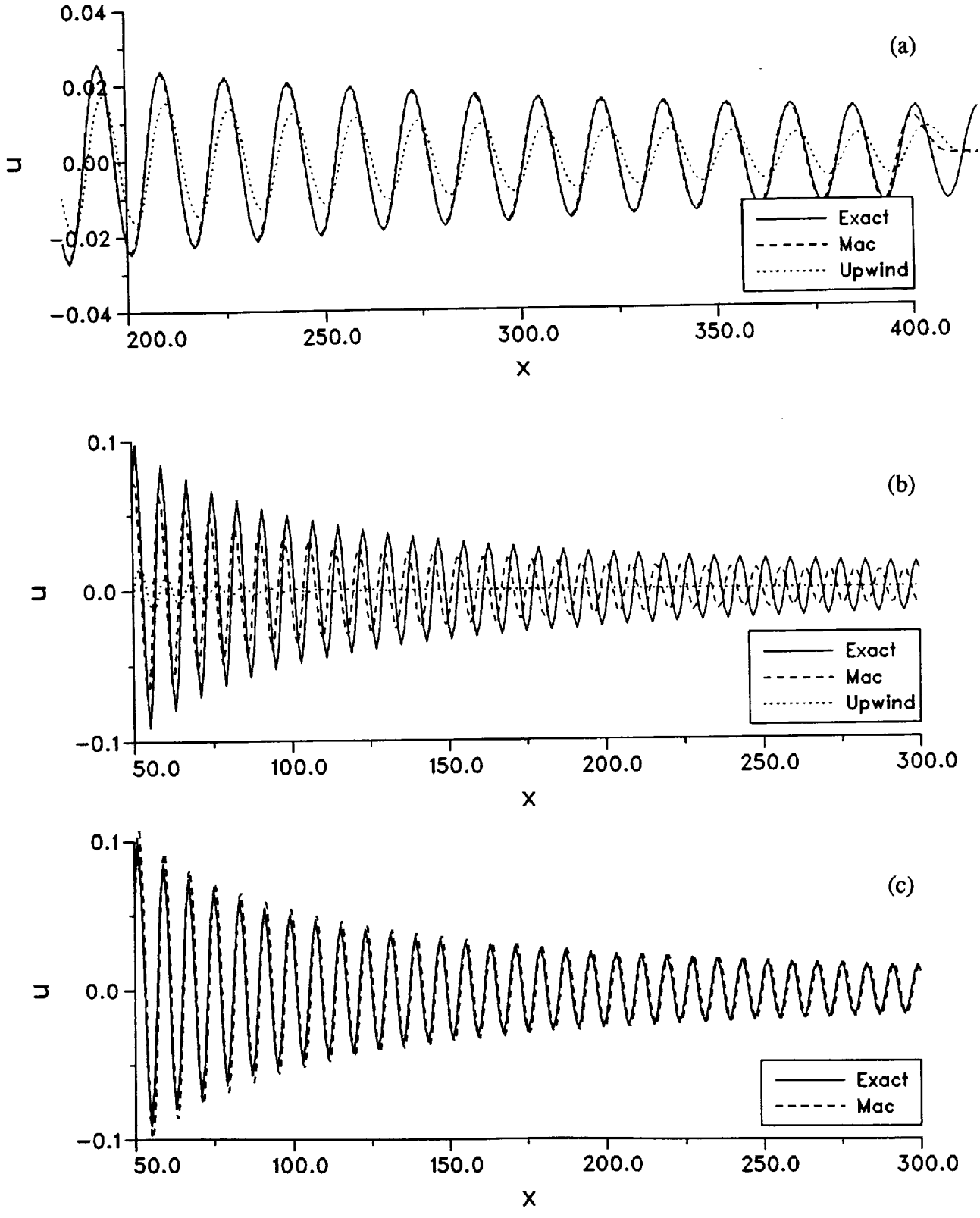

Figure 2. Comparison of exact and computed solutions of spherical wave propagation at time t=400. (a) $\omega=\pi/8$, $\Delta x=1.0$, $\Delta t=0.01$ (b) $\omega=\pi/4$, $\Delta x=1.0$, $\Delta t=0.01$ (c) $\omega=\pi/4$, $\Delta x=0.5$, $\Delta t=0.1$.

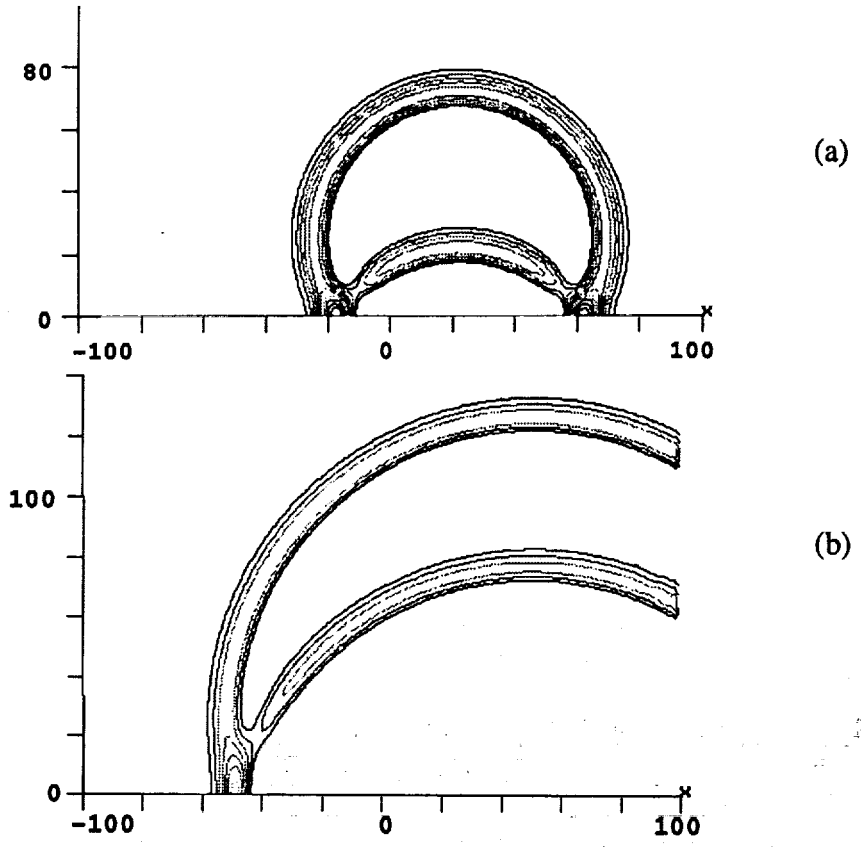

Figure 3. Pressure distributions obtained using 4-4 MacCormack scheme. (a) t=45 (b) t=100.

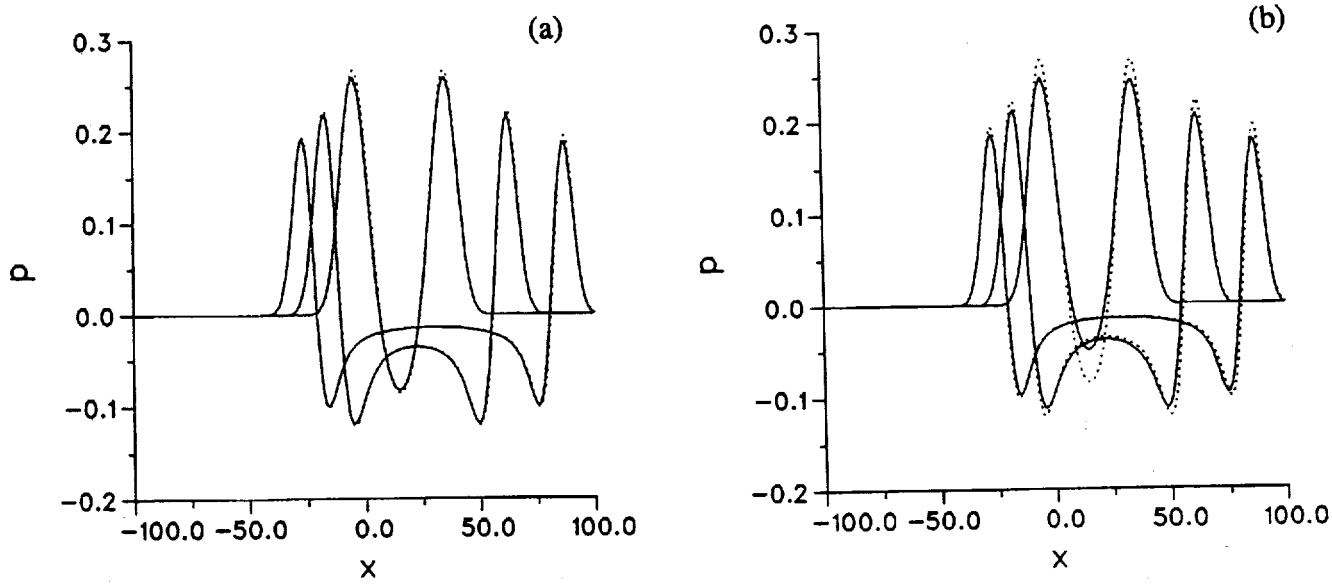

Figure 4. Comparison of computed wall pressure with exact solution. (a) 4-4 MacCormack scheme, t=30, 45, 60 (b) 4-3 upwind scheme, t=30, 45, 60 (c) 4-4 MacCormack scheme, t=75, 100, 150 (d) 4-3 upwind scheme, t=75, 100, 150.

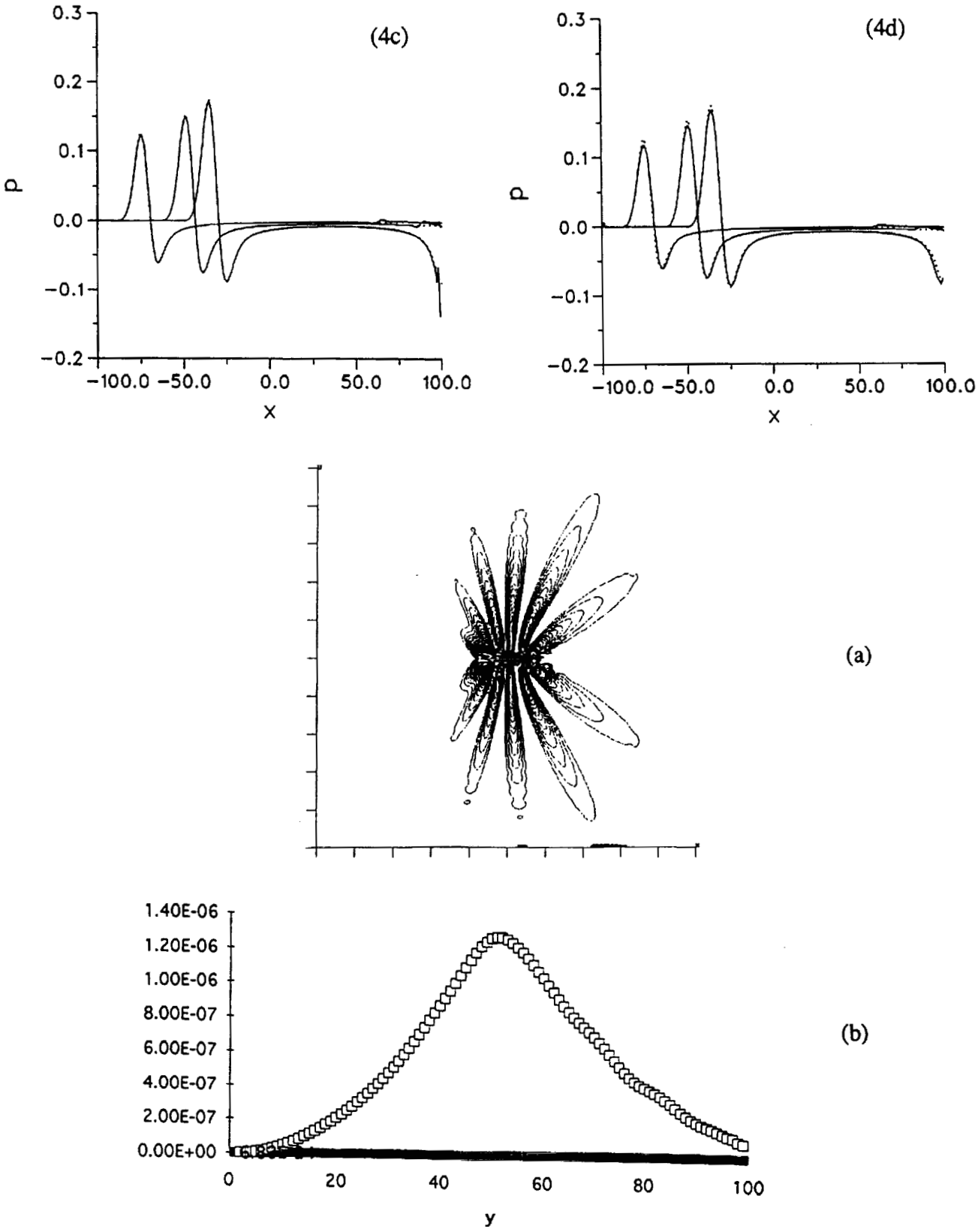

Figure 5. Noise radiated by flat plate in a gust. (a) root mean squared pressure contours (b) pressure distribution in the y direction. Open symbols: downstream, closed symbols: upstream boundary.

APPLICATION OF TRADITIONAL CFD METHODS TO NONLINEAR COMPUTATIONAL AEROACOUSTICS PROBLEMS [1]

Thomas S. Chyczewski and Lyle N. Long
Department of Aerospace Engineering
The Pennsylvania State University, University Park, PA 16802

SUMMARY

This paper describes an implementation of a high order finite difference technique and its application to the category 2 problems of the ICASE/LaRC Workshop on Computational Aeroacoustics (CAA). Essentially, a popular Computational Fluid Dynamics (CFD) approach (central differencing, Runge-Kutta time integration and artificial dissipation) is modified to handle aeroacoustic problems. The changes include increasing the order of the spatial differencing to sixth order and modifying the artificial dissipation so that it does not significantly contaminate the wave solution. All of the results were obtained from the CM5 located at the Numerical Aerodynamic Simulation Laboratory. It was coded in CMFortran (very similar to HPF), using programming techniques developed for communication intensive large stencils, and ran very efficiently.

INTRODUCTION

The occasion of this workshop is testimony to the fact that CAA has matured into a discipline that is somewhat distinct from CFD. Proper propagation of the high frequency, small amplitude waves (compared to hydrodynamic disturbances) associated with aeroacoustics is essential to any successful CAA algorithm, while they often are not considered in CFD. In fact, many CFD algorithms damp out these waves to accelerate the solution to a steady state.

The algorithm presented here is an adaptation of a popular CFD method. The original scheme, developed by Jameson [1], has many desirable features. These include robust shock capturing, good convergence rates and relaxed stability requirements. Also, since it is an explicit algorithm, it is simple to code and performs quite well on parallel processors.

Some of the features that make the original algorithm undesirable for noise predictions include the low order spatial differencing and the nature of the artificial dissipation. The second order spatial operator has very poor wave resolving capabilities. To properly propagate a wave, the second order scheme needs 30 to 40 grid points per wavelength. Considering the high frequency waves that must be resolved, very fine grids are necessary, making the problem computationally stiff.

The artificial dissipation, while having good shock resolving capabilities, can significantly contaminate the acoustic solution. In general, this scheme adds second order dissipation to the entire domain (although in small amounts) and is quite dispersive near discontinuities. Adding the second order dissipation terms to the smooth regions will hamper the advantages of increasing the order of the spatial operator. Also, the dispersion errors generated near discontinuities will likely

[1]Work supported by NASA GSRP Fellowship NGT-51118

convect into the smooth regions affecting the wave propagation there. The modified algorithm increases the order of the spatial operator and provides a dissipation that has good shock capturing qualities while keeping the scheme high order in smooth regions.

An additional advantage is the performance of the algorithm on parallel processors. Explicit schemes, such as the Jameson scheme, are known to run efficiently on these machines [2]. The modifications made here, though, certainly affect the parallel performance. For instance, increasing the spatial order increases the stencil size, thus increasing the interprocessor communication, which leads to poor performance. Modified coding strategies are implemented in the code to reduce the communication time. They have been evaluated and found to make the performance comparable to the original, efficient scheme [3].

NUMERICAL ALGORITHM

The Workshop problems considered here are designed to evaluate a scheme's ability to model nonlinear acoustics. The one dimensional Euler equations in conservative form are used to solve a wave steepening problem and the shock tube problem. The domain is sufficiently large so that there are no boundary condition effects. As mentioned earlier, an adaptation of the Jameson scheme is used. The second order spatial operator is replaced by a sixth order operator derived from Taylor series expansions. An alternative dissipation, considerate of CAA issues, is implemented as a replacement for the one proposed by Jameson. The dissipation has the form

$$\hat{F} = F + \begin{bmatrix} \frac{1}{4} D^2(Q) & \nu > \alpha \\ \frac{1}{64} D^6(Q) & \nu \leq \alpha \end{bmatrix} \tag{1}$$

where

$$\nu = \frac{|P_{i-1} - 2P_i + P_{i+1}|}{P_{i-1} + 2P_i + P_{i+1}} \tag{2}$$

$\hat{F}$ is the filtered flux, F is the unfiltered flux, $D^2(Q)$ is a second order dissipation operator, $D^6(Q)$ is a sixth order operator (both operating on the solution, Q) and α is a free parameter. For $\alpha \geq 1$ the second order dissipation is turned off, resulting in a sixth order scheme everywhere. When $\alpha \leq 0$ the scheme has second order dissipation everywhere. Finally, for $0 < \alpha < 1$ some regions may have second order dissipation while others have sixth, depending on the solution.

RESULTS

In this section, results for the category II problems are presented. For all calculations a CFL number of 0.5 was used. Two different values of α are used to generate the results. A value of 1 is used to illustrate the behavior of the sixth order scheme. Results for a combination of second and sixth order dissipation are also obtained by using $\alpha = \frac{1}{130}$. This number was obtained by trial and error on problem 1 (the same value is used on problem 2).

Figure 1 contains density traces at different sample times for the wave steepening problem (problem 1) for $\alpha = 1$. Noticeable oscillations are observed in front of and behind the shock.

There also appears to be a growth in amplitude of the wave before it shocks. These problems are somewhat suppressed when $\alpha = \frac{1}{130}$ is used. This is illustrated in figure 2. The oscillations are significantly attenuated. There is an undesirable damping of the wave amplitude before it shocks ($t = 10.0$). The wave amplitude at the final sample time ($t = 300.0$), though, is invariant with the type of dissipation.

Figures 3 and 4 contain density traces at different sample times for the shock tube problem. Again, nonphysical oscillations are observed near discontinuities when only sixth order dissipation is used. The addition of the second order dissipation damps these oscillations with minimal smearing of the shock.

CONCLUSIONS

An implementation of a high order finite difference technique and its application to the category 2 problems of the ICASE/LaRC Workshop on CAA is presented. The scheme is essentially an adaptation of the well known Jameson Runge Kutta scheme. The modifications include increasing the order of the spatial operator and implementing a more appropriate dissipation function. It has the advantages of being simple and getting good performance on parallel processors (a 3D Navier-Stokes version of this algorithm achieves 1.25 GFLOPS on a 128 processor CM5 [3]). It has been demonstrated in this paper that the scheme performs quite well on nonlinear problems.

References

[1] Jameson, A., Schmidt, W., and Turkel, E.; "Numerical Solutions of the Euler Equations by Finite Volume Methods Using Runge-Kutta Time-Stepping Schemes," AIAA-81-1259, 1981.

[2] Long, L. N., Khan, M. and Sharp, H. T. (1991) "A Massively Parallel Euler/Navier-Stokes method," *AIAA Journal*, **29**(5).

[3] Chyczewski, T. S. and Long, L. N., "An Efficient Higher Order Accurate Parallel Algorithm For Aeroacoustic Applications", AIAA-94-2265, 1994

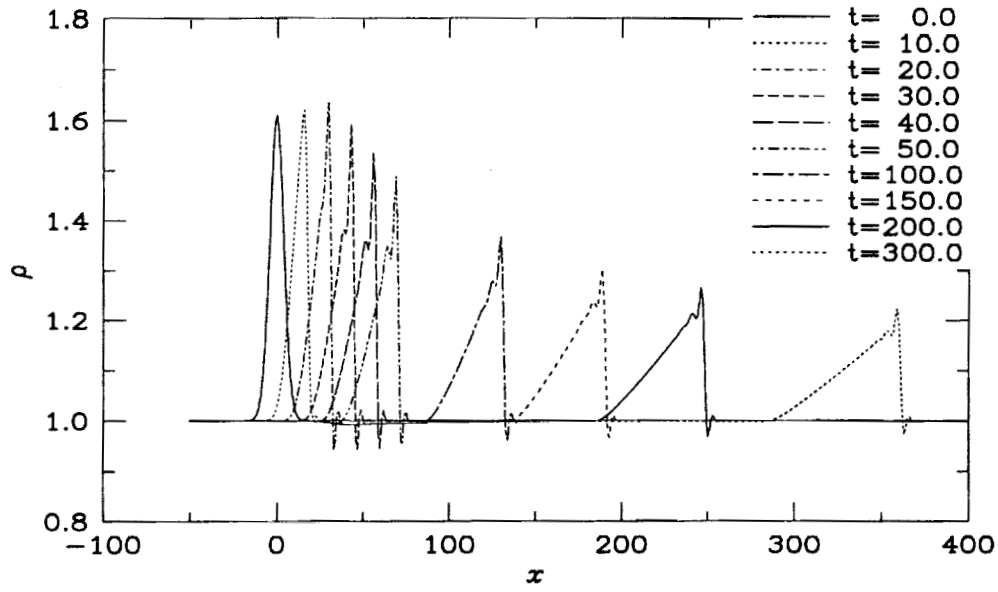

Figure 1: Density profiles, category 2, problem 1, sixth order dissipation

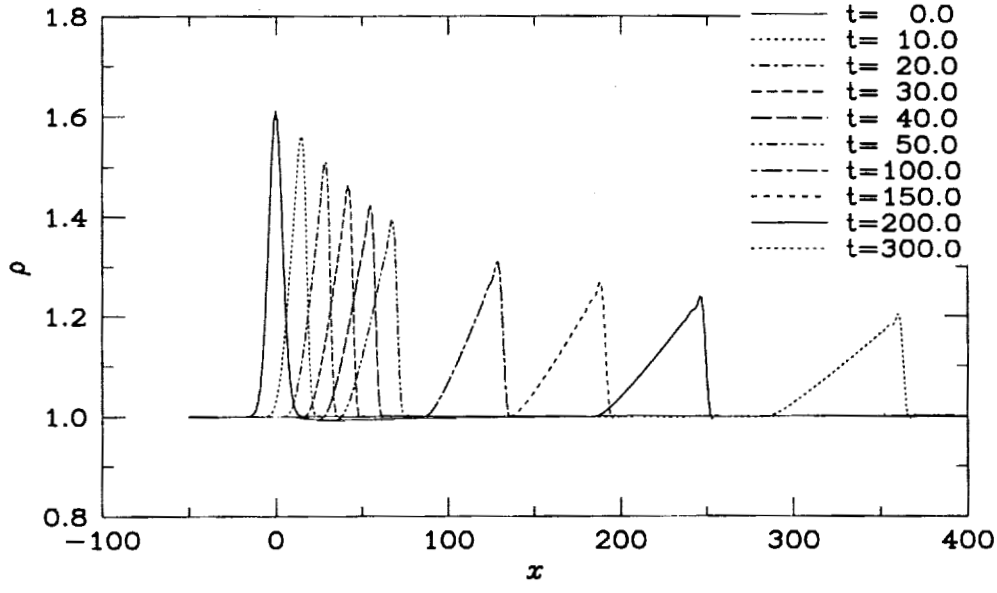

Figure 2: Density profiles, category 2, problem 1, sixth and second order dissipation

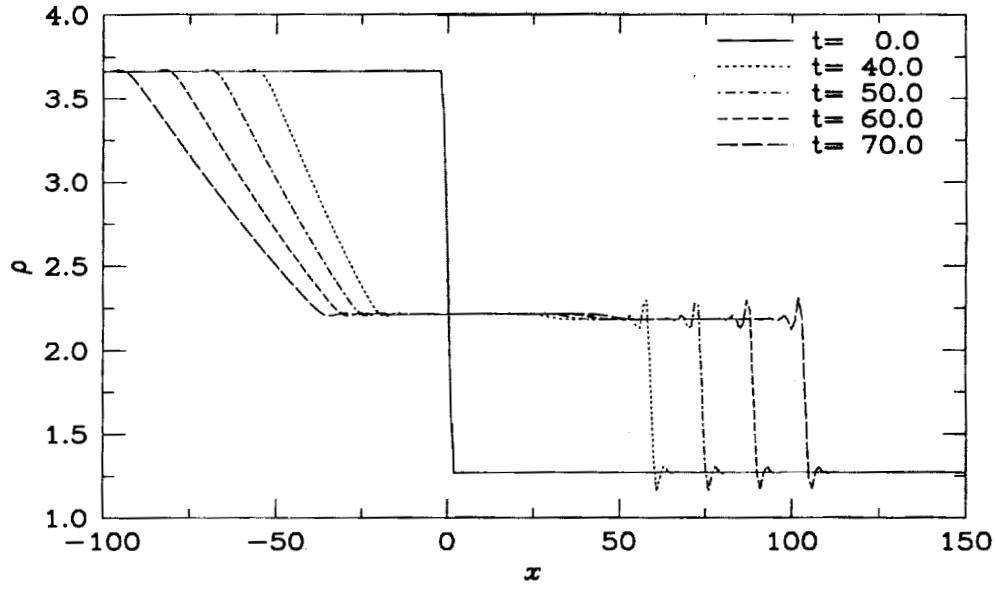

Figure 3: Density profiles, category 2, problem 2, sixth order dissipation

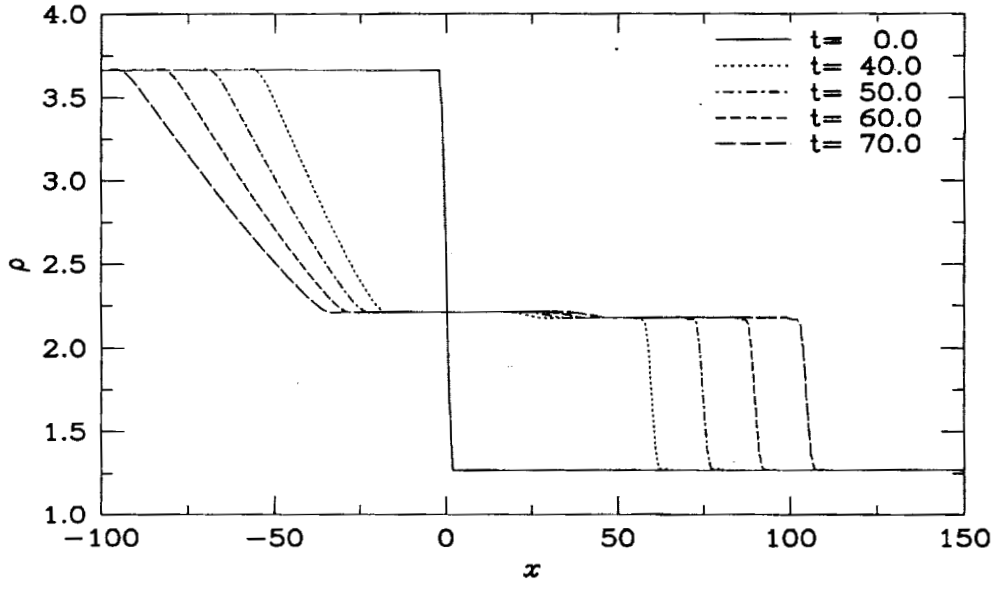

Figure 4: Density profiles, category 2, problem 2, sixth and second order dissipation

EVALUATION OF HIGH ORDER SCHEMES FOR NONLINEAR WAVE COMPUTATIONS

M. Ehtesham Hayder*
Institute for Computational Mechanics in Propulsion
Ohio Aerospace Institute
NASA Lewis Research Center
Cleveland, OH 44135

Abstract

We present results of benchmark problems of the category 2. This category of problems is designed to test the nonlinear wave propagation properties of a computational scheme. We chose three high order spatially accurate algorithms for our computations. These are the Dispersion- Relation- Preserving (DRP) scheme proposed by Tam and his colleagues, a fourth order extension of the MacCormack scheme proposed by Gottlieb and Turkel and an Essentially Non Oscillatory (ENO) scheme proposed by Shu and Osher.

1. Introduction

High order accurate schemes are essential for the computation of the noise source. These schemes have very little numerical dissipation. Numerical solutions with such schemes are very good in the smooth flow region. In this study, the test problems focus on the numerical solution of nonlinear waves. For this type of flow, high order schemes, because of their lack of numerical dissipation, usually generate spurious numerical oscillations near the shock. One may add artificial numerical dissipation to these schemes to suppress spurious oscillations. Tam and his colleagues developed a class of high order schemes, known as the DRP schemes[1, 2, 3] for aeroacoustic computations. They proposed adding a selective artificial damping to capture nonlinear waves in the flow field. Instead of adding artificial dissipation, one may also choose a scheme which is high order accurate and also sufficiently dissipative. The fourth order extension of the MacCormack scheme proposed by Gottlieb and Turkel[4], also known as the 2-4 scheme, is spatially fourth order accurate and is also dissipative. Inherent dissipation allows this scheme to capture weak shocks. There are many shock capturing schemes used for fluid dynamics simulations. Most of these schemes fail to maintain high order accuracy near the shock. As indicated earlier, high order of accuracy is essential for the noise computations and a low order shock capturing scheme may not be suitable for noise computations. Recently a class of high order shock capturing scheme has been developed. These schemes are known as the the Essentially Non Oscillatory (ENO) schemes[5, 6, 7]. They maintain high accuracy even very near the shock and may exhibit only minor oscillations.

In this study, we examine the DRP schemes with artificial dissipation[2, 3]. We also examine the fourth order extension of the MacCormack scheme by Gottlieb and Turkel[4] and an ENO scheme[6, 7]. We present the governing equations and the test problems in section 2. Descriptions of the schemes and discussion of the results of our test problems are presented in sections 3 and 4 respectively.

2. Test problem

We solve the one-dimensional Euler equation written in the following form

$$Q_t + f_x = 0$$

where

$$Q = \begin{pmatrix} \rho \\ \rho u \\ E \end{pmatrix}$$

$$f = \begin{pmatrix} \rho u \\ \rho u^2 + p \\ \rho u H \end{pmatrix}$$

$$P = (\gamma - 1)(E - \frac{1}{2}\rho u^2)$$

$$H = \frac{E + P}{\rho}$$

where ρ, u, P, E and H are the density, velocity, pressure, total energy and enthalpy respectively. We solve two model problems with the following initial conditions.

*Work funded by NASA Cooperative Agreement NCC3-233 through the ICOMP program.

2.1 Test Problem 1

Initial conditions are given as

$$u = \frac{1}{2}e^{-ln2(\frac{x}{9})^2}$$

$$P = \frac{1}{\gamma}(1 + \frac{\gamma-1}{2}u)^{\frac{2\gamma}{\gamma-1}}$$

$$\rho = (1 + \frac{\gamma-1}{2}u)^{\frac{2}{\gamma-1}}$$

The computational domain is -50 $\leq$ x $\leq$ 350.

2.2 Test Problem 2

Initial conditions are

$$\begin{aligned} u &= 0 \\ P &= 4.4, && x < -2 \\ P &= 2.7 + 1.7cos[\tfrac{(x+2)\pi}{4}], && -2 \leq x \leq 2 \\ P &= 1. && x > 2 \\ \rho &= (\gamma p)^{\frac{1}{\gamma}} \end{aligned}$$

The computational domain is -100 $\leq$ x $\leq$ 100.

3. Numerical Schemes

3.1 The DRP Scheme

Tam and Webb[1] developed a numerical algorithm known as the Dispersion Relation Preserving (DRP) scheme for computational acoustics. They chose the coefficients of their spatial discretization scheme by requiring the Fourier transform of the finite difference scheme be a close approximation of that of the partial derivatives. Coefficients of the finite difference time integration method were chosen such that the Laplace transform of the finite difference scheme is a good approximation of the partial derivative. In summary, their scheme for our test problem can be written as

$$K_i^n = -\frac{1}{\Delta x}\sum_{j=-3}^{3} a_j f_{i+j}^n \qquad (3.1)$$

$$Q_i^{n+1} = Q_i^n + \Delta t \sum_{j=0}^{3} b_j K_i^{n-j}$$

$a_0 = 0$, $a_1 = -a_{-1} = 0.79926643$, $a_2 = -a_{-2} = -0.18941314$, $a_3 = -a_{-3} = 0.02651995$, $b_0 = 2.30255809$, $b_1 = -2.49100760$, $b_2 = 1.57434093$ and $b_3 = -0.38589142$. This scheme is formally fourth order accurate in space and third order accurate in time. In a later paper Tam and Shen[3] revised the values of the coefficients a_j to obtain best overall numerical wave characteristics for a 7 point stencil. Revised a_j coefficients are $a_1 = -a_{-1} = 0.770882380518$, $a_2 = -a_{-2} = -0.166705904415$, and $a_3 = -a_{-3} = 0.029843142770$. We used these values of the a_j coefficients for our computations in this paper. Tam and his colleagues[2 3] proposed an artificial selective damping term to remove spurious numerical oscillation from the solution of nonlinear waves. Thus, the equation (3.1) becomes

$$K_i^n = -\frac{1}{\Delta x}\sum_{j=-3}^{3} a_j f_{i+j}^n - \frac{u_{stencil}}{\Delta x R_{stencil}}\sum_{j=-3}^{3} c_j Q_{i+j}^n$$

where $u_{stencil} = |u_{max} - u_{min}|$ is the difference between the maximum and the minimum velocity in the stencil. Unless otherwise mentioned, in this study, we chose all constants as recommended by Tam and Shen[3]. They are, $R_{stencil}$ =0.1, $c_0 = 0.327698660846$, $c_1 = -0.235718815308$, $c_2 = 0.086150669577$ and $c_3 = -0.01428118469$. Coefficients of the artificial damping are chosen to damp high frequency errors. Near a sharp gradient, the proposed scheme with the selective artificial damping loses its formal accuracy (in the sense of an expanded Taylor series).

3.2 Fourth Order MacCormack Scheme

Gottlieb and Turkel[4] extended the standard MacCormack scheme to a spatially fourth order accurate scheme. This is a widely used scheme in flow calculations. We used this scheme for jet flow simulations[8]. This scheme has a predictor and a corrector stage and for our test problem may be written as:

The predictor step with forward differences

$$\bar{Q}_i = Q_i^n + \frac{\Delta t}{6\Delta x}\{7(f_{i+1}^n - f_i^n) - (f_{i+2}^n - f_{i+1}^n)\}$$

The corrector step with backward differences

$$Q_i^{n+1} = \frac{1}{2}[\bar{Q}_i + Q_i^n$$

$$+\frac{\Delta t}{6\Delta x}\{7(\bar{f}_i - \bar{f}_{i-1}) - (\bar{f}_{i-1} - \bar{f}_{i-2})\}]$$

This scheme is second order in time and becomes fourth-order accurate in the spatial derivatives when alternated with symmetric variants. We define L_1 as a one dimensional operator with a forward difference in the predictor and a backward difference in corrector. Its symmetric variant L_2 uses a backward difference in predictor and a forward difference in the corrector. For our computations, the sweeps are arranged as

$$Q^{n+1} = L_1 Q^n$$

$$Q^{n+2} = L_2 Q^{n+1}$$

3.3 Essentially Non-oscillatory Scheme

Essentially Non-Oscillatory schemes were developed to capture shocks and maintain the high order accuracy of the solution. In this paper, we examine the ENO-Roe scheme for spatial discretization and a Runge-Kutta method for time integration. Both these schemes are proposed by Shu and Osher[6, 7]. For our present computations, we chose third order accuracy for both space and time. The Runge-Kutta scheme is may be written as

$$Q^1 = Q^n + \Delta t L(Q^n)$$

$$Q^2 = \frac{3}{4}Q^n + \frac{1}{4}Q^1 + \frac{1}{4}\Delta t L(Q^1)$$

$$Q^{n+1} = \frac{1}{3}Q^n + \frac{2}{3}Q^2 + \frac{2}{3}\Delta t L(Q^2)$$

where L is the finite difference approximation of $-f_x$. The ENO-Roe is an ENO scheme based on the fluxes and selects the locally 'smoothest' stencil using divided differences. The details of this scheme are given in Shu and Osher[7].

4. Results

We used 201 grid points for our computations of the test problems. Characteristic boundary conditions were used at the boundaries. In all our figures, we show profiles of pressure. In Figure 1.1, we show the evolution of the pulse in time. This solution was computed using the fourth order MacCormack scheme. The computed solutions with this scheme show undershoots ahead of the shock. In Figures 1.2 and 1.3, we compare solutions with three schemes at t=10 and t=200. We observe sharp shock profiles with the MacCormack scheme. Solutions of the test problem 2 are given in Figure 2. In Figure 2.1 we show the initial pressure profile and the solutions obtained by using three schemes at t=60. Details of the solutions at this time level are shown in Figures 2.2 and 2.3. In Figure 2.2 we see minor oscillations with the DRP scheme for $R_s = .1$. With $R_s = .05$, the artificial dissipation becomes larger and and it essentially eliminates all oscillations. However, in Figure 2.3 we observe a significant smearing of the shock due to the larger artificial damping. From these two test problems, we found that the fourth order MacCormack scheme gave a sharp shock, but it had a large undershoot ahead of the shock. We did not use any artificial damping with this scheme. The undershoot of the computed solution can likely be damped or eliminated by using artificial dissipation. The DRP scheme with the selective damping gave essentially smooth solutions. One needs to use the proper amount of artificial dissipation to ensure the quality of the solution. The third order ENO-Roe scheme gave clean shocks. The ENO schemes are likely to give very good solutions for problems with shocks. As is known, they can be very expensive to compute. Among the three schemes we studied, the fourth order MacCormack scheme was computationally the most inexpensive. The DRP scheme was observed to be a few times more expensive than the fourth order MacCormack scheme. Even though there were some oscillations and also smearing of the shock, in general solutions of with all three schemes appear to be reasonable within the range of our present study.

References

[1]Tam, C. K. W. and Webb, J. C., (1993), "Dispersion- Relation- Preserving Finite Difference Schemes for Computational Acoustics", *Journal of Computational Physics,* 107, pp 262-281.

[2]Tam, C. K. W., Webb, J. C. and Dong, Z., (1993), "A Study of the Short Wave Components in Computational Acoustics" Journal of Computational Acoustics, Vol. 1, No. 1, pp 1-30.

[3]Tam, C. W. K. and Shen, H., (1993), "Direct Computation of Nonlinear Acoustic Pulses Using High Order Finite Difference Schemes", *AIAA paper* 93-4325.

[4]Gottlieb, D. and Turkel, E. (1976), "Dissipative Two-Four Methods for Time Dependent Problems", *Math. Comp,* Vol 30, pp 703-723.

[5]Harten, A., Engquist, B., Osher, S. and Chakravarthy, S. R., (1987), "Uniformly High Order Accurate Essentially Non-Oscillatory Schemes, III", *Journal of Computational Physics,* 71, pp 231-303.

[6]Shu, C. and Osher, S., (1988), "Efficient Implementation of Essentially Non- oscillatory Shock- Capturing Schemes", *Journal of Computational Physics,* 77, pp 439-471.

[7]Shu. C. and Osher, S. (1989), "Efficient Implementation of Essentially Non- oscillatory Shock-Capturing Schemes, II", *Journal of Computational Physics,* 83, pp 32-78.

[8]Hayder, M. E., Turkel, E. and Mankbadi, R. R.(1993), "Numerical Simulations of a High Mach Number Jet Flow", *AIAA paper* 93-0653, NASA TM 105985.

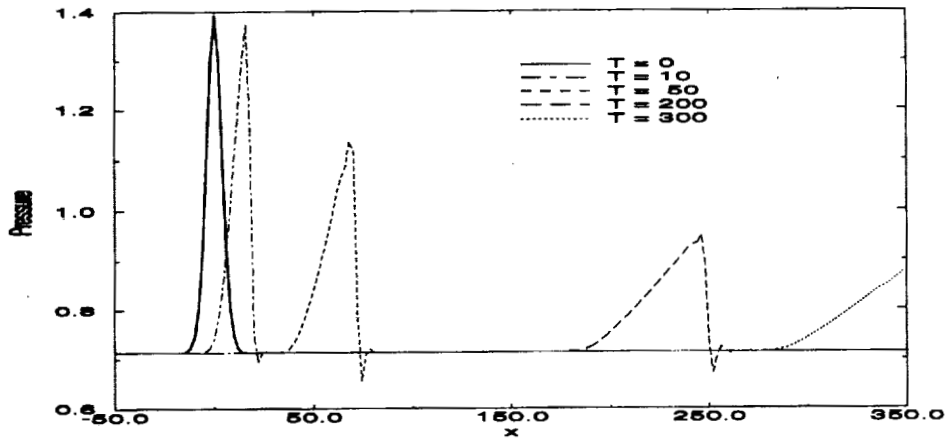

Figure 1.1: Evolution of the pulse

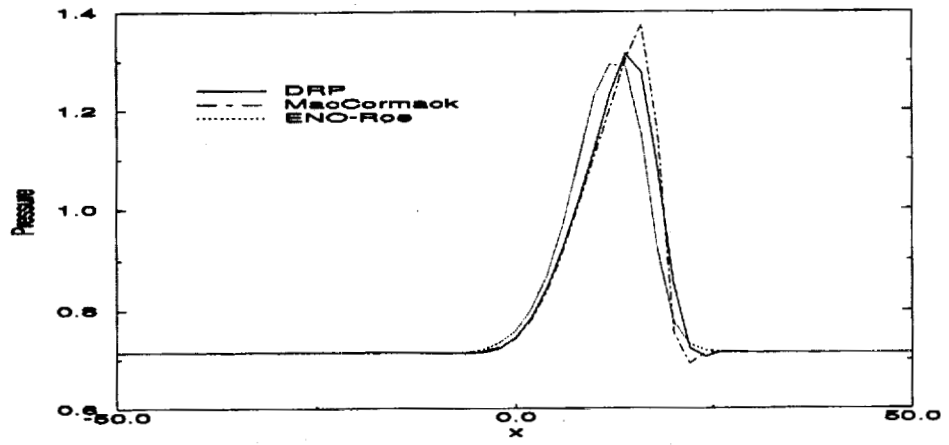

Figure 1.2: Pressure pulse at t=10

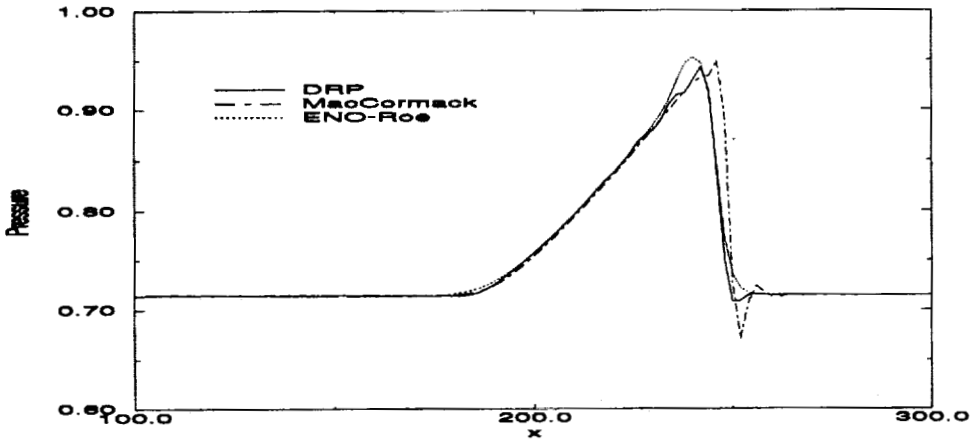

Figure 1.2: Pressure pulse at t=200

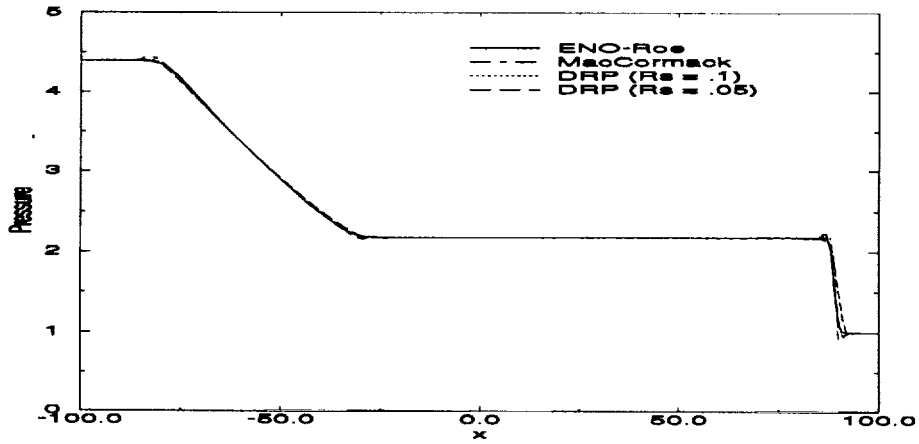

Figure 2.1

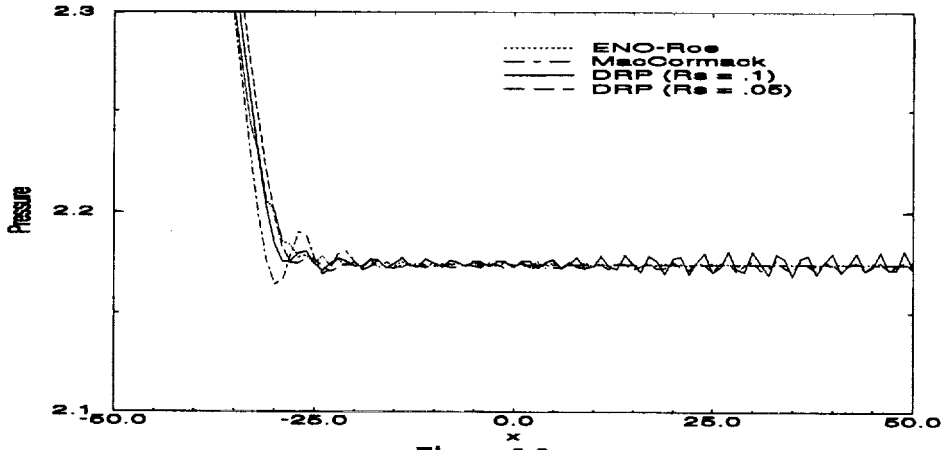

Figure 2.2

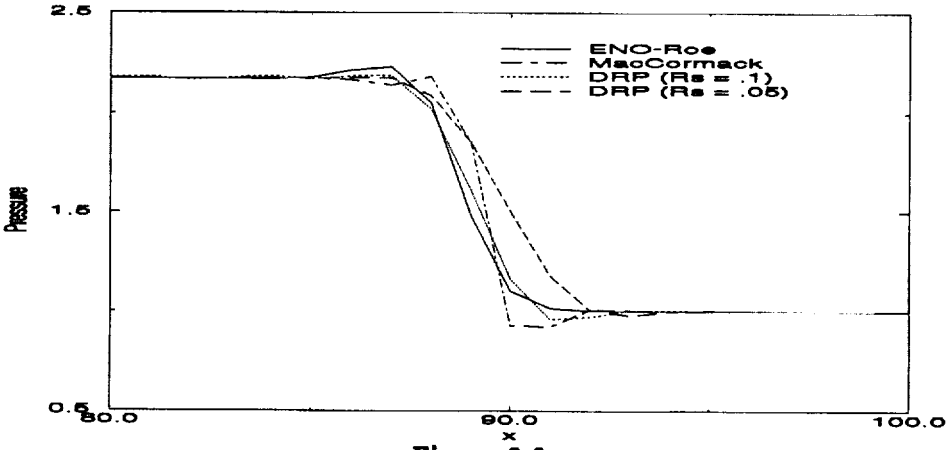

Figure 2.3

Figure 2: Pressure in the computed solution of problem 2 at t=60

TIME ACCURATE APPLICATION OF THE MACCORMACK 2-4 SCHEME ON MASSIVELY PARALLEL COMPUTERS[1]

Dale A. Hudson and Lyle N. Long
Department of Aerospace Engineering
The Pennsylvania State University, University Park, PA 16802

SUMMARY

Many recent computational efforts in turbulence and acoustics research have used higher order numerical algorithms. One popular method has been the explicit MacCormack 2-4 scheme. The MacCormack 2-4 scheme is second order accurate in time and fourth order accurate in space, and is stable for CFL's below 2/3. Current research has shown that the method can give accurate results but does exhibit significant Gibbs phenomena at sharp discontinuities. The impact of adding Jameson type second, third and fourth order artificial viscosity was examined here. Category II problems, the nonlinear traveling wave and the Riemann problem, were computed using a CFL number of 0.25. This research has found that dispersion errors can be significantly reduced or nearly eliminated by using a combination of second and third order terms in the damping. Use of second and fourth order terms reduced the magnitude of dispersion errors but not as effectively as the second and third order combination. The program was coded using Thinking Machine's CM Fortran, a variant of Fortran 90/High Performance Fortran, and was executed on a 2K CM-200. Simple extrapolation boundary conditions were used for both problems.

INTRODUCTION

What is called the MacCormack 2-4 scheme was published in 1976 by Gottlieb and Turkel [1]. The method is a predictor corrector scheme that is second order accurate in time and fourth order accurate in space. The fourth order accurate derivative in space is often cited as being needed to accurately resolve the nonlinear behavior of the flow, especially if turbulence quantities are to be resolved. The split accuracy makes the method truly time accurate when the time and space errors are of approximately equal magnitude. Simple tests such as solving the traveling wave problem for acoustic waves readily shows that wave speed is not accurately reproduced at CFL's significantly larger than 0.25. Therefore it can be said that time accuracy occurs at a CFL of about 0.25 while overall stability can be achieved for CFLs of 2/3 or less. As applied to the Euler equations in a single space direction, the stencil is given as

$$\frac{\partial Q}{\partial t} + \frac{\partial f}{\partial x} = 0$$

$$Q_j^{n+1/2} = Q_j^n - \tfrac{\Delta t}{6\Delta x}(-7f_j^n + 8f_{j+1}^n - f_{j+2}^n), \qquad j = 0, \ldots, N-2.$$

$$Q_j^{n+1} = \tfrac{1}{2}[Q_j^{n+1/2} + Q_j^n - \tfrac{\Delta t}{6\Delta x}(7f_j^{n+1/2} - 8f_{j-1}^{n+1/2} + f_{j-2}^{n+1/2})], \qquad j = 2, \ldots, N.$$

[1]Work supported by NASA Langley Research Center under grant NAG-1-1479

Similar to the second order MacCormack scheme, this method can be time split into separate spatial operators. The time split operator sequence is illustrated by the following equation.

$$Q_{i,j}^{n+2} = L_x(\Delta t_x) L_x(\Delta t_x) Q_{i,j}^{n}$$

Where $L_x(\Delta t_x)$ is the one dimensional predictor corrector operator sequences. Time splitting improves the size of time step for which the method is stable. The operators must be applied in a symmetric sequence to maintain order of accuracy. To avoid biasing errors, each spatial operator is alternated between between a forward-backward and backward-forward sequence of predictor corrector application. The MacCormack method, its characteristics and application are discussed in greater detail in Hudson [2].

The modified equation for the linear wave equation shows that the largest terms of the differencing error are second, third and fourth order derivatives of the solution variables. Artificial viscosity based on similar order terms was investigated. MacCormack and Baldwin [5] developed the use of the second derivative of pressure pressure as part of the coefficient to the damping terms. This feature causes the coefficients increase the applied damping in regions of strong gradients and to reduce damping in smooth regions. Second order differencing was used for the pressure derivative. Jameson *et al.* [4] is cited in Hirsch [3] as having developed the practice of using several derivatives of differing order as part of the damping function. The artificial viscosity terms applied in this work combine these two concepts. Three terms are developed representing second, third and fourth order damping. These terms are applied individually in two combinations; 1) second and third order damping terms and 2) second and fourth order damping terms. The coefficient of each damping term has a unique constant α that has been optimized for its effectiveness. The damping terms are applied to the conservative fluxes and yield the following set of equations.

$$f^{AV} = f - eps^{(2)} \frac{\partial U}{\partial x} - eps^{(3)} \frac{\partial^2 U}{\partial x^2} + eps^{(4)} \frac{\partial^3 U}{\partial x^3}$$

Where

$$eps_i^{(2)} = \alpha_2 \Delta x (|u| + c)_i \frac{|p_{i+1} - 2p_i + p_{i-1}|}{p_{i+1} + 2p_i + p_{i-1}}$$

$$eps_i^{(3)} = \alpha_3 \Delta x^2 (|u| + c)_i \frac{|p_{i+1} - 2p_i + p_{i-1}|}{p_{i+1} + 2p_i + p_{i-1}}$$

$$eps_i^{(4)} = \alpha_4 \Delta x^3 (|u| + c)_i \frac{|p_{i+1} - 2p_i + p_{i-1}|}{p_{i+1} + 2p_i + p_{i-1}}$$

For the workshop problems the constants had the following values: $\alpha_2 = 0.25, \alpha_3 = .9$, and $\alpha_4 = 0.1$. These constants were optimized for the traveling wave problem but were found to be very effective for both the traveling wave and the Riemann problem.

RESULTS

PROBLEM 1

Three cases of the traveling wave problem were solved: case 1 used the basic numerical scheme without any artificial damping, case 2 used second and third order damping terms and case 3 used second and fourth order damping terms. The wave calculation is presented in Figure 1 showing a composite of the nine solution times required. Only the density variable is shown since it adequately shows the wave profile and the numerical influences on the solution.

Significant dispersion error can be seen to occur early and to persist across solution times for case 1. The correct wave form should maintain peak wave magnitude until the shock forms. Solution time 20 occurs before the wave forms a shock and yet it shows dispersion increasing the wave magnitude. Beginning with solution time 30 the wave peak decreases in magnitude but the wave speed and the area under the wave curve were accurately maintained. The dispersion at the front and trailing edge of the wave is considered minor. However, the dispersion occurring at the top of the wave completely destroys any resemblance of a physically correct wave shape. The magnitude of the oscillations appears to be roughly proportional to the magnitude of the initial wave front.

Case 2 provides the best overall matching of the wave form and speed. A combination of second order dissipation and third order dispersion damping are used for this case. As expected it provided the best control of dispersion error in the solution. Figure 2 shows a composite of the nine solution times. The most significant improvement is the correct rendering of the wave magnitude at time 20. The wave magnitude maintains constant amplitude from the initial wave shape and shows only a small amount of wave shape distortion. The wave magnitude begins decreasing at time 30. The reduced dispersion makes the decreasing profile much smoother. The reduced dispersion also significantly reduces the distortion of the wave shape near the peak, but a lot of improvement is still desirable. The wave speed and overall shape are correct.

Case 3 uses second and fourth order dissipation damping. This solution was a significant improvement over the undamped case. The dispersion error was significantly reduced from the undamped case but was not quite as good as the case 2 results. Case 3 results are shown in Figure 3. The wave leading edge dispersion was also reduced in this case. The wave speed and general shape are accurately maintained. The purely dissipative damping of this case has produced significant improvements in the wave shape. But, it still lags the results produced by the combination of dissipative and dispersive damping of case 2.

PROBLEM 2

Problem 2 is the Riemann shock tube problem and the solutions have again been solved in a set of three cases: a) undamped, b) damped by second order dissipation and third order dispersion, and c) by a combination of second and fourth order dissipation. Figures 4, 5, and 6 show the results for these three cases respectively.

In the undamped solution (case a), variable magnitudes in each of the flat regions are accurately produced, as are the shock, contact surface, and front and back edges of the expansion wave. The

dispersion error at each of the discontinuities is the obvious problem with this solution. Oscillations at the top of the shock wave are the most significant.

Case b, use of second and third order damping, shows spectacular elimination of dispersive oscillatory errors. However, this improvement is not without cost. The shock has smeared; the contact surface speed has decreased; and, the point of increasing density at the beginning of the expansion wave has been smeared. But these effects are fairly minor. The expansion wave is still in the correct place. The contact surface has been delayed about the distance traveled in ten time units and the shock is not smeared any wider than one wavelength of the undamped oscillations in case a.

In case c, dissipation was again able to significantly reduce the magnitude of the dispersive errors in the solution. This solution would generally be acceptable for all discontinuities except the shock itself. Significant oscillations at the shock are still large and persist over a greater distance than the shock smearing that occurred in case b. Magnitudes and discontinuity speeds for this case were the same as for the undamped case, including the contact surface.

CONCLUSIONS

The results of this investigation show that combinations of damping terms can be very effective in reducing error introduced into the solution from the differencing scheme. Each damping term was found to contribute both dissipation and dispersion error. Yet, as according to conventional analysis, the even order terms contributed primarily dissipation and the odd order term contributed primarily dispersion behavior. The MacCormack 2-4 scheme has significant dispersion errors especially at the high pressure side of a shock. The addition of dissipation is limited in its ability to reduce these errors, as evidenced by the results of the second-fourth order combination. The second-third order combination produced the results most like the ideal wave forms for the test problems. Interestingly, the second-third order combination produced the only error in the speed of the contact surface for the Riemann problem. Overall, the combination of second and third order terms provided the best elimination of numerical errors.

References

[1] Gottlieb, D. and Turkell, E.;"Dissipative Two-Four Methods for Time-Dependent Problems," *Mathematics of Computation*, Vol. 30 No. 136 Oct 1976, pp 703-723.

[2] Hudson, Dale A.; "Computations of a Confined Shear Layers," Ph.D. Thesis, The Pennsylvania State University, to be published.

[3] Hirsch, C.; *Numerical Computation of Internal and External Flows, Volume 2: Computational Methods for Inviscid and Viscous Flows*, John Wiley and Sons, 1992.

[4] Jameson, A., Schmidt, W., and Turkel, E.; "Numerical Solutions of the Euler Equations by Finite Volume Methods Using Runge-Kutta Time-Stepping Schemes," AIAA Paper 81-1259, June 1981.

[5] MacCormack, R. W. and Baldwin, B. S.;"A Numerical Method for Solving the Time Splitting of Finite Difference Operators." AIAA 75-154, January 1975.

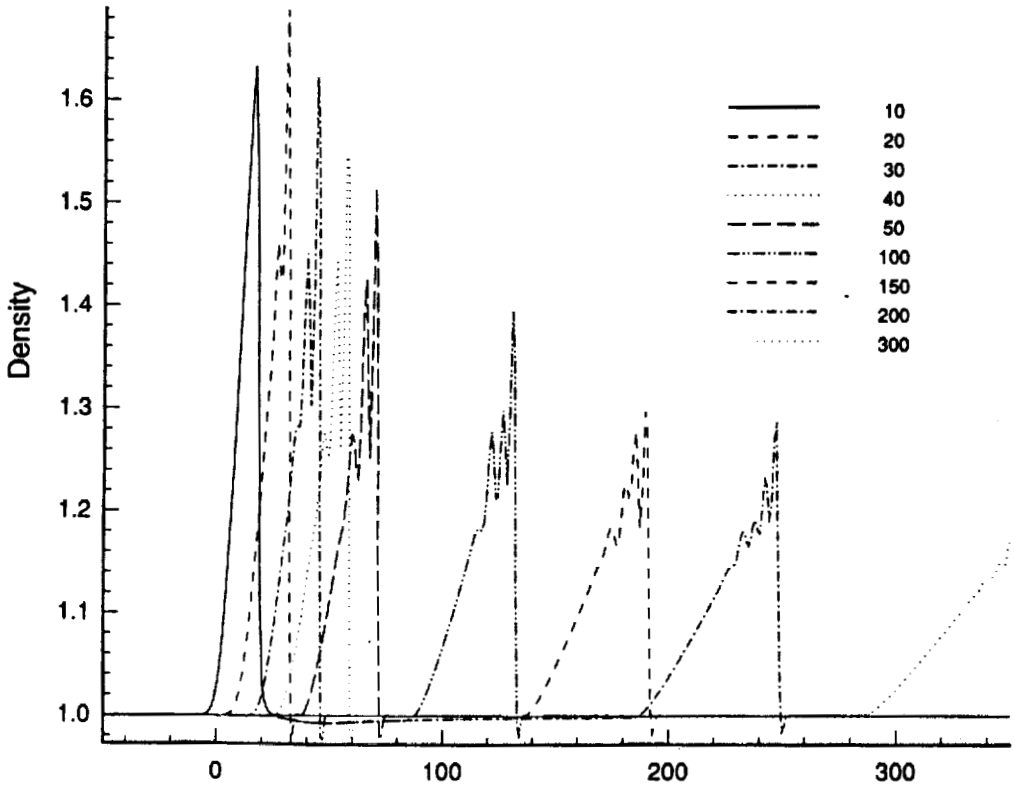

Figure 1. Catagory II Problem 1, Density profile of a traveling wave, solved with no damping, at solution times t=10,20,30,40,50,100,150,200, and 300.

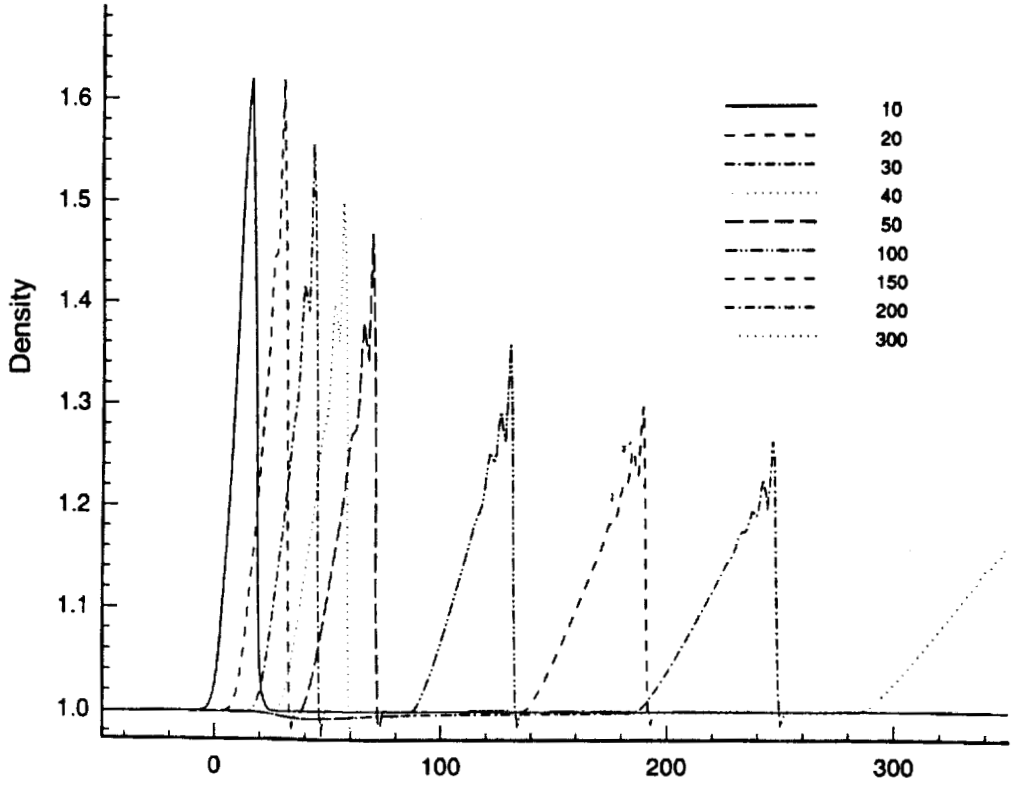

Figure 2. Catagory II Problem 1, Density profile of a traveling wave, solved with second and third order damping, at solution times t=10,20,30,40,50,100,150,200, and 300.

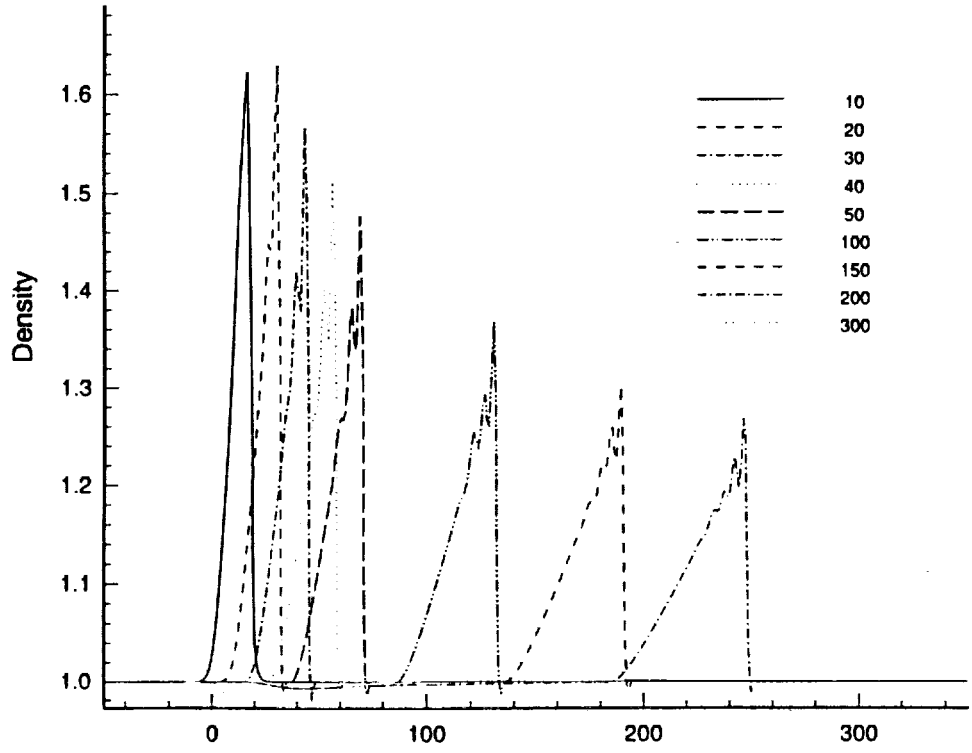

Figure 3. Catagory II Problem 1, Density profile of a traveling wave, solved with second and fourth order damping, at solution times t=10,20,30,40,50,100,150,200, and 300.

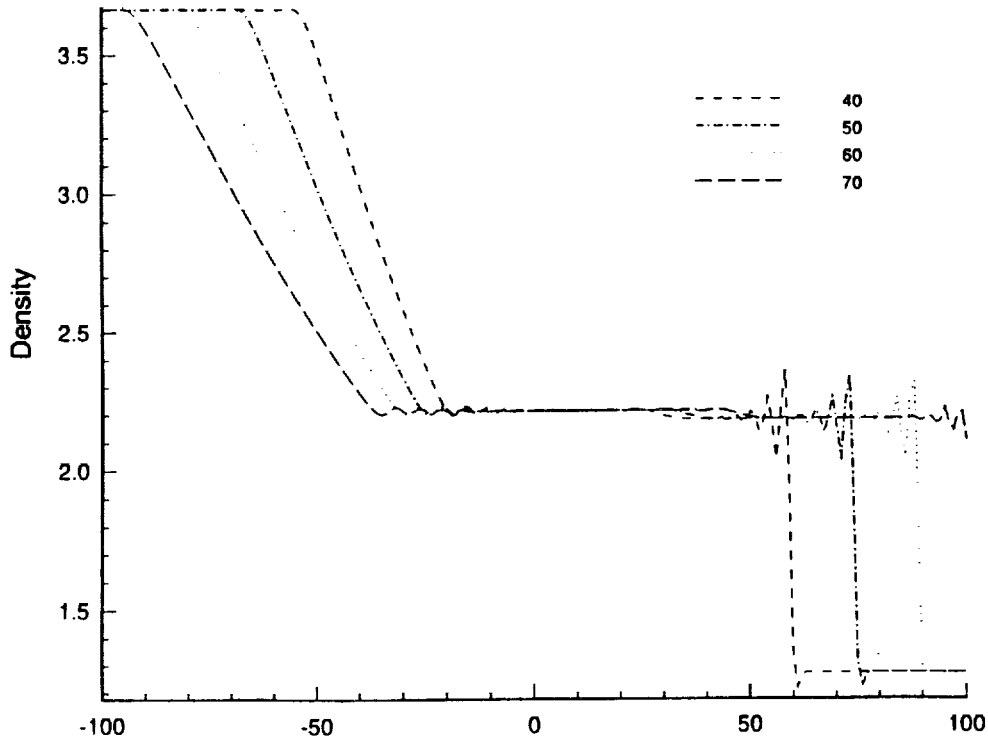

Figure 4. Catagory II Problem 2, Density profile for the Riemann shock tube problem, solved with no damping, at solution times t=40,50,60,and 70.

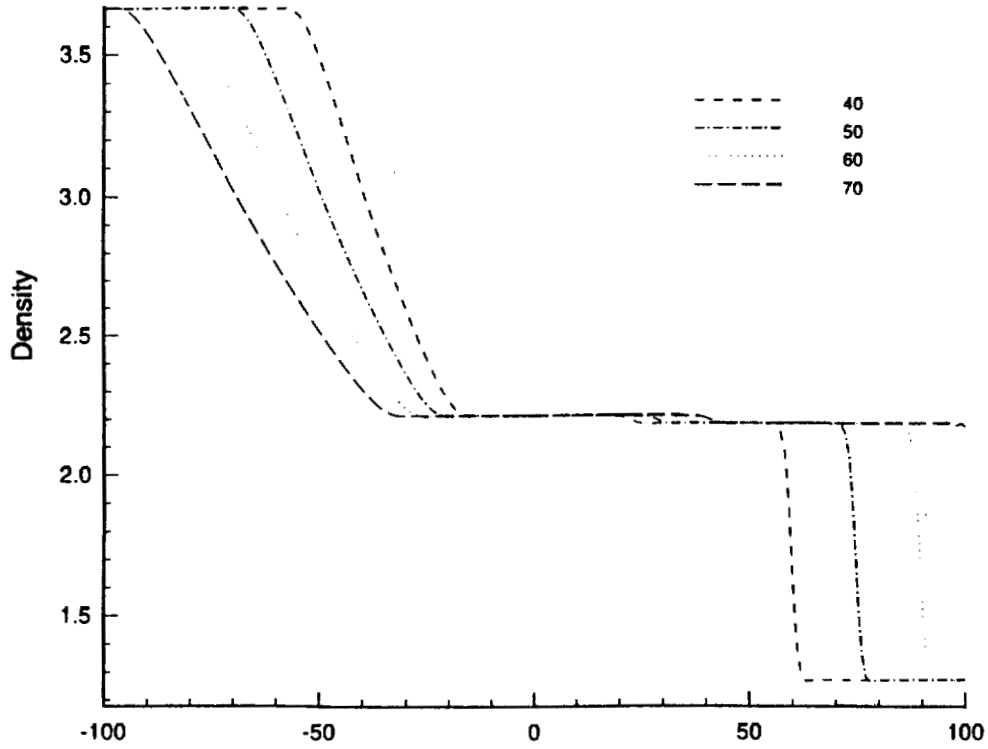

Figure 5. Catagory II Problem 2, Density profile for the Riemann shock tube problem, solved with second and third order damping, at solution times t=40,50,60,and 70.

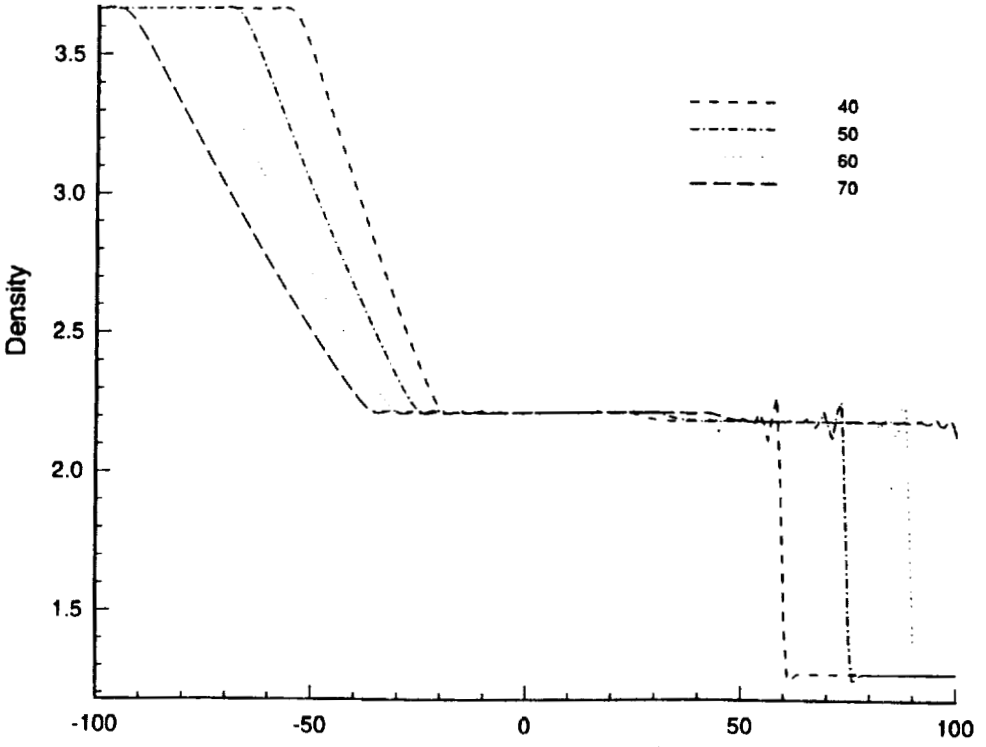

Figure 6. Catagory II Problem 2, Density profile for the Riemann shock tube problem, solved with second and fourth order damping, at solution times t=40,50,60,and 70.

NONLINEAR WAVE PROPAGATION USING THREE DIFFERENT FINITE DIFFERENCE SCHEMES*

(Category 2 Application)

D. Stuart Pope
Lockheed Engineering and Sciences Company
Hampton, VA

J. C. Hardin
NASA Langley Research Center
Hampton, VA

SUMMARY

Three common finite difference schemes are used to examine the computation of one-dimensional nonlinear wave propagation. The schemes are studied for their responses to numerical parameters such as time step selection, boundary condition implementation, and discretization of governing equations. The performance of the schemes is compared and various numerical phenomena peculiar to each is discussed.

INTRODUCTION

The emergence of computational aeroacoustics(CAA) as a discipline distinct from computational fluid dynamics has brought with it a need to develop efficient, reliable numerical schemes. Much is known from CFD concerning performance of particular algorithms, but their application to acoustic problems merits further investigation. In this work, the centered-time centered-space algorithm, and both the second and fourth-order MacCormack explicit predictor-corrector algorithms are applied to two model problems: nonlinear propagation of an acoustic pulse, and wave propagation in a shock tube. These schemes are examined for their ability to propagate discontinuities, damping and dispersion characteristics, and their sensitivities to various numerical considerations.

Common Numerical Considerations

For the schemes to be discussed, several numerical specifications are common to all three. For example, for problem 1, the grid used consisted of 401 evenly spaced points where $-50 \le x \le 350$ so that $\Delta x = 1.0$. Similarly for problem 2, a grid of 201 evenly spaced points is used in all computations with $-100 \le x \le 100$ so that again, $\Delta x = 1.0$. Additionally, a time step of either $\Delta t = .25$ or $\Delta t = .50$ is used in all computations. Initial calculations with $\Delta t = .75$ and $\Delta t = 1.0$ proved unstable for all schemes.

* Work done on contract at Lockheed Engineering and Sciences Company, NAS1-19000.

The boundary conditions used in all calculations are based on characteristics theory. By noting that along characteristic lines the quantity $\frac{2a_o}{\gamma-1}+u$ is conserved at inflow while $\frac{2a_o}{\gamma-1}-u$ is conserved at outflow, requiring no incoming acoustic or entropy waves reduces these quantities to $\frac{2}{\gamma-1}$ and the following relations can be obtained:

Inflow:

$$\frac{\partial \rho}{\partial t}+(u-a_o)\frac{\partial \rho}{\partial x}=0 \tag{1}$$

$$\frac{\partial u}{\partial t}+(u-a_o)\frac{\partial u}{\partial x}=0 \tag{2}$$

Outflow:

$$\frac{\partial \rho}{\partial t}+(u+a_o)\frac{\partial \rho}{\partial x}=0 \tag{3}$$

$$\frac{\partial u}{\partial t}+(u+a_o)\frac{\partial u}{\partial x}=0 \tag{4}$$

where

$$p=\frac{\rho^\gamma}{\gamma} \tag{5}$$

$$a_o^2=\rho^{\gamma-1} \tag{6}$$

and γ=1.4. Derivatives are implemented using first-order one-sided differences.

Centered-Time Centered-Space Algorithm

For linear problems, the centered-time centered-space(CTCS) scheme reproduces the exact solution with the proper selection of time step and is second-order accurate in both space and time[1]. Its marginal stability characteristics make it highly desirable for its ability to perfectly advect initial disturbances in applications where the propagation speed is constant. However, for our model problems, the propagation speed is not constant and it is natural to ask how the scheme performs in this case. The discretized equations are

$$\frac{\rho_i^{n+1}-\rho_i^{n-1}}{2\Delta t}+\frac{(\rho u)_{i+1}^n-(\rho u)_{i-1}^n}{2\Delta x}=0 \tag{7}$$

$$\rho_i^n\left(\frac{u_i^{n+1}-u_i^{n-1}}{2\Delta t}+u_i^n\frac{u_{i+1}^n-u_{i-1}^n}{2\Delta x}\right)=-\frac{p_{i+1}^n-p_{i-1}^n}{2\Delta x} \tag{8}$$

$$\frac{p_i^{n+1}-p_i^{n-1}}{2\Delta t}+u_i^n\frac{p_{i+1}^n-p_{i-1}^n}{2\Delta x}+\gamma p_i^n\frac{u_{i+1}^n-u_{i-1}^n}{2\Delta x}=0 \tag{9}$$

For both problems 1 and 2, this particular discretization(referred to as 'attempt 1') becomes unstable early in the flow evolution. Changing Δt from .50 to .25 does not help, though some high frequency content apparent in the solution for Δt= .50 is removed from the smaller time step calculations. In an

[1]Roache, Patrick J. Computational Fluid Dynamics. Hermosa Publishers, 1972, pp. 53-55.

effort to stabilize the calculations, equation(7) is re-discretized(attempt 2) wherein the momentum term is broken up, i.e.,

$$\frac{\rho_i^{n+1}-\rho_i^{n-1}}{2\Delta t}+\rho_i^n\frac{u_{i+1}^n-u_{i-1}^n}{2\Delta x}+u_i^n\frac{\rho_{i+1}^n-\rho_{i-1}^n}{2\Delta x}=0 \tag{10}$$

This discretization also fails to stabilize the calculations and the only noticeable change over attempt 1 is an introduction of undesirable high frequencies for both problems 1 and 2. In a further attempt at stabilization, the coefficients ρ_i^n and u_i^n of equation (10) can be spatially averaged:

$$\frac{\rho_i^{n+1}-\rho_i^{n-1}}{2\Delta t}+\left(\frac{\rho_{i+1}^n+\rho_{i-1}^n}{2}\right)\frac{u_{i+1}^n-u_{i-1}^n}{2\Delta x}+\left(\frac{u_{i+1}^n+u_{i-1}^n}{2}\right)\frac{\rho_{i+1}^n-\rho_{i-1}^n}{2\Delta x}=0 \tag{11}$$

This change(attempt 3) reduces the high frequency oscillations introduced by breaking up momentum in the continuity equation, but gives no real improvement. Finally, spatial averaging of difference coefficients may be applied to all three governing equations(attempt 4) which further removes the high frequency content and stabilizes the calculations to much later values of time. However, ultimately this attempt also fails to produce a stable solution. A snapshot of the four attempts is given in figure 1 for $\Delta t = .50$. For problem 2, the first three attempts become unstable almost immediately. The fourth attempt yields a somewhat stable, although erratic solution as depicted in figure 2. Note that the ill-behaved compression front is only slightly amplified as it travels to the right. The leftward propagating expansion wave remains somewhat well-behaved and as in problem 1, reducing Δt from .50 to .25 removes some of the high frequency oscillations. In summary, the CTCS scheme, despite all efforts at stabilization, fails to give acceptable results for either problem considered.

Second-Order MacCormack Scheme

Using MacCormack's method of second order, the discretized equations have the form:

Predictor

$$\rho_i^* = \rho_i^n - \frac{\Delta t}{\Delta x}\left[(\rho u)_i^n - (\rho u)_{i-1}^n\right] \tag{12}$$

$$u_i^* = u_i^n - \frac{\Delta t}{\Delta x}\left[u_i^n\left(u_i^n - u_{i-1}^n\right) + \frac{1}{\rho_i^n}\left(p_i^n - p_{i-1}^n\right)\right] \tag{13}$$

$$p_i^* = p_i^n - \frac{\Delta t}{\Delta x}\left[u_i^n\left(p_i^n - p_{i-1}^n\right) + \gamma p_i^n\left(u_i^n - u_{i-1}^n\right)\right] \tag{14}$$

$$(\rho u)_i^* = \rho_i^* u_i^* \tag{15}$$

Corrector

$$\rho_i^{n+1} = \frac{1}{2}\left\{\rho_i^n + \rho_i^* - \frac{\Delta t}{\Delta x}\left[(\rho u)_{i+1}^* - (\rho u)_i^*\right]\right\} \tag{16}$$

$$u_i^{n+1} = \frac{1}{2}\left\{u_i^n + u_i^* - \frac{\Delta t}{\Delta x}\left[u_i^*\left(u_{i+1}^* - u_i^*\right) + \frac{1}{\rho_i^*}\left(p_{i+1}^* - p_i^*\right)\right]\right\} \tag{17}$$

$$p_i^{n+1} = \frac{1}{2}\left\{p_i^n + p_i^* - \frac{\Delta t}{\Delta x}\left[u_i^*\left(p_{i+1}^* - p_i^*\right) + \gamma p_i^*\left(u_{i+1}^* - u_i^*\right)\right]\right\} \quad (18)$$

$$(\rho u)_i^{n+1} = \rho_i^{n+1} u_i^{n+1} \quad (19)$$

For this method, there is no problem with stability for either time step for either problem. However, for problem 1, the propagating wavefront becomes more spread out over space at later time as Δt is decreased from .50 to .25. For both time steps, the wavefront location as a function of time is the same. For the CTCS scheme, various forms of the discretization were used in attempts to achieve stability. While stability is not the issue for this scheme at these time steps, the same attempts at varying the form of the discretization are tried again to see their effects on a well-behaved scheme. It was found that breaking up the momentum term in the continuity equation discretization as well as averaging of the difference term coefficients in the governing equations made only slight changes in the results. One noticeable result for problem 2 is the introduction of high frequencies behind the compression front when Δt is lowered from .50 to .25. All attempts give very similar results and those of attempt 1 appear as figure 3.

Fourth-Order MacCormack Scheme

Both the CTCS and the MacCormack scheme examined so far are of second order in both time and space. A spatially fourth-order MacCormack scheme was implemented to study the effect of spatial order on the computations. The discretized equations for this method are the same as those of the second-order MacCormack except for the forward and backward spatial differencing operator used. In particular, differences are replaced with their fourth-order counterparts in all equations, i.e.,

$$\left(\frac{\partial \phi}{\partial x}\right)_i^* = \frac{7\phi_i^n - 8\phi_{i-1}^n + \phi_{i-2}^n}{6\Delta x} \quad (20)$$

$$\left(\frac{\partial \phi}{\partial x}\right)_i^{n+1} = \frac{-7\phi_i^* + 8\phi_{i+1}^* - \phi_{i+2}^*}{6\Delta x} \quad (21)$$

Adjacent to the computational boundaries, second-order differences are used. In the fourth-order results, fewer high frequency oscillations are observed than in the second-order results for both problems at both $\Delta t = .50$ and $\Delta t = .25$ and in general, the solutions are better resolved than those of the second-order MacCormack method. As in the second-order MacCormack method, the computations seem nearly insensitive to the form of the discretization used, so that breaking up the momentum term in continuity as well as spatial averaging of difference coefficients has negligible effect. A comparison of the two MacCormack methods for both problems is given in figure 4.

CONCLUSION

Three finite difference schemes commonly used in CFD have been examined for their application to acoustic propagation. The CTCS scheme appears inadequate for these nonlinear model problems and is, in fact, unstable. The two MacCormack schemes, while stable, fail to resolve the discontinuous wavefronts arising in the problem solutions and are perhaps, poor candidates for solution of these problems. This work illustrates the need for a thorough understanding of applied algorithms with regard to the impact of choices such as time step, forms of discretization, and boundary condition implementation, as all exert a strong influence on the quality of the computed solution.

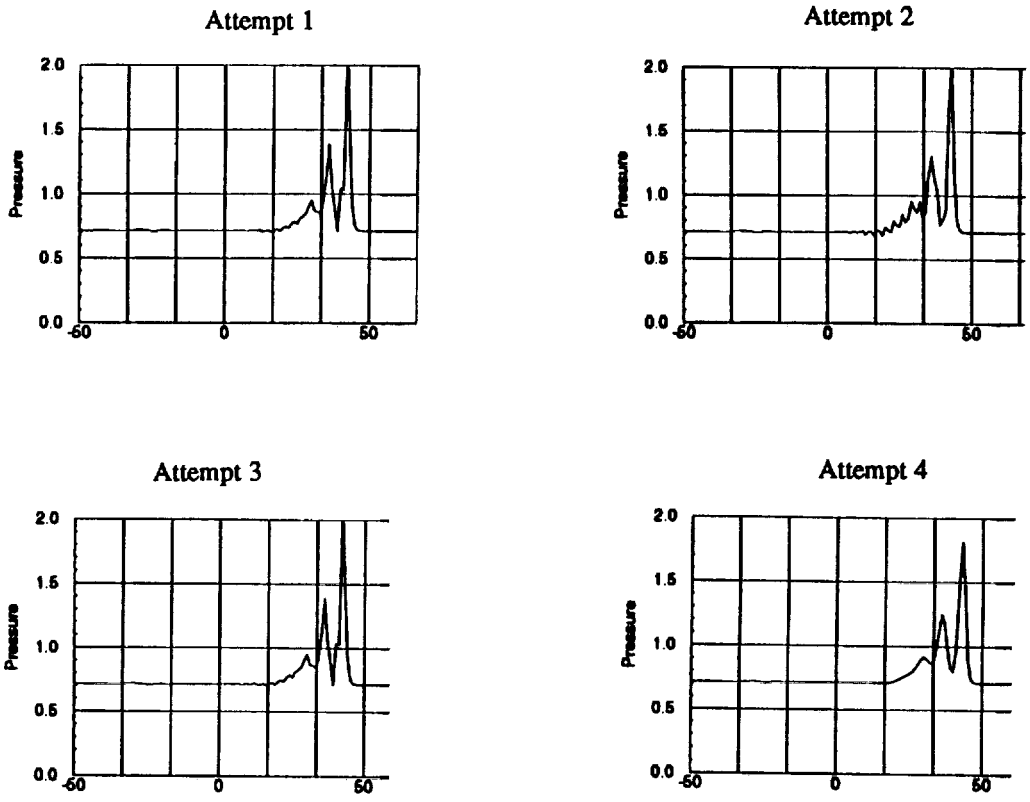

Figure 1 - CTCS pressure solution for problem 1, $\Delta t = .50$

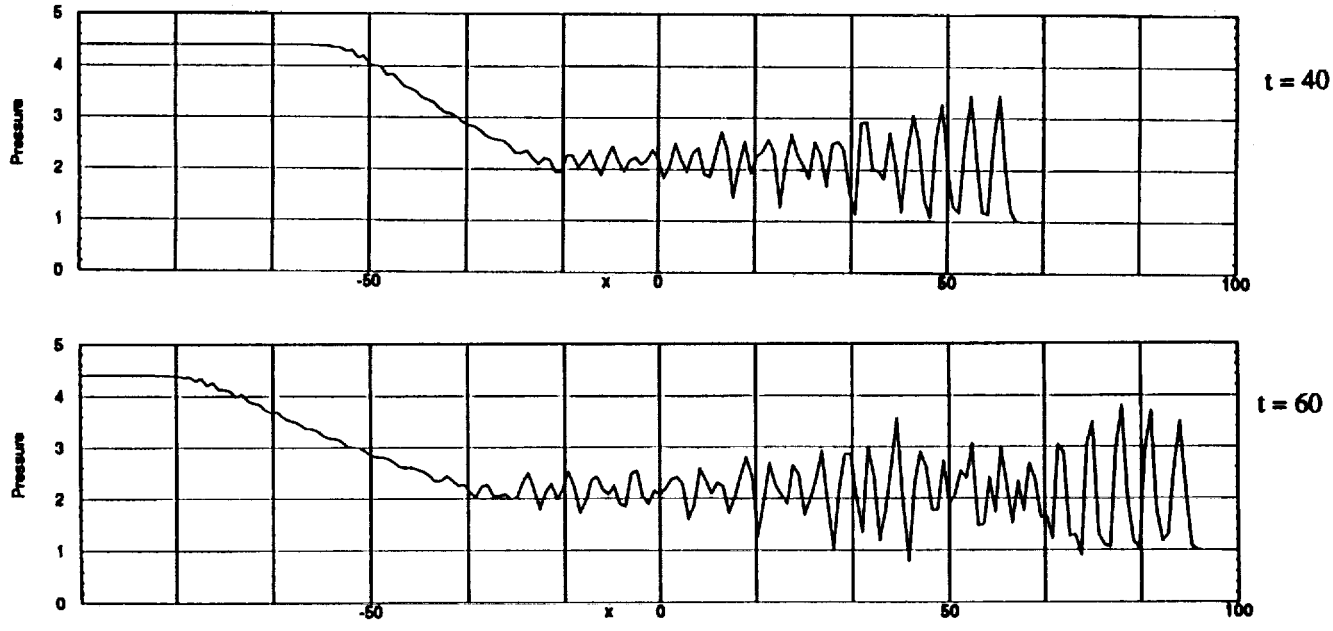

Figure 2 - CTCS pressure solution for problem 2, $\Delta t = .50$

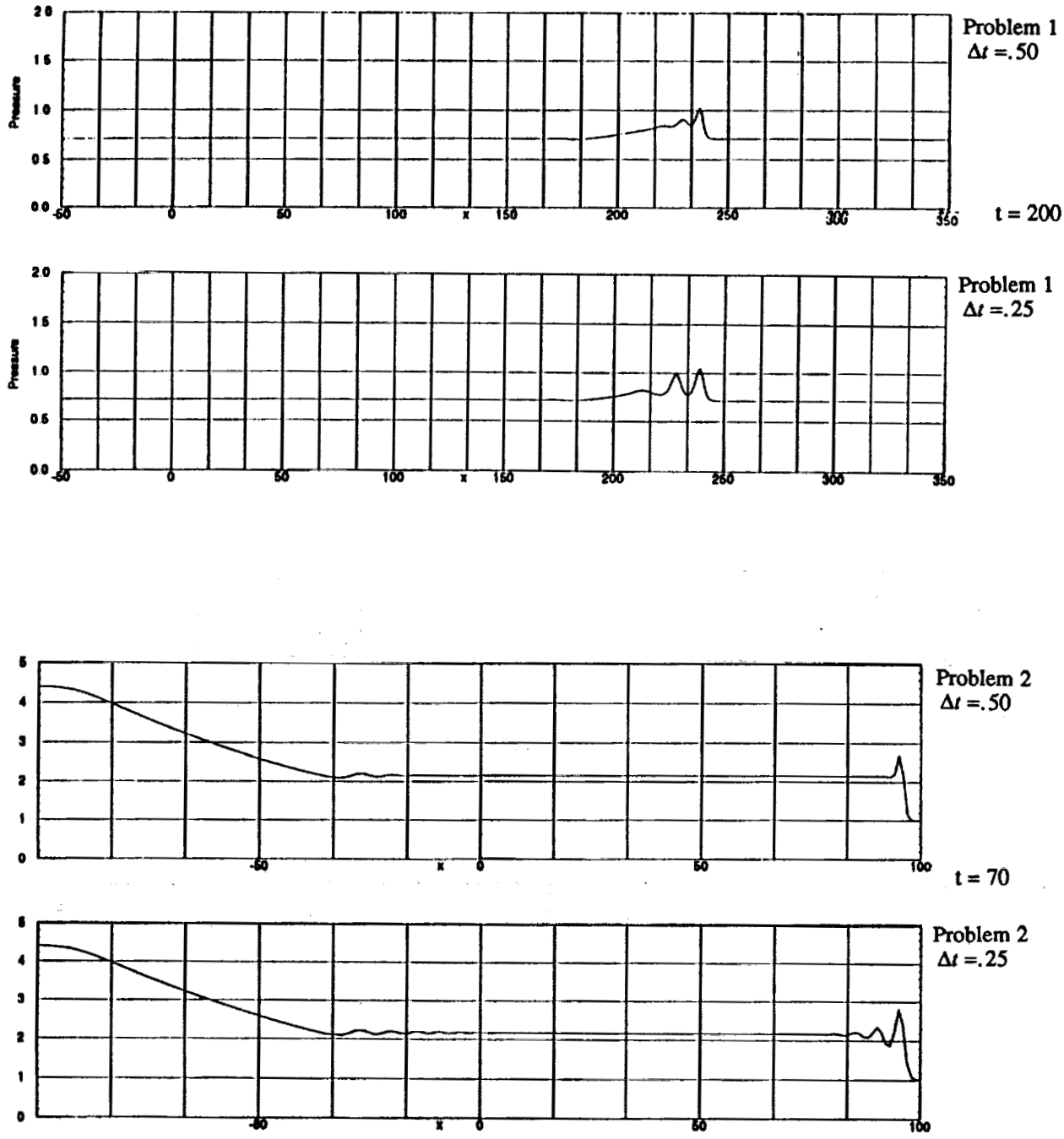

Figure 3 - MacCormack second-order pressure solution for problems 1 and 2, attempt 1

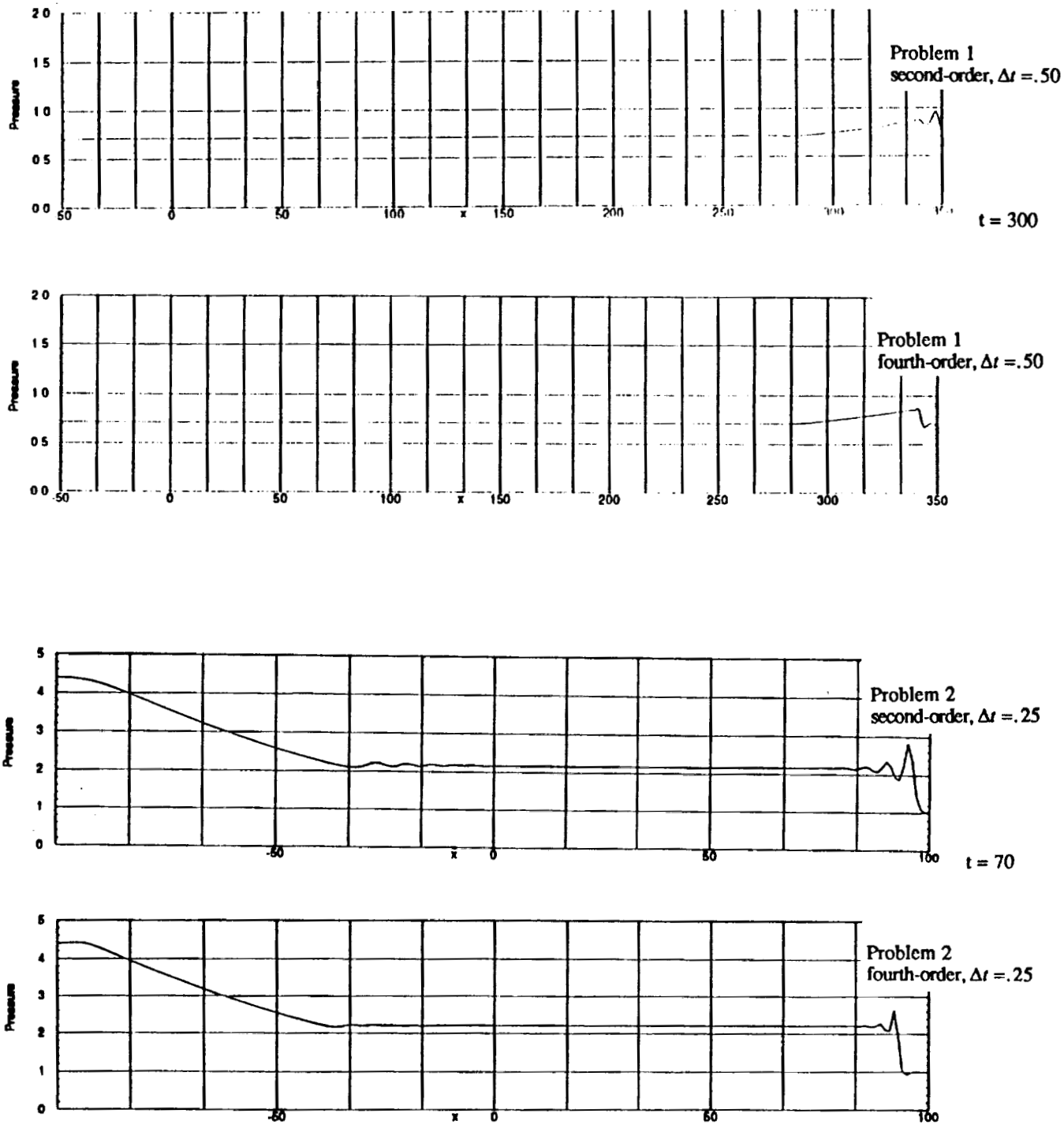

Figure 4 - Pressure solution for second and fourth order MacCormack scheme

WAVE PROPAGATION AND SCATTERING IN COMPUTATIONAL AEROACOUSTICS [1]

Cathy Chung[2] and Philip J. Morris[3]
Department of Aerospace Engineering
The Pennsylvania State University, University Park, PA 16802

ABSTRACT

This paper describes predictions of model problems in computational aeroacoustics. Two problem classes are considered. The first (Workshop Category III, Problem 1 and 2) considers two-dimensional wave propagation and non-reflecting boundary conditions in the presence of a mean flow. The second (Workshop Category IV, Problem 1) examines wall boundary conditions. For the last problem we introduce the Impedance Mismatch Method (IMM) to treat the solid wall boundaries. In this method the solid wall is simulated using a wall region in which the characteristic impedance is set to a different value to that in the fluid region. This method has advantages over traditional solid wall boundary conditions including simplicity of coding, speed of computations and the ability to treat curved boundaries efficiently. Several numerical examples are given in addition to the Workshop Problems. The discretization of the Euler equations is performed in all cases with a Dispersion-Relation-Preserving (DRP) algorithm. The numerical results are compared with either analytical solutions or solutions obtained using traditional solid wall boundary conditions.

INTRODUCTION

In aeroacoustic computations, special consideration must be given to the accuracy of the numerical scheme and the implementation of solid wall boundary conditions. Computational acoustic algorithms must describe unsteady, small scale, high-frequency quantities. This means that they must have high-order temporal and spatial accuracy, and minimize dispersion and dissipation. Recently, Tam and his co-workers introduced a Dispersion-Relation-Preserving (DRP) scheme (Tam and Webb, [1]). This algorithm is used in this paper. The philosophy behind the DRP scheme is that it attempts to reproduce the dispersion relationship of the partial differential equation in the discretized problem. This can only be achieved over a specified range of wavelengths with a known error in numerical dispersion and dissipation. The algorithm used in this paper is formally fourth-order accurate in space and second-order accurate in time; however, it was a seven-point spatial stencil and a four-time level discretization to achieve its optimized dispersion properties.

Another important problem is the implementation of solid wall boundary conditions. For inviscid flow the boundary condition at a solid wall is that the normal velocity is zero. For low-order finite-difference schemes or finite-volume schemes, the imposition of solid wall boundary conditions can usually be carried out in a straightforward manner. For high-order finite-difference schemes, treatment of this condition is complicated. Here we introduce a very efficient method to implement the solid wall boundary condition. We call this the Impedance Mismatch Method

[1]Work supported by NASA Langley Research Center under grant NAG-1-1479
[2]Research Assistant
[3]Boeing Professor of Aerospace Engineering, Associate Fellow AIAA

(IMM). This method can be applied easily to high-order finite difference schemes. Actually, in this method, no special wall boundary conditions need to be implemented at all. All that is needed is to define a wall region and set a different characteristic impedance in this region. Since this method does not involve any changes in the stencil, it can be used to represent the geometry of any object without difficulty. Also, it makes the computation much faster and the coding is very simple compared to other methods of dealing with solid wall boundary conditions.

WAVE PROPAGATION COMPUTATIONS USING THE DRP SCHEME
(Workshop Category III, Problem 1 and 2)

In this paper the two-dimensional linearized Euler equations are solved. The DRP method developed by Tam and Webb [1] has been used to discretize these equations. The DRP scheme is a fourth-order central finite difference scheme in space and is second-order in time. In addition, it is optimized to minimize the dispersion and dissipation over a specified range of wavelengths. The detailed procedure for the development of the scheme is given by Tam and Webb [1]. Here only a brief review of the DRP scheme is given. A seven-point stencil in space is used. The key point is how to fix the coefficients in the stencil to minimize the dispersion and dissipation over a specific range of wavelengths. The technique to evaluate the coefficients involves first taking the Fourier transform of the discretized spatial derivative with respect to the spatial variable. This leads to an expression for the numerical wavenumber as a function of the exact wavenumber. Four of the unknown coefficients in the algorithm are determined from a Taylor series expansion by the requirement of fourth-order accuracy in space. The remaining two coefficients are found by minimization of the difference between the numerical and exact wavenumbers over a finite range of wavenumbers. For a uniform grid the scheme is non-dissipative and the coefficients are symmetric. A similar procedure, using a Laplace transform is used to optimize the time derivatives.

It is known that high-order finite difference schemes invariably generate spurious waves. These oscillations are generated in regions of steep gradients that could be physical or numerical, such as a shock or a change in the grid spacing. The presence of these spurious oscillations inevitably renders the computed solution unacceptable. Artificial damping must be added to the numerical scheme to eliminate these spurious waves. In this paper selective artificial damping (Tam *et al* [2]) has been used. This damping has the characteristics that it removes the spurious short waves while having a negligible effect on the long waves which constitute the known useful band of wavelengths for the numerical simulation.

Non-reflecting boundary conditions are needed at the outer boundaries of the computational domain. The asymptotic, non-reflecting boundary conditions of Tam and Webb [1] have been used in this paper. These boundary conditions become increasingly accurate as more terms in the asymptotic expansion are used and as the boundary moves further from the source region. When only acoustic waves exit the computational domain, a radiation boundary condition is needed. When the outgoing waves include acoustic, entropy, and vorticity waves, the outflow boundary condition is used. For Workshop Category III, Problem 1, only the downstream boundary is the outflow boundary, the other three are radiation boundaries.

Figure 1 shows the computed density contour at time $t = 50$, $\Delta t = 0.07677$ for Problem III. 1. It can be seen that the entropy pulse has partially gone through the outflow boundary, no reflection is observed. Figure 2 is the corresponding density distribution along the x-axis. An interaction between the acoustic and entropy pulse has occurred. The computed results have been compared with published results and the agreement is good. This example demonstrates that the DRP scheme and the asymptotic non-reflecting boundary conditions work well.

When there is a mean flow in both the x and y directions, the non-reflecting boundary conditions must be modified; however, they can still be derived from the asymptotic analytical solutions. For a radiation boundary, the set of equations has the same form as that used in Problem 1; however, the polar coordinates are now based on the mean flow direction instead of the x-axis direction. For the outflow boundary, the pressure equation is the same as for the radiation boundary. The equations for the density and velocity are the Euler equations, with additional terms accounting for the y-direction mean flow. For problem 2, the outflow boundary conditions are applied on the upper and right boundaries. The radiation boundary conditions are used on the other two boundaries.

Figure 3 shows the computed density contour at time $t = 80$. Figure 4 is the corresponding density distribution along the $x = y$ axis. It can be seen that the whole wave pattern has been convected in the 45^o direction, and part of the wave has gone through the boundaries. No reflections are observed. The computed results have been compared with published results and the agreement is good. These examples demonstrate that the DRP and the asymptotic non-reflecting boundary conditions have good isotropic properties.

COMPUTATIONS OF ACOUSTIC REFLECTION AND SCATTERING USING THE IMPEDANCE MISMATCH METHOD
(Workshop Category IV, Problem 1)

From classical acoustics theory (Kinsler and Frey [4]), it is known that when a normal incident plane wave in a fluid medium impinges on the boundary of a contiguous second medium, a reflected wave is generated in the first medium and a transmitted wave appears in the second medium. The ratio of the pressure amplitudes of the reflected and transmitted waves to those of incident wave depend on the characteristic impedances ($\rho_0 a_0$) of the two media. When the second medium has a much higher characteristic impedance, then most of the wave energy is reflected. As the ratio of the characteristic impedance of the second medium to the first approaches infinity, all the incident waves are reflected. The second medium acts like a solid object. Thus, setting a higher impedance in a certain region can be used to simulate the effect of a solid object in this region. This was the basic idea of the IMM; however, the numerical implementation requires some modification of the problem.

Based on the above idea, the impedance of the scattering body may be set to 30 times that of the ambient region in numerical simulations. The speed of sound inside and outside the body is kept the same. This means that the wave speed is constant throughout the domain and permits the CFL number to be kept at almost the same value as when no object is present. For physical problems, the linearized Euler equations in non-conservative form have the mean density and speed of sound outside the spatial derivatives. At the interface the pressure and the normal velocity are continuous. When this method is used directly in two-dimensional cases, instability occurs, if the same time step size is used. This is because of the large discontinuity in the equation coefficients (ρ_0). In order to avoid this instability and maintain the time step size, an auxiliary problem is proposed.

For the auxiliary problem, new variables are defined: $\hat{\rho} = \rho/\rho_0$, $\hat{u} = u\rho_0$, $\hat{p} = p/\rho_0$. A set of equations, equivalent to the linearized Euler equations in a uniform density medium, are introduced in the form

$$\frac{\partial \rho}{\partial t} + \frac{\partial \hat{u}}{\partial x} = 0 \tag{1}$$

$$\frac{\partial u}{\partial t} + \frac{\partial \hat{p}}{\partial x} = 0 \tag{2}$$

$$\frac{\partial p}{\partial t} + a_0^2 \frac{\partial \hat{u}}{\partial x} = 0 \tag{3}$$

The equations are written in one-dimensional form for simplicity. This set of equations is the same as that in the physical problem in the fluid region and wall region, but not at the interface, since ρ_0 is piecewise uniform and has a jump at interface. We impose the condition that the new variables are continuous at the interface of the two media. If the second region is to mimic a solid wall, then the mean density in the wall region must be set to a very low value, instead of a higher value than that in first region. Since ρ_0 is alway unity in the first (or real fluid) region, the physical solution is then obtained in this region from the auxiliary problem. The accuracy of the computations depends on the density ratio; the smaller the value, the more closely the solution simulates the solid wall. However, test calculations have shown that this density ratio can not be set infinitely small to avoid instability.

In order to simulate the infinite wall using the IMM for the Workshop Category IV, Problem 1, an extra wall region is needed as shown in Figure 5. In this wall region, the mean density is set equal to 1/30. The thickness of this wall region is chosen to be $40\Delta y$. This thickness could be smaller, but in that case the source would be too close to the non-reflecting boundary of the computational domain, and some wave reflections would occur at the lower boundary. It will be seen in some following examples that this problem does not exist for scattering computations. An extra wall region is needed only when the source is close the boundary. In the new computational domain, the computations can be carried out directly. No stencil change is needed and no special solid wall boundary conditions are implemented. This makes the computation fast. Even though the extra wall region increases the computational domain size, the overall computation time is decreased. Figure 6 shows the calculated pressure contours associated with the acoustic pulse at $t = 100$, $\Delta t = 0.05$. At this time, the pulse has reached the wall and has been reflected, creating a double pulse pattern; one from the original source and the other from an image source below the wall. The mean flow convects the pulse so that the entire pressure pattern is moved downstream. Figure 7 shows the corresponding computed pressure wave form along the line $x = 50$, which passes through the center of the pulse. The analytical solution is also plotted on the same figure. It can be seen that the agreement is reasonable though some small errors can still be seen in the reflected wave form; both in the amplitude and phase. The amplitude error is mainly due to the choice of the wall mean density. The phase error is caused by the fact that the location of the wall can not be defined exactly. The error for the wall position is within one step size. However, this error can be minimized if enough grid points are used between the source and the wall.

A second example of the use of the IMM concerns the reflection of a periodic acoustic wave train by a solid wall in the absence of a mean flow. The geometry of the domain is the same as that in the previous example (Figure 5). The acoustic wave train is generated by a time periodic source in the energy equation. The simulation is carried out with zero initial conditions. After the transient solution has propagated out of the computational domain, the pressure fluctuation is periodic in time. 10 grid points per wavelength are used. Figure 8 shows the computed pressure contours adjacent to the solid wall at time $t = 180$ in the right half of the computational domain. The interference pattern is due to the cancellation between the incident wave and reflected wave. Figure 9 gives the corresponding pressure wave forms along the y-axis. The analytical solution is also plotted. The agreement between the computed and analytical solutions is good.

A third example given here is the scattering of a periodic acoustic wave train by a thin flat plate of finite length as shown in Figure 10. $L = 25$, $\lambda = L/4$; this is approximately 6 grid points per wavelength. The computations are conducted using two methods: the IMM and the solid wall boundary conditions developed by Tam and Dong [3]. The thickness of the plate must be Δy in the IMM, though the thickness is zero in the solid wall boundary condition method. That is, in the two rows of length L, the mean density is 1/30 in the IMM as the pressure on the two sides of the plate is different. Figure 11 shows the pressure contours computed using the IMM at time $t = 194$. The diffraction pattern behind the plate and the scattering pattern in front of the plate can be seen clearly. Figure 12 shows the corresponding pressure distributions along the upper boundary of the computational domain obtained from both the IMM and the solid wall boundary condition method. The agreement between the two solutions is good. The computation time for the IMM is 67 percent of that needed for the solid wall boundary condition method. The coding in the IMM is extremely simple, compared with the solid wall boundary condition method. In the IMM, the amount of coding work and the computing time do not change at all when there is an scattering object in the domain. This is the biggest advantage of the IMM.

CONCLUSIONS

In the first part of this paper a Dispersion-Relation-Preserving (DRP) scheme was used to compute the wave propagation of initially Gaussian pulses with mean flow in x-direction and at 45° to this direction. The numerical simulations demonstrated that the DRP and the asymptotic non-reflecting boundary conditions worked well in both cases. Then, the Impedance Mismatch Method was introduced to simulate solid wall boundaries. This method was applied to several two-dimensional reflection and scattering problems. The method was also compared with a traditional solid wall boundary condition method. Some advantages and disadvantages of this method have been revealed. The advantages of the IMM are: no special solid wall boundary conditions need to be implemented; no stencil changes are involved in the presence of solid objects; the coding is very easy; the computations are much faster than when the traditional solid wall boundary conditions are used; and there is no difficulty for any geometry. No matter whether the solid boundary is flat or curved, the amount of coding work and the computation time are the same. The disadvantages of the IMM are: the accuracy of computations depends on the value of the mean density in the wall region; there is an ambiguity in the wall position of one grid spacing; and an extra wall region is needed for sources and walls close to the edge of the computational domain. The IMM is a promising method for simulations of acoustic scattering, diffraction and reflection problems. Further development is underway to apply this method to three-dimensional problems.

References

[1] Tam, C. K. W. and Webb, J. C., "Dispersion-relation-preserving finite difference schemes for computational acoustics," *J. Comp. Physics*, 107,1993, pp. 262-281.

[2] Tam, C. K. W., Webb, J. C. and Dong, Z., "A study of the short wave components in computational acoustics," *J. Computational Acoustics*, 1, 1993, pp.1-30.

[3] Tam, C. K. W. and Dong, Z., "Wall boundary conditions for high order finite difference schemes in computational acoustics," *Theoretical and Computational Fluid Dynamics*, to appear 1994.

[4] Kinsler E. L. and Frey A. R., *Fundamentals of Acoustics*, 2nd. edition, 1962, John Wiley & Sons Inc., New York.

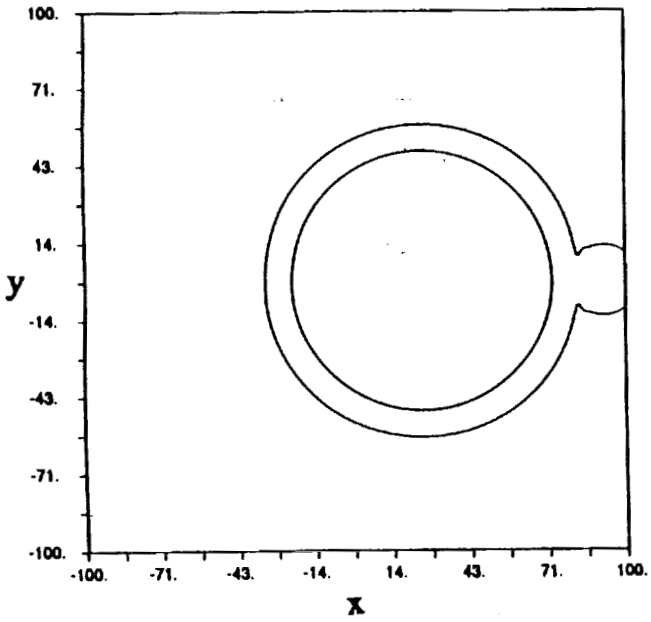

Figure 1: Density contour at $t = 50$.

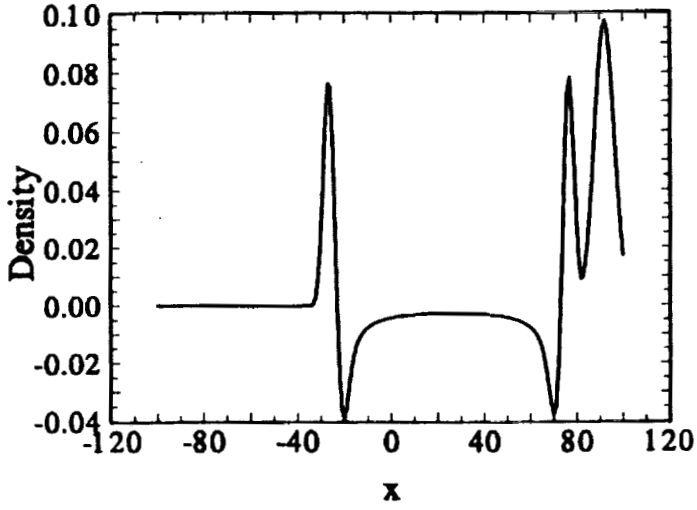

Figure 2: Density distribution along x-axis at $t = 50$.

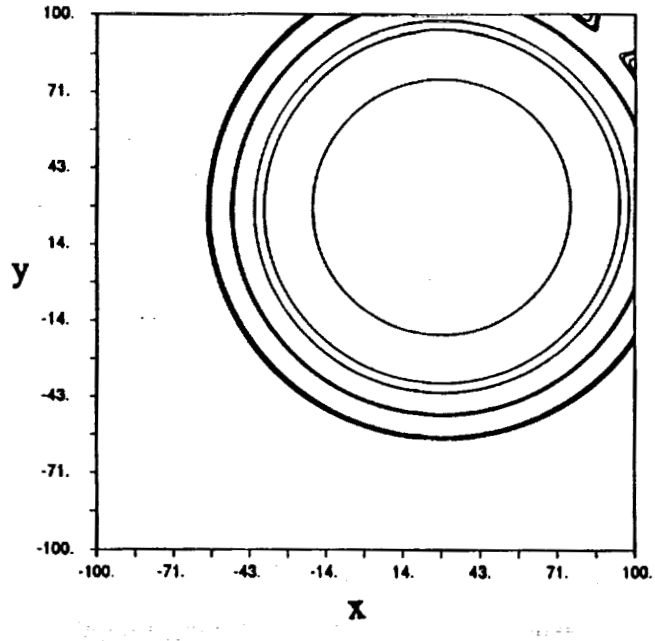

Figure 3: Density contour at $t = 80$.

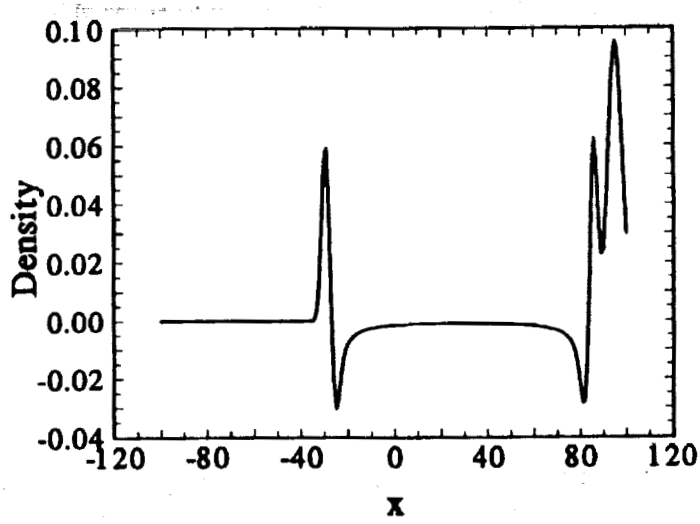

Figure 4: Density distribution along $x = y$ axis at $t = 80$.

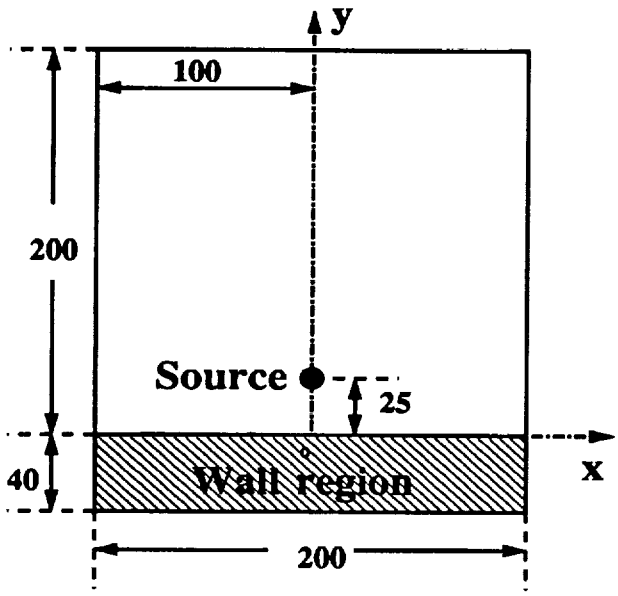

Figure 5: Sketch of computational domain for infinite wall reflection problem.

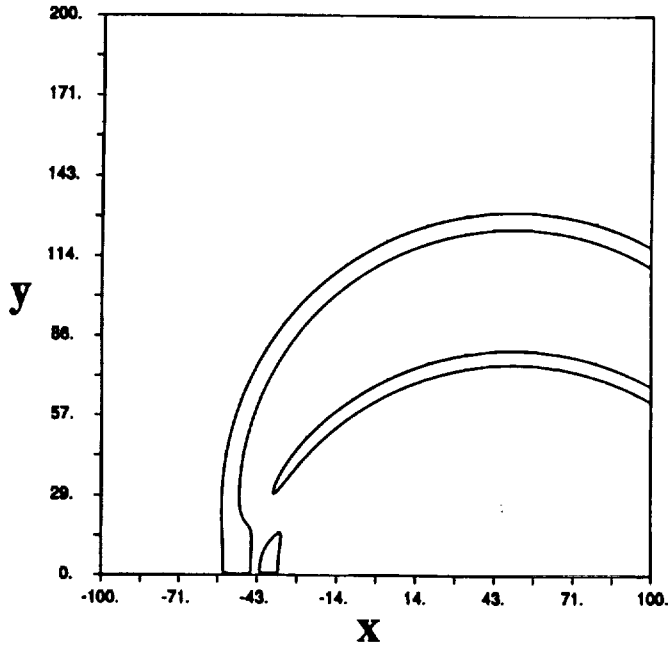

Figure 6: Pressure contour at $t = 100$ for reflection of acoustic pulse by infinite wall with mean flow Mach 0.5.

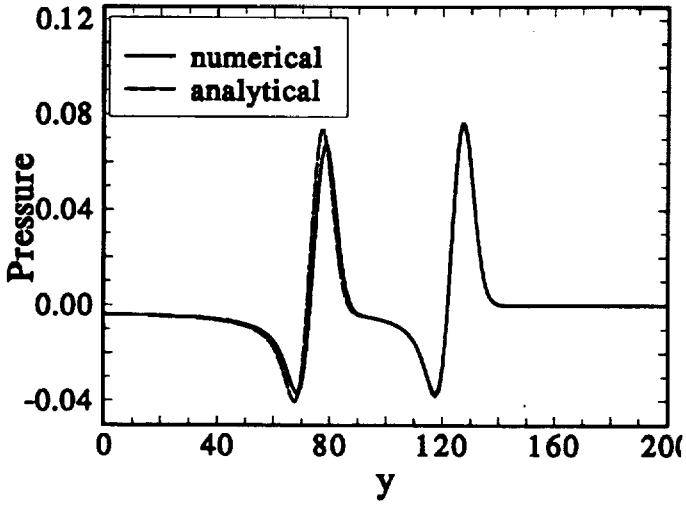

Figure 7: Pressure distribution along $x = 50$ axis at $t = 100$ for reflection of acoustic pulse by infinite wall with mean flow Mach 0.5.

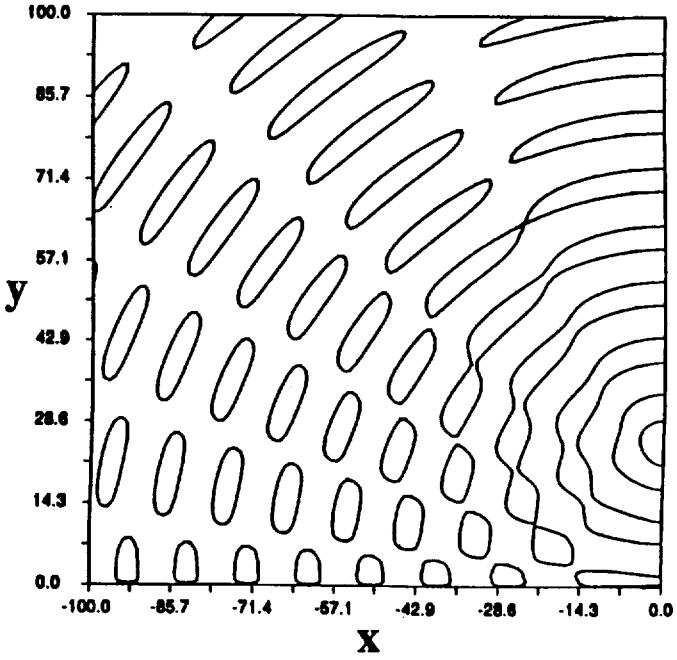

Figure 8: Pressure contour at $t = 180$ for reflection of acoustic wave train by infinite wall.

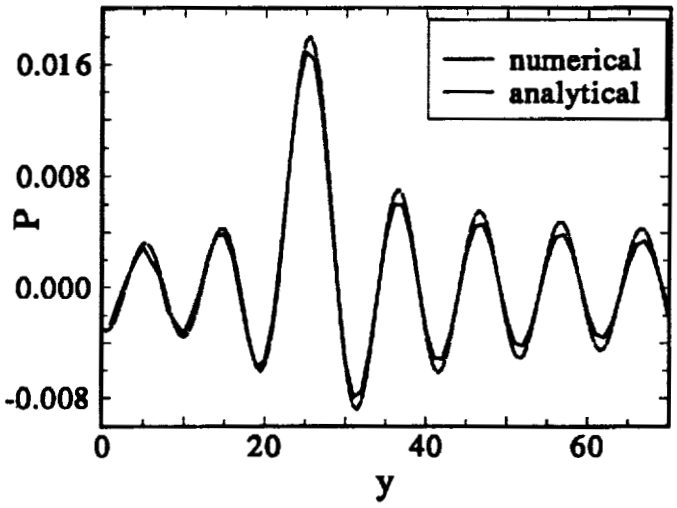

Figure 9: Pressure distribution along y-axis at $t = 180$ for reflection of acoustic wave train by infinite wall.

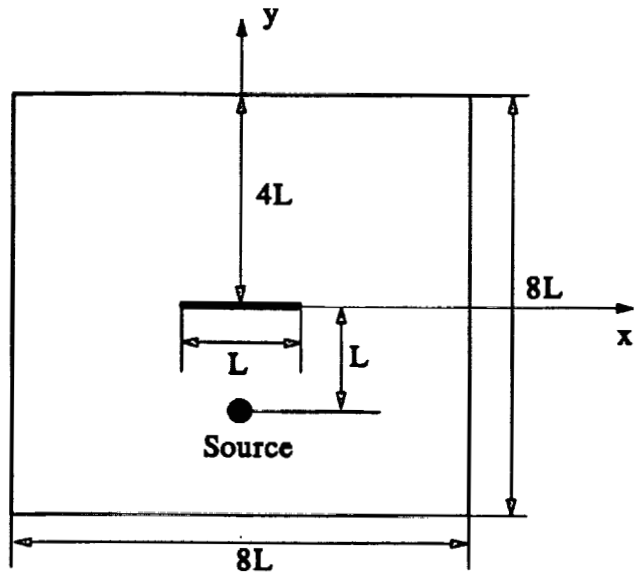

Figure 10: Sketch of computational domain for finite plate scattering problem.

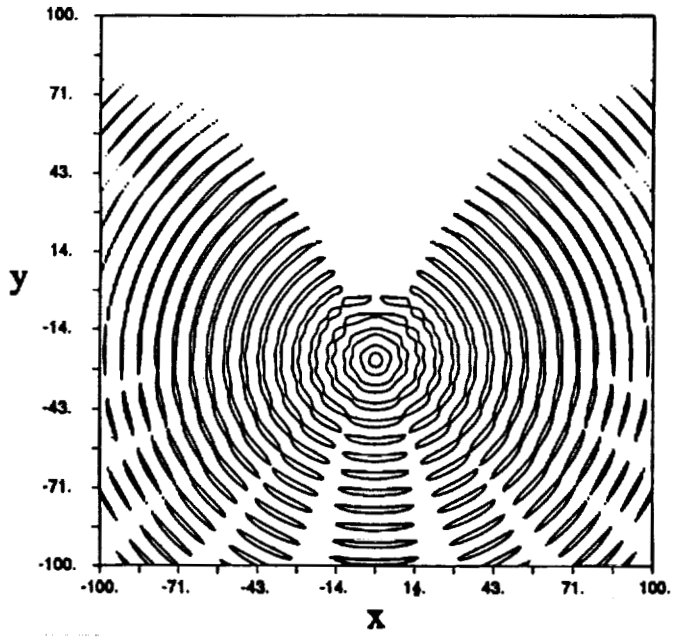

Figure 11: Pressure contour at $t = 194$ for scattering of acoustic wave train by finite plate.

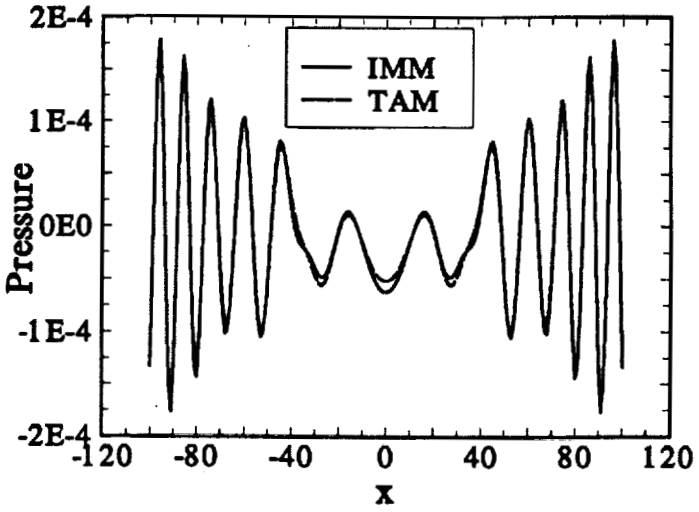

Figure 12: Pressure distribution along upper boundary at $t = 194$ for scattering of acoustic wave train by finite plate.

N95-30153

THE USE OF STAGGERED SCHEMES AND AN ABSORBING BUFFER ZONE FOR COMPUTATIONAL AEROACOUSTICS

Douglas M. Nark *
Joint Institute for Advancement of Flight Sciences
The George Washington University, Hampton, Virginia 23681

SUMMARY

Various problems from those proposed for the Computational Aeroacoustics (CAA) workshop were studied using second and fourth order staggered spatial discretizations in conjunction with fourth order Runge-Kutta time integration. In addition, an absorbing buffer zone was used at the outflow boundaries. Promising results were obtained and provide a basis for application of these techniques to a wider variety of problems.

INTRODUCTION

In this work, problems from categories three, four, and six were attempted which tested the chosen numerical scheme's ability to resolve acoustic waves with minimal isotropy, damping, and dispersion. Additionally, outflow and wall boundary conditions were required which would properly handle the particular problem geometry. A staggered spatial discretization was employed to resolve the difficulties in the interior domain. This arrangement was chosen because of the simplification of physical boundary treatment and an improvement in dispersion characteristics without addition of artificial damping. At the outflow boundaries, an absorbing buffer zone was used in which the original equations are modified in such a way that no wave will be reflected from the outer boundary of the buffer zone. The virtue of this treatment is that local acoustic boundary conditions need not be applied at the computational boundary.

The two approaches mentioned were used in all of the problem solutions. Any changes in implementation were a result of the inclusion of stationary or oscillatory solid boundaries. With this in mind, the rest of this discussion proceeds with a description of the staggered spatial discretization and the absorbing buffer zone. The problems that were attempted are then introduced beginning with category three, continuing to problem two of category four, and ending with category six. Each of these cases is presented with any special boundary treatment required by the geometry as well as the results. Finally, the work is closed with some conclusions and thoughts for future consideration.

STAGGERED DISCRETIZATION

The staggered technique, which has been used in the solution of a variety of problems [1, 2], entails calculating the primitive variables at only a specified collection of points. In this work, the scalar quantities were all solved at the same point, whereas the vector quantities were calculated at different points. In order to illustrate this, focus on a small portion of the grid in the interior of the domain comprised of five points (figure 1).

*This is a portion of research being conducted by the author for inclusion in a Doctoral Dissertation with The George Washington University.

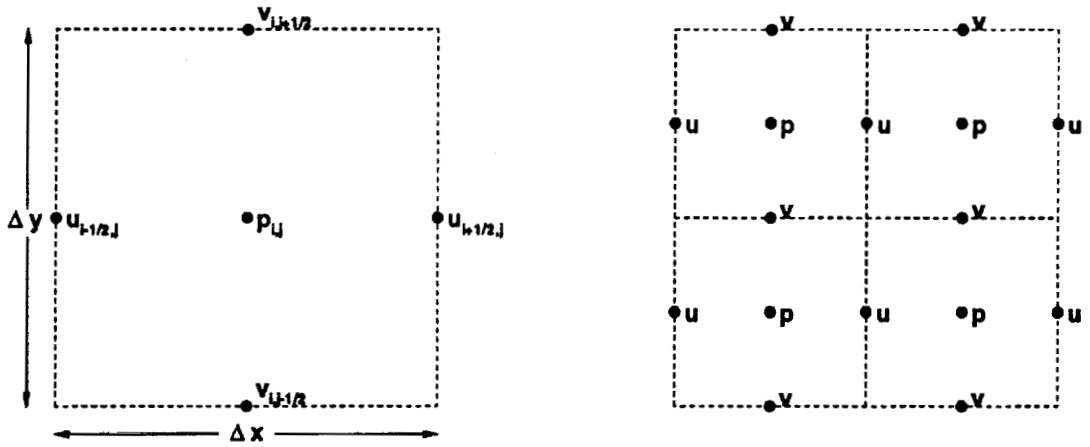

Figure 1: Staggered discretization for the linear problem.

This piece of the grid may be thought of as a cell with a grid point in the middle and a grid point at the midpoint of each cell wall. Scalar quantities are obtained at the cell center and the components of the vector quantities are calculated at the sides. The entire computational domain may be thought of as a collection of these cells with the variables determined at the specified points (figure 1).

Having set up the computational grid, the question now arises as to how to discretize equations on to this grid. The linearized Euler equations will serve as an example of how this is accomplished, since all of the problems investigated in this work involve their solution on a uniform grid. The linearized Euler equations in Cartesian coordinates may be written

$$\frac{\partial \rho}{\partial t} + \frac{\partial (M_x \rho + u)}{\partial x} + \frac{\partial (M_y \rho + v)}{\partial y} = 0 \tag{1}$$

$$\frac{\partial u}{\partial t} + \frac{\partial (M_x u + p)}{\partial x} + \frac{\partial (M_y u)}{\partial y} = 0 \tag{2}$$

$$\frac{\partial v}{\partial t} + \frac{\partial (M_x v)}{\partial x} + \frac{\partial (M_y v + p)}{\partial y} = 0 \tag{3}$$

$$\frac{\partial p}{\partial t} + \frac{\partial (M_x p + u)}{\partial x} + \frac{\partial (M_y p + v)}{\partial y} = 0 \tag{4}$$

where ρ and p are the density and pressure, u and v are the x and y components of velocity, and M_x and M_y are constant mean flow Mach numbers in the x and y directions.

A staggered semi-discrete form of the equations which has $O(\Delta x^2)$ accuracy is given by

$$\begin{aligned} \frac{\partial \rho_{i,j}}{\partial t} &= -\frac{M_x}{2\Delta x}\left(\rho_{i+1,j} - \rho_{i-1,j}\right) - \frac{M_y}{2\Delta y}\left(\rho_{i,j+1} - \rho_{i,j-1}\right) - \frac{1}{\Delta x}\left(u_{i+1/2,j} - u_{i-1/2,j}\right) \\ &\quad -\frac{1}{\Delta y}\left(v_{i,j+1/2} - v_{i,j-1/2}\right) \end{aligned} \tag{5}$$

$$\begin{aligned} \frac{\partial u_{i+1/2,j}}{\partial t} &= -\frac{M_x}{2\Delta x}\left(u_{i+3/2,j} - u_{i-1/2,j}\right) - \frac{M_y}{2\Delta y}\left(u_{i+1/2,j+1} - u_{i+1/2,j-1}\right) \\ &\quad -\frac{1}{\Delta x}\left(p_{i+1,j} - p_{i,j}\right) \end{aligned} \tag{6}$$

$$\frac{\partial v_{i,j+1/2}}{\partial t} = -\frac{M_x}{2\Delta x}\left(v_{i+1,j+1/2} - v_{i-1,j+1/2}\right) - \frac{M_y}{2\Delta y}\left(v_{i,j+3/2} - v_{i,j-1/2}\right) - \frac{1}{\Delta y}\left(p_{i,j+1} - p_{i,j}\right) \tag{7}$$

$$\frac{\partial p_{i,j}}{\partial t} = -\frac{M_x}{2\Delta x}\left(p_{i+1,j} - p_{i-1,j}\right) - \frac{M_y}{2\Delta y}\left(p_{i,j+1}p_{i,j-1}\right) - \frac{1}{\Delta x}\left(u_{i+1/2,j} - u_{i-1/2,j}\right) - \frac{1}{\Delta y}\left(v_{i,j+1/2} - v_{i,j-1/2}\right). \tag{8}$$

In many cases, higher order accuracy is desired, and in this investigation, both second and fourth order spatially accurate discretizations were used. Thus, an $O(\Delta x^4)$ accurate staggered semi-discretization of equations (1–4) is introduced and may be expressed as

$$\frac{\partial \rho_{i,j}}{\partial t} = -\frac{M_x}{12\Delta x}\left(-\rho_{i+2,j} + 8\rho_{i+1,j} - 8\rho_{i-1,j} + \rho_{i-2,j}\right) - \frac{M_y}{12\Delta y}\left(-\rho_{i,j+2} + 8\rho_{i,j+1} - 8\rho_{i,j-1} + \rho_{i,j-2}\right) - \frac{1}{24\Delta x}\left(-u_{i+3/2,j} + 27u_{i+1/2,j} - 27u_{i-1/2,j} + u_{i-3/2,j}\right) - \frac{1}{24\Delta y}\left(-v_{i,j+3/2} + 27v_{i,j+1/2} - 27v_{i,j-1/2} + v_{i,j-3/2}\right) \tag{9}$$

$$\frac{\partial u_{i+1/2,j}}{\partial t} = -\frac{M_x}{12\Delta x}\left(-u_{i+5/2,j} + 8u_{i+3/2,j} - 8u_{i-1/2,j} + u_{i-3/2,j}\right) - \frac{M_y}{12\Delta y}\left(-u_{i+1/2,j+2} + 8u_{i+1/2,j+1} - 8u_{i+1/2,j-1} + u_{i+1/2,j-2}\right) - \frac{1}{24\Delta x}\left(-p_{i+2,j} + 27p_{i+1,j} - 27p_{i-1,j} + p_{i-2,j}\right) \tag{10}$$

$$\frac{\partial v_{i,j+1/2}}{\partial t} = -\frac{M_x}{12\Delta x}\left(-v_{i+2,j+1/2} + 8v_{i+1,j+1/2} - 8v_{i-1,j+1/2} + v_{i-2,j+1/2}\right) - \frac{M_y}{12\Delta y}\left(-v_{i,j+5/2} + 8v_{i,j+3/2} - 8v_{i,j-1/2} + v_{i,j-3/2}\right) - \frac{1}{24\Delta y}\left(-p_{i,j+2} + 27p_{i,j+1} - 27p_{i,j-1} + p_{i,j-2}\right) \tag{11}$$

$$\frac{\partial p_{i,j}}{\partial t} = -\frac{M_x}{12\Delta x}\left(-p_{i+2,j} + 8p_{i+1,j} - 8p_{i-1,j} + p_{i-2,j}\right) - \frac{M_y}{12\Delta y}\left(-p_{i,j+2} + 8p_{i,j+1} - 8p_{i,j-1} + p_{i,j-2}\right) - \frac{1}{24\Delta x}\left(-u_{i+3/2,j} + 27u_{i+1/2,j} - 27u_{i-1/2,j} + u_{i-3/2,j}\right) - \frac{1}{24\Delta y}\left(-v_{i,j+3/2} + 27v_{i,j+1/2} - 27v_{i,j-1/2} + v_{i,j-3/2}\right). \tag{12}$$

Time Integration

The time integration may be handled several ways. Originally, staggered time differentiation was also attempted. However, this approach in combination with the staggered spatial operator

led to unstable schemes. Therefore, standard fourth order Runge-Kutta integration was used for both the second and fourth order spatial operators. Generally, for an equation in the form

$$\frac{\partial \mathbf{W}}{\partial t} + \mathbf{L}(\mathbf{W}) = 0, \tag{13}$$

where $\mathbf{W}$ is the unknown and $\mathbf{L}$ is a spatial operator, the $O(\Delta t^4)$ Runge-Kutta scheme to obtain the solution at time step $n+1$ is

$$\begin{aligned}
\mathbf{W}^{(0)} &= \mathbf{W}^n \\
\mathbf{W}^{(1)} &= \mathbf{W}^{(0)} - \frac{\Delta t}{2}\mathbf{L}(\mathbf{W}^{(0)}) \\
\mathbf{W}^{(2)} &= \mathbf{W}^{(0)} - \frac{\Delta t}{2}\mathbf{L}(\mathbf{W}^{(1)}) \\
\mathbf{W}^{(3)} &= \mathbf{W}^{(0)} - \Delta t\mathbf{L}(\mathbf{W}^{(2)}) \\
\mathbf{W}^{n+1} &= \mathbf{W}^{(0)} - \Delta t\left(\frac{1}{6}\mathbf{L}(\mathbf{W}^{(0)}) + \frac{1}{3}\mathbf{L}(\mathbf{W}^{(1)}) + \frac{1}{3}\mathbf{L}(\mathbf{W}^{(2)}) + \frac{1}{6}\mathbf{L}(\mathbf{W}^{(3)})\right).
\end{aligned}$$

ABSORBING BUFFER ZONE

Having set down the solution method for the governing equations, it is helpful to present the outflow boundary treatment before proceeding to the specific problems. The approach used at the outflow boundaries involves an absorbing buffer in which the governing equations are modified to minimize reflection. This idea has been successfully applied to different types of wave propagation problems [3, 4, 5, 6]. The modified equations are constructed by gradually changing the domain of dependence for the problem as one moves from the edge of the interior domain to the outer edge of the buffer zone. The implementation is usually very straightforward and begins with the addition of points to the original computational domain to form an outer buffer zone with the same spatial discretization (see figure 2). Within this zone, an artificial velocity field

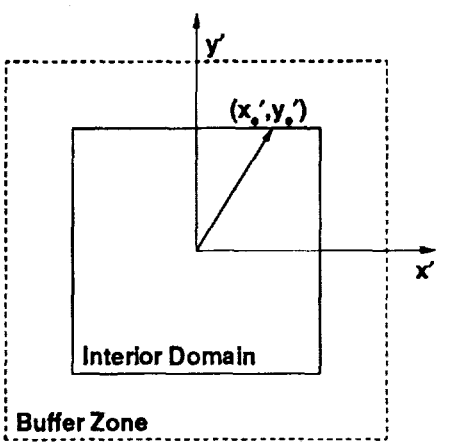

Figure 2: Computational domain with Cartesian grid overlaid.

$(\mathbf{U}' = (\mathbf{U}'_o, \mathbf{V}'_o))$ is introduced which is directed outward from the interior domain. This velocity field is set up such that its value is zero at the edge of the interior domain and its normal component is approximately 1.3 times larger than the maximum interior velocity at the outer edge

of the buffer zone. The value 1.3 was arbitrarily chosen to ensure that the flow was "supersonic" in the normal direction at the buffer zone edges.

A proper velocity profile may be illustrated by setting up a Cartesian grid with the origin at the center of the interior domain. The velocity is forced to be zero at the edge of the interior domain by writing

$$U'_o = \beta (x' - x'_e)^m , V'_o = 0 \tag{14}$$

on the $x' =$ const. sides, and

$$V'_o = \beta (y' - y'_e)^m , U'_o = 0 \tag{15}$$

on the $y' =$ const. sides. Here, (x', y') is the location of a point on the Cartesian grid and x_e and y_e are the values of x' and y' at the edges of the interior domain as shown in figure 2. The velocity field is made continuous at the corners of the buffer zone by considering it to be of the form

$$U'_o = \beta (x' - x'_e)^m , V'_o = \beta (y' - y'_e)^m \tag{16}$$

in these regions. The parameter β is used to impose the chosen value of 1.3 times the maximum interior velocity for the normal component at the outer edge of the buffer zone. Figure 3 shows the upper right hand corner of the buffer zone with superimposed radial velocity vectors. In this

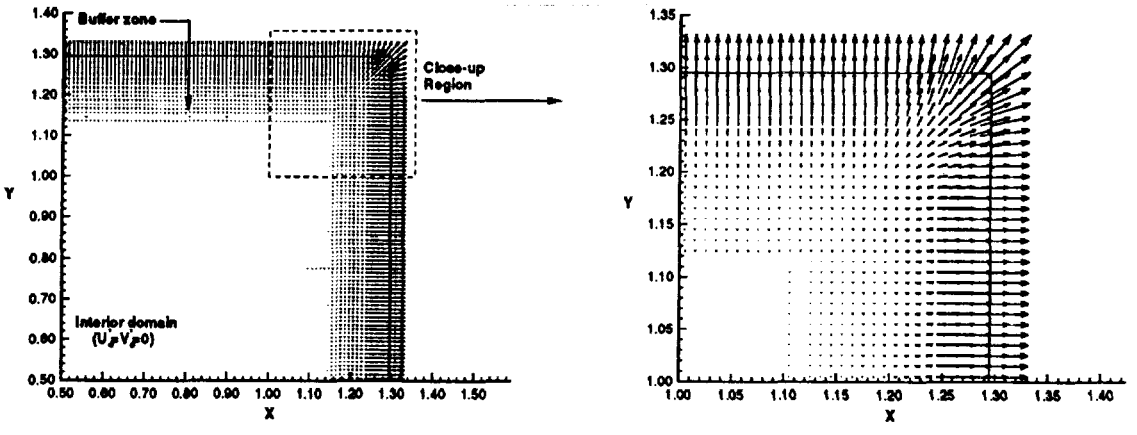

Figure 3: Radial velocity vectors of the buffer zone.

figure, and in the given results, the value of m was set to 8. This was chosen through numerical experimentation, and it should be noted that the effect of varying m or the entire imposed velocity profile is a point which could warrant further research. On the outer edge of the buffer zone, the finite difference stencil still requires some information from outside the domain. For this work, a simple solid wall condition was used, however, any reasonable condition could be employed.

Once the velocity field is established in the buffer zone, the equations must be modified in order for it to have an effect. This is achieved by adding an artificial mean flow term of the form $\nabla \cdot (\mathbf{U}'\varphi)$ to each equation where $\mathbf{U}'$ is the buffer zone velocity field and φ is the variable being computed. Note that the equations are unchanged in the interior since the imposed velocity field is zero there.

Time Stepping Consideration

A final point needs investigation before continuing; that is the effect of the buffer zone velocity field on the CFL number. In general, the CFL number is given as $\frac{U_{max}\Delta t}{\Delta x}$ where U_{max} is

the maximum velocity in the interior domain ($U_{max} = c + \sqrt{U_o^2 + V_o^2}$). By imposing a velocity field which has components which are approximately 1.3 times larger than U_{max}, it can be seen that the time step must be reduced in order to maintain stability. This lower time step then leads to increased computation time. One approach to alleviating this problem is to lower the wave speed in the buffer zone to counteract the increased velocity. This is accomplished by multiplying the actual operator by a variable μ. For instance, the equation $u_t + \mathrm{L}(u) = 0$ would be written $u_t + \mathrm{U}' \cdot \nabla u + \mu \mathrm{L}(u) = 0$. The value of μ is set to 1 on the interior and is decreased to .1 at the outer edge of the buffer zone. The decrease of μ from 1 to .1 in the buffer zone is accomplished by using the relation

$$\mu = 1 - \eta \left(x' - x'_e\right)^m \tag{17}$$

on the $x' =$ const. sides and

$$\mu = 1 - \eta \left(y' - y'_e\right)^m \tag{18}$$

on the $y' =$ const. sides. At the corners, the parameter takes the form

$$\mu = 1 - \eta \left(\left(x' - x'_e\right)^m + \left(y' - y'_e\right)^m \right), \tag{19}$$

where x', y', x'_e, y'_e are defined as before and η is a constant which allows the proper value of μ to be set at the edge of the buffer zone. This multiplication by μ allows one to maintain stability without lowering the CFL number. Thus, the final form of the governing equations (1–4) becomes

$$\frac{\partial \rho}{\partial t} + \frac{\partial (U'_o \rho)}{\partial x} + \frac{\partial (V'_o \rho)}{\partial y} + \mu \left[\frac{\partial (M_x \rho + u)}{\partial x} + \frac{\partial (M_y \rho + v)}{\partial y} \right] = 0 \tag{20}$$

$$\frac{\partial u}{\partial t} + \frac{\partial (U'_o u)}{\partial x} + \frac{\partial (V'_o u)}{\partial y} + \mu \left[\frac{\partial (M_x u + p)}{\partial x} + \frac{\partial (M_y u)}{\partial y} \right] = 0 \tag{21}$$

$$\frac{\partial v}{\partial t} + \frac{\partial (U'_o v)}{\partial x} + \frac{\partial (V'_o v)}{\partial y} + \mu \left[\frac{\partial (M_x v)}{\partial x} + \frac{\partial (M_y v + p)}{\partial y} \right] = 0 \tag{22}$$

$$\frac{\partial p}{\partial t} + \frac{\partial (U'_o p)}{\partial x} + \frac{\partial (V'_o p)}{\partial y} + \mu \left[\frac{\partial (M_x p + u)}{\partial x} + \frac{\partial (M_y p + v)}{\partial y} \right] = 0. \tag{23}$$

Previous work employing the staggered discretization and the absorbing buffer zone has shown that a buffer zone width of approximately 2.5 times the maximum wavelength of the propagating signal is necessary to achieve less than one percent error [7]. Thus, with this result in hand, the aforementioned techniques were applied to selected problems proposed for the Computational Aeroacoustics (CAA) workshop.

CATEGORY THREE

This category was devised in order to test the isotropy property of the computational algorithm as well as the capabilities of radiation, inflow, and outflow boundary conditions. Two problems were included which both involved the solution of the linearized Euler equations, but with different mean flow and initial conditions. The computational domain of both was -100 $\leq x \leq$ 100, -100 $\leq y \leq$ 100 embedded in free space with $\Delta x = \Delta y = 1$. Results were obtained through a straightforward implementation of the second and fourth order staggered spatial operators with fourth order Runge-Kutta time integration at a CFL number of .6. Additionally, a buffer zone of non-dimensional width 40 was employed at the boundaries to maintain one percent error as mentioned previously.

Problem 1

In this case, the mean flow was given as $M_x = .5, M_y = 0$ and the initial conditions were as described earlier in these proceedings. Solutions were obtained at successive times as the waves left the interior domain, however, only those at $t = 100$ are included. In figure 4, first a view of the entire domain is shown for the fourth order staggered solution. Then, a line plot of the density along the line y=0 is included for both the second and fourth order discretizations. The second

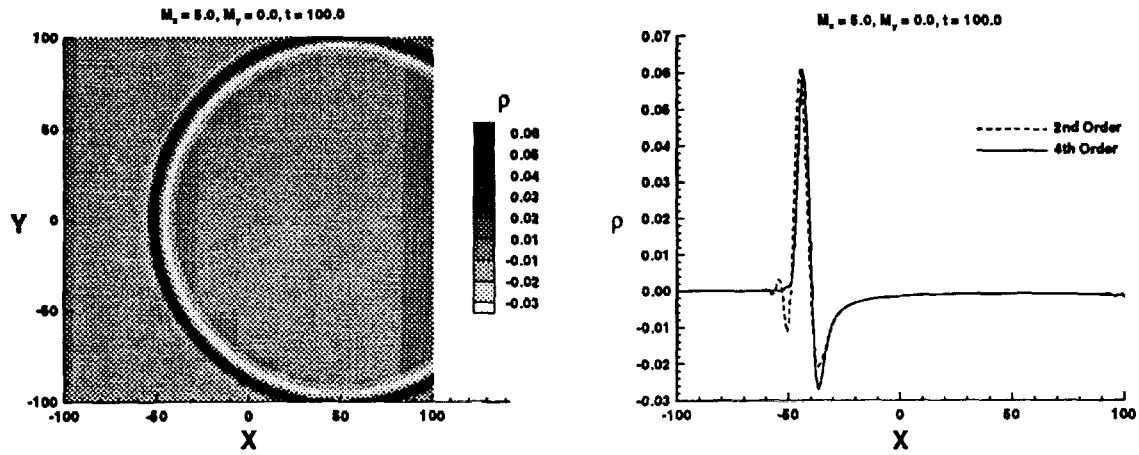

Figure 4: Results for Problem 1.

order scheme shows some dispersion error, which is diminished by the fourth order version. Overall, reasonable results were obtained and the schemes were therefore applied to problem two of this category.

Problem 2

This problem is very similar to problem one except that the mean flow is $M_x = M_y = 0.5\cos\left(\frac{\pi}{4}\right)$ and the initial conditions, as given in the problem description, are slightly different. The fact that the mean flow is directed toward the corner does not require special treatment by the buffer zone or the staggered discretization. The solution obtained by the fourth order scheme for t=100 is presented in figure 5. Also included is a line plot of the second and fourth order results along the line $y = x$. Here, part of the entropy and vorticity pulses are seen just leaving the interior domain at the upper corner. The second order result does again show some dispersion, but this is resolved by the fourth order code. The performance of both schemes was improved in comparison to problem one, and the staggered discretization and buffer zone handled these problems quite well. Therefore, having shown that these approaches may be used effectively together, the next step is to include a solid boundary. This geometry is found in category 4.

CATEGORY 4

In this category, the problems were set up to test the capabilities of wall boundary conditions, and for this work only problem two was investigated. It involves acoustic radiation from an oscillating piston in an infinite wall and is governed by the linearized Euler equations in cylindrical

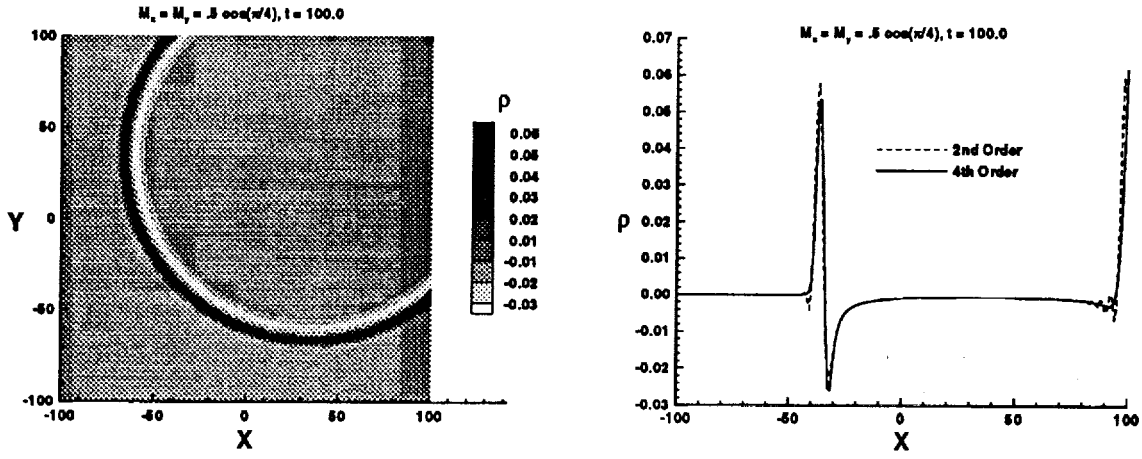

Figure 5: Results for Problem 2.

coordinates with axisymmetry. The piston (radius r=10) oscillates with normal velocity $u = 1.0^{-4} \sin \frac{\pi t}{5}$ into a computational domain $0 \leq x \leq 100$, $0 \leq r \leq 100$ with $\Delta x = \Delta r = 1$.

The geometry of this problem includes two radiation boundaries which may be handled using the absorbing buffer zone. In addition, the x-axis is a symmetry axis and the r-axis coincides with the rigid piston and wall as shown in figure 6. Also presented is the placement of the primitive variables. The symmetry axis is managed by setting the radial velocity component, v, equal to zero along its entirety and "reflecting" the other variables. The treatment of the piston and wall boundary depends on the size of the spatial stencil.

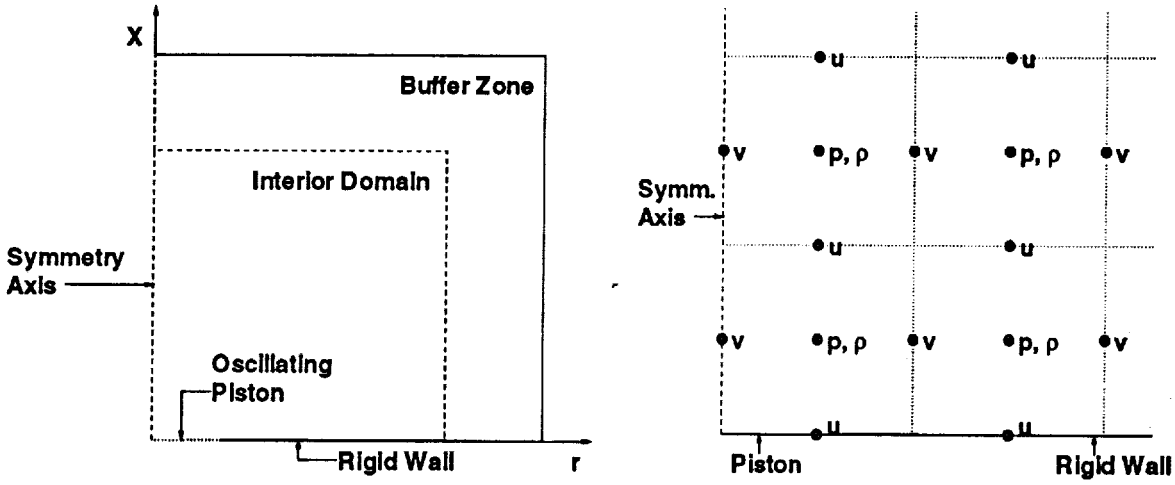

Figure 6: Geometry for Problem 2, Category 4.

For the second order scheme, no shifting of the spatial stencils is required. Only grid points for the normal component of velocity lay on the boundary, and this is given for the piston and is zero on the wall. Any of the stencils needed to discretize the governing equations remain in the interior and ghost points are not necessary. However, this is not the case for the fourth order version. Again, only grid points for the normal component of velocity fall precisely on the boundary, but the spatial stencils include more points and thus extend beyond the solid boundary. This problem was alleviated by following a procedure similar to that given by Tam and Dong [8].

Ghost points for pressure are obtained by using the momentum equation $\frac{\partial u}{\partial t} + \frac{\partial p}{\partial x} = 0$ along the piston and wall. This allows for a full spatial stencil to be used for the term $\frac{\partial p}{\partial x}$. The remaining spatial stencils are shifted at the boundary so that they require only known data points.

One more item should be considered before presentation of the results; that being the implementation of the time dependent boundary conditions on the piston for the Runge-Kutta integration. If a time dependent boundary condition for a system of equations described by equation (13) were given by $\mathbf{W}_i(0,t) = f(t)$, the standard treatment at each stage would be

$$\mathbf{W}_i^1 = f(t + \frac{\Delta t}{2}) \qquad \mathbf{W}_i^2 = f(t + \frac{\Delta t}{2}) \tag{24}$$

$$\mathbf{W}_i^3 = f(t + \Delta t) \qquad \mathbf{W}_i^{n+1} = f(t + \Delta t). \tag{25}$$

As mentioned by Carpenter *et. al* [9], higher order accuracy may be maintained at larger CFL numbers by the alternate implementation

$$\begin{aligned} \mathbf{W}_i^1 &= f(t) + \frac{\Delta t}{2} f'(t), \qquad \mathbf{W}_i^2 = f(t) + \frac{\Delta t}{2} f'(t) + \frac{(\Delta t)^2}{4} f''(t) \\ \mathbf{W}_i^3 &= f(t) + \Delta t f'(t) + \frac{(\Delta t)^2}{2} f''(t) + \frac{(\Delta t)^3}{4} f'''(t) \\ \mathbf{W}_i^{n+1} &= f(t + \Delta t). \end{aligned} \tag{26}$$

These expressions were used to specify the normal velocity of the oscillating piston. With the normal velocity on the rigid wall set equal to zero, the lower boundary was then handled and solutions could be obtained.

Results

In this case, a linearized analytic result is shown along with those from the second and fourth order schemes. In figure 7, these are presented in the form of line plots along the x and r axes at time $t = 160$ with a CFL number of .5005 and a buffer zone width of 25 units. These plots show

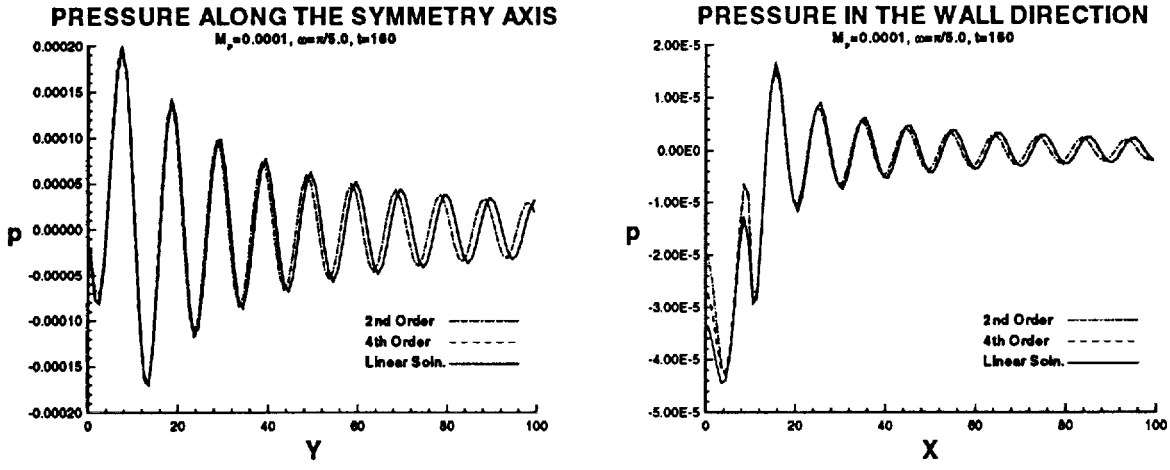

Figure 7: Results for Problem 2, Category 4 along the x and r axes.

that the fourth order scheme captures the solution quite well with only small errors along the

piston face. As in the category three problems, the second order version shows some dispersion which is evident in both directions. It should be noted however, that this problem was formerly solved with a second order MacCormack scheme and the results for the staggered schemes are an improvement over those obtained previously. Thus, with the staggered scheme and buffer zone continuing to show promise, the approaches were applied to the problem of category 6.

CATEGORY 6

The proposed problem of this category tests the scheme's ability to calculate sound generation by a gust-plate interaction and requires conditions on the flat plate as well as inflow, outflow, and radiation conditions. It is governed by the linearized Euler equations in Cartesian coordinates, and there is a mean flow in the x direction given by $M_\infty = 0.5$ which carries with it a gust velocity component in the y-direction of the form $v = 0.1 \sin\left[\frac{\pi}{8}\left(\frac{x}{M_\infty} - t\right)\right]$. A computational domain $-100 \leq x \leq 100$, $-100 \leq y \leq 100$ was used with $\Delta x = \Delta y = 1$.

As mentioned above, the problem geometry includes inflow and outflow boundaries. These are handled by the absorbing buffer zone technique as shown in figure 8. Additionally, the flat plate requires that the total normal velocity be zero on its surface. For the second order discretization, this is handled quite easily since only the grid points for the normal components of velocity fall on the plate surface, as seen in figure 8. Thus, the normal velocity may be specified and the other primitive variables calculated directly since the second order stencils do not extend beyond the plate. The fourth order implementation is only slightly more complicated and is accomplished in the same way as the piston and wall were handled in problem 2 of category 4. The grid points for the normal velocity are still the only grid points exactly on the plate, however the spatial stencils extend beyond the plate. Ghost points for pressure are obtained by using the momentum equation $\frac{\partial v}{\partial t} + \frac{\partial M_\infty v}{\partial x} + \frac{\partial p}{\partial y}$ along the plate surface. The stencils for the remaining variables are shifted so that they require only known data points.

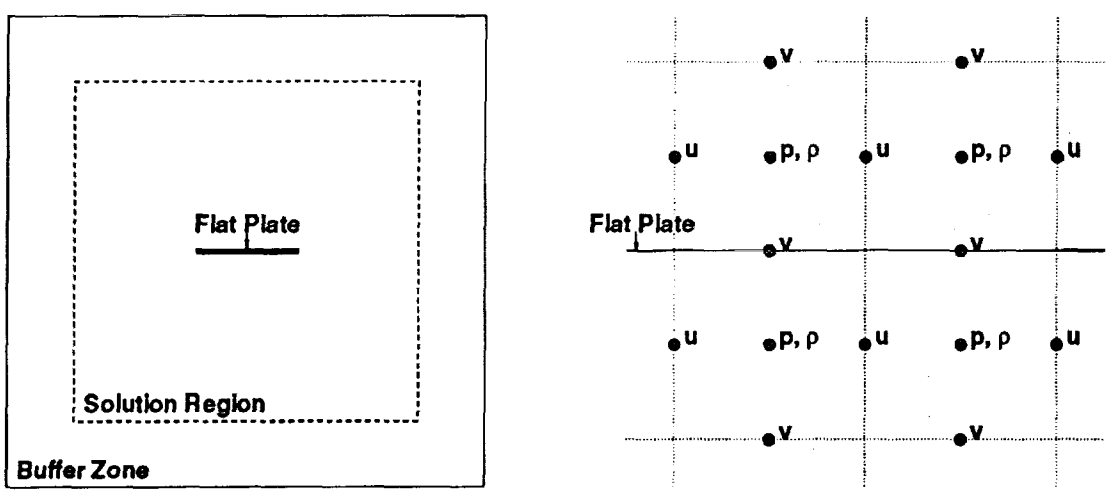

Figure 8: Geometry for Problem 1, Category 6.

Results

An analytic solution was not available for this problem, so the results included are those outlined in the problem description. In figure 9, the intensity of the radiated sound $\overline{p^2}$ along the

lines $x = \pm$ 95 is presented with a CFL number of .5625 and a buffer zone width of 40. This clearly shows the larger sound intensity being emitted behind the flat plate. The second line plot gives the intensity along the lines $y = \pm$ 95. In this case, the curves fall directly on top of one another showing that the sound field is symmetric above and below the plate. In addition, there are lobes evident in this solution which give insight into the directivity of the radiated sound. Although a direct comparison with an exact solution is not possible, the schemes seemed to give very reasonable results for this problem.

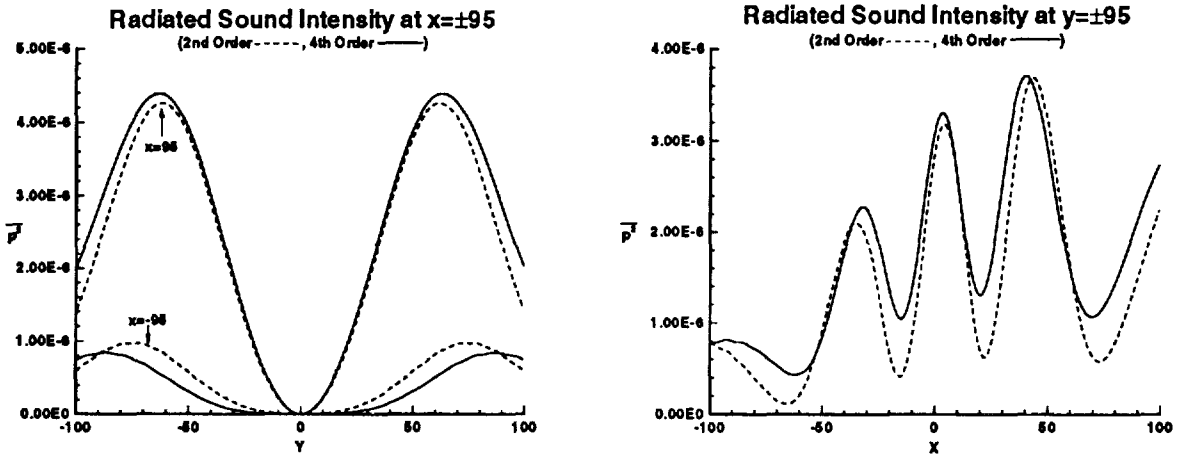

Figure 9: Results for Problem 1, Category 6.

CONCLUSIONS

The problems presented in this work have shown that the staggered schemes and buffer zone technique can perform quite well when properly employed. The staggered schemes have been found to exhibit some very nice properties. First, the schemes show an improvement in dispersion characteristics without the addition of any artificial damping. Also, the required stencils generally simplify the implementation of physical boundaries by requiring only certain quantities at specified locations. This aspect simplified the coupling with the outlow conditions as well.

The absorbing buffer zone conditions provide a straightforward way of handling outflow boundaries without the need for local acoustic boundary conditions which can be problematic. Additionally, there are modifications that could be made to improve the efficiency of the technique. The imposed velocity field in the buffer zone may be modified by using different ramping functions or optimizing those used in this work. This change may in turn lead to a decrease in reflection as a wave enters the zone. The spatial discretization in the buffer zone may also be a point of investigation. In these cases, the computational grid was unchanged in the buffer zone. It may be possible to increase the step size in the zone and achieve similar results with less computation. Possible improvements aside, the staggered schemes and buffer zone technique provided very good results as they were implemented and show promise in their use for a wider variety of more complicated problems.

ACKNOWLEDGEMENTS

The author would like to thank Shlomo Ta'asan for introducing him to the use of staggered schemes and absorbing buffer zones. Also, thanks to Dr. Jay C. Hardin for many helpful suggestions throughout this work.

REFERENCES

[1] Anderson, D. A., Tanehill, J. C., and Pletcher, R. H., *Computational Fluid Mechanics and Heat Transfer*, McGraw Hill, 1984.

[2] Yee, K. S., "Numerical Solution of Initial Boundary Value problems Involving Maxwell's Equations in Isotropic Media", *IEEE Trans. on Antennas and Propagation*, Vol. AP-14, No.3, pp. 302-307 (1966).

[3] Joslin, R. D., Streett, C. L., and Chang, C., "Validation of Three- Dimensional Incompressible Spatial Direct Numerical Simulation Code", NASA Technical Paper 3205, July 1992.

[4] Streett, C. L., and Macaraeg, M. G., "Spectral Multi-Domain for Large-Scale Fluid Dynamic Simulations", *Int. Journal Appl. Numer. Math.*, Vol. 6, pp. 123-139, (1989).

[5] Liu, C., and Liu, Z., "High Order Finite Difference and Multigrid Methods for Spatially Evolving Instability in a Planar Channel", *Journal of Computational Physics*, Vol 106, pp. 92-100 (1993).

[6] Kishoni, D., and Ta'asan, S., "Non-reflecting regions for finite difference methods in modeling of elastic wave propagation in plates", Review of Progress in Quantitative NDE, Vol 13, Edited by D.O. Thompson and Chimenti (Plenum Press, New York, 1994).

[7] Ta'asan, S., and Nark, D. M. "An Absorbing Buffer Zone Technique for Acoustic Wave Propagation", *Proceedings of the 33rd AIAA Aerospace Sciences Meeting*, Reno, NV, January 9-12, 1995.

[8] Tam, C. K. W., and Dong, Z., "Solid Wall Boundary Conditions for Computational Aeroacoustics". *Proceedings of the Forum on Computational Aero- and Hydro- Acoustics*, Washington, DC, June 20-24, 1993.

[9] Carpenter, M. H., Gottlieb, D., Abarbanel, S., and Don, W., "The Theoretical Accuracy of Runge-Kutta Time Discretizations for the Initial Value Problem: A Careful Study of the Boundary Error". NASA Contractor Report No. 93-83, November, 1993.

A NUMERICAL SOLUTION METHOD FOR ACOUSTIC RADIATION FROM AXISYMMETRIC BODIES*

John E. Caruthers
G. K. Raviprakash
The University of Tennessee Space Institute
Tullahoma TN 37388

SUMMARY

A new and very efficient numerical method for solving equations of the Helmholtz type is specialized for problems having axisymmetric geometry. It is then demonstrated by application to the classical problem of acoustic radiation from a vibrating piston set in a stationary infinite plane.

The method utilizes "Green's Function Discretization" [1], to obtain an accurate resolution of the waves using only 2-3 points per wave. Locally valid free space Green's functions, used in the discretization step, are obtained by quadrature.

Results are computed for a range of grid spacing/piston radius ratios at a frequency parameter, $\omega R/c_0$, of 2π. In this case, the minimum required grid resolution appears to be fixed by the need to resolve a step boundary condition at the piston edge rather than by the length scale imposed by the wave length of the acoustic radiation. It is also demonstrated that a local near-field radiation boundary procedure allows the domain to be truncated very near the radiating source with little effect on the solution.

INTRODUCTION

A method of discretizing the Helmholtz equation over a finite domain for the purpose of efficient numerical solution has recently been given by Caruthers, French, and Raviprakash [1]. The method proved to be nearly optimal in the sense that the accuracy of the discretization does not fail until the grid coarseness approaches 2 points/wave along the grid diagonal, while standard finite difference and finite element methods require approximately 10 points/wave to maintain adequate wave resolution.

As an intermediate step in the construction of the discretizing equations, free space Green's functions for the Helmholtz equation are used. For three-dimensional and two-dimensional planar problems these functions are simply given by $e^{-ikr}/4\pi r$ and $iH_0^{(2}(kr)/4$, respectively. A certain important class of practical problems, however, are quasi-three-dimensional in nature. For example, acoustic fields generated or scattered by axisymmetric bodies are generally three-dimensional but may be Fourier decomposed in the azimuthal coordinate yielding decomposed

* Work supported by Propeller and Acoustics Technology Branch of NASA Lewis Research Center, through grant NAG3-1516.

"modes" which are uncoupled in the radial-axial plane. Problems involving turbofan noise generation and propagation to the environment, for example, are often modeled in this manner. That is, letting $\hat{\phi}$ be the acoustic velocity potential

$$\hat{\phi}(r,z,\theta) = \sum_{\nu=-\infty}^{\infty} \phi_\nu(r,z)e^{i\nu\theta} \tag{1}$$

where

$$\frac{1}{r}\frac{\partial}{\partial r}\left(\frac{r\partial\phi_\nu}{\partial r}\right) + \frac{\partial^2\phi_\nu}{\partial z^2} + (k^2 - \frac{\nu^2}{r^2})\phi_\nu = 0 \;\; ; \;\; k = w/c \tag{2}$$

$$\nu = -\infty, \ldots, -1, 0, 1, \ldots, \infty$$

The corresponding free space Green's functions for equation (2) are harmonic ring source fields and are given in simple quadrature form in the following section. Fully axisymmetric problems, such as the benchmark circular piston radiation problem considered in this paper, correspond to the special case $\nu = 0$, but the method, as presented herein, is valid for $\nu \neq 0$ as well.

In the following we consider the solution of the acoustic problem of a circular disk set in a infinite wall (as indicated in Figure 1) and oscillating as a rigid body in simple harmonic motion normal to the surface. The Helmholtz equation for the acoustic velocity potential and boundary conditions are discretized using Green's Function Discretization [1] (summarized briefly in the following section) resulting in a large linear algebraic system of equations which is solved by a standard direct technique for sparse banded systems. The accuracy of the resulting solution is then examined by comparison with a solution obtained from the exact quadrature formula. At first a solution is obtained on a very large domain with high grid resolution (10 points/wave). Then the beneficial features of the method are highlighted by solving the same problem on a subdomain at grid densities of $10, 5, 4$, and 3 points/wave. The structure of the discretization method allows a convenient formulation of a local near-field radiation approximation which allows consideration of the small subdomain problems with negligible penalty in accuracy.

ANALYSIS

Summary of Green's Function Discretization

The foundation for Green's Function Discretization [1] (GFD) is the idea that the acoustic field may be approximated in the vicinity of each discrete point of the domain by a superposition of the acoustic fields generated by N hypothetical simple sources of strength γ_n located at N points $\mathbf{r}_n$ surrounding each discrete point. That is, dropping the subscript ν, with that implied

$$\phi(\mathbf{r}) = \sum_{n=1}^{N} \gamma_n G(\mathbf{r};\mathbf{r}_n) \tag{3}$$

where $G(\mathbf{r};\mathbf{r}_n)$, is the free space Green's function for equation (2) given by

$$G(\mathbf{r};\mathbf{r}_n) = \int_0^{2\pi} \frac{e^{-ikr'}}{4\pi r'} \rho_n e^{i\nu\theta} d\theta \tag{4}$$

where

$$r' = \sqrt{\rho^2 + \rho_n^2 - 2\rho\rho_n \cos\theta + (z - z_0)^2} \tag{5}$$

and where ρ and ρ_n are the cylindrical radial coordinates of $\mathbf{r}$ and $\mathbf{r}_n$ respectively. Then for each of M points in the local neighborhood where equation (3) is valid we have

$$\phi(\mathbf{r}_m) = \sum_{n=1}^{N} \gamma_n G(\mathbf{r}_m; \mathbf{r}_n) \; ; \; m = 1, 2, ..., M \tag{6}$$

In matrix notation

$$\boldsymbol{\phi} = \mathbf{G}\boldsymbol{\gamma} \tag{7}$$

where $\boldsymbol{\phi}$ and $\boldsymbol{\gamma}$ are $M \times 1$, and $N \times 1$ matrices respectively (i.e., column vectors) with elements $\phi(\mathbf{r}_m); m = 1, 2, ..., M$ and $\gamma_n; n = 1, 2, ..., N$, and $\mathbf{G}$ is an $M \times N$ matrix with elements $G(\mathbf{r}_m; \mathbf{r}_n)$. Intentionally letting $N > M$, *a* solution of equation (7) for the hypothetical source distribution $\boldsymbol{\gamma}$ having a minimum L^2 norm property is given by

$$\boldsymbol{\gamma} = \mathbf{G}^+ \boldsymbol{\phi} \tag{8}$$

where $\mathbf{G}^+$ is the so-called pseudo-inverse of the rectangular matrix $\mathbf{G}$.

Letting $\mathbf{g}$ represent the column vector with elements $g_n(\mathbf{r}) = G(\mathbf{r} : \mathbf{r}_n)$, equations (3) and (8) combine to give

$$\phi(\mathbf{r}) = \mathbf{g}^T \mathbf{G}^+ \boldsymbol{\phi} \tag{9}$$

The field discretization is now obtained simply by letting $\mathbf{r}$ take on successive values $\mathbf{r}_{i,j}$ at each lattice point of the grid while $\boldsymbol{\phi}$ refers to the corresponding set of M surrounding nodes which is different for each point. For uniform grids the row vector quantity $\mathbf{g}^T\mathbf{G}^+$ needs to be computed only once for the entire grid, yielding.

$$\phi(\mathbf{r}_{i,j}) = \mathbf{g}^T \mathbf{G}^+ \boldsymbol{\phi}_{i,j} \tag{10}$$

In this case, the discretizing relation is exactly the same for all field points just as it would be for standard finite difference or finite element discretization methods. In the current axisymmetric case, however, even uniform grid spacing in the axial-radial plane does not provide the necessary uniformity since the azimuthal scale of the grid varies with the radius. Then the quantity $\mathbf{g}^T\mathbf{G}^+$ must be recomputed for each lattice point of different radius so that

$$\phi(\mathbf{r}_{i,j}) = (\mathbf{g}^T \mathbf{G}^+)_j \boldsymbol{\phi}_{i,j} \tag{11}$$

It remains to select the number, N, and relative locations $\mathbf{r}_n$ of the hypothetical sources. The neighboring point set [i.e., the $\mathbf{r}_m$ and M of equation (6)] must also be selected. There is a degree of arbitrariness about this selection. For the purpose of computing the example of this paper we have chosen $N = 20$, and $M = 8$, with the locations as indicated in Figure 2.

Radiation Boundary Conditions

The upper and right boundaries of this problem are free radiating surfaces along which some condition must be applied, which implies that all disturbances present at this boundary had

their origin below the upper boundary and to the left of the right boundary. A procedure for applying such conditions in the near-field has been developed previously by the present authors for application to turbofan noise propagation problems and may be found developed in some detail in [2]. The procedure presents itself quite naturally, however, in the current context of the GFD method since one needs only to choose the discretizing point set in a manner similar to that shown in Figure 2 at the radiating boundaries and then choose the locations $\mathbf{r}_n; n = 1, 2, 3, \ldots, N$, all entirely within the bounded domain. This is all that is required to satisfy the conditions of a free radiating surface. No far-field property at the radiating boundary is implied by this simple procedure. Limiting the discretizing set of points to only the adjacent points makes this a "numerically local" method which has the advantage of preserving the block tridiagonal nature of the overall linear system of equations. Obviously, a numerically non-local procedure may be constructed by extending the discretizing set to more remote points at the expense of the overall linear system block band width. Numerical experimentation has shown this to be unnecessary. This near-field radiation procedure allowed consideration of the much smaller near-field subdomain in the example results.

Finally, in this regard, for the current example problem, one may take advantage of the limited extent of the radiating surface by choosing the hypothetical sources for each point along the radiation boundary to lie along the piston surface. Notice that hypothetical source strengths are not given (this would be cheating) but are calculated from equation (8) as for the field points. Indeed, each radiation boundary point may see a different distribution of hypothetical radiator sources.

Neumann Boundary Conditions

Along the piston and wall surface, as well as along the axis of symmetry for this example problem, Neumann boundary conditions are applied. Along the piston face $\frac{\partial \phi}{\partial z} \mid_{z=0} = 1$ represents the normalized velocity amplitude of the piston surface. Along the remaining wall $\frac{\partial \phi}{\partial z} \mid_{z=0} = 0$. The symmetry condition gives $\frac{\partial \phi}{\partial r} \mid_{r=0} = 0$ along the axis of symmetry.

To discretize these boundary conditions we merely select a one-sided set of neighboring points for the discretizing point set as depicted in Figure 2, and add constraint equations to the system of equations (7) to reflect the given values of $\frac{\partial \phi}{\partial n}$ at a chosen number of points (indicated by the solid dots) along the portion of boundary bound by the point set. It should be pointed out that it is possible to do this exactly only because the choice of $N > M$ yielded an underdetermined system of equations (7) to which up to $N - M$ additional constraints may be added without compromising the collocating property of the resulting interpolation [given by equation (9)]. The net result of this boundary procedure is a solution which is locally an exact solution to the Helmholtz equation all the way to the wall and satisfies the specified Neumann boundary conditions exactly at up to $N - M$ boundary points within each boundary lattice.

For the example problem considered in this paper, the jump discontinuity in the boundary condition at the piston edge presents a severe challenge to the boundary algorithm if accurate solutions are to be obtained using desirable coarse grids. It was found by numerical experimentation that the best results were achieved by applying the boundary conditions at the mid-points of the lattice as indicated in Figure 2 along the piston/wall surface.

RESULTS

The numerical solution of the Helmholtz equation is obtained in the large domain (10×10) using a 100×100 grid. The reduced frequency for the test problem is given by $k = \frac{\omega R}{c_0} = 2\pi$ (R is radius of the piston). The magnitude and phase contours of $p/(\rho_0 c_0 v_p)$ are plotted in Figures 3a1 and 3a2. In the plots, tick marks on the x and r axis correspond to the grid used. The accuracy of the solution obtained can be easily seen by plotting the corresponding exact solution as in Figures 3b1 and 3b2. It is difficult to distinguish the difference between the two solutions. In order to look at the near-field solution more closely, a 2×2 window is considered in the large domain. The solution obtained earlier is plotted in this window domain by a post solution interpolation procedure based on the interpolation formula given by equation (9), and is shown in Figures 4a1 and 4a2. This procedure uses the solution in the 20×20 grid window domain to interpolate the solution to a 100×100 subgrid in the same window domain. These results, in Figures 4a1 and 4a2, compare very well with those of the exact solution in Figures 4b1 and 4b2. It can be seen that the post solution interpolation procedure gives a very accurate representation inside each grid box. It can be noted that the maximum value of the amplitude of $p/(\rho_0 c_0 v_p)$ differs from the exact solution only by 0.5%.

To look at the effectiveness of the near-field local radiation boundary condition, a smaller subdomain (2×2) is considered for carrying out the basic solution. The numerical solution obtained in this subdomain with a 20×20 grid is plotted in Figures 5a and 5b. These results obtained in this subdomain are nearly identical to that obtained in the larger domain problem.

The power of the GFD method can be shown by using coarser grids to solve the same problem. The results for a 10×10 grid with 5 grid spaces on the piston, shown in Figures 6a and 6b, also compare very well with the exact solution.

The magnitude and phase contours for an 8×8 grid problem are shown in Figures 7a and 7b. The accuracy of the detailed solution that is obtained between grid points, by using post solution interpolation, can be easily seen now by looking at the grid box at $z = 0$, $y = 0.4$ in Figures 6a and 6b and at $z = 0$, $y = 0.5$ in Figures 7a and 7b. The maximum pressure $p/(\rho_0 c_0 v_p)$ amplitude in the 8×8 coarse grid problem differs by just 1.7% from the exact maximum pressure. The errors in magnitude normalized by the maximum value of $p/(\rho_0 c_0 v_p)$ in the domain are calculated for all these cases and are shown in Table I.

Table 1. Normalized Errors

Domain	Grid	No. of Grid Spaces on Piston	Error in Max Pressure	Max Error	Average Error
10×10	100×100	10	0.55×10^{-2}	1.112×10^{-2}	3.522×10^{-4}
10×10 (2 x 2 window in)	100×100	10	0.56×10^{-2}	1.314×10^{-2}	1.226×10^{-3}
2×2	20×20	10	0.55×10^{-2}	1.388×10^{-2}	1.188×10^{-3}
2×2	10×10	5	0.90×10^{-2}	2.955×10^{-2}	2.411×10^{-3}
2×2	8×8	4	1.70×10^{-2}	2.928×10^{-2}	4.327×10^{-3}
2×2	6×6	3	9.25×10^{-2}	0.162	2.310×10^{-2}

Finally a very coarse (6×6) grid with just 3 grid spacings on the piston is solved. The overall behavior of the solution looks reasonable, but the maximum pressure differs by 9.5% from the

exact maximum pressure (Figures 8a and 8b). Also the contours above the piston edge are not very accurate. It must be noted that any numerical method for this problem has to resolve jump boundary conditions at the piston edge as well as the wavelength of the radiating sound field. The inaccuracy in the above solution is more likely due to the insufficient resolution of the jump condition at the piston edge than failure to resolve the resulting wave structure which is already < 3 points/wave along the primary direction of wave propagation.

CONCLUSIONS

The Green's Function Discretization technique has been successfully adapted to quasi-three-dimensional boundary value problems for the Helmholtz equation. The accuracy and efficiency of the method have been demonstrated by application to the classic problem of acoustic radiation from an harmonically oscillating circular piston set in an infinite plane wall.

Once the discretization process is completed, resulting in a large linear system of equations, the number of arithmetic operations required to solve the system goes like $2n_r^3 n_z$ for large n_r, where n_r is the number of grid points in the radial direction and n_z is the number in the axial direction. This translates into work station computer solution times measured in tiny fractions of a second for all the subdomain example solutions of the benchmark piston radiation problem considered here. By far the greatest computing effort is spent in forming the initial discretization and producing the post-solution interpolation for high resolution display.

The need to resolve the jump discontinuity in the boundary condition at the piston edge, on a scale small relative to the piston radius, appears to set the minimum grid spacing required for accurate solution of this example problem.

Finally, the utility and simplicity of the GFD method in accurately implementing both Neumann and radiation type boundary conditions with a discretization procedure almost identical to that for the field points have been demonstrated.

REFERENCES

[1] Caruthers, J. E.; French, J. C.; and G. K. Raviprakash: Green's Function Discretization for Numerical Solution of the Helmholtz Equation. Accepted for publication by the *Journal of Sound and Vibration*, February 1994, to appear in October 1995.

[2] Raviprakash, G. K.: Ph.D. dissertation The University of Tennessee. A Computational Method for the Analysis of Acoustic Radiation from Turbofan Inlets. May 1992.

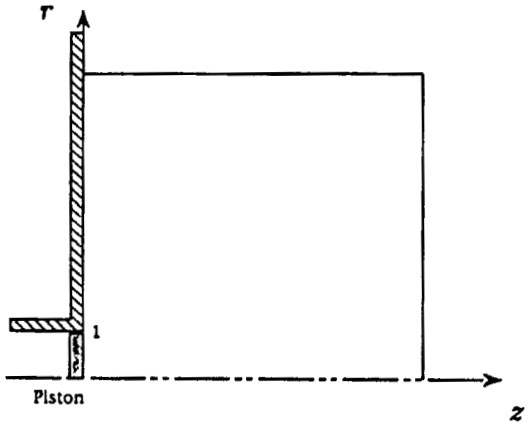

Figure 1. ICASE/LaRC benchmark problem: acoustic field of an oscillating circular piston in a wall.

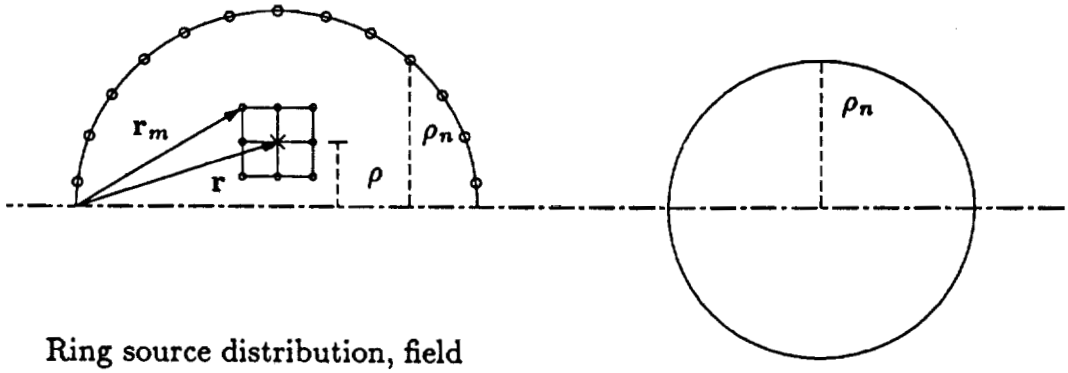

Ring source distribution, field point, and the neighboring points.

Axial view of ring source n at ρ_n.

2a. Field point.

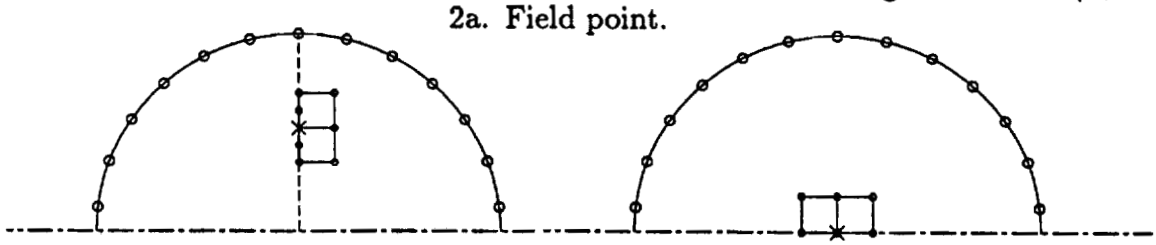

2b. Points along the wall boundary and on the piston.

2c. Points along the axis.

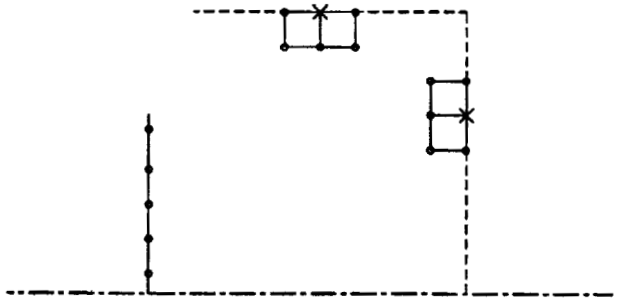

2d. Points along the radiating boundary.

Figure 2. Illustration of the ring source GFD method.

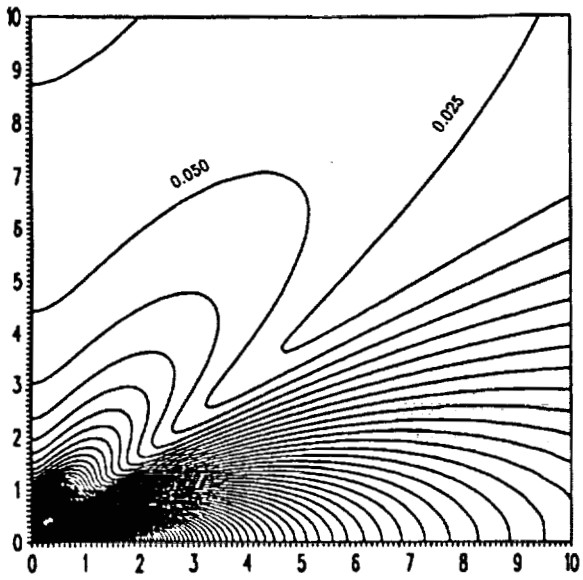

3a1. Numerical solution contours of $|p/(\rho_0 c_0 v_p)|$ in 0.025 intervals, max = 2.01.

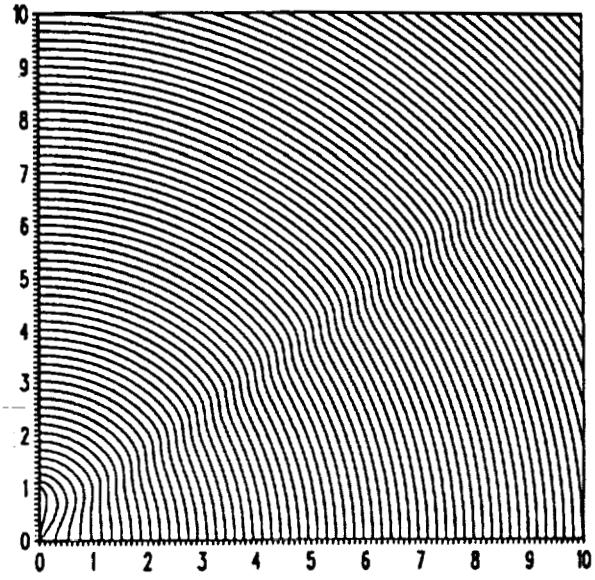

3a2. Numerical solution contours of phase in 60° intervals.

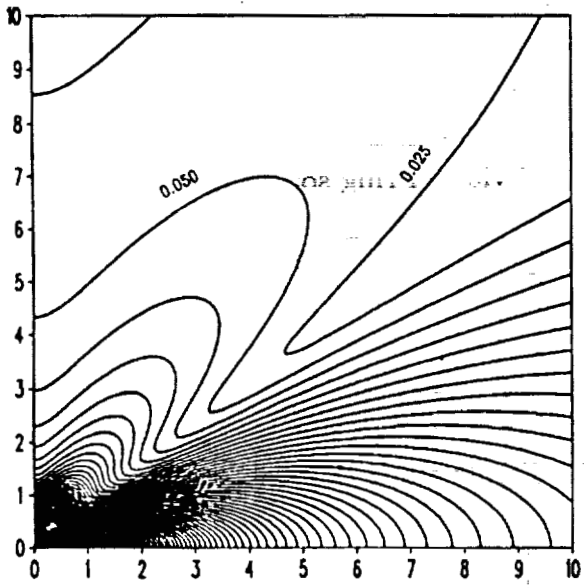

3b1. Exact solution contours of $|p/(\rho_0 c_0 v_p)|$ in 0.025 intervals, max = 2.0.

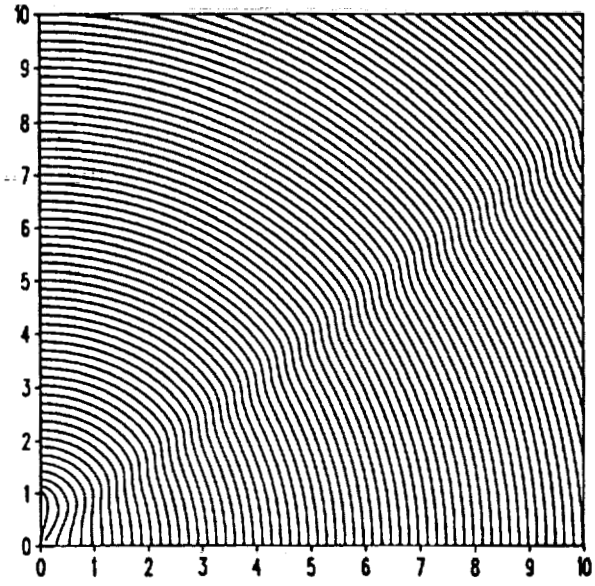

3b2. Exact solution contours of phase in 60° intervals.

Figure 3. Acoustic field of an oscillating circular piston (large domain solution).

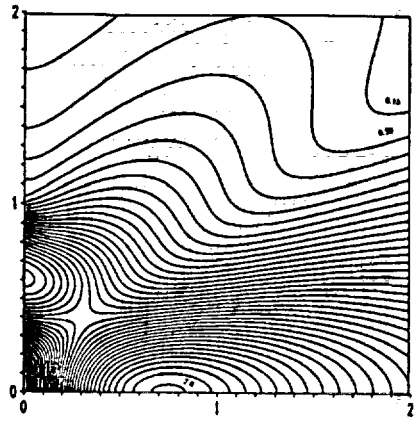

4a1. Numerical solution contours of $|p/(\rho_0 c_0 v_p)|$ in 0.05 intervals, max = 2.012.

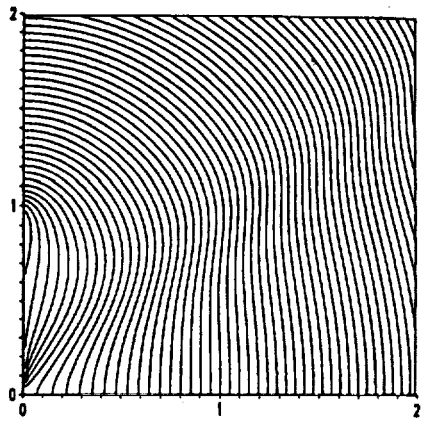

4a2. Numerical solution contours of phase in 15° intervals.

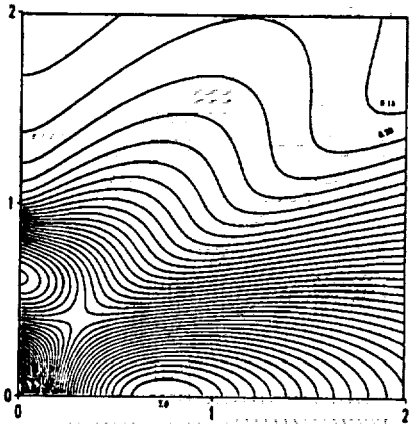

4b1. Exact solution contours of $|p/(\rho_0 c_0 v_p)|$ in 0.05 intervals, max = 2.0.

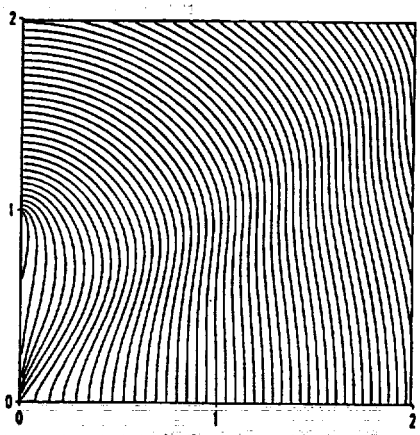

4b2. Exact solution contours of phase in 15° intervals.

Figure 4. Acoustic field of an oscillating circular piston (solution inside 2 × 2 window of the large domain).

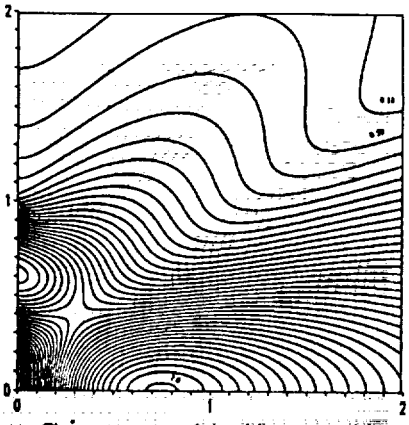

5a. Contours of $|p/(\rho_0 c_0 v_p)|$ in 0.05 intervals, max = 2.011.

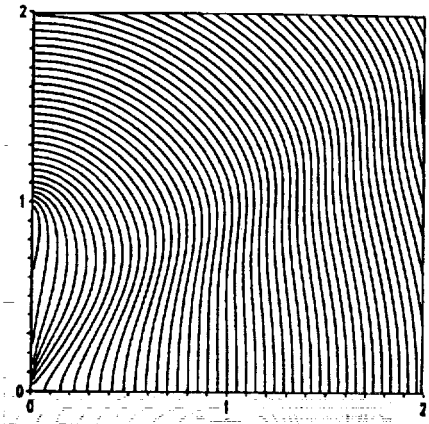

5b. Contours of phase in 15° intervals.

Figure 5. Subdomain numerical solution using local near-field radiation boundary conditions (20 × 20).

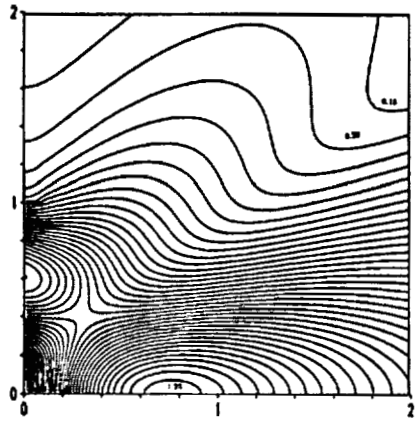

6a. Contours of $|p/(\rho_0 c_0 v_p)|$ in 0.05 intervals, max = 1.982.

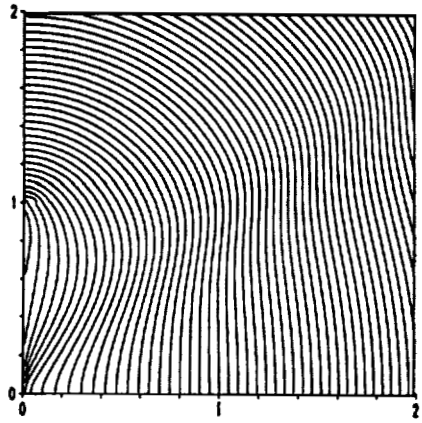

6b. Contours of phase in 15° intervals.

Figure 6. Coarse grid solution 1 (10 × 10 grid).

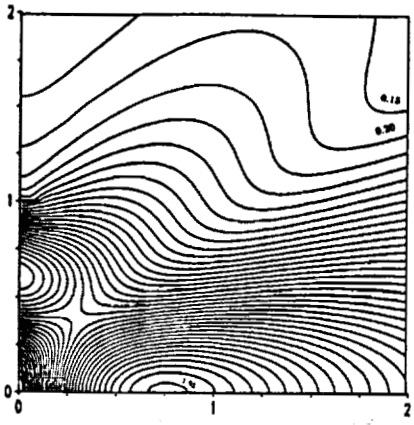

7a. Contours of $|p/(\rho_0 c_0 v_p)|$ in 0.05 intervals, max = 1.966.

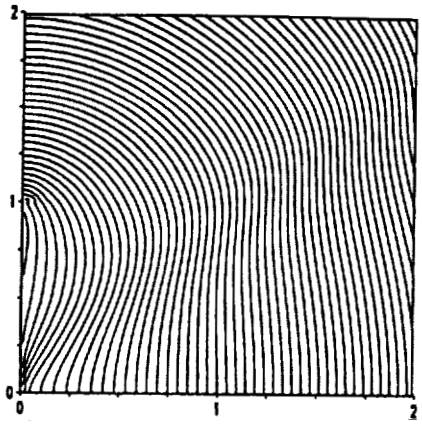

7b. Contours of phase in 15° intervals.

Figure 7. Coarse grid solution 2 (8 × 8 grid).

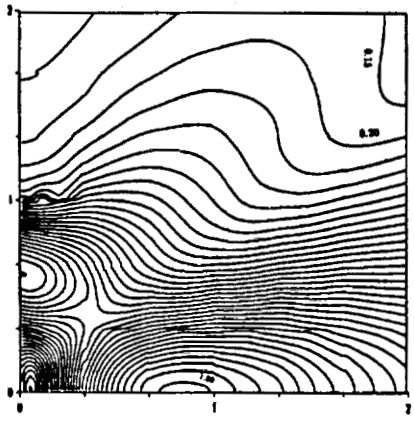

8a. Contours of $|p/(\rho_0 c_0 v_p)|$ in 0.05 intervals, max = 1.815.

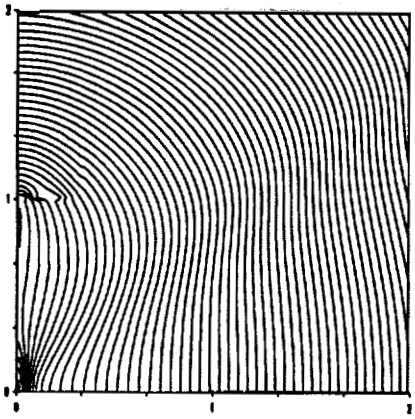

8b. Contours of phase in 15° intervals.

Figure 8. Coarse grid solution 3 (6 × 6 grid).

APPLICATION OF A NEW FINITE DIFFERENCE ALGORITHM FOR COMPUTATIONAL AEROACOUSTICS

John W. Goodrich
NASA Lewis Research Center
Cleveland, Ohio

INTRODUCTION

Accoustic problems have become extremely important in recent years because of research efforts such as the High Speed Civil Transport program (see [5]). Computational aeroacoustics (CAA) requires a faithful representation of wave propagation over long distances, and needs algorithms that are accurate and boundary conditions that are unobtrusive (see [4]). This paper applies a new finite difference method and boundary algorithm to the Linearized Euler Equations (LEE) for acoustic propagation in two space dimensions.

THE ALGORITHM

We will consider the LEE in two space dimensions in the form of the system

$$\begin{aligned} \frac{\partial u}{\partial t} + M_x \frac{\partial u}{\partial x} + M_y \frac{\partial u}{\partial y} + \frac{\partial p}{\partial x} &= 0, \\ \frac{\partial v}{\partial t} + M_x \frac{\partial v}{\partial x} + M_y \frac{\partial v}{\partial y} + \frac{\partial p}{\partial y} &= 0, \\ \frac{\partial p}{\partial t} + M_x \frac{\partial p}{\partial x} + M_y \frac{\partial p}{\partial y} + \frac{\partial u}{\partial x} + \frac{\partial v}{\partial y} &= 0, \end{aligned} \tag{1}$$

for the pressure p, the x velocity u, and the y velocity v. System (1) is in nondimensional form, and M_x and M_y are the constant mean convection Mach numbers in the the x and y directions. The density is not included in (1) since it affects neither the pressure nor the velocities.

The new algorithm uses a twenty one point symmetric stencil obtained from the twenty five point 5×5 square stencil by deleting the four corner points. This algorithm can be written most efficiently as an explicit finite difference method, with each new solution value obtained as a particular linear combination of the known data on the twenty one point stencil. The algorithm can be written in this form as

$$\begin{aligned} u_{i,j}^{n+1} &= \sum_{\{q,r\} \in IS} \left[a u_{q,r} u_{i+q,j+r}^{n} + a v_{q,r} v_{i+q,j+r}^{n} + a p_{q,r} p_{i+q,j+r}^{n} \right], \\ v_{i,j}^{n+1} &= \sum_{\{q,r\} \in IS} \left[b u_{q,r} u_{i+q,j+r}^{n} + b v_{q,r} v_{i+q,j+r}^{n} + b p_{q,r} p_{i+q,j+r}^{n} \right], \\ p_{i,j}^{n+1} &= \sum_{\{q,r\} \in IS} \left[c u_{q,r} u_{i+q,j+r}^{n} + c v_{q,r} v_{i+q,j+r}^{n} + c p_{q,r} p_{i+q,j+r}^{n} \right], \end{aligned} \tag{2}$$

where IS is the appropriate index set for the stencil. The one hundred and eighty nine constants will not be given here because of space limitations. Method (2) is a single step explicit finite difference algorithm with a symmetric central stencil, it is fourth order accurate in both space and time, it is isotropic in the sense that the computational error is not significantly affected by the angle between the grid and either the mean convection velocity or the propagating wave front, and it is stable if the ratio of the time to space step sizes is less than one over one plus the mean convection speed. For subsonic flows, grid ratios up to at least $\frac{1}{2}$ may be used. Details are provided in Goodrich [1].

Hagstrom [3] has developed a new outflow boundary condition that we will use. At the $+x$ or downstream outflow boundary, the outflow boundary condition is most easily presented in terms of the diagonalization of system (1) in the x variable, replacing (1) with equivalent equations for the three variables $\omega_1 = u - p$, $\omega_2 = v$, and $\omega_3 = u + p$. The partial differential equation for ω_1 is

$$\frac{\partial \omega_1}{\partial t} + (M_x - 1)\frac{\partial \omega_1}{\partial x} + M_y \frac{\partial \omega_1}{\partial y} - \frac{\partial \omega_2}{\partial y} = 0. \tag{3}$$

For subsonic flows $M_x - 1 \leq 0$, and ω_1 is conventionally described as incoming at the outflow boundary. Hagstrom's new boundary condition replaces equation (3) for ω_1 by the system

$$\begin{aligned}
&\frac{\partial \omega_1}{\partial t} + M_y \frac{\partial \omega_1}{\partial y} - M_x \frac{\partial \omega_2}{\partial y} + \sum_j (f_j + g_j) = 0, \\
&\frac{\partial f_j}{\partial t} + (M_x + \alpha_j)(1 - M_x^2)^{\frac{1}{2}} \frac{\partial f_j}{\partial y} = \frac{\beta_j}{2}(1 - M_x^2)\frac{\partial^2 p}{\partial y^2}, \\
&\frac{\partial g_j}{\partial t} + (M_x - \alpha_j)(1 - M_x^2)^{\frac{1}{2}} \frac{\partial f_j}{\partial y} = \frac{\beta_j}{2}(1 - M_x^2)\frac{\partial^2 p}{\partial y^2},
\end{aligned} \tag{4}$$

where the f_j and g_j are auxiliary variables. Notice that all of the spatial derivatives in (4) are parallel to the outflow boundary. Condition (4) uses no assumptions about the data, and no geometric information about the solution. Details are provided in Hagstrom [3]. In this paper we use $j = 2$, with $\alpha_1 = Cos(\frac{\pi}{5})$, $\alpha_2 = Cos(\frac{2\pi}{5})$, $\beta_1 = \frac{2}{5}Sin^2(\frac{\pi}{5})$, and $\beta_2 = \frac{2}{5}Sin^2(\frac{2\pi}{5})$. Condition (4) has been implemented as a local single step explicit algorithm, similar to method (2), with a central stencil and fourth order accuracy in both space and time. Details are provided in Goodrich and Hagstrom [2].

THE CATEGORY FOUR WALL PULSE PROBLEM

Data for the category four ICASE CAA workshop problem will be shown. In these computations the mesh is $\Delta x = 1$, $\Delta y = 1$, for (x, y) in the domain $[-100, 100] \times [0, 200]$, representing 40401 grid points. The mean convection velocity is $M_x = 0.5$ and $M_y = 0$. The initial data is the Gaussian

$$p(x, y, 0) = exp[-(\frac{x^2 + (y - 25)^2}{25})ln[2]],$$

with $u \equiv 0$ and $v \equiv 0$. The boundary conditions along the wall at $y = 0$ are $v = 0$ and $\frac{\partial p}{\partial y} = 0$, with u obtained from method (2) with interior differencing. The outflow boundary condition at

$x = +100$ is to solve for ω_1 with condition (4), and for ω_2 and ω_3 with method (2) using interior differencing. The boundaries at $x = -100$ and $y = 200$ are never reached by the evolving wave dynamics within the workshop simulation time limit of $t = 150$, so they are handled by a simple characteristic type of condition. We will use the grid ratio $\frac{\Delta t}{\Delta x} = \frac{1}{4}$, so that data at $t = 150$ requires 600 time steps. In figure (1) at $t = 15$, the pressure wave has expanded until the outer pressure contours are just touching the wall. In figure (2) at $t = 45$, the pressure wave front has a substantial reflection from the wall, with details near the wall of the interference between the expanding and the reflecting wave fronts. The data at $t = 15$ and $t = 45$ show complete and undistorted circular wave fronts except for near the wall where the wall boundary comes into play, with the expected spatial symmetry in x. In figure (3) at $t = 75$, a significant amount of the pressure structure has already passed through the outflow boundary, and the angle between the wave fronts and the artificial boundary has increased from the initial parallel contact to approximately forty five degrees. In figure (4) at $t = 150$, the pressure structure is approximately halfway out of the downstream boundary. The incomplete pressure structures at $t = 75$ and 150 show wavefronts that are still perfectly circular, with no visible distortion because of the outflow boundary, even at $t = 150$ when the wave front is nearly perpendicular to the artifical boundary. The mean convection speed is subsonic, so the wave dynamic will have a significant upstream effect that continues from the moment that any part of the pressure structure passes through the artifical boundary. There is no apparant disruption of this upstream propagation from the pressure stucture that is downstream of the outflow bouondary, even as a cumulative error from the moment of contact between the pressure front and the outflow boundary at $t \approx 60$ until the final simulation time at $t = 150$. During the overall review of all of the data submitted for this problem at the workshop, the workshop organizers said that this solution was correct.

SUMMARY AND CONCLUSIONS

The results in this paper have demonstrated the ability of a new fourth order propagation algorithm to accurately simulate the genuinely multidimensional wave dynamics of acoustic propagation in two space dimensions with the linearized Euler equations. The results have also shown the ability of a new outflow boundary condition and fourth order algorithm to pass the evolving solution from the computational domain with no perceptible degradation of the solution remaining within the domain.

BIBLIOGRAPHY

[1] J. W. Goodrich, "An Approach To The Development Of Numerical Algorithms For First Order Linear Hyperbolic Systems In One And Two Space Dimensions," in preparation.

[2] J. W. Goodrich and T. Hagstrom, in preparation.

[3] T. Hagstrom, "On High Order Radiation Boundary Conditions," to appear in Proc. of the IMA Workshop on Comput. Wave Prop., (Minneapolis, Minn., Sept., 1994).

[4] J. Hardin, "Numerical Considerations For Computational Aeroacoustics," in *Computational Aeroacoustics*, edited by J. Hardin and J. Hussaini, (Springer-Verlag, New York, 1993).

[5] J. M. Seiner and E. A. Krejsa, "Supersonic Jet Noise and the High Speed Civil Transport," AIAA Paper No. 89-2358.

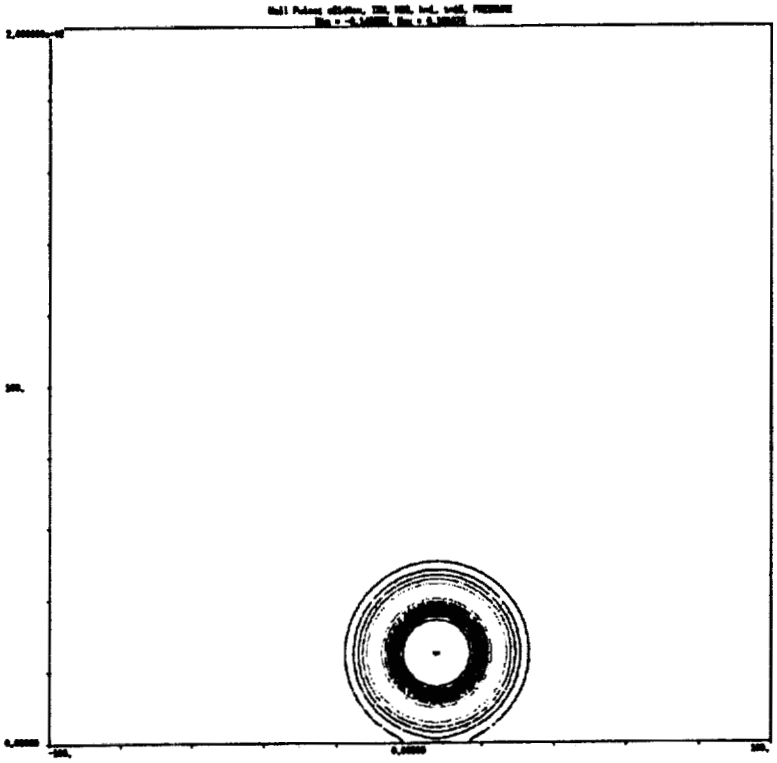

Figure 1: Pressure Contours at t = 15.

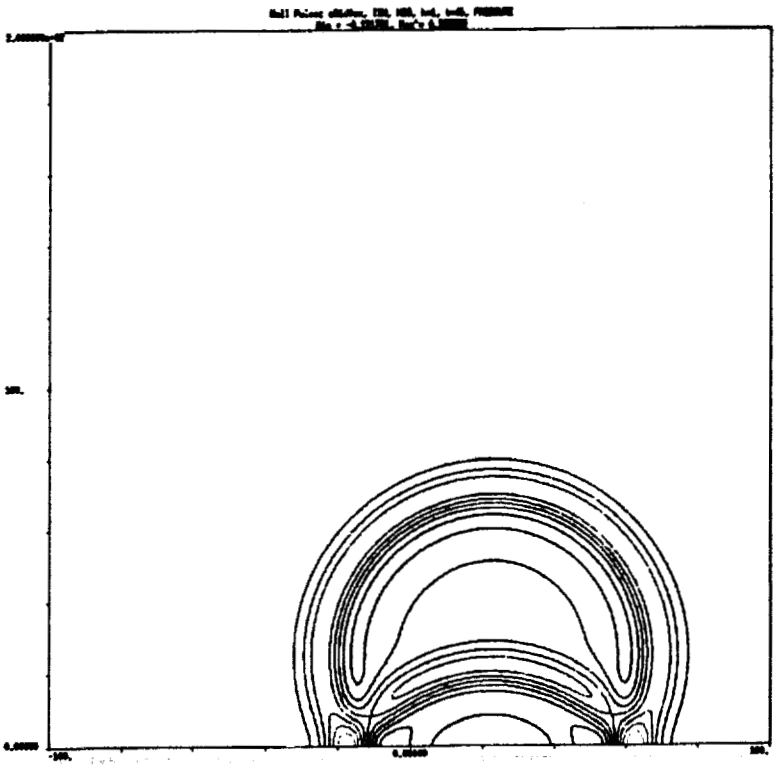

Figure 2: Pressure Contours at t = 45.

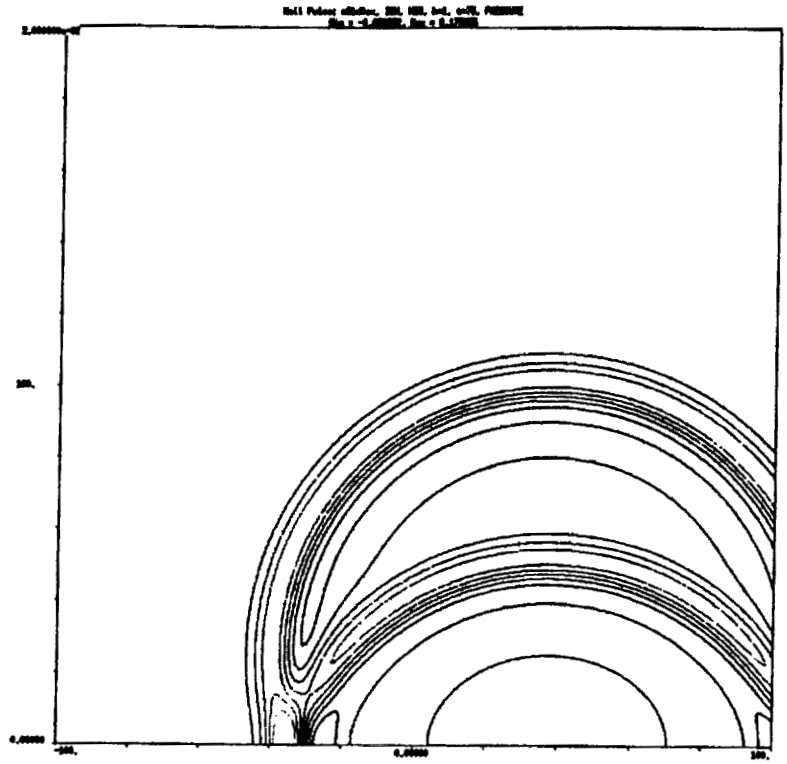

Figure 3: Pressure Contours at t = 75.

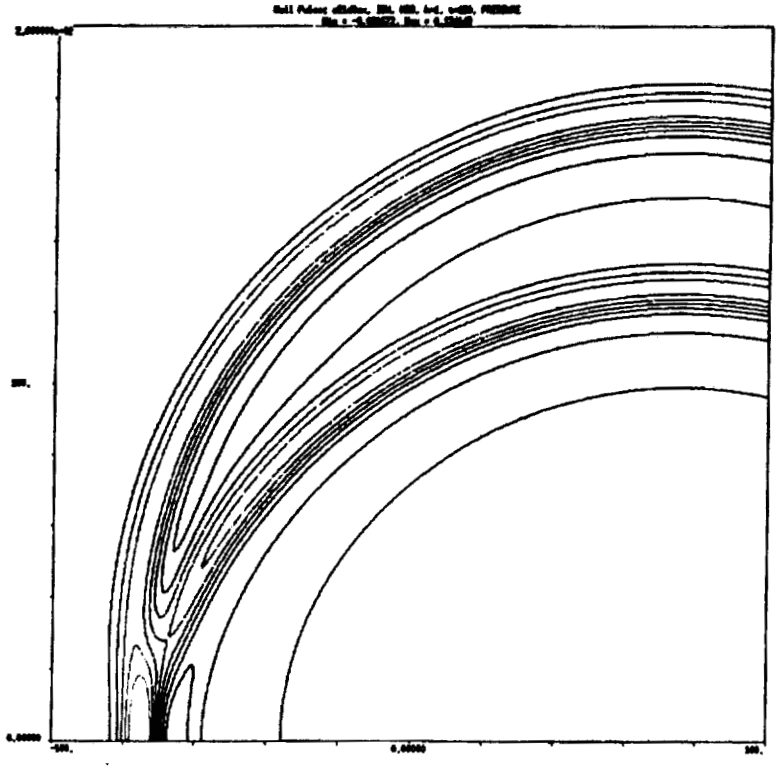

Figure 4: Pressure Contours at t = 150.

COMPUTATIONAL AEROACOUSTICS ON MASSIVELY PARALLEL COMPUTERS[1]

Yusuf Özyörük and Lyle N. Long
Department of Aerospace Engineering
The Pennsylvania State University, University Park, PA 16802

SUMMARY

A computational fluid dynamics (CFD) technique is employed to solve aeroacoustics problems on massively parallel computers. The algorithm is based on a 4th order accurate central finite difference and 4th order accurate 4-stage Runge-Kutta time integration method that solves the 3-D full Navier-Stokes/Euler equations on a curvilinear coordinate system. The code has been developed to predict noise radiation from ducted fans [1]. A specific application of this code is made here to the oscillating circular piston problem (Workshop Category IV, Problem 2) by solving the full Euler equations with nonreflecting boundary conditions in the axisymmetric mode. The features of the code that apply to this particular problem are described in this paper.

INTRODUCTION

There is a large variety of algorithms for integrating the time dependent system of equations of fluid dynamics for aeroacoustics applications. Among these the most commonly used are the classical leapfrog, MacCormack, central finite difference [2] , and compact finite difference methods [3] as well as the recently introduced dispersion relation preserving (DRP) scheme [4]. The computational requirements of the aeroacoustics problems are usually very high; long run times and large amounts of memory are required. One has to consider two things in the choice of the numerical algorithm for it to be a useful design tool: accuracy and speed (effectiveness).

Massively parallel computers offer the computational power, and the classical explicit finite difference algorithms offer the effectiveness on these machines. Specifically, a 4-stage, noncompact Runge-Kutta time stepping scheme with a fourth-order-accurate central finite difference stencil is used. This algorithm is briefly described below, and results for the current problem are discussed.

NUMERICAL ALGORITHM

The Euler equations are integrated in the interior of the physical domain, together with the nonreflecting boundary conditions on the outer boundaries. Accurate and effective nonreflecting boundary conditions are essential for a successful aeroacoustic simulation. In cases of a mean flow, the far-field boundaries may be composed of inflow and outflow boundaries, which then require different conditions depending on the characteristics. At a subsonic inflow boundary, the only outgoing information is associated with the acoustic waves, and therefore, the radiation boundary conditions are applied. At a subsonic outflow boundary, the outgoing information is associated

[1]Work supported by NASA Langley Research Center under grant NAG-1-1367

with acoustic waves, entropy waves, and vorticity waves. Therefore, at such boundaries outflow boundary conditions are solved. Specifically, the B_1 operator of Bayliss and Turkel [5] is applied to all perturbation variables (deviations to density, three velocity components, and pressure from their respective undisturbed values) at an inflow boundary. In the absence of vorticity each of these variables satisfies the convective wave equation, which is the basis of this boundary condition operator. At an outflow boundary this operator is applied only to the pressure perturbation and the other variables are obtained from the linearized Euler equations.

The current algorithm is essentially a cell-centered finite difference method. That is, the state variables are stored at the cell centers, and fluxes are differenced using the cell centered fluxes, as opposed to cell-face-based fluxes of a finite volume technique. In this approach grid singularities are avoided, and the solid surface boundary conditions are implemented in a convenient manner. Ghost cells are introduced at the solid wall. The normal velocity at the wall is prescribed, and the ghost normal velocity is then obtained via interpolation. The tangential velocity for the ghost cell is extrapolated from the interior. The continuity equation is used to solve for the density at the wall. The ghost cell density is then obtained via interpolation, and the pressure is calculated using the isentropic relation $p_g = p_\infty(\rho_g/\rho_\infty)^\gamma$, where p and ρ are the pressure and density, respectively, γ is the ratio of specific heats, and the index g indicates the ghost cell, and ∞ the undisturbed quantity.

Time integration is performed using the well-known four-stage Runge-Kutta (R-K) technique which yields a fourth-order-accurate algorithm. Spatial derivatives are computed using fourth order accurate central differencing in the interior, which requires a 5-point stencil. Biased differencing is used at or near the boundaries. Von Neumann analysis of this R-K finite difference algorithm applied to a 1-D advection equation indicates that the scheme is stable for a Courant number (CFL) less than approximately 2.06. The four stage Runge-Kutta method is known to be stable up to a CFL of $2\sqrt{2}$ if the spatial discretization is ignored. Figure 1a presents the amplification factor as a function of $k\Delta x$, where k is the wave number and Δx is the grid spacing, for various CFL numbers. The corresponding phase error is illustrated in Figure 1b. Waves at high frequencies propagate at the wrong speed. Therefore, one uses artificial dissipation to suppress these waves.

The current algorithm employs a blend of second order and fourth order dissipation, or a blend of second order and sixth order dissipation, similar to that of Jameson *et al.* [6]. Figure 1c shows the effect of adding a fourth order dissipation term and a sixth order dissipation term alone on the stability characteristics of the 1-D scalar advection equation. These terms are given by $D^{(4)}(u) = -(\varepsilon_4/\Delta t)\Delta x^4 \partial^4 u/\partial x^4$, and $D^{(6)}(u) = (\varepsilon_6/\Delta t)\Delta x^6 \partial^6 u/\partial x^6$, respectively, where D is the dissipation flux added to the right-hand side of the governing equation, u is the solution variable, ε is a constant coefficient, and Δt is the time increment. As seen in Figure 1c, in the absence of these terms the high frequency waves are propagated, and they will be diffused as they propagate with artificial dissipation. The addition of these terms alters the wave speed only slightly due to the coupling of the R-K stages (Figure 1d).

Since the current algorithm has been programmed to run on massively parallel computers using Fortran 90, one tries to avoid performing computations in portions of the computational domain sequentially. This normally occurs when one has to solve different sets of governing equations for the interior points and the far-field boundary points. In this case the definitions of the fluxes, and the solution variables differ. The most time consuming process on data parallel computers is the communication among its processors. In the current computer program, the spatial derivatives of the far-field and the interior points are evaluated simultaneously, cutting down the communication time significantly. The artificial dissipation is computed for every grid

point in the computational domain for the full solution variables, and then the artificial dissipation for the perturbation variables at the far-field boundary points are obtained via linearization, reducing the communication time by half.

RESULTS

In this section results for the Workshop Category IV, Problem 2 are presented. This problem has been solved using the Euler equations in axisymmetric coordinates, with radiation boundary conditions on the outer boundaries of the computational domain. The size of the computational domain is $100\Delta x \times 100\Delta r$ with $\Delta x = \Delta r$, where x and r are the axial and radial coordinates, respectively. The radius of the piston is $10\Delta r$, and its axial velocity is $u(t) = 10^{-4}\sin(\frac{\pi t}{5})$ in nondimensional coordinates.

First a grid refinement study was performed using only a 4th order filter. Figures 2a-c show the normalized acoustic pressure along the $r = 0.5\Delta r$ constant line (half cell size off the centerline) for an increasing number of cells per wavelength, respectively. The solid line indicates the exact solution and the dashed line indicates the Euler solution. The improvement in the numerical solution is such that the root mean square error between the numerical and the exact solutions decreases proportional to $O(\Delta x^4)$ as the number of the cells per wavelength is increased, as shown in Figure 2d. This is in fact the spatial order of accuracy of the algorithm. Figures 3a and 3b illustrate the acoustic pressures along the wall and the 45-degree line from the wall, respectively. These figures correspond to the same number of cells per wavelength as Figure 2b, which is the specified number of cells for the test problem. Due to the piston velocity discontinuity, some spurious waves occur in the vicinity of the piston. Other than this, the overall agreement between the exact solution and the current solution is excellent for the specified number of cells. These results were obtained using a CFL number of 0.1. When the CFL number is increased to 0.5, the phase error starts to show up near the source (piston), but the accumulation of this phase error over space remains about the same. Also it was observed that using a sixth order filter slightly improved the dissipation characteristics of the algorithm on this problem over a fourth order filter.

CONCLUSIONS

A spatially and temporarily fourth order accurate Runge-Kutta finite difference algorithm has been applied to an oscillating circular piston problem on the Connection Machine. It has been shown that the numerical scheme needs about 10 cells per wavelength to give results without significant phase error. A comparison of a fourth order filter and a sixth order filter indicated that the amplitude error properties of the algorithm are improved using the sixth order filter. Increasing the CFL number causes an early but negligible development of the phase error at the wall.

References

[1] Ozyoruk, Y. and Long, L. N.; "A Navier-Stokes/Kirchhoff Method for Noise Radiation from Ducted Fans ," AIAA Paper 94-0462, Jan. 1994.

[2] Anderson, D. A., Tannehill, J. C., and Pletcher, R. H.; *Computational Fluid Mechanics and Heat Transfer*, Hemisphere Pub. Corp., 1984.

[3] Lele, S. K.; "Compact Finite Difference Schemes with Spectral-like Resolution," *J. Comp. Physics*, Vol. 103, pp. 16-42, 1992.

[4] Tam, C. K. W., and Webb, J. C.; "Dispersion Relation Preserving Finite Difference Schemes for Computational Acoustics," *J. Comp. Physics*, vol. 107, pp. 262-281.

[5] Bayliss, A. and Turkel, E.; "Far Field Boundary Conditions for Compressible Flow," *J. Comp. Physics*," Vol. 48, 1982, pp. 182-199.

[6] Jameson, A., Schmidt, W., and Turkel, E.; "Numerical Solutions of the Euler Equations by Finite Volume Methods Using Runge-Kutta Time-Stepping Schemes," AIAA Paper 81-1259, June 1981.

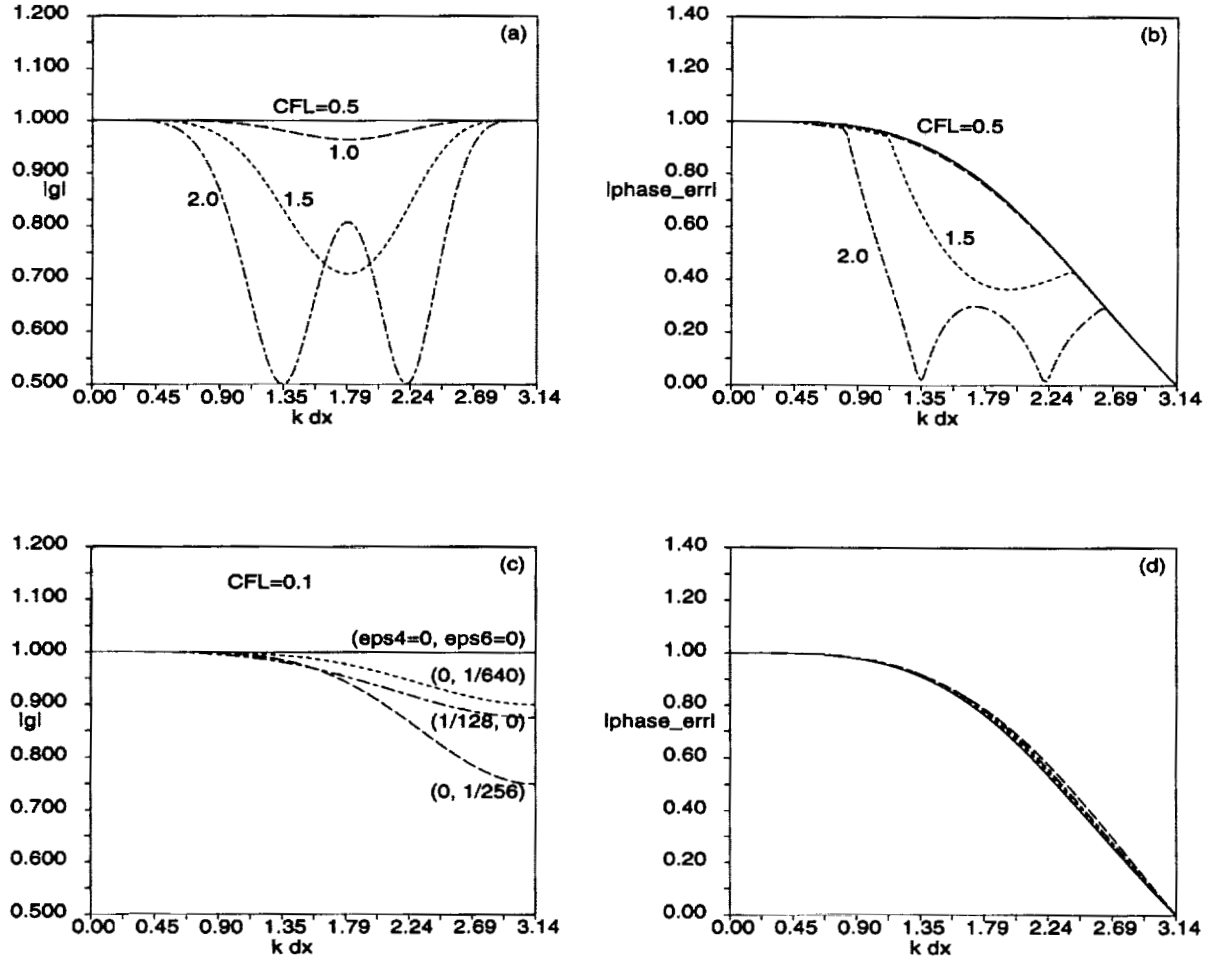

Figure 1: Von Neumann stability analysis: Amplification factor and phase error. (a),(b) with no dissipation; and (c),(d) with dissipation.

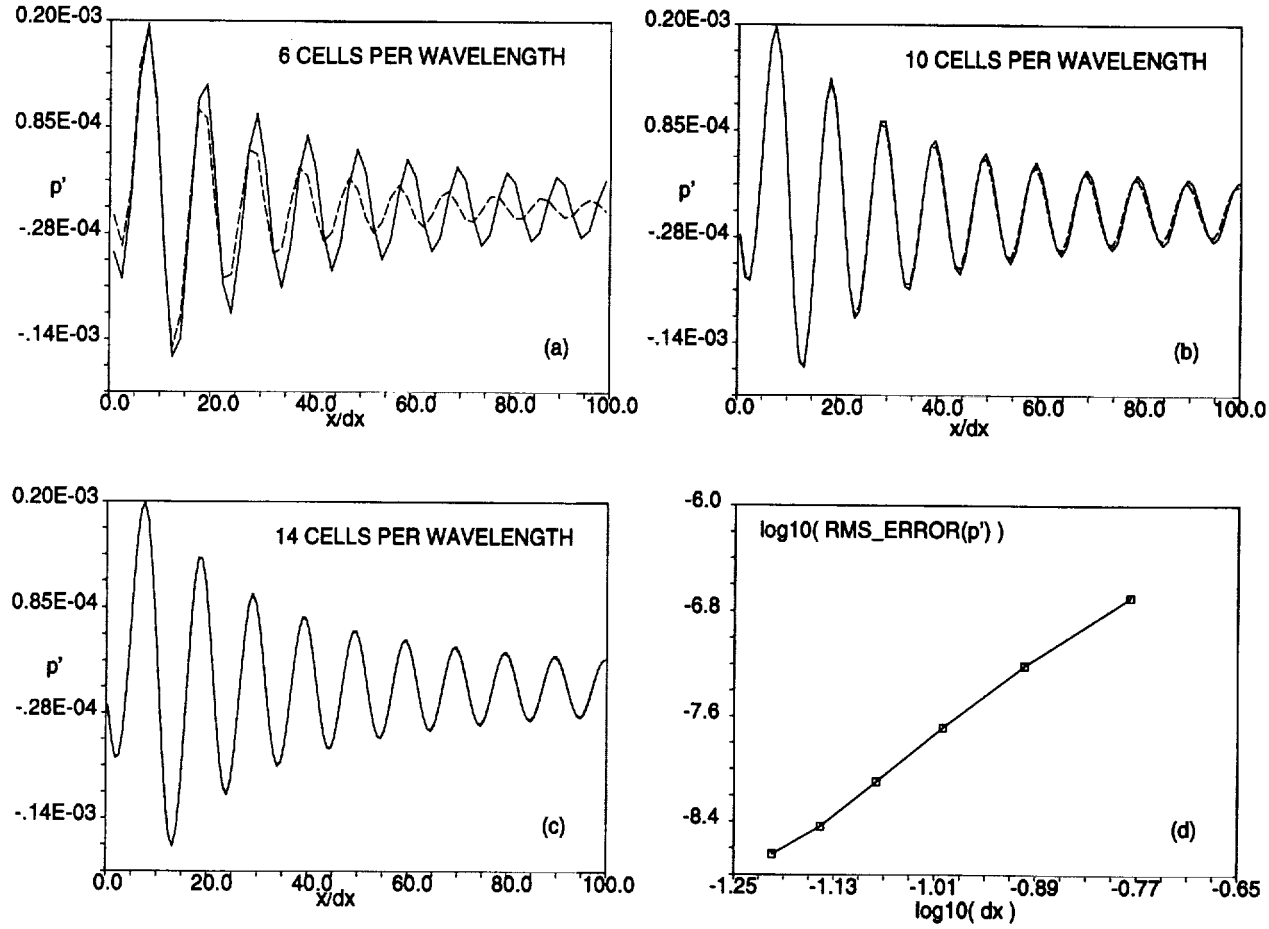

Figure 2: Grid refinement: Centerline pressure for (a) 6 cells per wavelength, (b) 10 cells, (c) 14 cells per wavelength, and (d) Order of accuracy of the algorithm.

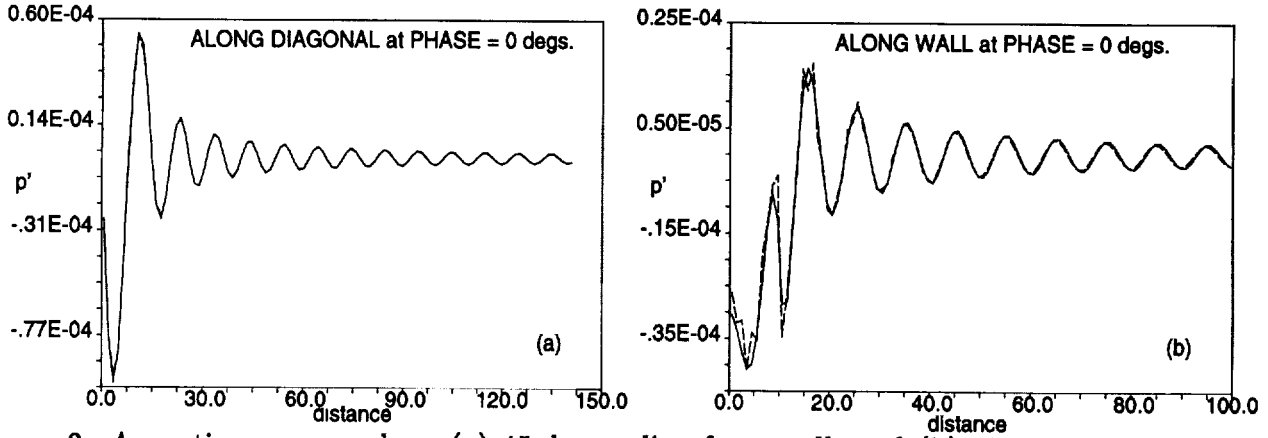

Figure 3: Acoustic pressure along (a) 45-degree line from wall, and (b) along wall, 10 cells per wavelength.

CATEGORY 5 PROBLEM
SOLUTION USING AN UNSTRUCTURED FINITE VOLUME ALGORITHM

Trong T. Bui and Reda R. Mankbadi
NASA Lewis Research Center
Cleveland, Ohio

INTRODUCTION

For the simulation of flows with complex geometries, unstructured finite volume methods have proven to be very popular, and simulations of a large number of flows have been done with good results using this approach. Since most of the simulations to date were done for steady flows, it is not clear that present unstructured finite volume algorithms can accurately track the unsteady propagation of acoustic waves in a computation. Therefore, there is a need to assess the accuracy of these methods for acoustic calculations.

In this paper, we perform the numerical simulation of a very small amplitude acoustic wave incident on the non-uniform steady flow in a quasi-1D convergent-divergent nozzle using an unstructured finite volume algorithm with piece-wise linear, least square reconstruction, Roe flux difference splitting, and second-order MacCormack time marching. First, the spatial accuracy of the algorithm is evaluated for the steady flow by running the simulation with a sequence of successively finer meshes. Then the unsteady numerical solution with the acoustic perturbation is presented.

NUMERICAL PROCEDURE

The governing equation used for this study is the quasi-1D Euler equation in the following form:

$$\frac{\partial U}{\partial t} + \frac{\partial F}{\partial x} = Q \tag{1}$$

Where

$$U = \begin{bmatrix} \rho \\ \rho u \\ E_t \end{bmatrix} \qquad F = \begin{bmatrix} \rho u \\ \rho u^2 + P \\ (E_t + P)\, u \end{bmatrix} \qquad Q = \begin{bmatrix} -\frac{1}{S}\frac{\partial S}{\partial x}\rho u \\ -\frac{1}{S}\frac{\partial S}{\partial x}\rho u^2 \\ -\frac{1}{S}\frac{\partial S}{\partial x}(E_t + P)\, u \end{bmatrix} \tag{2}$$

The above equation is discretized using the finite volume approach. In this approach, eq. (1) is integrated over a finite volume which reduces to a single strip of length Δx for the one-dimensional case. The major steps in the solution procedure are: (1) reconstruction, (2) flux computation, and (3) evolution. This is a standard finite volume solution procedure that has been used in previous works, and it is described in detail in ref. 1.

Step 1: Reconstruction - A cell-centered scheme is used in the current work. A piece-wise linear, least square reconstruction procedure similar to those described in refs. 1 and 2 is used. Each of the three conservation variables is assumed to vary linearly within a finite volume as:

$$U(x) = \bar{U} + \phi U_x (x - \bar{x}) \tag{3}$$

The overbar denotes cell-averaged values, and φ is a gradient limiter. The gradient limiter is needed so that eq. (3) does not produce new extrema that are outside the range of the cell-averaged data used in the reconstruction process. A different gradient limiter is used for each conservation variable. Note that the cell-averaged value of the unknown is recovered when eq. (3) is integrated over the finite volume.

$\bar{U}$ is updated in step 3 below. Following ref. 2, U_x is computed using a least square procedure that minimizes the differences between the cell averages of the reconstructed polynomial and the cell averages of the support set. For this 1-D problem, the support set consists of the immediate left and right neighboring cells, and U_x can be computed as:

$$U_x = \frac{\sum \bar{U}_i (\bar{x}_i - \bar{x}) - \bar{U} \sum (\bar{x}_i - \bar{x})}{\sum (\bar{x}_i - \bar{x})^2} \tag{4}$$

Where the i index denotes the left and right neighboring cells used in the support set.

Step 2: Flux computation - With a piece-wise linear reconstruction of the solution unknowns, the conservation variables are continuous and assumed to vary linearly within a control volume. However, there is no guarantee that they will be continuous across adjacent volumes, since a different linear function is used in each volume. As the result, a flux formula is needed to compute a single flux at a control volume boundary given fluxes from the adjacent volumes. A popular flux formula used in finite volume codes is the Roe flux difference splitting, and it is used here.

Step 3: Evolution - A large number of time marching algorithms is available to advance the solution unknowns in time. Since the problem is unsteady, an accurate time marching algorithm is desired. In the current work, the two-stage, second-order MacCormack time marching algorithm is used because of its simplicity. A CFL number of 0.9 based on the minimum Δx and maximum (u + a) is used in all computations, where u and a are the local flow speed and speed of sound, respectively.

BOUNDARY CONDITIONS

Boundary conditions are needed to provide the incoming flux that is going into the first control volume at the nozzle inlet and the outgoing flux that is passing out of the last volume at the exit. A number of different boundary condition implementations were tried, and an implementation that gives the best results is described below.

Inflow - The incoming flow is always subsonic for this benchmark case, so the boundary conditions used are:

1. Specified P_{tot}
2. Specified T_{tot}
3. $\frac{\partial P}{\partial t} - \rho c \frac{\partial u}{\partial t} = -(u - c)\left(\frac{\partial P}{\partial x} - \rho c \frac{\partial u}{\partial x}\right)$

The outgoing compatibility relation 3 is solved with $\frac{\partial P}{\partial x}$ and $\frac{\partial u}{\partial x}$ discretized using information from the computational domain.

For the acoustic computations, the inlet values of P_{tot} and T_{tot} are specified as functions of time.

Outflow - The outgoing flow is supersonic. The applicable compatibility relations are:

1. $\frac{\partial \rho}{\partial t} - \frac{1}{c^2}\frac{\partial P}{\partial t} = -u\left(\frac{\partial \rho}{\partial x} - \frac{1}{c^2}\frac{\partial P}{\partial x}\right)$
2. $\frac{\partial P}{\partial t} + \rho c \frac{\partial u}{\partial t} = -(u + c)\left(\frac{\partial P}{\partial x} + \rho c \frac{\partial u}{\partial x}\right) - \frac{1}{S}\frac{\partial S}{\partial x}\rho u c^2$
3. $\frac{\partial P}{\partial t} - \rho c \frac{\partial u}{\partial t} = -(u - c)\left(\frac{\partial P}{\partial x} - \rho c \frac{\partial u}{\partial x}\right) - \frac{1}{S}\frac{\partial S}{\partial x}\rho u c^2$

RESULTS AND DISCUSSIONS

Computations were done on an IBM RS 6000 workstation using double precision floating point arithmetic (64 bit). Converged steady state solutions were obtained to machine precision. At convergence, the residual values typically have decreased by about 14 orders of magnitude. The steady state computations were started from zero flow velocity everywhere in the nozzle, and the acoustic computations were started from the converged steady state solutions. To assess the spatial accuracy of the method for the steady flow, computations were performed using a sequence of successively finer meshes. From the log-log plot of the L_1 norm of the error versus the number of mesh points, the spatial order of accuracy of the method was found to be better than two.

Fig. 1 shows the results of the acoustic calculations for a series of successively finer meshes. For the case with 280 cells, it can be seen that there are some spurious pressure oscillations near

the nozzle inlet. In ref. 3, it was found that the piece-wise linear reconstruction with the Barth's limiter can produce spurious pressure oscillations in the numerical simulation of the supersonic vortex, and a similar thing might be happening here. These oscillations are visibly reduced when a finer mesh of 600 cells was used, and they are essentially gone for a mesh of 1200 cells.

Fig. 2 plots the time history of the pressure at the nozzle exit. It can be seen that the coarse mesh solutions have a small phase error as compared with the fine mesh solution. However, as the mesh is refined, the phase error is significantly reduced, and the coarse mesh solutions are seen to converge to the fine mesh solution.

CONCLUSIONS

Numerical simulation of an acoustic wave incident on the steady flow inside a quasi-1D convergent-divergent nozzle was performed using an unstructured finite volume algorithm with piece-wise linear least square reconstruction, Roe flux difference splitting, and second order MacCormack time marching. For steady flow, the spatial order of accuracy of the above method was found to be better than two for this problem. The above method successfully tracked the propagation of a very small amplitude acoustic wave in the nozzle.

REFERENCES

1. Barth, T. J., "Recent Developments in High Order K-Exact Reconstruction on Unstructured Meshes," AIAA Paper 93-0668, Jan. 1993.
2. Coirier, W. J., "An Adaptively-Refined, Cartesian, Cell-Based Scheme for the Euler and Navier-Stokes Equations," NASA TM 106754, Oct. 1994.
3. Aftosmis, M., Gaitonde, D., and Tavares T. S., "On the accuracy, Stability and Monotonicity of Various Reconstruction Algorithms for Unstructured Meshes," AIAA paper 94-0415, Jan. 1994.

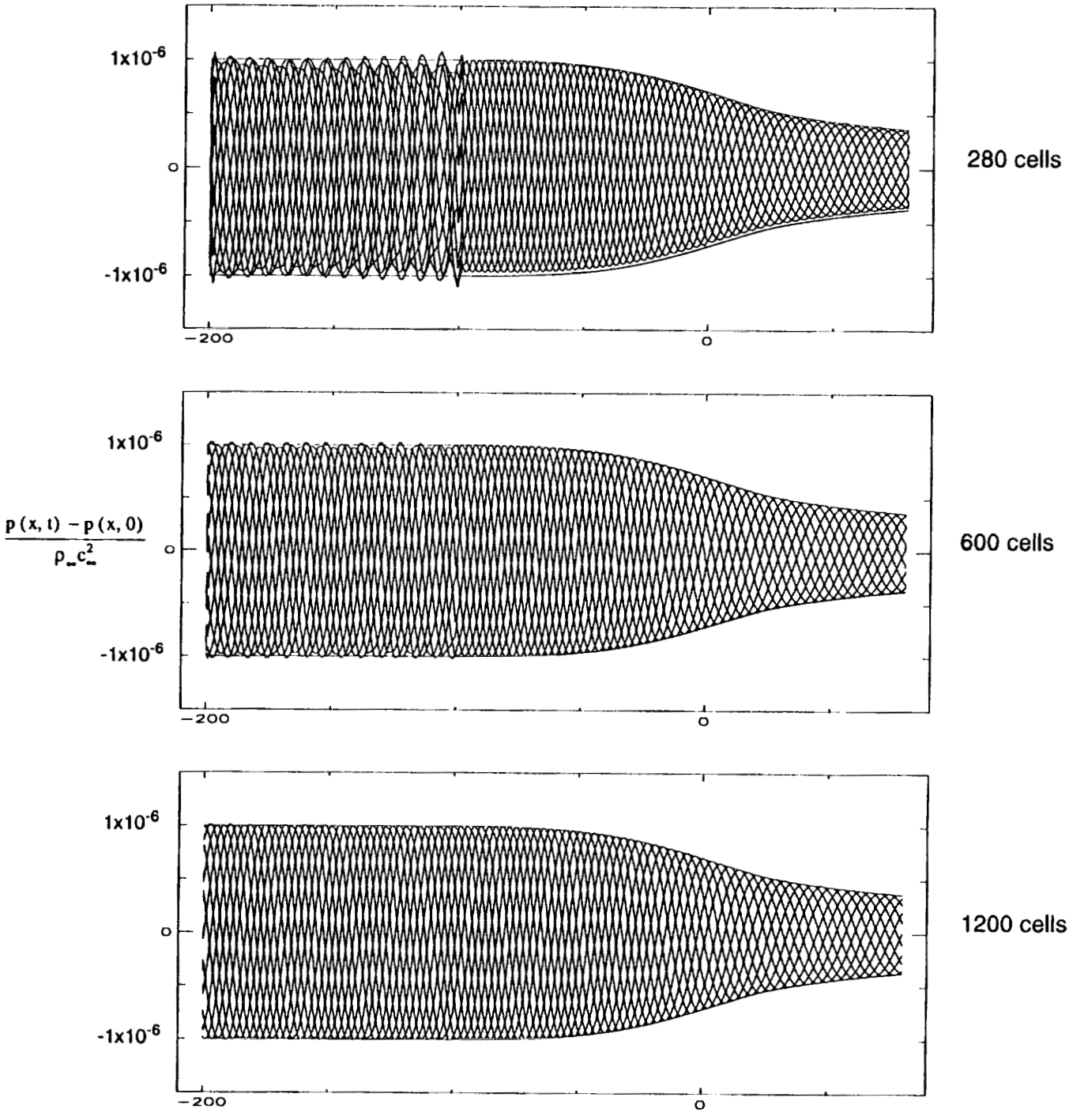

Figure 1. Acoustic results with grid refinement

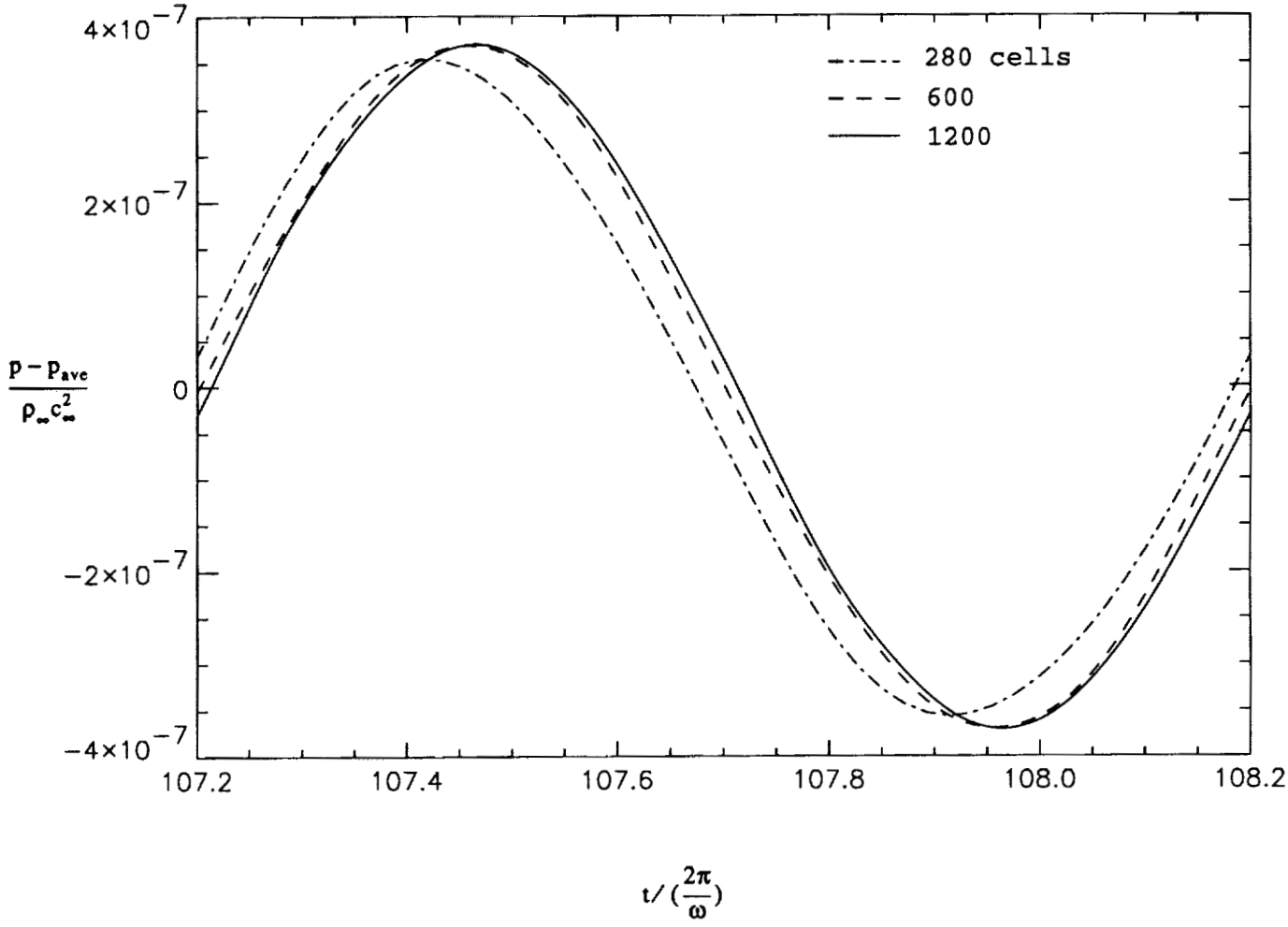

Figure 2. Time history of the nozzle exit pressure with acoustic perturbation

C-4.

COMPARISON OF SPATIAL NUMERICAL OPERATORS FOR DUCT-NOZZLE ACOUSTICS

A. B. Cain and W. W. Bower
McDonnell Douglas Corporation
St. Louis, MO

SUMMARY

A production Navier-Stokes/Euler CFD code, NASTD, developed for aircraft flowfield analysis has been modified to analyze acoustic fields associated with propulsion exhaust systems. The modified code has been applied to the Category 5 nozzle problem using six different spatial discretization schemes combined with a third-order, compact storage Runge-Kutta time integration. NASTD was found capable of tracking pressure disturbances normalized by the freestream value of order 10^{-6}, even with lower-order schemes, for the benchmark problem.

INTRODUCTION

In the past three years McDonnell Douglas Aerospace (MDA) has computed Navier-Stokes simulations of the noise generated by high-speed jet flows. Such simulations require a significantly greater accuracy than that required for standard computational fluid dynamics (CFD) calculations for the following primary reasons: 1) The wide range of frequencies and scales associated with turbulence-generated noise necessitates high-order temporal and spatial accuracy. 2) The simulations are performed on a finite computational domain that must represent the infinite domains in which measurements are made, so the acoustic and turbulence energy must be allowed to exit the computational domain without generating spurious perturbations. 3) The numerical scheme must contain some dissipation to ensure stability and provide good shock capturing, but the dissipation should not be sufficiently large to alter the acoustic field. To assess current capability in these areas, both von Neumann modified wavenumber analysis on a variety numerical algorithms and direct numerical calculations are performed.

To satisfy these requirements the NASTD code, which has been used extensively at MDA for CFD simulations of a variety of complete military aircraft flowfields, has been modified to permit high-resolution acoustics calculations applied primarily to propulsion exhaust systems. NASTD is a finite-volume Navier-Stokes/Euler solver with a multi-block structure and an overlapping (or Chimera) capability to address arbitrarily complex geometries. Higher-order temporal and spatial discretization schemes have been included in the code. In addition, specially developed boundary conditions to maintain irrotational freestream inflow and to eliminate acoustic-wave boundary reflections have also been incorporated.

This paper summarizes the discretization schemes and boundary conditions contained in NASTD which are necessary for aeroacoustics calculations and presents solutions for a Category 5 problem of the ICASE/LaRC Workshop "Benchmark Problems in Computational Aeroacoustics". This specific test case was constructed to test numerical scheme and boundary condition accuracy in analyzing a very small amplitude acoustic wave superimposed on the steady flow in a converging-diverging nozzle.

NUMERICAL PROCEDURE

In the point-wise discretization of a partial differential equation in space and time for the propagation of an acoustic wave, one of the most significant numerical problems is numerical dispersion. This occurs when the phase speed becomes a function of the spatial and/or temporal discretization interval. How this numerical artifact arises becomes apparent through discretization of the one-dimensional scalar wave equation.

$$\frac{\partial f}{\partial t} + c\frac{\partial f}{\partial x} = 0, \tag{1}$$

where the propagation speed is constant. The harmonic solution of this equation is $f(x, t) = \exp[i(kx - \omega t)] = \exp[ik(x - ct)]$, where $c = \omega/k$. For a discretized point in space and time, $(x_m, t_n) = (x_o + m\Delta x, t_o + n\Delta t)$, the discretized spatial derivative is represented by:

$$\left(\frac{\delta f}{\delta x}\right)_{m,n} = ik' f_{m,n}, \tag{2}$$

where Equation (2) defines the so-called numerical "modified wave number" k'.

The truncation error TE associated with numerical spatial difference approximations can be expressed in terms of the ratio of the modified to the actual wave number,

$$TE = (k / k') - 1. \tag{3}$$

If (k'/k) is real, then the only errors in the solution for f at a later time (due to errors in k') will be errors in the phase (no errors in amplitude). On the other hand, errors in the imaginary component of k' will produce amplitude errors, which will have an exponential impact with either unbounded artificial growth (unstable) or decay. A detailed von Neumann linear error analysis of various discretization schemes, including their application to stretched grids, is contained in Reference 1. An analogous study of "optimized" schemes relevant to aeroacoustics calculations for uniform grids is presented in Reference 2.

Figure 1(a) depicts the real and imaginary components of k'/k versus $k\Delta$ for first-order upwind, second-order upwind, second-order central difference, third-order upwind biased, fourth-order upwind biased and fifth-order upwind biased schemes. These cases are on a reference uniformly spaced grid (grid stretching ratio r = 1). It should be noted that $k\Delta = \pi$ corresponds to two points per wavelength, $k\Delta = \pi/2$ corresponds to four points per wavelength, etc.

The boundary conditions employed in NASTD are of the first-order characteristic type (Reference 3). This standard scheme is augmented by the implementation of an irrotational inflow condition and second- and/or fourth-order damping locally in the boundary region. The boundary damping is derived and imposed so that the highest wave number resolved is completely damped in

one time step at the boundary and tapered to zero impact in the interior. In the present application, the characteristic boundary condition is applied downstream of the sampling point with no discernible error.

RESULTS

The category 5 test problem dealing with a small amplitude (10^{-6}) sound wave incident on a convergent-divergent nozzle is illustrated in Figure 2. The intent of this problem is to test the suitability of the numerical scheme for the direct simulation of very small amplitude acoustic waves superimposed on a non-uniform mean flow in a semi-infinite duct. The normalizing parameters, area distribution of the nozzle, and incoming acoustic wave are defined in Figure 2. The desired solution is the transmitted sound wave at the nozzle exit.

Simulations were performed with NASTD in the Euler mode. A third-order, compact storage, Runge-Kutta time integration was implemented in combination with the following spatial schemes: 1) first-order upwind, 2) second-order upwind, 3) second-order physical space upwind biased, 4) third-order upwind biased, 5) fourth-order upwind biased, and 6) fifth-order upwind biased. The acoustic wave propagation problem was solved in two steps. First, a given spatial operator is chosen, and the numerical steady flow solution is computed to a residual level of 10^{-9}. This converged solution is then used as an initial condition for an unsteady simulation with the imposed time harmonic inflow condition.

The normalized perturbation pressure as a function of dimensionless time at the downstream nozzle station $x = 80.0$ is presented in Figure 3 for the various spatial schemes with 15 points per wavelength and in Figure 4 with 7.5 points per wavelength. The phase relations in the solutions are indeterminate since all were started from steady solutions that converged at differing times depending on the starting value and the algorithm used. A comparison of the results shows that the fourth- and fifth-order upwind schemes give the same solution when the finest resolution is used. The amplitude of the wave is diminished when the resolution is reduced, even for the highest-order scheme. It is interesting to note that even in the crudest case (the first-order upwind algorithm) the harmonic distribution is clearly identifiable even though the wave amplitude is significantly diminished due to the highly dissipative formulation.

CONCLUSIONS

NASTD, a production Navier-Stokes/Euler code for aircraft flowfield simulations, with use of appropriate discretization algorithms and boundary conditions was found to accurately track acoustic disturbances in the Category 5 duct-mode acoustics problem. A modified von Neumann wave number analysis performed on the spatial operators determined the basic behavior of the first- through fifth-order spatial algorithms used. Solutions were generated for these cases with 7.5 and 15 points per wavelength ($\Delta x=4$ and $\Delta x=2$). It was found that with the fine resolution grid independence was achieved with the fourth-order algorithm.

REFERENCES

1. Cain, A. B. and Bush, R. H., "Numerical Wave Propagation Analysis for Stretched Grids," AIAA-94-0172, 1994.

2. Tam, C.K.W. and Webb, J.C., "Dispersion-Relation-Preserving Finite Difference Schemes for Computational Acoustics," J. Comp. Phys., August 1993.

3. Bush, R. H., "External Compressor Inlet Predictions Using an Implicit Upwind, Multiple Zone Approach, AIAA-85-1521, 1985.

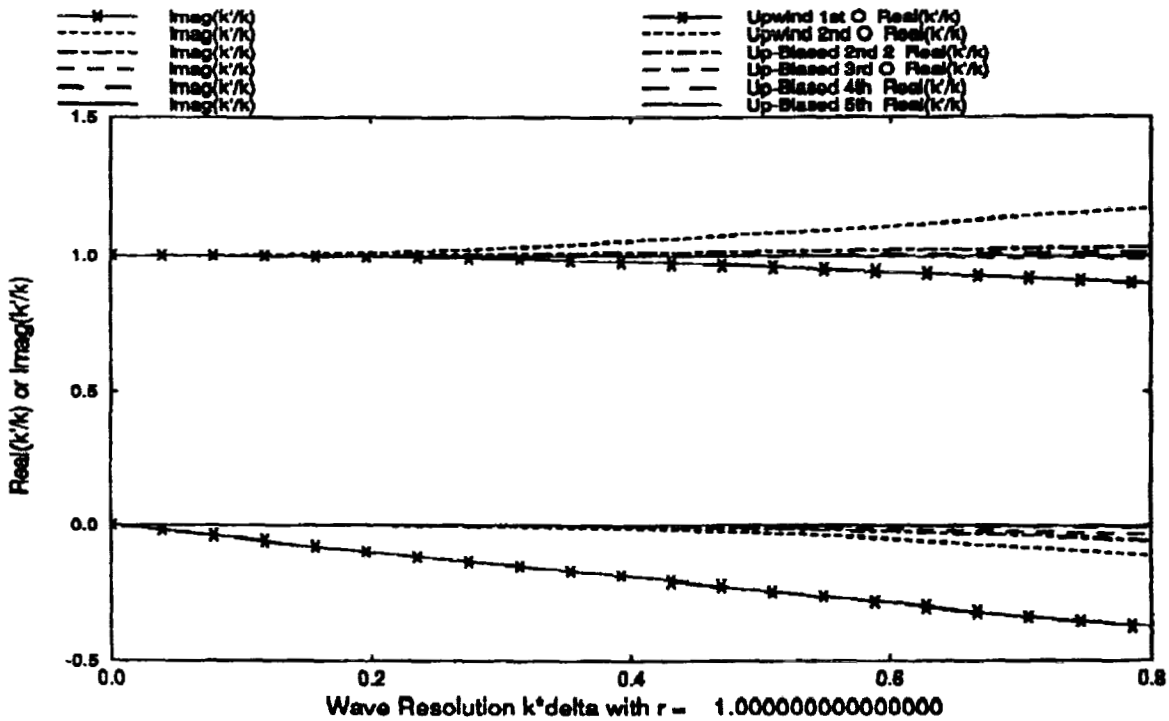

Figure 1. Modified Wavenumber Analysis on a Uniform Grid; Results for Real and Imaginary Modified Wavenumber

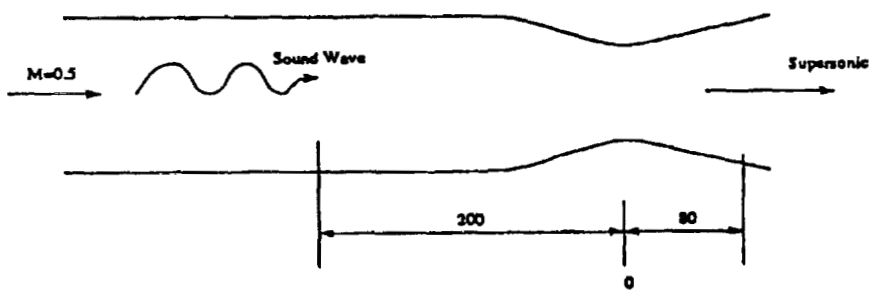

Δx = length scale

a_∞ (sound speed far upstream) = velocity scale

$\frac{\Delta x}{a_\infty}$ = time scale

ρ_∞ (density of gas upstream) = density scale

$\rho_\infty a_\infty^2$ = pressure scale

$$A(x) = \begin{cases} 134 & x \le -100 \\ 117.00583090379 - 16.99416909621 \cos\left(\frac{\pi x}{100}\right) & -100 \le x \le 19 \\ 97.24858634138 + 0.300089327538911x & 19 \le x \le 80 \end{cases}$$

Figure 2. Category 5 Problem: Small Amplitude Acoustic Waves Superimposed on a Non-Uniform Mean Flow in a Semi-Infinite Duct

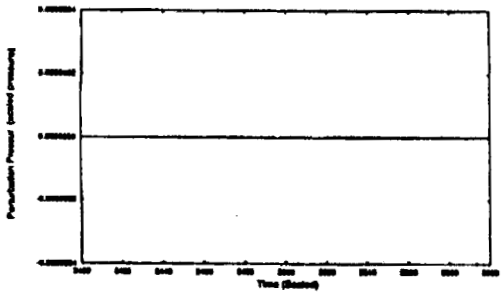

First-Order Upwind
15 Points/Wavelength

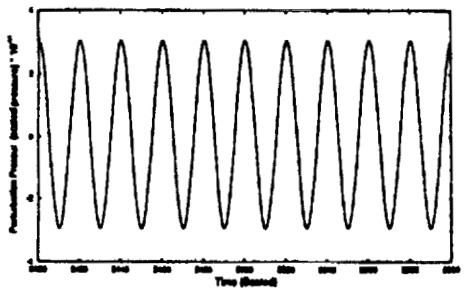

First-Order Upwind Expanded
Scale 15 Points/Wavelength

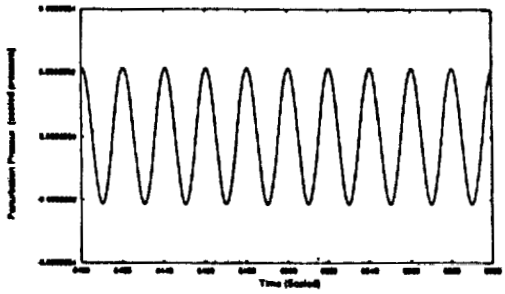

Second-Order Upwind
15 Points/Wavelength

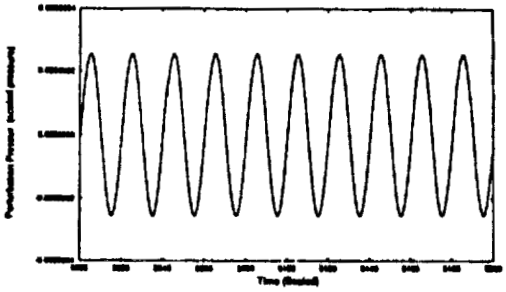

Second-Order Physical Space
15 Points/Wavelength

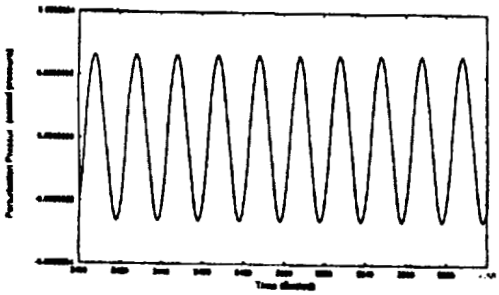

Third-Order Upwind Biased
15 Points/Wavelength

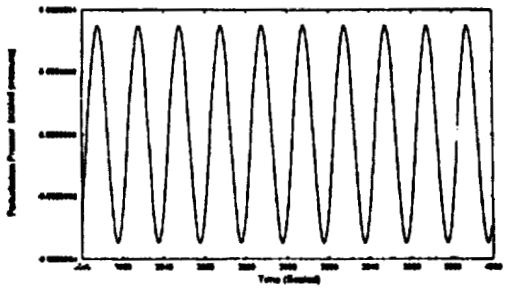

Fourth-Order Upwind Biased
15 Points/Wavelength

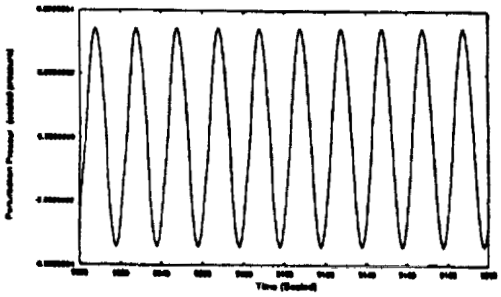

Fifth-Order Upwind Biased
15 Points/Wavelength

Figure 3. Perturbation Pressure History for Various Spatial Discretization Schemes (x=80)

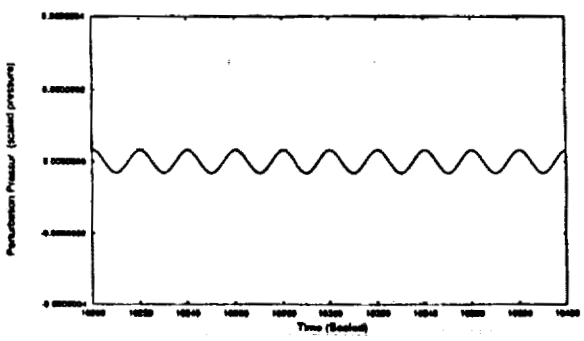

Second-Order Spatial
7.5 Points/Wavelength

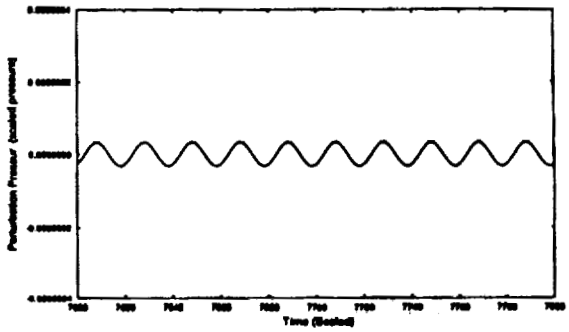

Third-Order Upwind Biased
7.5 Points/Wavelength

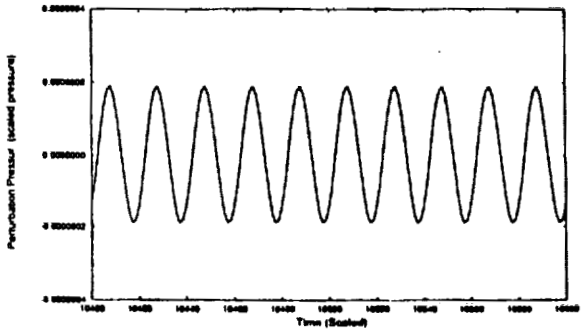

Fifth-Order Upwind Biased
7.5 Points/Wavelength

Figure 4. Perturbation Pressure History for Various Spatial Discretization Schemes (x = 80)

HIGH-ORDER ESSENTIALLY NON-OSCILLATORY METHODS FOR COMPUTATIONAL AEROACOUSTICS*

Jay Casper
ViGYAN, Inc.
Hampton, VA

INTRODUCTION

The desire to obtain acoustic information from the numerical solution of a nonlinear system of equations is a demanding proposition for a computational algorithm. High-order accuracy is required for the propagation of high-frequency, low-amplitude waves. In addition, it is desirable to highly resolve discontinuities that can develop in the solutions of the Euler or Navier-Stokes equations. The class of essentially non-oscillatory (ENO) shock-capturing schemes[1,2] has been designed to have both of these properties. The dual capacity of ENO schemes for high-order accuracy and non-oscillatory shock-capturing is achieved through the use of adaptive stenciling, which makes these schemes highly nonlinear. These schemes are briefly described and referenced herein. A fourth-order algorithm is then applied to the solution of an acoustic wave in a quasi-one-dimensional converging-diverging nozzle.

NUMERICAL METHOD

For the sake of brevity, the necessary details of the ENO schemes to be used in this work are presented within the context of a one-dimensional scalar equation,

$$\frac{\partial}{\partial t}u + \frac{\partial}{\partial x}f(u) = 0 \tag{1}$$

A control-volume formulation is obtained by integrating Eq. 1 on an interval $[x_{i-1/2}, x_{i+1/2}]$ with center x_i and "volume" Δx_i. The one-dimensional scalar conservation law can then be written

$$\frac{\partial}{\partial t}\bar{u}_i(t) = \frac{-1}{\Delta x_i}\Big[f(\,u(x_{i+1/2},t)\,) - f(\,u(x_{i-1/2},t)\,)\Big] \tag{2}$$

where

$$\bar{u}_i(t) = \frac{1}{\Delta x_i}\int_{x_{i-1/2}}^{x_{i+1/2}} u(x,t)\,dx \tag{3}$$

is the cell average of u on the i-th interval at time t. Temporal integration of Eq. 2 can be accomplished by treating Eq. 2 as a system of ordinary differential equations, via a method-of-lines approach. In particular, the Runge-Kutta methods of Shu and Osher[2] will be used. These methods are high-order accurate and total-variation diminishing (TVD) in the sense that the temporal operator does not increase the solution's total variation in time. The right-hand

*Work done on contract at NASA Langley Research Center, Hampton, VA, NAS1-19672.

side of Eq. 2 is approximated in a manner similar to that introduced by Harten, *et al.*[1]; a brief description follows.

To approximate the right-hand side of Eq. 2 to high-order accuracy, the spatial operator must include a high-order pointwise approximation to $u(x,t)$. However, at a given time t, only the cell averages in Eq. 3 are available. Therefore, a pointwise "reconstruction" of the solution from its cell averages is required. To this end, let R be an operator which reconstructs the cell averages and yields a piecewise polynomial $R(x\,;\bar{u}(t))$ of degree $r-1$ which approximates $u(x,t)$ to high order, wherever $u(x,t)$ is sufficiently smooth. This operator R acts in a piecewise manner in that the solution is locally reconstructed within each cell. Let $\mathcal{P}_i$ denote the polynomial of degree $r-1$ which approximates $u(x,t)$ in the i-th cell, at time t, *i.e.*

$$\mathcal{P}_i(x) \equiv R(x;\bar{u}(t)) = u(x,t) + O(h^r), \quad x_{i-1/2} \le x \le x_{i+1/2} \tag{4}$$

The specific method used in this work is the "reconstruction by primitive" proposed by Harten *et al.*[1] and is not detailed here.

This piecewise reconstruction can cause jumps in the approximate solution at the cell interfaces that are $O(h^r)$ in smooth regions and $O(1)$ near discontinuities. The fluxes in Eq. 2 are then approximated by solving the local Riemann problems at the cell interfaces. Thus, the right-hand side of Eq. 2 is replaced by its high-order approximation, which yields

$$\frac{\partial}{\partial t}\bar{u}_i(t) = \frac{-1}{\Delta x_i}\left[\,\hat{f}_{i+1/2}(t) - \hat{f}_{i-1/2}(t)\right] \tag{5a}$$

where

$$\hat{f}_{i+1/2}(t) = f^{\mathrm{Rm}}(\,\mathcal{P}_i(x_{i+1/2})\,,\,\mathcal{P}_{i+1}(x_{i+1/2})\,) \tag{5b}$$

and $f^{\mathrm{Rm}}(u_L,u_R)$ denotes the flux that is associated with the solution of the Riemann problem whose initial states are u_L and u_R. Upon temporal integration of Eq. 2 with an appropriately high-order Runge-Kutta method,[2] the scheme in Eq. 5 is locally r-th-order accurate in the L_1 sense.[1] The extension of these schemes to hyperbolic systems that is used in this work can be found in Ref. 1.

The most unique aspect of the reconstruction operator R is its use of adaptive stenciling. That is, the interpolation set used for the approximation of $u(x,t)$ within a given cell is allowed to shift in an attempt to use the smoothest possible information. In this way, ENO schemes can approximate the smooth regions of a piecewise continuous function to high-order accuracy without the oscillatory behavior that is associated with interpolation across steep gradients. Furthermore, adaptive stenciling enables high-resolution shock-capturing. Previous research has shown that the accuracy of these schemes can degenerate when the stencils are allowed to freely adapt.[3] Further research indicates that this accuracy problem can be remedied by biasing the stencils toward those that are linearly stable.[4,5] For present purposes, the desired reconstruction stencils are centered if r is odd and one cell upwind if r is even. In this manner, the resulting schemes have an upwind biased flux, as shown for the cases $r=3$ and $r=4$ in Fig. 1. In the next section, the above methodology is applied to the direct simulation of the propagation of an acoustic wave in a converging-diverging nozzle.

CATEGORY 5: ACOUSTIC WAVE IN A QUASI-ONE-DIMENSIONAL NOZZLE

The high-order ENO methods discussed above are now applied to the solution of an acoustic wave in a quasi-one-dimensional converging-diverging nozzle. The governing equations are the quasi-one-dimensional Euler equations:

$$\frac{\partial}{\partial t}(AU) + \frac{\partial}{\partial x}(AF) = H \tag{6a}$$

where

$$U = \begin{bmatrix} \rho \\ \rho u \\ \rho E \end{bmatrix}, \quad F = \begin{bmatrix} \rho u \\ \rho u^2 + P \\ (\rho E + P)u \end{bmatrix}, \quad H = \begin{bmatrix} 0 \\ P\frac{dA}{dx} \\ 0 \end{bmatrix} \tag{6b}$$

The variables ρ, u, P, E, and A are the density, velocity, pressure, total specific energy, and nozzle area, respectively. The equation of state is

$$P = (\gamma - 1)\rho(E - \frac{1}{2}u^2)$$

where γ is the ratio of specific heats which is assumed to have a constant value of 1.4. The flow variables are normalized with respect to stagnation conditions as described in Category 5 of the Workshop Test Cases. The prescribed area distribution $A(x)$ and its derivative are illustrated in Fig. 2. Note that $A(x)$ has only one continuous derivative at $x = -100$ and $x = 19$.

A steady-state solution (Fig. 3) is obtained by implementing a fourth-order ($r = 4$) ENO scheme with a biased stencil algorithm until residuals are driven to machine zero. It should be noted that this numerically converged initial condition cannot be obtained with a freely adaptive stencil algorithm. Fig. 4 illustrates the density error of the steady state solution on four successively refined meshes. The error is only second order near $x = -100$ and $x = 19$, as expected, but is fourth order away from these points.

After the steady state is achieved, an acoustic disturbance is introduced at the inlet, $x = -200$:

$$\begin{aligned} P(t) &= P_i[1 + \epsilon \sin(\omega(x/(M+1) - t))] \\ \rho(t) &= \rho_i\left[\frac{P(t)}{P_i}\right]^{1/\gamma} \\ u(t) &= u_i + \frac{2}{\gamma - 1}[c(t) - c_i] \end{aligned}$$

where the subscript i denotes the steady inlet state, ω is the circular frequency, ϵ is the amplitude, and $c = \sqrt{\gamma P/\rho}$ is the local sound speed. The calculation is performed on a uniform mesh of 280 cells, with $\omega = 0.1\pi$ and $\epsilon = 10^{-6}$. The time-dependent part of the calculation is computed with a fourth-order Runge-Kutta method[2] with a Courant number of 0.8. Time-accurate, nonreflecting numerical boundary conditions[6] are employed at inflow and outflow for both the initial steady solution and the time-dependent solution. The inflow is perturbed for $0 < t/T_\lambda \leq 110$, where $T_\lambda = 2\pi/\omega$ is one period of the incoming acoustic wave.

The mean flow pressure $\bar{P}(x)$ is averaged at the nozzle exit for $20 \leq t/T_\lambda \leq 100$. The averaging is done for $t/T_\lambda > 20$ to avoid the initial transient. The pressure perturbation δP is

$$\delta P(x,t) = P(x,t) - \bar{P}(x)$$

Fig. 5 depicts this pressure perturbation as a function of the nozzle length, at 10 equally spaced time intervals, during one period of the incoming acoustic wave. The required pressure perturbation at the nozzle exit is

$$\delta P(80,t) = P(80,t) - \bar{P}(80)$$

and is measured for $100 \leq t/T_\lambda \leq 110$. The data in Fig. 6 represent one period within this time interval.

CONCLUDING REMARKS

The modifications that have been suggested by other authors[4,5] in regard to the biasing of stencils toward those that are linearly stable have been demonstrated to serve their purpose in a smooth flow. Clearly, this particular Workshop problem does not require the adaptive stenciling feature of the ENO methods described. However, the numerical methods discussed and applied herein have also been shown to work well when applied to shocked flows. For more discussion and numerical solutions of a similar problem in which an acoustic wave must interact with a shock in a nozzle, the interested reader is referred to Refs. 7 and 8.

REFERENCES

1. Harten, A., Engquist, B., Osher, S., and Chakravarthy, S., "Uniformly High Order Accurate Essentially Non-oscillatory Schemes III," *Journal of Computational Physics*, Vol. 71, No. 2, 1987, pp. 231-323.
2. Shu, C. and Osher, S., "Efficient Implementation of Essentially Non-Oscillatory Shock-Capturing Schemes," *Journal of Computational Physics*, Vol. 77, No. 2, 1988, pp. 439-471.
3. Rogerson, A. and Meiberg, E. "A Numerical Study of the Convergence Properties of ENO Schemes," *Journal of Scientific Computing*, Vol. 5, No. 2, 1990, pp. 151-167.
4. Shu, C., "Numerical Experiments on the Accuracy of ENO and Modified ENO Schemes," *Journal of Scientific Computing*, Vol. 5, No. 2, 1990, pp. 127-150.
5. Atkins, H., "High-Order ENO Methods for the Unsteady Navier-Stokes Equations," AIAA 91-1557, June, 1991.
6. Atkins, H. and Casper, J., "Non-Reflective Boundary Conditions for High-Order Methods," *AIAA Journal*, Volume 32, No. 3, pp. 512-518, March, 1994.
7. Meadows, K., Caughey, D., and Casper, J., "Computing Unsteady Shock Waves for Aeroacoustic Applications," *AIAA Journal*, Volume 32, No. 7, pp. 1360-1366, July, 1994. 8
8. Casper, J. and Meadows, K.R., "Using High-Order Accurate Essentially Non-Oscillatory Schemes for Aeroacoustic Applications ," AIAA 95-0163, January, 1995.

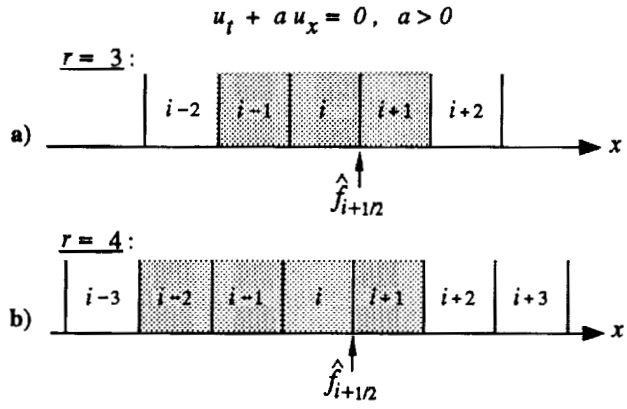

Figure 1. Preferred reconstruction stencils that result in fluxes that are a) one-half cell upwind and b) one cell upwind.

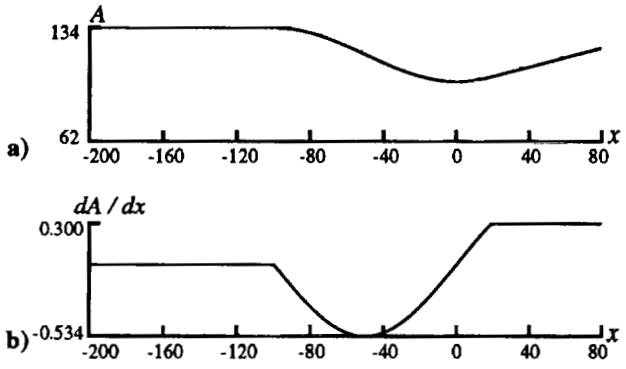

Figure 2. a) Nozzle area $A(x)$, and b) area derivative dA/dx.

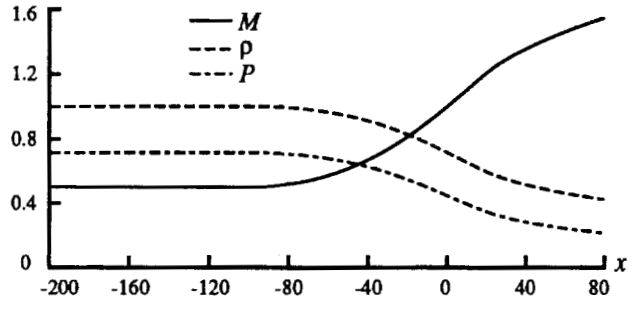

Figure 3. Initial steady-state solution.

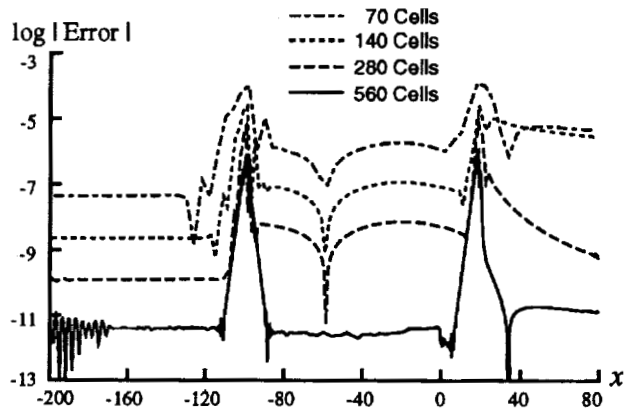

Figure 4. Density error distribution of steady-state solution.

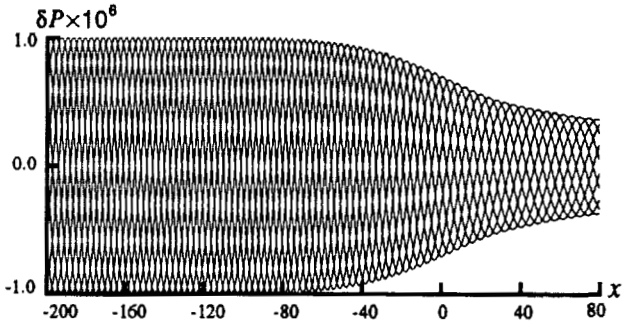

Figure 5. Envelop of pressure perturbation.

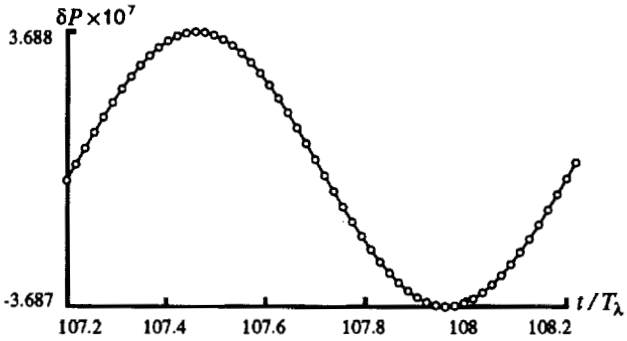

Figure 6. Pressure perturbation at nozzle exit.

NUMERICAL SIMULATIONS OF SMALL AMPLITUDE ACOUSTIC WAVE PROPAGATION IN A CONVERGING-DIVERGING NOZZLE

Thomas Z. Dong
NASA Lewis Research Center
Cleveland, OH

Reda. R. Mankbadi
NASA Lewis Research Center
Cleveland, OH

SUMMARY

Numerical simulations of the small amplitude acoustic wave propagation in a converging-diverging nozzle proposed in Category 5 are performed and presented here. The quasi 1-D unsteady flow equations in conservative form are discretized by the DRP scheme with the artificial damping developed by Tam and Webb [1]. Characteristic boundary conditions are used at both the inlet and outlet of the nozzle. The effect of different numerical implementations of the subsonic inflow boundary conditions on the convergence of the solution to the steady state is studied. In the case of a subsonic outflow in which a shock is formed in the nozzle, the interaction between acoustics and the shock is also investigated.

1. INTRODUCTION

Category 5 problem is set to study the feasibility of capturing the acoustic waves with amplitude many orders of magnitude smaller than the mean flow and the local truncation error of the numerical scheme. It has been recognized that high order schemes, when properly formulated, can successfully resolve waves with wavelength equal to 8-10 mesh points even for long distance propagation problems due to the low numerical dispersion and dissipation associated with the schemes. This is demonstrated again by the results of the present paper. But there are also drawbacks in using high order schemes such as more spurious solutions, slow convergence to steady state and difficulty with the implementation of boundary conditions. These drawbacks are worth to be aware before using these schemes. In the present paper, the steady state solution is computed as the first step. The acoustic source is turned on after the steady state is reached. The effect of different numerical implementations of the characteristic subsonic inflow boundary condition on the convergence of the solution to the steady state is also studied. The results of this study may help in explaining why some high order schemes have slow convergence or even no convergence to the steady state. To study the capability of DRP scheme in solving problems involving both shocks and acoustic waves, the proposed problem is modified by an increase in exit pressure. A shock is, therefore, formed inside the nozzle. Both the mean flow with a shock and the acoustic waves which propagate through the shock are computed by DRP scheme with selective artificial damping and compared with the analytical results.

2. INTERIOR SCHEME

The numerical scheme used here to discretize the governing differential equations is the 7-point 4-level Dispersion-Relation-Preserving finite difference scheme with selective artificial damping terms developed by Tam and Webb [1]. Assume that the governing equations are in the conser-

vative form

$$\frac{\partial \mathbf{U}}{\partial t} + \frac{\partial \mathbf{G}}{\partial x} + \mathbf{F} = 0 \tag{1}$$

where $\mathbf{U} = (\rho A, \rho u A, eA)'$ and $\mathbf{G}$ and $\mathbf{F}$ contains ρ, u, p and the area of the nozzle $A(x)$ and its spatial derivative. The discretization of DRP scheme is formulated in the following way;

$$\frac{\partial \mathbf{U}}{\partial t}\Big|_l^n = -\frac{1}{\Delta x}\sum_{k=-3}^{3} c_k \mathbf{G}_{l-k}^n - \mathbf{F}_l^n - \frac{1}{R}\sum_{k=-3}^{3} d_k \mathbf{U}_{l-k}^n \tag{2}$$

and

$$\mathbf{U}_l^{n+1} = \mathbf{U}_l^n + \Delta t \sum_{q=0}^{3} b_q \frac{\partial \mathbf{U}}{\partial t}\Big|_l^{n-q} \tag{3}$$

where l is the spatial index and n is the time index. The last term in equation (2) is the selective artificial damping term and the R is the mesh Reynolds number. The coefficients for spatial and temporal discretizations and damping given in [1] are $c_0 = 0$, $c_1 = -c_{-1} = 0.770882380518225552$ $c_2 = -c_{-2} = -0.166705904414580469$ $c_3 = -c_{-3} = 0.0208431427703117643$ and $b_0 = 2.3025580888383$ $b_1 = -2.4910075998482$, $b_2 = 1.5743409331816$, $b_3 = -0.38589142217163$ and $d_0 = 0.287392842460216014$, $d_1 = d_{-1} = -0.22614695180872$ $d_2 = d_{-2} = 0.10630357876989$ $d_3 = d_{-3} = -0.023853048191278$

3. BOUNDARY AND INITIAL CONDITIONS

The compatibility equations of the original governing equations are

$$\frac{\partial p}{\partial t} - \rho a \frac{\partial u}{\partial t} + (u-a)\left(\frac{\partial p}{\partial x} - \rho a \frac{\partial u}{\partial x}\right) + [\rho u a^2 A_x / A] = 0 \tag{R1}$$

$$\frac{\partial p}{\partial t} - a^2 \frac{\partial \rho}{\partial t} + u\left(\frac{\partial p}{\partial x} - a^2 \frac{\partial \rho}{\partial x}\right) = 0 \tag{R2}$$

$$\frac{\partial p}{\partial t} + \rho a \frac{\partial u}{\partial t} + (u+a)\left(\frac{\partial p}{\partial x} + \rho a \frac{\partial u}{\partial x}\right) + [\rho u a^2 A_x / A] = 0 \tag{R3}$$

3.1. Subsonic Inflow ($A_x = 0$)

At the subsonic inflow, R2 and R3 are the incoming entropy and acoustic waves which must be specified by the known boundary conditions and R1 is the outgoing acoustic wave which must be computed from the interior. To illustrate the effect of different numerical implementations, three different types of boundary treatments are tried.

Linear Version (LV) This is considered the ideal version since the amplitude of the acoustic wave is so small relative to the mean flow and the formulation of the characteristics is mathematically sound. After linearization about the mean flow, the above compatibility equations become

$$\begin{aligned} p - u &= F(x - (M_0 - 1)t) \\ p - \rho &= G(x - M_0 t) \\ p + u &= H(x - (M_0 + 1)t) \end{aligned} \tag{4}$$

With G = 0 and H provided by the analytical incoming acoustic solutions, the differential forms of these boundary equations become

$$\frac{\partial}{\partial t}\begin{bmatrix}\rho \\ u \\ p\end{bmatrix} + (M_0 - 1)\frac{\partial}{\partial x}\begin{bmatrix}\rho \\ u \\ p\end{bmatrix} = -\begin{bmatrix}1 \\ 1 \\ 1\end{bmatrix}\frac{2\epsilon\omega}{M_0 + 1}\cos\left[\omega\left(\frac{x}{M_0 + 1} - t\right)\right] \tag{5}$$

The derivatives, which represent the outgoing information, are computed with backward differencing.

Non-linear Version (NV) In this approach, the spatial derivatives along the incoming characteristics in the compatibility equations are computed from analytical expressions of the incoming acoustic waves. The outgoing one is still computed from interior by the backward differencing. This is the Thompson's type implementation with the specification of the incoming waves, instead of no incoming waves [4]. The differential forms of the boundary equations become

$$\begin{aligned}
\frac{\partial p}{\partial t} &= -\frac{1}{2}[(u-a)(\frac{\partial p}{\partial x} - \rho a \frac{\partial u}{\partial x}) + (u+a)(1+\rho a)\frac{\epsilon\omega}{M_0+1}\cos[\omega(\frac{x}{M_0+1} - t)] \\
\frac{\partial \rho}{\partial t} &= \frac{1}{a^2}\frac{\partial p}{\partial t} \\
\frac{\partial u}{\partial t} &= \frac{1}{\rho a}[\frac{\partial p}{\partial t} + (u-a)(\frac{\partial p}{\partial x} - \rho a \frac{\partial u}{\partial x})]
\end{aligned} \tag{6}$$

Finite Difference Version (FV) In this version, the computation of the outgoing characteristic stays the same as LV and NV. The spatial derivatives along the incoming characteristics are computed with central differencing. The values of the flow variables outside the computation domain are provided by the given analytical expressions of the incoming acoustic waves.

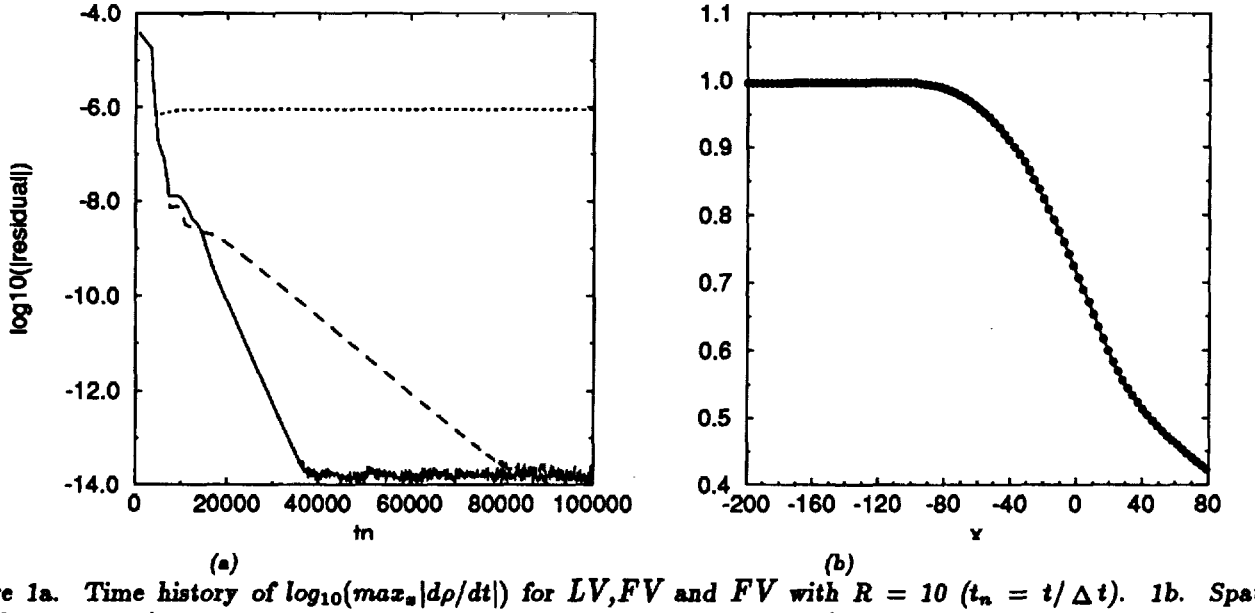

Figure 1a. Time history of $log_{10}(max_n|d\rho/dt|)$ for LV,FV and FV with R = 10 ($t_n = t/\Delta t$). 1b. Spatial distribution of $d\rho/dt$ and $-\alpha\rho$ at $t = 100000\Delta t$ where the solid line is for $d\rho/dt$ and circles are for $-\alpha\rho$

The time histories of residuals for all three versions are plotted in Figure 1a. The mesh Reynolds number is chosen to be 10 which hardly has any effect on the acoustic waves (see Tam, Webb and Dong [2]). The computations with *FV* and *NV* versions converge to steady state at different speeds, in which the *FV* version converges faster. But the solution with the ideal *LV* version does not converge anymore after the residual reaches about 10^{-6}. It is further found that an almost neutral solution of the form $df/dt = -\alpha f$ where $\alpha = 0.89442538 \times 10^{-6}$ has appeared as shown in Figure 1b. It will take extremely long time for this solution to decay to zero or in practice the computation does not converge. This solution must be one of those spurious solutions associated with the discretized system coupled with boundary equations. Because the amplitude of this spurious solution is very small, which is true in most cases, it shows up after all the other time dependent solutions have vanished. An increase of damping will only affect the speed of

convergence of FV case. One way to eliminate this solution is to slightly modify the boundary condition implementation so the boundary equations do not support this solution anymore as it is done in the present paper. Another way to remove this solution is to subtract out this solution from the governing equations as it is described by Tam and Dong [3]. It is also noticed that both LV and NV versions require a smooth function to turn on the acoustic disturbance gradually or the mean will be distorted. The FV version is used in the present computations. Besides the advantage of having higher speed of convergence, the FV version requires only the values of flow variables, instead of analytical expressions. The computed acoustic results are shown in Figure 2a. One can see that with the choice of DRP scheme and FV implementation, the numerical dissipation experienced by the acoustic waves is very small. To illustrate the advantage in using DRP scheme for solving acoustics problems, a case with $\omega = 0.3\pi$ is run and the results is plotted in Figure 2b. In this case, the acoustic wave length contains only 11 grid points (10 Δx). The results still agree well with the exact solutions.

3.2. Supersonic Outflow Boundary Condition

Because the flow is supersonic at the outflow, all the spatial derivatives are discretized with the backward (interior) differencing and the compatibility equations are the same as the interior equations.

3.3. Initial Condition

The initial conditions are computed by integrating the steady state governing equations analytically. They are very good approximations to, but not exactly, the steady state solutions of the finite difference equations.

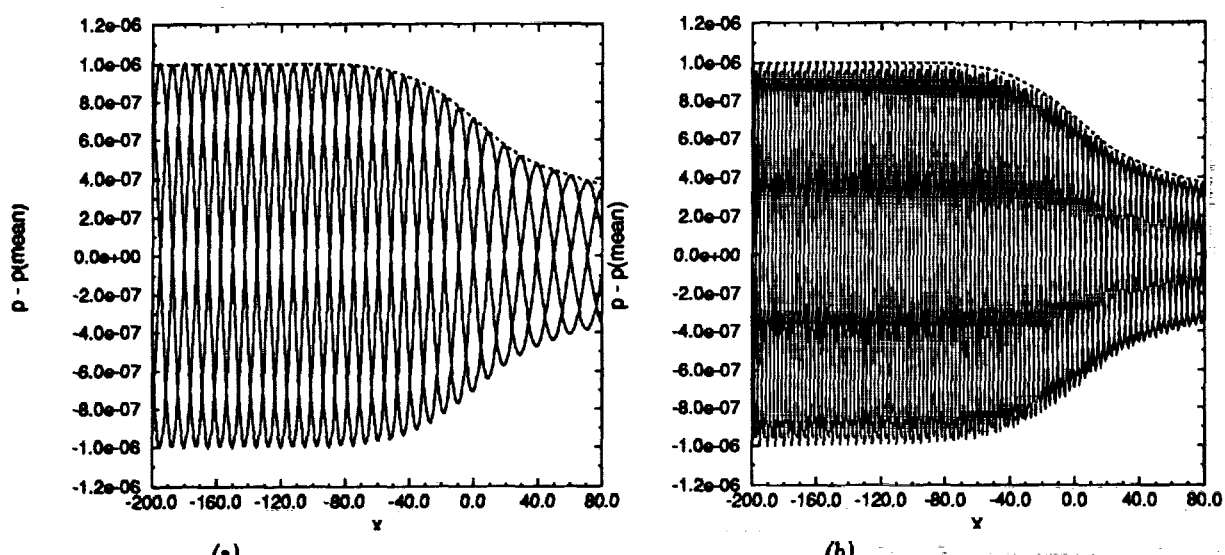

Figure 2. Several snapshots of the spatial distribution of the pressure disturbances ($R = 10$). The dotted lines are the maximum pressure disturbances from the analytical results. a. $\omega = 0.1pi$ (30 meshes per wavelength). b. $\omega = 0.3\pi$ (10 meshes per wavelength).

4. SHOCK PROBLEM

A shock is formed in the nozzle by increasing the exit pressure. The flow becomes subsonic at the outlet. Characteristics $R2$ and $R3$ are outgoing and $R1$ is incoming. Along $R1$,

$$\frac{\partial p}{\partial t} - \rho a \frac{\partial u}{\partial t} = 0$$

is assumed to suppress reflections. This approximation would generate some reflections due to the non-constant nozzle area at the outlet. Interior differencings are used on $R2$ and $R3$. Stronger damping with mesh Reynolds number equal to 0.2 is used at the shock to suppress the high frequency oscillations. A Gaussian function is used to smooth the transition between this strong damping and the weak damping in the smooth region. A variable damping method can also be found in [5]. Both the mean flow and acoustic waves are plotted in Figure 3. The frequency of the acoustic disturbance is still equal to 0.1π. The pressure ratios which are the ratios of the after-shock pressure to pre-shock pressure for both mean and acoustics are compared with the analytical results in Figure 4. The analytical acoustic result is obtained from the linear theory [6]. One could notice that some oscillations are visible on the envelope curve of the pressure disturbance due to the reflection from the outlet.

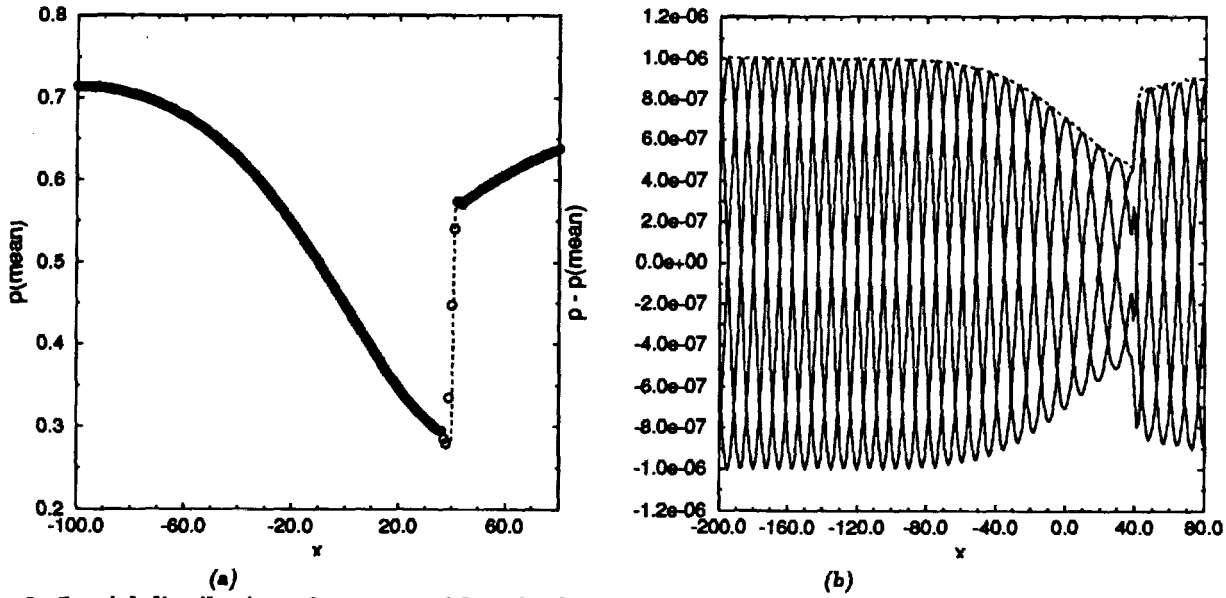

Figure 3. Spatial distribution of pressure with a shock at x=40. a. Mean pressure. The dotted line is the analytical mean pressure. b. Pressure disturbance ($\omega = 0.1\pi$). The dotted line is the computed max. pressure disturbance

5. CONCLUSIONS

By comparing the simulated acoustic solution with the exact solution (the envelope) in Figure 2, It is concluded that the DRP scheme has captured the propagation of the small amplitude acoustic waves very well due to its low numerical dispersion and dissipation . But one should also be aware that low dissipation will usually slow down the convergence of the computation to steady state. Besides, high order finite difference system can also support spurious solutions which are almost neutral, namely will take extremely long time to vanish. Special techniques are needed in order to remove these die-hard spurious solutions. It is also found that with a good selective artificial damping technique, well-formulated high order schemes such as DRP schemes can also produce high quality solutions for problems involving shock and acoustics without introducing much complication.

6. REFERENCES

[1] Tam, C.K.W., Webb, J.C.: Dispersion-Relation-Preserving Finite Difference Schemes For Computational Acoustics. J. of Comput Phys., Vol. 107, No. 2, PP 262-281, 1993.

[2] Tam, C.K.W., Webb, J.C., Dong, T.Z.: A Study of the Short Wave Components in Computational Acoustics. J. of Comput. Acoustics., Vol. 1, No. 1, PP 1-30. 1993

[3] Tam, C.K.W., Dong, T.Z.: Radiation and Outflow Boundary Conditions for Direct Computation of Acoustics and Flow Disturbances in a Non-uniform Mean Flow. Submitted to J. of Comput. Phys. 1994

[4] Thompson, K.W.: Time Dependent Boundary Conditions for Hyperbolic Systems. J. of Comput. Phys., Vol. 68, PP1-24, 1987

[5] Tam, C.K.W., Shen, H.: Direct Computation of Nonlinear Acoustic Pulses Using High Order Finite Difference Schemes. AIAA-93-4325, 1993

[6] Meadows, K.R., Casper, J., Caughey, D.A.: A Numerical Investigation of Sound Amplification by a Shock. Computational Aero- and Hydro- Acoustics ASME, FED-Vol. 147, PP 47-52, 1993

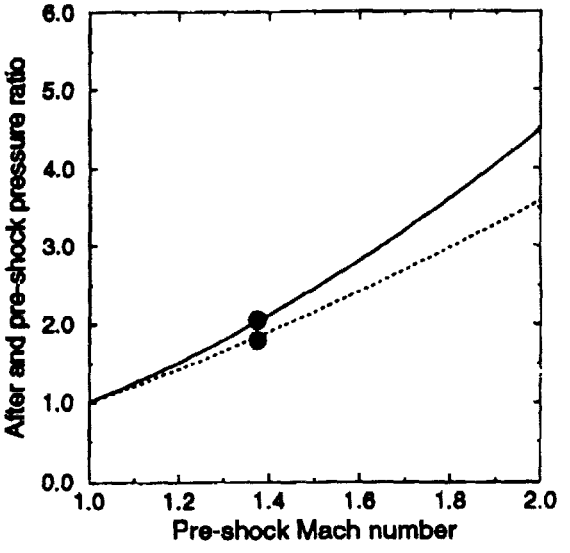

Figure 4. Ratios of the after-shock pressure to the pre-shock pressure versus pre-shock Mach number. The lines are from the analytical results (solid for mean and dotted for disturbance) and the circles are the computed results

THE PRESSURE FIELD OF A GUST INTERACTING WITH A FLAT PLATE

Hafiz M. Atassi * and Sheryl M. Patrick †
University of Notre Dame
Notre Dame, Indiana 46556

A semianalytical solution is presented for the unsteady pressure field of a vortical gust interacting with a flat-plate airfoil in subsonic flow. The solution will serve as a benchmark for evaluating the accuracy and efficiency of time dependent numerical schemes. The specific case considered corresponds to the ICASE benchmark problem number 6. The results are compared with those of asymptotic theories for high frequency and show excellent agreement.

INTRODUCTION

The treatment of a two-dimensional gust impinging on a flat plate airfoil at subsonic speed is a classical problem in unsteady aerodynamics. The assumption of a mean uniform flow uncouples the unsteady flow problem from the mean flow and leads to the linearized Euler equations with constant coefficients. The physical problem depends on two parameters, the reduced frequency k_1 which is a measure of the convective time scale to the gust period, and the Mach number M which is the ratio of the mean flow velocity U_∞ to the speed of sound a_∞. Although, the mathematical problem may appear to be relatively simple, *no exact* solution exists for the general case. In the early treatments, the problem was often formulated in terms of Possio's integral equation and solutions were obtained by collocation techniques [1, 2]. More recently, frequency-domain finite-difference solutions were obtained by Scott and Atassi [3]. Because of the widespread applications of unsteady airfoil theory to flutter and forced vibrations, asymptotic solutions were derived for the unsteady pressure jump along the plate surface for the low frequency [4, 5] and the high frequency cases [6, 7]. For more details, the reader is referred to a recent review article by Atassi [8].

Interest in the far-field acoustic radiation has motivated the development of methods to calculate the unsteady pressure field. Amiet [9] gave an expression for the far-field acoustic power produced by an airfoil in subsonic turbulent flow. However, he considered *only* the dipole contribution to the far-field sound. Martinez and Widnall [10] gave an exact expression for the far-field acoustic pressure in the limit of high frequency. Atassi et al. [11] derived an expression for the unsteady pressure everywhere in terms of the unsteady pressure jump along the plate surface for arbitrary values of the parameters k_1 and M. They calculated the unsteady pressure jump along the plate by solving Possio's integral equation. Their results show that as the frequency parameter $K_1 = \omega c/(2a_\infty\beta^2)$ becomes larger than $\pi/2$, quadrupole and noncompact source effects become *significant*. Here, ω is the circular frequency, c is the plate chord length and $\beta^2 = 1 - M^2$.

*Professor
†Fellow, Center for Applied Mathematics

In the present paper, we use the method of Atassi et al. [11] to calculate the unsteady pressure resulting from a gust interacting with a flat-plate airfoil. The specific case considered corresponds to ICASE problem 6 for which the Mach number is 0.5 and the sinusoidal transverse gust has a reduced frequency $k_1 = \omega c/(2U_\infty) = 15\pi/4$. Since our solution relies on a Possio solver and thus is semianalytical, the results for both the unsteady pressure jump along the plate surface and the acoustic pressure in the far-field are compared with high frequency asymptotic theories [7, 10].

MATHEMATICAL FORMULATION

Details of the mathematical derivation are given in [11]. The results can be summarized as follows. For an inviscid, non-heat conducting uniform mean flow, with an imposed upstream vortical disturbance, the linearized unsteady velocity field can be split into a convected vortical part and a potential part. Since the problem is linear, without loss of generality, we may consider a single Fourier component for the vortical part. Therefore, the velocity can be written as

$$\vec{V}(\vec{x},t) = U_\infty \vec{i}_1 + \vec{a} e^{i(\omega t - \vec{k}\cdot\vec{x})} + \vec{\nabla}\phi(\vec{x},t) \tag{1}$$

where $\vec{a} = (a_1, a_2, a_3)$ is the amplitude vector of the vortical disturbance, $\vec{k} = (k_1, k_2, k_3)$ is its wave number vector, and $\vec{\nabla}\phi$ is the potential part of the unsteady velocity. It is customary to normalize lengths with respect to half the chord, $c/2$, and velocities with respect to U_∞. The unsteady pressure p' is given by $p' = -\rho_\infty D_0\phi/Dt$. where $D_0/Dt \equiv \partial/\partial t + U_\infty \partial/\partial x_1$. The unsteady pressure p' is governed by the convective wave equation

$$\frac{1}{a_\infty^2}\frac{D_0^2}{Dt^2}p' - \nabla^2 p' = 0 \tag{2}$$

and a similar equation can be derived for ϕ. By introducing

$$P = \frac{p'}{\rho_0 a_2 U_\infty} e^{-i(k_1 t + MK_1\tilde{x}_1 - k_3\tilde{x}_3/\beta)} \tag{3}$$

equation (2) reduces to the two-dimensional Helmholtz equation in the Prandtl-Glauert coordinate system

$$\left(\tilde{\nabla}^2 + K^2\right) P = 0 \tag{4}$$

where the Prandtl-Glauert coordinates are $\tilde{x}_1 = x_1$, $\tilde{x}_2 = \beta x_2$, $\tilde{x}_3 = \beta x_3$, with $K_1 = k_1 M/\beta^2$, and $K^2 = K_1^2 - k_3^2/\beta^2$. Traditionally the boundary value problem for P has been formulated in terms of a singular integral equation [1]. This equation is solved by direct collocation and gives the unsteady pressure along the plate, $\Delta p'$.

The unsteady pressure field is then obtained using Green's theorem [11],

$$p'(\vec{\tilde{x}}) = \frac{-i}{4} K \tilde{x}_2 \int_{-1}^{1} \Delta p'(\tilde{y}_1) e^{iMk_1(\tilde{x}_1 - \tilde{y}_1)} \frac{H_1^{(2)}(K|\vec{\tilde{x}} - \vec{\tilde{y}}|)}{|\vec{\tilde{x}} - \vec{\tilde{y}}|} d\tilde{y}_1 \tag{5}$$

where $\Delta p' = p'(y_1, 0+) - p'(y_1, 0-)$ is the pressure jump along the plate surface, and $H_1^{(2)}$ is the Hankle function. This expression gives the unsteady pressure field everywhere in the plane. It accounts for both dipole and quadrupole effects. For large distance ($r = |\vec{x}| \to \infty$) this expression can be simplified and the unsteady pressure can be cast in terms of the Fourier transform of $\Delta p'$ [11].

$$p'(r, \theta) = \frac{\beta K^{1/2}}{\sqrt{8\pi}} \frac{e^{i(\pi/4)}}{\sqrt{r}} \frac{sin\theta}{(1 - M^2 sin^2\theta)^{3/4}} exp\{-ir[K(1 - M^2 sin^2\theta)^{1/2} - MK_1 cos\theta]\}$$

$$X \int_{-1}^{1} \Delta p'(y_1) e^{i\alpha y_1} dy_1 \tag{6}$$

where

$$\alpha = K \frac{cos\theta}{\sqrt{1 - M^2 sin^2\theta}} - MK_1$$

ICASE BENCHMARK PROBLEM 6

In this case we have a transverse gust defined as

$$v = 0.1 a_\infty sin\left[\frac{\pi}{8}\left(\frac{x}{M_\infty} - t\right)\right] \tag{7}$$

where the normalization for the velocity is with respect to a_∞; length, with respect to $\Delta x = 1$; and time, with respect to $\Delta x / a_\infty$. The Mach number is given as 0.5, and the chord is 30 units. Using the usual normalization, we get $k_1 = 15\pi/4 = 11.781$, and $a_2 = 0.2$. This corresponds to $K_1 = 7.85$, a high frequency case.

The unsteady pressure is to be calculated on a box surrounding the flat plate as shown in figure (1). The sides of the box are located at dimensional positions of $x = \pm 95$ and $y = \pm 95$. When nondimensionalized by the semichord the values are $x = \pm 6.333$, $y = \pm 6.333$. Thus, the box boundaries are not located in the far field and as a result, (5) must be used instead of its far-field expansion.

The fact that K_1 is relatively large allows us to compare our results for both $\Delta p'$ and the far-field acoustic pressure with the high frequency asymptotic theories [7, 10]. The results shown are for the normalized pressure

$$p = \frac{p'}{\rho_\infty a_\infty^2} \tag{8}$$

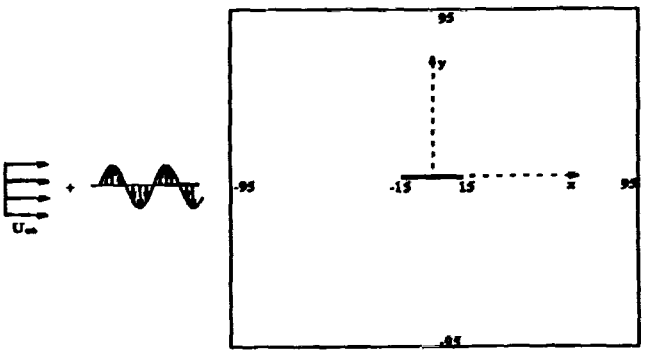

Figure 1: ICASE benchmark problem 6

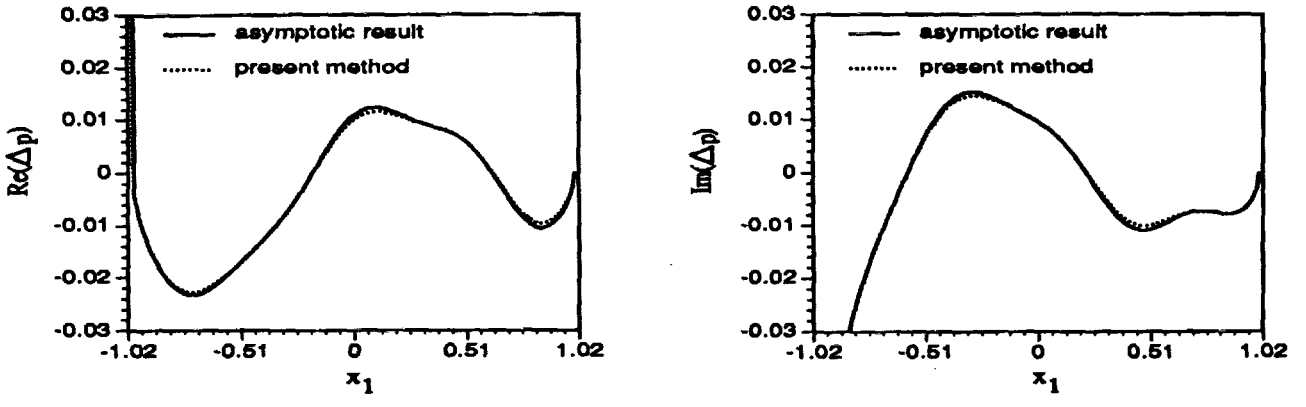

Figure 2: Unsteady pressure jump across airfoil

Figure 2 shows plots of the real and imaginary parts of the pressure jump Δp using the present method and the asymptotic expression derived by Amiet [7] and Martinez and Widnall [10]. The excellent agreement shows the high accuracy of our results.

In order to compare our acoustic pressure with the far-field asymptotic expression of Martinez and Widnall [10], we used the far field expansion of (5). Figure 3 shows a comparison between directivity plots of $|p|\sqrt{r}$, using the two methods. Again the agreement is excellent.

The mean square pressure, $\overline{p^2}$ is now calculated at the ICASE box boundaries. Figure 4 shows the variation of $\overline{p^2}$ on the top boundary of the box. Because the pressure is antisymmetric with respect to the y axis, the values at the bottom boundary are the same as on the top boundary. Figure 5 shows the variation of $\overline{p^2}$ along the left and right boundaries of the box, respectively.

The authors would like to point out that the data for $\overline{p^2}$ presented a the workshop were calculated for a gust of amplitude $0.1U_\infty$, while the gust amplitude of the present data is $0.1a_\infty$ (see equation (7)). Therefore, the workshop data must be multiplied by 4.0 to conform with the present data.

The authors would like to thank Professor S. I. Hariharan for presenting their results at the workshop.

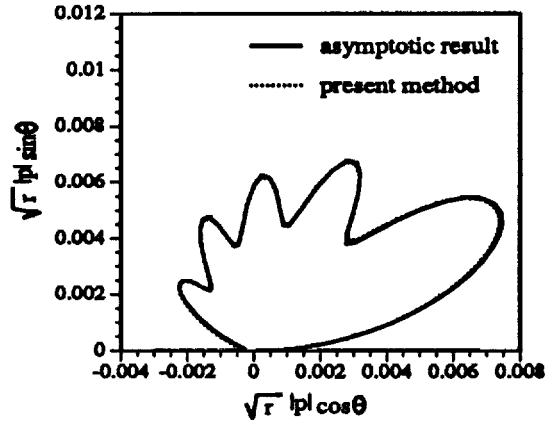

Figure 3: Directivity of unsteady pressure

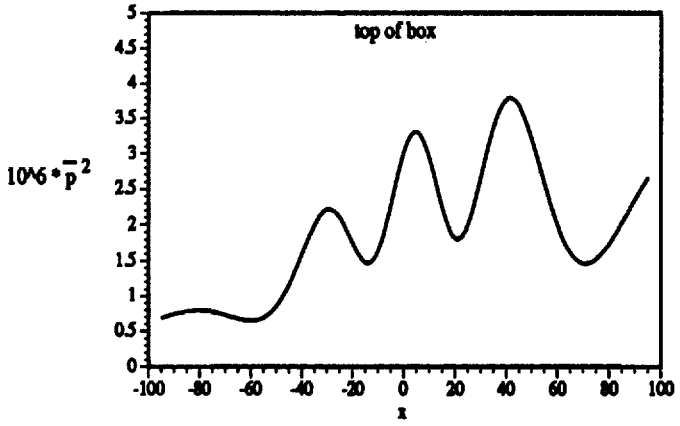

Figure 4: Unsteady pressure on top of the box for t = 0

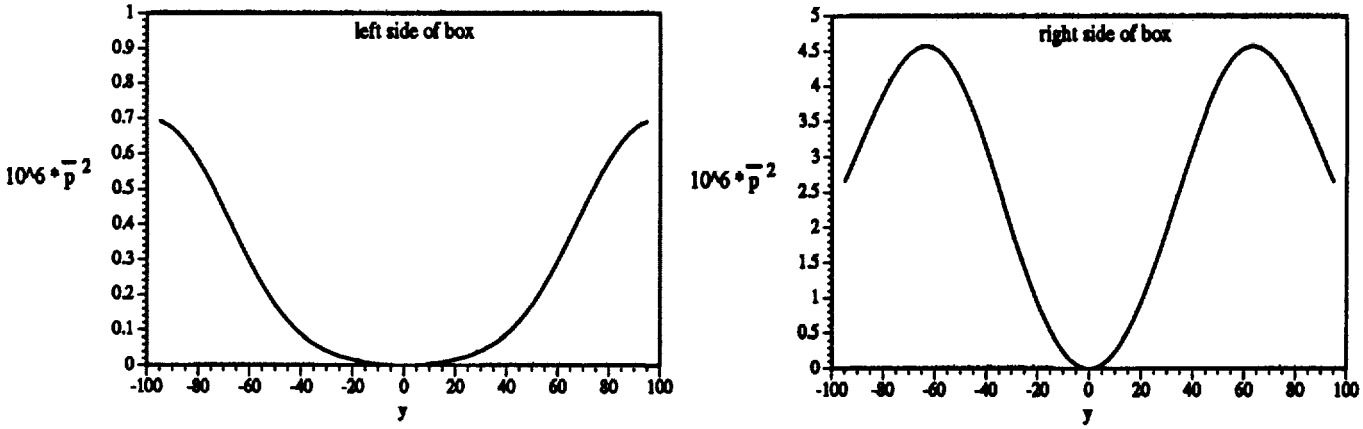

Figure 5: Unsteady pressure on left and right sides of the box for t = 0

REFERENCES

[1] Possio, D.: L'Azione Aerodinamica sul Prodilo Oscillante in un Fluido Compressible a Velocita Ipsonora. *L'Aerotecnica*, vol. XVIII, no. 4, 1938.

[2] Graham, J. M. R.: Similarity Rules for Thin Airfoils in NOn-Stationary Subsonic Flows. *Journal of Fluid Mechanics*, vol. 43, pt. 4, 1970, pp.753-766.

[3] Scott, J. S.; and Atassi, H. M.: A Finite Difference Frequency-domain Numerical Scheme for the Solution of the Linearized Euler Equations. NASA CP 3078, 1991.

[4] Osborne, C.: Unsteady Thin-Airfoil Theory for Subsonic Flow. *AIAA Journal*, vol. 11, no. 2, 1973, pp. 205-209.

[5] Amiet, R. K.: Compressibility Effects in Unsteady Thin-Airfoil Theory. *AIAA Journal*, vol. 12, no. 2, 1974, pp.253-255.

[6] Adamczyk, J. J.: The Passage of an Infinite Swept Airfoil Through an Oblique Gust. *Journal of Aircraft*, vol. 11, no. 4, 1974, pp. 281-187.

[7] Amiet, R. K.: High Frequency Thin-Airfoil Theory for Subsonic Flow. *AIAA Journal*, vol. 14, no. 8, 1976, pp.1076-1082.

[8] Atassi, H. M.: Unsteady Aerodynamics and Vortical Flows: Early and Recent Developments. *Aerodynamics and Aeroacoustics*, Editor, K. Y. Fung, World Scientific, 1994, pp. 119-169.

[9] Amiet, R. K.: Acoustic Radiation from an Airfoil in a Turbulent Stream. *Journal of Sound and Vibration*, vol. 41, no. 4, 1974, pp. 407-420.

[10] Martinez, R.; and Widnall, S. E.: Unified Aerodynamic-Acoustic Theory for a Thin Rectangular Wing Encountering a Gust. *AIAA Journal*, vol. 18, no. 5, 1980, pp.638-645.

[11] Atassi, H. M.; Dusey, M.; and Davis, C. M.: Acoustic Radiation from a Thin Airfoil in Nonuniform Subsonic Flow. *AIAA Journal*, vol. 31, 1993, pp 12-19.

N95-30162

AEROACOUSTIC COMPUTATION OF A GUST-PLATE INTERACTION VIA MACCORMACK SCHEMES

James E. Martin
Department of Mathematics
Christopher Newport University
Newport News, Virginia 23606

ABSTRACT

We apply second, fourth, and sixth order spatially accurate variations of the MacCormack scheme to calculate the noise radiated by the interaction of a flat plate with an oncoming gust. For the given gust wavelength and numerical discretization, the fourth and sixth order schemes each are effective in capturing the occurring acoustic waves. However, for the case of the sixth order scheme, the high order of extrapolation applied at the far field boundaries necessitates an extension of the computational boundaries from their prescribed location.

1. INTRODUCTION

For many aeroacoustic problems, simple adaptation of standard CFD schemes is unsuitable due to the additional challenges involved in computing the sound field. Hardin (1993) lists many of the additional challenges inherent in aeroacoustic computation. These include: (1) the small size of the quantities to be computed, (2) the high frequencies involved, (3) a sensitive dependence of the acoustic field upon phase, damping, and dispersion, and (4) the temporal dependence of the far field boundary conditions. Radiation boundary conditions which minimize reflections at the far field boundaries have been derived and successfully tested by Tam and Webb (1993). With their dispersion relation preserving schemes, Tam and Webb have furthermore developed numerical schemes which, unlike many finite difference schemes, maintain the dispersive qualities of the occurring acoustic waves. One aim of the present study is to test the effectiveness of a typical CFD scheme, which lacks the tailoring of the dispersion relation preserving schemes, on a given benchmark problem in computational aeroacoustics. In the present study, using the radiation boundary conditions derived by Tam and Webb, we investigate the ability of three variations of the MacCormack scheme to capture the occurring acoustic waves in the given flow field.

As part of the Workshop on Benchmark Problems in Computational Aeroacoustics, the following problem was posed. Determine the intensity of radiated sound generated by the interaction of an infinitesimally thin, flat plate with an oncoming gust which contains a two component, mean velocity. The gust has uniform mean velocity in x with Mach number, M_∞, equal to 0.5. The gust's mean velocity in y is of smaller amplitude and is given by

$$v = f(x - M_\infty t) = 0.1 \sin\left[\frac{\pi}{8}\left(\frac{x}{M_\infty} - t\right)\right].$$

Hariharan *et al.* (1992) investigated a similar flow arrangement using a finite difference scheme with second order, spatial and temporal accuracy.

In the present study, we concentrate on the effectiveness of the MacCormack scheme applied to the above problem. We focus on the fourth order spatially accurate variation of this scheme and compare our results with those we obtain using second and sixth order spatially accurate versions. The outline of this paper is as follows: in section 2, we will review the numerical approach we have applied to the given problem. In section 3, we will describe and discuss the results, and in section 4, we will give a short summary and conclusions.

2. NUMERICAL APPROACH

For the calculation, a computational domain extending in x and in y from -100 to 100 is prescribed. The following scales are to be used: length scale, Δx; velocity scale, a_∞; density scale, ρ_∞; and pressure scale, $\rho_\infty a_\infty^2$. Here Δx is the computational grid spacing. ρ_∞ and a_∞ are, respectively, the ambient density and sound speed. Viscous effects are to be ignored. Therefore, we solve the problem using the non-dimensional, compressible Euler equations. After linearization about the mean flow, these equations have the following form:

$$\frac{\partial}{\partial t}\begin{bmatrix} u' \\ v' \\ p' \end{bmatrix} + \frac{\partial}{\partial x}\begin{bmatrix} M_\infty u' + p' \\ M_\infty v' \\ M_\infty p' + u' \end{bmatrix} + \frac{\partial}{\partial y}\begin{bmatrix} 0 \\ p' \\ v' \end{bmatrix} = 0 \tag{1}$$

in which u', v' and p' are the disturbance streamwise velocity, transverse velocity, and pressure. Since the equations for the disturbance density and pressure are identical, we remove the equation for density from our system and correspondingly reduce the magnitude of the calculation. At the far field computational boundaries, we apply the radiation boundary conditions derived by Tam and Webb (1993). The only physical boundary is the plate located at $y = 0$ and $-15.0 \leq x \leq 15.0$. On the plate, we satisfy the no normal flow condition by specifying $v' = -f(x - M_\infty t)$. The transverse gust velocity will create discontinuities across the plate in the pressure and the streamwise velocity. We determine the pressure on each side of the plate using a one-sided Taylor expansion with $\partial p'/\partial y = 0$ at the plate. Off the plate, pressure must be continuous. Continuity of u' in x however, may lead to discontinuities in u' across $y = 0$ all along the centerline. For the results presented here, we perform all calculations over only the upper half domain (thus, only one value for each of the discontinuous variables along the centerline at $y = 0$ is monitored) and we utilize symmetry conditions of the pressure and the velocities about $y = 0$.

When applied to waves of high frequency, the Fourier-Laplace transform of standard finite difference schemes begins to deviate from that of the derivatives they attempt to approximate. Tam and Webb's results indicate that for the given gust frequency and numerical discretization, using a standard finite difference scheme, minimal fourth order spatial accuracy is necessary to adequately represent the occurring acoustic waves. Thus, for the numerical integration of equation (1), we tested an unsplit, 2-4 variation of the MacCormack scheme (second order accurate in time, fourth order accurate in space) developed by Gottlieb and Turkel (1976). For an equation of the form $U_t = F_x$, the two stages of this scheme have the following form:

$$\overline{U}_i = U_i^n + \frac{\Delta t}{6\Delta x}\left[7\left(F_{i+1}^n - F_i^n\right) - \left(F_{i+2}^n - F_{i+1}^n\right)\right]$$

$$U_i^{n+1} = \frac{1}{2}\left\{U_i^n + \overline{U}_i + \frac{\Delta t}{6\Delta x}\left[7\left(\overline{F}_i - \overline{F}_{i-1}\right) - \left(\overline{F}_{i-1} - \overline{F}_{i-2}\right)\right]\right\}. \quad (2)$$

For comparison purposes, we have also implemented the standard 2-2 MacCormack scheme as well as the 2-6 variation alluded to by Bayliss *et al.* (1985). For the MacCormack schemes, flow information is required at locations external to the computational domain. With each scheme implemented, to obtain information at these external locations we apply an extrapolation formula with accuracy which is one order less than the spatial accuracy of the numerical scheme. Below, we list the first, third, and fifth order extrapolation formulas used with the second, fourth, and sixth order spatially accurate schemes

$$F_{N+1} = 2F_N - F_{N-1} \quad (3)$$

$$F_{N+1} = 4F_N - 6F_{N-1} + 4F_{N-2} - F_{N-3} \quad (4)$$

$$F_{N+1} = 6F_N - 15F_{N-1} + 20F_{N-2} - 15F_{N-3} + 6F_{N-4} - F_{N-5}. \quad (5)$$

3. RESULTS

Figure 1 contains contours of the disturbance pressure from the 2-4 MacCormack calculation at the time $t = 500.0$. By time 500.0, the flow is fully time periodic. The pattern of acoustic wave emission is visible, with five distinct waves radiating from each side of the plate. The strongest waves emit from the trailing edge, with intensity and wavelength decreasing for waves emitting closer to the leading edge. In figure 1 the jump in disturbance pressure which occurs across the plate can be seen. The directivity pattern for this calculation (figure 2(a)), measured by computing the product of the radius, r, and $\overline{p'^2}(r)$ along the $x = \pm 95$ and $y = \pm 95$ coordinate lines, contains five lobes in each half domain. The lobes fan out in an approximate 90 degree sector. Each of the waves emitting from the plate increases in magnitude with increasing downstream direction, with the strongest waves leaving the trailing edge at an approximate 30 degree angle.

Throughout the calculation, the wake remains silent. The radiation boundary conditions create no noticeable reflections of the waves back into the computational domain. As a test of the effectiveness of our solution near the far field boundaries, we perform a second calculation using a computational domain which extends in x and in y from -200 to 200. The directivity pattern, again computed along the $x = \pm 95$ and $y = \pm 95$ coordinate lines, matches the directivity pattern shown in figure 2(a), thus indicating the effectiveness of the far field boundary conditions used. As further validation of our solution, we find good agreement between our results using the prescribed grid and those we obtain using instead a grid with one half the prescribed grid spacing.

We have also tested the second and sixth order spatially accurate variations of the MacCormack scheme on the given problem. The fifth order extrapolation used with the 2-6 scheme, proves too

intrusive. The one-dimensional, unphysical extrapolation formulas (3)-(5), become more problematic as their stencil size increases and information closer to the sound source is utilized. As a result, very early in our calculation using the 2-6 scheme, contours of the disturbance pressure indicate significant reflections near the far field boundaries. This results in a more jagged directivity pattern (figure 2(b)) than that obtained using the 2-4 scheme. Using instead an extended computational domain, the 2-6 scheme again produces a solution in good qualitative agreement with that obtained using the 2-4 scheme (figure 2(c)). Finally, in figure 2(d), we show the directivity pattern obtained using the standard 2-2 MacCormack scheme. As predicted by the Tam and Webb findings, the second order spatially accurate scheme is unable to accurately represent the occurring acoustic waves in the given problem.

4. CONCLUSIONS

We have tested three variations of the MacCormack scheme, a scheme widely used for CFD calculations, on the given benchmark problem in computational aeroacoustics. For a Mach 0.5, sinusoidal gust mean flow field, our results reveal a pattern of sound wave emission with five dominant waves of different intensity and wavelength each emitting from the solid body source. When used with minimal fourth order spatial accuracy, the MacCormack scheme has proven effective at capturing the occurring acoustic waves. Third order extrapolation used in conjunction with the 2-4 MacCormack scheme yields an accurate solution. However, as we have shown with our sixth order accurate calculation, the arbitrariness of one-dimensional extrapolation may become problematic when larger extrapolation stencils are used with increased accuracy schemes.

Acknowledgments

I would like to acknowledge the many helpful discussions with Jay Hardin. This work has been supported by a 1994 NASA/ASEE Summer Faculty Fellowship. Computing resources were provided by the Institute for Computational Applications in Science and Engineering.

References

1. Hardin, J.C.: Regarding numerical considerations for computational aeroacoustics, in: *Computational Aeroacoustics*, eds. J.C. Hardin and M.Y. Hussaini, Springer Verlag, 1993, pp. 216-228.

2. Tam, C.K.W.; and Webb, J.C.: Dispersion-relation-preserving finite difference schemes for computational acoustics. *J. Comput. Phys.*, vol. 107, no. 2, Aug. 1993, pp. 262-281.

3. Hariharan, S.I.; Ping, Y.; and Scott, J.R.: Time domain numerical calculations of unsteady vortical flows about a flat plate airfoil. *J. Comput. Phys.*, vol. 101, no. 2, Aug. 1992, pp. 419-430.

4. Gottlieb, D.; and Turkel, E.: Dissipative two-four methods for time-dependent problems. *Math. Comp.*, vol. 30, Oct. 1976, pp. 703-723.

5. Bayliss, A.; Parikh, P.; Maestrello, L.; and Turkel, E.: A fourth-order scheme for the unsteady, compressible Navier-Stokes equations. AIAA-85-1694, July 1985.

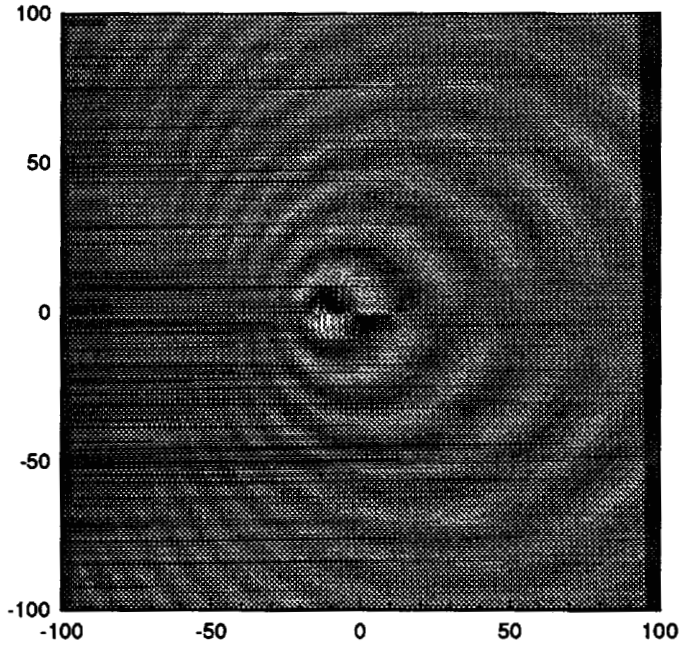

Figure 1: Contours of the disturbance pressure at time $t = 500.0$. Note the discontinuity in pressure which occurs across the plate located at $y = 0$ and $-15 \leq x \leq 15$. We observe five dominant acoustic waves emerging off each side of the plate, with the strongest waves emitting from the trailing edge at an approximate 30 degree angle.

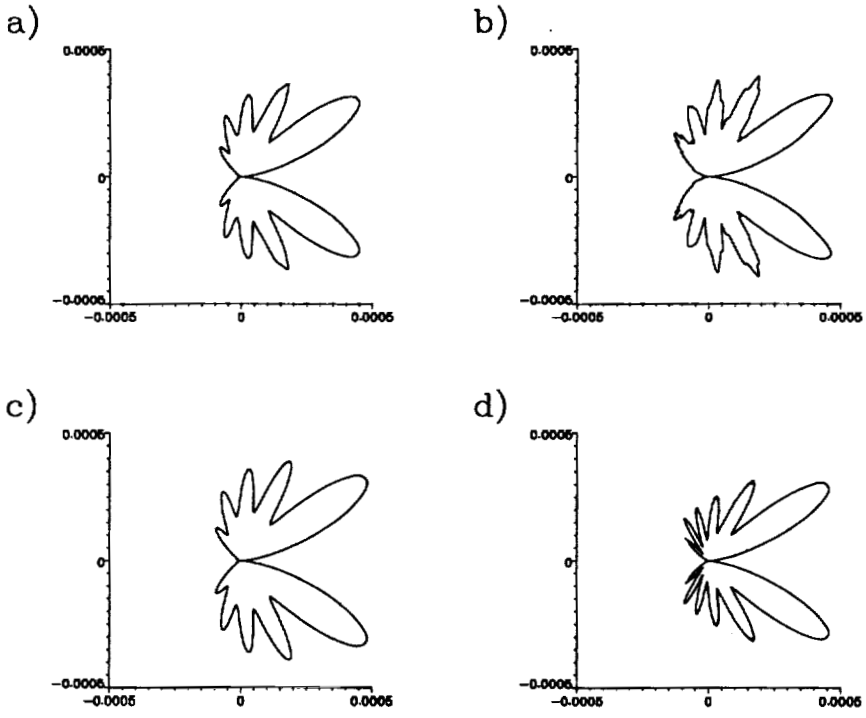

Figure 2: Directivity patterns obtained using the following versions of the MacCormack scheme: (a) 2-4 scheme, (b) 2-6 scheme, (c) 2-6 scheme with extended computational domain, and (d) 2-2 scheme.

EVALUATION OF NUMERICAL SCHEMES FOR THE ANALYSIS OF SOUND GENERATION BY BLADE-GUST INTERACTION

J. N. Scott

Department of Aeronautical and Astronautical Engineering
The Ohio University
Columbus, OH 43210

S. I. Hariharan[1]

Department of Mathematical Sciences
University of Akron, Akron, OH 44325-4002, U.S.A.

R. Mankbadi

NASA Lewis Research Center
21000 Brook Park Road, Cleveland, OH 44135

Abstract

In this investigation three different numerical algorithms have been utilized to compute the flow about a flat plate in the presence of a transverse gust described by a sinusoidal disturbance. The three schemes include the MacCormack explicit finite difference scheme which is second order accurate in both time and space, the Gottlieb and Turkel modification of MacCormack's scheme which is fourth order accurate in space and second order accurate in time, (referred to as the 2-4 scheme), and a two step scheme developed by Bayliss et. al. which has second order temporal accuracy and sixth order spatial accuracy (a 2-6 scheme). The flow field results are obtained with these schemes by using the same code with the only difference being the implementation of the respective solution algorithms. The problem is set up so that the sinusoidal disturbance is imposed at the surface of the flat plate as a surface boundary condition. Thus the problem is treated as scattering problem. The computed results include the time average of the acoustic pressure squared along grid lines five points away from the boundaries. distribution throughout the computational domain is monitored at various times. The numerical results are compared with an exact solution obtained by Atassi, Dusey, and Davis.

INTRODUCTION

Unsteady flow associated with the interaction of a gust with a blade is encountered in all types of rotating machinery including compressors, turbines, fans, and helicopter rotors. This unsteady flow is a major contributor to the generation and propagation of acoustic disturbances. The use of computational methods in the analysis of such unsteady flow and the resultant far field acoustic radiation requires care in the application of any numerical scheme. In particular, the dissipation and dispersion characteristics of the numerical scheme are critical to the accuracy of the solution. Dissipative schemes tend to damp natural unsteady or oscillatory disturbances while dispersive schemes generate non-physical oscillations. Either can degrade or contaminate the numerical solution of acoustic propagation to the point that it is unreliable. In general, there are three types of waves present in unsteady flows. These include acoustic waves which

[1]Support for the first two authors was provided by ICOMP, NASA Lewis Research Center

are isotropic, non-dispersive, non-dissipative, and propagate at the speed of sound, C, as well as entropy and vorticity waves which are non-dispersive, non-dissipative and highly directional and propagate at the mean convection speed of the flow. Acoustic phenomena are generally considered to be governed by the linearized Euler equations.

A major effort in calculating solutions for unsteady linearized Euler equations has been pursued by Atassi and his coworkers. A nicely documented history of formulations from previous results to the state-of-the-art results are reported by Atassi [2]. Further, the first computational effort for the sound radiation problem is due to Atassi et. al. [3]. In this work the near field calculations were performed using a numerical scheme developed by Scott and Atassi [8]. For the current problem involving a flat plate airfoil, the first numerical solution in the frequency domain was obtained by Scott and Atassi [9] and in the time domain by Hariharan et. al. [5]. In these works the focus was the near field calculations. For the far field calculations, again the work in [3] appears to be the first in the literature. Despite the nature of this classical problem, computational efforts clearly are rather new. In fact, for the flat plate - gust interaction solution of Atassi et. al. [4], semi-analytical results have been presented with the aid of numerical and asymptotic approximations. The current results are compared with these results.

The present results are obtained in the search for an efficient scheme that will not only predict the near field behavior, but also the far field acoustic radiation simultaneously. The numerical schemes that are used to simulate the results are simple to handle. Moreover, the boundary treatment on the artificial boundary is simple and does not involve specialized treatments, such as a nontrivial differencing or adding terms to stabilize the results. The conditions are derived using progressive wave solutions implemented in the ongoing work by Hagstrom and Hariharan[1]. They have the asymptotic behavior of the solution built in. In this case, the results can be improved if necessary, by enlarging the computational domain. In fact a sample result is presented in later sections to demonstrate the asymptotic behavior of the boundary conditions. The numerical solution schemes we choose belong to the same family as the classical McCormack scheme. In addition to this scheme we use one proposed by Gottlieb and Turkel [6] which is a fourth order scheme in space and an extension proposed by Bayliss et. al. [7] which is sixth order accurate in space. The assessment of these results are presented in light of the semi-analytical (numerical) results of [4].

TEST PROBLEM

The linearized Euler equations yield the following non-dimensional linear equations:

$$(\frac{\partial}{\partial t} + M\frac{\partial}{\partial x})p + div\mathbf{u} = 0, \tag{1}$$

$$(\frac{\partial}{\partial t} + M\frac{\partial}{\partial x})\mathbf{u} + \nabla p = 0. \tag{2}$$

where $\mathbf{u} = (u, v)$ is the acoustic propagation velocity and p is the acoustic pressure. In this linearization the isentropic relation is used so that $p = \rho$ at this order. Therefore, the current problem is to solve the above equation subject to an incident gust at $x = -\infty$ and in the presence of a flat plate centered at the origin. This problem is then reformulated as a scattering problem in the following sense: let the total disturbed velocity field be

$$\mathbf{u} = \mathbf{u}_i + \mathbf{u}_s \tag{3}$$

where $\mathbf{u}_i$ is the incident gust disturbance velocity and $\mathbf{u}_s$ is the scattered field velocity. We note that that the following properties are satisfied by the incident gust velocity:

- Gust disturbance is solenoidal, i.e., $divu_i = 0$. One such form is $u_i = (0,\, g(x,t))$.
- Gust disturbances are convected with the flow, i.e., $(\frac{\partial}{\partial t} + M\frac{\partial}{\partial x})\mathbf{u}_i = \mathbf{0}$. This property imposes the further restriction that $\mathbf{u}_i = (0, f(\frac{x}{M} - t))$ where f is an arbitrary function of the indicated argument. For the specific test problem under consideration $f(\frac{x}{M} - t)) = .1\sin(\frac{\pi}{8}(\frac{x}{M} - t))$.

Now substituting the decomposition (3) into equations (1) and (2), we have

$$(\frac{\partial}{\partial t} + M\frac{\partial}{\partial x})p + div\mathbf{u}_s = 0, \tag{4}$$

$$(\frac{\partial}{\partial t} + M\frac{\partial}{\partial x})\mathbf{u}_s + \nabla p = 0. \tag{5}$$

Note that with $\mathbf{u}_s = (u, v)$ the governing equations are identical to those for the total velocity field and they are:

$$(\frac{\partial}{\partial t} + M\frac{\partial}{\partial x})p + \frac{\partial u}{\partial x} + \frac{\partial v}{\partial y} = 0 \tag{6}$$

$$(\frac{\partial}{\partial t} + M\frac{\partial}{\partial x})u + \frac{\partial p}{\partial x} = 0 \tag{7}$$

$$(\frac{\partial}{\partial t} + M\frac{\partial}{\partial x})v + \frac{\partial p}{\partial y} = 0 \tag{8}$$

A major advantage to this formulation is that the far field conditions become homogeneous, since $\mathbf{u} \to \mathbf{u}_i$ as $x \to -\infty$, $\mathbf{u}_s \to 0$ as $x \to -\infty$. The scattering formulation now originates from the boundary condition on the flat plate airfoil. On the flat plate the total velocity is given by $\mathbf{v} = M\mathbf{i} + \mathbf{u}_i + \mathbf{u}_s = (M + u, v + f(\frac{x}{M} - t)$. Since the boundary condition on the plate is $\mathbf{v}\cdot\mathbf{j} = 0$ (i.e., the normal component of the total velocity is zero), we have

$$v = -f(\frac{x}{M} - t). \tag{9}$$

Again for the specific problem in hand $v = -.1\sin(\frac{\pi}{8}(\frac{x}{M} - t))$. The problem then is to solve equations (6),(7),(8) together with the boundary condition on the surface of the plate prescribed by equation (9) and appropriate radiation conditions which will be discussed next.

The radiation boundary conditions used for this problem are based on the work of Hagstrom and Hariharan [1]. The conditions are derived from the progressive wave solutions for the acoustic part. For this purpose equations (6),(7) and (8) are recast in cylindrical coordinates. They have the form

$$\mathbf{u}_t + \mathbf{A}\,\mathbf{u}_r + \frac{1}{r}\mathbf{B}\,\mathbf{u}_\theta = \mathbf{0} \tag{10}$$

where

$$\mathbf{u} = \begin{pmatrix} p \\ u \\ v \end{pmatrix}$$

For these transformed equations, solutions are sought in the form:

$$\mathbf{u} = \frac{f_0(t - r\,g(\theta))}{r^{1/2}}\,\mathbf{a}_0(\theta) + \frac{f_1(t - r\,g(\theta))}{r^{3/2}}\,\mathbf{a}_1(\theta) + \cdots \tag{11}$$

Substitution of (11) into (10) yields $O(\frac{1}{r^{1/2}})$ terms:

$$[\mathbf{I} - g(\theta)\,\mathbf{A} - g'(\theta)\,\mathbf{B}]\;\mathbf{a}_0 = \mathbf{0} \tag{12}$$

Therefore, nontrivial solutions of equation (12) at $O(\frac{1}{r})$ are restricted by an 'eikonal function' $g(\theta)$ corresponding to the wave propagation given by the system of equations (6)-(9). Calculation of this function yields:

$$g(\theta) = \frac{\sqrt{1 - M^2 \sin^2\theta} - M\cos\theta}{1 - M^2} \tag{13}$$

This function plays the role in constructing higher order boundary conditions for the convective wave equation in two dimensions as discussed in [11]. With this $g(\theta)$ equation (12) determines the eigenvector $\mathbf{a}_0(\theta)$. Solutions of equation (12) are given by

$$\mathbf{a}_0 = h_0(\theta) \begin{pmatrix} 1 \\ \frac{Q}{1-MQ} \\ \frac{R}{1-MQ} \end{pmatrix} = h_0(\theta) \begin{pmatrix} 1 \\ r_2 \\ r_3 \end{pmatrix}$$

where

$$Q = g\cos\theta - g'\sin\theta$$

$$R = g\sin\theta + g'\cos\theta$$

Substituting this solution into the progressive wave solution, we obtain the following relationship for the acoustic variables:

$$\begin{pmatrix} p \\ u \\ v \end{pmatrix} = \frac{h_0(\theta) f_0(t - r\,g(\theta))}{r^{1/2}} \begin{pmatrix} 1 \\ r_2 \\ r_3 \end{pmatrix} \tag{14}$$

From this it follows two relations

$$u = r_2 p \tag{15}$$

$$v = r_3 p \tag{16}$$

The above two relations were prescribed as two boundary conditions at the inflow boundaries and (15) at the outflow boundary in the x direction and (16) at the outflow boundary in y direction.

NUMERICAL SCHEMES

The numerical schemes that are used here are explicit, two-level, second order time accurate schemes. In all cases un-split versions of these schemes are used to maintain the accuracy. The description of the schemes will use the following notation for the system (6)-(8):

$$\mathbf{u}_t + \mathbf{f}_x + \mathbf{g}_y = 0 \tag{17}$$

We denote the solutions $\mathbf{u}(x(i), y(j), n\Delta t)$ by $\mathbf{u}^n_{i,j}$, where $x(i) = -100 + (i-1), i = 1, ..., 201$ and $y(j) = -100 + (j-1), j = 1, .., 201$.

McCormack Scheme

The first scheme for the above equations utilizes the original predictor - corrector formulation as follows:

$$\bar{\mathbf{u}}_{i,j} = \mathbf{u}^n_{i,j} - \frac{\Delta t}{\Delta x}(\mathbf{f}^n_{i+1,j} - \mathbf{f}^n_{i,j}) - \frac{\Delta t}{\Delta y}(\mathbf{g}^n_{i,j+1} - \mathbf{g}^n_{i,j}) \tag{18}$$

$$\mathbf{u}^{n+1}_{i,j} = .5(\bar{\mathbf{u}}_{i,j} + \mathbf{u}^n_{i,j} - \frac{\Delta t}{\Delta x}(\bar{\mathbf{f}}_{i,j} - \bar{\mathbf{f}}_{i-1,j}) - \frac{\Delta t}{\Delta y}(\bar{\mathbf{g}}_{i,j} - \bar{\mathbf{g}}_{i,j-1})) \tag{19}$$

This equation has second order spatial accuracy and the scheme is implemented on the entire grid in the computational domain. As such the fluxes are undefined a row ahead (and behind). The scheme is supplanted by a first order flux extrapolations given by

$$\mathbf{f}_{N+1,j} = 2\mathbf{f}_{N,j} - \mathbf{f}_{N-1,j} \tag{20}$$

at the right termination point in the x direction and

$$\bar{\mathbf{f}}_{0,j} = 2\bar{\mathbf{f}}_{1,j} - \bar{\mathbf{f}}_{2,j} \tag{21}$$

at the left termination point respectively. Here $N = 201$ is the number of grid points in the x direction. A similar extrapolation is used in the y direction for the g fluxes. Clearly solutions are defined up to the boundary.

Gottlieb-Turkel Scheme

This scheme developed by Gottlieb and Turkel is described in [6] and is similar to the the McCormack scheme but has fourth order spatial accuracy. The scheme is as follows:

$$\bar{\mathbf{u}}_{i,j} = \mathbf{u}^n_{i,j} - \frac{\Delta t}{6\Delta x}(7(\mathbf{f}^n_{i+1,j} - \mathbf{f}^n_{i,j}) - (\mathbf{f}^n_{i+2,j} - \mathbf{f}^n_{i+1,j})) - \frac{\Delta t}{\Delta y}(7(\mathbf{g}^n_{i,j+1} - \mathbf{g}^n_{i,j}) - (\mathbf{g}^n_{i,j+2} - \mathbf{g}^n_{i,j+1})) \tag{22}$$

$$\mathbf{u}^{n+1}_{i,j} = .5(\bar{\mathbf{u}}_{i,j} + \mathbf{u}^n_{i,j} - \frac{\Delta t}{6\Delta x}(7(\bar{\mathbf{f}}_{i,j} - \bar{\mathbf{f}}_{i-1,j}) - (\bar{\mathbf{f}}_{i-1,j} - \bar{\mathbf{f}}_{i-2,j})) - \frac{\Delta t}{6\Delta y}(7(\bar{\mathbf{g}}_{i,j} - \bar{\mathbf{g}}_{i,j-1}) - (\bar{\mathbf{g}}_{i,j-1} - \bar{\mathbf{g}}_{i,j-2})) \tag{23}$$

Clearly, fluxes need to be defined at two points ahead and behind the termination points. The flux extrapolations used here as suggested in [6] ahead the termination point in the x direction are third order ones given by

$$\mathbf{f}_{N+1,j} = 4\mathbf{f}_{N,j} - 6\mathbf{f}_{N-1,j} + 4\mathbf{f}_{N-2,j} - \mathbf{f}_{N-3,j} \tag{24}$$

and

$$\mathbf{f}_{N+2,j} = 4\mathbf{f}_{N+1,j} - 6\mathbf{f}_{N,j} + 4\mathbf{f}_{N-1,j} - \mathbf{f}_{N-2,j} \tag{25}$$

A similar treatment is given behind the left termination point.

Bayliss et. al. sixth order scheme

This scheme has sixth order spatial accuracy (see [7]). It is constructed as an extension of the fourth order scheme described above. The scheme proposed in [7] is described for a one dimensional analysis. However, it is used here as an extension to two dimensional equations and the analysis remains to be shown in the future. The scheme is as follows:

$$\bar{\mathbf{u}}_{i,j} = \mathbf{u}^n_{i,j} - \frac{\Delta t}{30\Delta x}(37D\mathbf{f}^n_{i+1,j} - 8D\mathbf{f}^n_{i+2,j} + D\mathbf{f}^n_{i+3,j}) - \frac{\Delta t}{30\Delta y}(37D\mathbf{g}^n_{i,j+1} - 8D\mathbf{g}^n_{i,j+2} + D\mathbf{g}^n_{i,j+3}) \tag{26}$$

$$\mathbf{u}^{n+1}_{i,j} = .5(\bar{\mathbf{u}}_{i,j} + \mathbf{u}^n_{i,j} - \frac{\Delta t}{30\Delta x}(37D\bar{\mathbf{f}}_{i,j} - 8D\bar{\mathbf{f}}_{i-1,j} + D\bar{\mathbf{f}}_{i-2,j}) - \frac{\Delta t}{30\Delta y}(37D\bar{\mathbf{g}}_{i,j} - 8D\bar{\mathbf{g}}_{i,j-1} + D\bar{\mathbf{g}}_{i,j-2})) \tag{27}$$

where $D\mathbf{f}^n_{i+1,j} = \mathbf{f}^n_{i+1,j} - \mathbf{f}^n_{i,j}$ and $D\mathbf{g}^n_{i,j+1} = \mathbf{g}^n_{i,j+1} - \mathbf{g}^n_{i,j}$. Similar definitions are deduced for the other terms involving these operators. As in the above two numerical schemes flux extrapolations are required at the end points of the computational domain. A fifth order extrapolation is

proposed [10] at these points. Again we list one set of such extrapolations and others follow in a similar manner. At the right boundary the sequence of extrapolations are:

$$f_{N+1,j} = 6f_{N,j} - 15f_{N-1,j} + 20f_{N-2,j} - 15f_{N-3,j} + 6f_{N-4,j} - f_{N-5,j} \tag{28}$$

$$f_{N+2,j} = 6f_{N+1,j} - 15f_{N,j} + 20f_{N-1,j} - 15f_{N-2,j} + 6f_{N-3,j} - f_{N-4,j} \tag{29}$$

$$f_{N+3,j} = 6f_{N+2,j} - 15f_{N+1,j} + 20f_{N,j} - 15f_{N-1,j} + 6f_{N-2,j} - f_{N-3,j} \tag{30}$$

NUMERICAL RESULTS

The numerical results for each of the three numerical schemes are presented for the unsteady pressure field in relatively close proximity to the boundary on each of the four sides of the computational domain. Specifically the computed pressures along lines at $x = \pm 95$ and $y = \pm 95$ are plotted for each of the three numerical schemes. These results are compared with each other as well as the analytical result of Atassi, et.al.

Initially the numerical results were examined for a grid of 200 x 200 points and a time of 10 periods of the scheme. These results were compared with the analytical results of Atassi and found to be in poor agreement. This was attributed to the reflections that accumulate from the boundary conditions used. Thus, solutions were obtained for a larger domain consisting of 600 points in each direction equally spaced. These results clearly revealed the benefits of much longer run times improving the accuracy of the numerical prediction of critical flow features. These results are shown at locations of $x = \pm 95$ in figures 1 and 2 and at $y = \pm 95$ in figures 3 and 4. As noted previously these lines are in close proximity to each of the boundaries. These figures show the far field acoustic pressure computed with each of the three schemes as well as the analytical results of Atassi, et.al. In each case the numerical results show the time average of the oscillatory behavior of the pressure waves near each of the boundaries. Along the inflow and outflow boundaries the symmetry of the incoming and outgoing waves is in good agreement with the exact solution with agreement improving with order of accuracy. Similarly the numerical solutions near the side boundaries clearly show the presence of four peaks giving a good representation of the trends shown by the exact solution.

It is particularly important to note that solutions should start from a state of rest to avoid propagation of discontinuities. Moreover the waves impinge on the plate from the left. To simulate these considerations the boundary condition on the plate is modified as follows

$$v = -.1 \sin(\frac{\pi}{8}(\frac{(x+L)}{M} - t))H(\frac{\pi}{8}(\frac{(x+L)}{M} - t)) \tag{31}$$

where $H(z)$ is the Heaviside function. In addition to the pressure data described above, the time variation of the pressure field for the entire computational domain was monitored with time. The computed pressure values are shown as surface plots at times corresponding to time step levels 720 and 1440 in figures 5 and 6 respectively. These results are obtained using the 6th order scheme of Bayliss and his associates. In these figures, the time evolution of the waves is seen as they propagate outward from the plate. These results clearly show that the waves pass out through the boundaries of the computational domain in a stable manner and that there are no reflections or non-physical disturbances produced at the boundaries as the waves pass through them.

Another feature that is observed in these figures is the development of the wake at the trailing edge of the plate and its subsequent growth downstream. This behavior is a good representation of the results anticipated from classical theory and experimental observations and is achieved in this case with no special treatment along the wake line.

CONCLUSIONS

The objective of this effort was to investigate the application of numerical schemes to the analysis of unsteady flow characteristics produced by the interaction of a transverse gust impinging on a flat plate and to assess the prediction of the acoustic far field which results from the unsteady flow. In this study three different numerical schemes were utilized to solve the linearized Euler equations as prescribed in the ICASE CAA Benchmark Problem description designated as Category 6. As noted in previous sections the three different numerical schemes utilized are of the same predictor-corrector explicit differencing family of algorithms. These are the well known MacCormack scheme which is second order accurate in both time and space, the Gottlieb- Turkel extension to fourth order spatial accuracy while maintaining second order temporal accuracy and an extension to sixth order spatial accuracy developed by Bayliss and his associates. The numerical results are compared with the analytical results obtained by Atassi, et.al. Clearly the agreement of the numerical results with the exact solution improves dramatically with increasing order of accuracy of the numerical scheme. The prediction of the far field acoustic pressure shown in figures 1-4 shows that the use of these type of schemes has promise for computing the acoustic radiation produced by unsteady flow effects. Further, the results obtained with these methods generally compare quite favorably with other methods presented for the solution of CAA Benchmark Problem category 6.

References

[1] T. Hagstrom and S. I. Hariharan, *Numerical simulations of time-dependent compressible flows in open domains*, in preparation.

[2] H. M. Atassi, *Unsteady Aerodynamics of Vortical Flows: Early and Recent Developments, Symposium on Aerodynamics and Aeroacoustics*, Tucson, Arizona, February 28 - March 2, 1993.

[3] H. M. Atassi, S. Subramaniam and J. R. Scott., *Acoustic Radiation from Lifting Airfoils in Compressible Subsonic Flows*, AIAA Paper 90-3911, October,1990.

[4] H. M. Atassi, M. Dusey and C. M. Davis, *Acoustic Radiation from a Thin Airfoil in Nonuniform Subsonic Flows*, AIAA Paper 90-3910, October, 1990.

[5] S. I. Hariharan, Yu Ping and J. R. Scott, *Time Domain Numerical Calculations of Unsteady Vortical Flows about a Flat Plate airfoil*, J. Comput. Phys., Vol. 101, No. 2, (1992), pp. 419 - 430.

[6] D. Gottlieb and E. Turkel, *Dissipative Two-Four Methods for Time Dependent Problems*, Math. Comp., 30 (1976), pp. 703-723.

[7] A. Bayliss, P. Parikh, L. Maestrello and E. Turkel, *A Fourth-Order Scheme for the Unsteady Compressible Navier Stokes Equations*, ICASE Report No. 85-44 (1985).

[8] J. R. Scott and H. M. Atassi *A Finite-Difference, Frequency-Domain Numerical Scheme for the Solution of the Gust Response Problem*, J. Comput. Phys. (to appear)

[9] J. R. Scott and H. M. Atassi Numerical Solution of Periodic Vortical Flows about a Thin Airfoil, NASA TM - 101998, (1989).

[10] Private Communications with Alvin Bayliss(1994).

[11] T. Hagstrom and S.I. Hariharan, "Far Field Expansion for Anisotropic Wave Equations," *Proceedings of the Second IMACS Symposium on Computational Acoustics*, North Holland, Eds. D. Lee, A. Cakmak and R. Vichnevetsky, (1990), pp. 283-294.

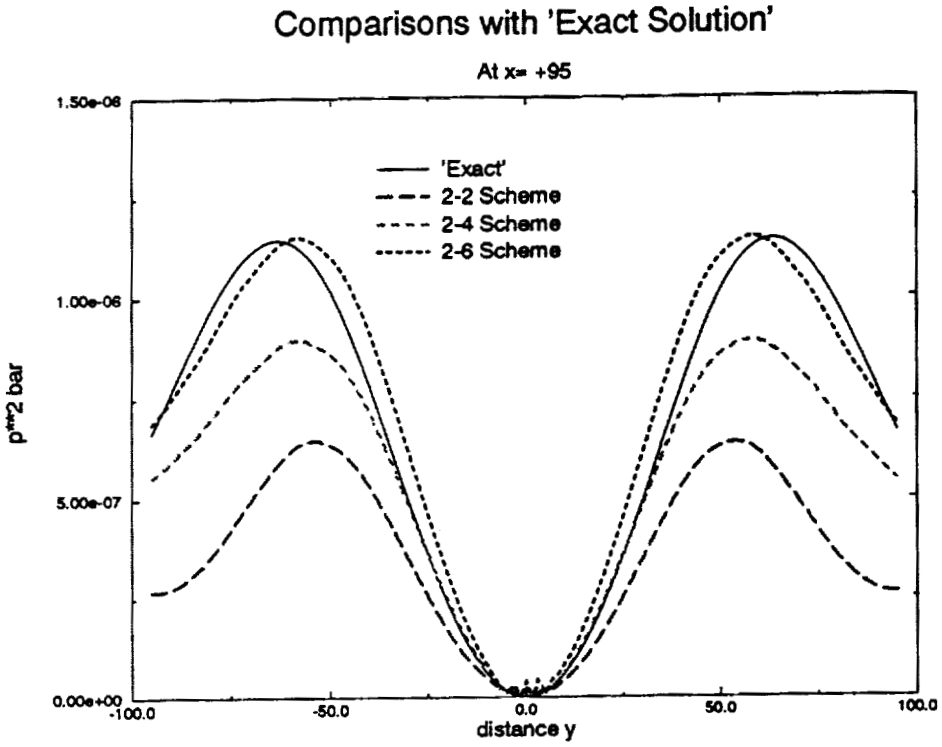

Figure 1: Comparison of numerical results with exact solution at x = +95

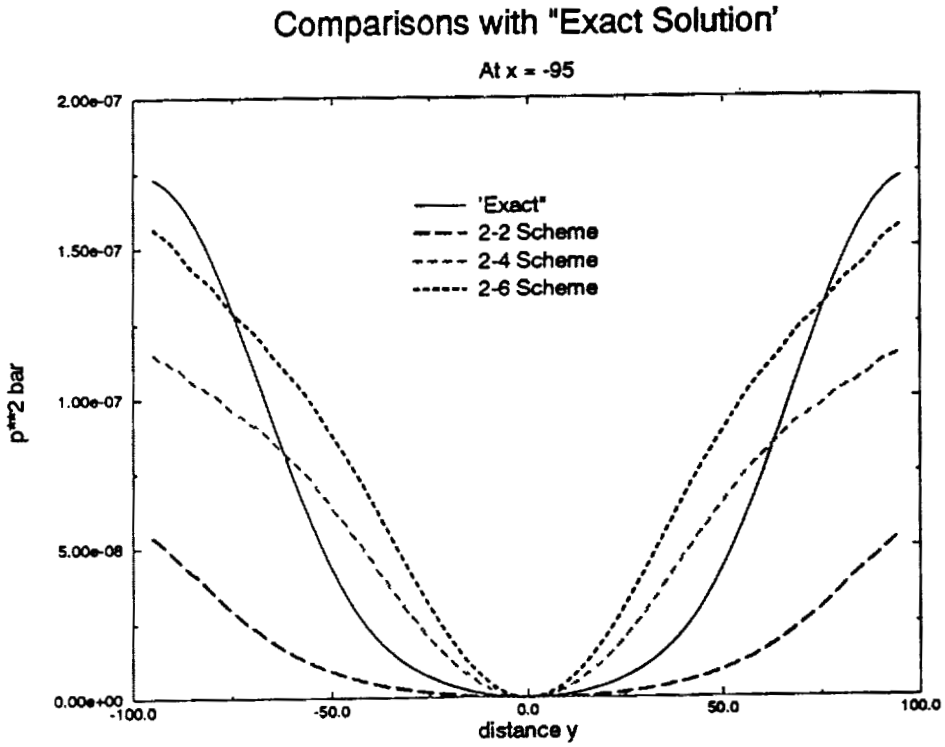

Figure 2: Comparison of numerical results with exact solution at x = -95

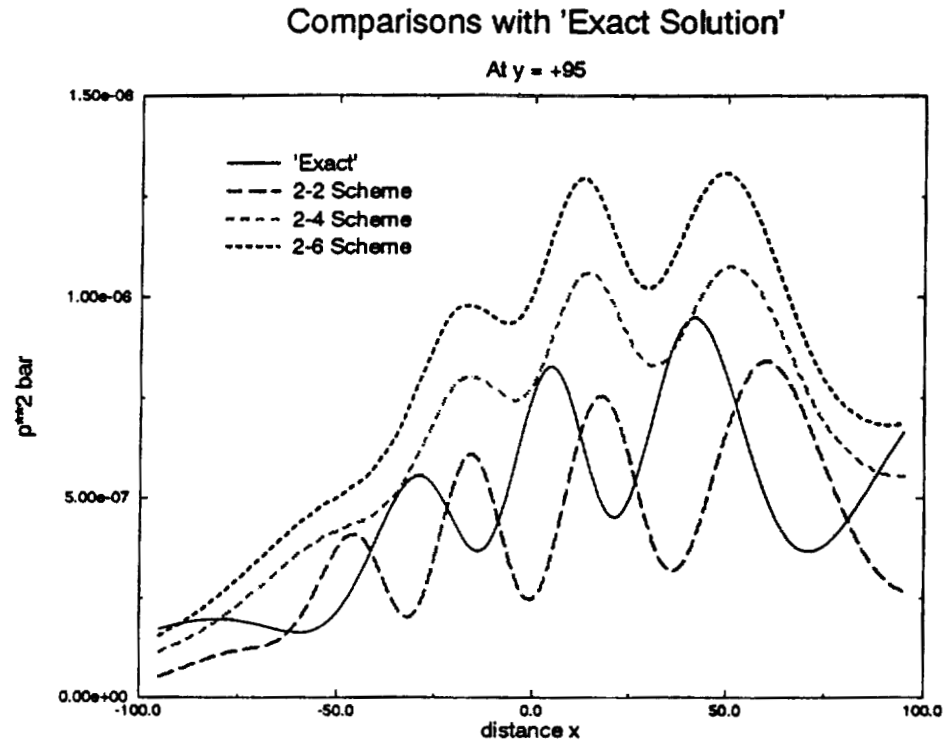

Figure 3: Comparison of numerical results with exact solution at y = +95

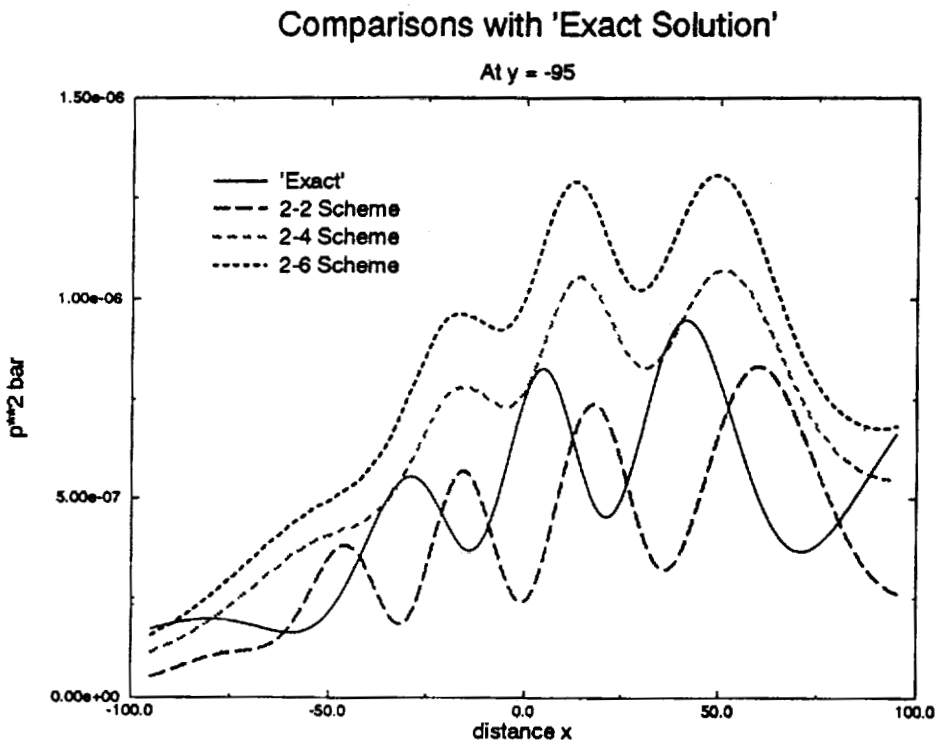

Figure 4: Comparison of numerical results with exact solution at y = -95

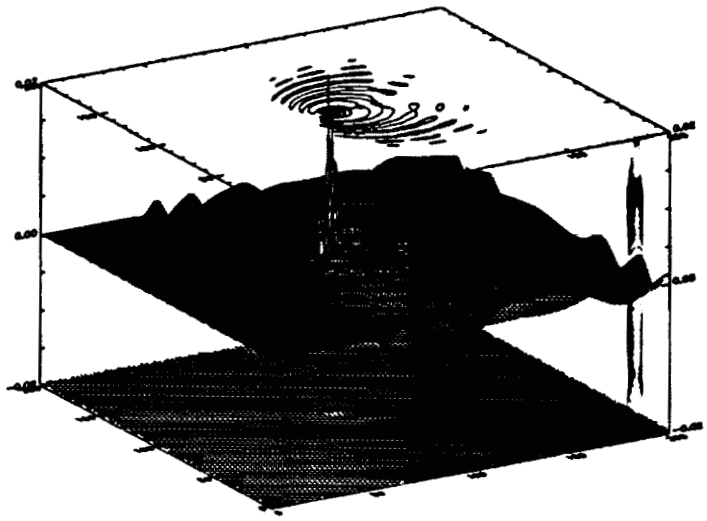

Figure 5: Solution at time step 720

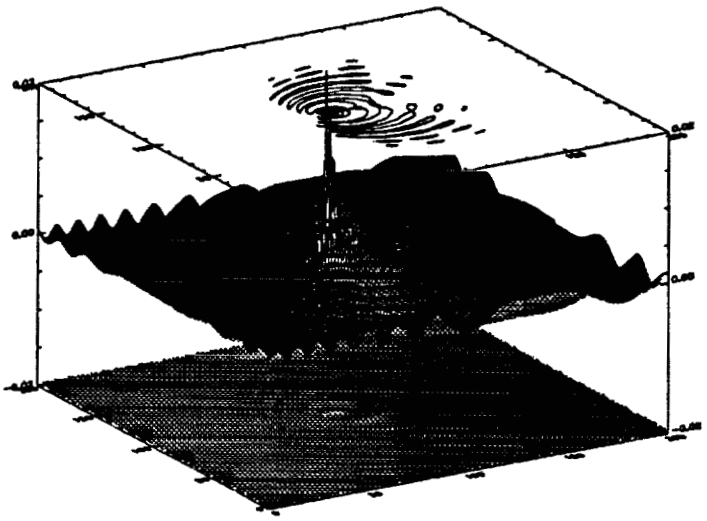

Figure 6: Solution at time step 1440

OVERVIEW OF COMPUTED RESULTS

Christopher K.W. Tam

As a requirement for making a presentation in the workshop, each participant was asked to submit a set of the computed results, in a standard format, to the Scientific Committee. In the pages to follow, a part of the submitted data are shown together with the exact or approximate analytical solutions (except the Category 6 problem). The data requested by the Scientific Committee are quite extensive. Only a selected portion, which is deemed to provide critical tests of accuracy or other important aspects of the computations, are shown below.

Numerical solutions are subjected to many types of errors. The dominant type of error may vary from one class of problems to another. Thus, a numerical scheme, designed specifically for one type of problem, may do poorly when used for solving problems unanticipated by the original developer. Sometimes, compromises are made so that a numerical scheme may work reasonably well for a larger class of problem. Such a scheme may be fine-tuned to perform better if only a smaller restricted class of problems is considered. For the above reasons, the Scientific Committee has left it to the readers to form their own opinion as to the accuracy, limitations, advantages and disadvantages of each method presented in the workshop.

In formulating the benchmark problems, emphasis was placed on spatial resolution. It has not been found feasible to test spatial resolution and temporal resolution simultaneously. It was felt that the CPU time needed for each benchmark problem was too short for meaningful comparison of computation efficiency. As a result, the choice of time step was left open to the participants.

Overall, the workshop has been very successful as evidenced not only by the number of participants but also by the quality of the computation methods presented. Upon reviewing the submitted data and presentations, it is possible to report the following observations.

1. A number of computational schemes presented in the workshop appear to have low dispersion and low dissipation errors (over a distance of 400 mesh points) even for waves with wave lengths of only 6 to 8 mesh spacings. These schemes are obviously suitable for use in CAA applications.

2. High-quality numerical radiation and outflow boundary conditions are presently available. These boundary conditions seem to work well even for cases where the sound waves are incident at an oblique angle to the boundary of the computation domain and in the presence of

a mean outflow with a significant tangential component.

3. Many of the schemes presented have low numerical noise levels. For these schemes, direct computation of acoustic waves and mean flow simultaneously is feasible. This is so even when the amplitude of the acoustic waves is several orders of magnitude smaller than that of the mean flow.

Christopher K.W. Tam
Department of Mathematics
Florida State University
Tallahassee, FL 32306-3027

Category 1, Problem 1

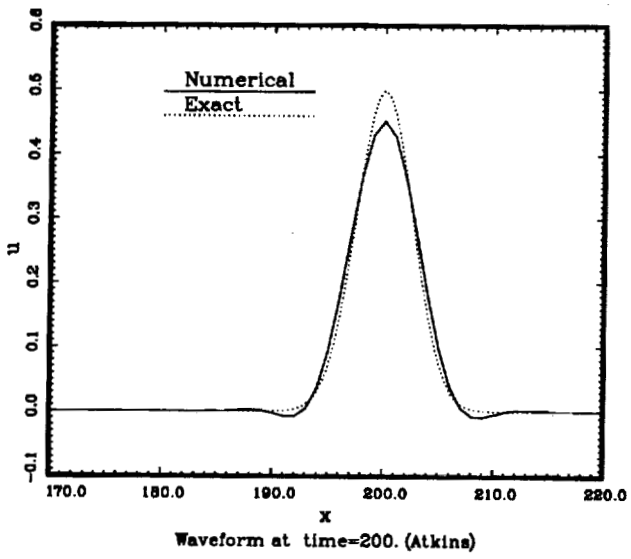

Waveform at time=200. (Atkins)

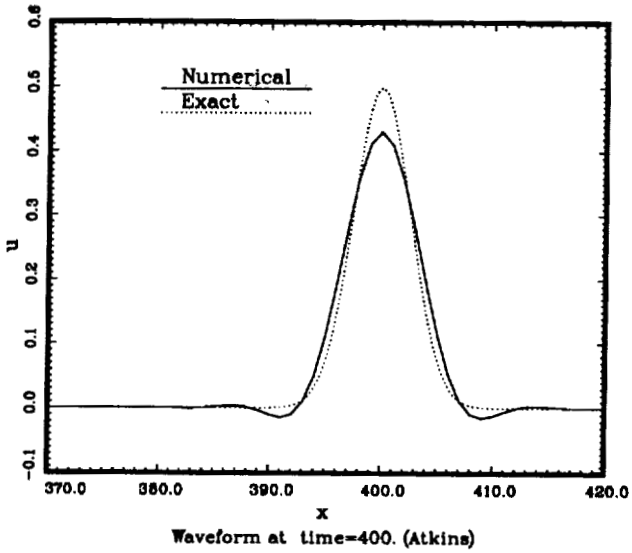

Waveform at time=400. (Atkins)

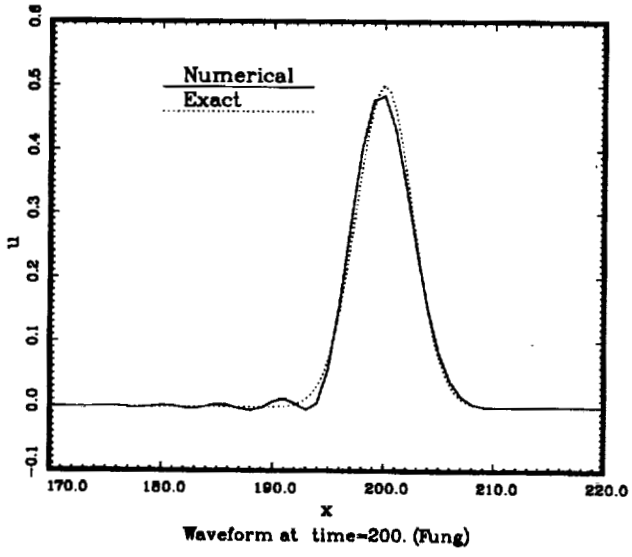

Waveform at time=200. (Fung)

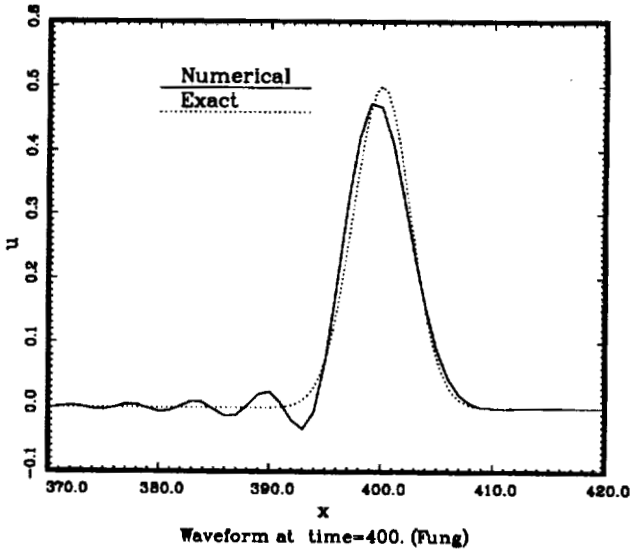

Waveform at time=400. (Fung)

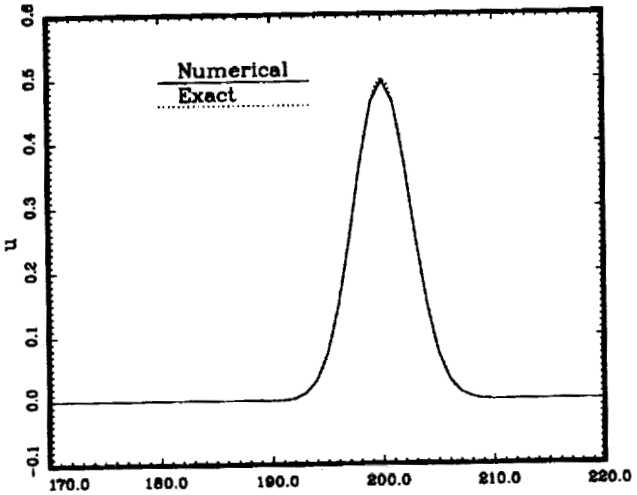

Waveform at time=200. (Hu)

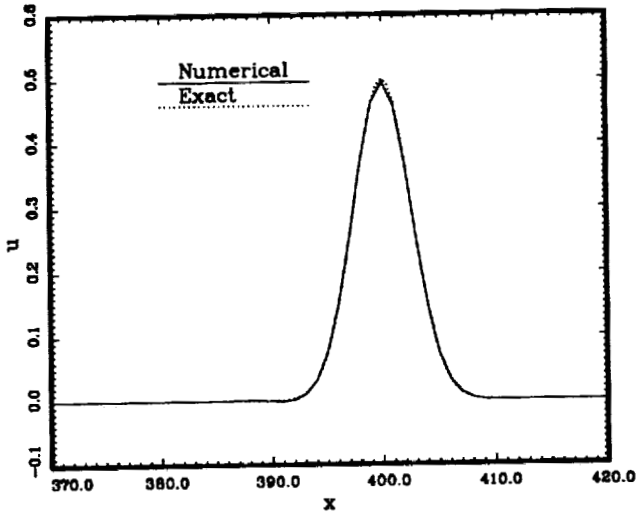

Waveform at time=400. (Hu)

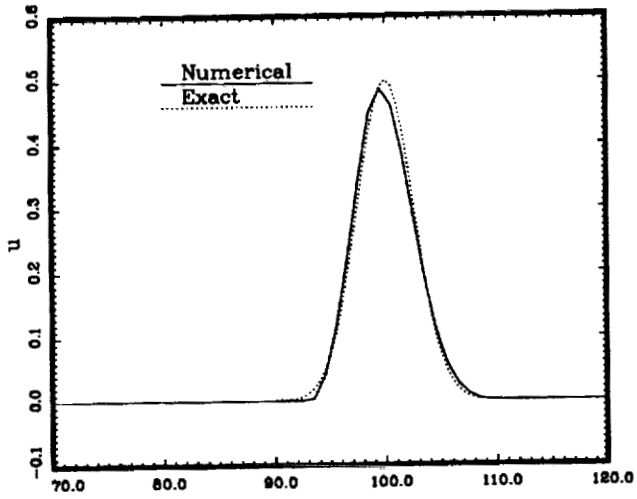

Waveform at time=100. (Hunyh -ord2)

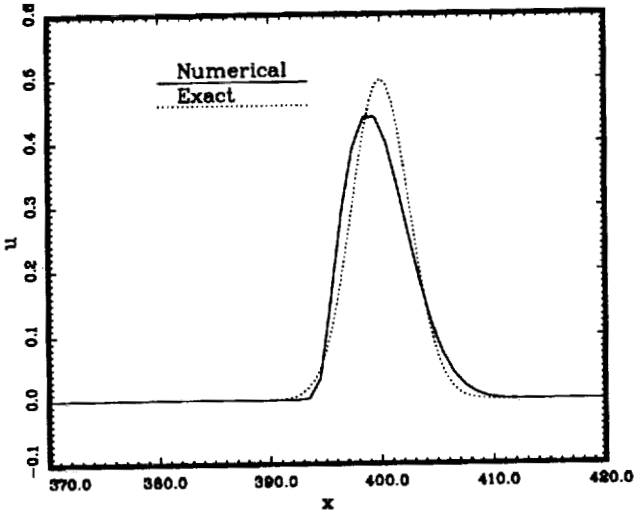

Waveform at time=400. (Hunyh -ord2)

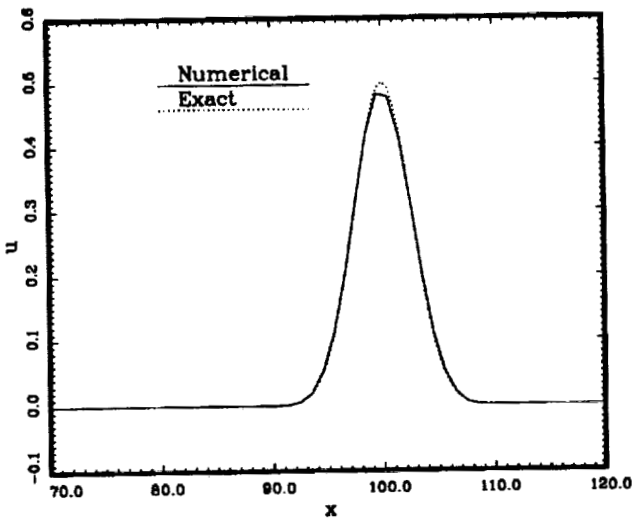

Waveform at time=100. (Hunyh -ord3)

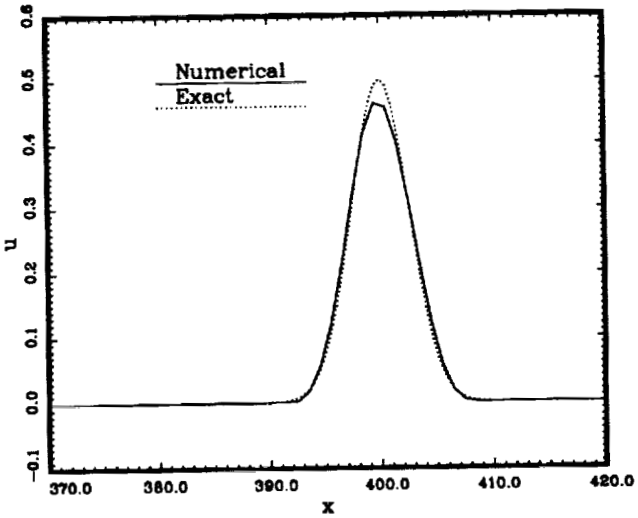

Waveform at time=400. (Hunyh -ord3)

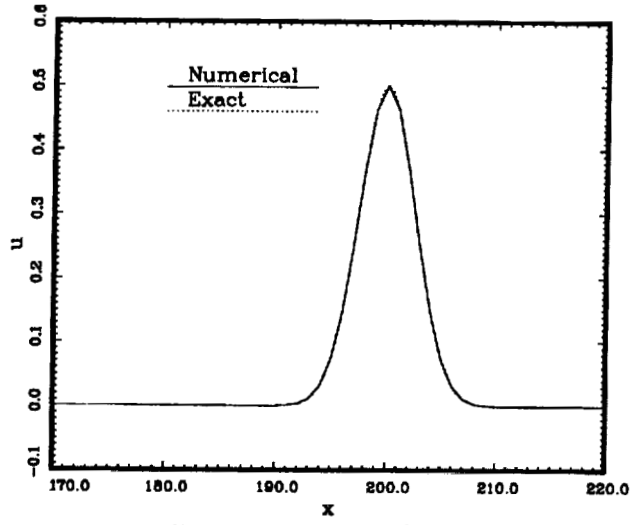

Waveform at time=200. (Kopriva)

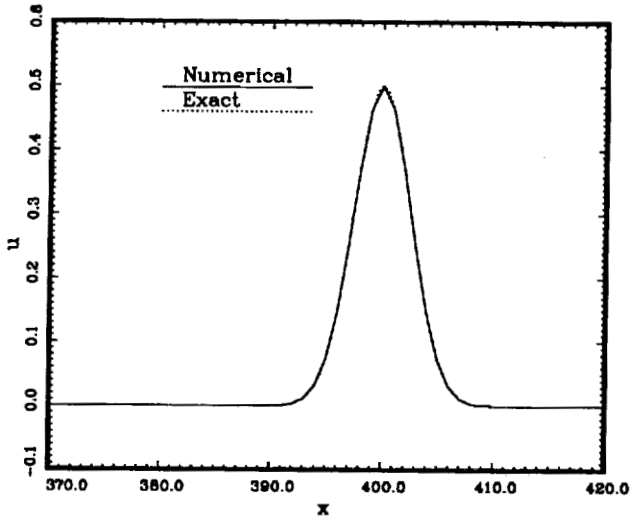

Waveform at time=400. (Kopriva)

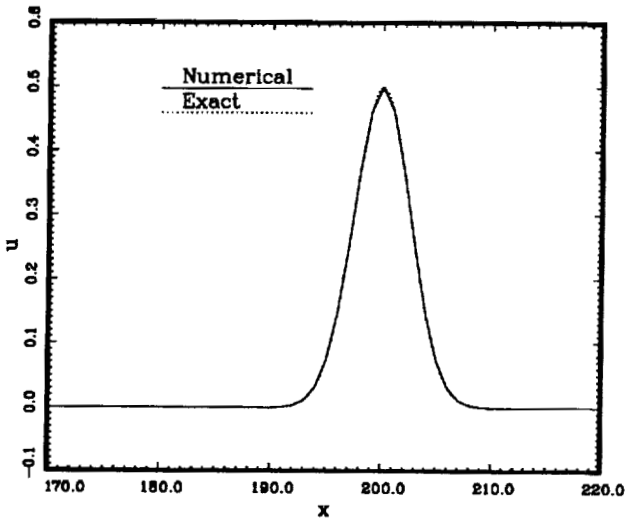

Waveform at time=200. (Lafon)

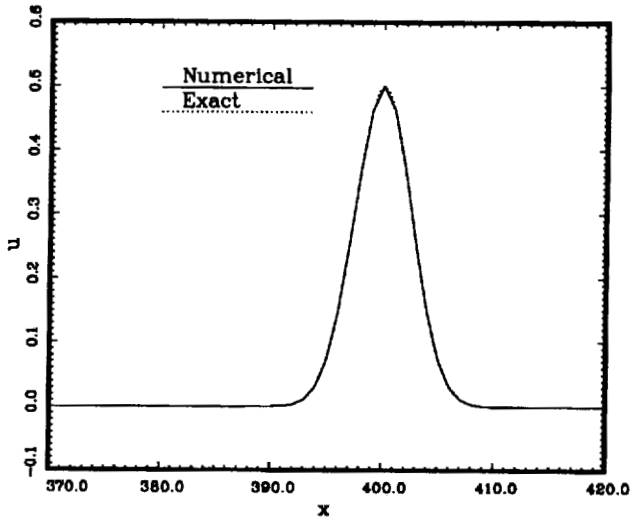

Waveform at time=400. (Lafon)

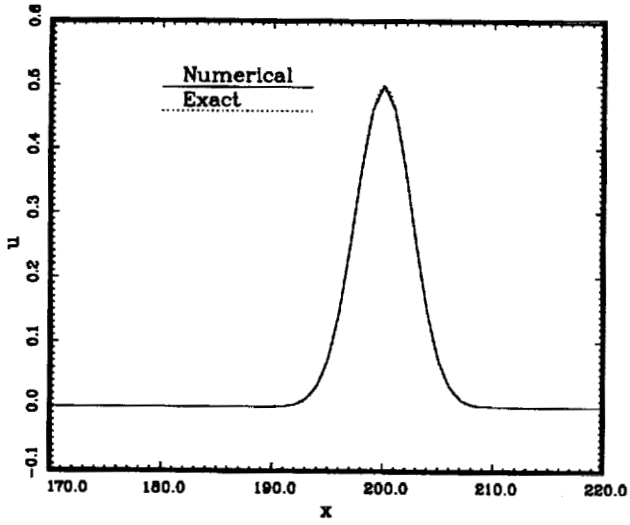

Waveform at time=200. (Sparrow)

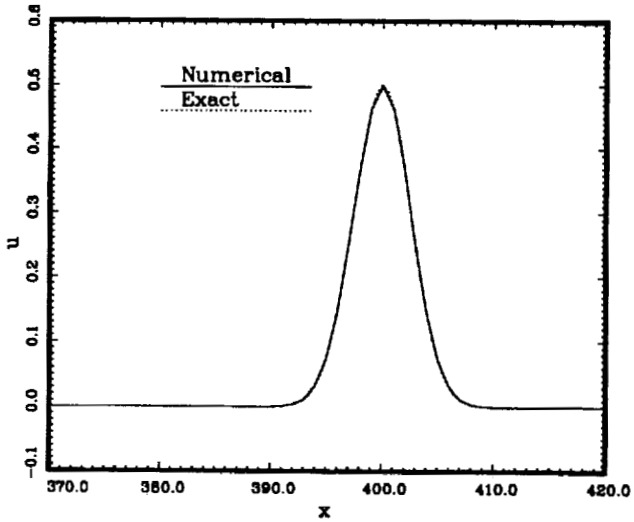

Waveform at time=400. (Sparrow)

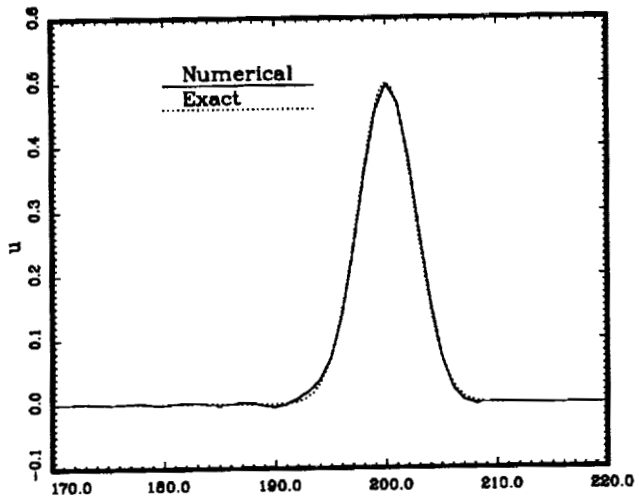

Waveform at time=200. (Tam)

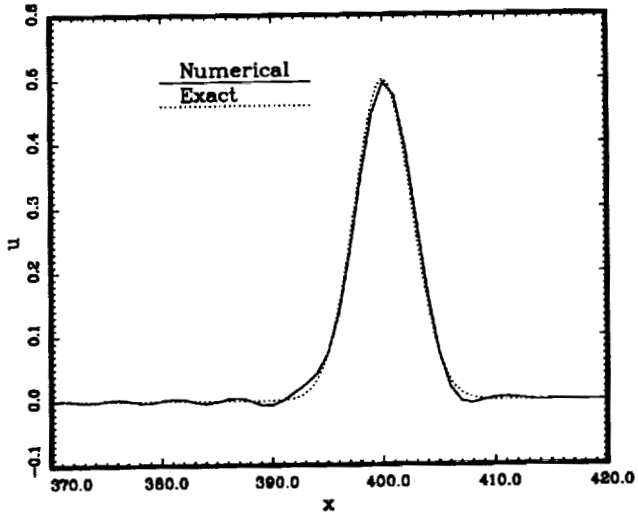

Waveform at time=400. (Tam)

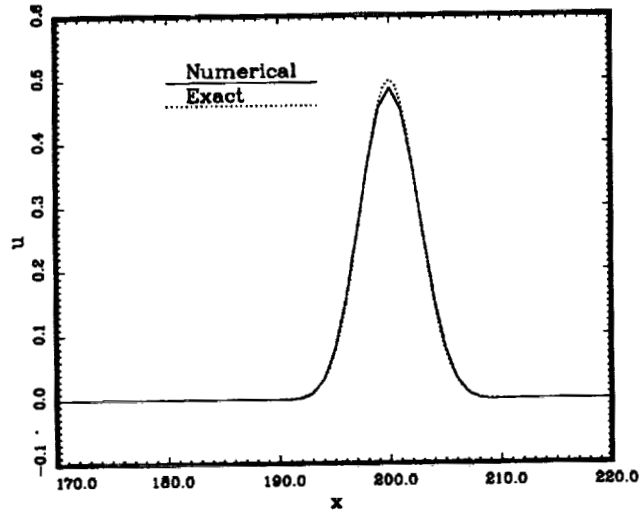

Waveform at time=200. (Tang)

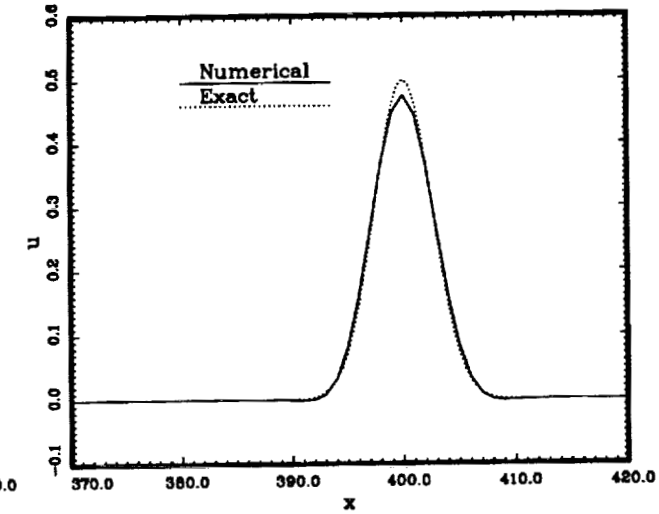

Waveform at time=400. (Tang)

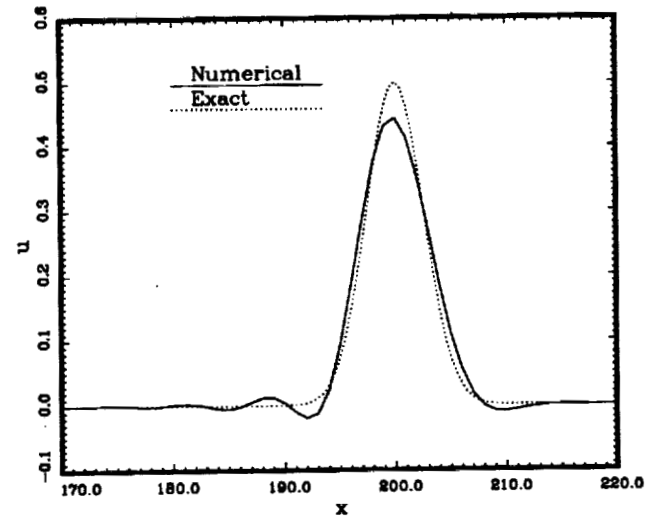

Waveform at time=200. (Viswanathan)

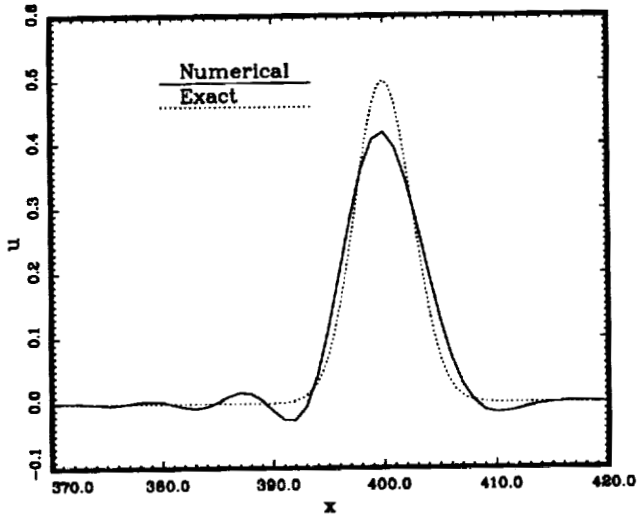

Waveform at time=400. (Viswanathan)

Category 1, Problem 2

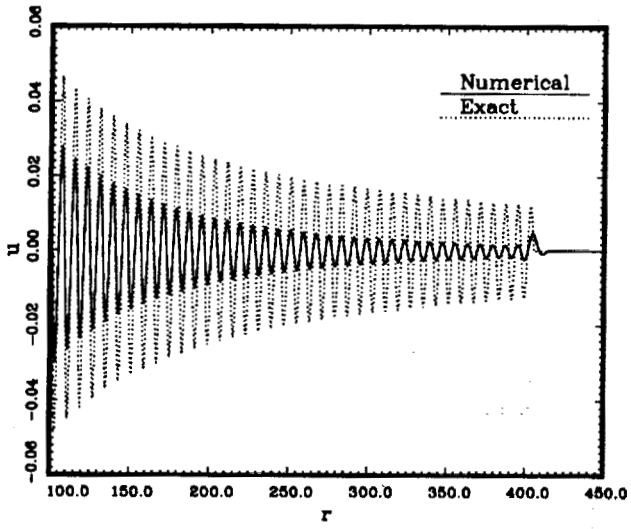

Spatial distribution of waves at time=400, $\omega = \pi/4$. (Atkins)

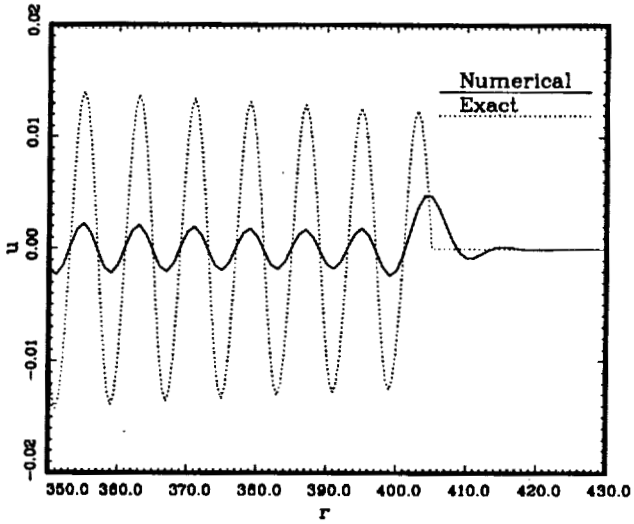

Spatial distribution of waves at time=400, $\omega = \pi/4$. (Atkins)

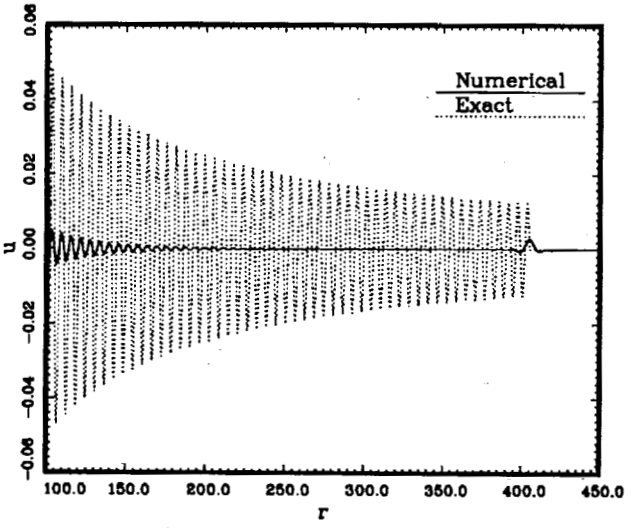

Spatial distribution of waves at time=400, $\omega = \pi/3$. (Atkins)

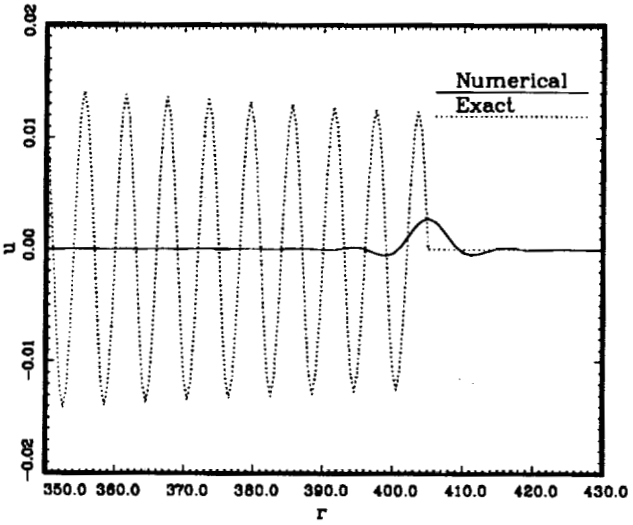

Spatial distribution of waves at time=400, $\omega = \pi/3$. (Atkins)

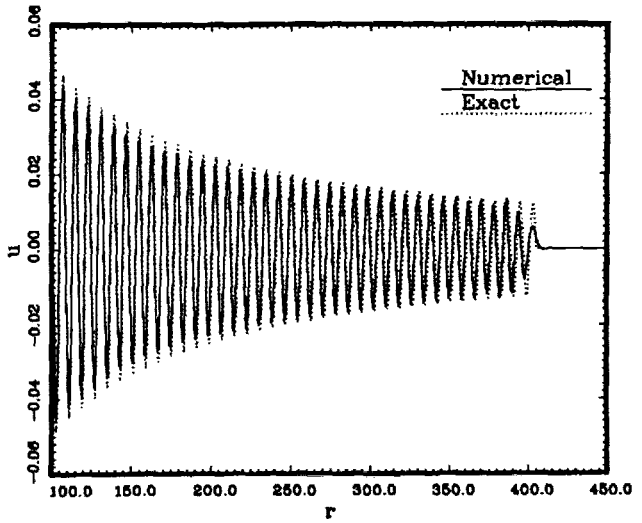

Spatial distribution of waves at time=400, $\omega = \pi/4$. (Fung)

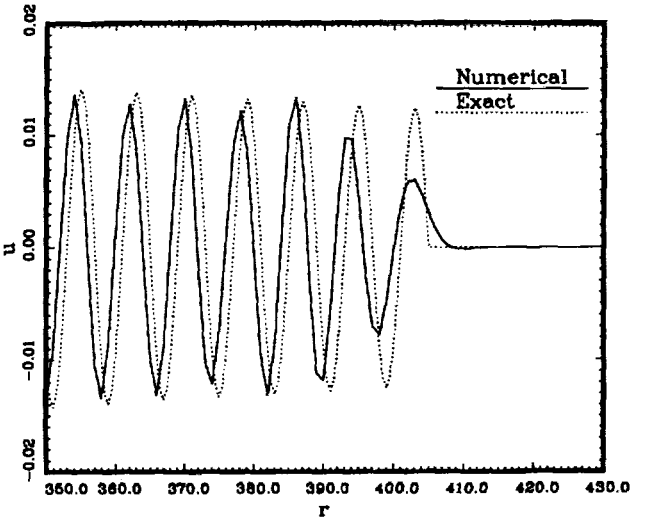

Spatial distribution of waves at time=400, $\omega = \pi/4$. (Fung)

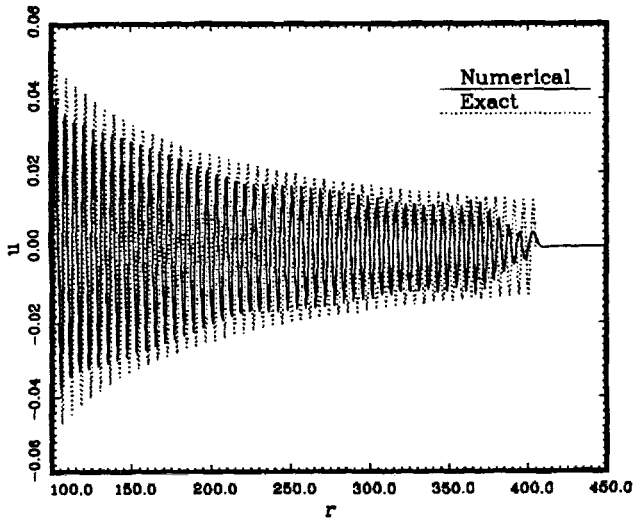

Spatial distribution of waves at time=400, $\omega = \pi/3$. (Fung)

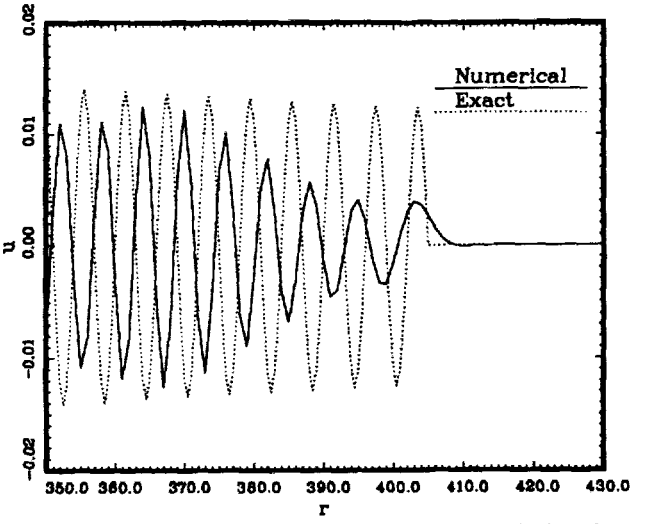

Spatial distribution of waves at time=400, $\omega = \pi/3$. (Fung)

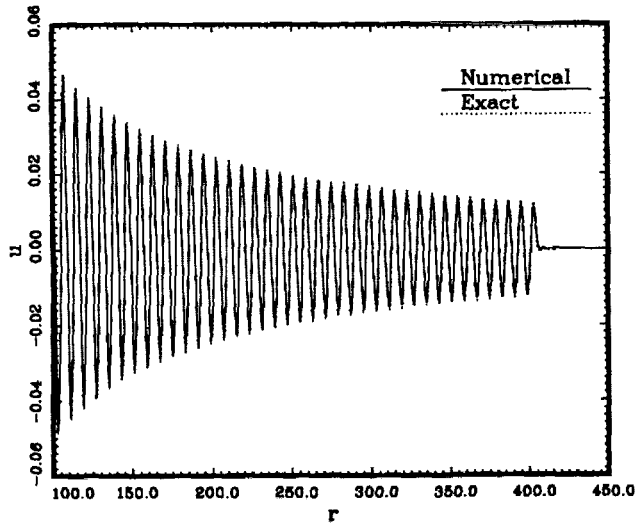

Spatial distribution of waves at time=400, $\omega = \pi/4$. (Hu)

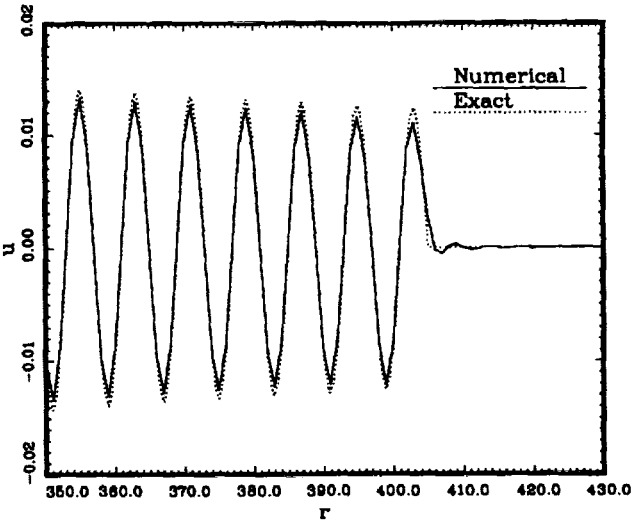

Spatial distribution of waves at time=400, $\omega = \pi/4$. (Hu)

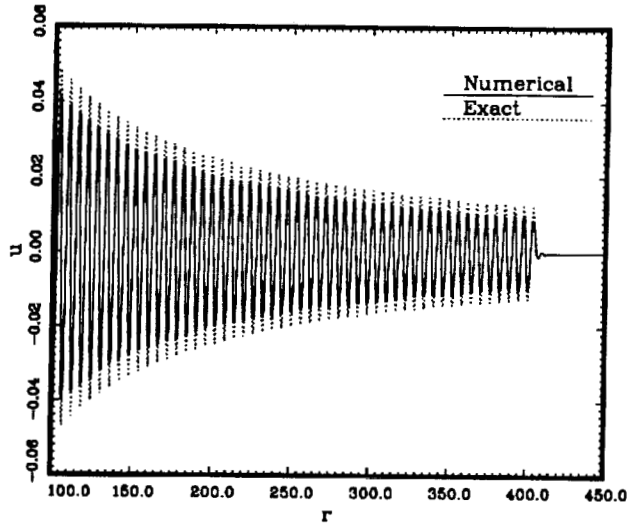

Spatial distribution of waves at time=400, $\omega = \pi/3$. (Hu)

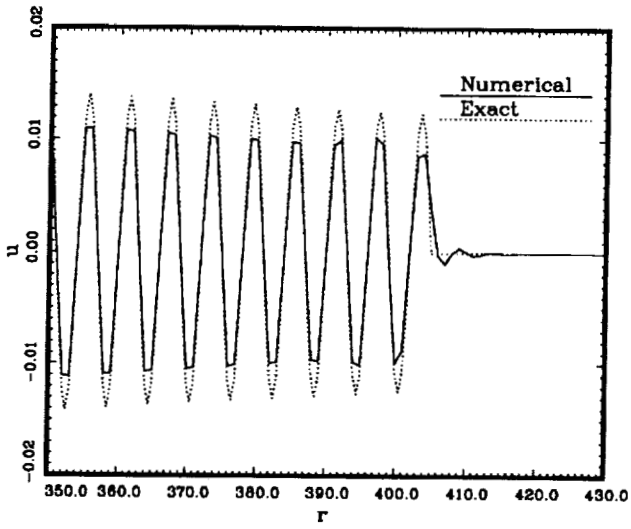

Spatial distribution of waves at time=400, $\omega = \pi/3$. (Hu)

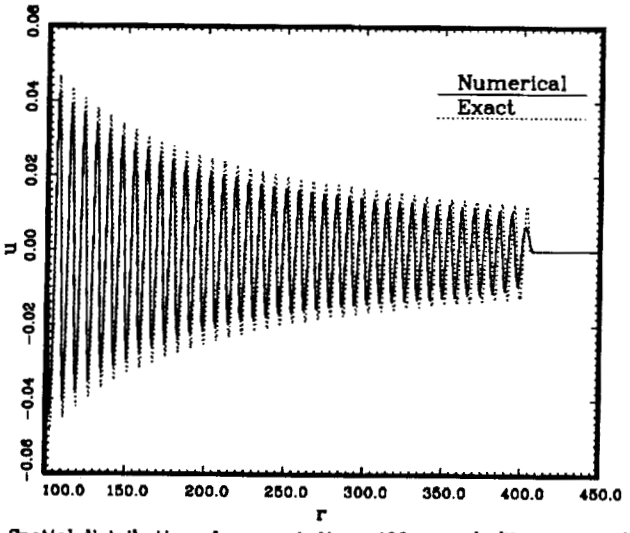

Spatial distribution of waves at time=400, $\omega = \pi/4$. (Hunyh −ord2)

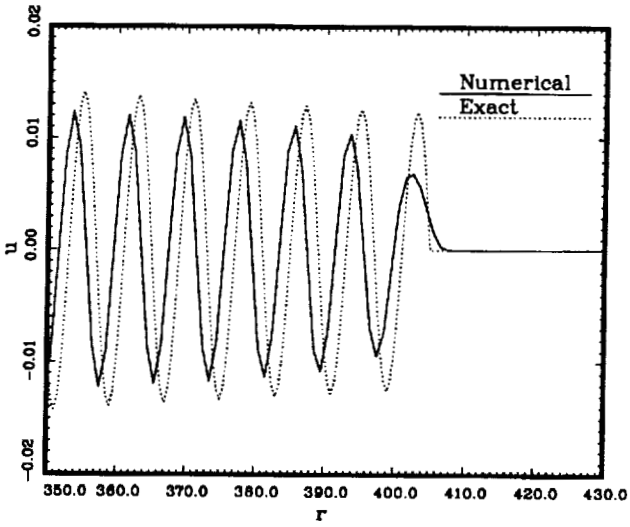

Spatial distribution of waves at time=400, $\omega = \pi/4$. (Hunyh −ord2)

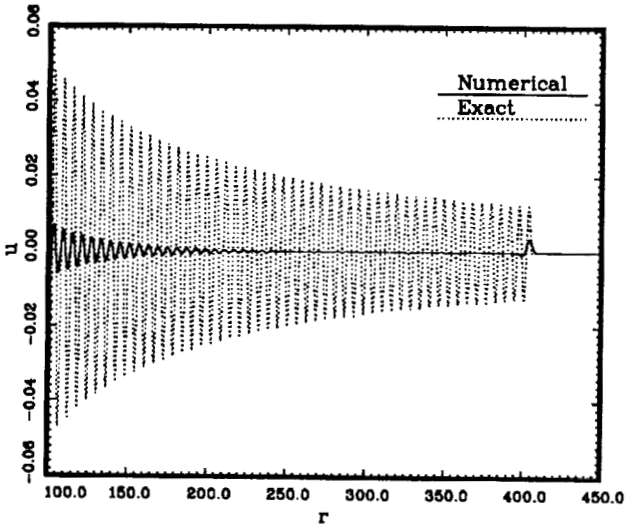

Spatial distribution of waves at time=400, $\omega = \pi/3$. (Hunyh −ord2)

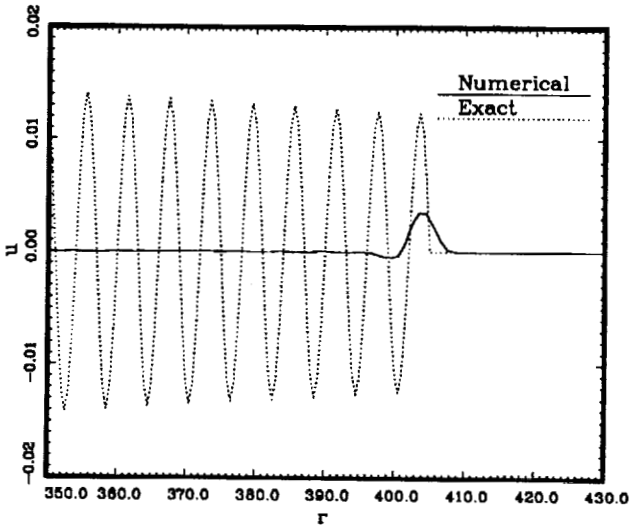

Spatial distribution of waves at time=400, $\omega = \pi/3$. (Hunyh −ord2)

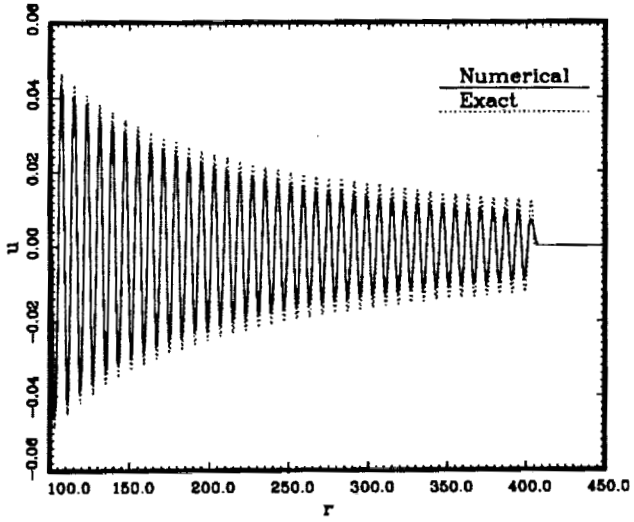

Spatial distribution of waves at time=400, $\omega = \pi/4$. (Hunyh −ord3)

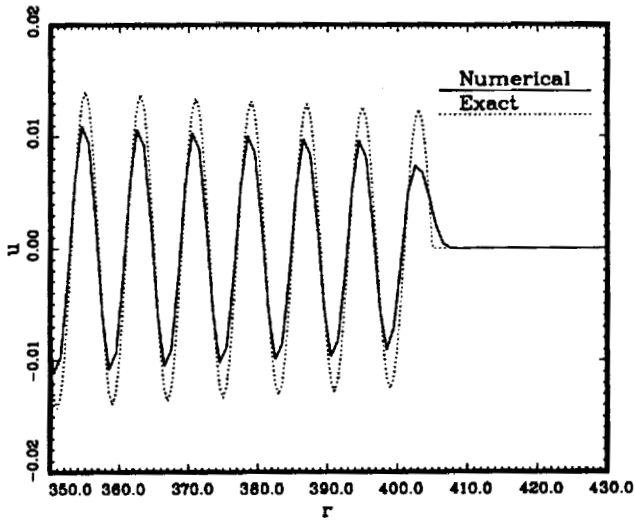

Spatial distribution of waves at time=400, $\omega = \pi/4$. (Hunyh −ord3)

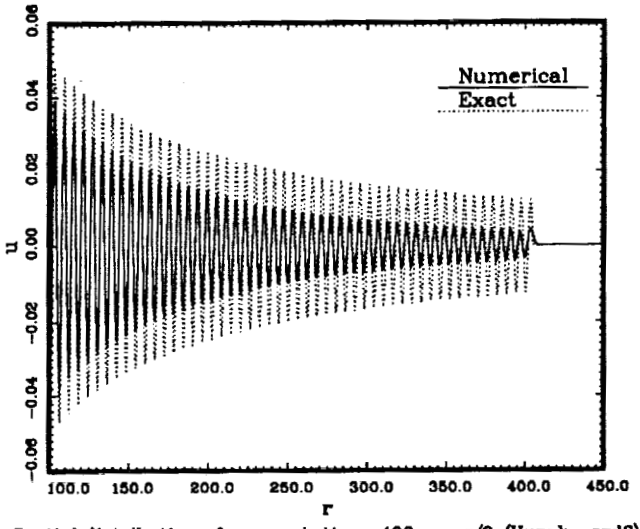

Spatial distribution of waves at time=400, $\omega = \pi/3$. (Hunyh −ord3)

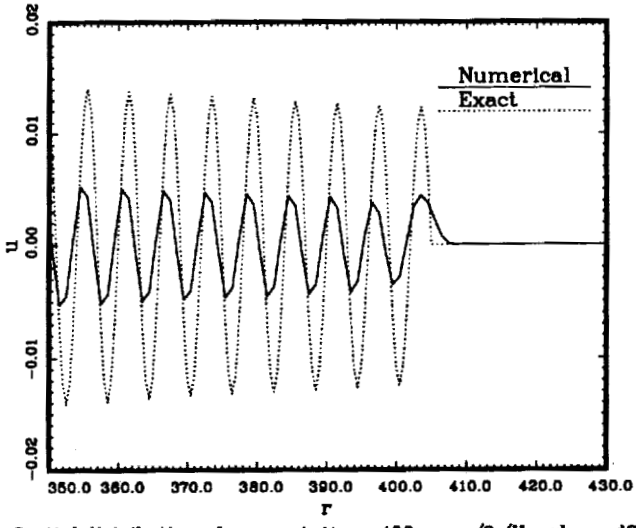

Spatial distribution of waves at time=400, $\omega = \pi/3$. (Hunyh −ord3)

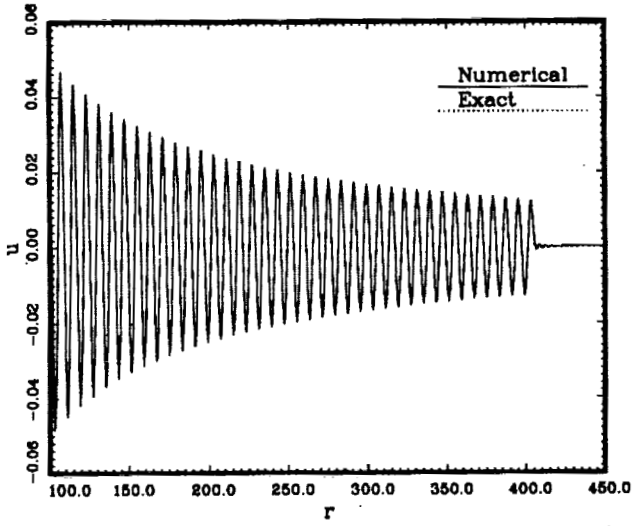

Spatial distribution of waves at time=400, $\omega = \pi/4$. (Kopriva)

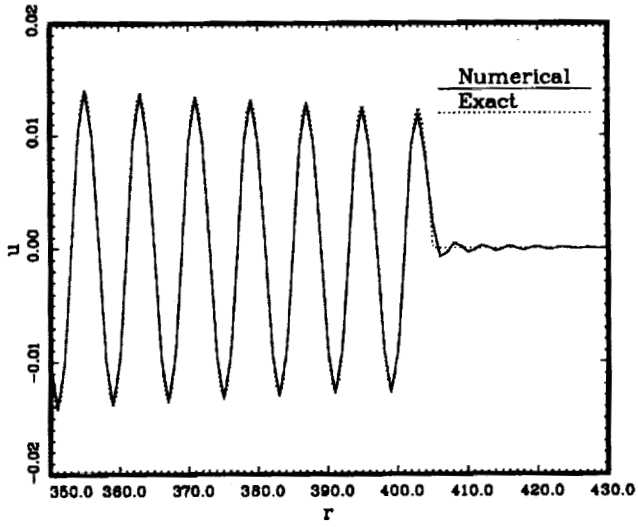

Spatial distribution of waves at time=400, $\omega = \pi/4$. (Kopriva)

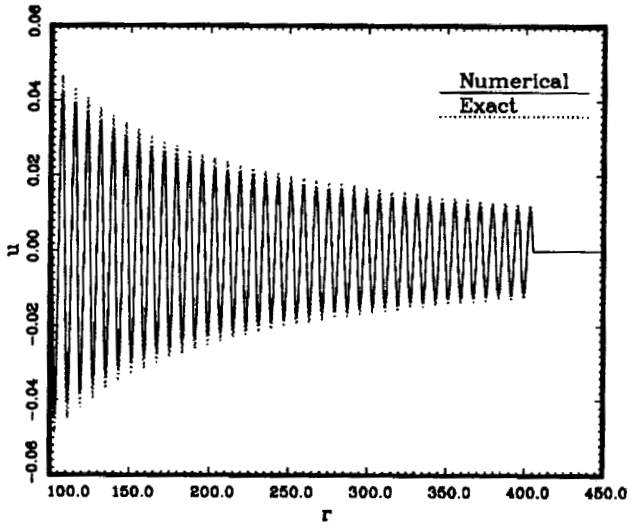

Spatial distribution of waves at time=400, $\omega = \pi/4$. (Lafon)

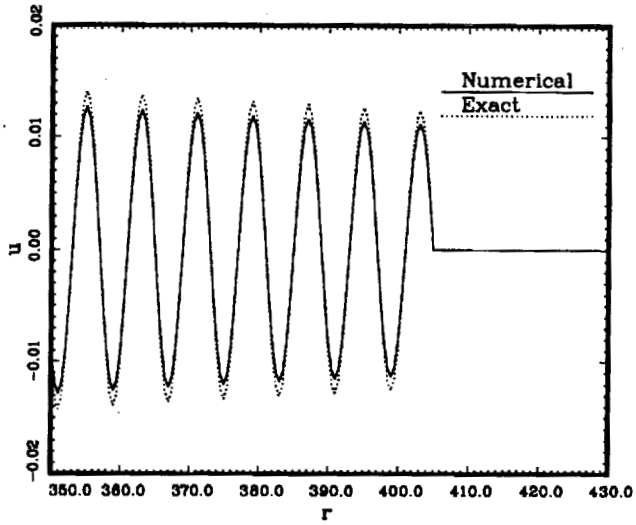

Spatial distribution of waves at time=400, $\omega = \pi/4$. (Lafon)

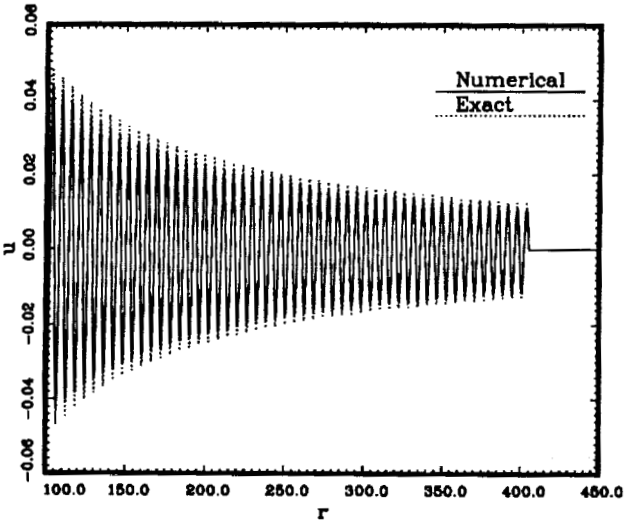

Spatial distribution of waves at time=400, $\omega = \pi/3$. (Lafon)

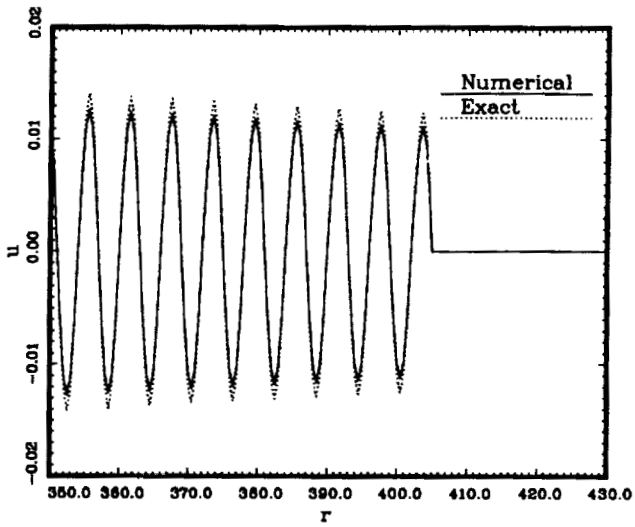

Spatial distribution of waves at time=400, $\omega = \pi/3$. (Lafon)

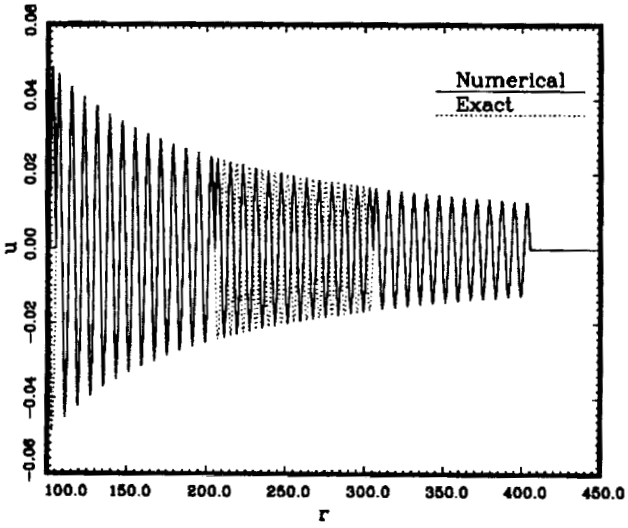

Spatial distribution of waves at time=400, $\omega = \pi/4$. (Sparrow)

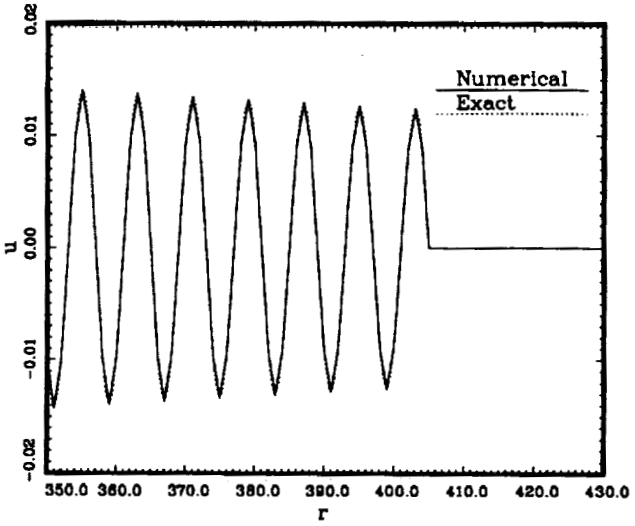

Spatial distribution of waves at time=400, $\omega = \pi/4$. (Sparrow)

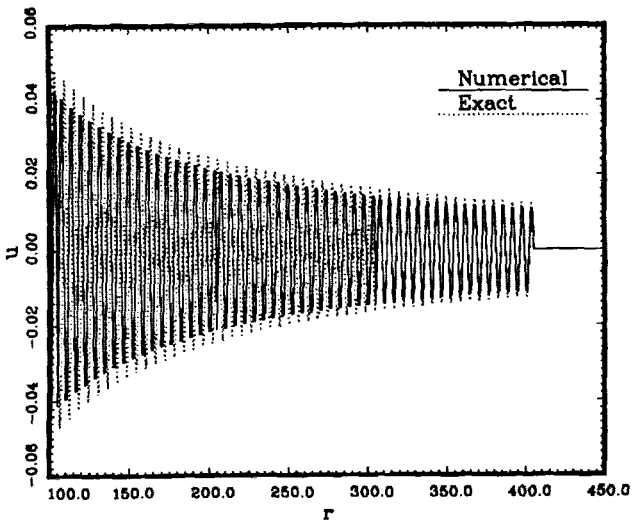

Spatial distribution of waves at time=400, $\omega = \pi/3$. (Sparrow)

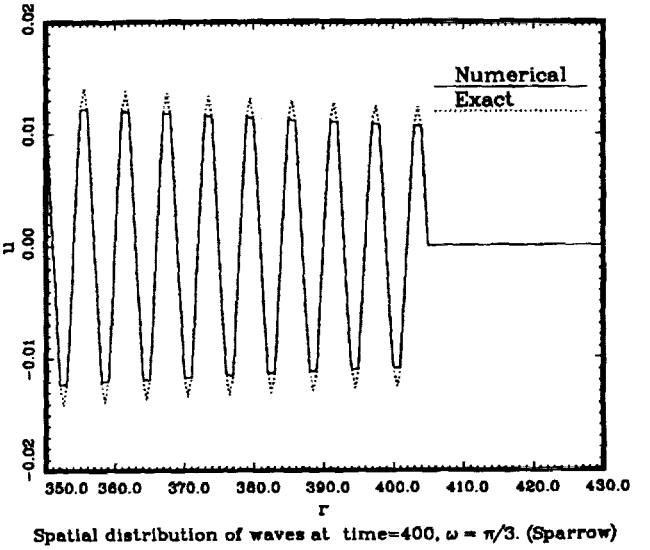

Spatial distribution of waves at time=400, $\omega = \pi/3$. (Sparrow)

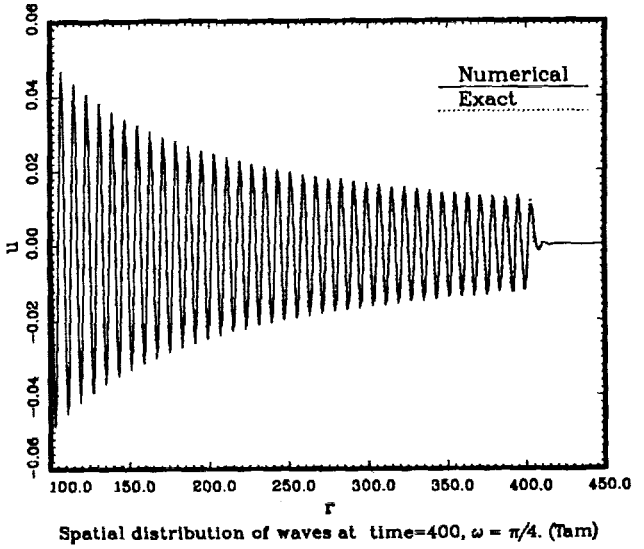

Spatial distribution of waves at time=400, $\omega = \pi/4$. (Tam)

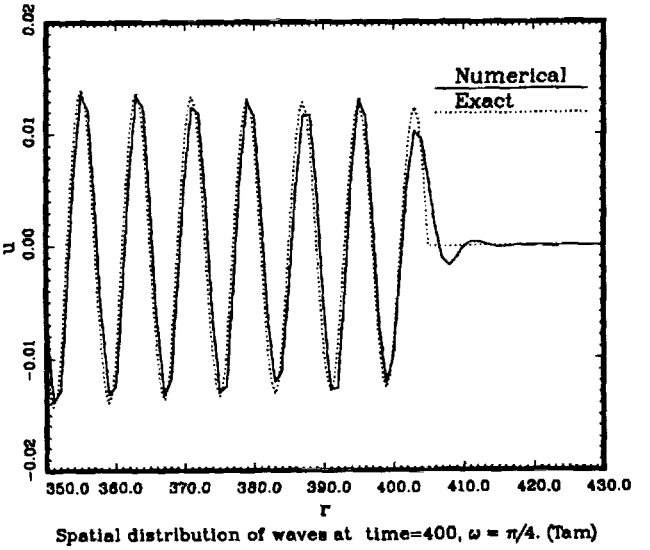

Spatial distribution of waves at time=400, $\omega = \pi/4$. (Tam)

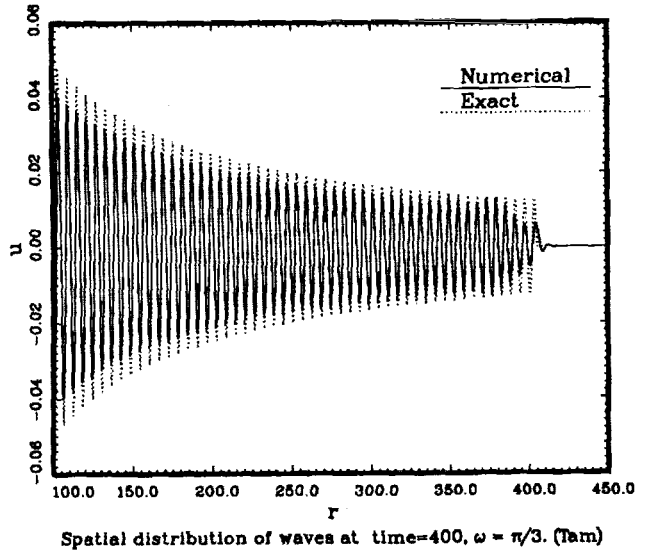

Spatial distribution of waves at time=400, $\omega = \pi/3$. (Tam)

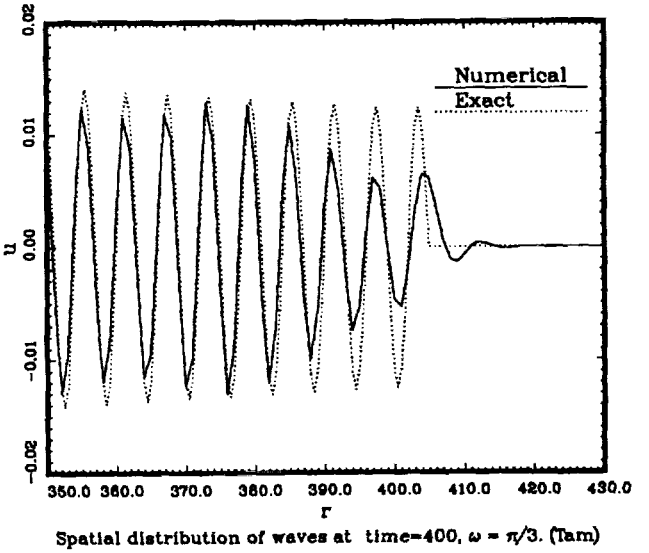

Spatial distribution of waves at time=400, $\omega = \pi/3$. (Tam)

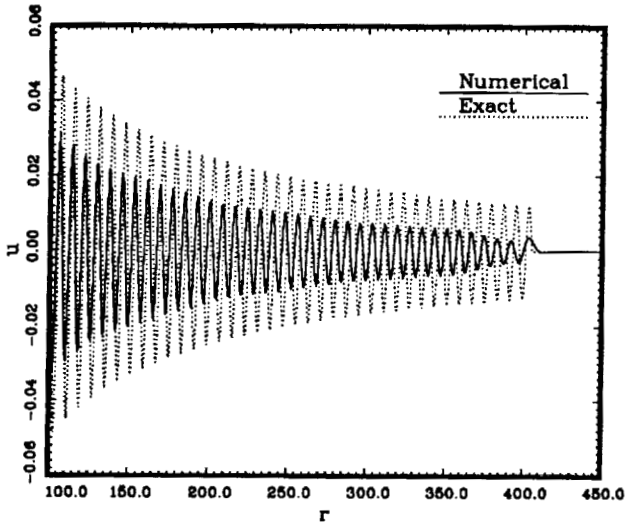

Spatial distribution of waves at time=400, $\omega = \pi/4$. (Viswanthan)

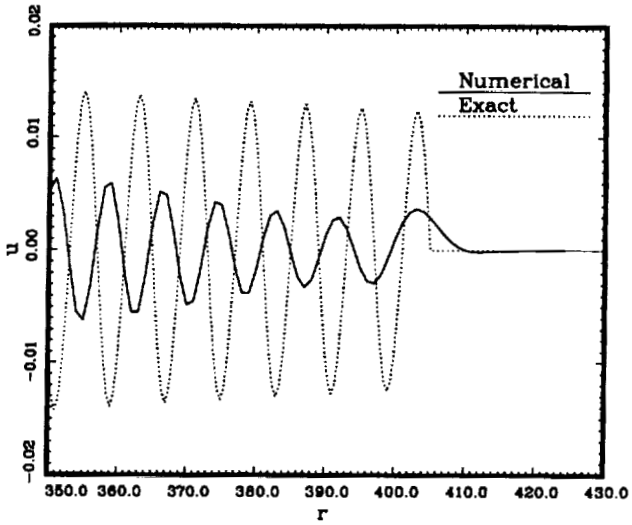

Spatial distribution of waves at time=400, $\omega = \pi/4$. (Viswanthan)

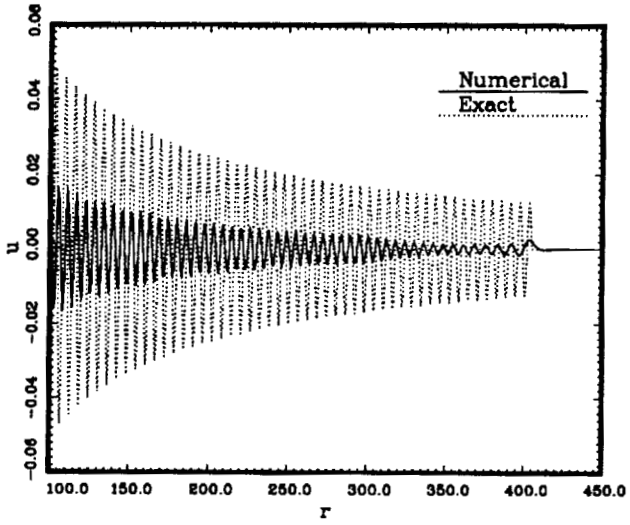

Spatial distribution of waves at time=400, $\omega = \pi/3$. (Viswanthan)

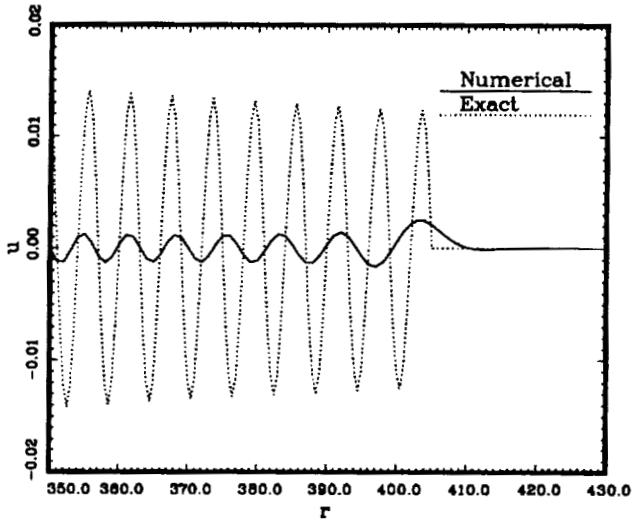

Spatial distribution of waves at time=400, $\omega = \pi/3$. (Viswanthan)

Category 2, Problem 1

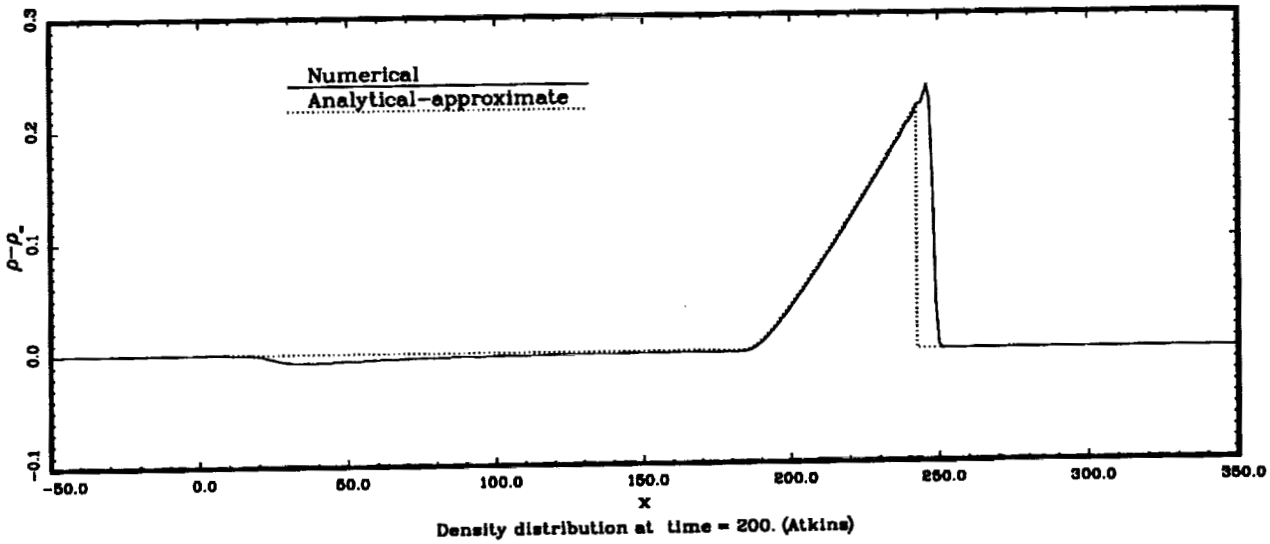

Density distribution at time = 200. (Atkins)

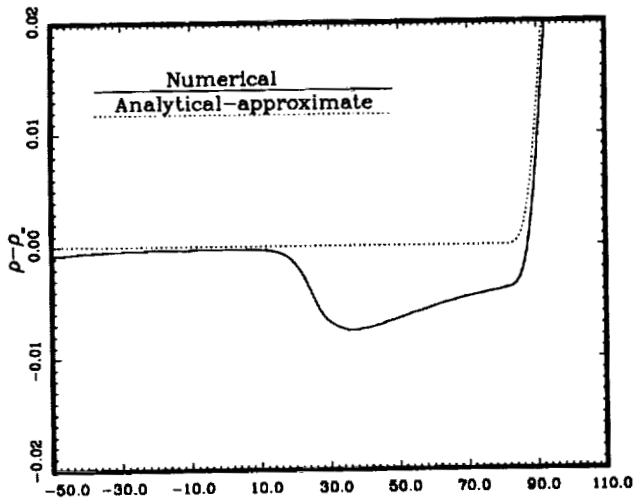

Density distribution at time = 100. (Atkins)

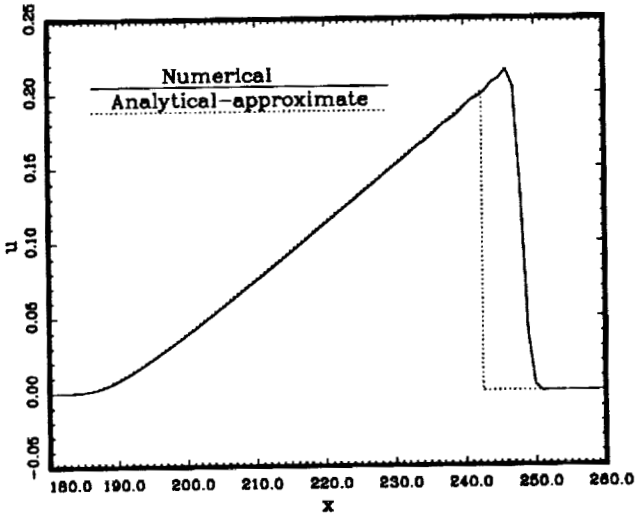

Velocity distribution at time = 200. (Atkins)

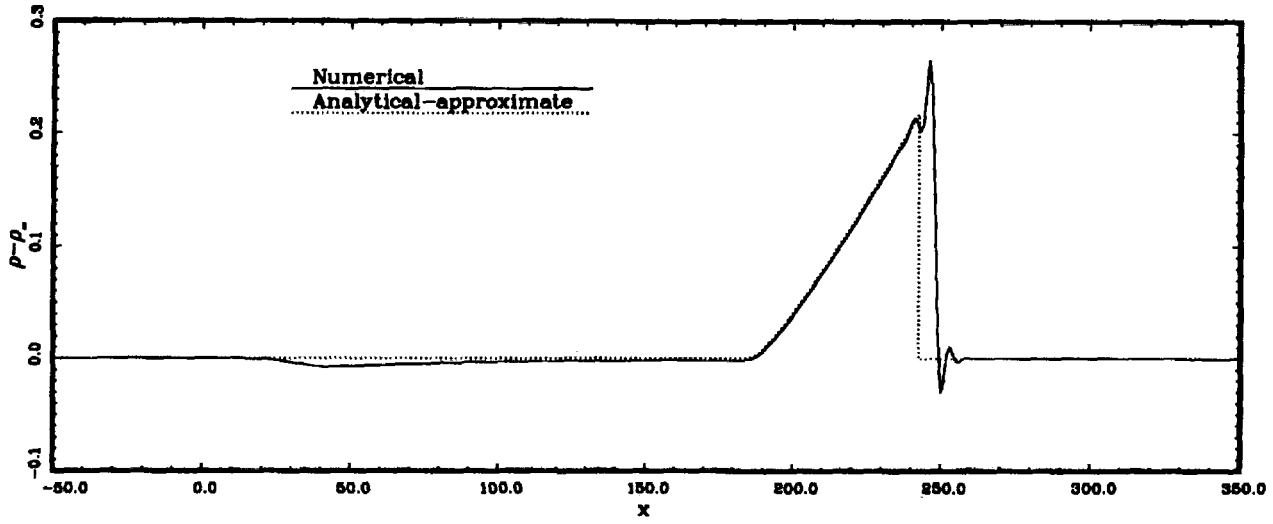

Density distribution at time = 200. (Chyczewski-a)

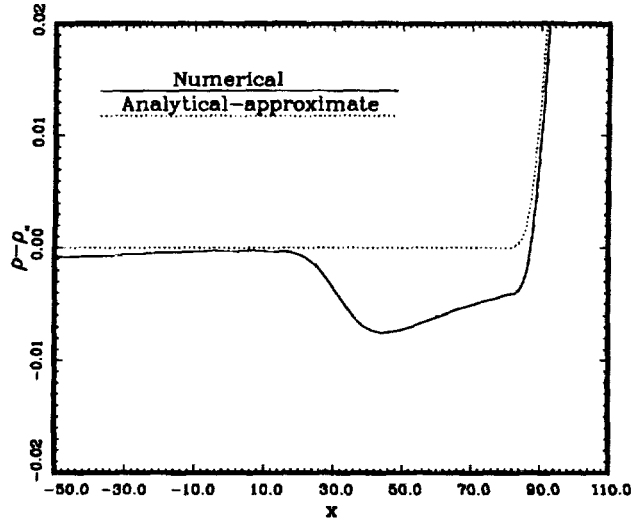

Density distribution at time = 100. (Chyczewski-a)

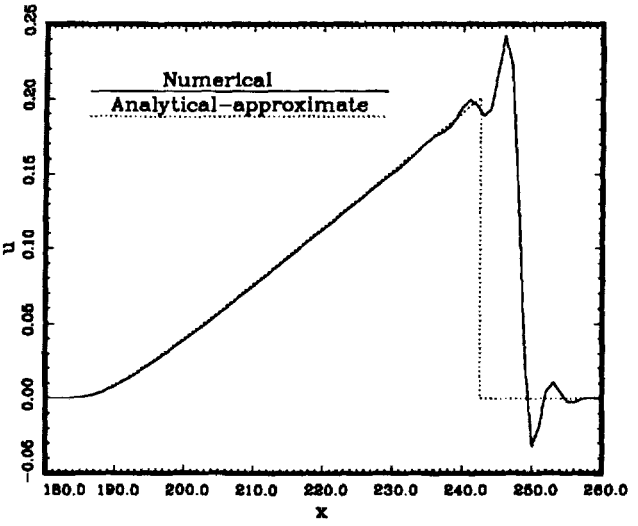

Velocity distribution at time = 200. (Chyczewski-a)

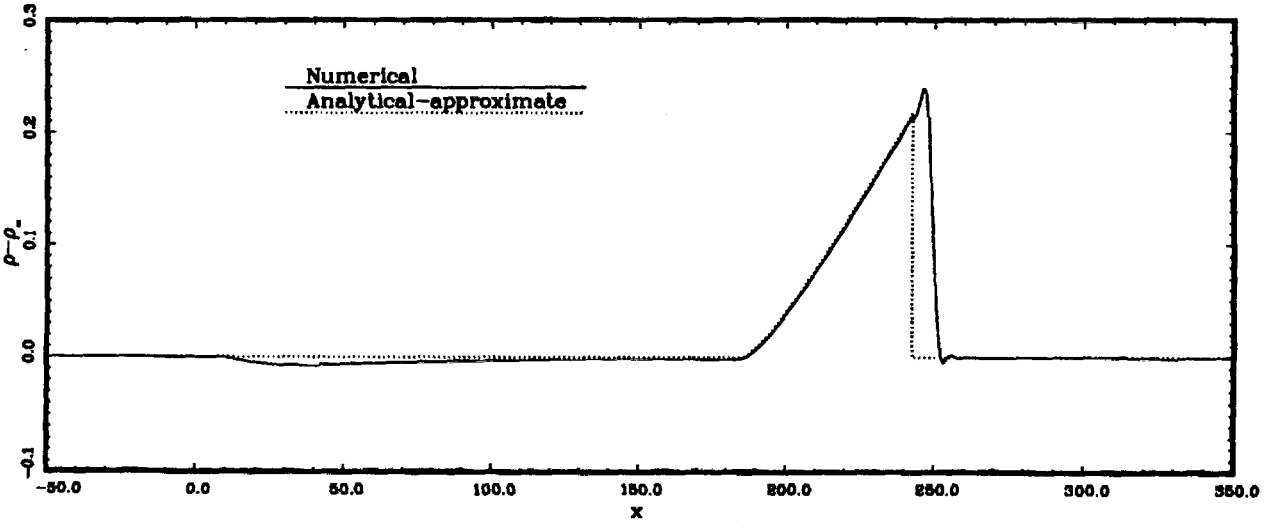

Density distribution at time = 200. (Chyczewski-b)

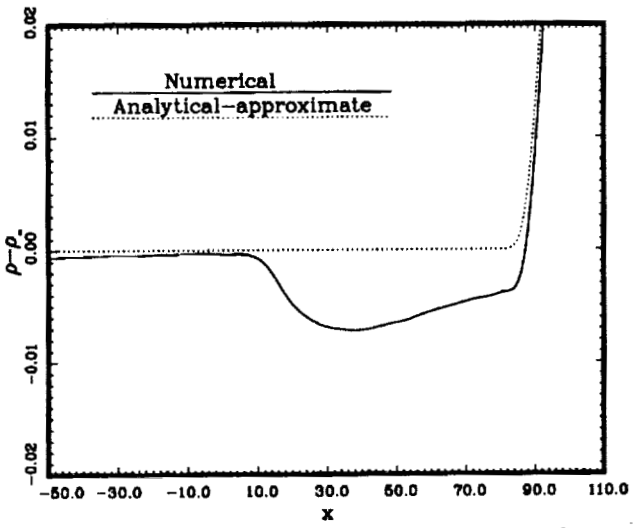

Density distribution at time = 100. (Chyczewski–b)

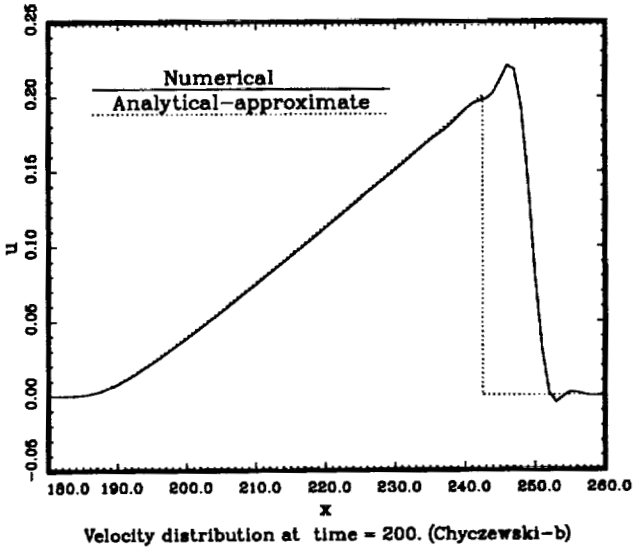

Velocity distribution at time = 200. (Chyczewski–b)

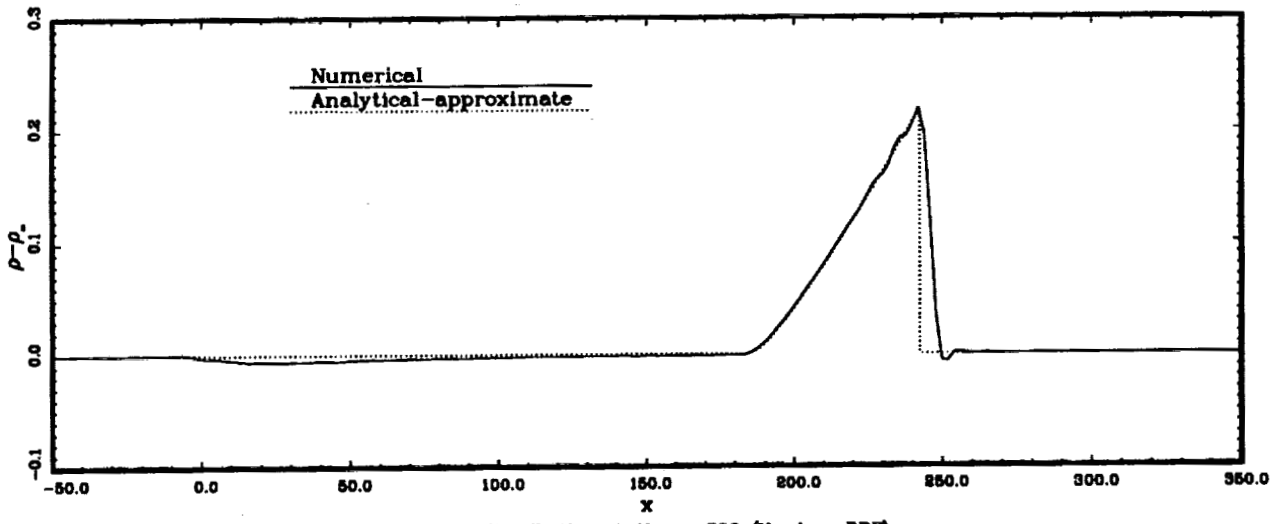

Density distribution at time = 200. (Hayder –DRP)

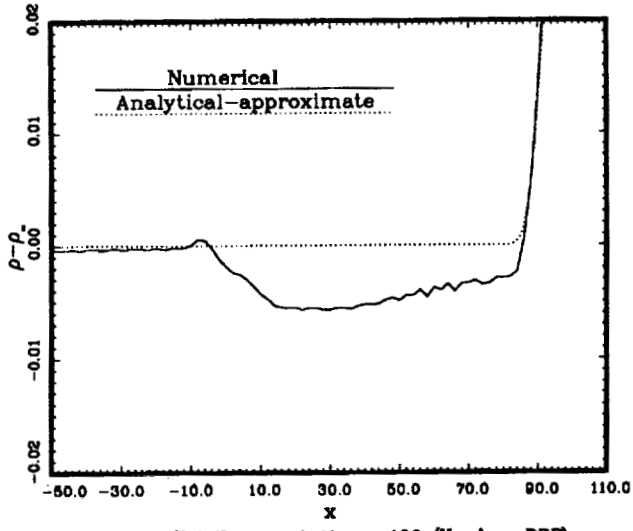

Density distribution at time = 100. (Hayder –DRP)

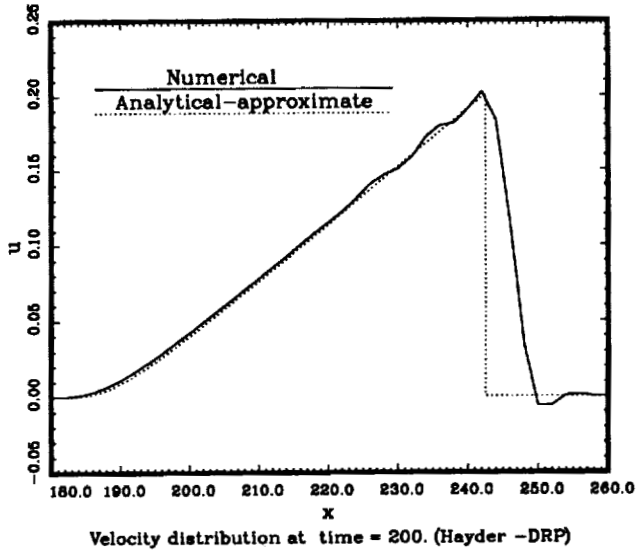

Velocity distribution at time = 200. (Hayder –DRP)

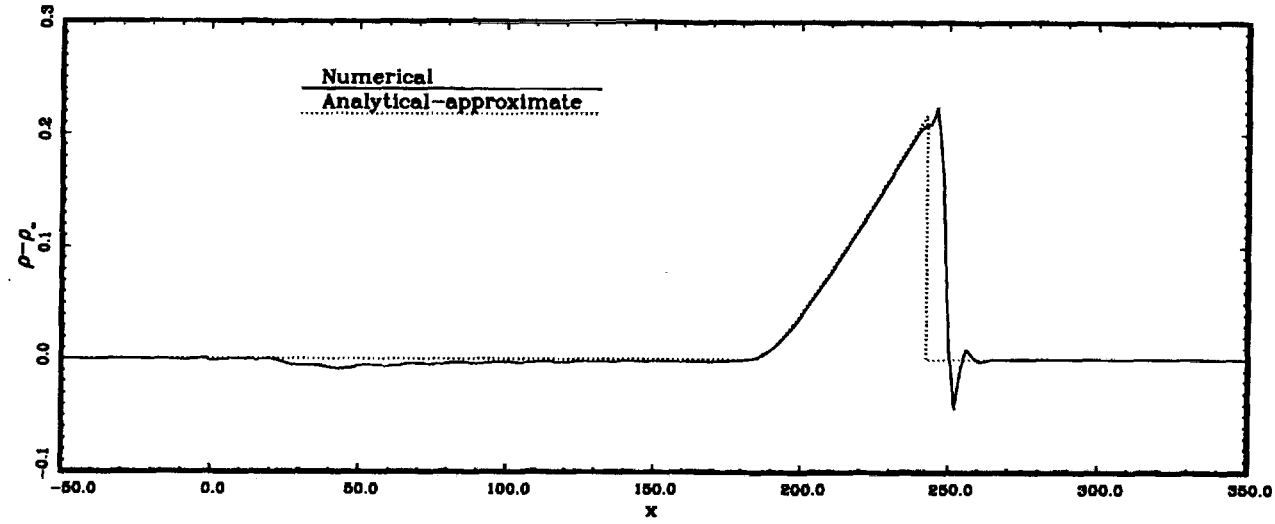

Density distribution at time = 200. (Hayder -MacCormack 2-4)

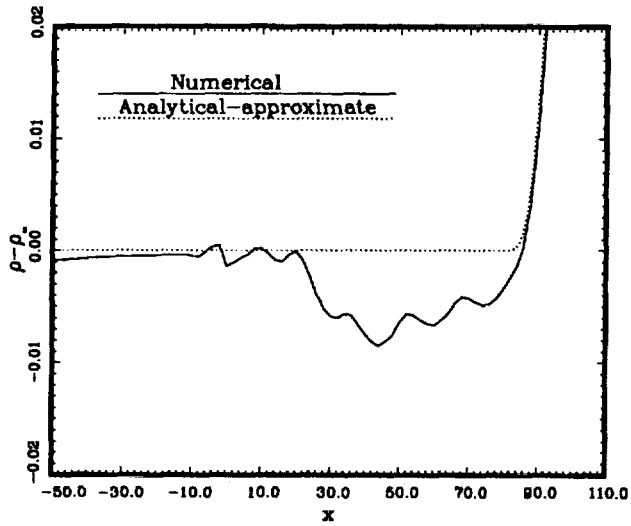

Density distribution at time = 100. (Hayder -MacCormack 2-4)

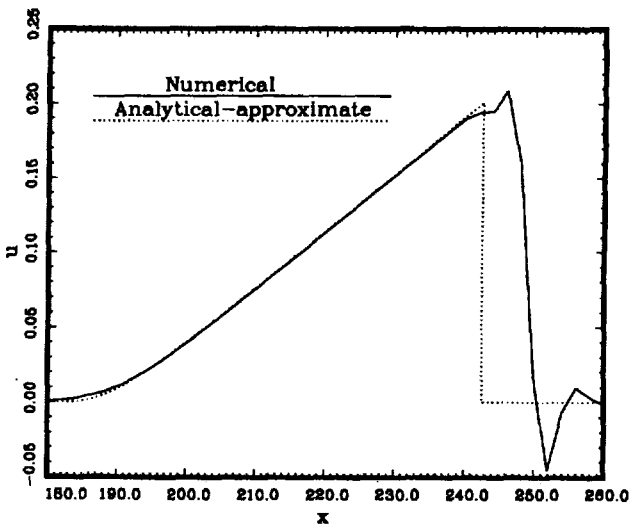

Velocity distribution at time = 200. (Hayder -MacCormack 2-4)

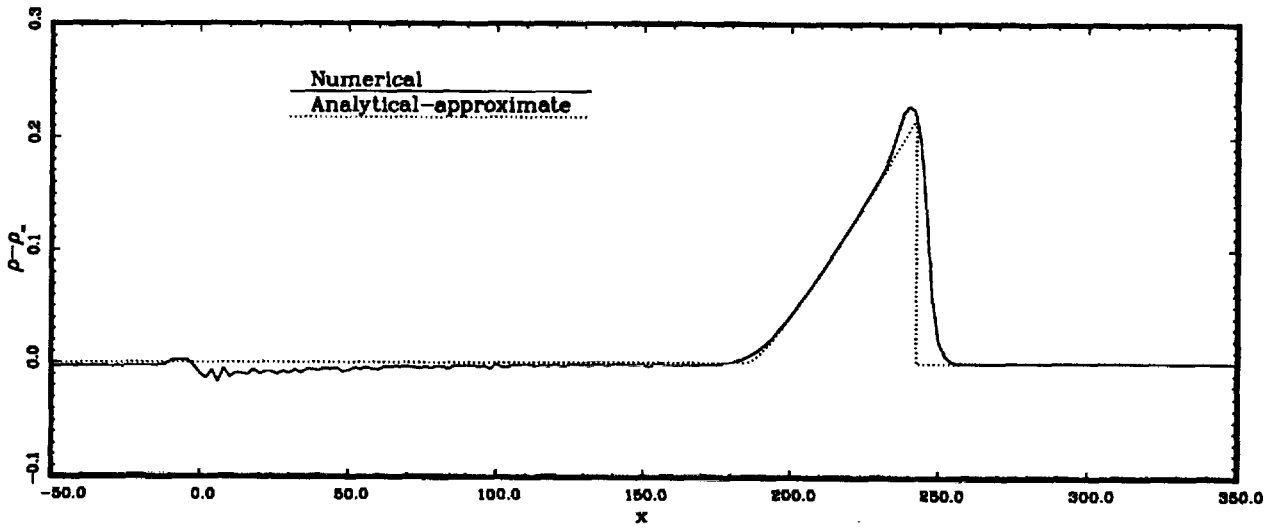

Density distribution at time = 200. (Hayder -ENO-ROE)

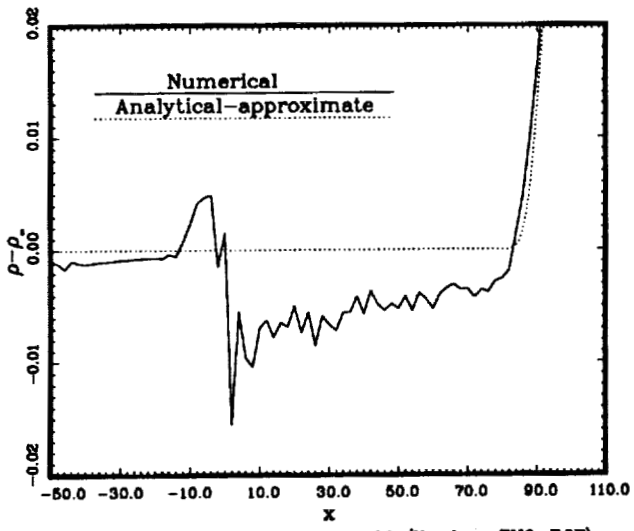

Density distribution at time = 100. (Hayder –ENO–ROE)

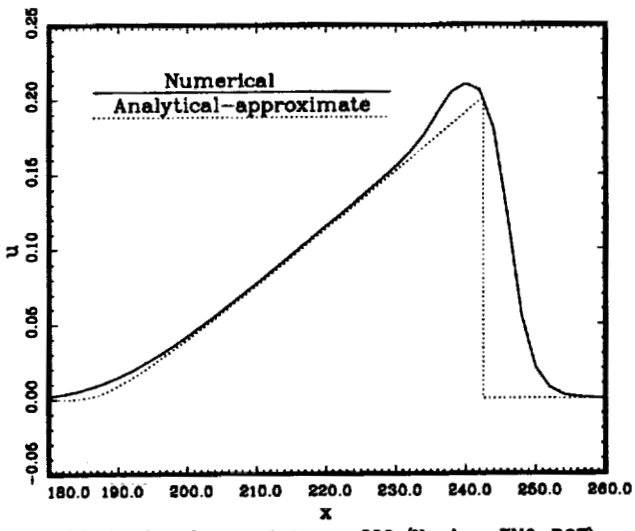

Velocity distribution at time = 200. (Hayder –ENO–ROE)

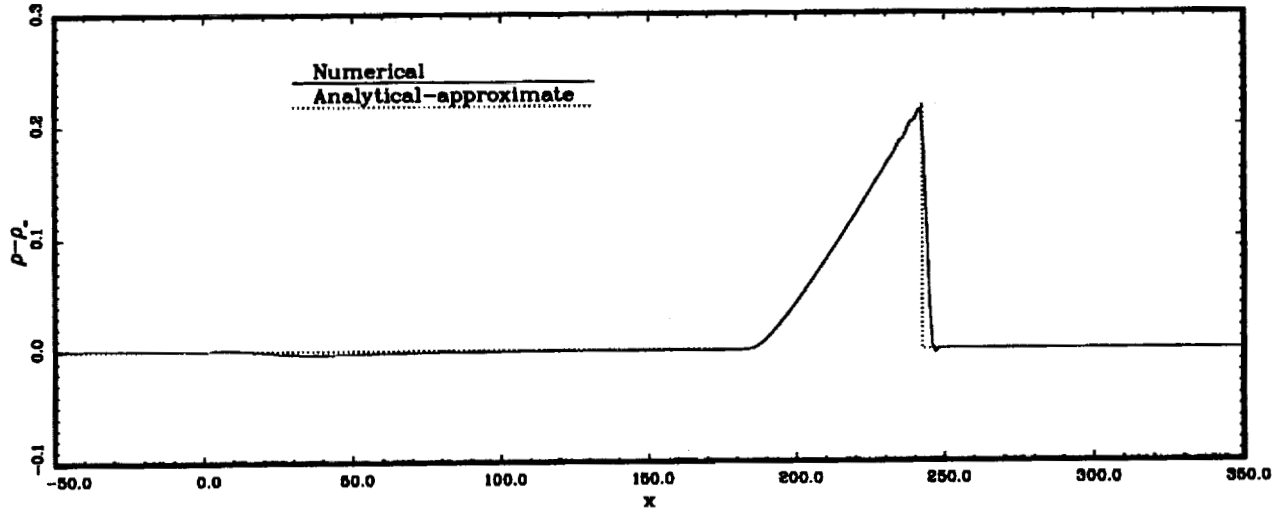

Density distribution at time = 200. (Hu)

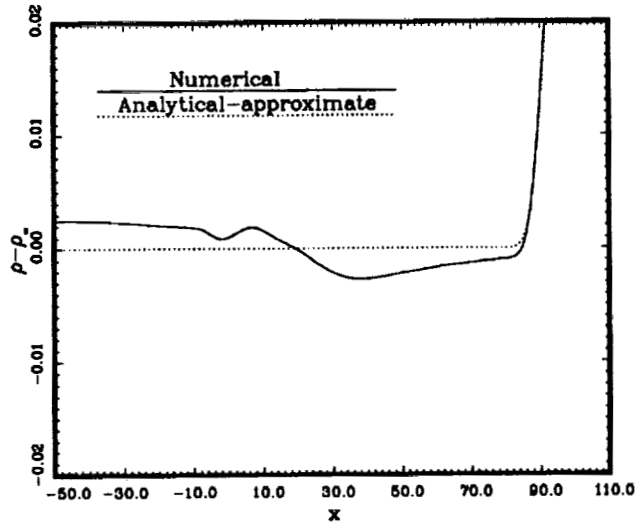

Density distribution at time = 100. (Hu)

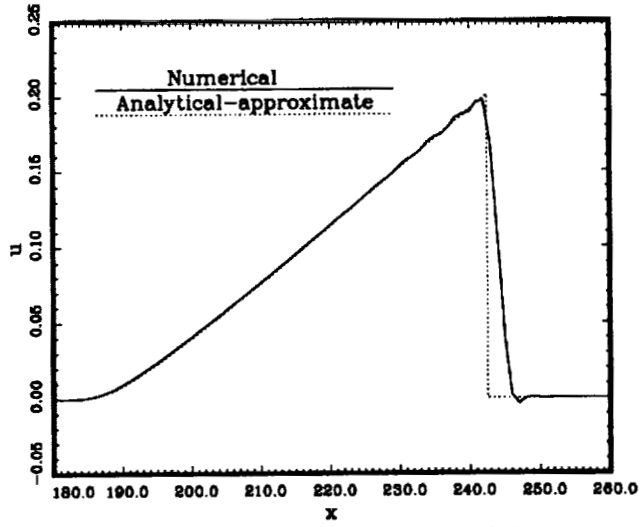

Velocity distribution at time = 200. (Hu)

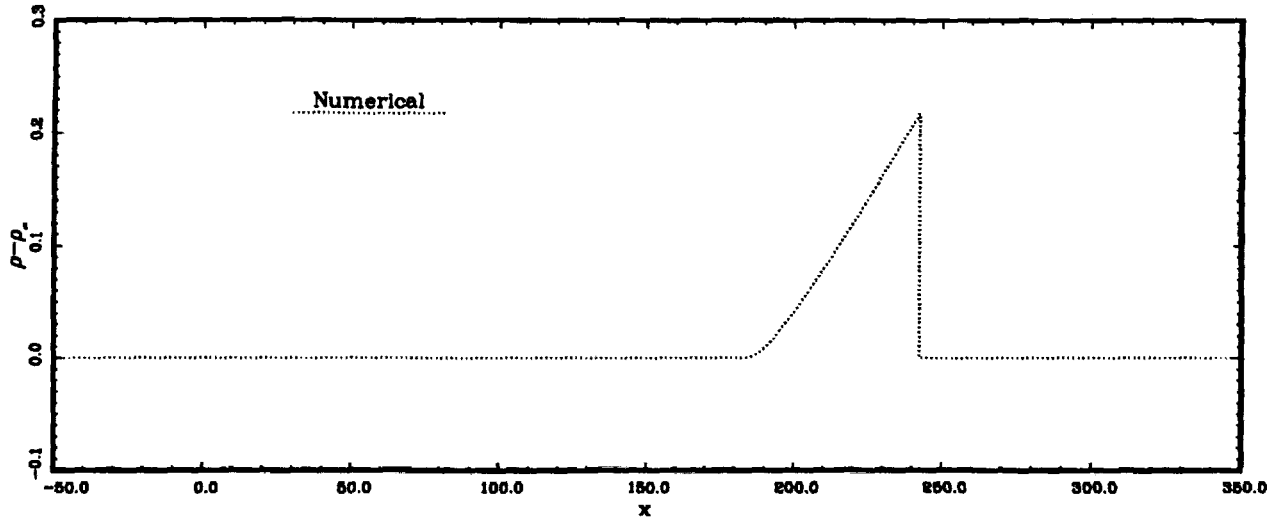

Density distribution at time = 200. (Hudson – with AV)

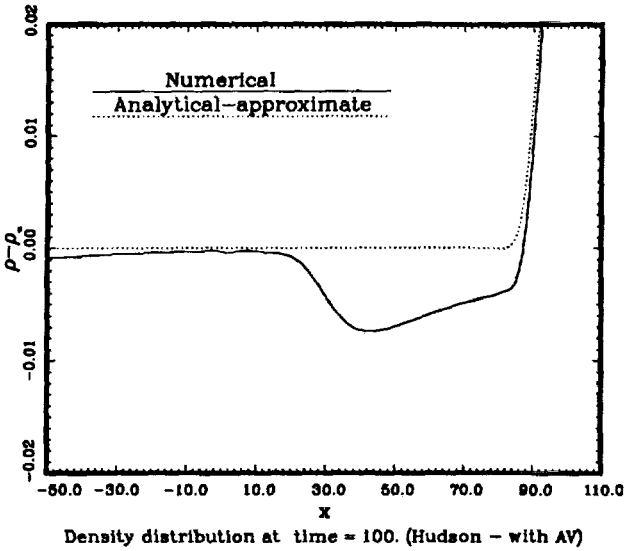

Density distribution at time = 100. (Hudson – with AV)

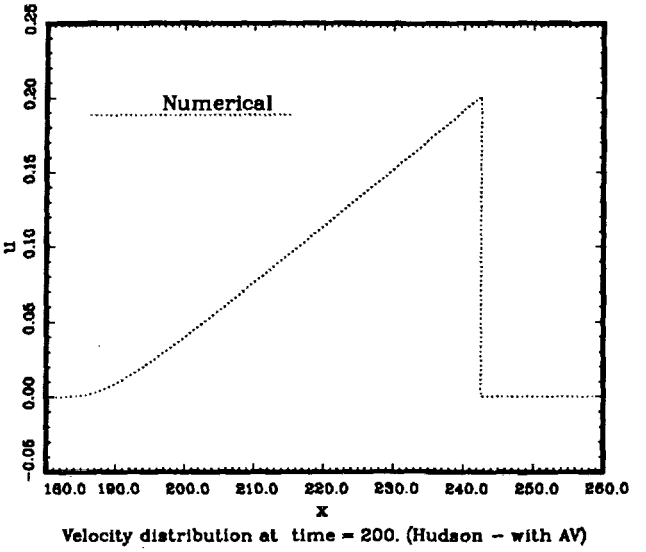

Velocity distribution at time = 200. (Hudson – with AV)

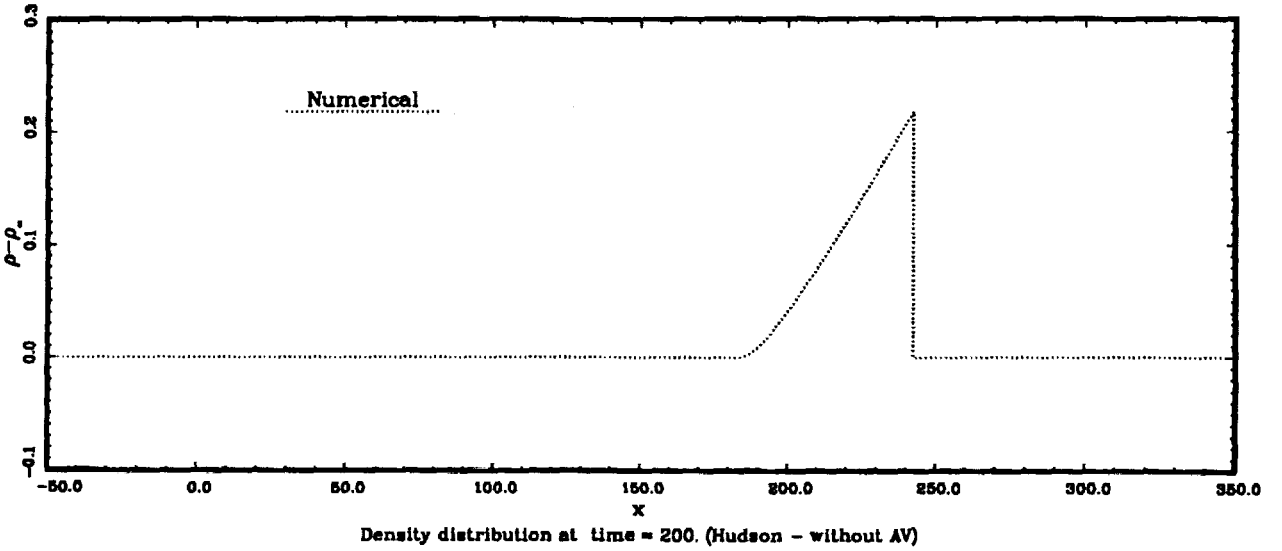

Density distribution at time = 200. (Hudson – without AV)

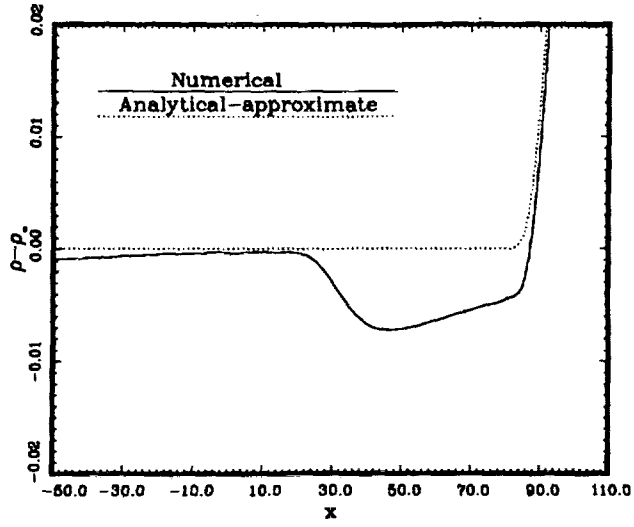

Density distribution at time = 100. (Hudson – without AV)

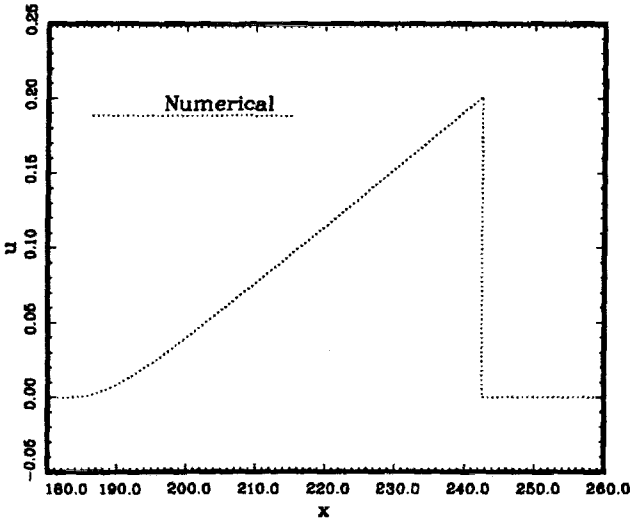

Velocity distribution at time = 200. (Hudson – without AV)

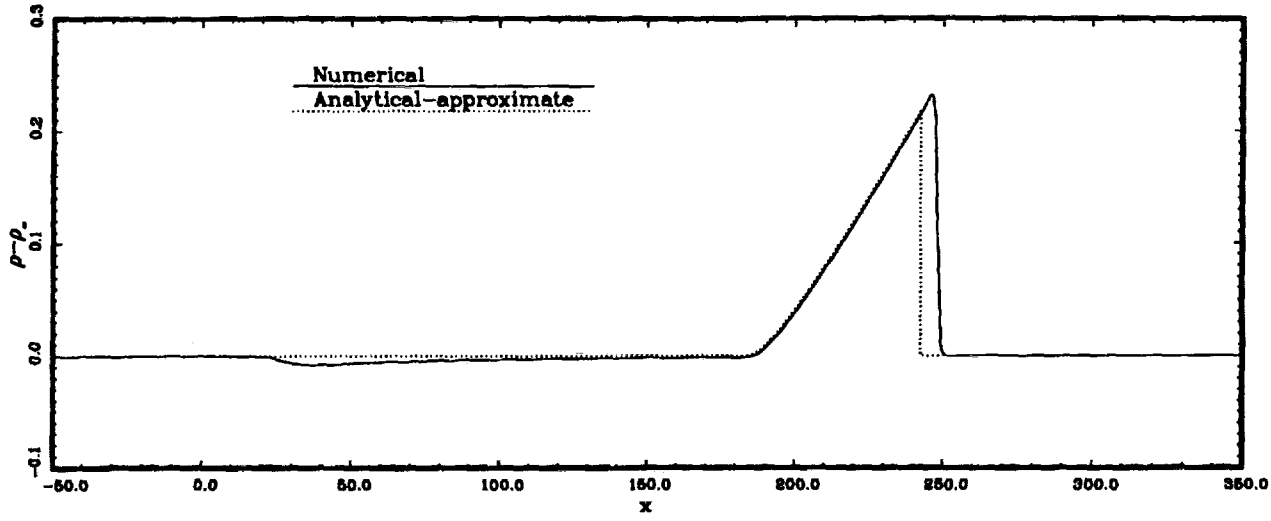

Density distribution at time = 200. (Hunyh –ord 2)

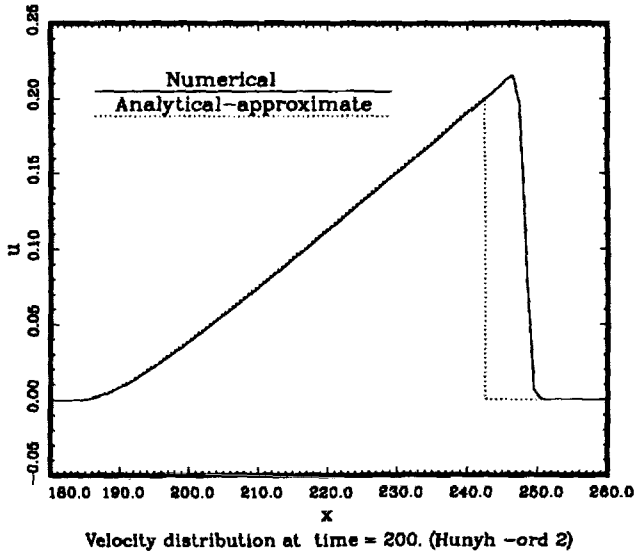

Velocity distribution at time = 200. (Hunyh –ord 2)

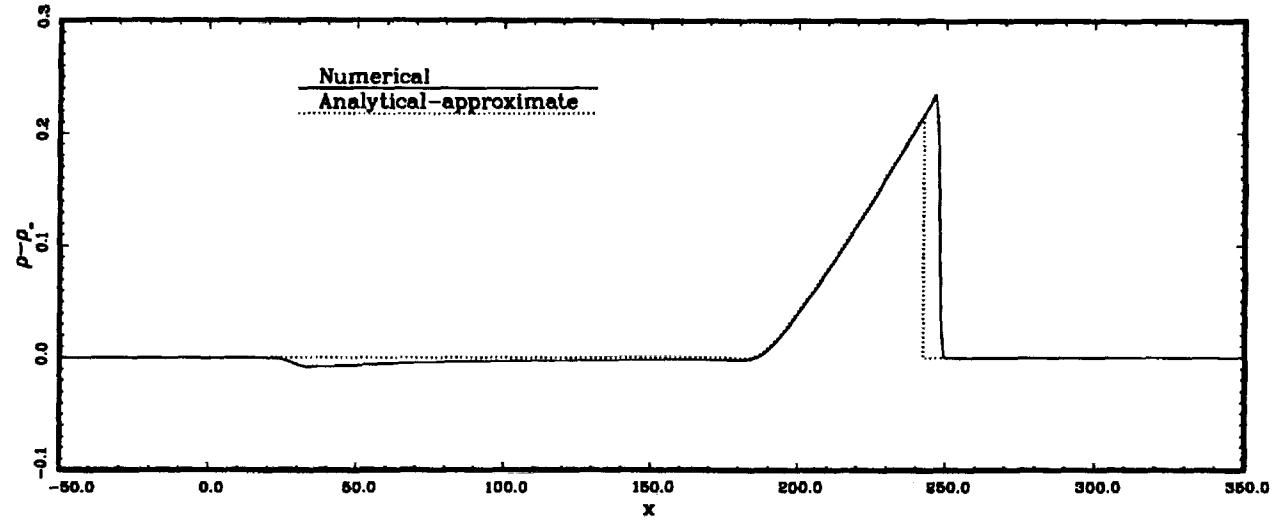

Density distribution at time = 200. (Hunyh -ord 3)

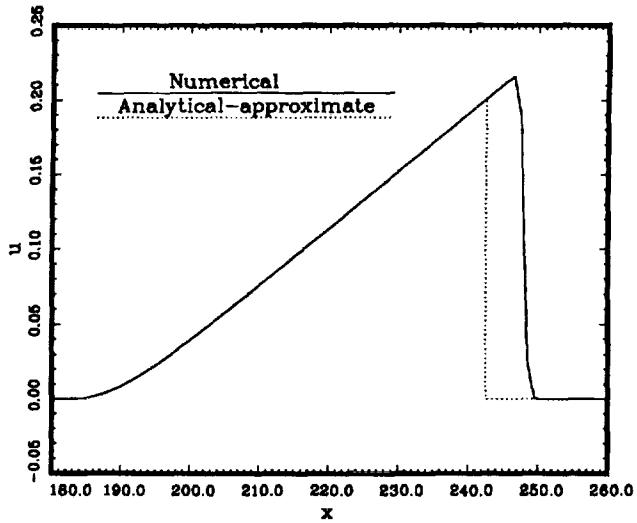

Velocity distribution at time = 200. (Hunyh -ord 3)

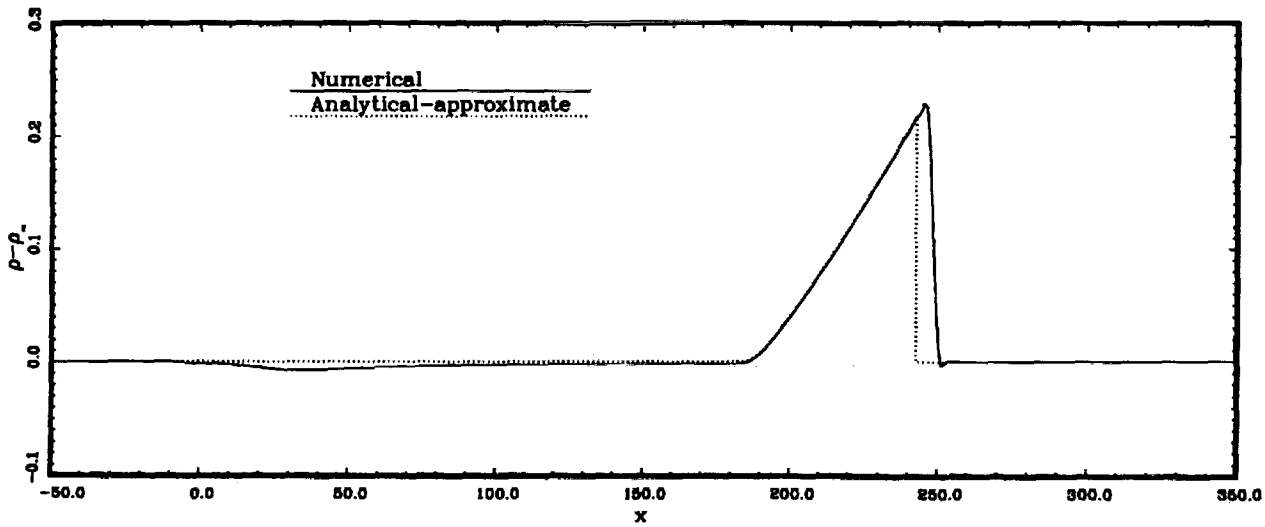

Density distribution at time = 200. (Tam)

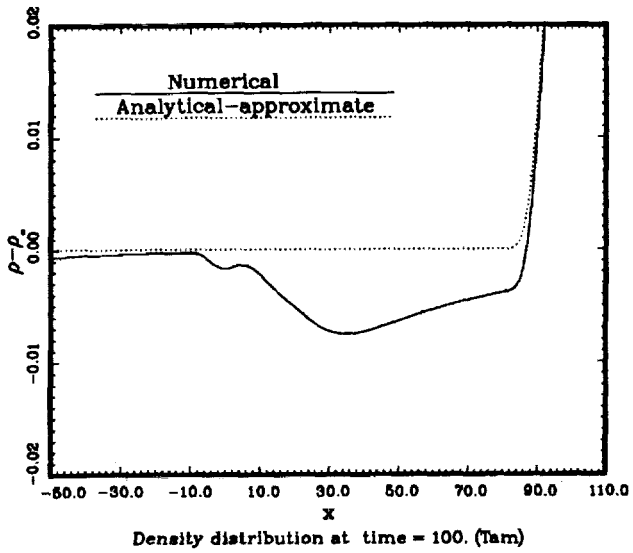

Density distribution at time = 100. (Tam)

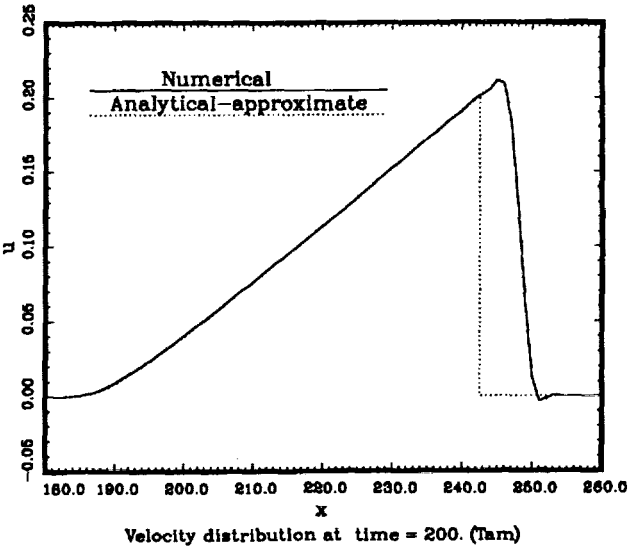

Velocity distribution at time = 200. (Tam)

Category 2, Problem 2

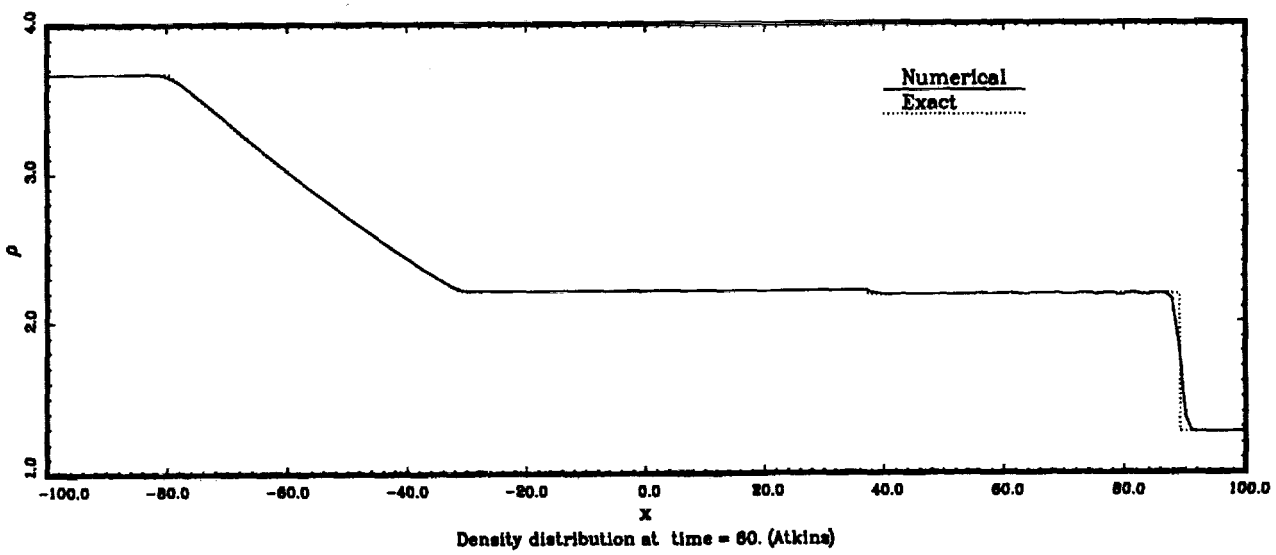

Density distribution at time = 60. (Atkins)

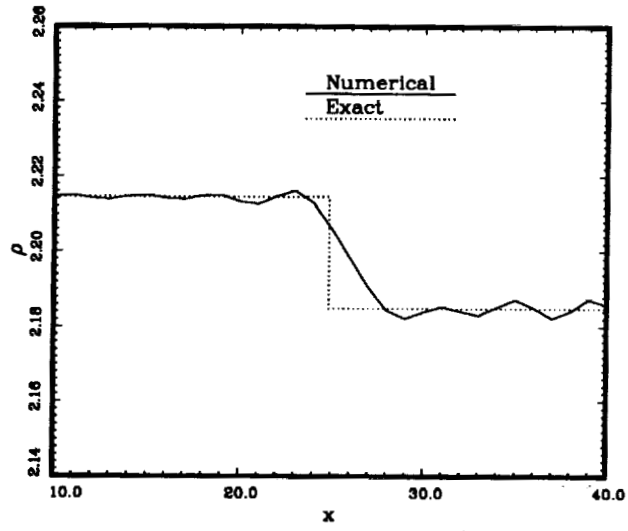

Density distribution at time = 40. (Atkins)

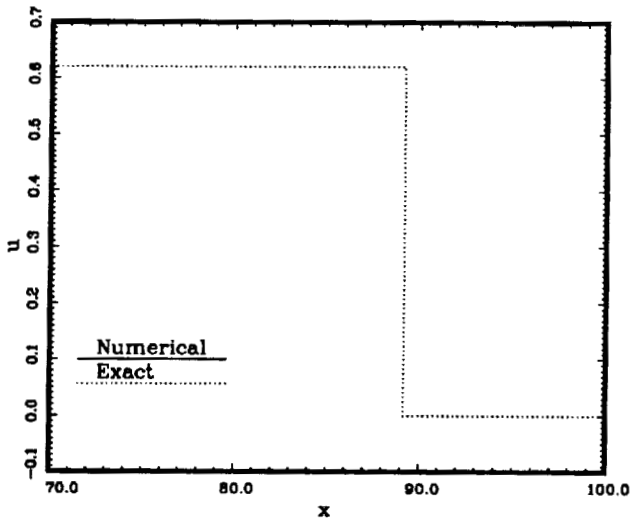

Velocity distribution at time = 60. (Atkins)

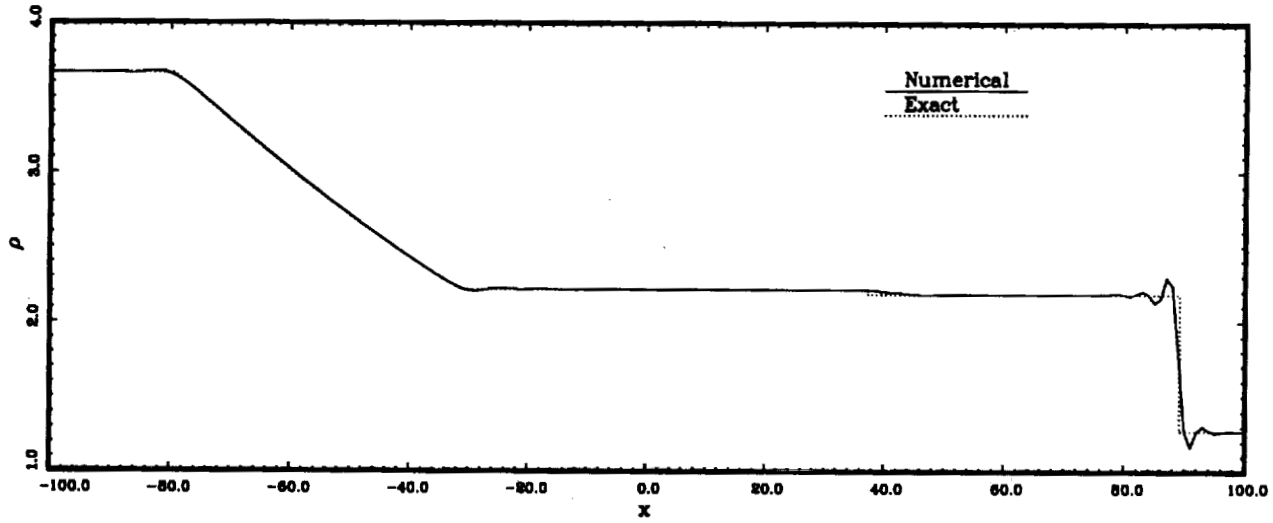

Density distribution at time = 60. (Chyczewski-a)

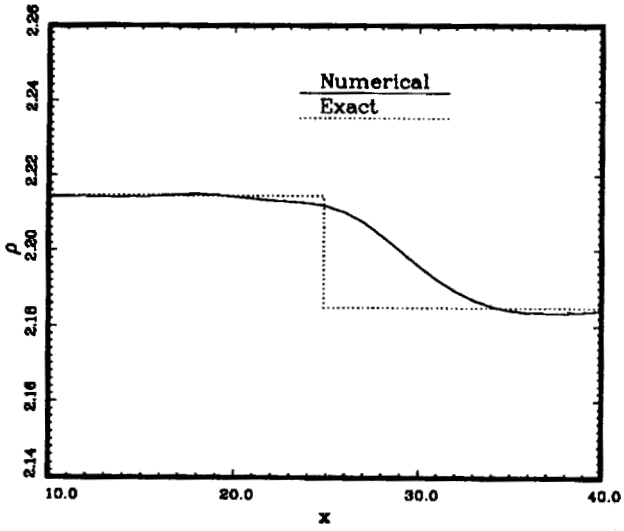

Density distribution at time = 40. (Chyczewski-a)

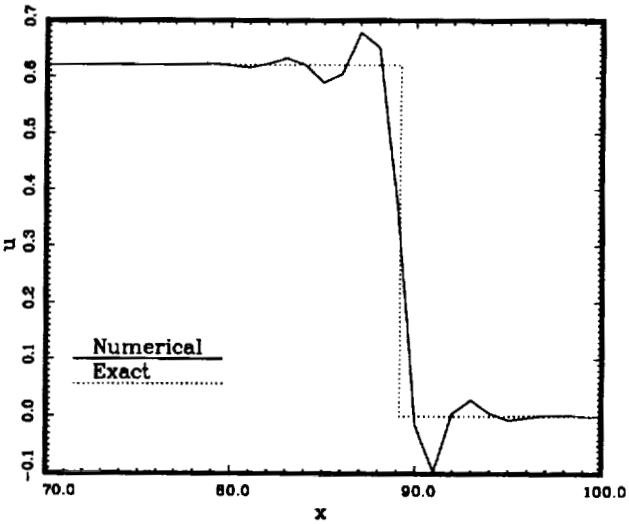

Velocity distribution at time = 60. (Chyczewski-a)

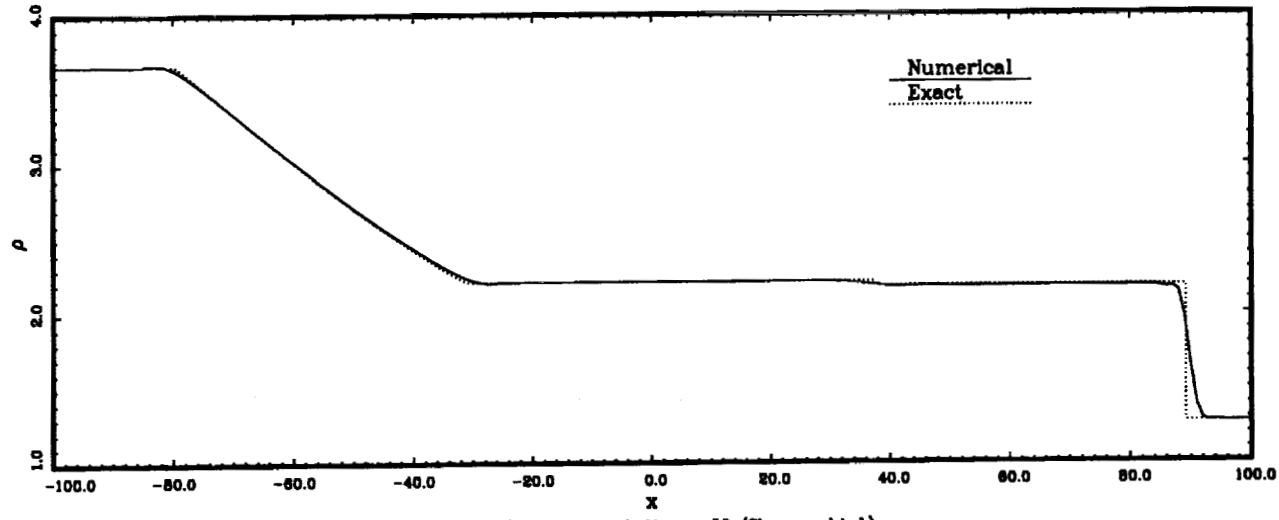

Density distribution at time = 60. (Chyczewski-b)

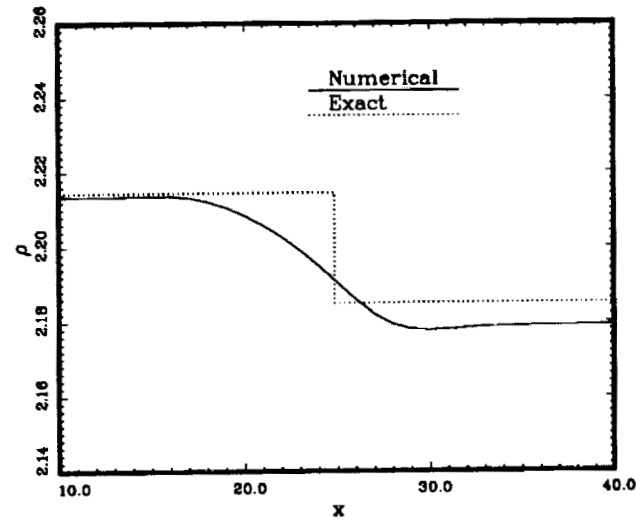

Density distribution at time = 40. (Chyczewski-b)

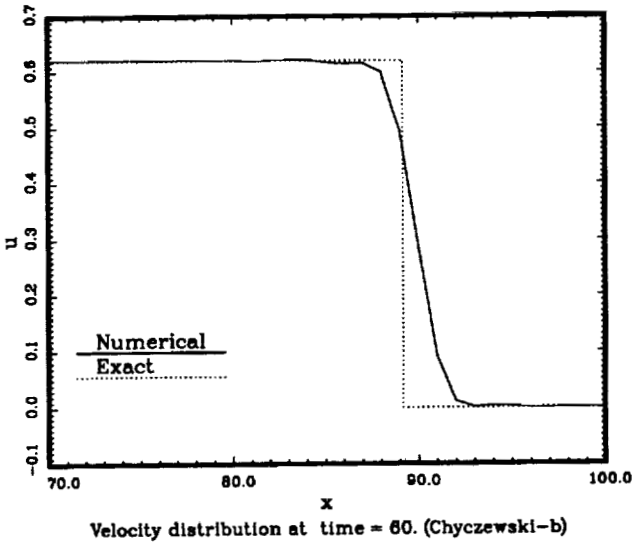

Velocity distribution at time = 60. (Chyczewski-b)

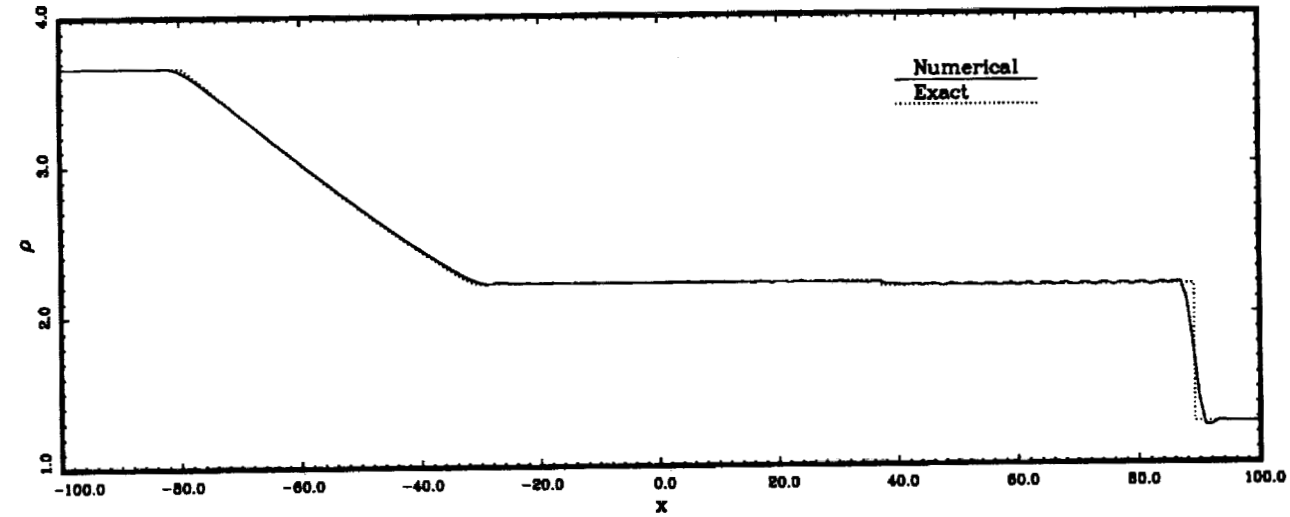

Density distribution at time = 60. (Hayder -DRP)

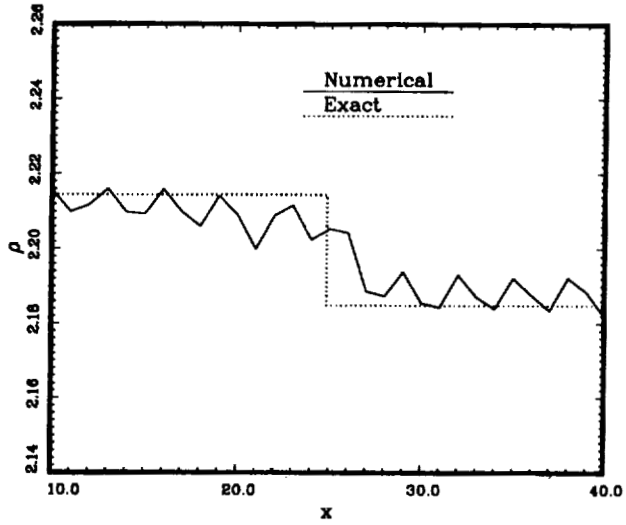

Density distribution at time = 40. (Hayder –DRP)

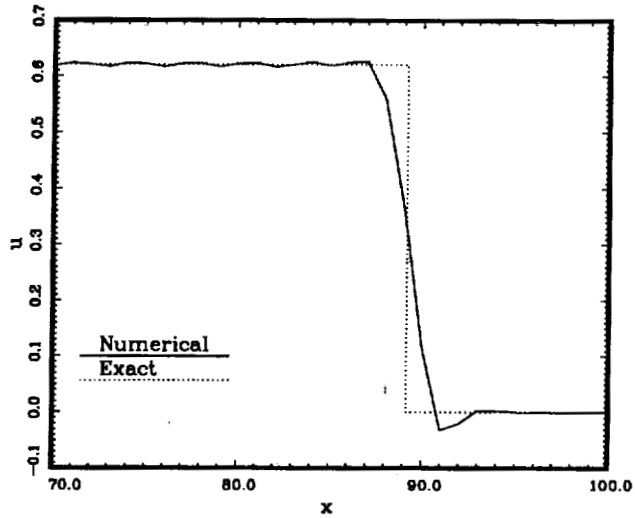

Velocity distribution at time = 60. (Hayder –DRP)

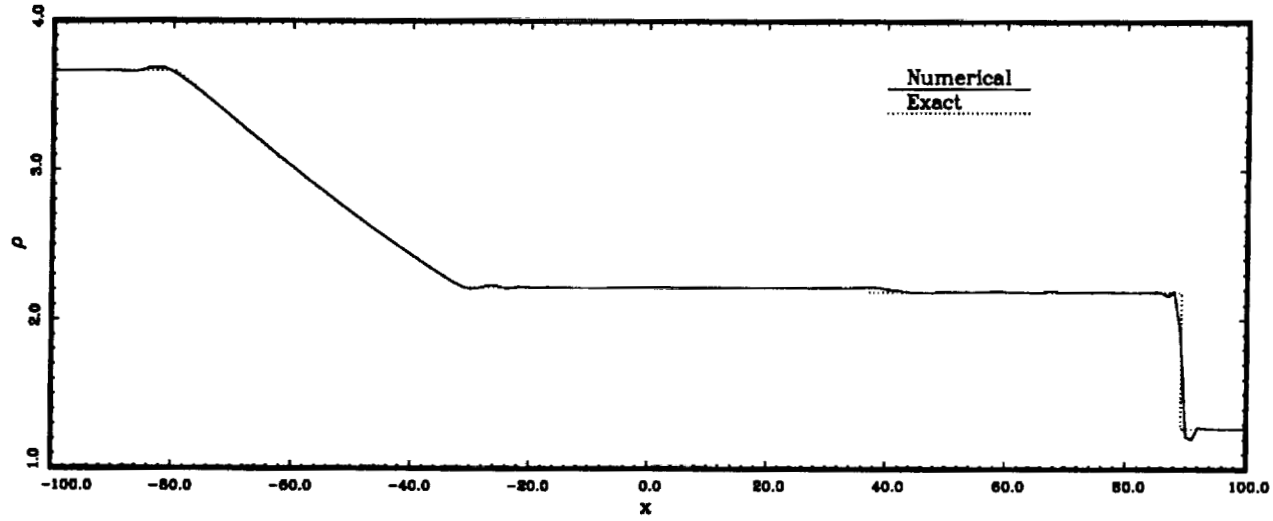

Density distribution at time = 60. (Hayder –MacCormack 2–4)

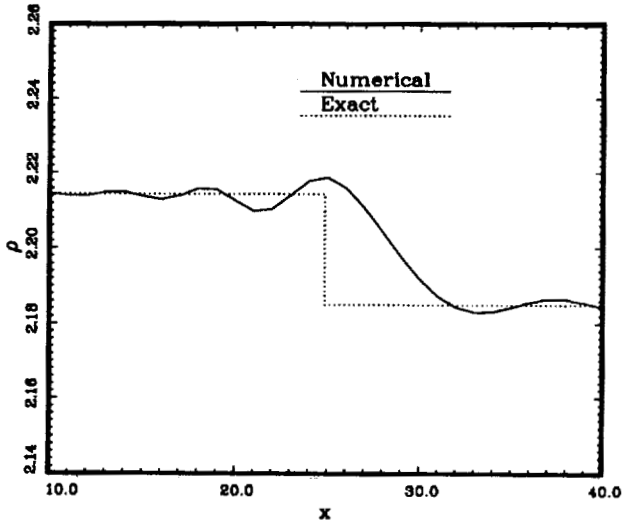

Density distribution at time = 40. (Hayder –MacCormack 2–4)

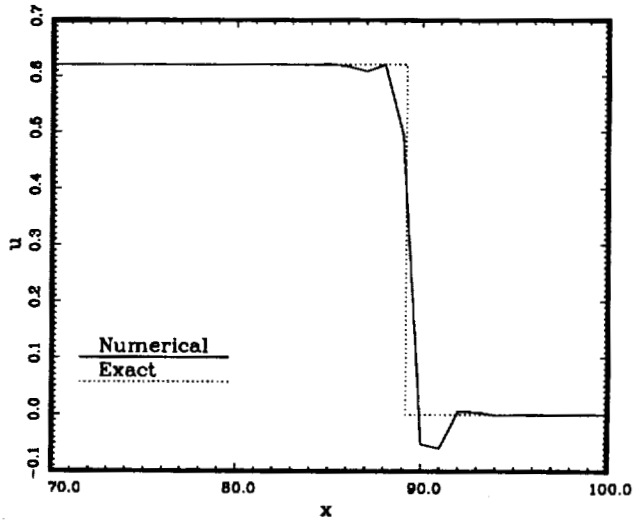

Velocity distribution at time = 60. (Hayder –MacCormack 2–4)

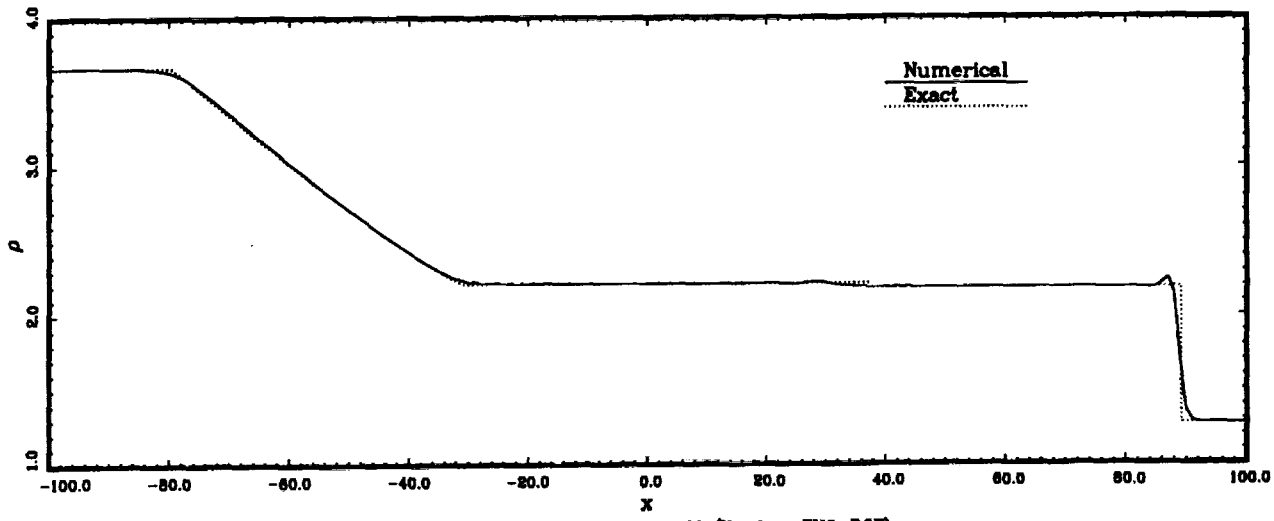

Density distribution at time = 60. (Hayder –ENO–ROE)

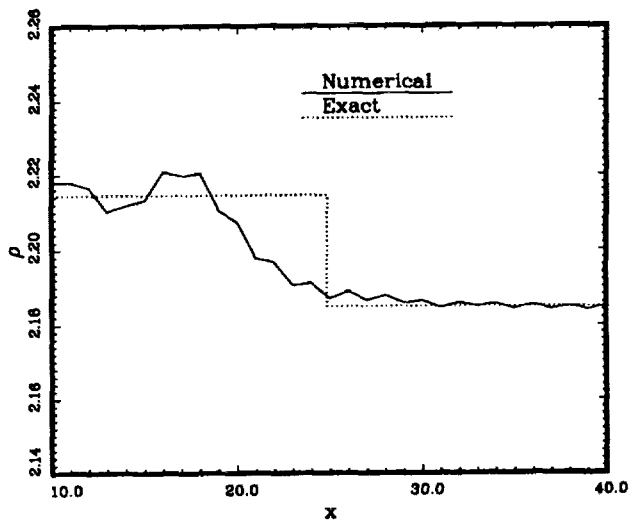

Density distribution at time = 40. (Hayder –ENO–ROE)

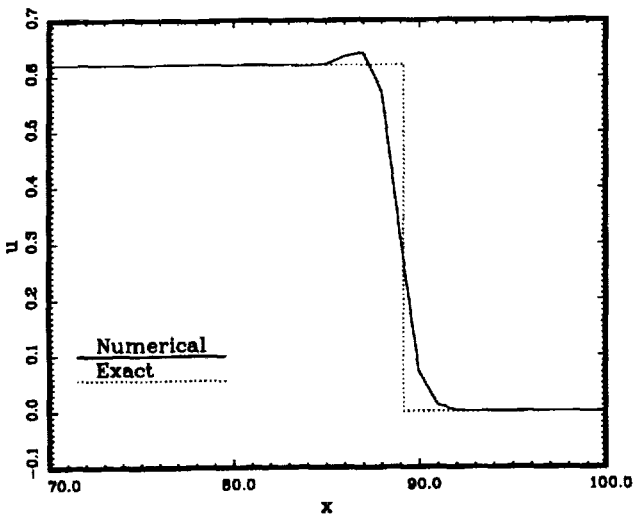

Velocity distribution at time = 60. (Hayder –ENO–ROE)

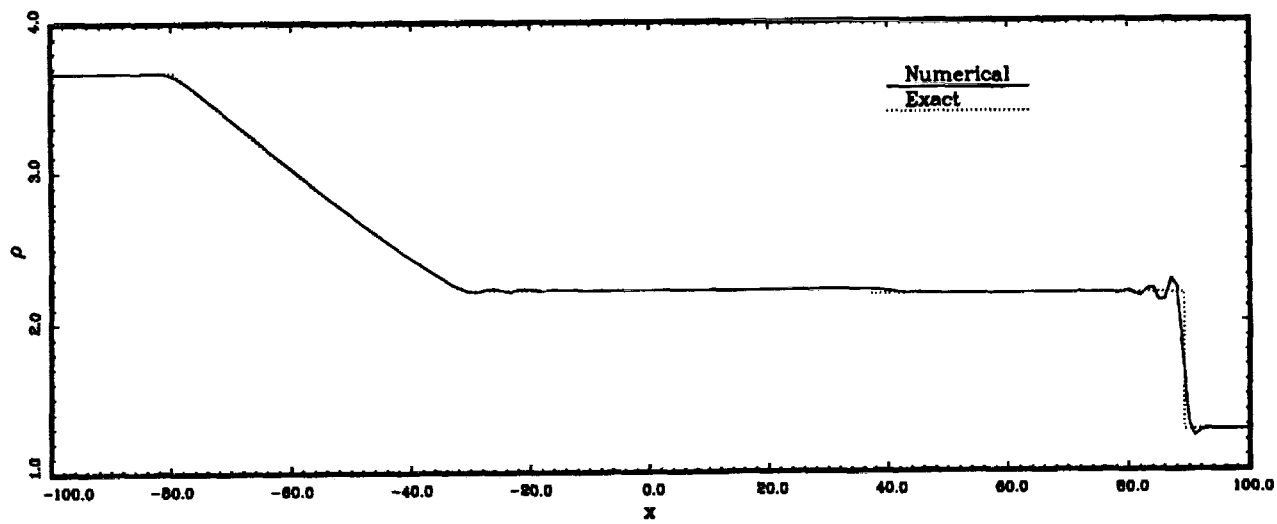

Density distribution at time = 60. (Hudson – with AV)

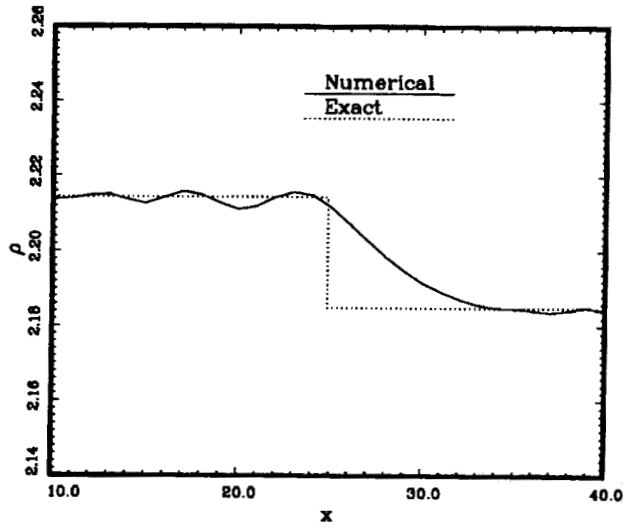

Density distribution at time = 40. (Hudson – with AV)

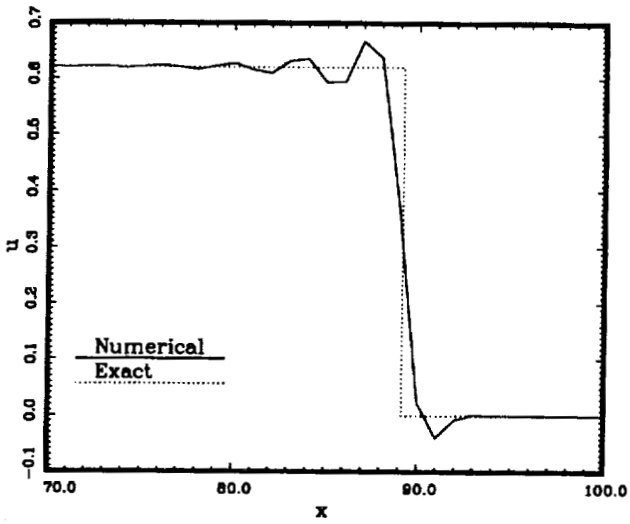

Velocity distribution at time = 60. (Hudson – with AV)

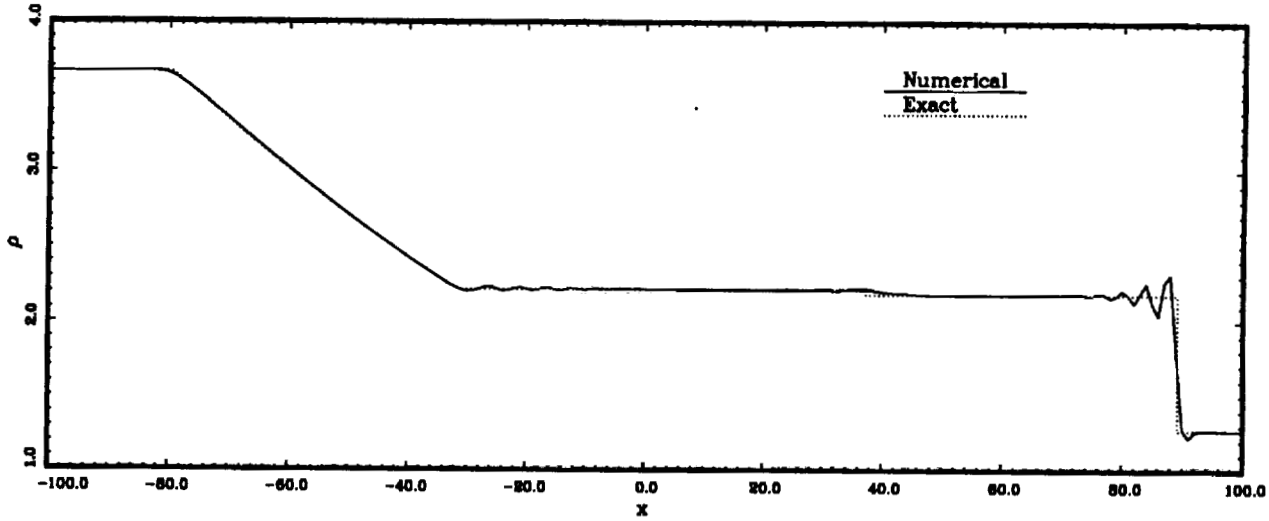

Density distribution at time = 60. (Hudson – without AV)

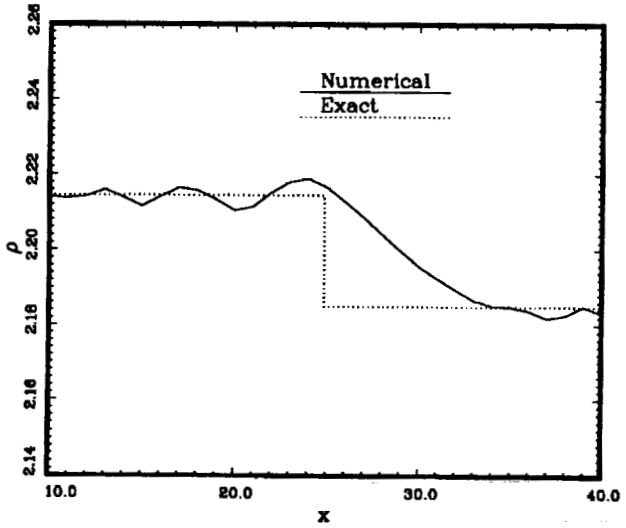

Density distribution at time = 40. (Hudson – without AV)

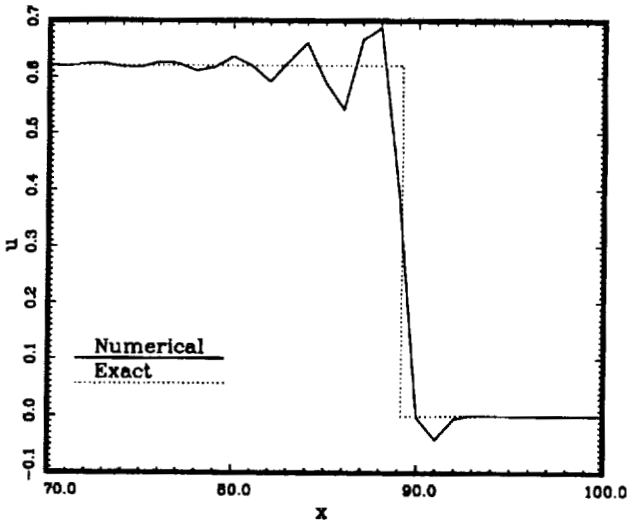

Velocity distribution at time = 60. (Hudson – without AV)

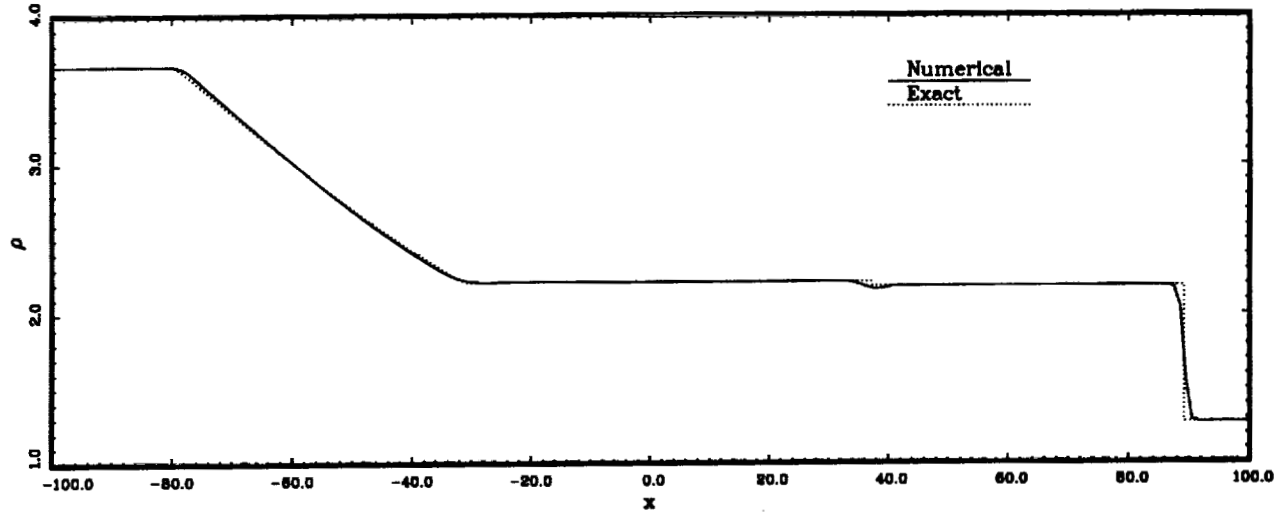

Density distribution at time = 60. (Hunyh –ord 2)

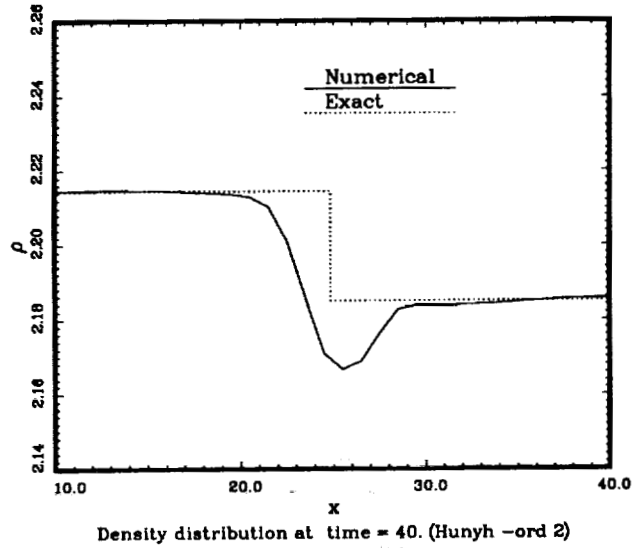

Density distribution at time = 40. (Hunyh –ord 2)

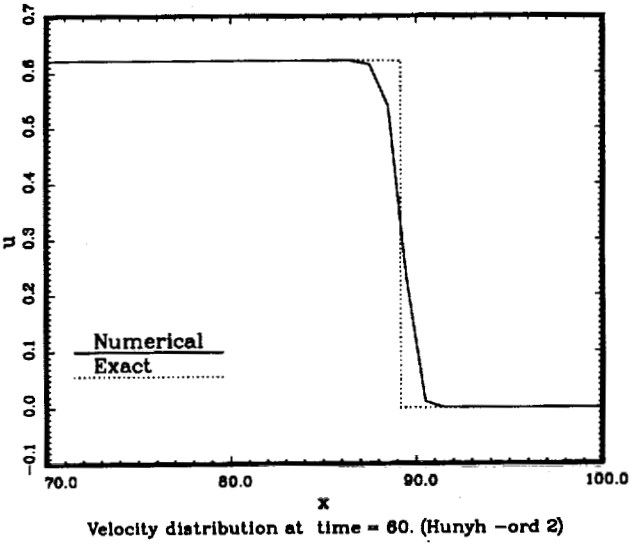

Velocity distribution at time = 60. (Hunyh –ord 2)

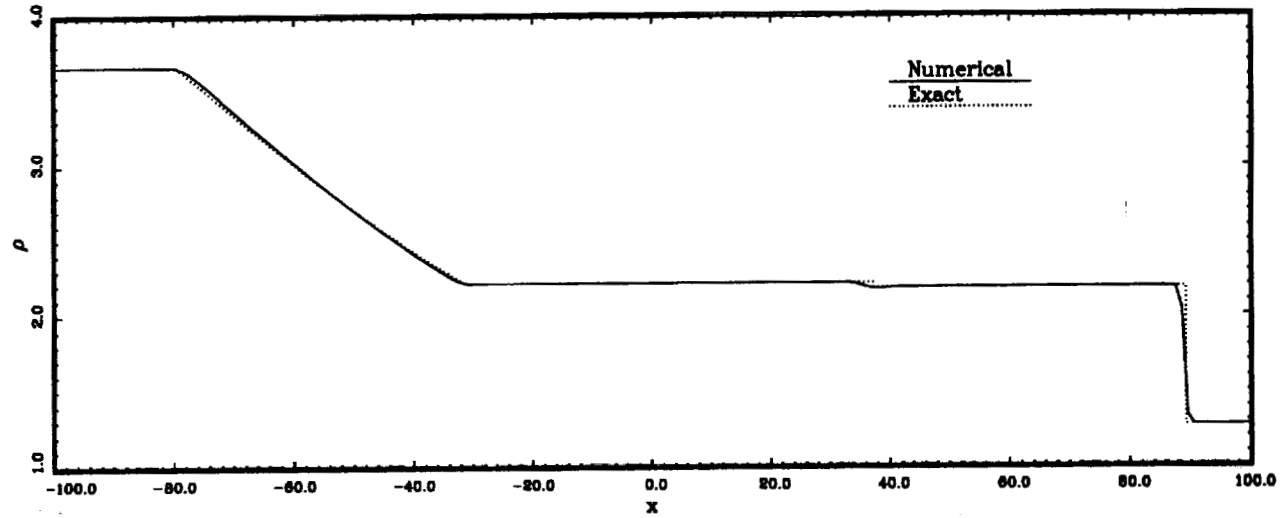

Density distribution at time = 60. (Hunyh –ord 3)

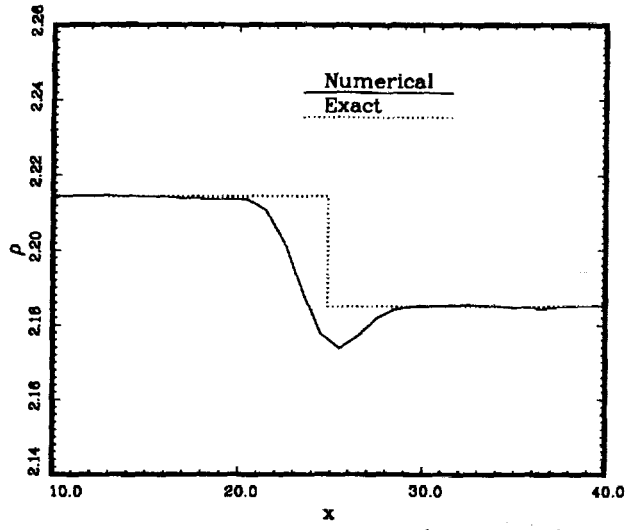

Density distribution at time = 40. (Hunyh –ord 3)

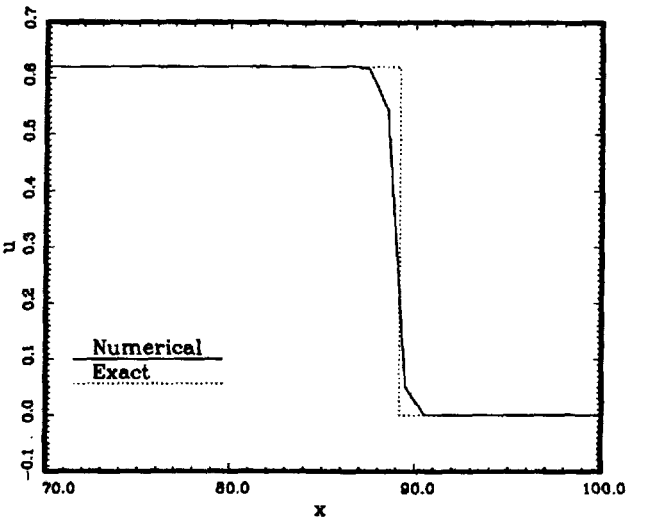

Velocity distribution at time = 60. (Hunyh –ord 3)

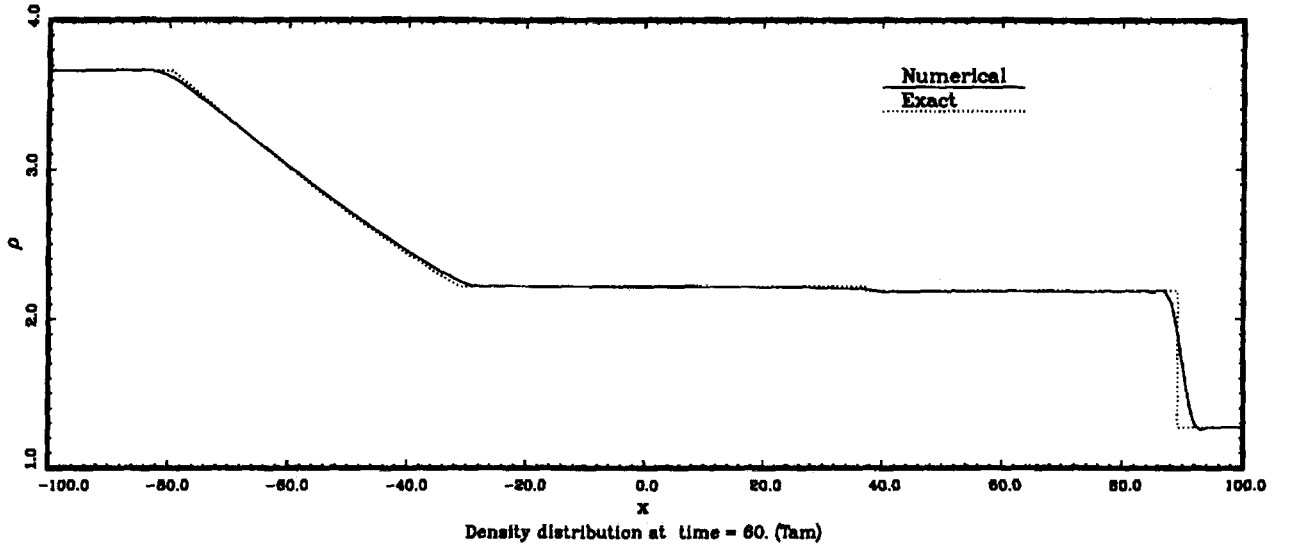

Density distribution at time = 60. (Tam)

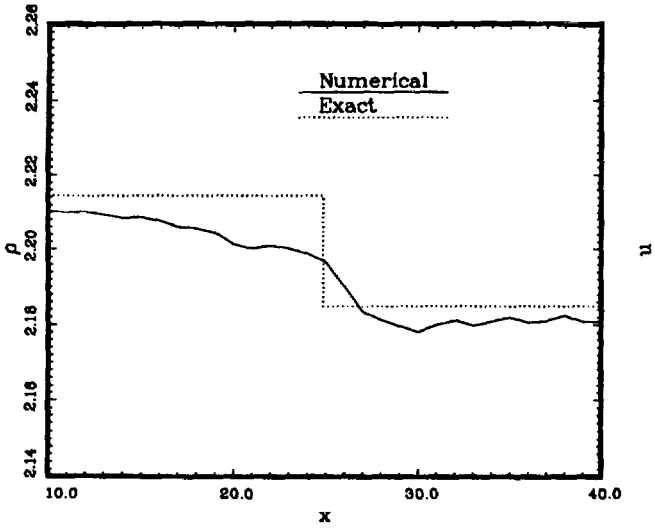

Density distribution at time = 40. (Tam)

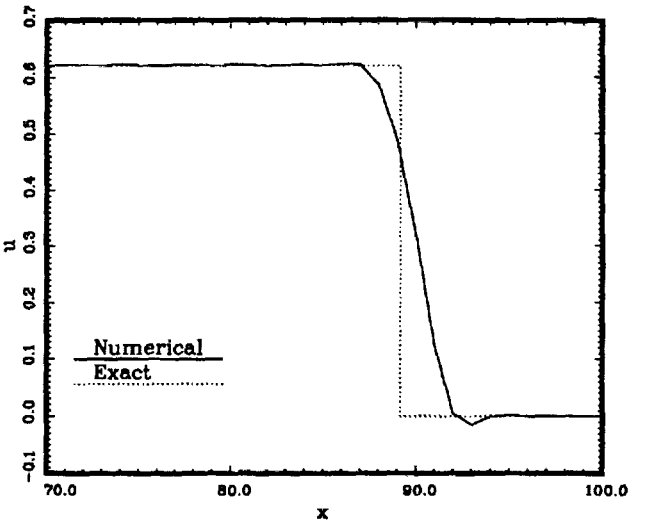

Velocity distribution at time = 60. (Tam)

Category 3, Problem 1

Density contours.

- -	$4x10^{-2}$
——·——·——·——·——·——·——	$2x10^{-2}$
————————————————————	$1x10^{-4}$
—— — —— — —— — —	$-2x10^{-2}$
.....	exact

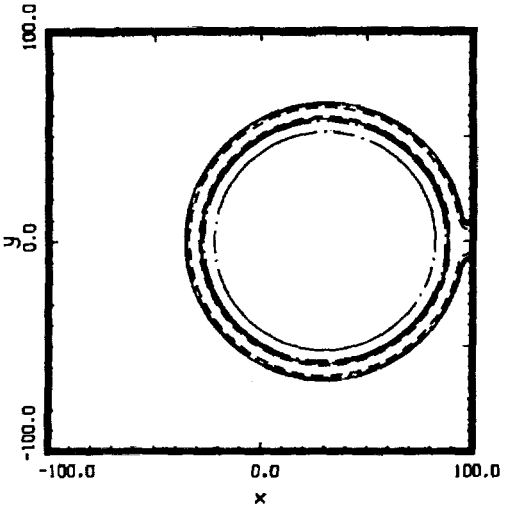

Density contours. t=60. (*Atkins*)

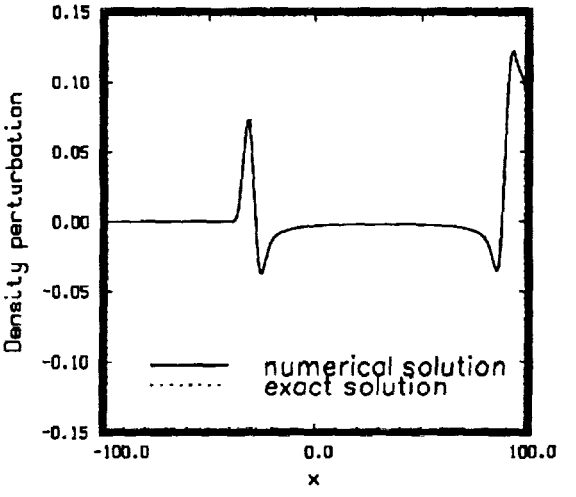

Density waveform along x-axis. t=60. (*Atkins*)

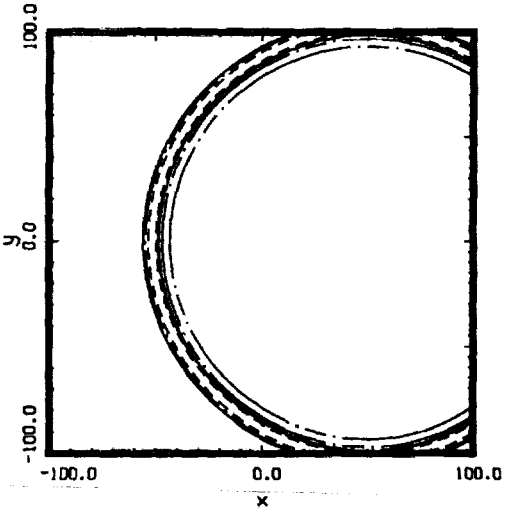

Density contours. t=100. (*Atkins*)

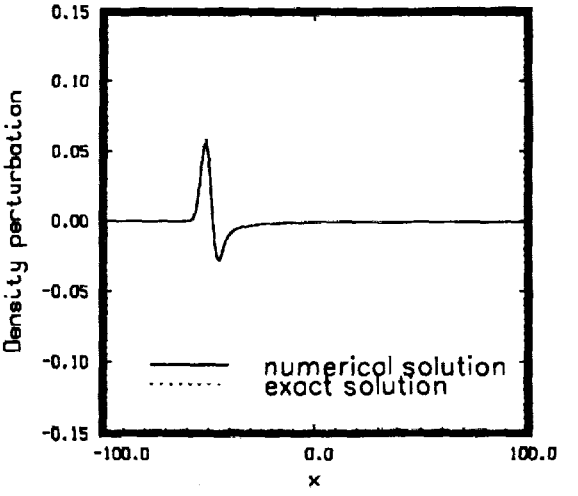

Density waveform along x-axis. t=100. (*Atkins*)

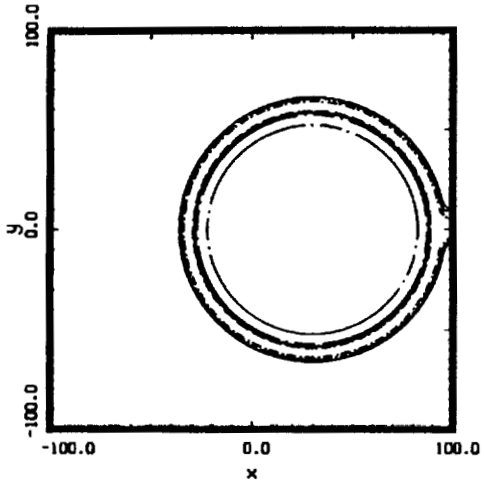

Density contours. t=60. (*Fung*)

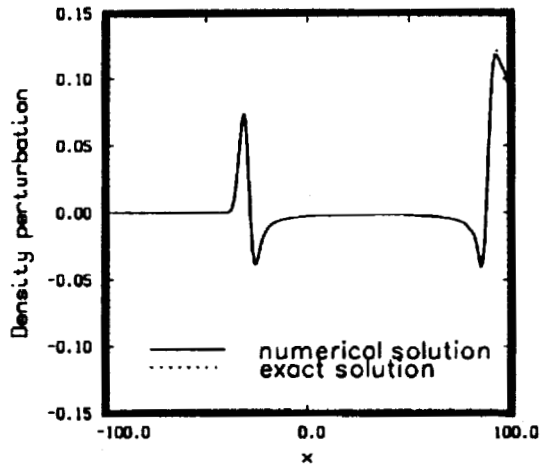

Density waveform along x-axis. t=60. (*Fung*)

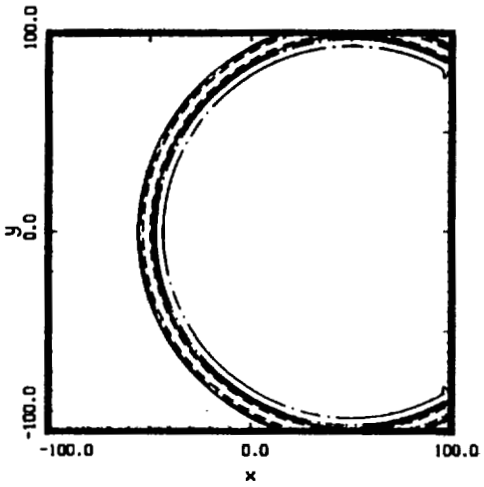

Density contours. t=100. (*Fung*)

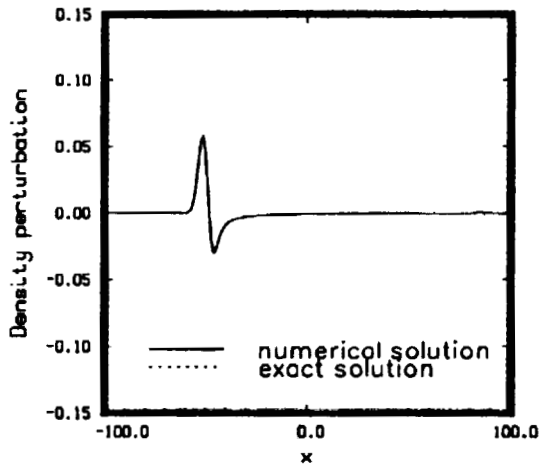

Density waveform along x-axis. t=100. (*Fung*)

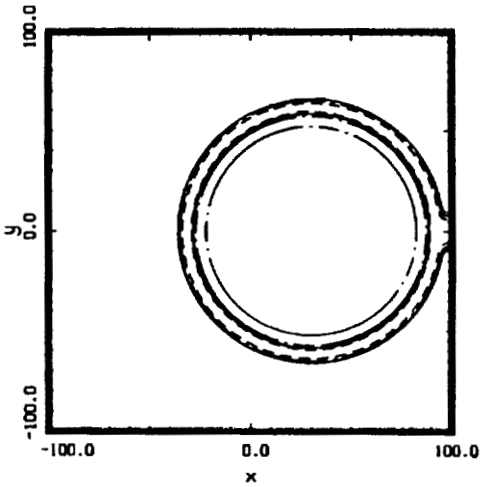

Density contours. t=60. (*Hu*)

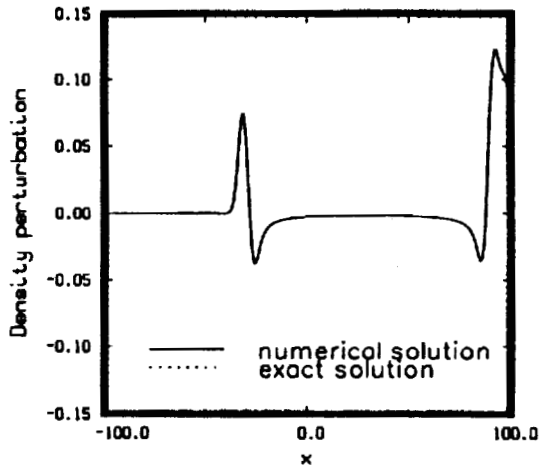

Density waveform along x-axis. t=60. (*Hu*)

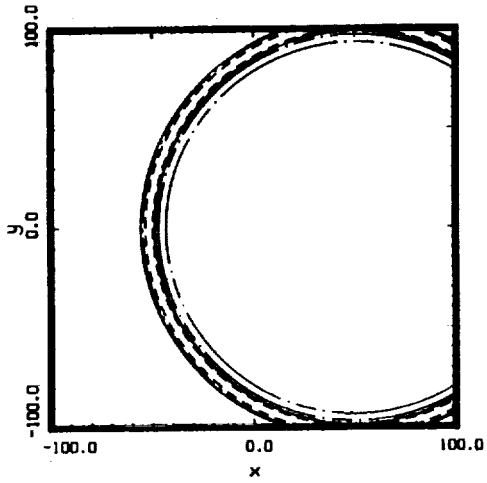

Density contours. t=100. (*Hu*)

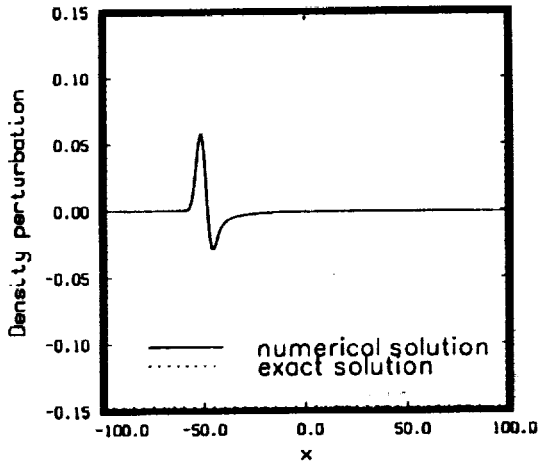

Density waveform along x-axis. t=100. (*Hu*)

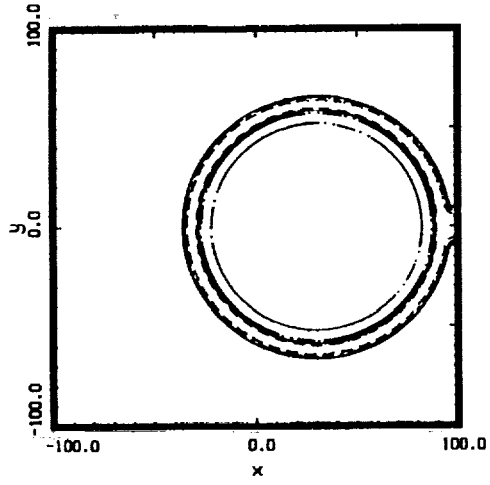

Density contours. t=60. (*Morris/Chung*)

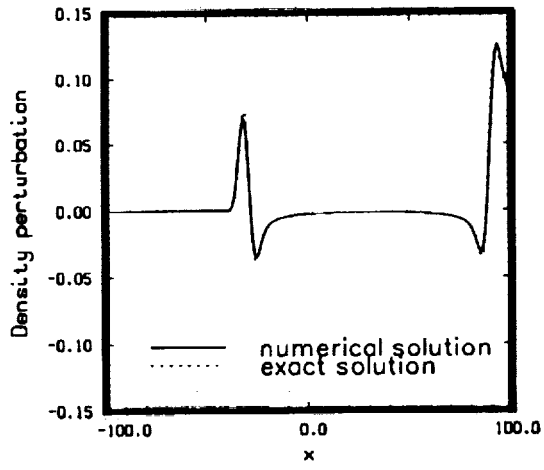

Density waveform along x-axis. t=60. (*Morris/Chung*)

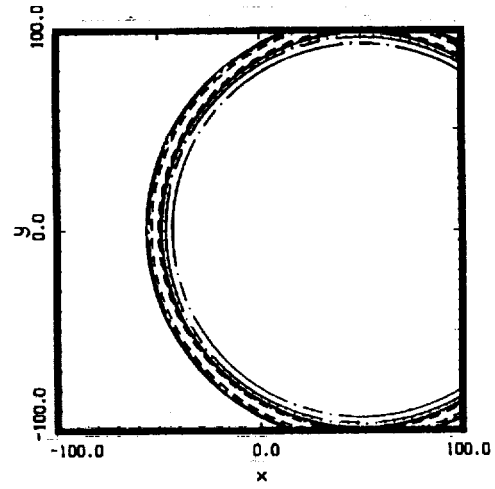

Density contours. t=100. (*Morris/Chung*)

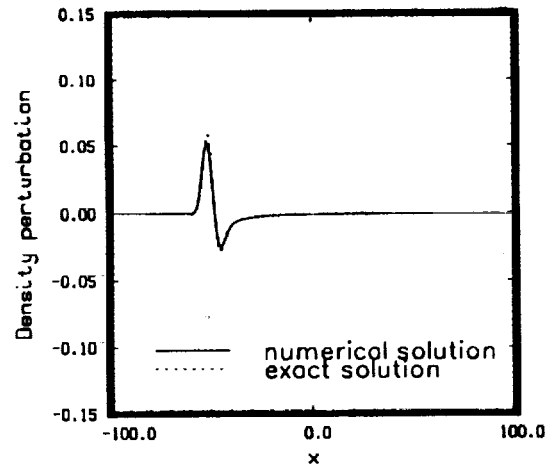

Density waveform along x-axis. t=100. (*Morris/Chung*)

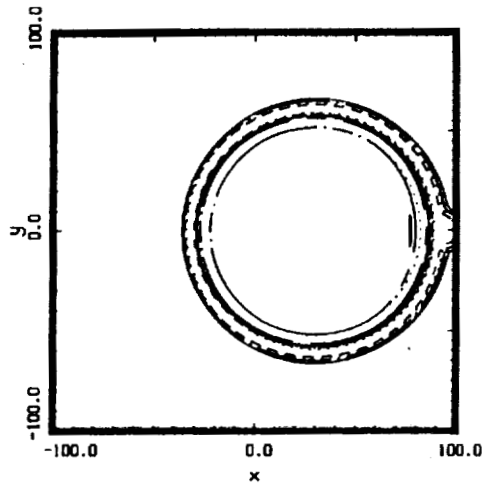

Density contours. t=60. (*Nark, 1*)

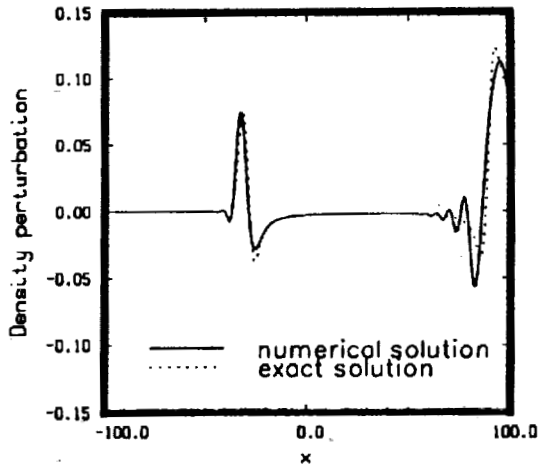

Density waveform along x-axis. t=60. (*Nark, 1*)

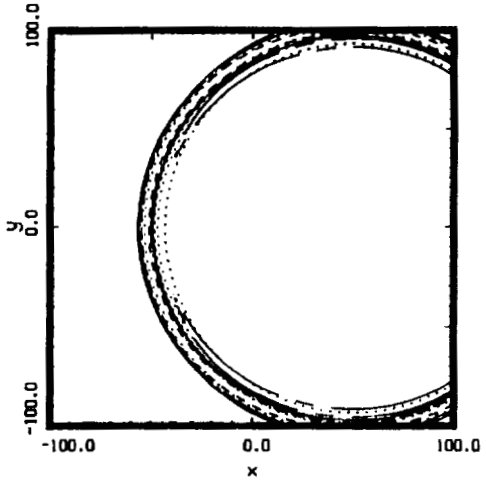

Density contours. t=100. (*Nark, 1*)

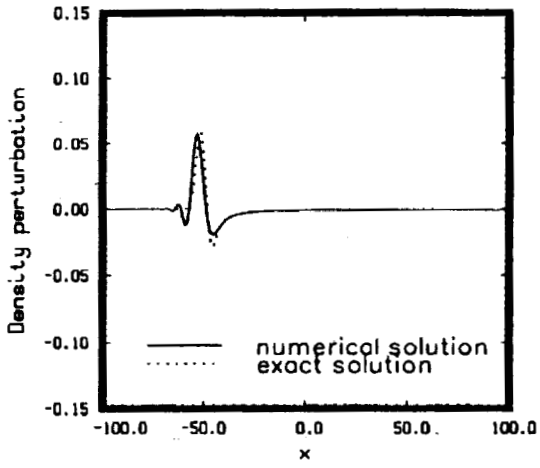

Density waveform along x-axis. t=100. (*Nark, 1*)

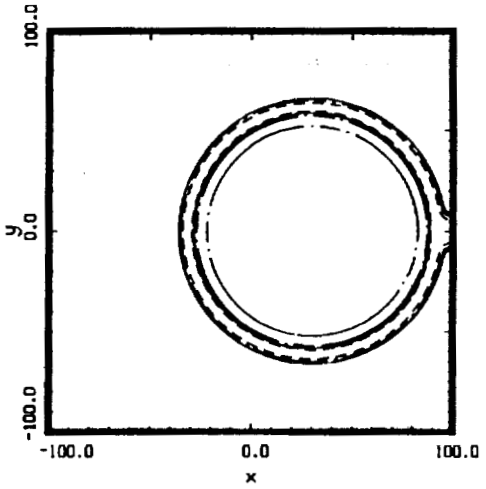

Density contours. t=60. (*Nark, 2*)

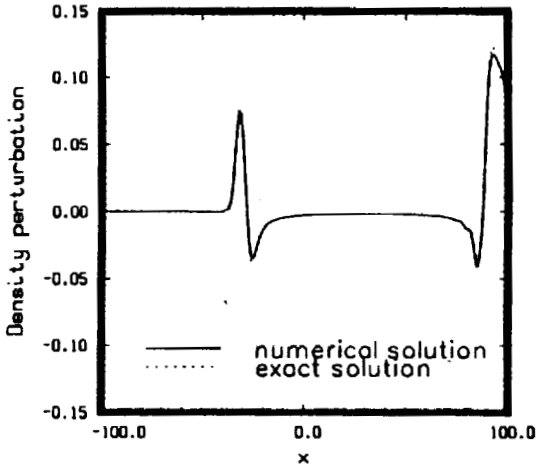

Density waveform along x-axis. t=60. (*Nark, 2*)

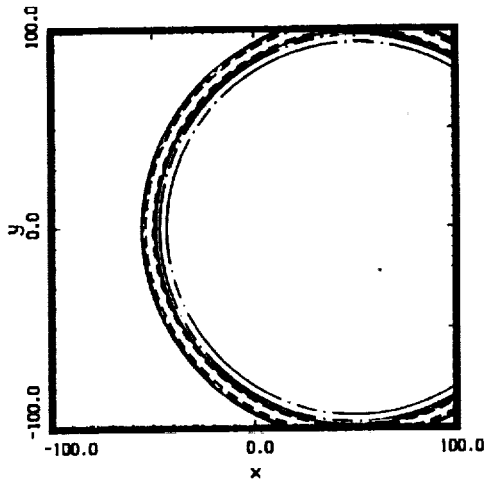

Density contours. t=100. (*Nark,2*)

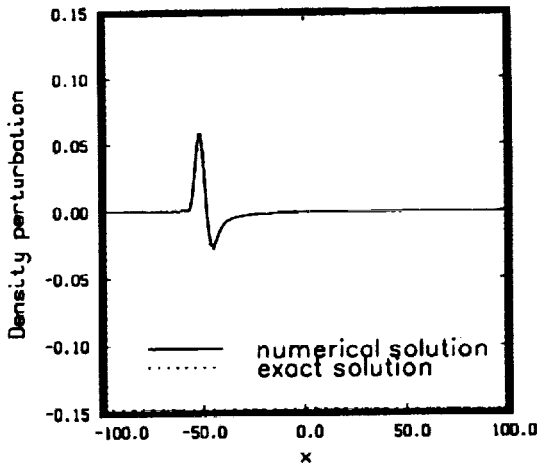

Density waveform along x-axis. t=100. (*Nark,2*)

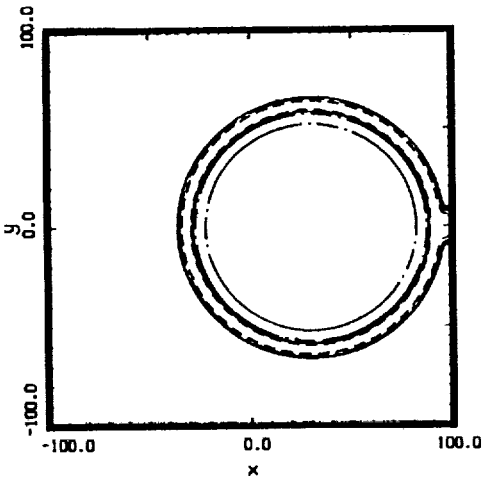

Density contours. t=60. (*Tam*)

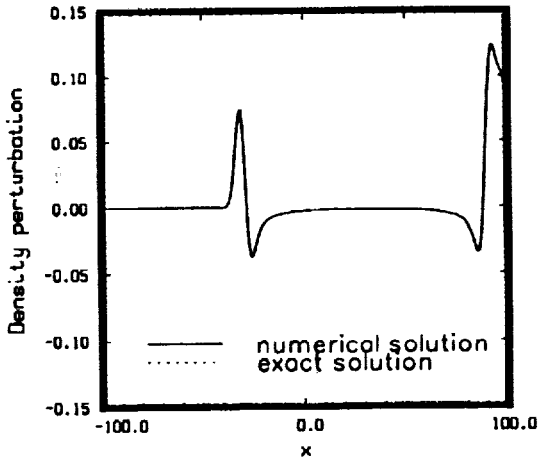

Density waveform along x-axis. t=60. (*Tam*)

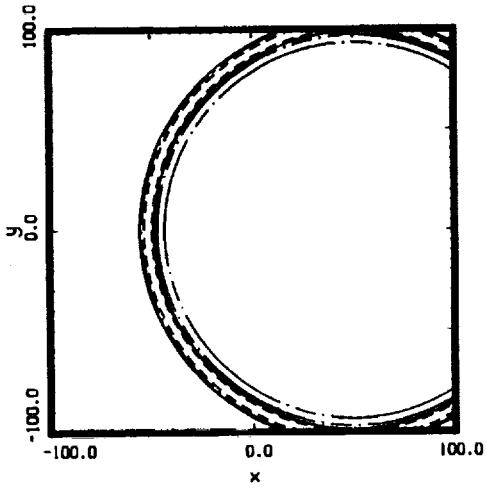

Density contours. t=60. (*Tam*)

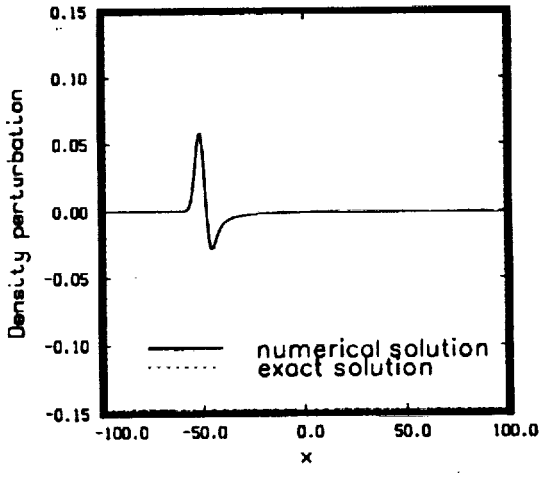

Density waveform along x-axis. t=100. (*Tam*)

Category 3, Problem 2

Density contours.

- -	4×10^{-2}
——— · ——— · ——— · ——— · ——— · ——— · ———	2×10^{-2}
———————————————————————————————	1×10^{-4}
——— – ——— – ——— – ——— – ——— – ——— – ———	-2×10^{-2}
.....	exact

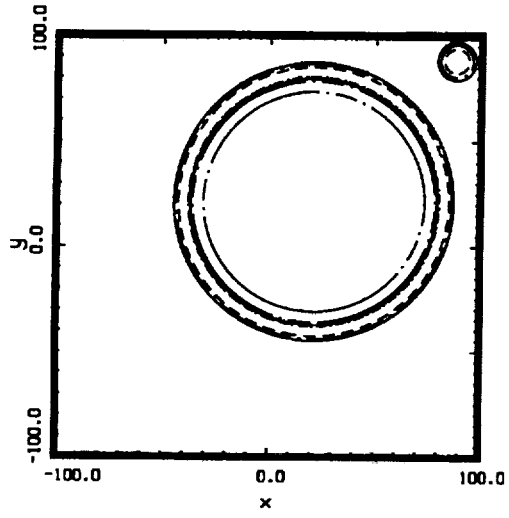

Density contours. t=60. (*Fung*)

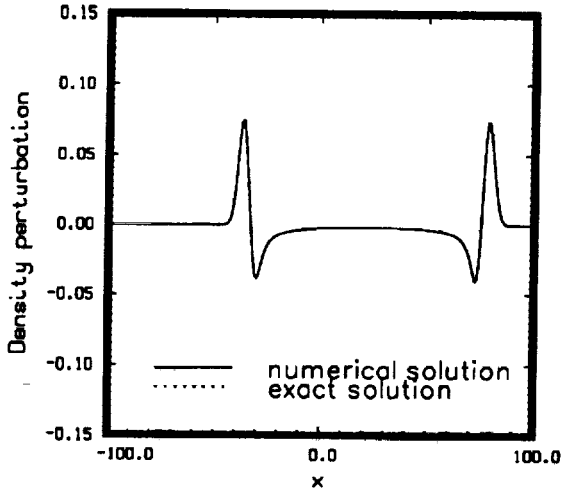

Density waveform along x-axis. t=60. (*Fung*)

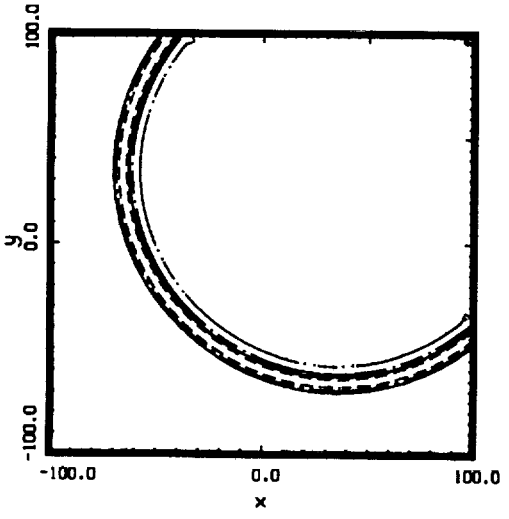

Density contours. t=100. (*Fung*)

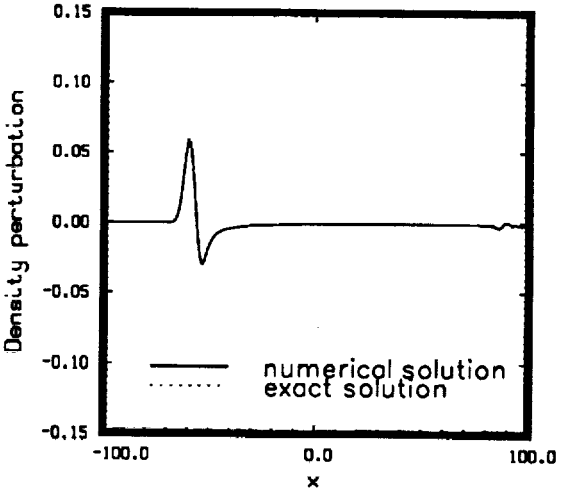

Density waveform along x-axis. t=100. (*Fung*)

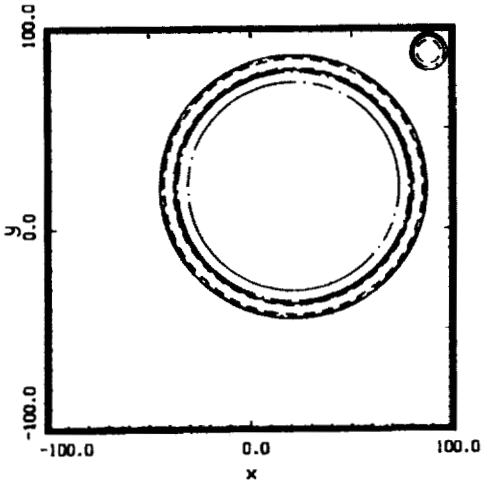

Density contours. t=60. (*Hu*)

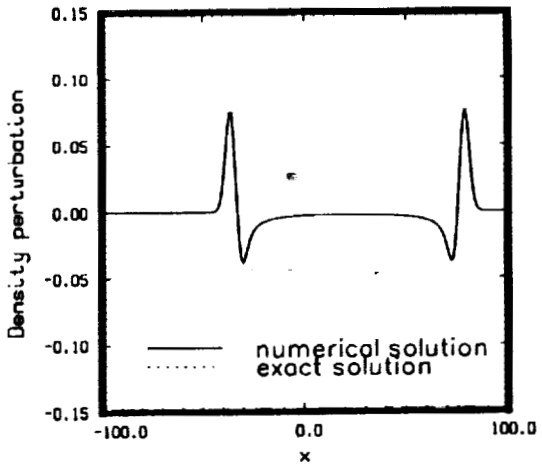

Density waveform along x-axis. t=60. (*Hu*)

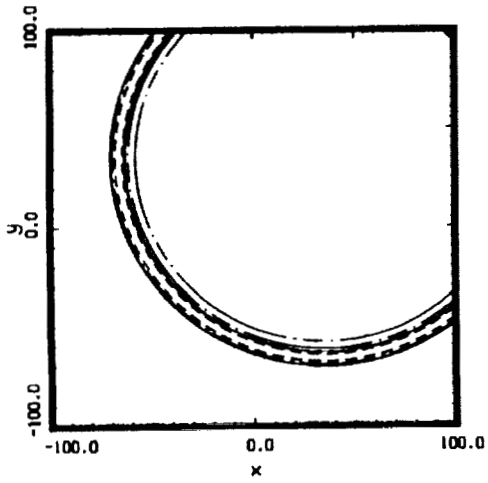

Density contours. t=100. (*Hu*)

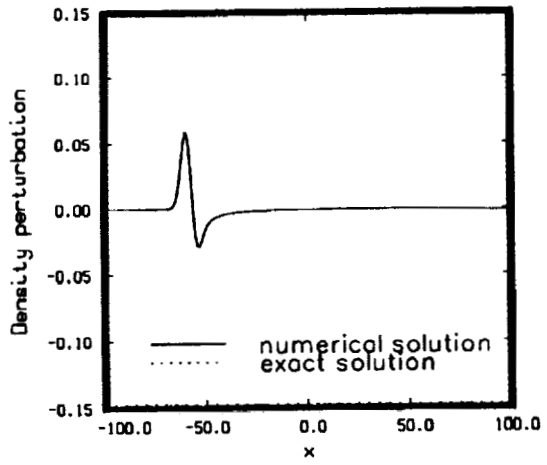

Density waveform along x-axis. t=100. (*Hu*)

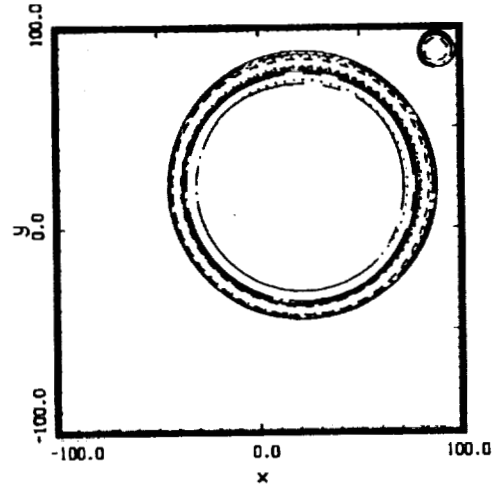

Density contours. t=60. (*Nark, I*)

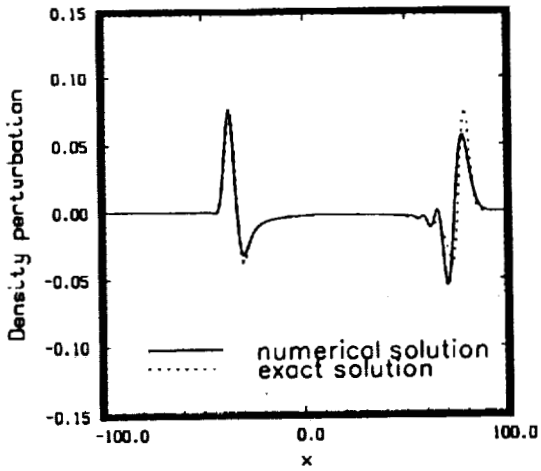

Density waveform along x-axis. t=60. (*Nark, I*)

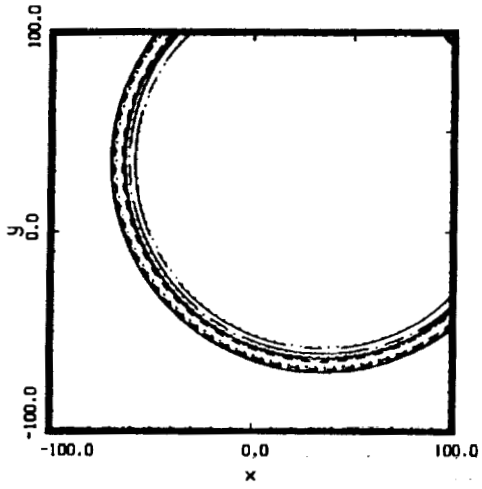

Density contours. t=100. (*Nark, 1*)

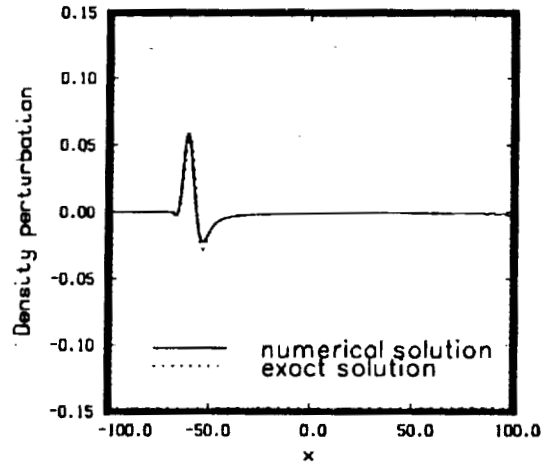

Density waveform along x-axis. t=100. (*Nark, 1*)

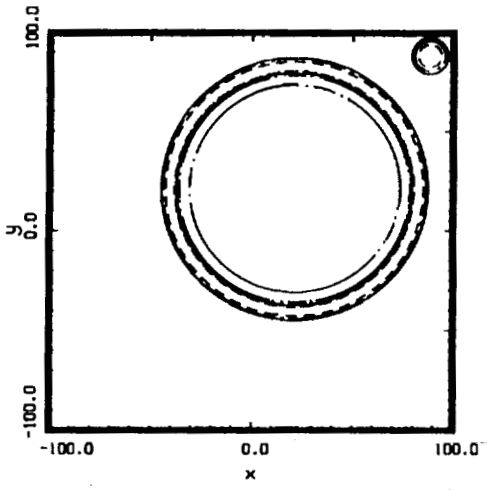

Density contours. t=60. (*Nark, 2*)

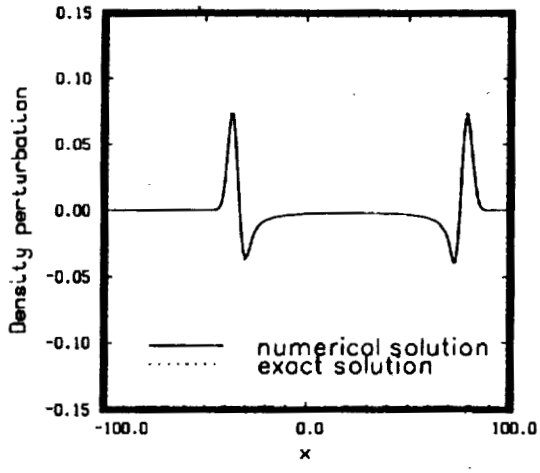

Density waveform along x-axis. t=60. (*Nark, 2*)

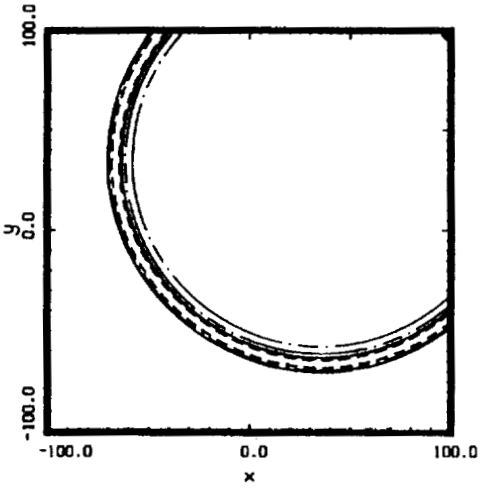

Density contours. t=100. (*Nark, 2*)

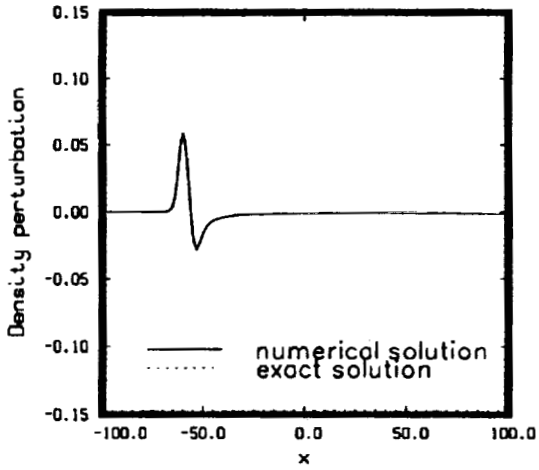

Density waveform along x-axis. t=100. (*Nark, 2*)

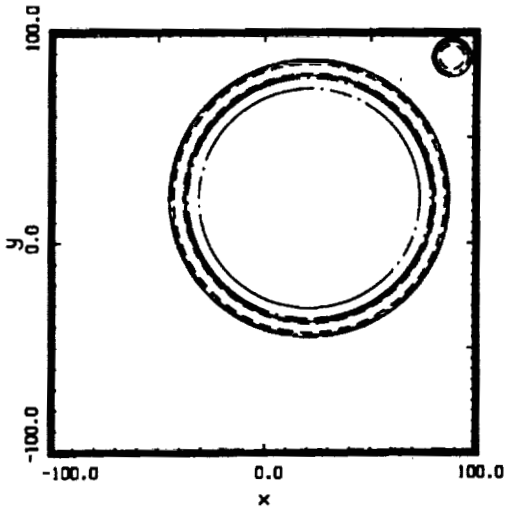

Density contours. t=60. (*Tam*)

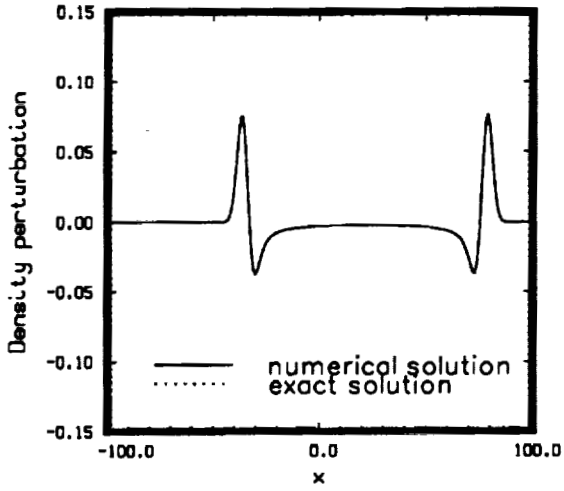

Density waveform along x-axis. t=60. (*Tam*)

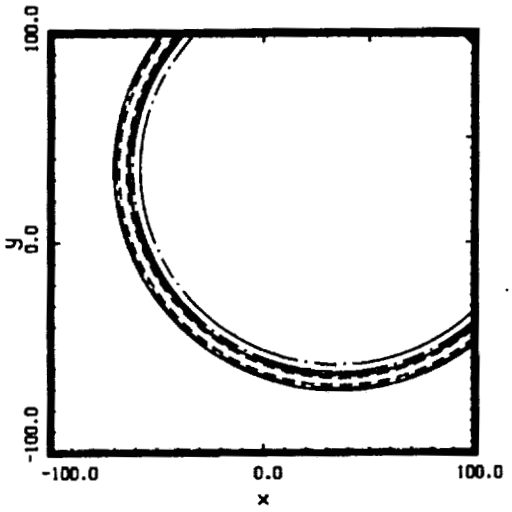

Density contours. t=60. (*Tam*)

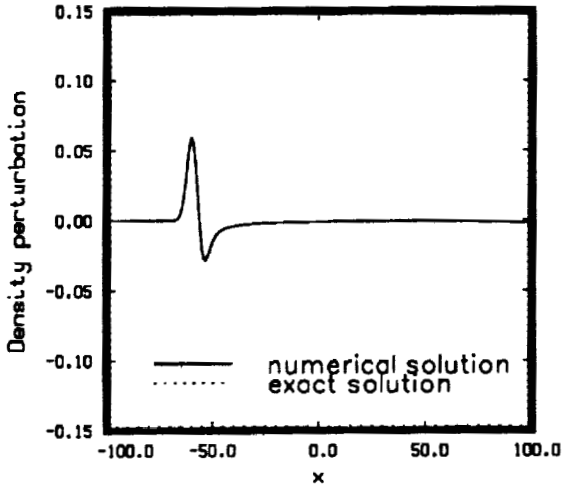

Density waveform along x-axis. t=100. (*Tam*)

Category 4, Problem 1

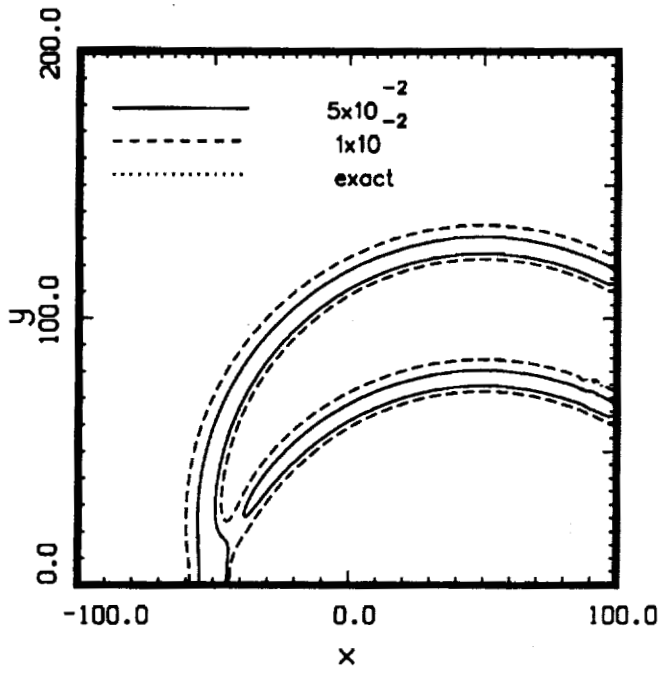

Pressure contours. t=100. (*Fung*)

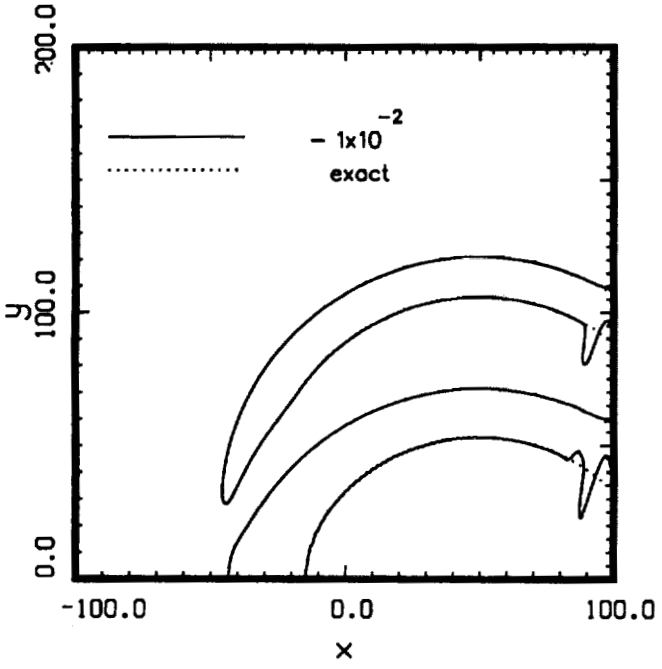

Pressure contours. t=100. (*Fung*)

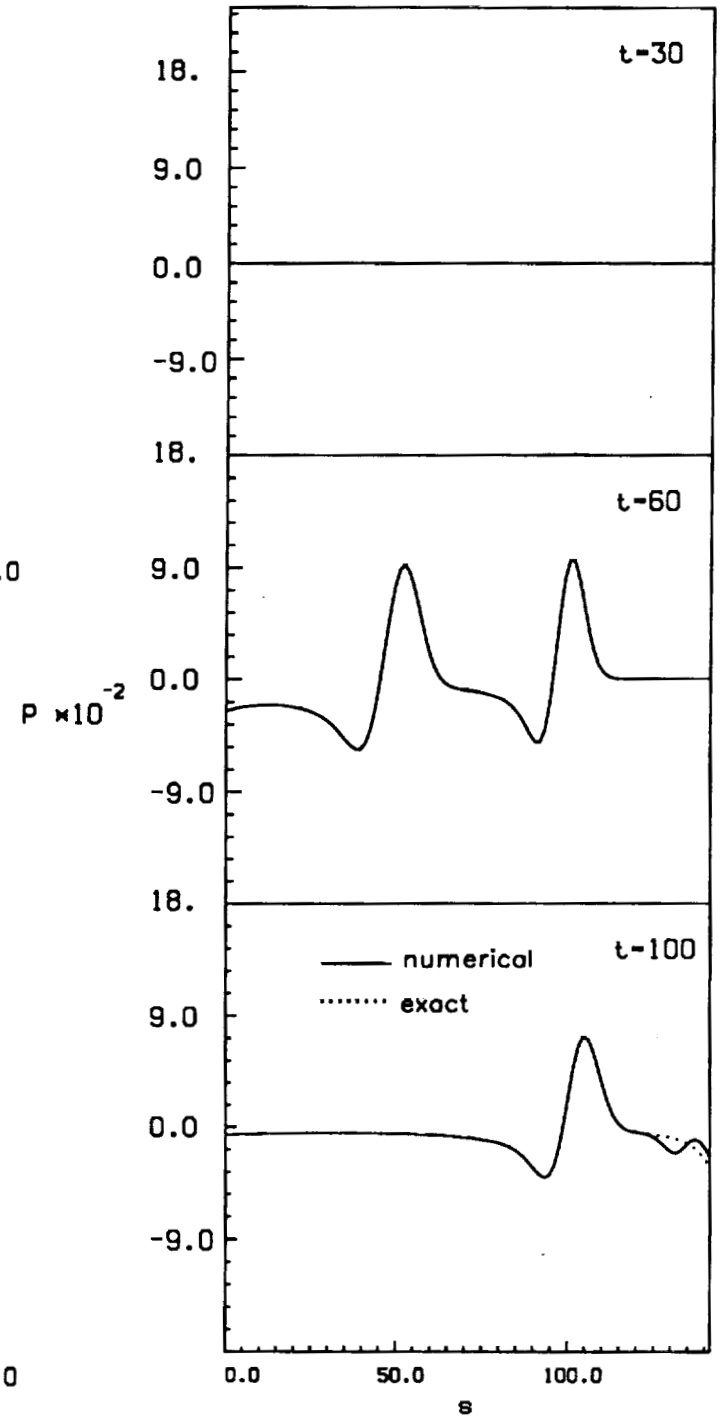

Pressure waveforms along the line x = y. (*Fung*)

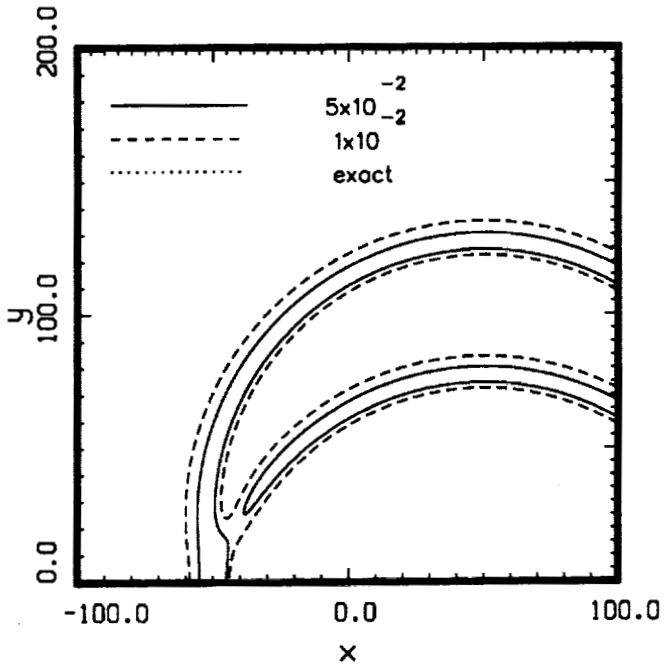

Pressure contours. t=100. (*Goodrich*)

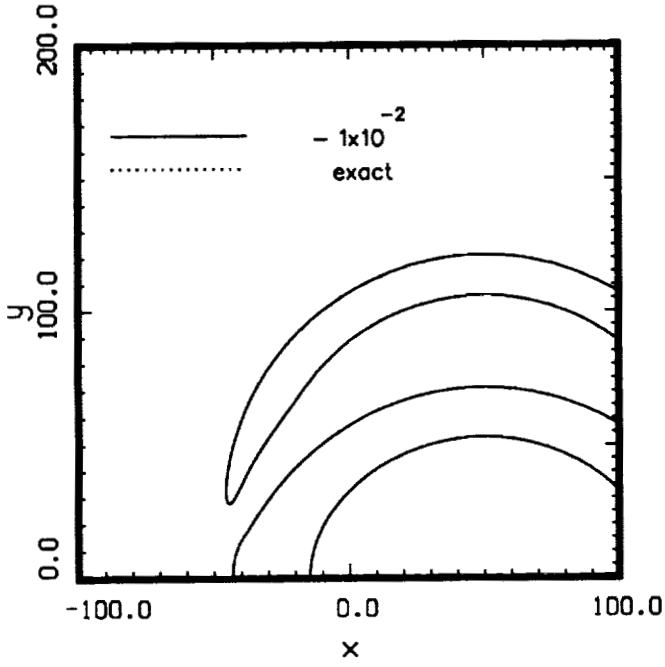

Pressure contours. t=100. (*Goodrich*)

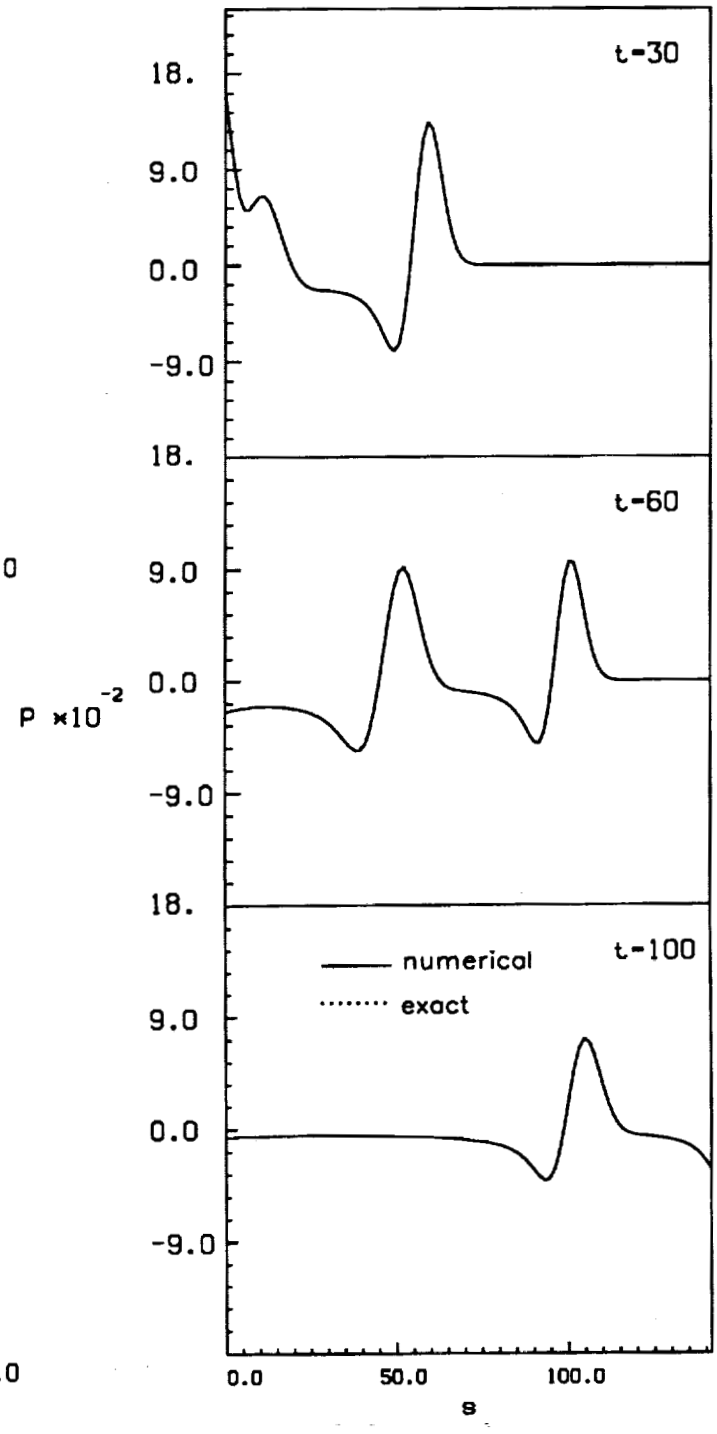

Pressure waveforms along the line x = y. (*Goodrich*)

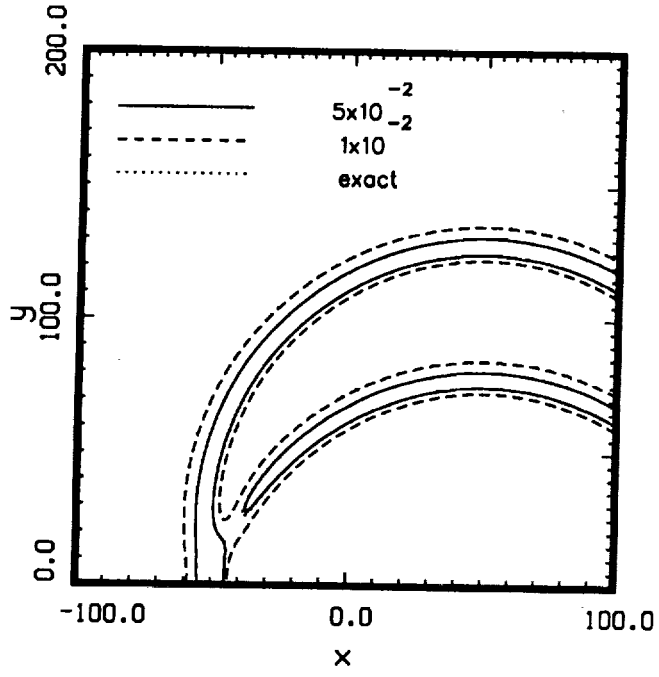

Pressure contours. t=100. (*Hu*)

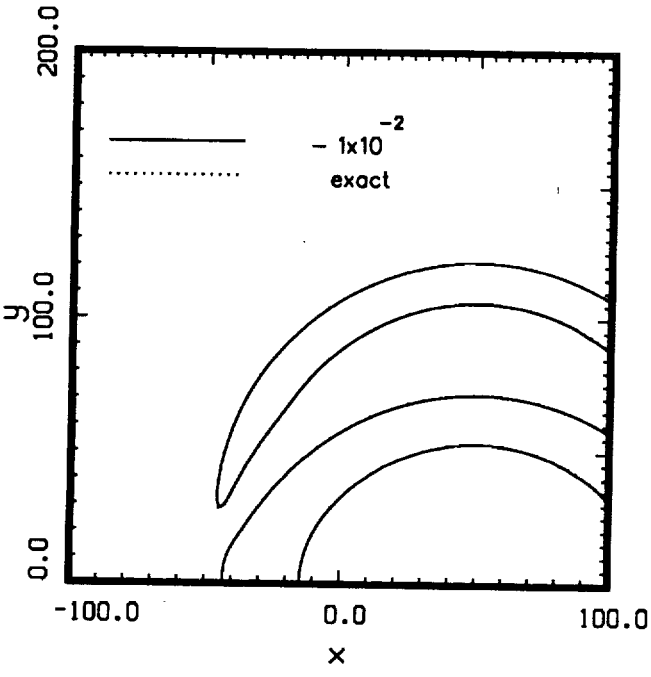

Pressure contours. t=100. (*Hu*)

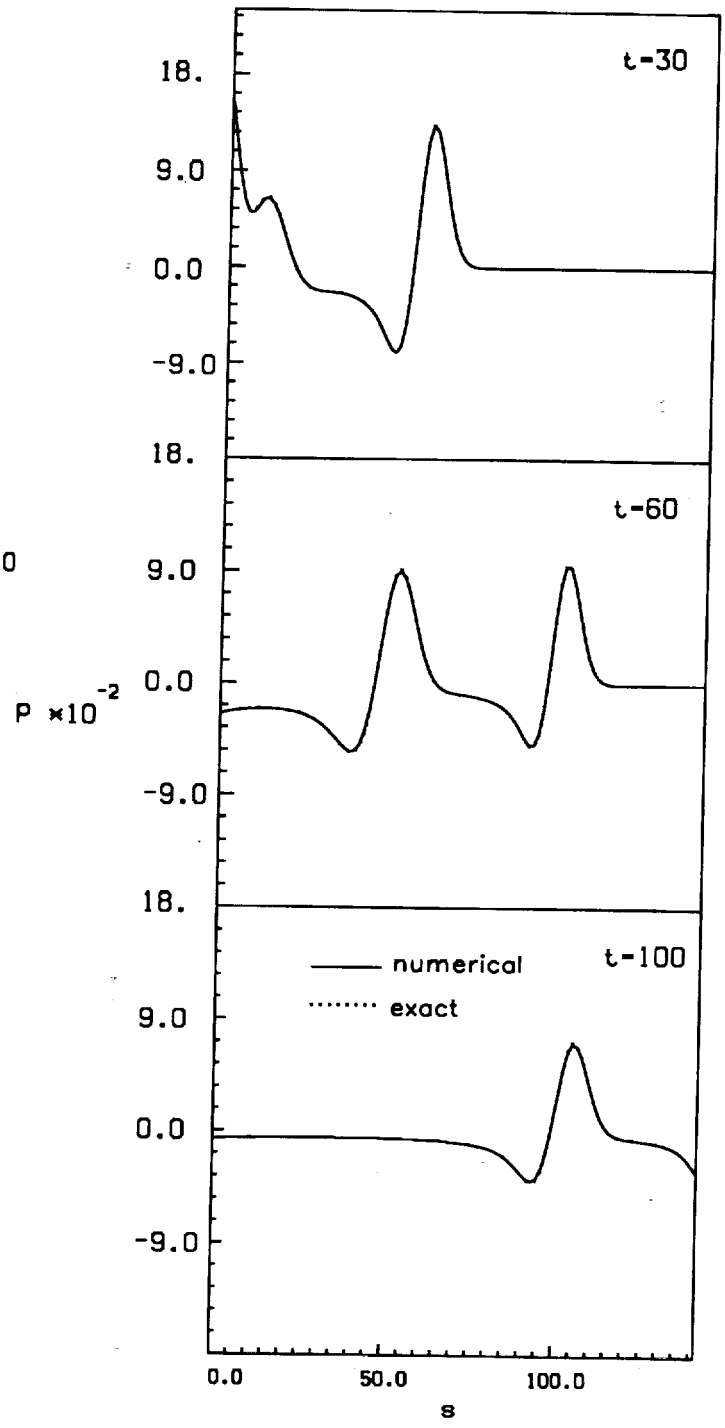

Pressure waveforms along the line x = y. (*Hu*)

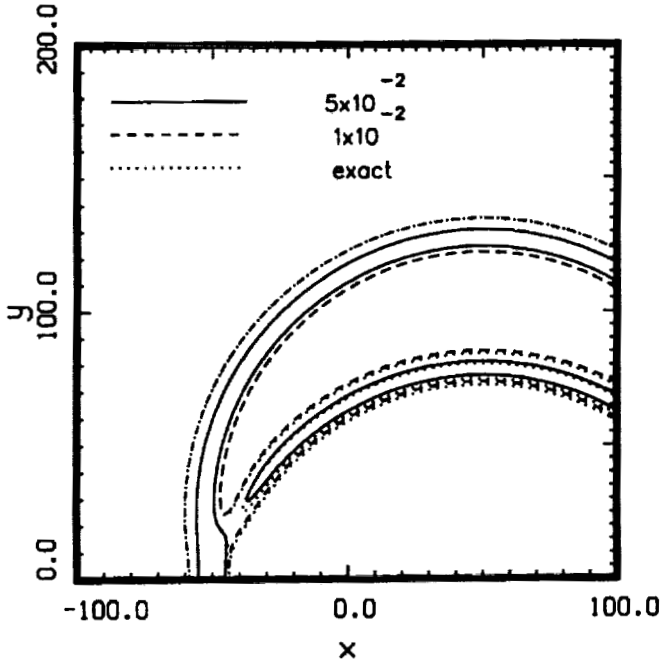

Pressure contours. t=100. (*Morris*)

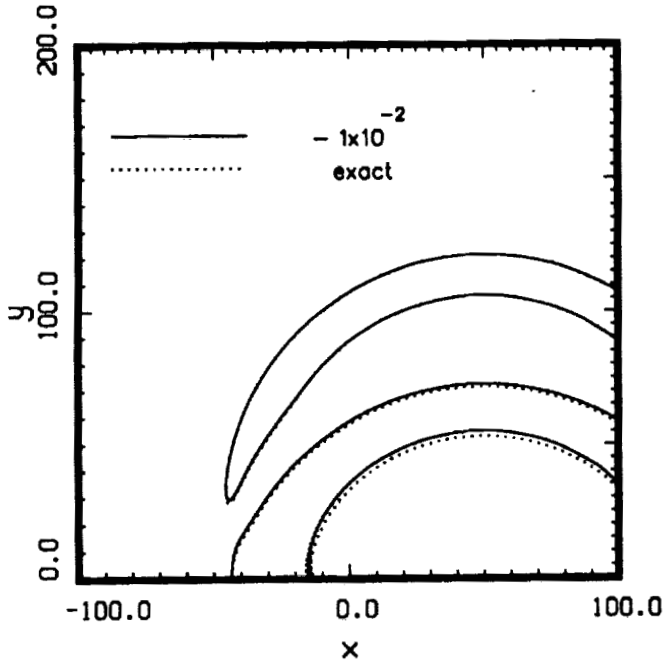

Pressure contours. t=100. (*Morris*)

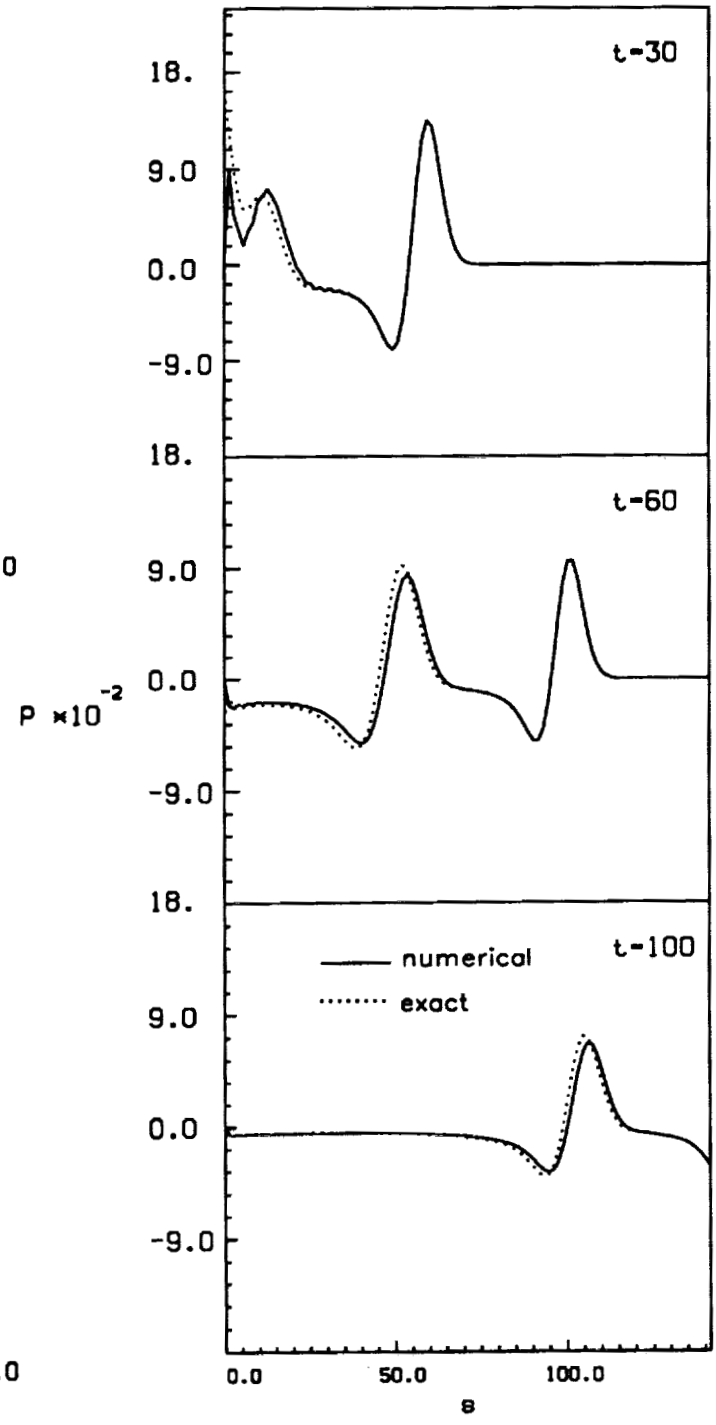

Pressure waveforms along the line x = y. (*Morris*)

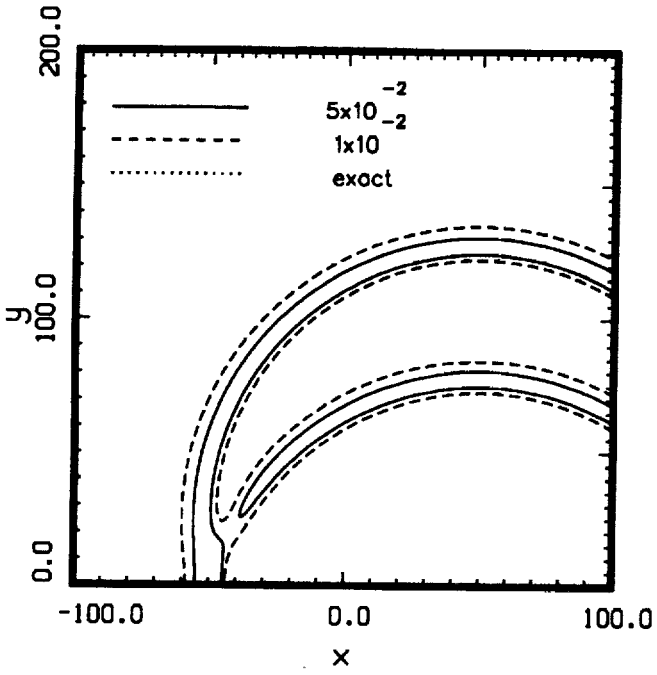

Pressure contours. t=100. (*Tam*)

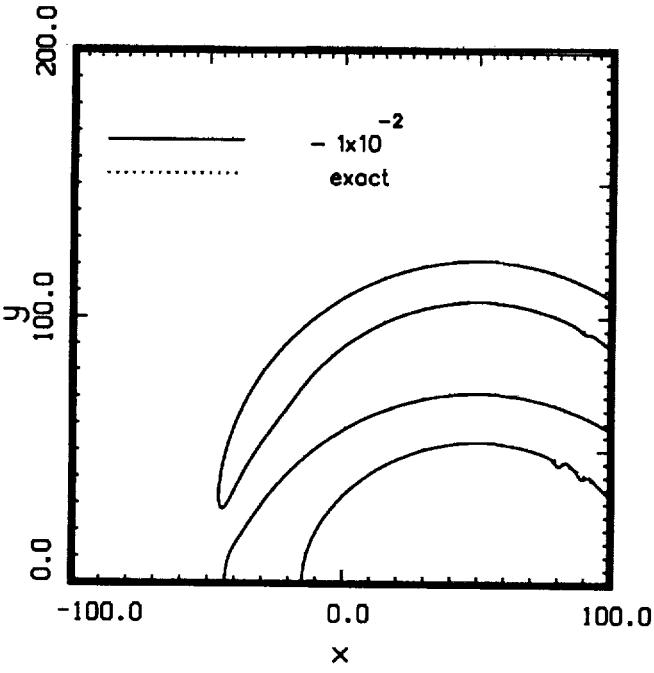

Pressure contours. t=100. (*Tam*)

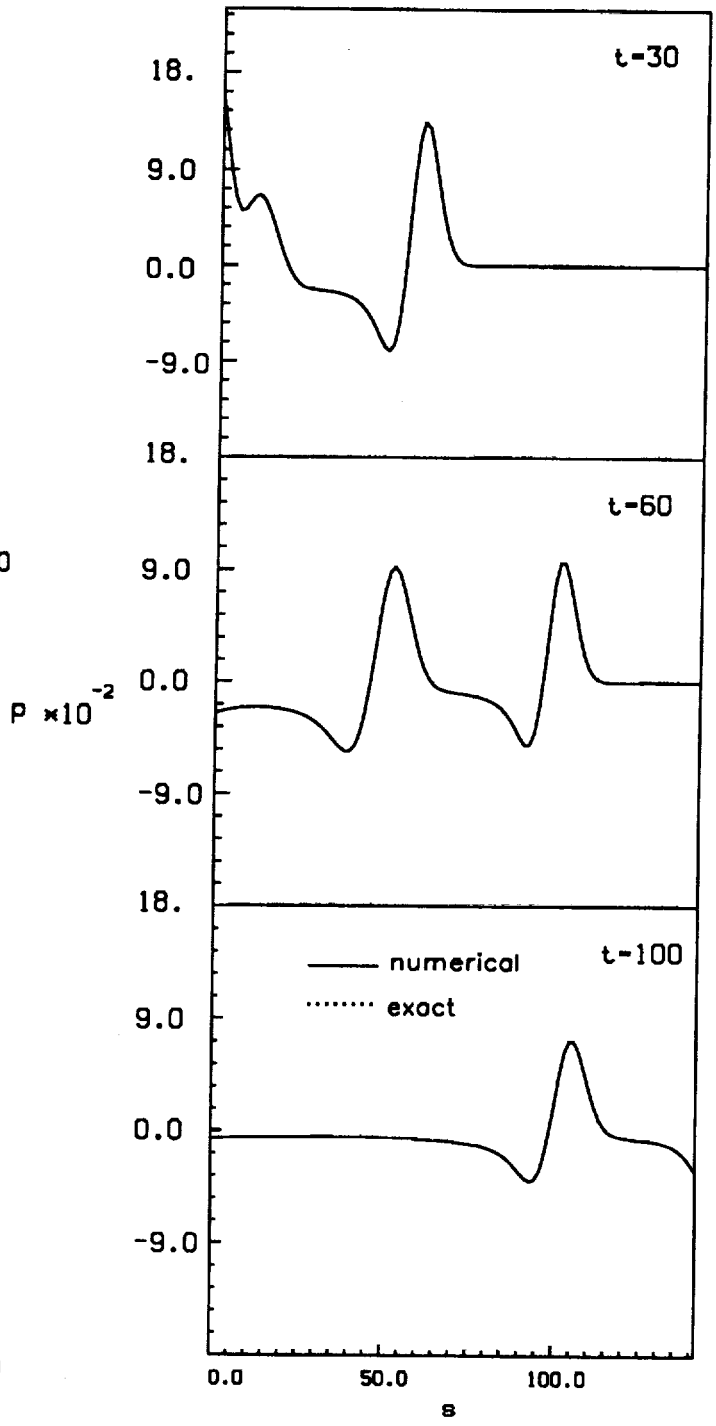

Pressure waveforms along the line x = y. (*Tam*)

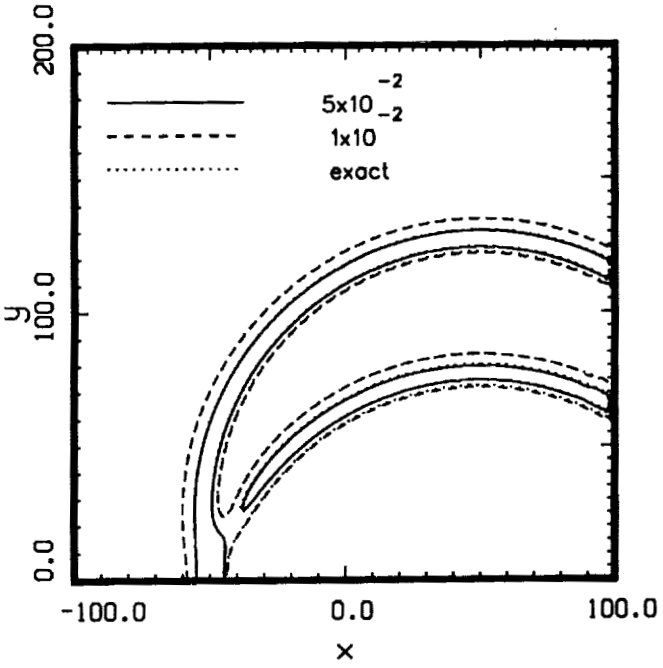

Pressure contours. t=100. (*Viswanathan*)

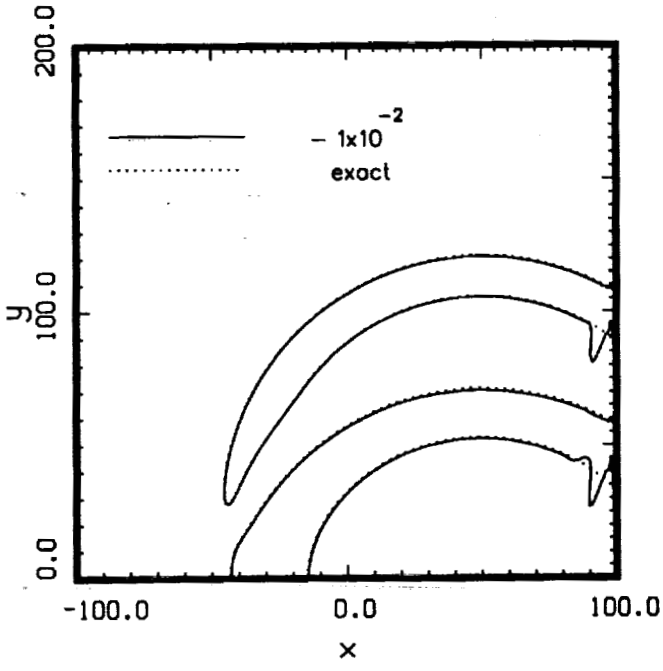

Pressure contours. t=100. (*Viswanathan*)

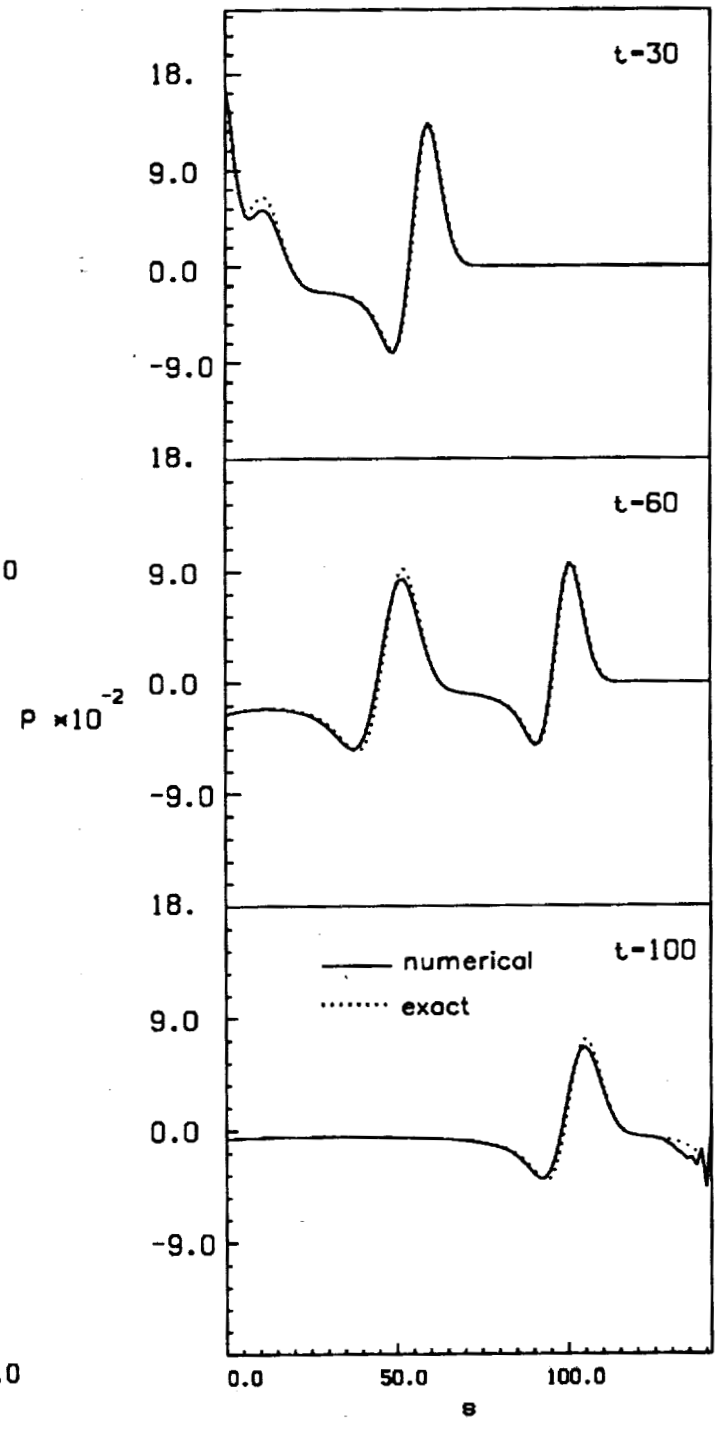

Pressure waveforms along the line x = y. (*Viswanathan*)

Category 4, Problem 2

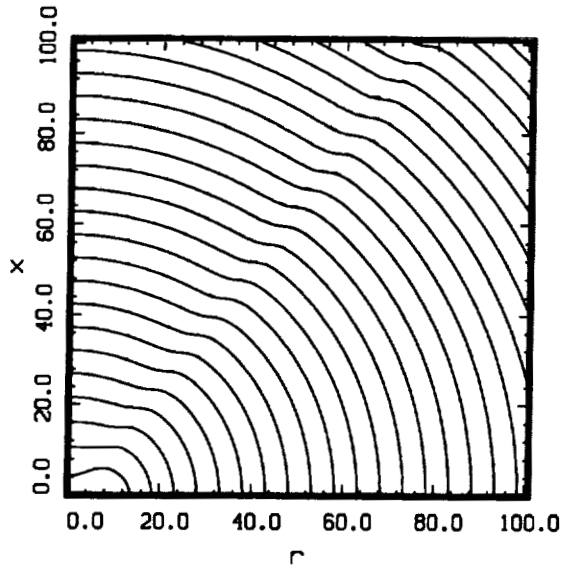

Pressure contours (p = 0) at the beginning of a cycle. (*Caruthers*)

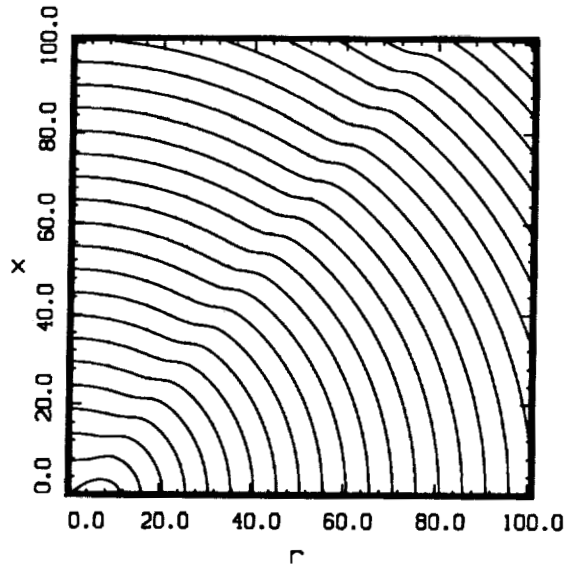

Pressure contours (p = 0) at one quarter of the cycle period. (*Caruthers*)

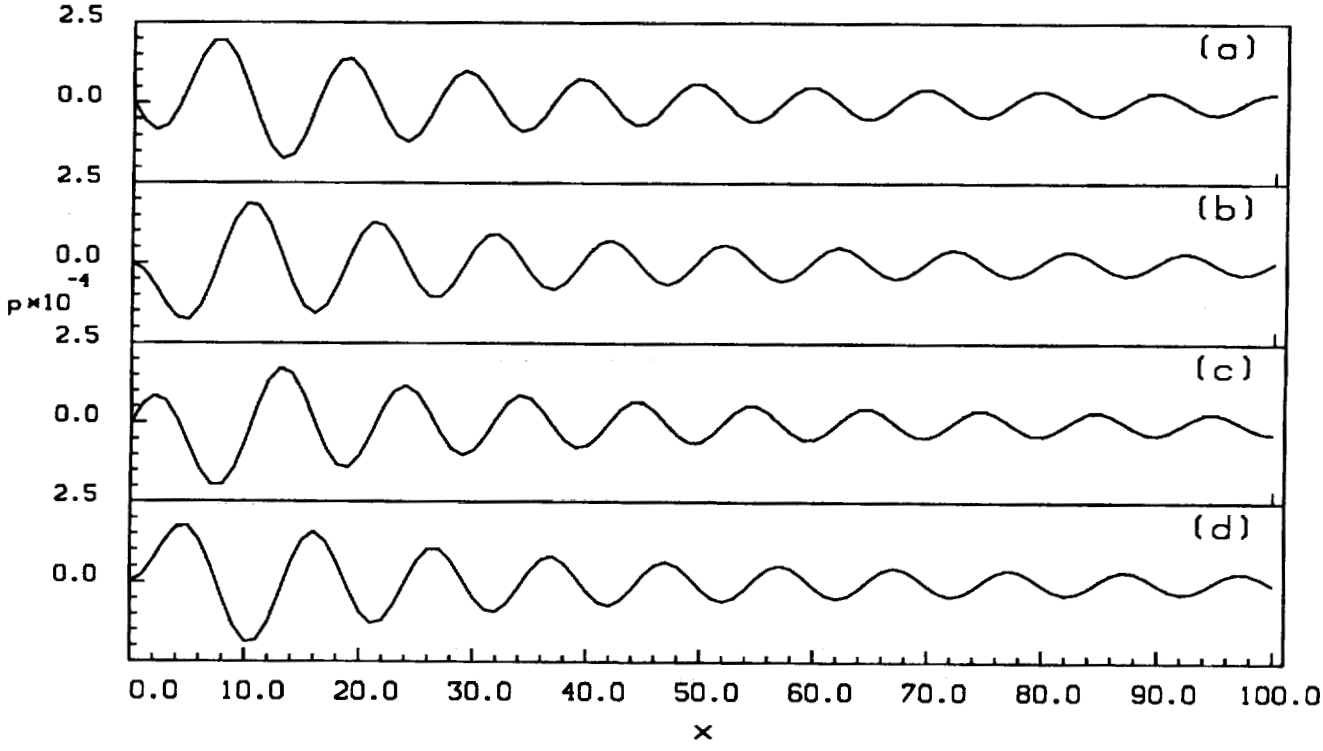

Pressure distribution along the axis (r = 0) of the piston at: (*Caruthers*)

(a) the beginning of a cycle,
(b) one quarter of a cycle,
(c) half a cycle,
(d) three quarters of a cycle.

——— **numerical**
- - - - - **exact**

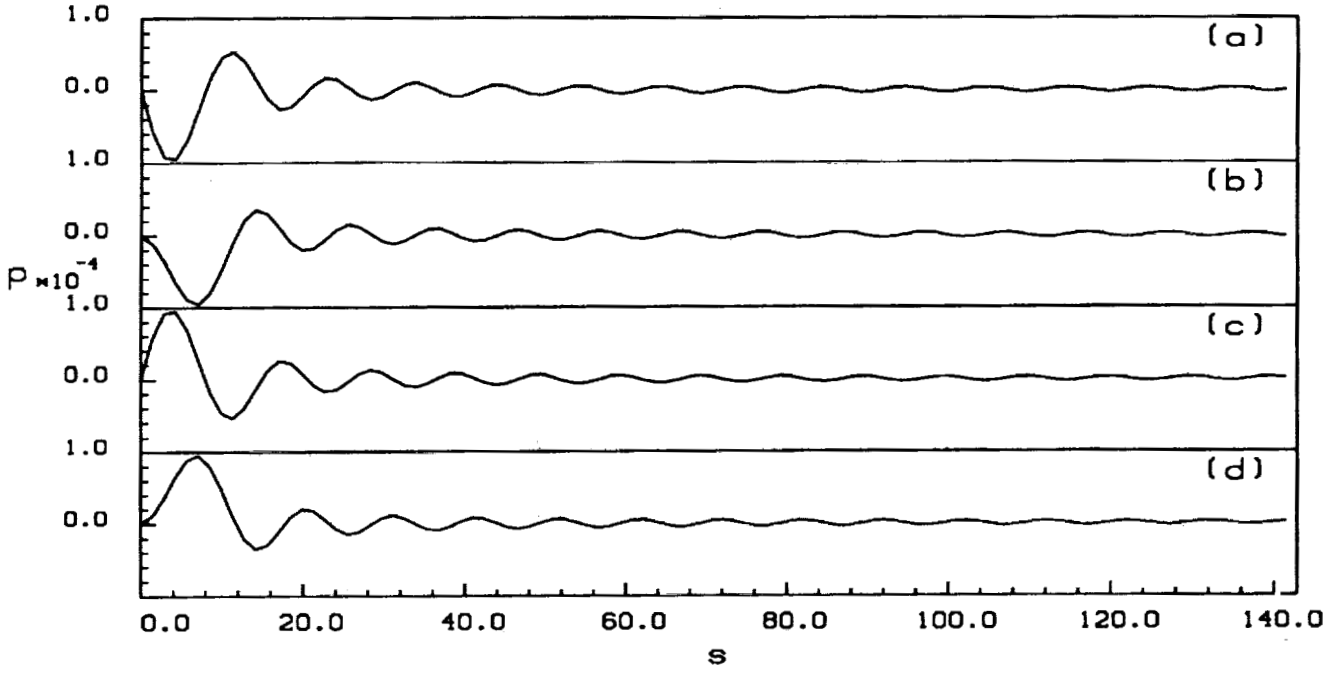

Pressure distribution along the line (r = x). (*Caruthers*)

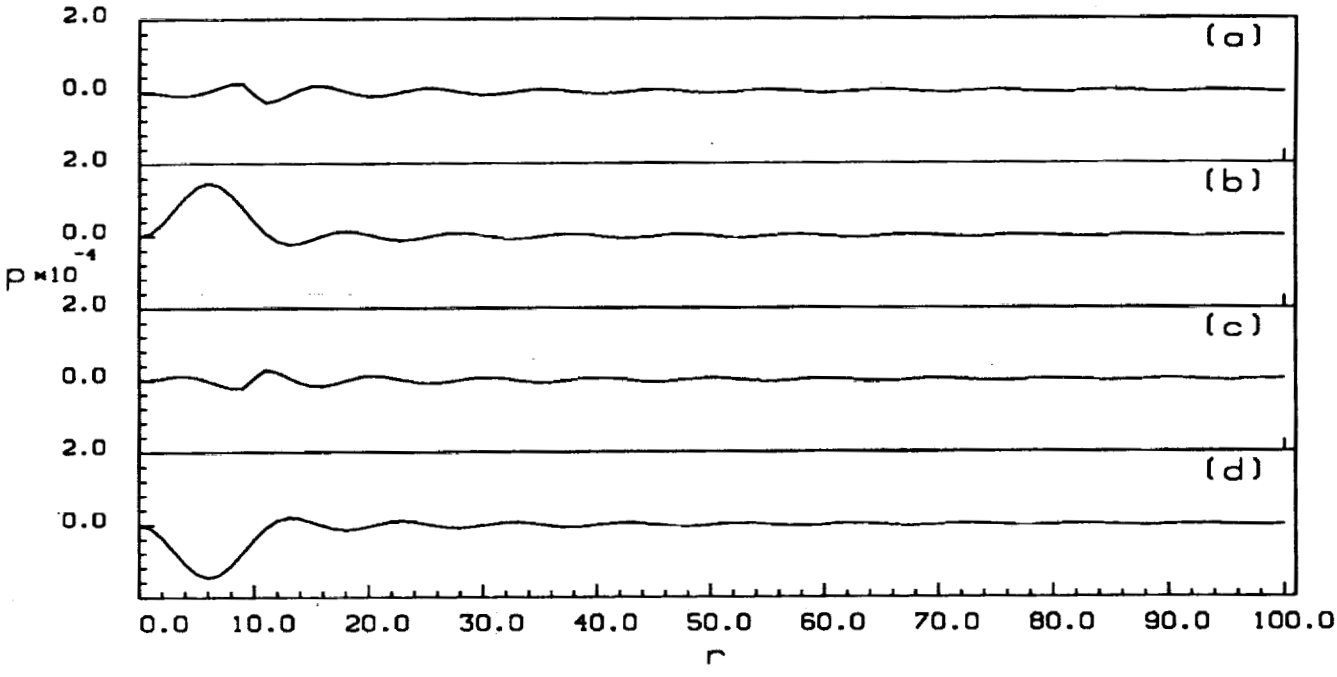

Pressure distribution along the wall (x = 0). (*Caruthers*)

(a) the beginning of a cycle,
(b) one quarter of a cycle,
(c) half a cycle,
(d) three quarters of a cycle.

——— **numerical**
- - - - - **exact**

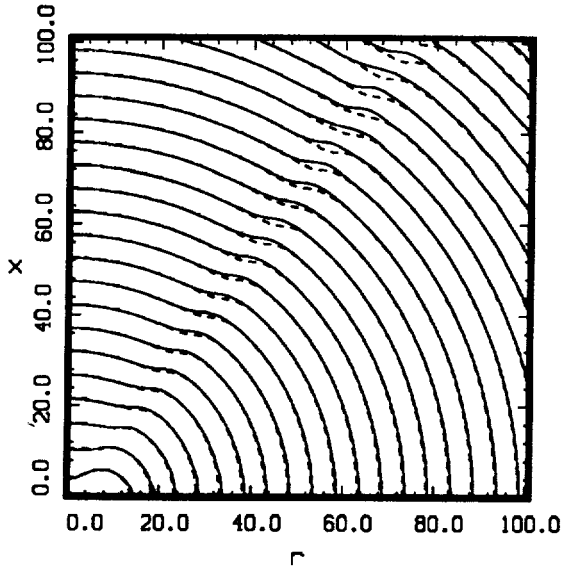

Pressure contours (p = 0) at the beginning of a cycle. (*Fung*)

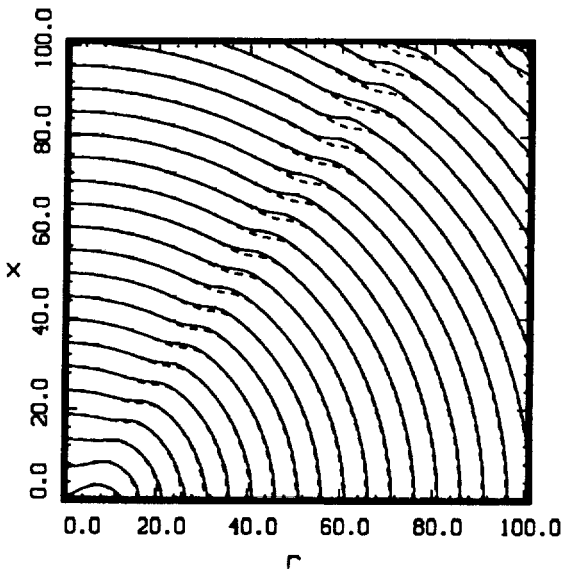

Pressure contours (p = 0) at one quarter of the cycle period. (*Fung*)

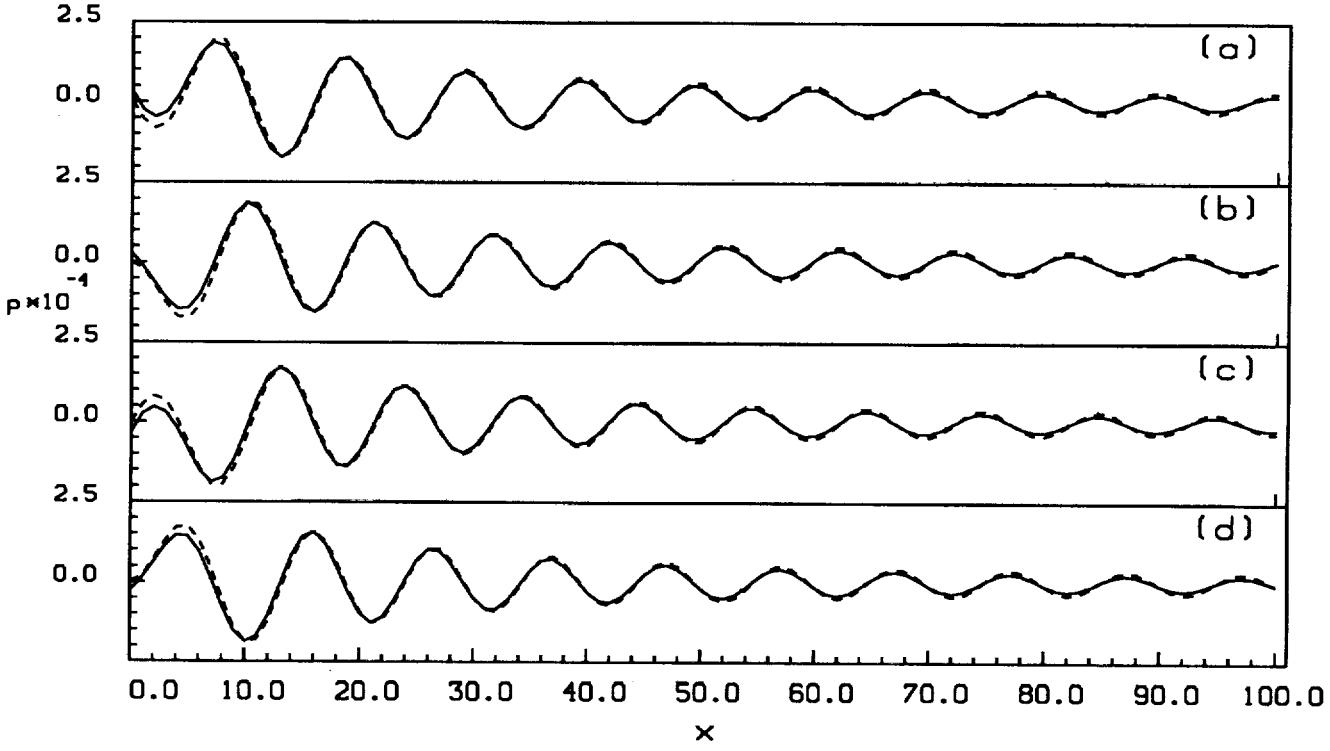

Pressure distribution along the axis (r = 0) of the piston at: (*Fung*)

(a) the beginning of a cycle,
(b) one quarter of a cycle,
(c) half a cycle,
(d) three quarters of a cycle.

——— **numerical**
- - - - - **exact**

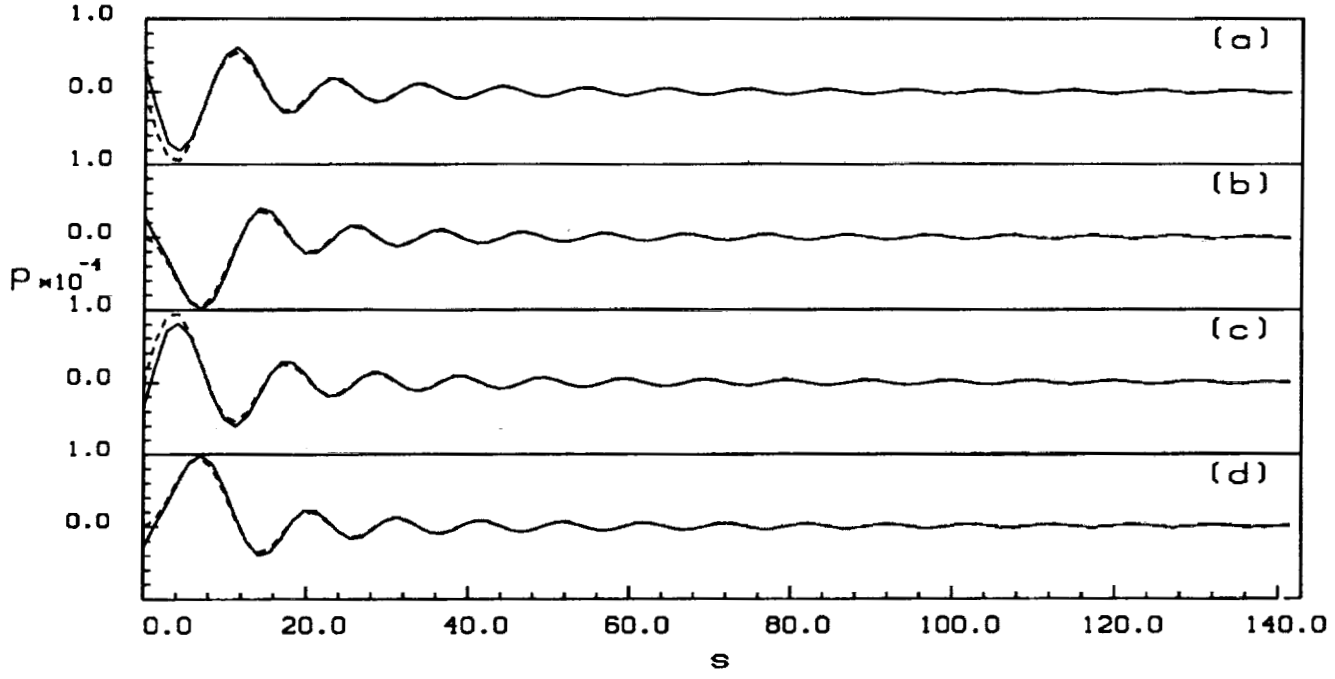

Pressure distribution along the line (r = x). (*Fung*)

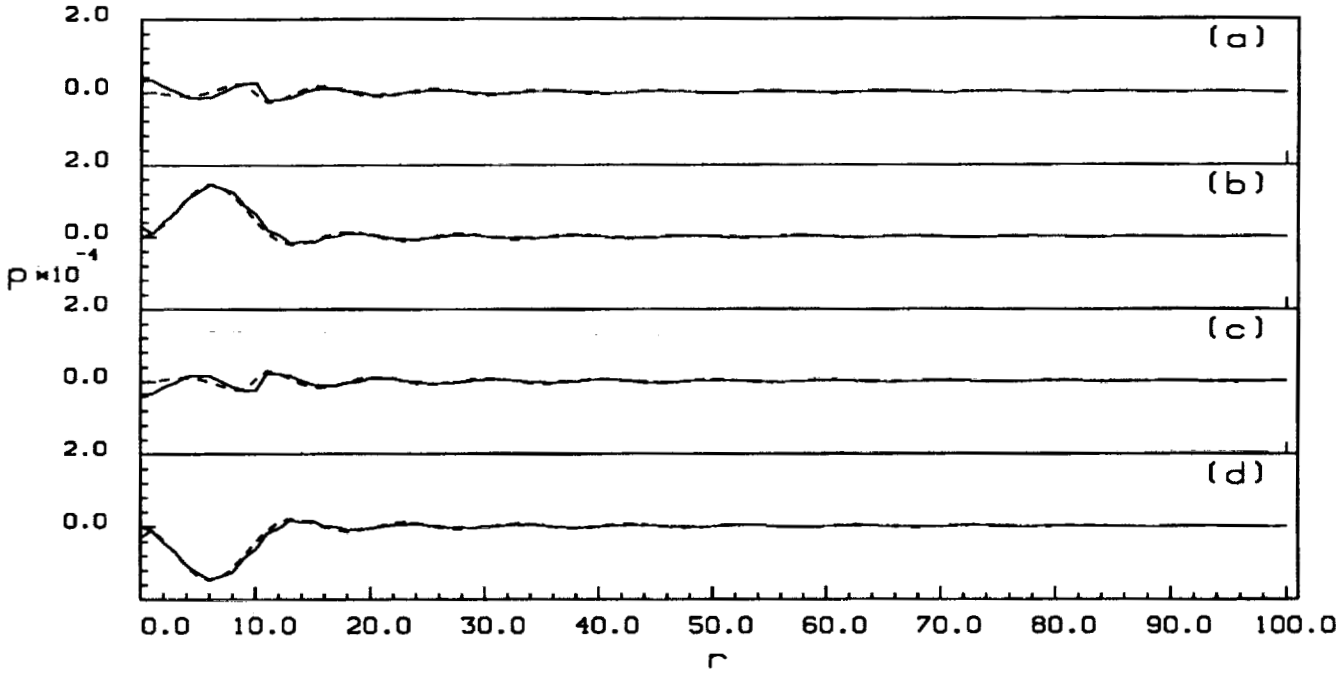

Pressure distribution along the wall (x = 0). (*Fung*)

(a) the beginning of a cycle,
(b) one quarter of a cycle,
(c) half a cycle,
(d) three quarters of a cycle.

——— **numerical**
- - - - - **exact**

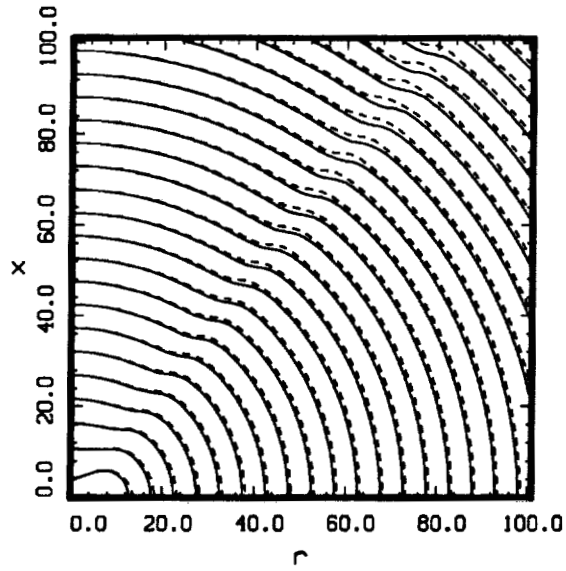

Pressure contours (p = 0) at the beginning of a cycle. (*Lafon*)

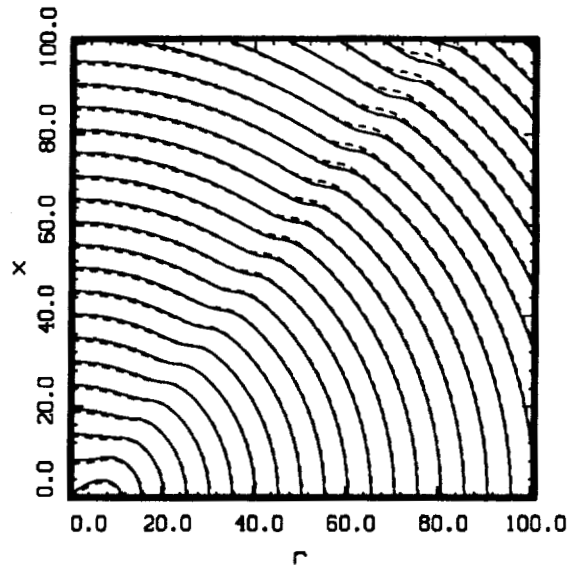

Pressure contours (p = 0) at one quarter of the cycle period. (*Lafon*)

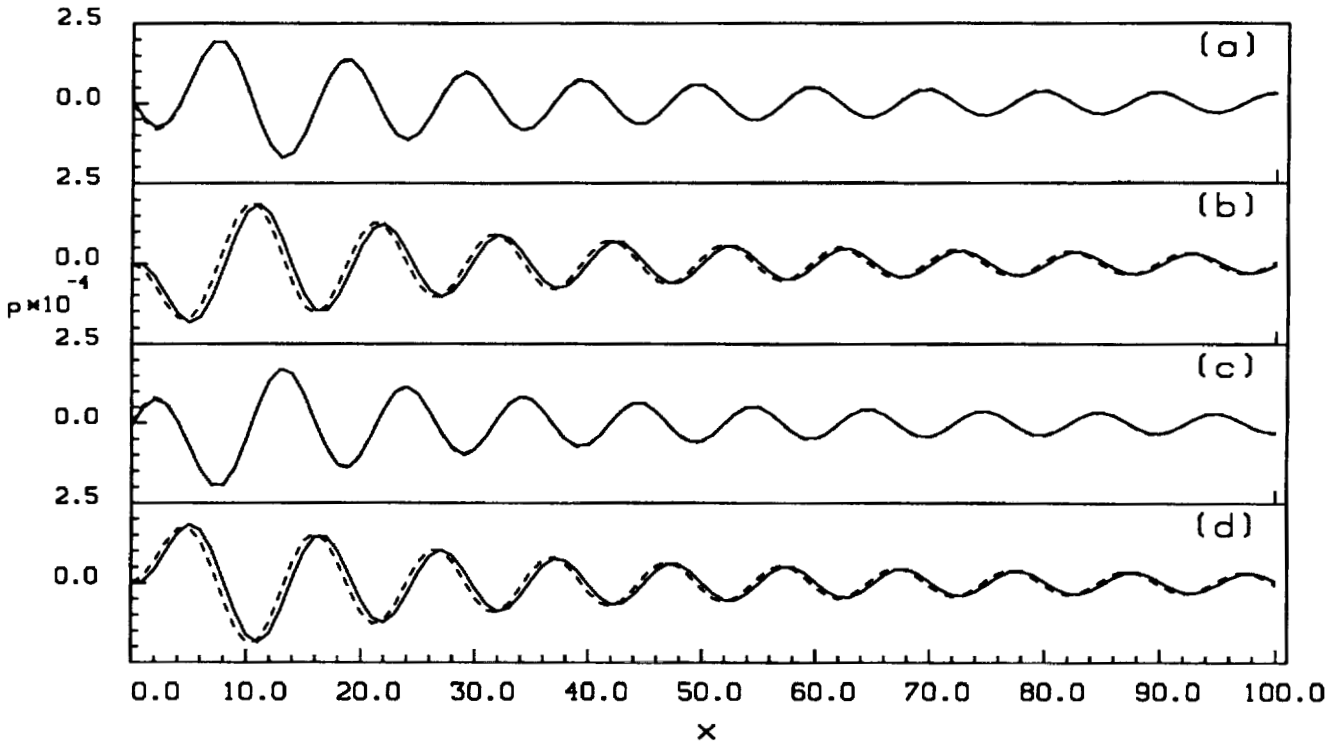

Pressure distribution along the axis (r = 0) of the piston at: (*Lafon*)

(a) the beginning of a cycle,
(b) one quarter of a cycle,
(c) half a cycle,
(d) three quarters of a cycle.

——— **numerical**
- - - - - **exact**

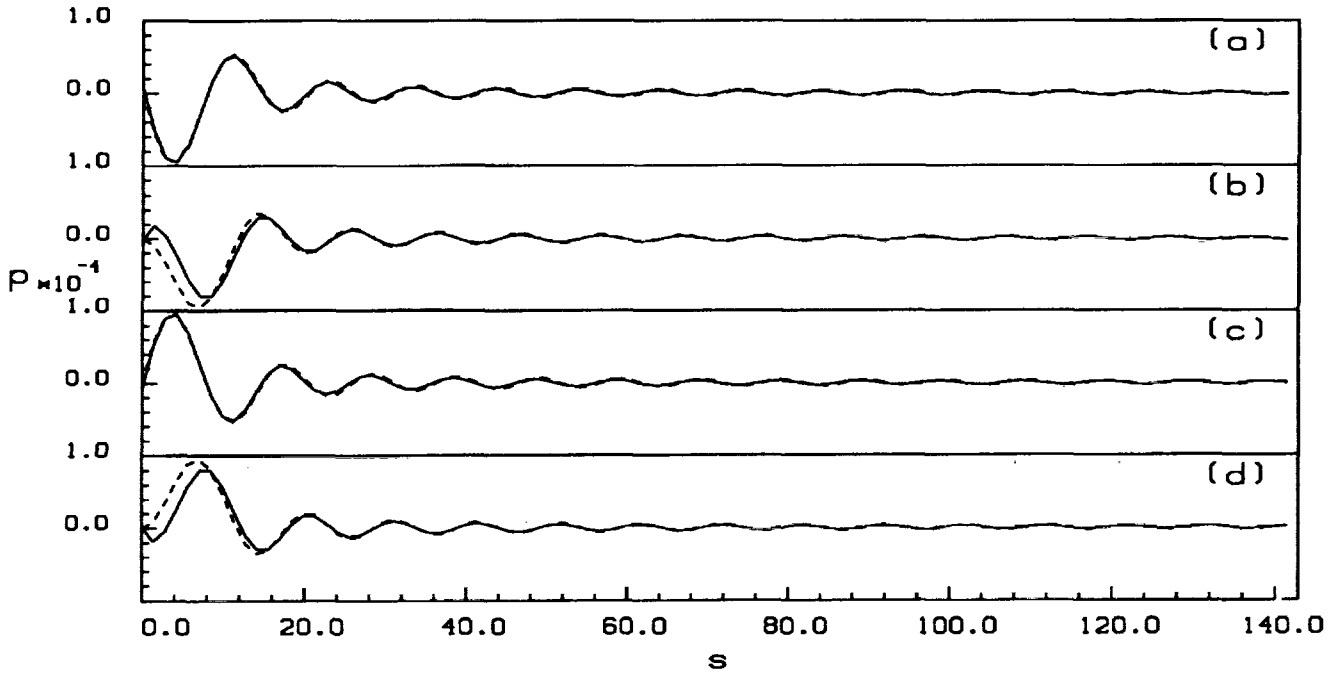

Pressure distribution along the line (r = x). (*Lafon*)

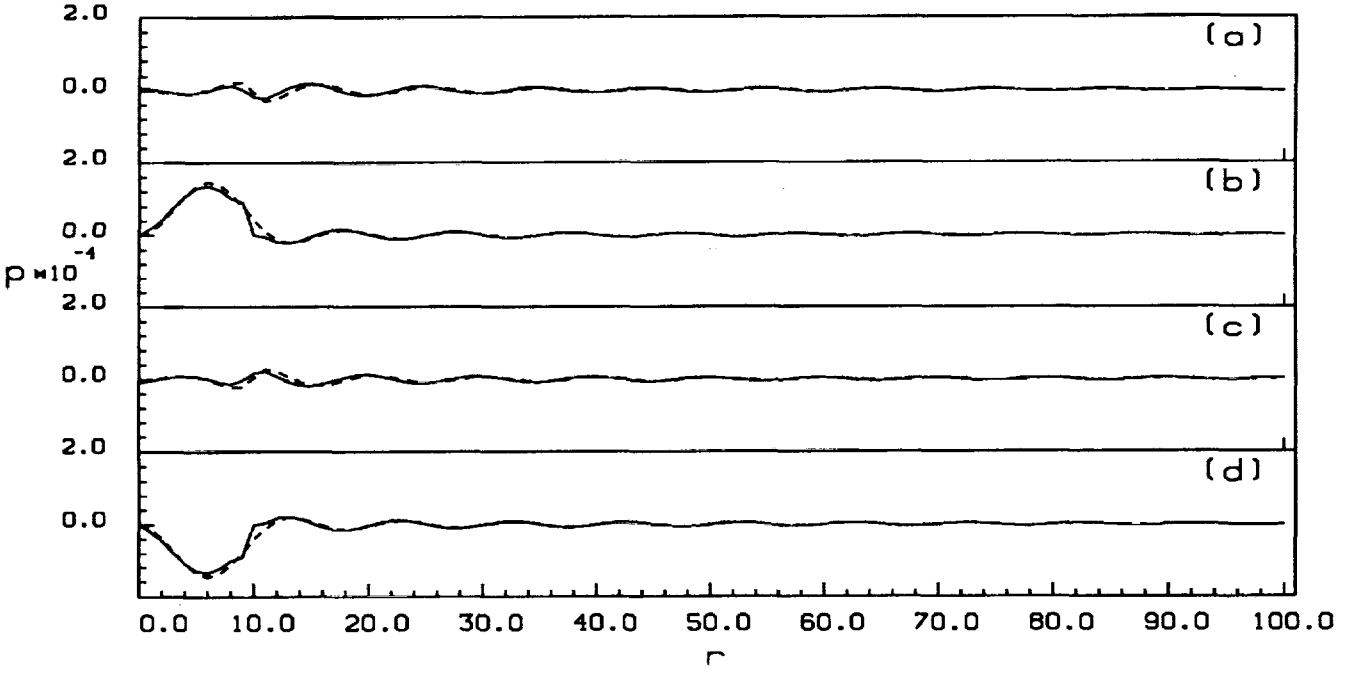

Pressure distribution along the wall (x = 0). (*Lafon*)

(a) the beginning of a cycle,
(b) one quarter of a cycle,
(c) half a cycle,
(d) three quarters of a cycle.

——— **numerical**
- - - - - **exact**

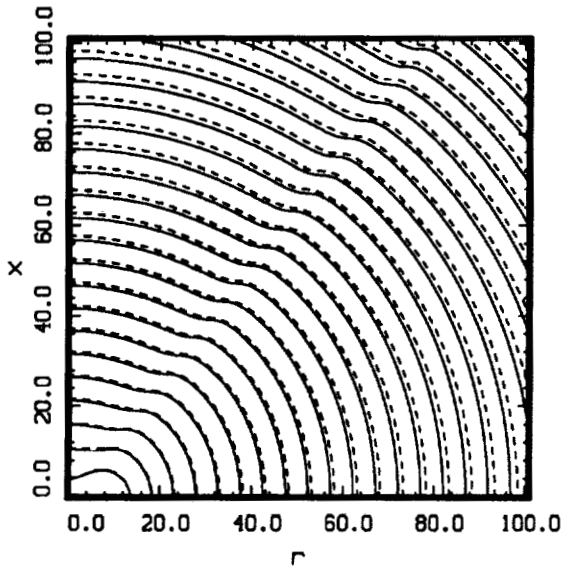

Pressure contours (p = 0) at the beginning of a cycle. (*Nark, 1*)

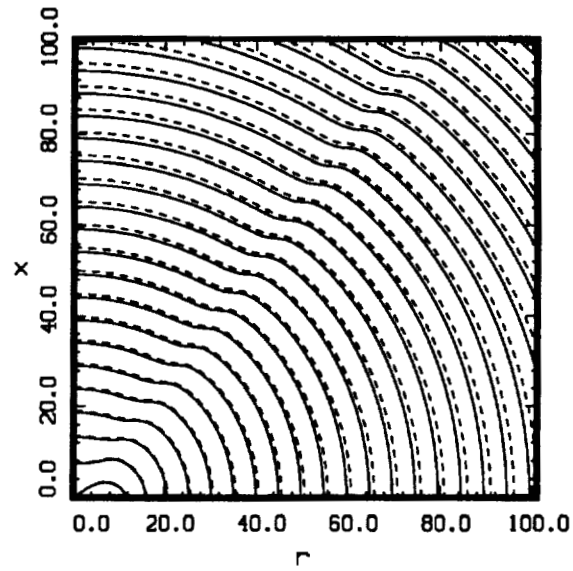

Pressure contours (p = 0) at one quarter of the cycle period. (*Nark, 1*)

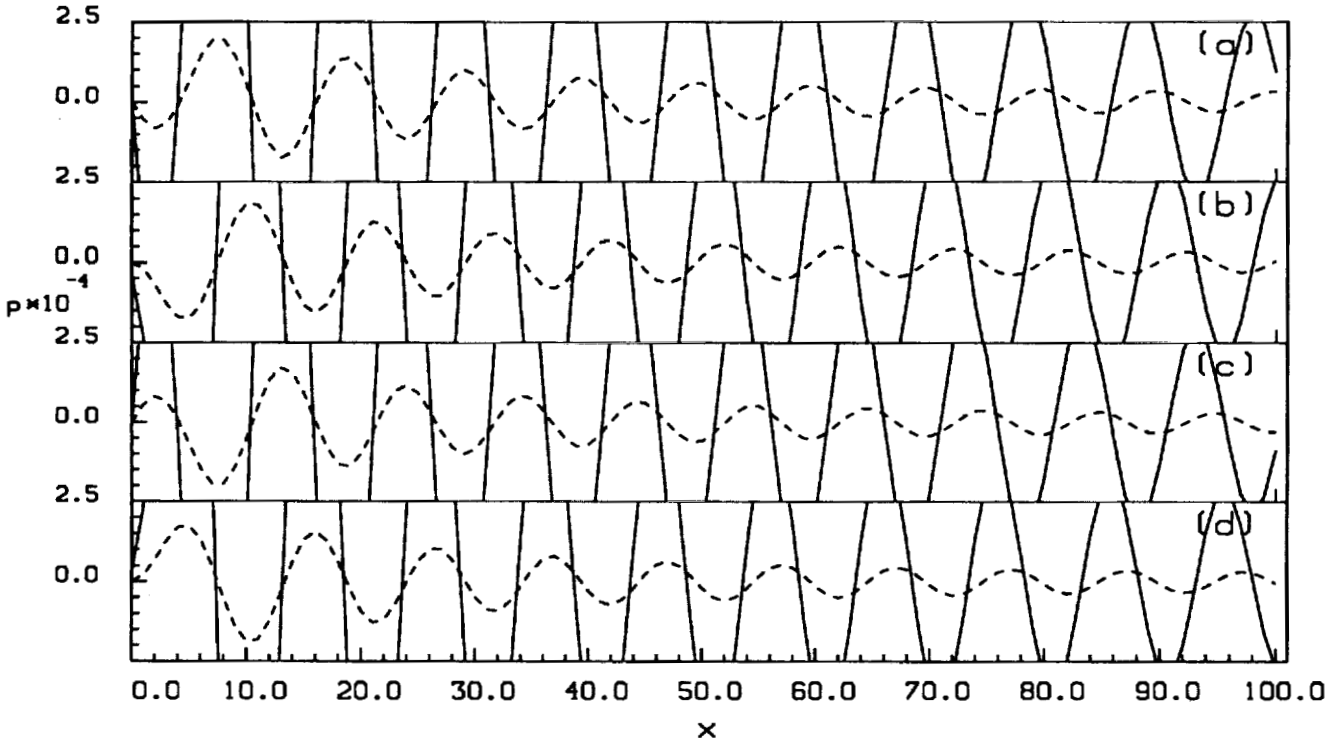

Pressure distribution along the axis (r = 0) of the piston at: (*Nark, 1*)

(a) the beginning of a cycle,
(b) one quarter of a cycle,
(c) half a cycle,
(d) three quarters of a cycle.

——— **numerical**
- - - - - **exact**

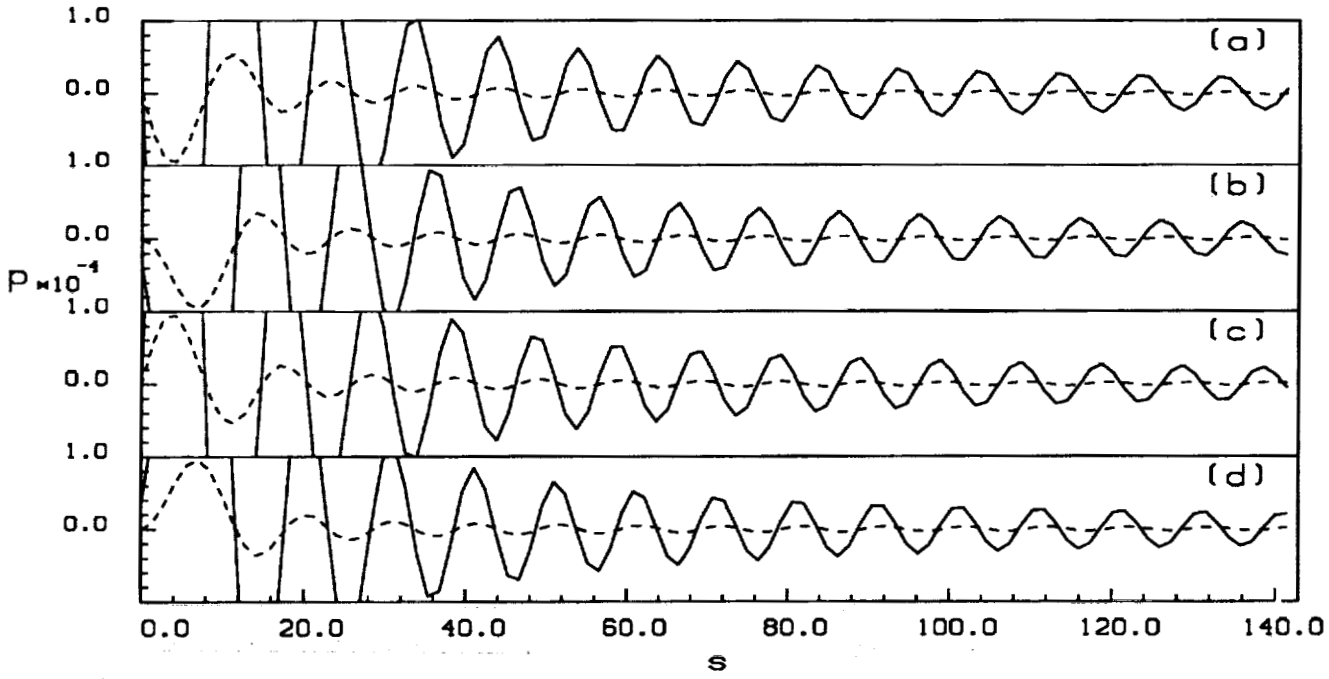

Pressure distribution along the line (r = x). (*Nark, 1*)

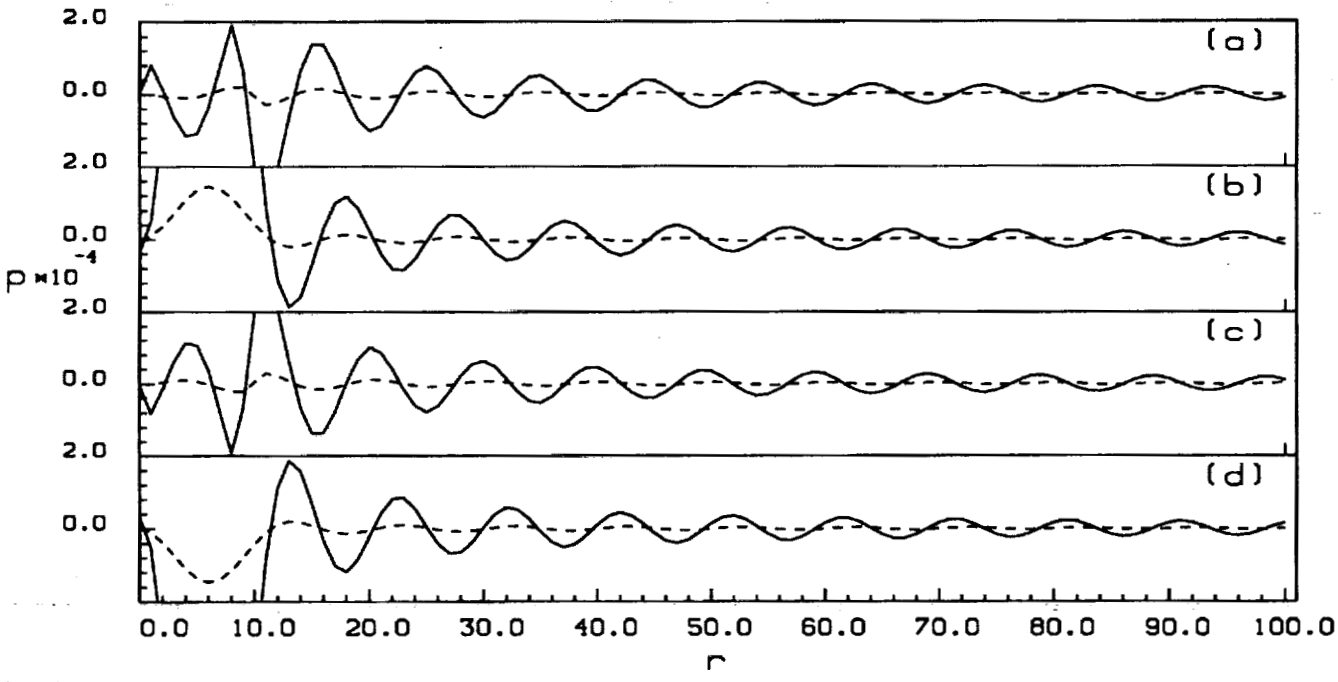

Pressure distribution along the wall (x = 0). (*Nark, 1*)

(a) the beginning of a cycle,
(b) one quarter of a cycle,
(c) half a cycle,
(d) three quarters of a cycle.

——— **numerical**
- - - - - **exact**

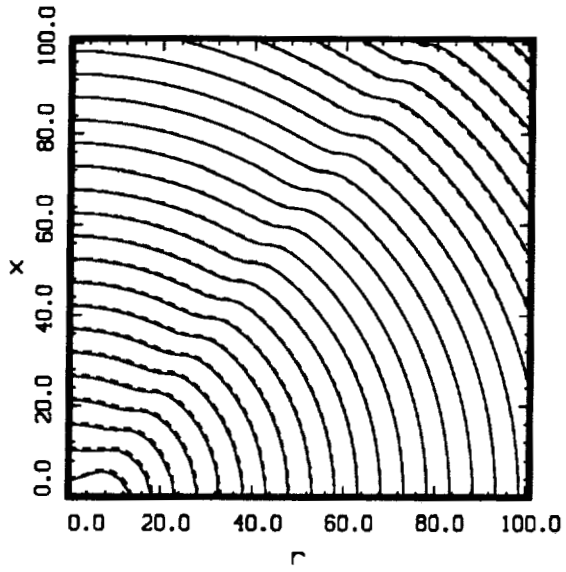

Pressure contours (p = 0) at the beginning of a cycle. (*Ozyoruk*)

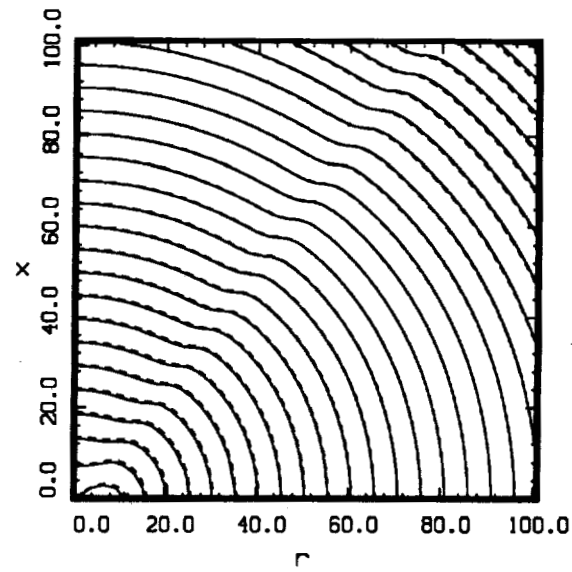

Pressure contours (p = 0) at one quarter of the cycle period. (*Ozyoruk*)

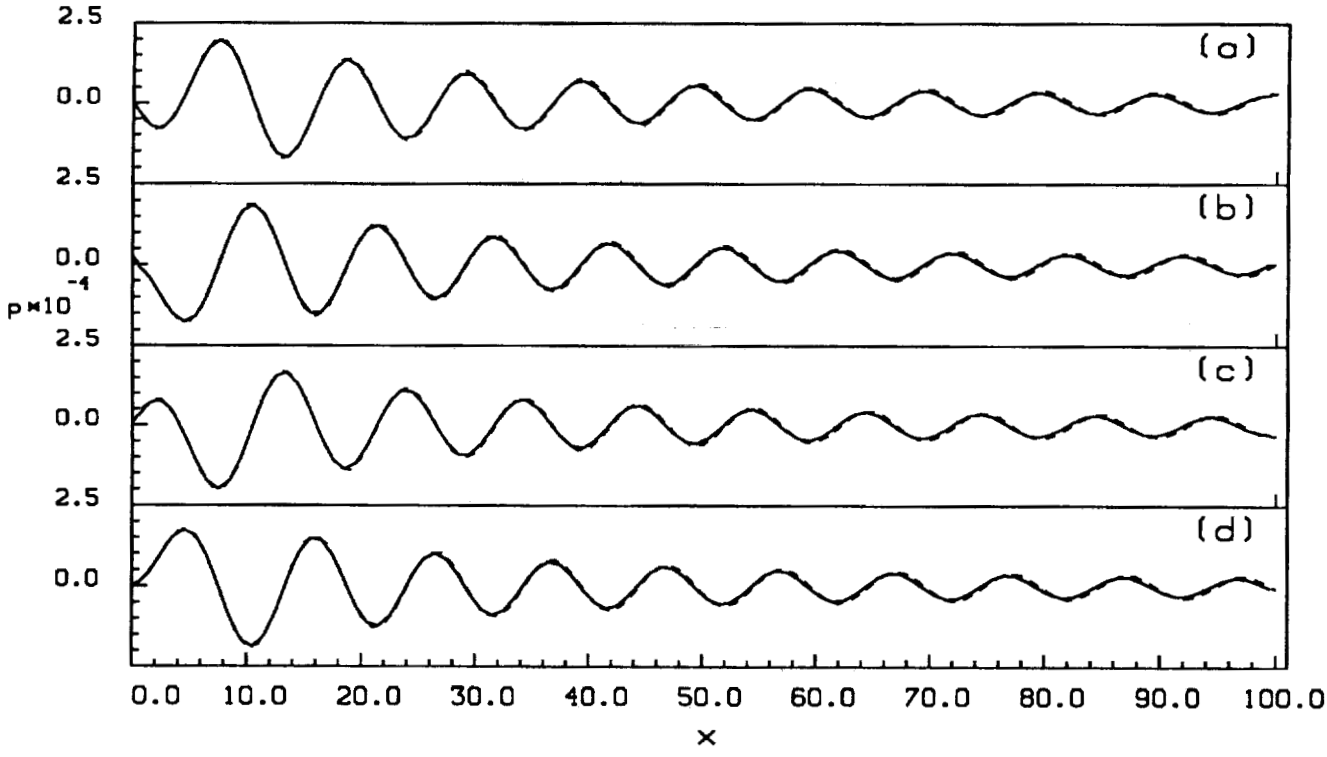

Pressure distribution along the axis (r = 0) of the piston at: (*Ozyoruk*)

(a) the beginning of a cycle,
(b) one quarter of a cycle,
(c) half a cycle,
(d) three quarters of a cycle.

——— **numerical**
- - - - - **exact**

@-5.

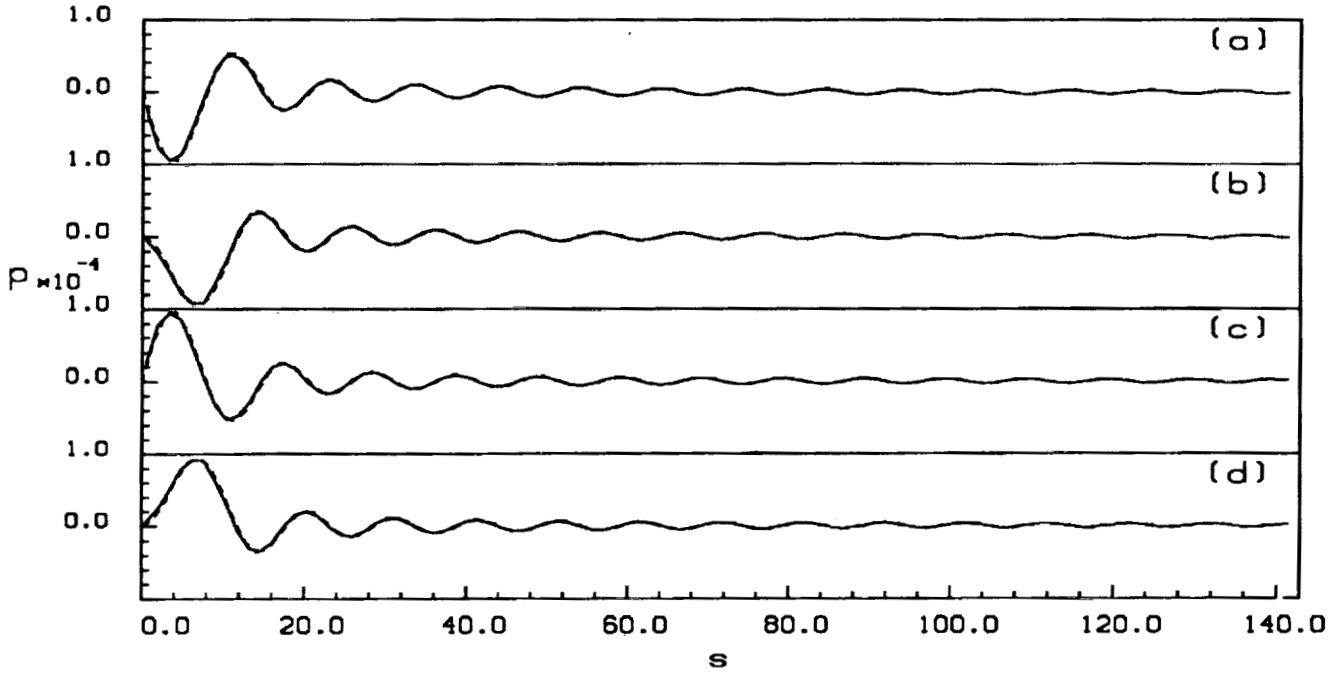

Pressure distribution along the line (r = x). (*Ozyoruk*)

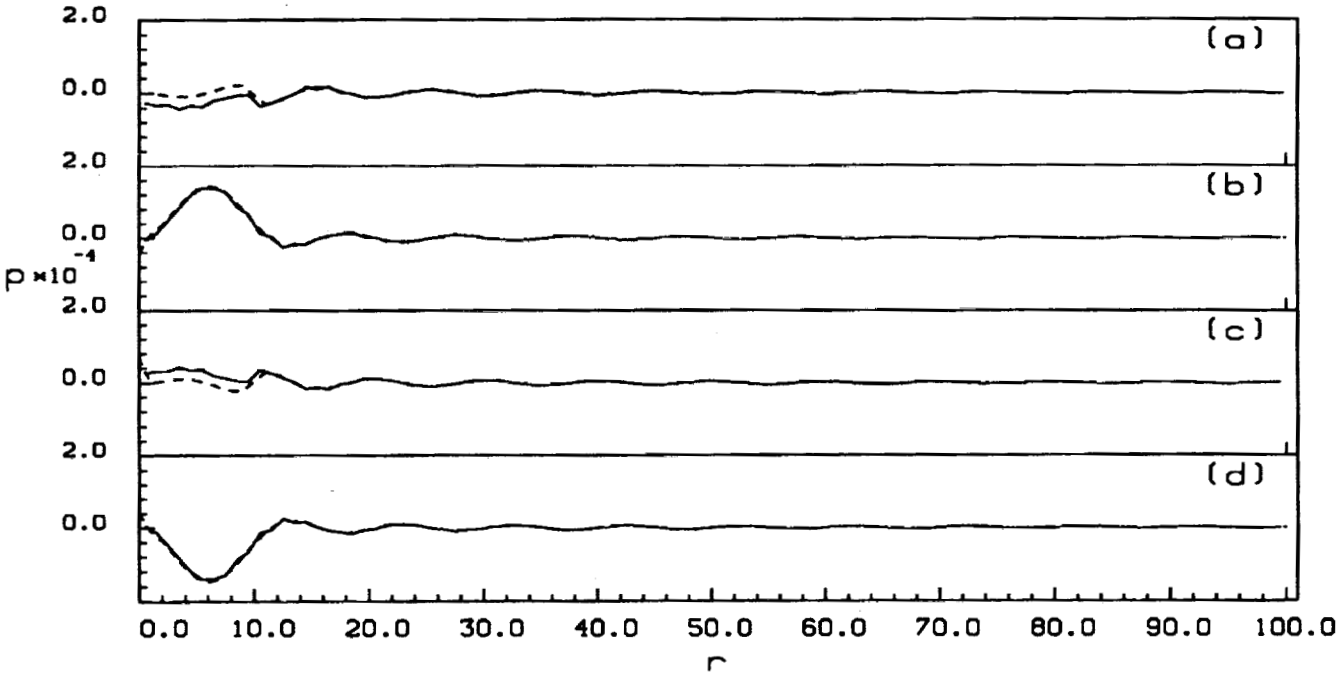

Pressure distribution along the wall (x = 0). (*Ozyoruk*)

(a) the beginning of a cycle,
(b) one quarter of a cycle,
(c) half a cycle,
(d) three quarters of a cycle.

——— **numerical**
- - - - - **exact**

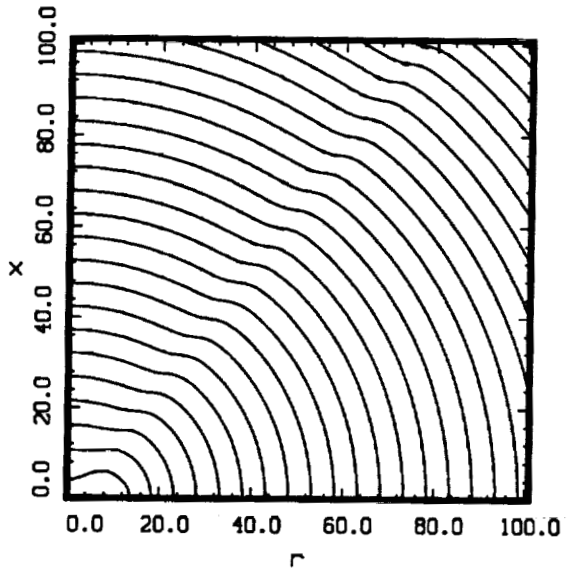

Pressure contours (p = 0) at the beginning of a cycle. (*Tam et al.*)

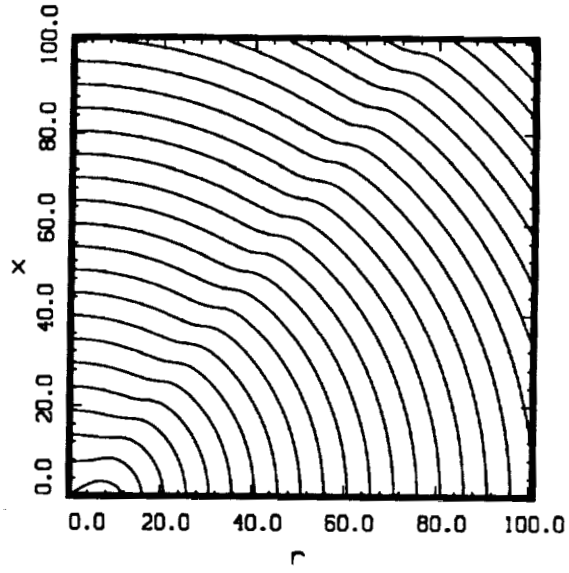

Pressure contours (p = 0) at one quarter of the cycle period. (*Tam et al.*)

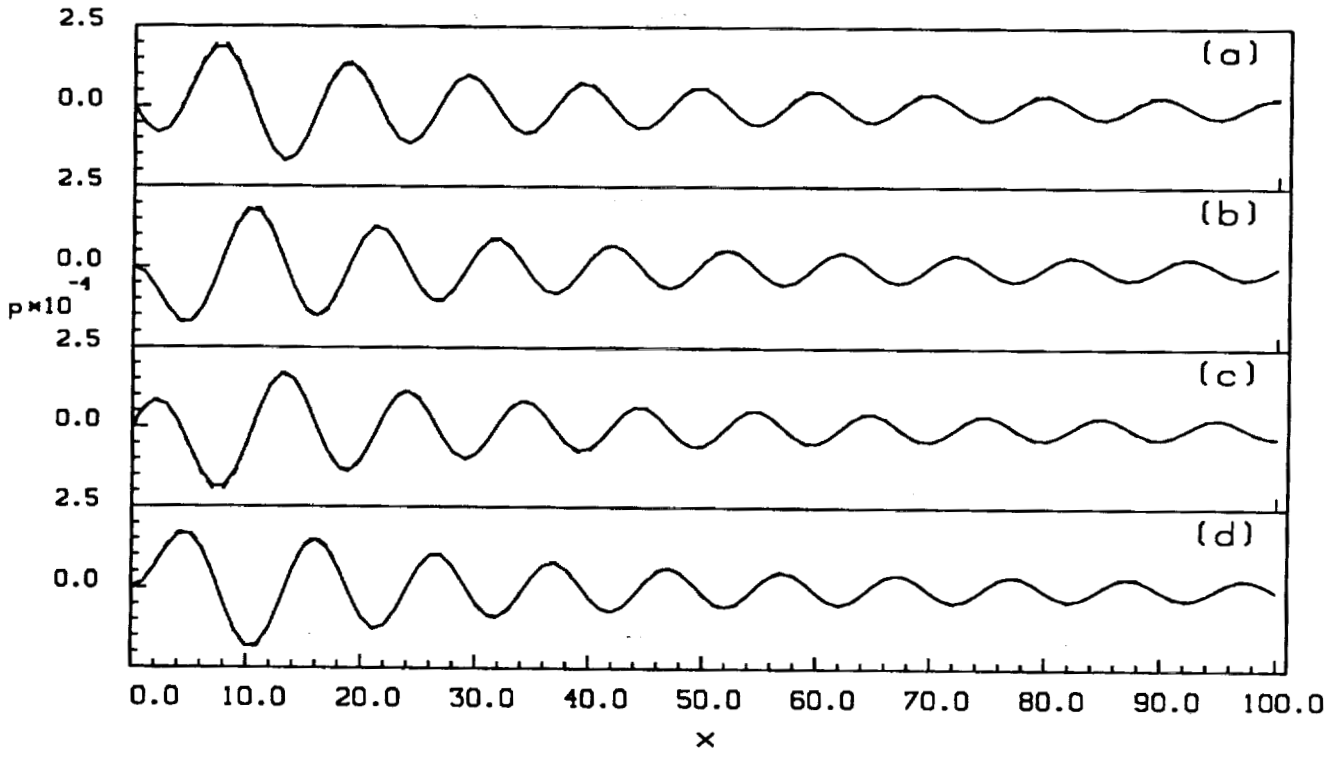

Pressure distribution along the axis (r = 0) of the piston at: (*Tam et al.*)

(a) the beginning of a cycle,
(b) one quarter of a cycle,
(c) half a cycle,
(d) three quarters of a cycle.

——— **numerical**
- - - - - **exact**

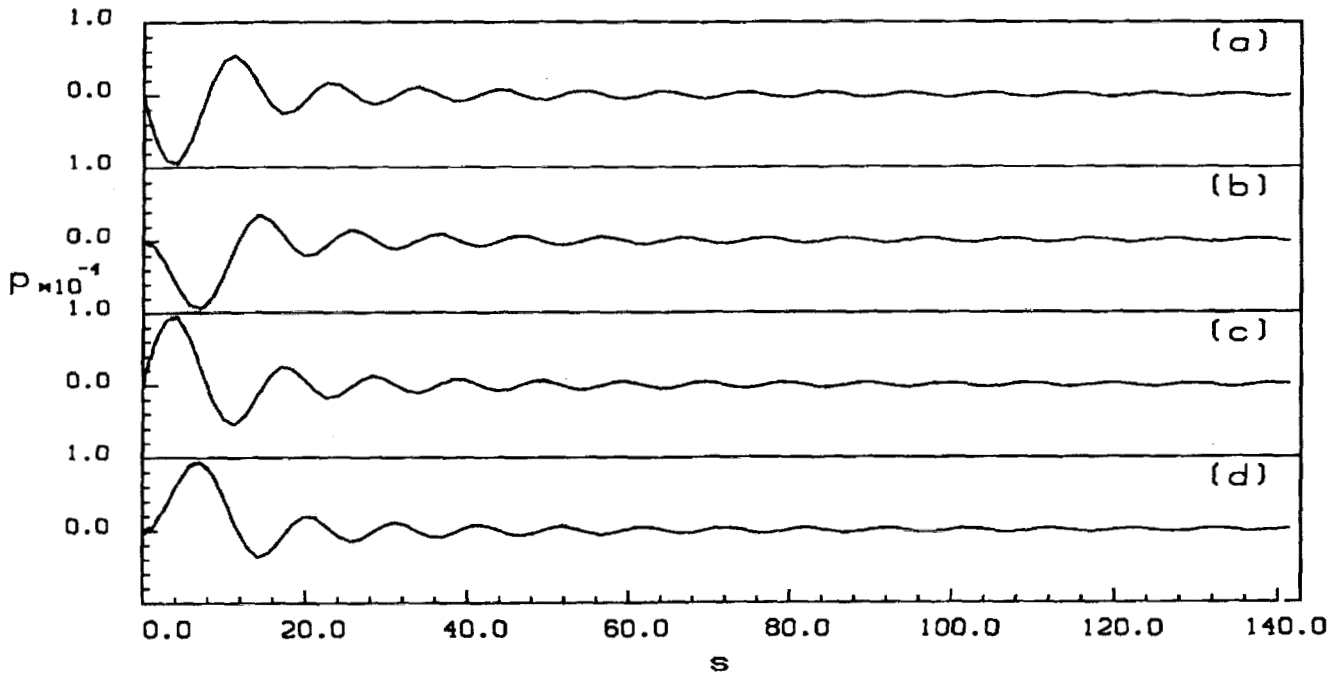

Pressure distribution along the line (r = x). (*Tam et al.*)

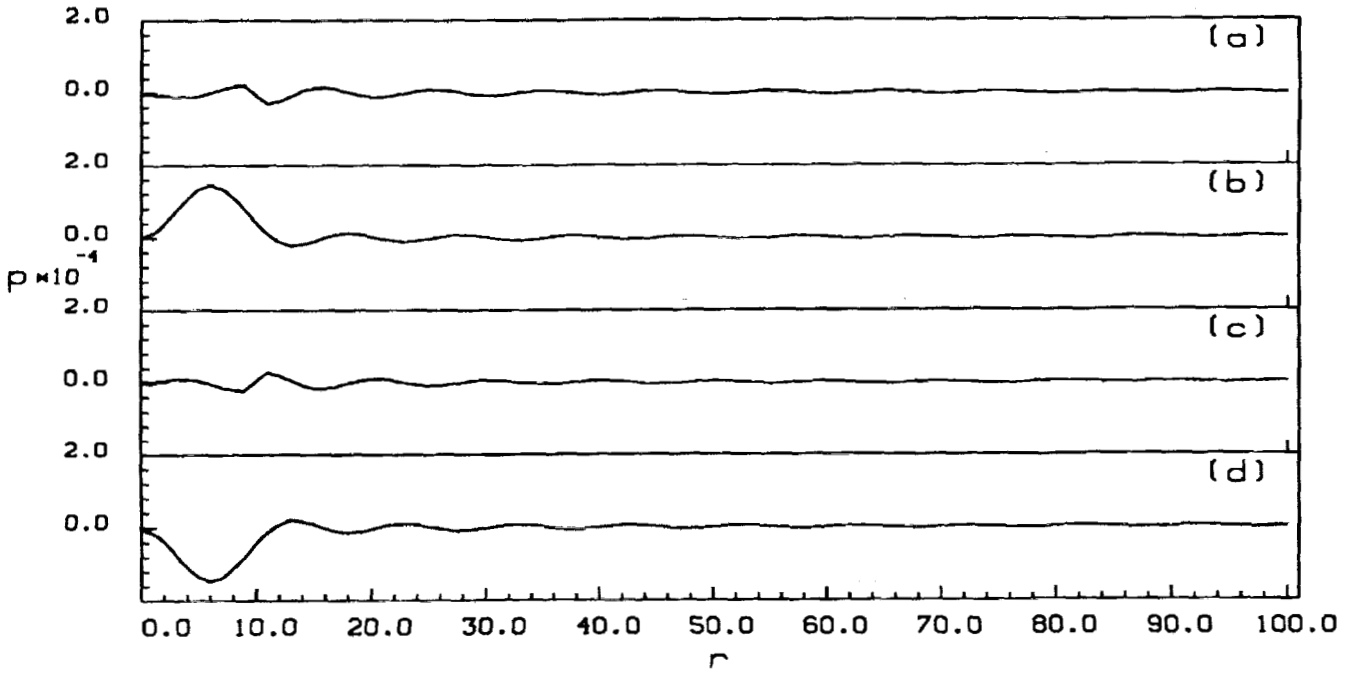

Pressure distribution along the wall (x = 0). (*Tam et al.*)

(a) the beginning of a cycle,
(b) one quarter of a cycle,
(c) half a cycle,
(d) three quarters of a cycle.

——— **numerical**
- - - - - **exact**

Category 5 :

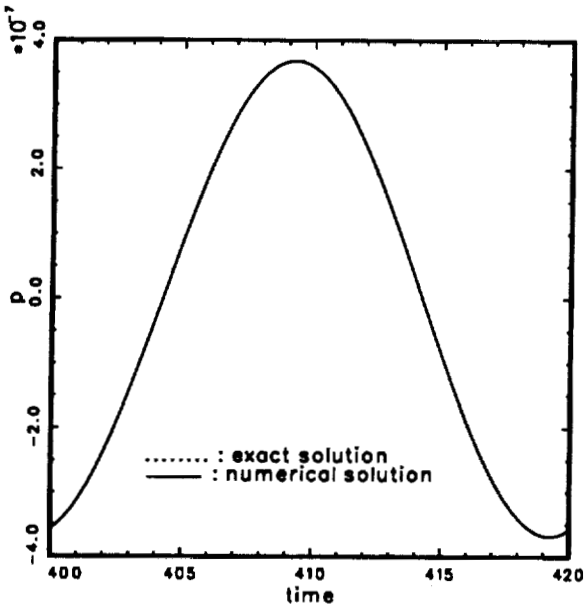

Pressure at nozzle exit as a function of time (Atkins).

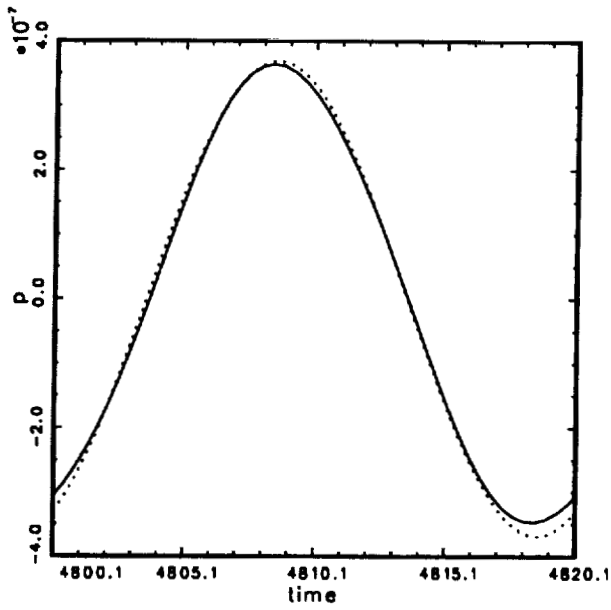

Pressure at nozzle exit as a function of time (Bui et al).

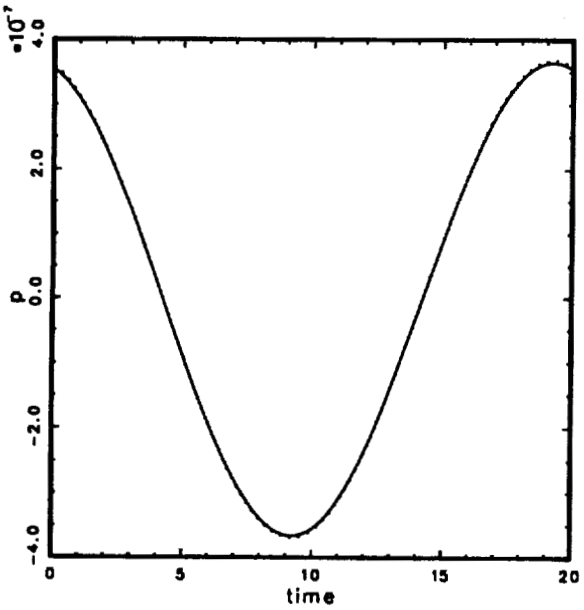

Pressure at nozzle exit as a function of time (Dong et al).

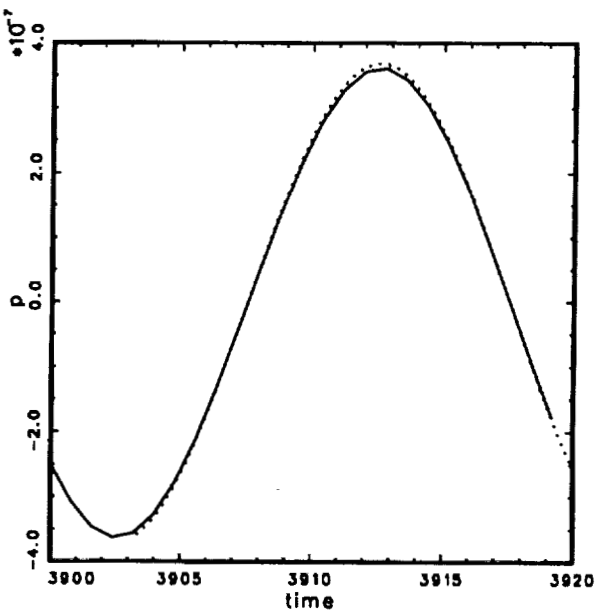

Pressure at nozzle exit as a function of time (Hu et al).

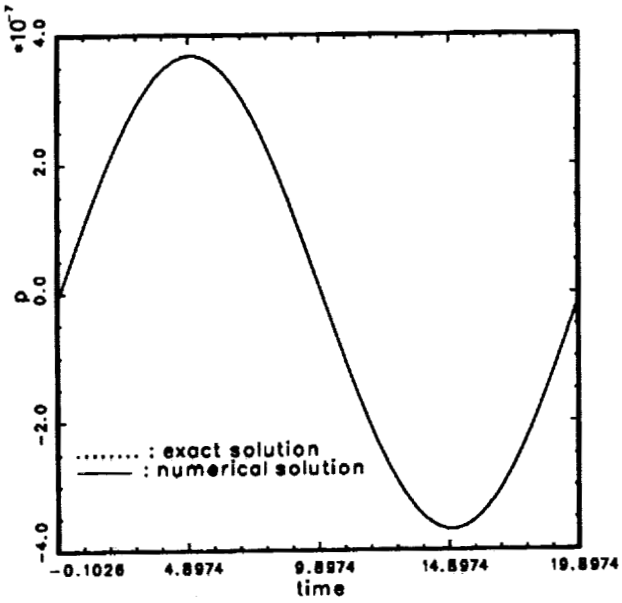

Pressure at nozzle exit as a function of time (Huynh–2nd ord).

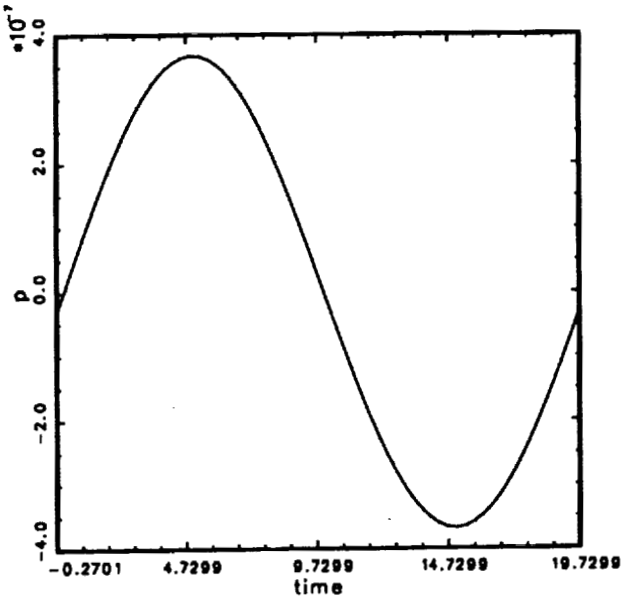

Pressure at nozzle exit as a function of time (Huynh–3nd ord).

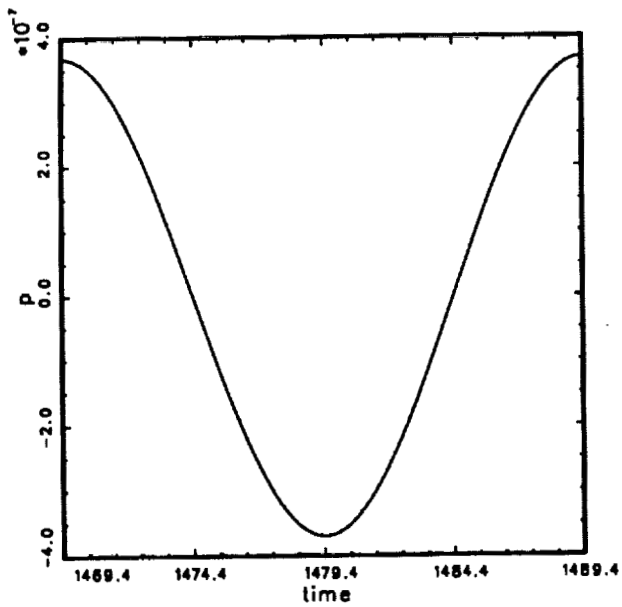

Pressure at nozzle exit as a function of time (Kopriva).

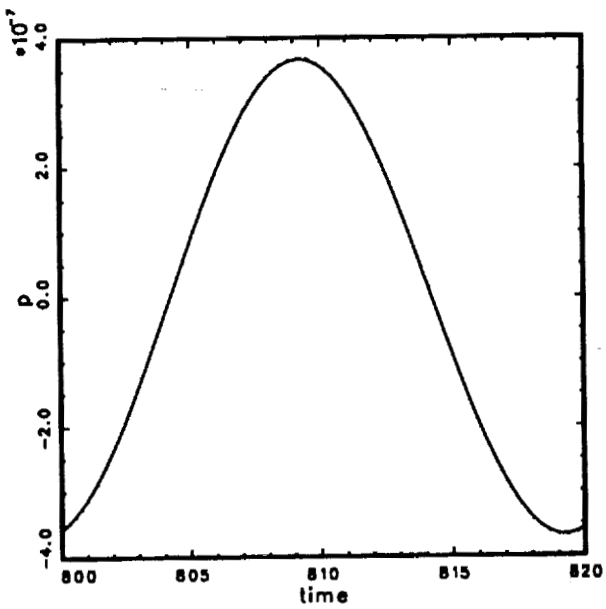

Pressure at nozzle exit as a function of time (Tam et al).

Category 6

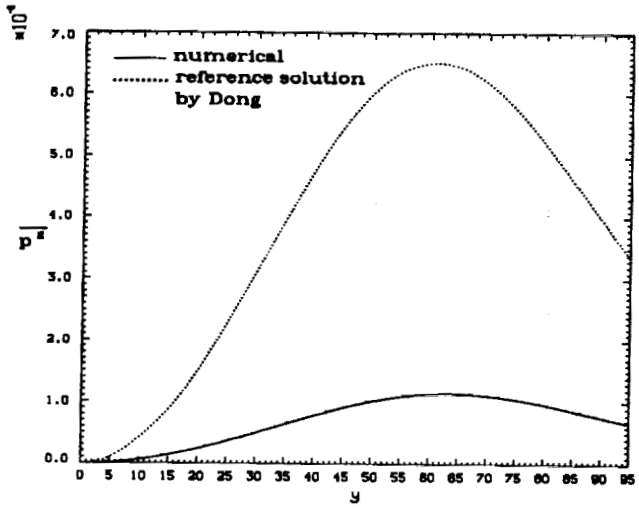

Intensity of radiated sound, $\overline{p^2}$, along x=95. (Atassi)

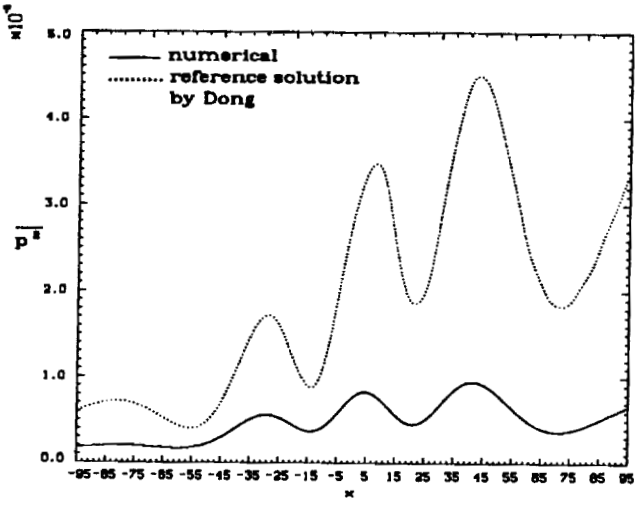

Intensity of radiated sound, $\overline{p^2}$, along y=95. (Atassi)

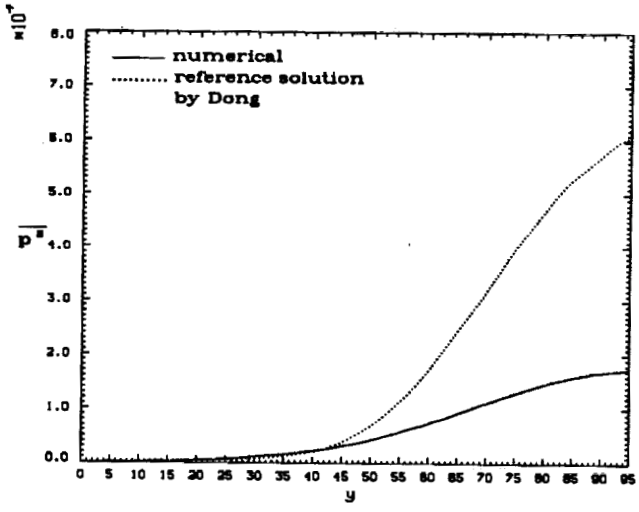

Intensity of radiated sound, $\overline{p^2}$, along x=−95. (Atassi)

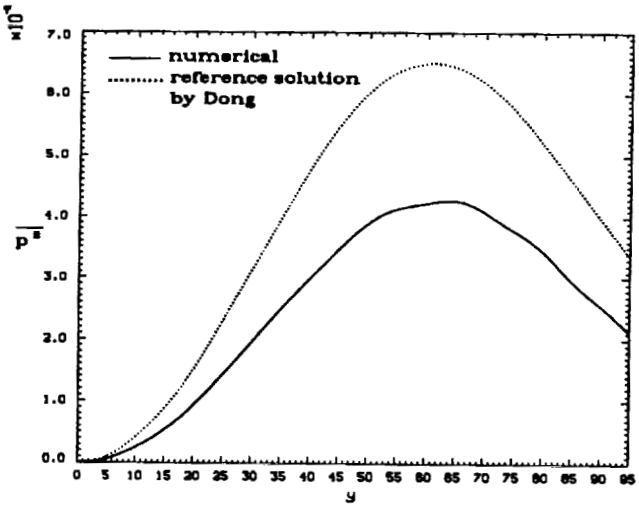

Intensity of radiated sound, $\overline{p^2}$, along x=95. (Hu)

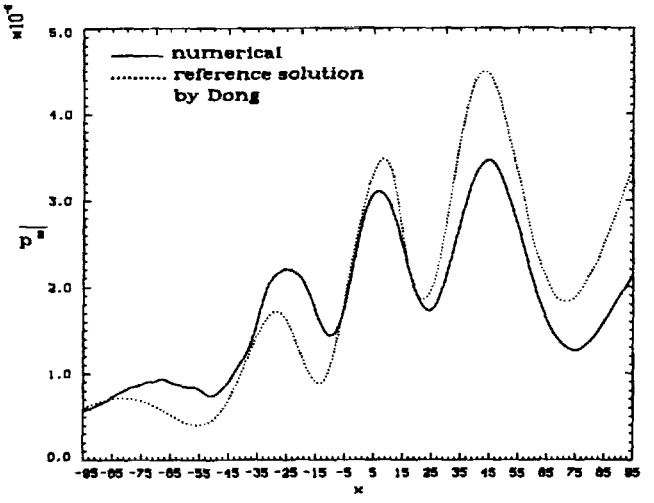

Intensity of radiated sound, $\overline{p^2}$, along y=95. (Hu)

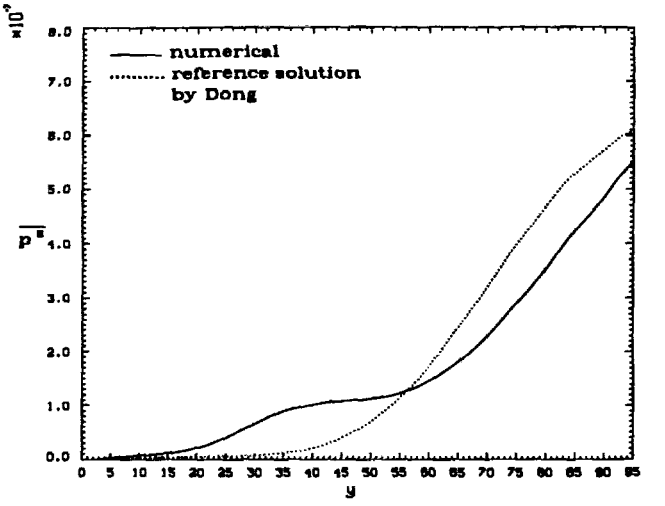

Intensity of radiated sound, $\overline{p^2}$, along x=−95. (Hu)

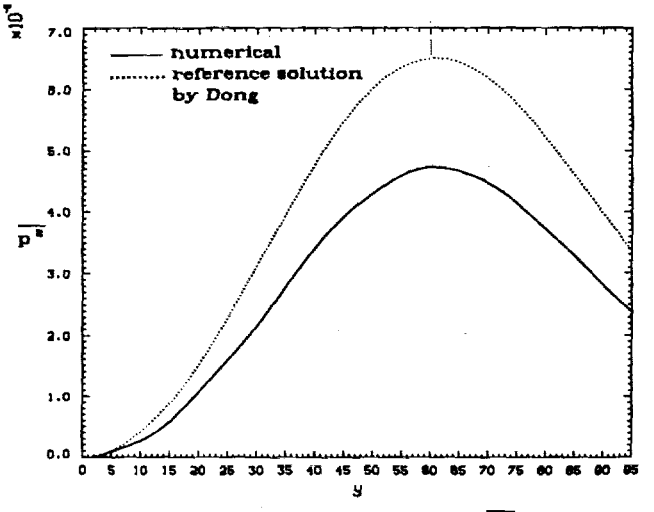

Intensity of radiated sound, $\overline{p^2}$, along x=95. (Martin)

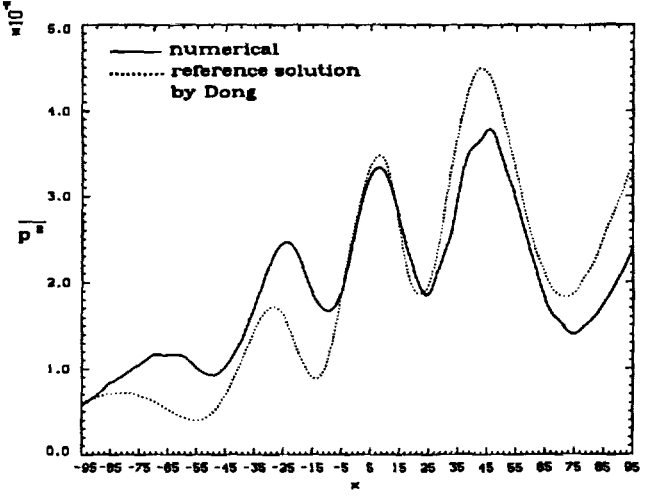

Intensity of radiated sound, $\overline{p^2}$, along y=95. (Martin)

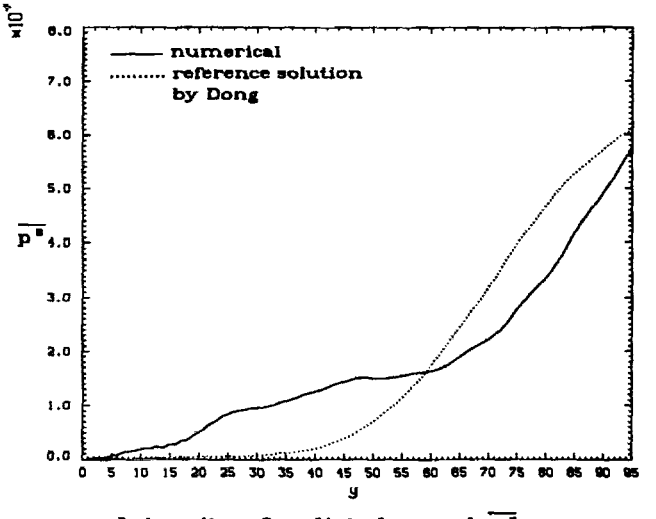

Intensity of radiated sound, $\overline{p^2}$, along x=−95. (Martin)

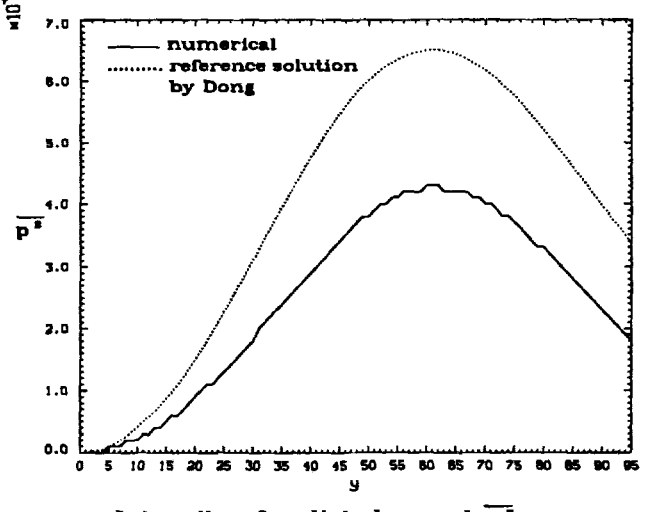

Intensity of radiated sound, $\overline{p^2}$, along x=95. (Nark, version 1)

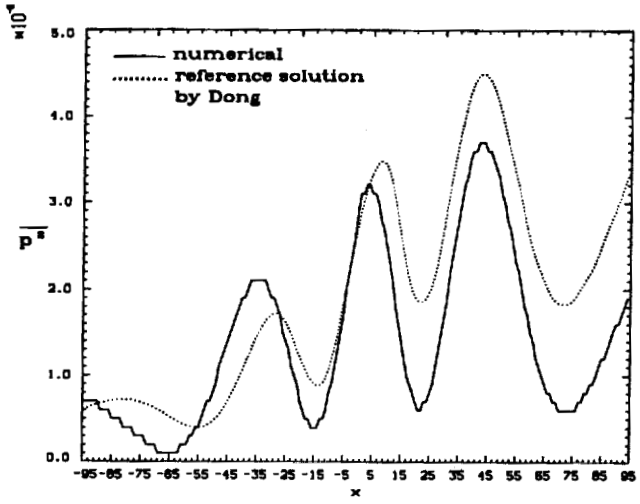

Intensity of radiated sound, $\overline{p^2}$, along y=95. (Nark, version 1)

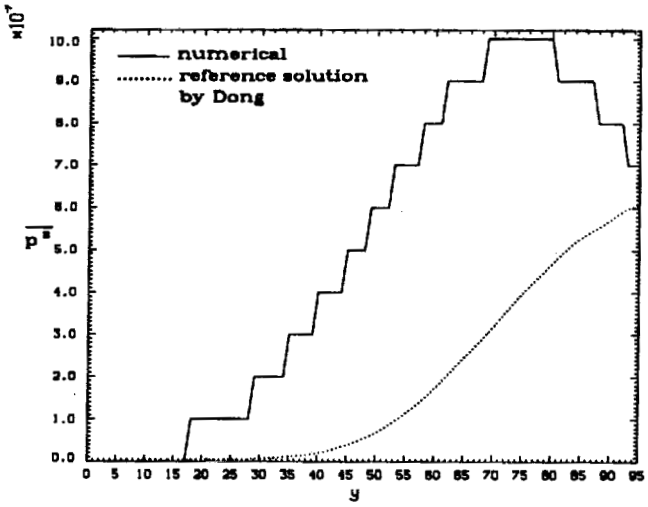

Intensity of radiated sound, $\overline{p^2}$, along x=−95. (Nark, version 1)

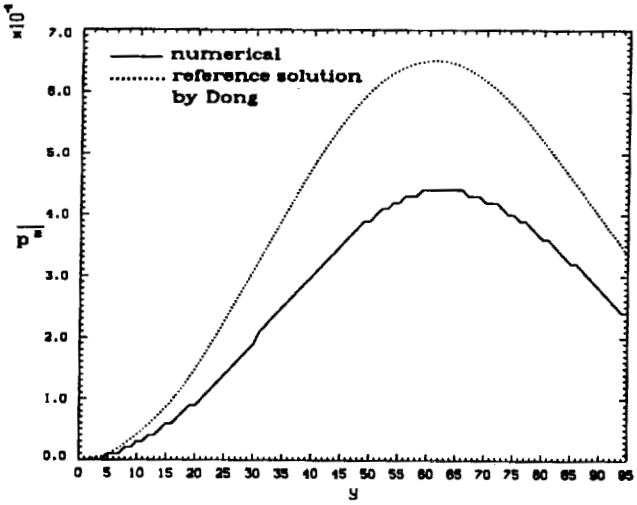

Intensity of radiated sound, $\overline{p^2}$, along x=95. (Nark, version 2)

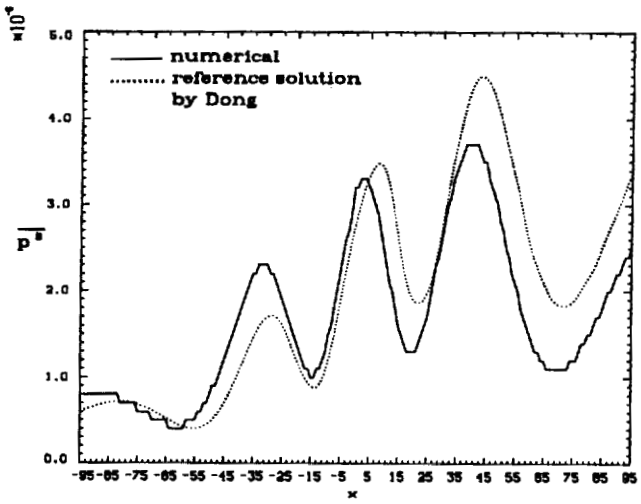

Intensity of radiated sound, $\overline{p^2}$, along y=95. (Nark, version 2)

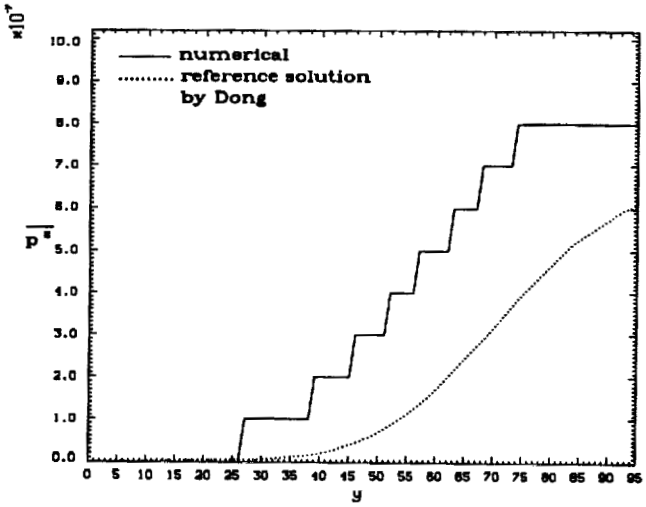

Intensity of radiated sound, $\overline{p^2}$, along x=−95. (Nark, version 2)

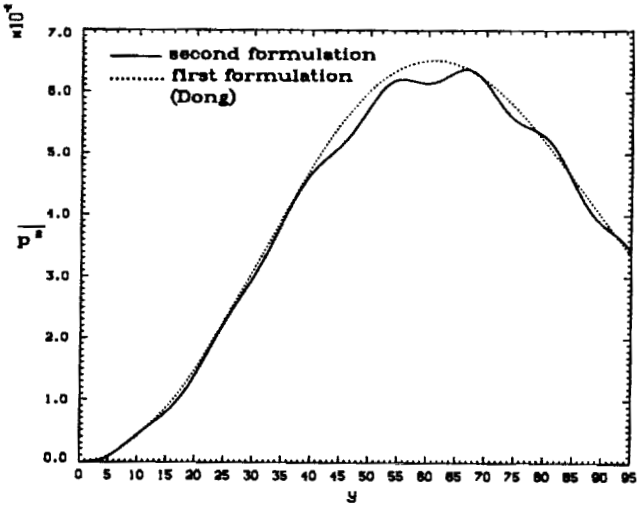

Intensity of radiated sound, $\overline{p^2}$, along x=95. (Tam et al)

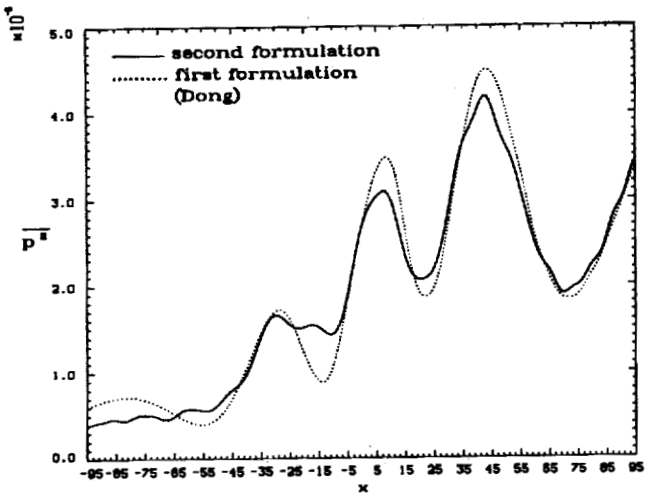

Intensity of radiated sound, $\overline{p^2}$, along y=95. (Tam et al)

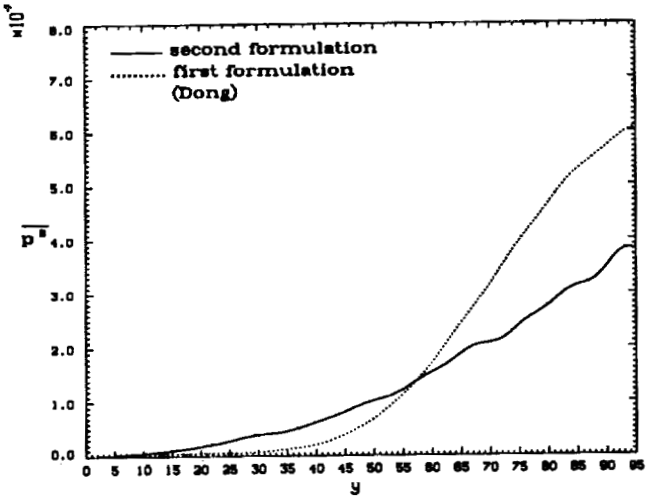

Intensity of radiated sound, $\overline{p^2}$, along x=−95. (Tam et al)

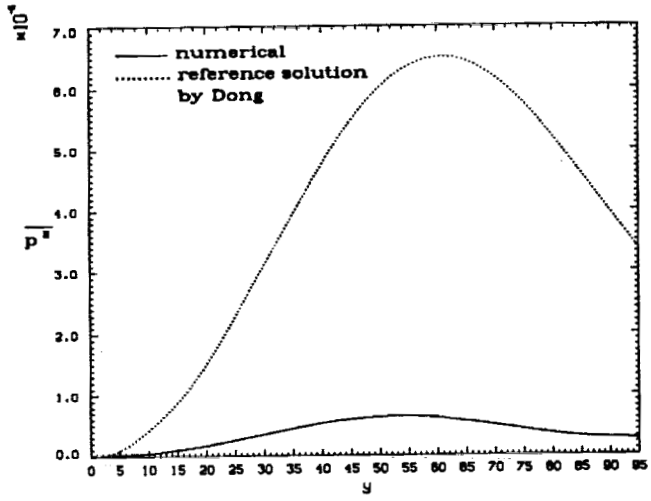

Intensity of radiated sound, $\overline{p^2}$, along x=95. (Hariharan, version 1)

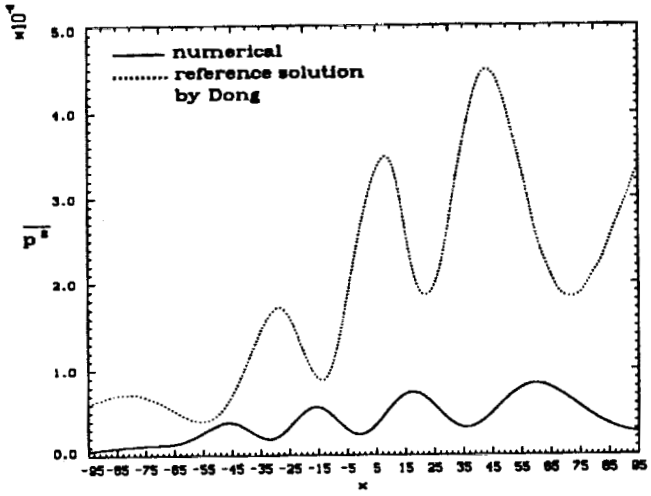

Intensity of radiated sound, $\overline{p^2}$, along y=95. (Hariharan, version 1)

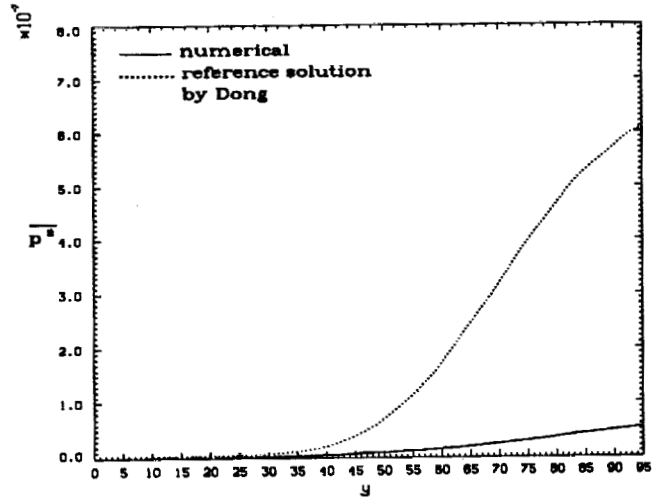

Intensity of radiated sound, $\overline{p^2}$, along x=−95. (Hariharan, version 1)

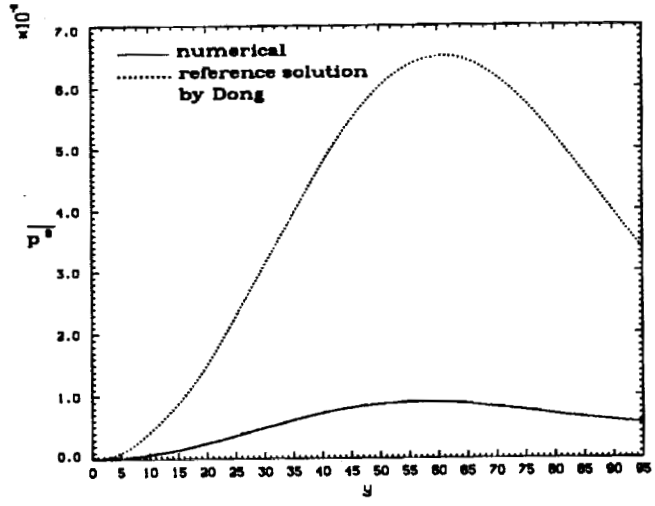

Intensity of radiated sound, $\overline{p^2}$, along x=95. (Hariharan, version 2)

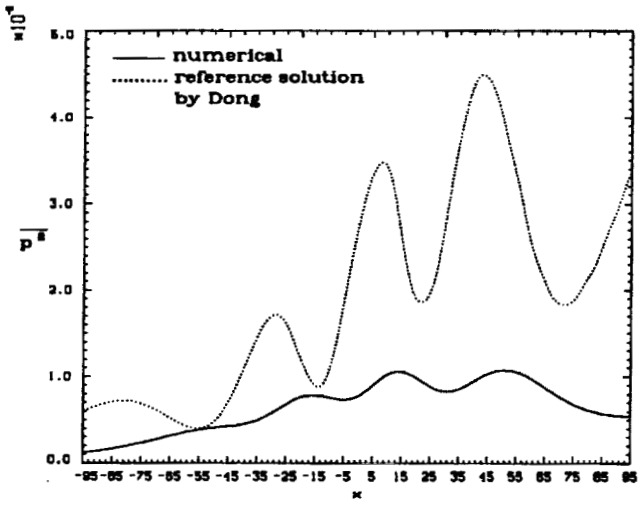

Intensity of radiated sound, $\overline{p^2}$,
along y=95. (Hariharan, version 2)

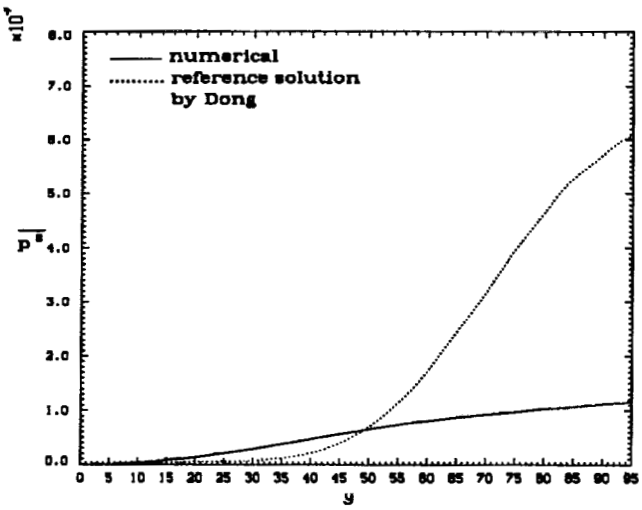

Intensity of radiated sound, $\overline{p^2}$,
along x=−95. (Hariharan, version 2)

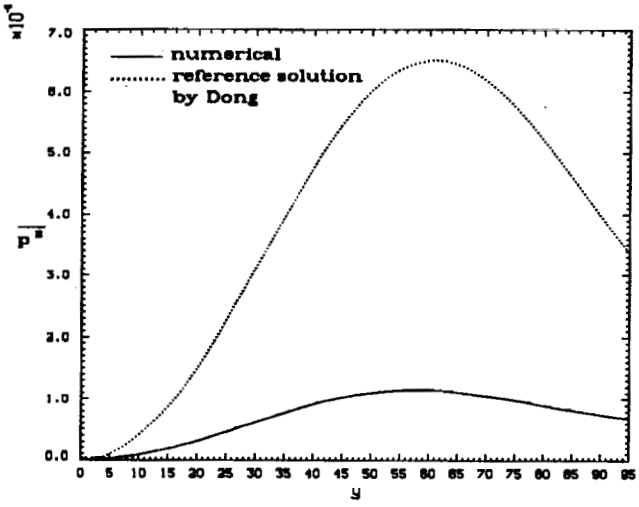

Intensity of radiated sound, $\overline{p^2}$,
along x=95. (Hariharan, version 3)

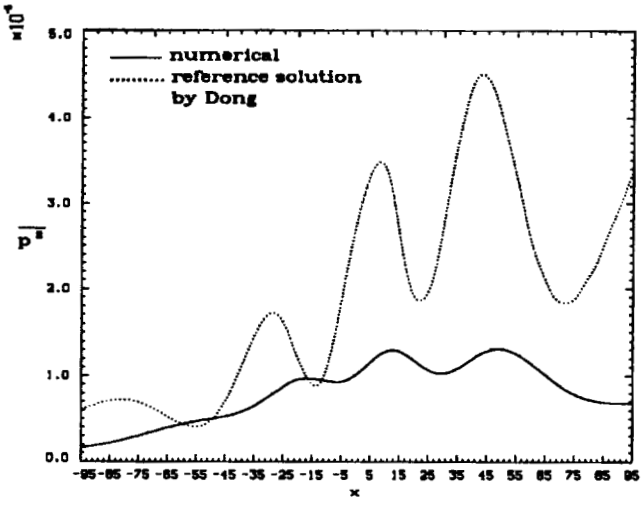

Intensity of radiated sound, $\overline{p^2}$,
along y=95. (Hariharan, version 3)

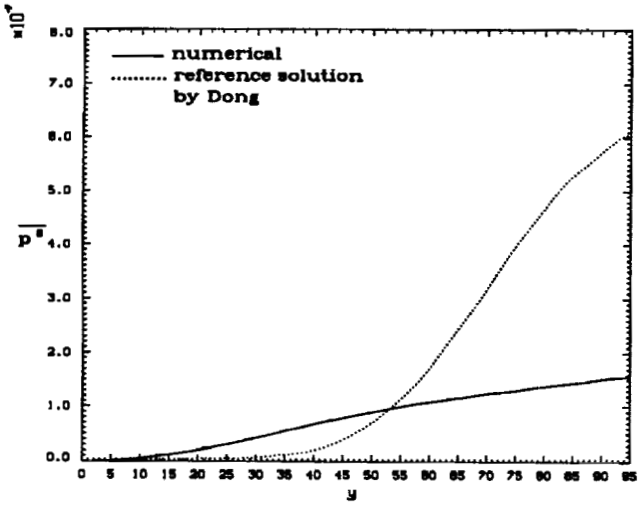

Intensity of radiated sound, $\overline{p^2}$,
along x=−95. (Hariharan, version 3)

INDUSTRY PANEL PRESENTATIONS AND DISCUSSIONS

N.N. Reddy
Lockheed Aeronautical Systems Company
Marietta, GA 30063

The workshop organizers invited representatives from the aircraft industry to organize an industry panel and participate in the workshop. The primary purpose of the panel was to present and discuss the industry needs in acoustic technology in general and in computational aeroacoustics in particular. Also to provide guidance to the researchers and scientists by identifying the current and future issues related to acoustic technology.

The panel presentations and discussions were moderated by Jay Hardin of NASA-LaRC. The following representatives attended the workshop and participated in the presentations and discussions.

Thomas Barber	United Technologies Research Center
Leo Dadona	Boeing D/SG Helicopter Division
Wen-Huel Jou	Boeing Commercial Airplane Group
N.N. Reddy	Lockheed Aeronautical Systems Co.

Philip Gliebe of GE Aircraft Engines and Mahendra Joshi of McDonnell Douglas were also invited but unable to attend the workshop. They provided, however, the information that was presented and discussed. This section presents the views of GE and McDonnell Douglas in addition to those presented at the workshop panel. The following paragraph summarizes the panels' view of noise sources, critical noise issues and current engineering practices.

NOISE SOURCES

The aircraft acoustic sources contributing to the community noise are illustrated in Figures 1 to 3. Gas turbine engine noise sources are shown in Figure 1. Fan and compressor noise sources have similar characteristics. However, their propagating properties are different and depend on the nacelle geometry (inlet and exhaust). The typical characteristics of the sources as a function of time are shown in Figure 1b. The compressor noise levels are relatively small compared to other sources. The turbine and combustion noise generally propagate through the primary exit nozzle. The jet noise is generated by the process of jet exhaust mixing with the entrained ambient flow. The relative importance of the various noise sources of a turbofan engine is shown in Figure 1c as a function of engine bypass ratio. It is evident from this figure that at low bypass ratio, the jet noise dominates, and as the bypass

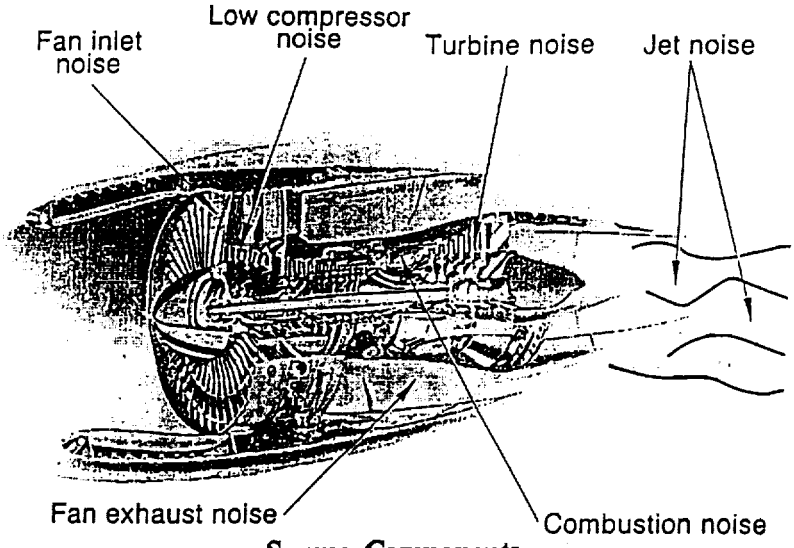

a. Source Components

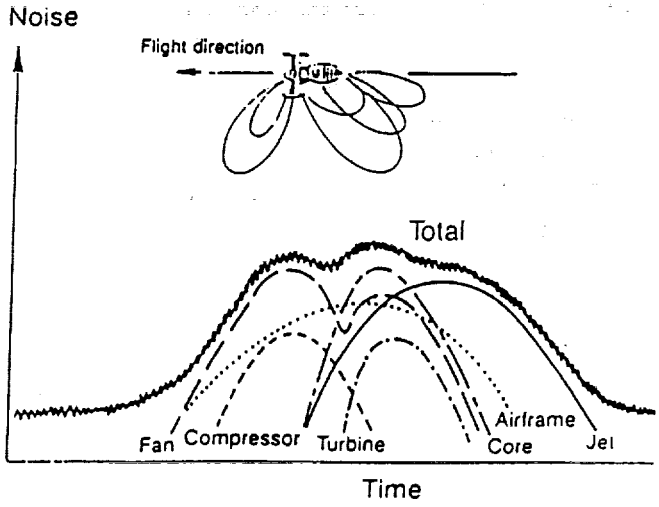

b. Relative Source Strengths During Flight

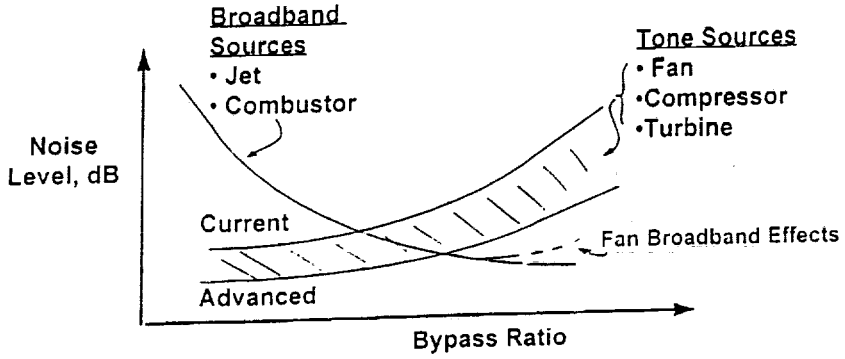

c. Importance of Sources as a Function of Bypass Ratio

Figure 1. Gas Turbine Engine Noise Sources and Their Characteristics

ratio increases the turbomachinery noise sources become important. To predict and reduce the

noise levels, it is necessary to recognize the critical sources and understand their generating mechanisms.

Airframe noise sources are shown in Figure 2. The airframe noise is defined as the noise generated by the aerodynamic flow interacting with the aircraft surfaces during flight. The important airframe noise sources are identified in this figure. In addition, the interaction of the jet stream with wing/flap components and the wakes from wing, landing gear and other components interacting with the flap components also contribute to the airframe noise.

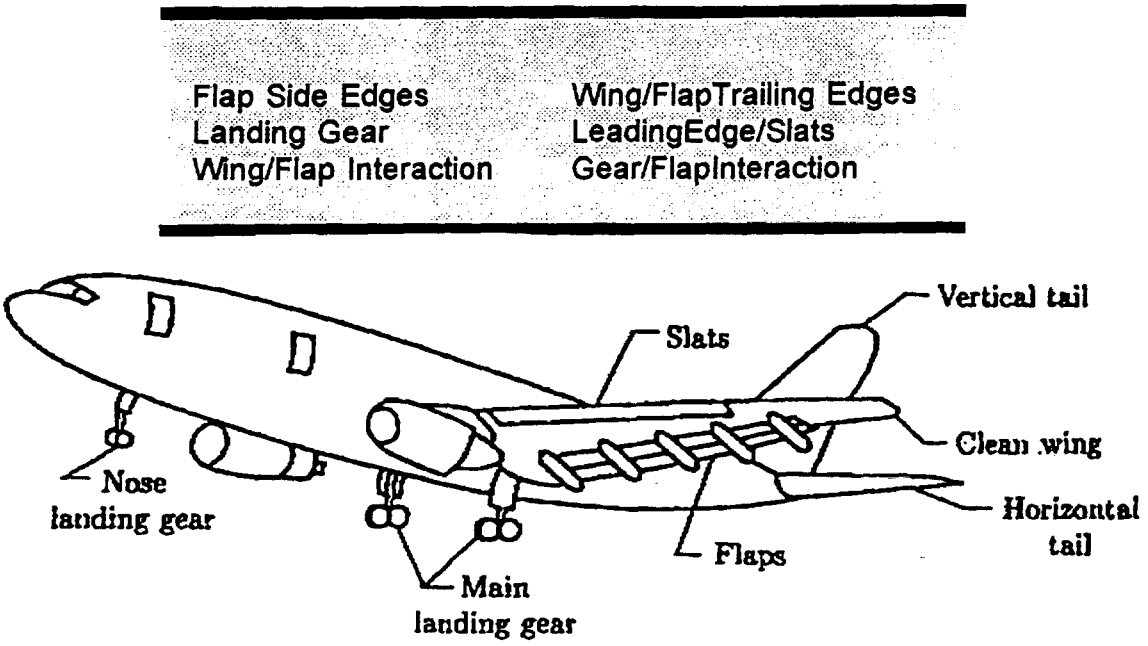

Figure 2. Airframe Noise Sources

In the case of propeller aircraft, the important sources are free-propeller noise, engine noise, propeller/engine/airframe installation effects. Inflow angle has a significant effect on propeller noise. Amongst several rotorcraft noise sources, the Blade Vortex Interaction (BVI)is dominant. This source is illustrated in Figure 3.

CRITICAL NOISE ISSUES

There are several noise issues which require new and innovative technology development.

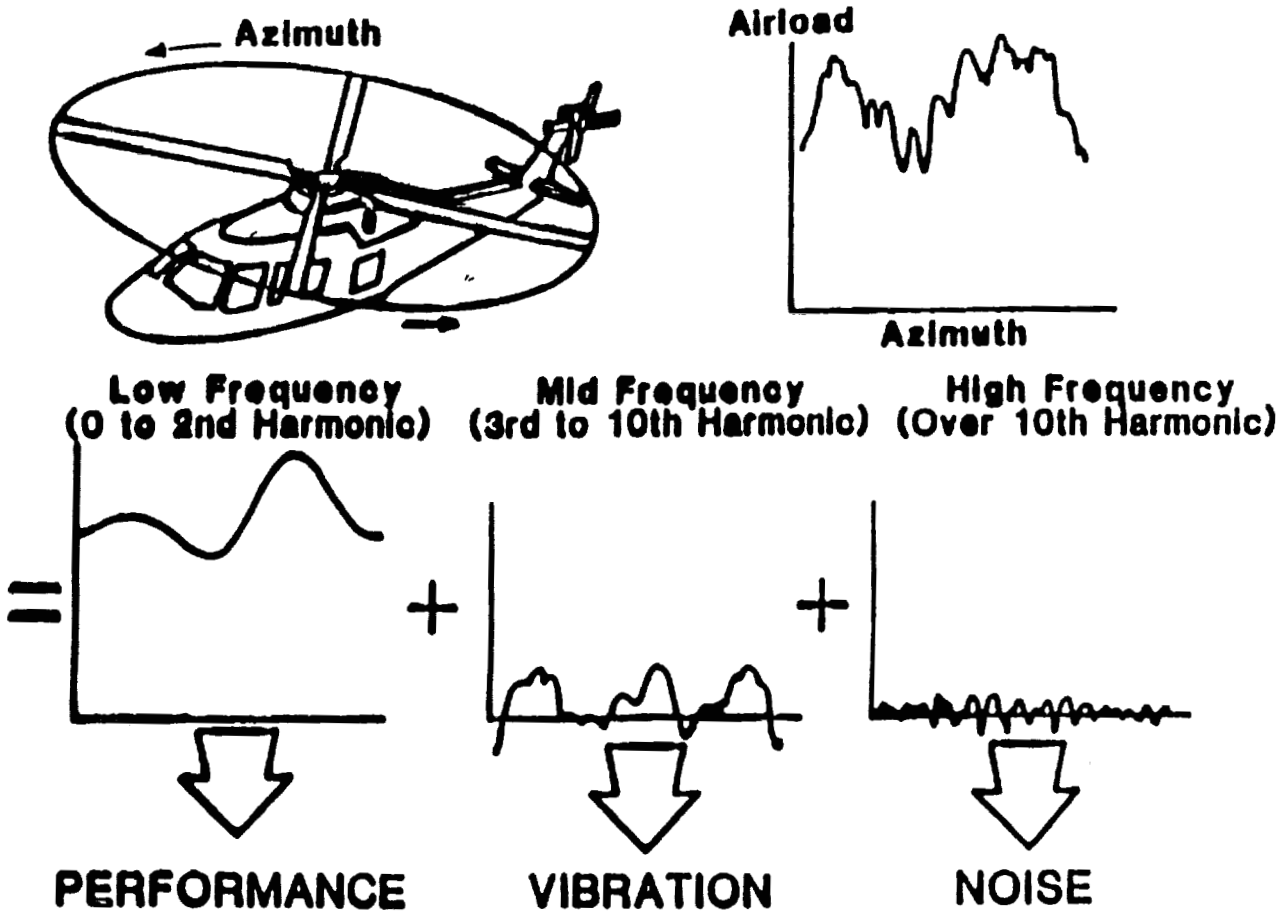

Figure 3. Rotor Performance, Vibration and Noise

The following are a few of the critical issues. 1) It is anticipated that the aircraft noise regulations will be more stringent than the existing ones. Therefore, the community noise levels in the vicinity of airports need to be reduced. 2) The interior noise levels need to be reduced to make the noise environment acceptable to the passengers. 3) It is necessary to accurately predict the noise/vibration environment on the aircraft structural components and sensitive avionic equipment. The following paragraphs discuss the particular issues which require immediate attention.

Current Engines

It is necessary to improve the modeling capability for fan-core internal mixing. This will provide better understanding of noise characteristics which will help in developing noise reduction concepts. Liner technology must be improved, to develop a low noise nacelle with minimum performance penalty. This involves understanding fan noise generation and propagation through the ducts, and acoustic properties of liner materials and optimization techniques.

Advanced Subsonic Engines

The present empirical models for jet noise are not adequate. Analytical models based on sound theoretical models need to be developed for fan noise and liner technology.

Advanced Supersonic Jet Engines

New and innovative jet noise suppressors with minimum performance losses are urgently needed. Understanding of fan/inlet interactions and inlet noise suppression techniques need to be developed.

Airframe Noise

As the propulsion noise levels reduce with improved technology, airframe noise will become the dominant source, particularly during approach. The noise mechanisms contributing to the total airframe noise need to be identified. It is essential to quantify the flow and geometrical parameters that influence these sources. Noise/flow and propagation models and prediction methods for these sources need to be developed. Flap side edge noise source is one of the critical airframe components to be modeled and evaluated. It is also necessary to determine the effect of flow and geometrical variations on the total airframe noise.

Helicopter/Tilt Rotor Noise

In addition to the various rotor noise sources, Blade Vortex Interaction (BVI) noise is an important source. To control the noise, it is important to understand the flow characteristics responsible for this noise component. Models must be developed to determine the magnitude,

spectra and directivity of this source.

Propeller Noise

Major issues in the propeller noise are the installation effects. These include the inflow angles and the presence of wing/fuselage. Improved models for advanced propellers and methods to evaluate the installation effects on noise generation are needed.

Flow/Surface Interaction Noise

This noise is generated when the jet flow and propeller/rotor wake flow interact with the aircraft surfaces. It is necessary to understand the source mechanism and develop analytical/computational models.

CURRENT ENGINEERING PRACTICES

At the present time the noise prediction methods for different sources are primarily semi-empirical. The following paragraphs discuss the present methods.

Jet Mixing Noise

There are several methods available to predict jet mixing noise. The application of each of the methods depends on the nozzle configuration. All the methods were developed using test data and known theoretical understanding. For single stream circular nozzles, SAE ARP 876 method is used. This method appears to be quite reasonable for subsonic jets. However, this method is not adequately validated for supersonic jets. For co-axial circular nozzles, two methods, SAE ARP 876 and Boeing JEN6 are used. For coaxial circular nozzles with inverted velocity profiles (IVP), the Pao method is used. This method is incorporated in NASA Aircraft Noise Prediction Program (ANOPP). Pratt & Whitney uses their own inhouse semi-empirical method known as Larson's method for IVP jet noise. A prediction code known as MGB Method was developed at GE several years ago under the sponsorship of NASA Lewis Research Center. Recently NASA has undertaken to improve the MGB Method by using CFD calculated flow parameters as input.

Jet Shock Noise

There are two methods available to predict shock associated noise from supersonic jets. A prediction method was developed in late 70's by Harper-Bourne and Fisher. This is an empirical method based on experimental data. This method was adapted in SAE ARP 876 and in NASA ANOPP. Lockheed and Tam recently developed a procedure to predict the shock associated broad band noise for imperfectly expanded supersonic jets. This method is based on the shock noise theory developed by Tam. The method is validated using laboratory data and has been incorporated in NASA ANOPP as a module. In addition to the laboratory data, this method is being validated using F/16 flyover test data.

Fan Noise

Tyler/Sofrin cutoff model is used for blade-wake interaction effects. Broadband noise is predicted empirically using test data. Semi-empirical methods are used to predict noise propagation through inlet and exhaust. For example, for forward radiated (inlet) noise, the method developed by Rice at NASA Lewis Research Center, and for aft radiated noise, a method developed by Dean of Pratt and Whitney are used. These methods are calibrated using simulated laboratory and engine data.

Propeller Noise

SAE AIR 1407 is a simple empirical method based on correlation of the laboratory and flight test data. This method is primarily used during the preliminary design. The method is applicable for tractor installations with level flyovers and flight speed greater than 35 knots.

Hamilton Standard under FAA sponsorship, has developed a prediction method, "V/STOL Rotary Propulsion System Noise Prediction." This method is capable of predicting tone noise levels (steady loading, unsteady loading and thickness) and broadband noise for free-air propellers.

Farassat of NASA-LaRC has developed a time domain theoretical method to predict propeller noise. Hanson of Hamilton Standard has also developed a frequency domain theoretical method. These methods require the blade geometry and aerodynamic loads as input. These methods are used in understanding the noise source characteristics and propeller design. Based on Hanson's theory, Hamilton Standard developed a prediction method which consists of modules for tone noise, broadband noise, propagation effects, and calculations of noise metrics. This method predicts both near- and far-field noise.

A computer module, Propeller Analysis System (PAS) was developed by NASA-LaRC and incorporated in NASA ANOPP. This program predicts both performance and noise. This is based on Farassat's solution to the Ffowcs Williams and Hawkings equation and is primarily used for small propellers (general aviation).

NASA-LeRC, Georgia Institute of Technology, Allison engine company and others are developing prediction methods using computational techniques.

In addition to these methods, Rolls Royce of U.K., ONERA of France, DLR of Germany and FFA of Sweden have prediction capabilities and are developing theoretically based methods.

Helicopter/Rotor Noise

ROTONET as a part of NASA ANOPP is the prediction method widely used by industry to predict the rotorcraft noise levels. This method is based on test data correlations. The rotorcraft industry relies extensively on test data and 'engineering' methods using acoustic analogy to reduce noise levels.

Airframe Noise

Airframe noise prediction method developed by Fink of United Technologies is used by industry. This method is incorporated in the NASA ANOPP prediction method as a module. This is a semi-empirical method based on some theoretical developments for flow/surface interaction noise and test data. Several important noise sources (e.g., flap side edge) are not included in this method.

Flow/Surface Interaction Noise

There is no industry standard for predicting flow/surface interaction noise. Each company uses their own method based on the proprietary data.

COMPUTATIONAL AEROACOUSTICS (CAA) ROLE

Jet Noise

Properly developed numerical simulation of the jet noise, (small scale turbulence for subsonic jets and large scale turbulence for supersonic jets) is necessary. In the case of supersonic jets, it is also necessary to develop models for interaction of large scale turbulence with shock cells and discrete tone noise. This not only will improve the prediction capability, but also will help in the development of viable noise control techniques. Extending the CFD methods by reducing the grid size and time increments for unsteady flow will require the computer capabilities which are not available at the present time. Therefore it is necessary to develop the new and innovative computational techniques to solve these acoustic problems.

Turbomachinery Noise

Turbomachinery noise generation process is very complex, because of the interaction of stator/rotors. The available CFD formulations may be utilized to understand the upstream wakes, inflow distortions and turbulence, flow downstream of the blade, and fluctuating lift/drag on rotor/stator of fan/compressor. Properly developed CAA by using the acoustic wave energy principle to determine acoustic wave mode number and frequency as a function of number of blades and unsteady flow structure will help designing noise reduction techniques. CAA can also be used to simulate the spinning and radial modal patterns of propagation through ducts (inlet and exhaust). It is necessary to extend this simulation to provide directivity and spectra of radiated sound field.

Helicopter/Rotor Noise

The biggest challenge in rotorcraft noise is the understanding, prediction and reduction of Blade-Vortex Interaction (BVI) noise. Figure 4 illustrates complexity of the instantaneous blade loading and wake rollup mechanism. Development of CAA models to simulate the rotor wake flow and noise characteristics (directivity and spectra) is essential for industry.

Airframe Noise

Modification of CFD programs within the constraints of present computer technology

will not be adequate to understand the airframe noise source mechanisms and to predict the radiated sound field. It is necessary to model the airframe noise sources with appropriate simplifications to suit the modern computers and to capture the essential physics related to noise generation. The primary interest is to model the sources of flap side edge noise, wing/flap leading/trailing edges, and landing gears.

LESSONS LEARNED FROM CFD

It is obvious that CFD has made impressive progress during the last twenty years. CFD

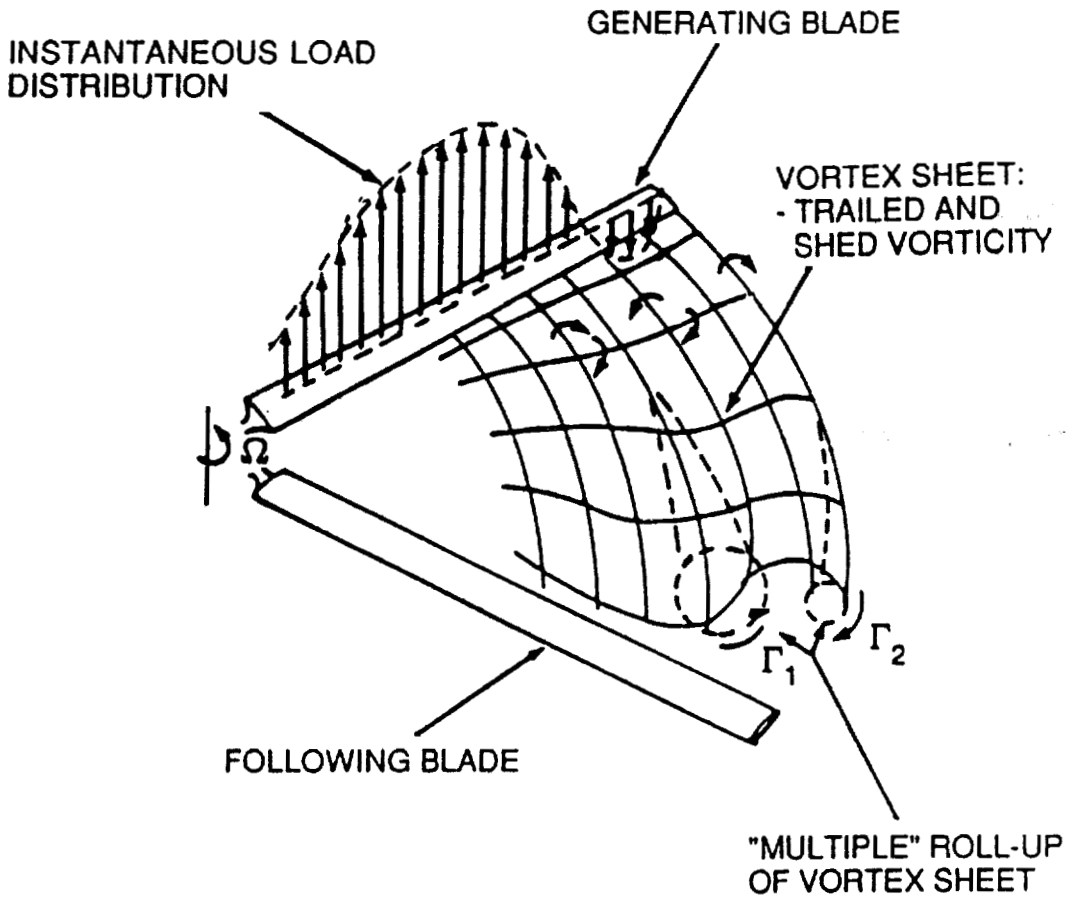

Figure 4. Schematic of Rotor Wake

has been used extensively as an aircraft design tool in airframe, engine, and aircraft integration design procedures. It is essential, however, to realize that aeroacoustic problems are distinctly different from those encountered in aerodynamics. One may think that at the present time CAA is in the same status as CFD twenty years ago. Since aeroacoustics involves the flow, it is possible to learn some of the flow properties required in acoustics from CFD. However, modification of CFD methods without understanding the acoustic requirements will not yield a noise design tool with the existing (modern) computers. Therefore it is necessary to recognize the differences between aeroacoustics and aerodynamics and the limitations of computer capability and develop numerical techniques to be used as a noise design tool.

PARTICIPANTS

Krishnan Ahuja
GTRI/AERO
Georgia Institute of Technology
Atlanta, GA 30332-0800
U.S.A.
(404) 528-7054
krishan.ahuja@gtri.gatech.edu

Vineet Ahuja
Department of Aerospace Engineering
The Pennsylvania State University
233 Hammond Building
University Park, PA 16802
U.S.A.
(814) 865-0396

Natalia Alexandrov
Mail Stop 159
NASA Langley Research Center
Hampton, VA 23681-0001
U.S.A.
(804) 864-7059
natalia@tab00.larc.nasa.gov

Marc Amerigo
Department of Aerospace Engineering
University of Maryland
College Park, MD 20742
U.S.A.
(301) 405-1107

Eyal Arian
ICASE
Mail Stop 132C
NASA Langley Research Center
Hampton, VA 23681-0001
U.S.A.
(804) 864-8010
arian@icase.edu

Harold Atkins
Mail Stop 128
NASA Langley Research Center
Hampton, VA 23681-0001
U.S.A.
(804) 864-2308
h.l.atkins@larc.nasa.gov

James Baeder
Department of Aerospace Engineering
University of Maryland
College Park, MD 20742
U.S.A.
(301) 405-1107
baeder@eng.umd.edu

Ashok Bangalore
School of Aerospace Engineering
Georgia Institute of Technology
Atlanta, GA 30332
U.S.A.
(404) 894-3014
gt5455a@prism.gatech.edu

Thomas J. Barber
United Technologies Research Center
Mail Stop 20
Silver Lane
East Hartford, CT 06108
U.S.A.
(203) 727-7619
bar@utrc.utc.com

Richard Barnwell
Mail Stop 128
NASA Langley IResearch Center
Hampton, VA 23681-0001
U.S.A.
(804) 864-4129
r.w.barnwell@larc.nasa.gov

Oktay Baysal
Department of Aerospace Engineering
Old Dominion University
KDH-241
Norfolk, VA 23529-0247
U.S.A.
(804) 683-3729
baysal@aero.odu.edu

Thonse Bhat
Old Dominion University
Mail Stop 219
NASA Langley Research Center
Hampton, VA 23681-0001
U.S.A.
(804) 864-6706
t.r.s.bhat@larc.nasa.gov

Kenneth S. Brentner
Mail Stop 128
NASA Langley Research Center
Hampton, VA 23681-0001
U.S.A.
(804) 864-3630
k.n.brentner@larc.nasa.gov

Trong Bui
Mail Stop 5-11
NASA Lewis Research Center
21000 Brookpark Road
Cleveland, OH 44135
U.S.A.
(216) 433-5639
bui@lerc.nasa.gov

Alan Cain
McDonnell Douglas Corporation
Mail Code 106-4126
P. O. Box 516
St. Louis, MO 63166
U.S.A.
(314) 233-2526

Michael Card
Mail Stop 110
NASA Langley Research Center
Hampton, VA 23681-0001
U.S.A.
(804) 864-8987
m.f.card@larc.nasa.gov

Mark Carpenter
Mail Stop 128
NASA Langley Research Center
Hampton, VA 23681-0001
U.S.A.
(804) 864-2318
carpentr@tab00.larc.nasa.gov

John E. Caruthers
The University of Tennessee Space Institute
Tullahoma, TN 37388
U.S.A.
(615) 393-7468

Jay Casper
Vigyan, Inc.
30 Research Drive
Hampton, VA 23666
U.S.A.
(804) 864-2238
casper@cmb17.larc.nasa.gov

Meelan Choudhari
High Technology Corporation
Mail Stop 156
NASA Langley Research Center
Hampton, VA 23681-0001
U.S.A.
(804) 864-2240
meelan@cmb00.larc.nasa.gov

Cathy Chung
Department of Aerospace Engineering
The Pennsylvania State University
233P Hammond Building
University Park, PA 16802
U.S.A.
(814) 863-0157

Thomas Chyczewski
The Pennsylvania State University
233P Hammond Building
University Park, PA 16802
U.S.A.
(814) 865-0396
tsc@penser.psu.edu

Leo Dadone
Boeing Helicopters
P. O. Box 16858
Mail Stop P32-74
Philadelphia, PA 19142-0858
U.S.A.
(610) 591-7367
dadonel.pgate.he.boeing.com

Kristian Dahl
Department of Mathematics
Christopher Newport University
50 Shoe Lane
Newport News, VA 23606
U.S.A.
(804) 594-7647
kdahl@pcs.cnu.edu

Sanford Davis
Mail Stop 260-1
NASA Ames Research Center
Moffett Field, CA 94035-1000
U.S.A.
(415) 804-4197
davis@fml.arc.nasa.gov

Ayodeji Demuren
Department of Mechanical Engineering and Mechanics
Old Dominion University
Norfolk, VA 23529-0247
U.S.A.
(804) 683-6363
demuren@icase.edu

Thomas Z. Dong
Mail Stop 5-9
NASA Lewis Research Center
21000 Brookpark Road
Cleveland, OH 44135
U.S.A.
(216) 433-6680
fsdong@elaina.lerc.nasa.gov

Nabil El-Hady
Advanced Technology
P. O. Box 1007
Yorktown, VA 23693-1007
U.S.A.
(804) 867-9573
75114.1257@compuserve.com

Charles C. Fenno
Mail Stop 463
NASA Langley Research Center
Hampton, VA 23681-0001
U.S.A.
(804) 864-3579
fenno@acod73.larc.nasa.gov

K.-Y. Fung
Department of Mechanical Engineering
University of Miami
Coral Gables, FL 33124
U.S.A.
(305) 284-3287
kyfung@coeds.eng.miami.edu

James Geer
Watson School of Engineering
State University of New York
Binghamton, NY 13902
U.S.A.
(607) 777-2897
jgeer@bingsuns.cc.binghamton.edu

John Goodrich
Mail Stop 5-11
NASA Lewis Research Center
Cleveland, OH 44135
U.S.A.
(216) 433-5922
fsgdrch@jgoodrich.lerc.nasa.gov

Kenneth Hall
Department of Mechanical Engineering and Materials Science
Duke University
Box 90300-0300
Durham, NC 27708-0300
U.S.A.
(919) 660-5328
hall@euler.egr.duke.edu

Jay Hardin
Mail Stop 461
NASA Langley Research Center
Hampton, VA 23681-0001
U.S.A.
(804) 864-3622
hardin@tab00.larc.nasa.gov

Nathan Hariharan
School of Aerospace Engineering
Georgia Institute of Technology
Atlanta, GA 30332
U.S.A.
(404) 853-0489
gt0430d@prism.gatech.edu

S. I. Hariharan
Department of Mathematical Sciences
University of Akron
Akron, OH 44325
U.S.A.
(216) 972-6994
hari@math.uakron.edu

M. Ehtesham Hayder
ICOMP
Ohio Aerospace Institute
22800 Cedar Point Road
Brook Park, OH 44142
U.S.A.
(216) 962-3146
fshyder@icomp01.lerc.nasa.gov

Duane Hixon
Ohio Aerospace Institute
Mail Stop 5-11
NASA Lewis Research Center
Cleveland, OH 44135
U.S.A.
(216) 433-6681
fshixon@muskie.lerc.nasa.gov

Fang Hu
Department of Mathematics
Old Dominion University
Norfolk, VA 23529
U.S.A.
(804) 683-3325
fhu@icase.edu

Dale Hudson
Department of Aerospace Engineering
The Pennsylvania State University
233 Hammond Building
University Park, PA 16802
U.S.A.
(804) 865-0396
dah@penser.psu.edu

M. Y. Hussaini
ICASE
Mail Stop 132C
NASA Langley Research Center
Hampton, VA 23681-0001
U.S.A.
(804) 864-2174
myh@icase.edu

H.T. Huynh
Mail Stop 5-11
NASA Lewis Research Center
Cleveland, OH 44135
U.S.A.
(216) 433-5852
tshung@freya.lerc.nasa.gov

Lee Jamieson
ICASE
Mail Stop 132C
NASA Langley Research Center
Hampton, VA 23681-0001
U.S.A.
(804) 864-2174

Ronald Joslin
Mail Stop 170
NASA Langley Research Center
Hampton, VA 23681-0001
U.S.A.
(804) 864-2234
r.d.joslin@larc.nasa.gov

Wen-Huei Jou
Boeing Commercial Airplane Group
M/S 7C-36
P. O. Box 3707
Seattle, WA 98124-2207
U.S.A.
(206) 865-6102

David Keyes
ICASE
Mail Stop 132C
NASA Langley Research Center
Hampton, VA 23681-0001
U.S.A.
(804) 864-6873
keyes@icase.edu

Harsh Khanna
Department of Aerospace Engineering
University of Maryland
College Park, MD 20742
U.S.A.
(301) 405-1107

David Kopriva
Department of Mathematics
The Florida State University
SCRI B-186
Tallahassee, FL 32306
U.S.A.
(904) 644-7037
dak@scri.fsu.edu

Philippe Lafon
Department Acoustique et Mecanique Vibratoire
Direction des Etudes et Recherches
Electricite de France
1, avenue du General de Gaulle
Clamart Cedex, 92141
FRANCE
011 33 147653708
philippe.lafon@der.edf.fr

Patrick Le Tallec
INRIA
BP 105
Le Chesnay, 78153
FRANCE
011 33 139 635483
letallec@menusin.inria.fr

David Lockhard
Department of Aerospace Engineering
The Pennsylvania State University
233P Hammond Building
University Park, PA 16802
U.S.A.
(814) 865-9611
david@penser.psu.edu

Lyle N. Long
Department of Aerospace Engineering
The Pennsylvania State University
233P Hammond Building
University Park, PA 16802
U.S.A.
(814) 865-1172
lnl@psu.edu

Anastasios Lyrintzis
School of Aeronautics & Astronautics
Purdue University
1282 Grissom Hall
West Lafayette, IN 47907-1282
U.S.A.
(317) 494-5142
lyrintzi@ecn.purdue.edu

Michele Macaraeg
Mail Stop 156
NASA Langley Research Center
Hampton, VA 23681-0001
U.S.A.
(804) 864-3630
macaraeg@tab00.larc.nasa.gov

Lucio Maestrello
Mail Stop 463
NASA Langley Research Center
Hampton, VA 23681-0001
U.S.A.
(804) 864-1067
l.maestrello.larc.nasa.gov

Roberto Marsilio
ICASE
Mail Stop 132C
NASA Langley Research Center
Hampton, VA 23681-0001
U.S.A.
(804) 864-4746
marsilio@icase.edu

James E. Martin
Department of Mathematics
Christopher Newport University
50 Shoe Lane
Newport News, VA 23606
U.S.A.
(804) 594-7945
jamie@pcs.cnu.edu

Megan McCluer
Department of Aerospace Engineering
University of Maryland
College Park, MD 20742
U.S.A.
(301) 405-1107

Kristine Meadows
Mail Stop 128
NASA Langley Research Center
Hampton, VA 23681-0001
U.S.A.
(804) 864-3624
k.r.meadows@larc.nasa.gov

Philip J. Morris
Department of Aerospace Engineering
The Pennsylvania State University
233P Hammond Building
University Park, PA 16802
U.S.A.
(814) 863-0157
pjm@cac.psu.edu

Douglas Nark
George Washington University
Mail Stop 461
NASA Langley Research Center
Hampton, VA 23681-0001
U.S.A.
(804) 864-3623
nark@acodux.larc.nasa.gov

Yusuf Ozyoruk
Department of Aerospace Engineering
The Pennsylvania State University
233P Hammond Building
University Park, PA 16802
U.S.A.
(814) 865-0396
yusuf@penser.psu.edu

Vasudev Parameswaran
Department of Aerospace Engineering
University of Maryland
College Park, MD 20742
U.S.A.
(301) 405-1107

D. Stuart Pope
Lockheed Engineering & Sciences Company
144 Research Drive
Hampton, VA 23666
U.S.A.
(804) 766-9717
pope@vortex.larc.nasa.gov

Freda Porter-Locklear
Department of Mathematics and Computer Science
Pembroke State University
P. O. Box 1359
Pembroke, NC 28372
U.S.A.
(910) 521-6412
fpl@pembvax1.pembroke.edu

G. K. Raviprakash
University of Tennessee Space Institute
Tullahoma, TN 37388
U.S.A.
(615) 393-7505

Narayana N. Reddy
Lockheed Aeronautical Systems Company
Acoustics, Department 73-47
Zone 0685
Marietta, GA 30063-0685
U.S.A.
(404) 494-2944
reddy@fspc9.lasc.lockheed.com

Ray Ristorcelli
ICASE
Mail Stop 132C
NASA Langley Research Center
Hampton, VA 23681-0001
U.S.A.
(804) 864-2197
jrrjr@icase.edu

Philip Roe
Department of Aerospace Engineering
University of Michigan
Ann Arbor, MI 48109-2140
U.S.A.
(313) 764-3394
philroe@caen.engin.umich.edu

Lakshmi N. Sankar
School of Aerospace Engineering
Georgia Institute of Technology
Atlanta, GA 30332
U.S.A.
(404) 894-3014

James R. Scott
Department of Aeronautical and Astronautical Engineering
Ohio State University
2036 Neil Avenue Mall
Columbus, OH 43210
U.S.A.
(614) 292-3828
jscott@mps.ohio-state.edu

Asher Shamam
Department of Mathematics
University of California, Los Angeles
Los Angeles, CA 91405
U.S.A.
(818) 909-0309
ashamam.edu.ucla.math

Rajneesh Singh
Department of Aerospace Engineering
University of Maryland
College Park, MD 20742
U.S.A.
(301) 405-1107

Patricia Slechta-Shah
Boston University
College of Engineering
110 Cummington Street
Boston, MA 02215
U.S.A.
(617) 734-0389
plshah@acs.bu.edu

Scot Slimon
General Dynamics
75 Eastern Point Road
Groton, CT 06340
U.S.A.
(203) 433-5785

Marilyn Smith
Georgia Tech Research Institute
CCRF - Aero Bldg. 2
Atlanta, GA 30332
U.S.A.
(404) 528-7804
msmith@aerob.gatech.edu

Victor W. Sparrow
Graduate Program in Acoustics
The Pennsylvania State University
157 Hammond Building
University Park, PA 16802
U.S.A.
(814) 865-3162
sparrow@helmholtz.psu.edu

Craig Streett
Mail Stop 170
NASA Langley Research Center
Hampton, VA 23681-0001
U.S.A.
(804) 864-2230
c.l.streett@larc.nasa.gov

Christopher Tam
Department of Mathematics
The Florida State University
Tallahassee, FL 32306-3027
U.S.A.
(904) 644-2455
tam@math.fsu.edu

Lei Tang
Department of Aerospace Engineering
University of Maryland
College Park, MD 20742
U.S.A.
(301) 405-1107

James Thomas
Mail Stop 128
NASA Langley Research Center
Hampton, VA 23681-0001
U.S.A.
(804) 864-2163
j.l.thomas@larc.nasa.gov

V. Venkatakrishnan
ICASE
Mail Stop 132C
NASA Langley Research Center
Hampton, VA 23681-0001
U.S.A.
(804) 864-2183
venkat@icase.edu

K. Viswanathan
Lockheed Aeronautical Systems Company
Acoustics Department 73-47
Zone 0685
Marietta, GA 30063-0685
U.S.A.
(404) 494-8583
vishy@grumpy.lasc.lockheed.com

Willie Watson
Mail Stop 460
NASA Langley Research Center
Hampton, VA 23681-0001
U.S.A.
(804) 864-5290
w.r.watson@larc.nasa.gov

Ye Zhou
ICASE
Mail Stop 132C
NASA Langley Research Center
Hampton, VA 23681-0001
U.S.A.
(804) 864-2281
zhou@icase.edu

REPORT DOCUMENTATION PAGE

Form Approved
OMB No. 0704-0188

1. AGENCY USE ONLY *(Leave blank)*	2. REPORT DATE	3. REPORT TYPE AND DATES COVERED
	May 1995	Conference Publication

4. TITLE AND SUBTITLE
ICASE/LaRC Workshop on Benchmark Problems in Computational Aeroacoustics (CAA)

5. FUNDING NUMBERS
505-90-52-01

6. AUTHOR(S)
J. C. Hardin, J. R. Ristorcelli, and C. K. W. Tam, Editors

7. PERFORMING ORGANZATION NAME(S) AND ADDRESS(ES)
NASA Langley Research Center
Hampton, VA 23681-0001 and
Institute for Computer Applications in Science and Engineering
NASA Langley Research Center
Hampton, VA 23681-0001

8. PERFORMING ORGANIZATION REPORT NUMBER
L-17497

9. SPONSORIING/MONITORING AGENCY NAME(S) AND ADDRESS(ES)
National Aeronautics and Space Administration
Washington, DC 20546-0001

10. SPONSORING/MONITORING AGENCY REPORT NUMBER
NASA CP-3300

11. SUPPLEMENTARY NOTES

12a. DISTRIBUTION/AVAILABILITY STATEMENT
Unclassified–Unlimited
Subject Category 71
Availability: NASA CASI (301) 621-0390

12b. DISTRIBUTION CODE

13. ABSTRACT *(Maximum 200 words)*

The proceedings of the Benchmark Problems in Computational Aeroacoustics Workshop held at NASA Langley Research Center are the subject of this report. The purpose of the Workshop was to assess the utility of a number of numerical schemes in the context of the unusual requirements of aeroacoustical calculations. The schemes were assessed from the viewpoint of dispersion and dissipation - issues important to long time integration and long distance propagation in aeroacoustics. Also investigated were the effect of implementation of different boundary conditions.

The Workshop included a forum in which practical engineering problems related to computational aeroacoustics were discussed. This discussion took the form of a dialogue between an industrial panel and the workshop participants and was an effort to suggest the direction of evolution of this field in the context of current engineering needs.

14. SUBJECT TERMS
Aeroacoustics; Numerical methods; Wave propogation; Sound; Acoustic boundary conditions

15. NUMBER OF PAGES
408

16. PRICE CODE
A18

17. SECURITY CLASSIFICATION OF REPORT	18. SECURITY CLASSIFICATION OF THIS PAGE	19. SECURITY CLASSIFICATION OF ABSTRACT	20. LIMITATION OF ABSTRACT
Unclassified	Unclassified	Unclassified	Unclassified